C O N T E N T

PREFACE

The 2nd Conference "Isotopic and Molecular Processes" held in Cluj-Napoca, Romania, on September 27-29, 2001, was organized by the National Institute of Isotopic and Molecular Technologies together with Babes-Bolyai University Cluj-Napoca. There were more than 100 participants, including 9 foreigners from 7 countries.

The scientific program of the conference included papers on original research and covered the full range of isotopic and molecular processes and their application in physics, chemistry, chemical physics and biophysics. Except lectures by invited speakers, there were oral communications and poster sessions. The plenary lectures were held in the morning, followed by oral communications presented in two parallel sessions. The papers scheduled as posters were presented in the afternoon at the poster session arranged in the Hall of the "Raluca Ripan" Chemistry Institute, Cluj-Napoca. All the received materials are published in this volume, which, unfortunately, does not contain any trace of our fruitful discussion upon the presented works. This opportunity of personal exchange of ideas is, in our opinion, the most stimulating and indispensable part of any successful meeting.

At the opening ceremony the Governor of Cluj County, Prof. Dr. Ing. Vasile Soporan welcomed the participants. The conference was then opened by the Director of the National Institute of Isotopic and Molecular Technologies, Dr. Mircea Bogdan, after which Acad. Marius Peculea addressed the conference.

During the conference a reception was held in the Glass Hall of the Institute and a Conference Dinner in the "Stadion" Hotel restaurant.

The research laboratories of the Institute were open to visitors during the conference.

On behalf of the Organizing Committee we wish to express to everyone who helped in the successful organization of the 2nd "Isotopic and Molecular Processes" conference, our most cordial thanks for their hard work, enthusiasm and co-operation. Finally, we wish to thank the chairmen, plenary lecturers and all the participants who made the Conference a stimulating scientific event.

Mircea Bogdan and Viorel Cosma
Chairman-Organizing Committee

ACKNOWLEDGEMENTS

The organizers are indebted to many organizations for effective help in the preparation of the Conference.

The financial support given by the Ministry of Education and Research was greatly appreciated. The substantial help received from the Cluj County Council is gratefully acknowledged.

The Babes-Bolyai University Cluj-Napoca has provided its outstanding hotel accommodation facilities for the conference.

Special thanks are due to the following sponsors:

- Romanian Commercial Bank
- S.C. "Tehnofrig" S.A.
- "Romceh import - export" S.R.L. Focsani
- S.C. "Prodvinalco" S.A. Cluj-Napoca
- S.C. "Ursus" S.A. Cluj-Napoca
- S.C. "Napolact" S.A. Cluj-Napoca
- "Peisagistica" S.R.L. Cluj-Napoca
- "Edenland" S.R.L. Cluj-Napoca
- S.C. "Coca-Cola" S.A. Oradea
- S.C. "Farmec" S.A. Cluj-Napoca
- S.C. "Comcereal" S.A. Cluj-Napoca
- Statiunea de Cercetari Pomicole Cluj-Napoca
- RATUC S.A. Cluj-Napoca
- S.C. "Alcom" S.A.
- S.C. "Valcele" S.A.

STUDIA UNIVERSITATIS BABEŞ-BOLYAI, PHYSICA, SPECIAL ISSUE, 2001

INSTITUTUL NAȚIONAL DE CERCETARE - DEZVOLTARE PENTRU TEHNOLOGII IZOTOPICE ŞI MOLECULARE, CLUJ-NAPOCA - 50 DE ANI DE EXISTENȚĂ -

GHEORGHE VĂSARU

INCDTIM
E-mail: infovision@mail.dntcj.ro

Institutul Național de Cercetare - Dezvoltare pentru Tehnologii Izotopice şi Moleculare din Cluj-Napoca, principalul organizator al conferințelor "PIM", a împlinit, în anul 2000, 50 de ani. Jumătate de secol de existență reprezintă un bun motiv pentru a trece în revistă, fie şi fugitiv, etapele mai importante ale devenirii sale.

Institutul îşi are originile în anul 1950 când a luat ființă la Cluj, o secție a Institutului de Fizică de la Măgurele. În anul 1952 această Secție a trecut sub patronajul Filialei din Cluj a Academiei Române. În perioada de început a funcționării, au fost abordate tematici de cercetare cu un pronunțat caracter aplicativ, solicitate, în majoritatea cazurilor, de industrie. Un exemplu este realizarea unei tehnologii de obținere a acetilenei prin cracarea gazului metan în arc electric. Această tehnologie stă la baza unui procedeu industrial de obținere a acetilenei utilizate ca materie primă în sinteza cauciucului. Pentru creşterea randamentului reacției, metanul nedescompus, evacuat din reactor, s-a separat de celelalte gaze printr-un procedeu de difuzie, obținându-se astfel randamente de recuperare de 90 %. Pentru monitorizarea procesului de separare, au fost elaborate metode de analiză a amestecurilor de gaze, realizându-se şi aparatura analitică necesară.

În anul 1956, după înființarea Institutului de Fizică Atomică din Bucureşti-Măgurele, Secția din Cluj a fost trecută în cadrul acestui institut, cu un profil de cercetare axat pe fizica şi chimia izotopilor stabili, tematică în care se putea valorifica, la un nivel superior, experiența câştigată în domeniul separărilor. Activitatea de cercetare s-a desfăşurat abordând probleme legate de abundența naturală a izotopilor, separarea, analiza şi aplicațiile izotopilor stabili ai elementelor uşoare, fiind singura unitate de cercetare din țară cu acest obiect de activitate.

În paralel cu preocupările legate de izotopii stabili, în cadrul Secției și-a început activitatea și un laborator de radioactivitate, destinat aplicațiilor industriale ale radioizotopilor în Transilvania, precum și studiilor de abundență a radionuclizilor în mediul ambiant.

În anul 1970, Secția din Cluj a Institutului de Fizică Atomică a devenit „Institutul de Izotopi Stabili", unitate dependentă de Comitetul de Stat pentru Energia Nucleară (CSEN), iar în anul 1976 a fost denumit „Institutul de Tehnologii Izotopice și Moleculare".

În anul 1999, Institutul a fost acreditat ca **institut național de cercetare și dezvoltare** devenind actualul „Institut Național de Cercetare - Dezvoltare pentru Tehnologii Izotopice și Moleculare".

De-a lungul celor 50 de ani de existență, au fost abordate câteva domenii de cercetare, de importanță deosebită pentru dezvoltarea economică a României. În continuare sunt descrise câteva dintre acestea.

1. Fizico - chimia deuteriului

În comparație cu celelalte secții din cadrul Institutului de Fizică Atomică, tematica de cercetare a Secției din Cluj avea un caracter aparte. Acestei secții i s-a trasat sarcina să abordeze fizico-chimia separării deuteriului, respectiv a apei grele, materiale nucleare de importanță vitală pentru reactorii nucleari energetici, moderați si răciți cu apă grea, de tip CANDU.

Cercetările au început în condiții grele: pe de o parte, posibilitățile de informare erau foarte precare din cauza secretului foarte sever menținut asupra cercetărilor legate de separarea acestui izotop, pe de altă parte, dotarea Secției era sub nivelul cerut de atacarea unei cercetări de o asemenea anvergură. Este meritul conducerii de atunci a Secției din Cluj că, bazându-se probabil pe îndrăzneala și exuberanța unui colectiv tânăr, a știut să-i insufle acestuia încrederea în reușita cercetărilor.

În prima etapă s-a pornit la drum pe trei direcții:

- prospectarea surselor de deuteriu din țară;
- elaborarea de metode de analiză izotopică H/D;
- elaborarea de metode de separare a deuteriului.

Pe lângă utilizările din domeniul energeticii nucleare, au fost luate în considerare și alte aplicații. Astfel, studiind răspândirea deuteriului în natură, s-au explorat principalele râuri, sondele de metan și țițeiului din țară, punându-se baza unor cercetări de hidrologie și geologie izotopică. Datele culese în decursul anilor relativ la distribuția deuteriului în circuitul natural al apei au permis elucidarea unor aspecte legate de originea și evoluția diferitelor cursuri de ape sau a unor surse de apă minerală.

Prin măsurarea conținutului de deuteriu a zăcămintelor de hidrocarburi, s-a constatat existența unor „curbe de nivel" izotopic (izoconcentrate), la zăcămintele dintr-o anumită zonă. Cu ajutorul acestor „curbe de nivel" s-a putut determina care

este punctul de maximă concentrare de hidrocarburi din regiune. De asemenea, s-a putut determina direcția şi viteza de deplasare a masei de hidrocarburi, deplasare cauzată de procesul de exploatare (care introduce dezechilibre barice) şi de injecția de apă. Acest gen de cercetări a deschis un câmp larg de aplicații în industria extractivă de țiței şi gaze.

Pentru a duce la bun sfârşit cercetările legate de determinarea abundenței naturale a deuteriului în sursele din țară, precum şi pentru controlul oricărui proces de separare, trebuia rezolvată problema analizei izotopice H/D. Cercetările inițiale legate de analiza deuteriului s-au axat pe metode nespectrometrice, deoarece achiziționarea unui spectrometru de masă din import era imposibilă la data aceea. Astfel au fost puse la punct:

- **metode densimetrice** pentru analiza izotopică totală a apei (D/H şi $^{18}0/^{l6}0$) utilizând o variantă a metodei picăturilor, capabilă să determine diferențe de densitate în domeniul abundentelor naturale, la performanțe superioare celor obținute pe plan mondial la acea dată;

- **metode optice**, construindu-se un spectrometru Fabry-Perot cu baleiaj magnetostrictiv şi prin variație de presiune, care a dat rezultate comparabile cu alte metode;

- **cromatografîa în fază gazoasă**, folosită pentru analiza conținutului de deuteriu, atât din amestecuri de hidrogen cât şi din hidrocarburi şi substanțe marcate cu deuteriu. Cercetările, începute în anul 1958, s-au soldat cu proiectarea şi construcția a numeroase tipuri de gaz-cromatografe, precum şi a accesoriilor necesare acestei tehnici analitice (coloane de separare, umpluturi, detectori, etc). Ulterior, cercetările în domeniul cromatografiei în fază gazoasă - pentru dezvoltarea de metode analitice şi pentru proiectarea şi realizarea de aparatură - au constituit o direcție cu mare pondere în activitatea institutului. A fost luată în considerare realizarea de cromatografe de gaze pentru industria chimică şi petrochimică, industria farmaceutică, pentru laboratoarele de chimie, biologie, etc.

În paralel cu cercetările legate de determinarea cu precizie a abundenței naturale a deuteriului şi de analizele izotopice H/D, a fost demarat şi un program amplu în vederea **separării** acestui izotop. Pe plan mondial, pentru noua generație de uzine de apă grea care se construiau în perioada anilor 1955 - 1960, ca metode competitive pentru îmbogățirea primară a deuteriului s-au impus metodele bazate pe **reacțiile de schimb izotopic**. Procedeul de separare ales era însă diferit de la țară la țară. Ținându-se seama de posibilitățile țării noastre, s-a optat pentru metoda schimbului izotopic dintre apă şi hidrogen, catalizat eterogen, în fază de vapori şi catalizat omogen în fază lichidă. S-a elaborat un proces elementar de separare care combină un schimb izotopic între hidrogen si vapori de apă pe un strat catalitic poros, cu o evaporare-condensare de pe suprafața unui film de apă. Procesul a fost studiat atât în etapele lui intermediare cât şi ca proces global. Reacția catalitică în fază gazoasă s-a studiat cu ajutorul catalizatorilor de nichel pe suporți oxidici, determinându-se procesele de la interfețe. S-a constatat că nichelul este elementul

catalitic activ, suportul având doar rolul de a mări suprafața metalului. Catalizatorii utilizați în proces au fost la rândul lor studiați şi preparați în laboratoarele institutului. Aceste cercetări s-au dezvoltat în timp, în institut formându-se un puternic colectiv în domeniul catalizatorilor metalici suportați.

Procedeul de separare a fost experimentat pe un pilot de laborator, compus dintr-o coloană de separare cuplată cu un electrolizor ca şi convertor de fază. Deşi pilotul nu s-a dovedit competitiv pentru o îmbogățire primară în deuteriu, totuşi experimentarea lui a constituit o şcoală pentru atacarea problemei separării apei grele la nivel de pilot industrial. Experiența acumulată a permis colectivului să-şi aducă o contribuție importantă la proiectarea pilotului de apă grea de la Uzina G, din Râmnicu-Vâlcea.

Un alt grup de cercetări legat de sistemul H-D a vizat procesul de stocare a izotopilor hidrogenului în rețeaua cristalină a unui metal sau a unor aliaje, prin formarea de hidruri metalice. S-au dezvoltat cercetări legate de utilizarea hidrogenului ca sursă de energie. S-a studiat procesul de electroliză cu randament mărit, ca posibil generator de hidrogen şi stocarea acestuia sub forma de hidrură în metale şi aliaje adecvate în vederea arderii lui catalitice.

2. Separări de izotopi ai elementelor uşoare

Preocupările privind separarea izotopilor s-au amplificat, trecându-se de la cercetările legate strict de separarea deuteriului la separarea altor elemente uşoare. Astfel au fost efectuate studii teoretice privind procesele de separare, au fost elaborate tehnologii de separare şi s-au redactat şi publicat peste 20 de monografii şi bibliografii în acest domeniu, atât în țară cât şi în străinătate.

Deşi prezintă unele inconveniente (cantități mici de produs şi consum relativ ridicat de energie, **termodifuzia** a fost una dintre primele metode de separare adoptată în institut. Pentru aceasta metodă s-au efectuat studii legate de calculul factorilor de separare şi de stabilire a timpului de echilibrare pentru diferite amestecuri izotopice gazoase (H/D, $^{12}C/^{13}C$, $^{14}N/^{15}N$, $^{16}O/^{18}O$). S-au construit şi experimentat coloane de termodifuzie de diferite tipuri, ale căror performanțe de separare au fost stabilite atât în condiții de operare izolate cât şi legate, în regim de cascadă.

Primul izotop stabil separat în perioada 1967 - 1968 prin această metodă a fost izotopul greu al azotului, ^{15}N, folosind ca materie primă azotul de înaltă puritate chimică şi concentrație izotopică naturală. În acest scop s-a proiectat şi construit o cascadă compusă din 4 coloane, cu o lungime totală de 10 m.

Ulterior s-a realizat o îmbogățire a izotopului greu al carbonului, ^{13}C, până la 20%, folosind ca materie primă metanul natural (1,1% ^{13}C). Pentru aceasta s-a folosit o cascadă compusă din 19 coloane.

Termodifuzia este şi în momentul de față una din cele mai bune metode pentru separarea izotopilor gazelor nobile. Tot prin această metodă s-au separat izotopii neonului (^{20}Ne, ^{22}Ne) cu ajutorul unei cascade compusă din 8 coloane, obținându-se o îmbogățire de 99 % pentru ambii izotopi.

Pentru separarea izotopilor ^{36}Ar, ^{79}Kr şi ^{86}Kr s-a utilizat o cascadă cu 36 coloane, obținându-se o îmbogățire la 99 % a ^{36}Ar şi la 90 % a ^{86}Kr, materia primă fiind argonul respectiv kriptonul de înaltă puritate.

Dezvoltarea aplicațiilor bazate pe utilizarea substanțelor marcate cu izotopul ^{15}N în agricultura şi biologie au determinat o cerere tot mai mare de astfel de substanțe, atât pe piața internă cât şi pe plan mondial. Această cerere a determinat abordarea investigațiilor legate de separarea acestui izotop prin metoda schimbului izotopic dintre acidul azotic şi oxizii de azot (metoda Spindel-Taylor). A fost realizat un pilot în institut, compus din două etaje de separare care asigură o îmbogățire a ^{15}N de peste 99,8 %.

Prin schimbul izotopic dintre oxizii de azot în fază gazoasă şi soluția de acid azotic în fază lichidă s-a realizat şi separarea izotopului ^{18}O. Instalația respectivă a fost cuplată pe instalația productivă de ^{15}N, utilizând astfel, ca materie primă, acidul azotic furnizat de aceasta.

În institut s-a elaborat şi o metodă de separare a ^{10}B, necesar unor cercetări nucleare. Metoda se bazează pe schimbul izotopic dintre trifluorura de bor şi un complex organic al acesteia. S-au obținut concentrații de 80 % ^{10}B.

Un alt sistem studiat a fost ^{6}Li - ^{7}Li, punându-se la punct o tehnologie de separare şi optimizarea procesului.

Cercetările în direcția separării izotopilor au impus, pe lângă realizarea instalațiilor de separe şi studiul, proiectarea şi construirea unei serii de instalații şi utilaje anexe, standuri de pregătire a materiilor prime, de preparare a compuşilor marcați, pompe de vehiculare a fluidelor capabile să opereze în condiții speciale, debitmetre, aparatură de control.

În anul 1980 s-a abordat o nouă tematică, legată de separarea izotopilor prin excitare selectivă cu radiație laser. Această cercetare a concentrat o însemnată forță umană şi mijloace materiale, atât în institut cât şi în cadrul a numeroase colaborări cu unități specializate din țară. În cadrul acestui program s-a construit o instalație laser cu CO_2 în impulsuri, cu excitare transversală, la presiunea atmosferică, cu care s-a pus în evidență efectul izotopic de separare pentru izotopii sulfului şi carbonului. Pentru elucidarea procesului elementar de separare, laserul cu CO_2 a fost încorporat într-o instalație complexă. Ca domenii conexe cercetărilor legate de separarea izotopilor prin tehnici laser, a apărut necesitatea elaborării unei serii de detectori piroelectrici pentru domeniul IR, care se utilizează ca energimetre. Pentru asigurarea ferestrelor necesare celulelor de analiză şi a celorlalte componente optice în IR s-au construit instalații de creştere de cristale transparente în acest domeniu spectral, elaborându-se şi tehnologiile de prelucrare a lor.

În perioada 1987 – 1995 a fost elaborată o bază de date privind metoda de separare izotopică a uraniului prin tehnică laser, varianta atomică (AVLIS - U), materializată în 20 de rapoarte interne.

3. Construcția de aparatură și dezvoltarea de metode de analize izotopice și structurale, studii de fizica ionilor

Separarea izotopilor stabili, sinteza compușilor marcați cu acești izotopi și dezvoltarea metodelor bazate pe concentrația izotopilor stabili presupun metode de analiză de mare acuratețe. Abordarea acestui domeniu a dus la extrapolarea cercetărilor de la elaborarea de metode de analiză izotopică, la investigarea unor structuri moleculare complexe, studiul fragmentării moleculelor și a ionilor, reacții ion -moleculă, studiul ionilor metastabili și al efectelor izotopice ce pot interveni în aceste procese. A fost demarat un program de construcție de aparatură menit să compenseze dificultățile existente la vremea aceea în achiziționarea de echipament analitic din import. Efortul de cercetare a fost canalizat pe două direcții principale: realizarea de aparatură de cromatografie în fază gazoasă și realizarea de spectrometre de masă.

Pe parcurs s-au realizat diverse tipuri de gaz-cromatografe, începând cu cele destinate analizelor de deuteriu și a altor amestecuri gazoase, până la aparate complexe capabile să efectueze analize solicitate de industria chimică și petrochimică, industria alimentară, industria farmaceutică, etc. Dintre aparatele complexe realizate menționăm cromatografele M9, M9A și apoi GCL-90, instrumente îndeplinind toate funcțiunile unor aparate moderne, existând și posibilitatea interfațării lor cu echipament de calcul. Institutul a devenit un furnizor de gaz-cromatografe pentru analize chimice, acoperind, în acest domeniu, atât necesitățile din institut cât și solicitări din economie. De asemenea evidențiem realizarea pentru Centrala Nuclearo-Electrică de la Cernavodă a unui aparat complex pentru analiza gazelor din atmosfera reactorului.

Demararea cercetărilor în domeniul construcției de aparatură spectrometrică de masă se datorează, de asemenea, nevoii de a dispune de instrumente de analiză izotopică pentru controlul instalațiilor de separare.

Încă din anul 1956 în institut s-a format un colectiv de cercetare în domenii de vârf ca: optica ionică, tehnica vidului, detecția și prelucrarea semnalelor, proiectarea și realizarea de unități electronice de mare stabilitate și fiabilitate. Pornind la început cu o echipă de câțiva oameni preocupați de exploatarea rațională a unui spectrometru de masă de tip Dempster, de joasă rezoluție, institutul și-a clădit treptat, în această direcție, un grup puternic de cercetare de construcție și de exploatare. Au fost studiate numeroase geometrii de analizoare de masă cu simplă și dublă focalizare, statice și dinamice. Institutul a fost și a rămas singurul constructor de spectrometre de masă din țară, servind o gamă largă de cercetări, atât în domeniul nuclear cât și în cel al chimiei. Menționăm, în ordine cronologică, câteva tipuri mai importante de spectrometre de masă proiectate și realizate în institut:

- spectrometrul de masă automat, pentru măsurători de concentrații de deuteriu în domeniul concentrațiilor naturale, în regim dinamic. Spectrometrul are o sursă de ioni cu impact electronic şi sistem de introducere a probei cu două derivații, permițând obținerea unei precizii de măsurare de 1,4 % pentru deuteriu, în domeniul concentrațiilor naturale;

- spectrometrul de masă tandem cu cameră de ciocnire, destinat studiului reacțiilor ion - moleculă. Aparatul constă dintr-un spectrometru primar, monocromator, cu sistem de retardare a ionilor primari, o cameră de ciocnire şi un al doilea spectrometru care analizează produsele de reacție.

- spectrometrul de masă cu simplă focalizare pentru analize izotopice şi chimice în probe gazoase şi lichide. Este un aparat de concepție modulară realizat şi în varianta cu cuplaj de gaz-cromatograf. Domeniul de masă este de 2 - 400 uam. Limita de detecție este de 10 ppm, iar precizia de măsurare de 0,5 %.

- spectrometru de masă cu dublă focalizare, a fost o realizare deosebită a institutului. Aparatul poate opera în cuplaj cu gaz-cromatograf. Rezoluția măsurată la 50 % din înălțimea picului atinge valoarea 10.000. Lucrează în domeniul de mase 1 -1000 uam cu o reproductibilitate de 1 %. Pentru realizarea acestui aparat s-au efectuat studii conexe de optică ionică a filtrului Wien, cu câmpuri magnetice neomogene, precum şi studii teoretice şi experimentale asupra aberațiilor de imagine;

- spectrometrul de masă pentru analiza deuteriului, realizat pentru echiparea Combinatului Chimic de la Drobeta-Turnu Severin (Uzina de apă grea, ROMAG). Aparatul este destinat măsurării abundenței izotopice a hidrogenului atât în probe gazoase cât şi lichide.

- prin participarea institutului la programul de cercetări spațiale "Intercosmos" s-a realizat un tip de spectrometru de masă cuadrupolar, destinat analizei compoziției straturilor superioare ale atmosferei. Aparatul a fost lansat în cosmos şi a cules date în domeniul de mase 1-50 uam. Analizorul acestui aparat a fost perfecționat şi folosit pentru realizarea unor spectrometre de masă de laborator.

- spectrometrul de masă - detector de neetanşeități, cu heliu. Este destinat detectării şi localizării neetanşeității unor sisteme vidate, putându-se evalua şi mărimea fluxului de scurgere;

- detector de neetanşeități portabil. Este un aparat destinat detectării şi localizării neetanşeităților pentru instalații presurizate cu orice gaz, exceptând aerul.

- spectrometrul de masă cu ionizare termică. Este destinat analizei izotopice a elementelor chimice care nu au compuşi volatili sau la care compuşii volatili sunt instabili ori greu de manipulat (Li, K, Cs, Ru, Sr, U, Pb, etc) Domeniul de masă pentru care se poate folosi este cuprins între 5 şi 500 uam. Se pot efectua analize izotopice prin ionizare termică începând cu izotopii litiului şi terminând cu cei ai uraniului.

Aparatul este conceput pentru urmărirea unor procese de separare izotopică, pentru măsurători de interes în geologia izotopică (datări, etc), precum şi pentru controlul gestiunii combustibilului nuclear.

Tipurile de spectrometre de masă realizate în Institut, cu unele modificări, se pot adapta şi pentru alte domenii de cercetare decât acelea pentru care au fost concepute. Un exemplu în acest sens îl constituie spectrometrul de masă cuadrupolar, care a fost adaptat pentru analiza gazelor respiratorii, urmarindu-se procesul de desorbție al azotului din țesuturi pe parcursul aducerii scafandrilor la suprafață.

4. Aplicații ale izotopilor stabili

Utilizarea izotopilor stabili pentru rezolvarea unor probleme specifice în diferite domenii de cercetare este larg răspândită şi de o importanță deosebită. Preocuparea Institutului în acest domeniu a fost aceea de a introduce şi lărgi aria acestor aplicații.

O utilizare eficientă şi-au găsit-o izotopii stabili mai ales în domeniul ştiințelor agricole şi biologice. Încă din anul 1964 Institutul a fost solicitat să efectueze analize izotopice, precedate de prelucrarea chimică a probelor marcate cu ^{15}N provenite din experimentările efectuate în cadrul Programului de cercetare coordonat de FAO-AIEA privind utilizarea izotopilor la urmărirea eficienței îngrăşămintelor. Acest program de cercetare continuă pe plan internațional de peste 20 de ani.

Pentru a-i face față, în institut s-a pus la punct o tehnică de prelucrare chimică a probelor, precum şi o metodologie de analiză izotopică (prin spectrometria optică şi spectrometria de masă). Au fost sintetizați compuşi marcați cu ^{15}N, obținut în instalația proprie de separare. În acest scop s-a construit o instalație de conversie a acidului azotic în amoniac marcat, o instalație de obținere a sărurilor de amoniu (sulfat, azotat, clorură), a ureei, ureoformului marcat, etc.

Cercetările privind aplicațiile ^{15}N în domeniul agriculturii au fost efectuate in colaborare cu diferite institute de cercetări agronomice din țară. Scopul acestora a fost acela de a stabili randamentul de utilizare al îngrăşămintelor azotoase la diferite culturi.

Institutul a menținut relații de colaborare cu Institutul Medico-Farmaceutic din Cluj, legate de utilizarea aminoacizilor marcați cu ^{15}N în procese biomedicale. In acest scop, în institut, s-au preparat aminoacizi marcați cu acest izotop şi s-a efectuat analiza izotopică a probelor biologice.

In momentul de față se menține o preocupare permanentă legată de lărgirea sortimentului de compuşi marcați cu izotopi stabili. Astfel, s-au preparat solvenți organici cu deuteriu pentru utilizarea lor în RMN. De asemenea, au fost preparați, la cerere, compuşi marcați cu ^{15}N, ^{6}Li, ^{7}Li, ^{10}B şi s-au oferit, pentru cercetări, izotopi ai gazelor nobile.

Experiența analitică dobândită de colectivele de cercetare ale institutului au permis prestarea de servicii constând în identificarea unor compuşi necunoscuți, determinări de structuri moleculare, analize ale unor amestecuri multicomponent, etc. Colaborări fructuoase s-au stabilit cu Institutul de petrochimie, pentru analize

cromatografice, studii de catalizatori, etc. Centrala medicamentului, a fost partener în cercetări pentru studii de testare a unor medicamente româneşti, prin tehnica RMN. Institute geologice din Baia Mare şi Bucureşti au colaborat cu institutul nostru în domeniul geologiei izotopice. Institutul de cercetări pentru Delta Dunării din Tulcea a colaborat cu colective de cercetare din institutul nostru, pentru studii privind dinamica apelor subterane în zona Deltei.

5. Relațiile institutului cu comunitatea ştiințifică internațională

În decursul timpului Institutul a stabilit relații de colaborare cu diferite institute din străinătate. Dintre aceste contacte, foarte fructuoasă s-a dovedit colaborarea pe o perioadă de mai bine de 20 de ani dintre institutul nostru şi Institutul de izotopi stabili din Leipzig. În cadrul convenției de colaborare cu acest institut au fost efectuate schimburi de cercetători, lucrări de cercetare în comun, participări la congresele şi conferințele cu caracter internațional, organizate de cele două institute.

Cercetători din institutul nostru au efectuat stagii de specializare în institute şi universități de renume din Europa şi SUA (Departamentul de Izotopi Stabili, Saclay, Institutele de cercetări nucleare din Toulouse şi Grenoble, Institutul Max-Planck din Mainz, Şcoala Politehnică din Lausanne, Universitatea din Canberra, Universitatea Princeton şi MIT-Boston, Institutul de Tehnologie şi Universitatea din Tokyo, Institutele de Fizică ale Academiei din Rusia, etc. etc.). Începând din anul 1971 Institutul a participat la programul spațial "Intercosmos". fn cadrul acestui program studiile efectuate de cercetătorii noştri au vizat analiza compoziției chimice şi izotopice a straturilor superioare ale atmosferei. În acest scop, în Institut s-au construit un spectrometru de masă şi o balanță piezoelectrică de mare sensibilitate.

După anul 1989, institutul a participat la mai multe proiecte susținute de Comunitatea Europeana (COST, Inco-Copemicus, BRITE-EURAM), participa la mai multe programe interguvenamentale de cooperare în domeniul cercetării ştiințifice (România - Spania, România - Ungaria) şi are convenții bilaterale de cooperare ştiințifică cu institute şi universități din Ungaria, Austria, Germania, Elveția, Franța, Anglia, Statele Unite, Africa de Sud, Republica Populara Chineză, Japonia.

În ultimul deceniu, pe lângă continuarea cercetărilor în domeniile care l-au consacrat, Institutul a abordat direcții noi de cercetare, în special în domeniul fizicii moleculare şi biofizicii.

În încheiere, se cuvine să elogiem memoria celor care, în decursul acestei jumătăți de secol, şi-au închinat o parte importantă din viața şi activitatea lor dezvoltării Institutului şi prin aceasta progresului ştiinței româneşti: Prof. Dr. Doc. Aurel Ionescu, Prof. Dr. Doc. Victor Mercea - membru corespondent al Academiei Române -, Ing. Alexandru Mihăilă, Dr. Alexandru Ştefan Olaru, Dr. Constantin Mirel, Dr. Costică Ungureanu, Dr. Mircea Paşcalău, Dr. Ioan Deac, Fiz. Flaviu Băliban, şi alții.

STUDIA UNIVERSITATIS BABEŞ-BOLYAI, PHYSICA, SPECIAL ISSUE, 2001

CUM AM ÎNVĂȚAT CRIOGENIE

MARIUS PECULEA

Romanian Academy, Bucharest

ABSTRACT. Cryogenics object as well as its application domain, inclusively the development in Romania of oxygen/nitrogen production capabilities by liquid air distillation, are described. Five criteria are presented which differentiate cryogenics from the refrigeration processes based on vapor condensation: the lamination process / adiabatic expansion; vaporization heat; radiation; energy; heat exchange. The main cryogenic refrigeration processes are characterized, for instance the cold gas cycle, for which the cooling stage and the heat pump used in distillation are defined. the hydrogen isotopes distillation plant and the helium extraction and production plant are exemplified. The most important experimental results obtained at ICSI R>mnicu V>lcea were: the determination of the heat transfer in convection and boiling, the testing of the isotopic equilibrium elements in hydrogen distillation; the determination of the behavior of a filled column for the isotopic distillation of hydrogen and its equivalence with a wet wall distillation column, heat exchange for thermic regenerators operated in nonstationary regime. The accumulated experience was the basis for the construction of an industrial pilot for deuterium and tritium separation.

Obiectivul Uzinei G din Râmnicu Vâlcea a fost elaborarea tehnologiei de separare şi producere a apei grele şi asimilarea echipamentelor specifice, obiectiv convergent la a cărui finalizare institutul urma să-şi reducă drastic activitatea, rămânând un consultant al fabricii de apă grea pentru a-i menține competitivitatea. A fost momentul ca, bazându-ne pe toate cunoştințele obținute pentru separarea deuteriului, să ne îndreptăm preocupările către cel de-al treilea izotop al hidrogenului, tritiul, în vederea separării lui din moderatorul reactorilor nucleari de la C. N. Cernavodă. Tehnologia aleasă a fost cea de distilare izotopică a hidrogenului lichid, o tehnologie criogenică, criogenia fiind o disciplină cu perspective de dezvoltare divergente.

Domeniul criogeniei începe cu temperatura de vaporizare a metanului în condiții normale (111,7 K) şi tinde către zero absolut. Domeniul şi obiectivele criogeniei pot fi urmărite în figura 1. In figura 2 este descrisă evoluția producției de oxigen, respectiv de azot, din industria românească, tehnologia de lichefiere şi de distilare a aerului lichid fiind una dintre cele mai reprezentative tehnologii criogenice din țară [1].

O remarcă referitoare la figura 1: ”Arborele criogenic” este separat în partea de jos (rădăcina) de ştiințele care susțin criogenia, iar în partea de sus (coroana) apare dezvoltarea, valorificarea ei. De observat că tehnologiile criogenice sunt mari consumatoare de energie specifică şi operarea lor impune reguli de strictă securitate deoarece trebuie luat în considerare faptul că nu se poate vorbi despre ingineria criogenică fără a stăpâni lichefierea gazelor, separarea şi purificarea lor înaintată.

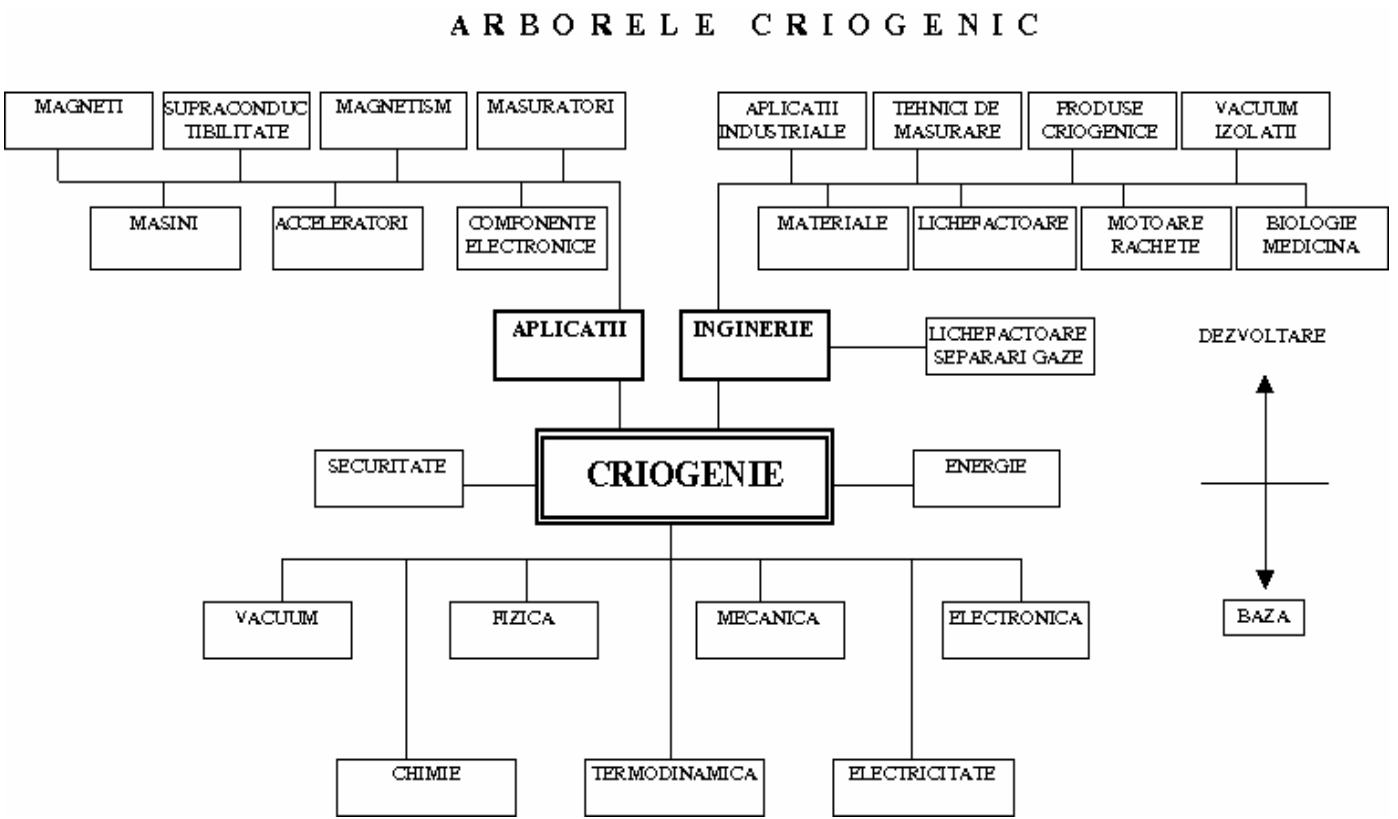

Fig. 1. Arborele criogenic

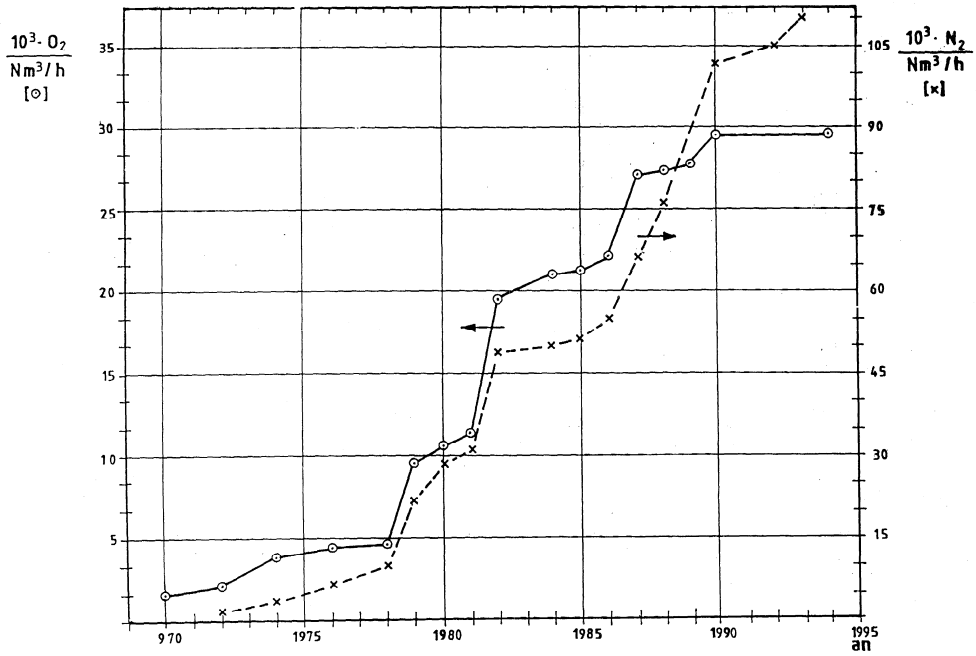

Fig. 2. Producția de oxigen şi azot din industria chimică din România

Cu o dotare de ultimă oră a laboratorului de criogenie al Uzinei G (1981) nu însemna că persoanele cunosc criogenie, prin urmare s-a procedat la un sistem – este adevărat costisitor – de instruire, desigur citind şi făcând – cu sublinierea cuvântului făcând –, adică prin experimentare şi verificare. Față de procesele clasice de tehnica frigului bazate pe ciclul de comprimare cu vapori, procesele de răcire în criogenie prezintă o serie de particularități [2].

a) Scăderea temperaturii agentului de lucru se poate obține prin două procese: laminare (destindere la entalpie constantă), sau prin detentă (destindere la entropie constantă). Răcirea prin laminare este limitată de domeniul cuprins de curba de inversiune a agentului; pentru diferite gaze, acest proces este reprezentat în diagrama din figura 3. Răcirea prin detentă reprezintă o adiabată care nu este limitată de un anumit domeniu, după cum rezultă din figura 4. In majoritatea proceselor de răcire şi în toate care reprezintă o lichefiere, sunt utilizate ambele procese: prerăcirea gazului prin detentă şi lichefierea propriu zisă prin laminare.

b) de răcire şi în toate care reprezintă o lichefiere sunt utilizate ambele procese: prerăcirea gazului se face utilizând detentoare, lichefierea propriu-zisă se realizează prin laminare.

c) O particularitate a agenților criogenici (gaze lichefiate) este scăderea căldurii latente de vaporizare odată cu scăderea temperaturii. Diagrama din figura 5 ilustrează aceasta, însă o reprezentare mai sugestivă în partea de jos a figurii este cea a cantității

de lichid vaporizat pentru introducerea în sistem a unui watt timp de 24 de ore. De aici rezultă pe de o parte consumul mare de energie specifică pentru lichefiere, pe de altă parte importanța izolației termice.

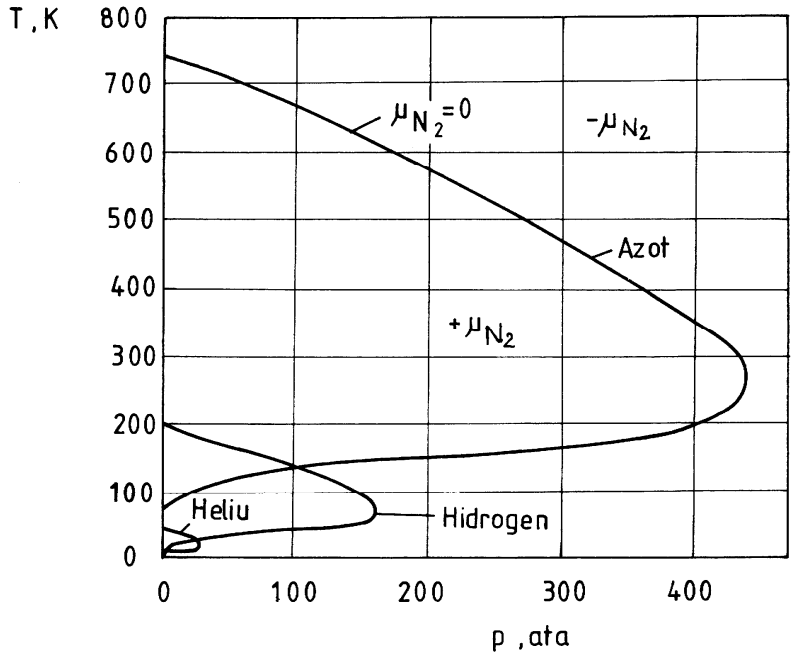

Fig. 3. Curbele de inversiune pentru azot, hidrogen şi heliu

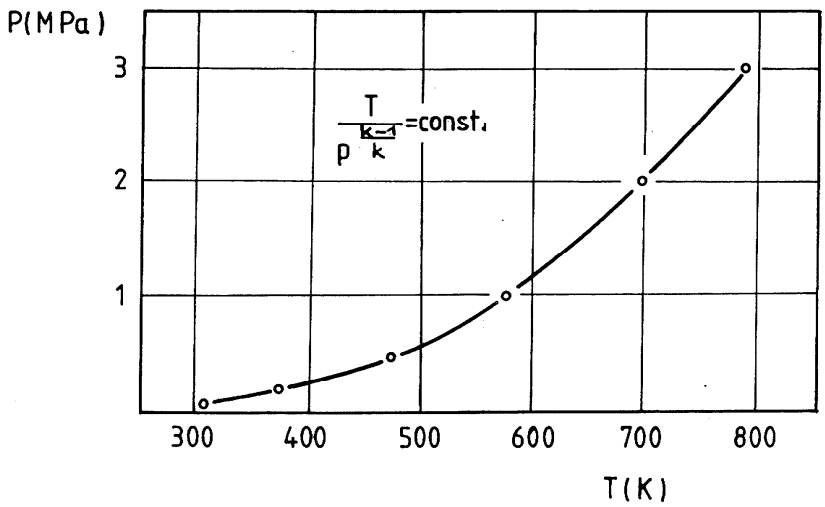

Fig. 4. Variația adiabatei (T, p)

d) Conducția este controlată prin reducerea la minim a dimensiunilor echipamentelor; convecția este practic anulată prin introducerea echipamentelor în incinte vidate (10^{-6} torr); problema este ridicată de radiație, care este proporțională cu puterea a patra a temperaturii:

$$Q_R = \text{prop}(T_2^4 - T_1^4) \qquad (1)$$

și cum temperatura de lucru T_1 tinde către zero, temperatura mediului ambiant care este T_2 = 300 K practic controlează radiația, respectiv Q_R = prop. $\cdot$ $8.1 \cdot 10^9$. Remediul este ecranul de radiație [3] (aceasta fiind una dintre primele lucrări cu care am început instruirea noastră). Experimentele realizate la nivelul azotului lichid (≈ 80 K) au arătat capacitatea de reducere a pierderilor de căldură prin radiație în funcție de numărul de ecrane, experimente ilustrate în diagrama din figura 6.

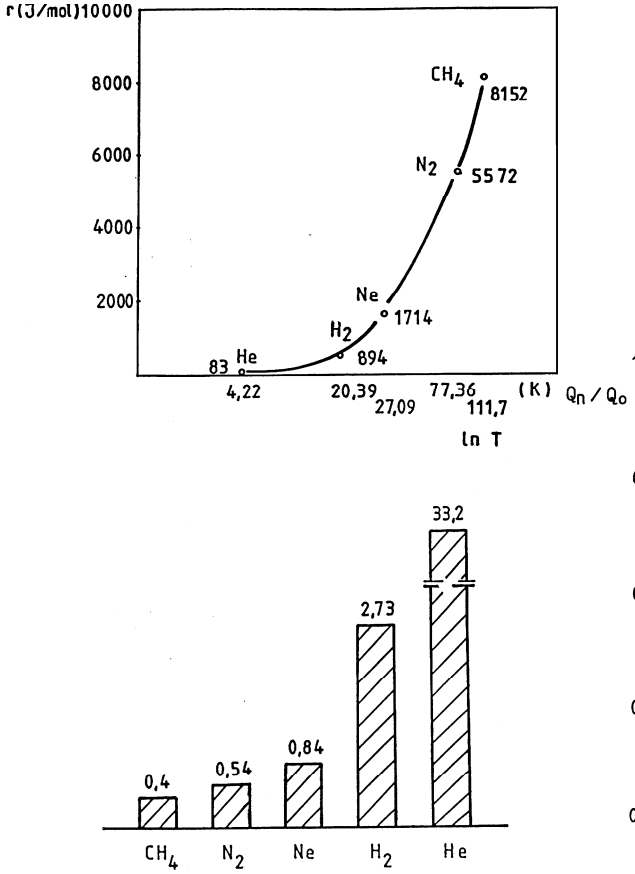

Fig. 5. Varia⇔ia căldurii de vaporizare cu temperatura, respectiv cantitatea de lichid evaporat pentru 1 W/zi energie

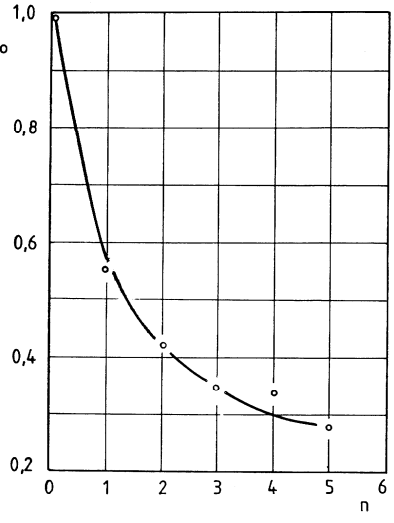

Fig. 6. Efectul ecranelor de radia⇔ie asupra pierderilor de căldură

e) Analiza energetică a pierderilor în schimbătoarele de căldură prin creşterea de entropie $\Delta E_p = T_0 \cdot \Delta S_{ir}$, descrise în final de relaţiile:

$$\Delta E_Q = T_0 \frac{T_2 - T_1}{T_2 \cdot T_1} \qquad (2)$$

pentru transmiterea de căldură, şi:

$$\Delta E_P = T_0 \int_0^{\Delta P} \frac{v_1}{T_1} d(\Delta P) \qquad (3)$$

pentru căderea de presiune, ne arată că, datorită tinderii temperaturii T_1 către zero, ambele pierderi devin foarte mari. Minimizarea acestor pierderi înseamnă transmiterea căldurii la diferenţe cât mai mici de temperatură ($T_2 = T_1$ reprezintă un proces reversibil) şi secţiuni mari de curgere pentru ΔP cât mai mic. S-au elaborat în acest scop schimbătoare de căldură multistrat cu aripioare, din aluminiu, executate cu competenţă tehnică la fabrica de radiatoare din Bistriţa. Acest tip de schimbător de căldură, pe unitatea de masă, este caracterizat de o suprafaţă mare de schimb şi căderi minime de presiune. Testele efectuate asupra acestor tipuri de schimbătoare de căldură ne-au permis să tragem următoarele concluzii:

- relaţiile de calcul din literatura de specialitate cu privire la transmiterea căldurii prin convecţie la curgerea în contracurent sunt utilizate cu rezultate bune, lucru atestat de experimentele proprii la nivele de temperatură cuprinse între 20 şi 80 K, prezentate comparativ în diagrama din figura 7.
- la transmiterea de căldură cu schimbarea stării de agregare, la condensare se respectă legea lui Nusselt, în schimb la fierbere, după cum se poate observa în reprezentările din figura 8, se recomandă verificarea experimentală. Măsurătorile noastre efectuate la fierberea hidrogenului lichid sunt marcate cu semnul *; sunt de remarcat diferenţele mici de temparatură realizate la schimbul termic, care vin în sprijinul observaţiilor de mai sus.

Obţinerea de temperaturi joase şi foarte joase în condiţii economice se realizează prin cascadarea procesului criogenic, cascadare care se aplică cu succes la ciclurile de răcire cu gaz (Brayton). Prin asemănare cu cascadarea proceselor de separare izotopică, s-a definit elementul de cascadă criogenică (etaj) ca fiind format dintr-un detentor şi un schimbător de căldură, conform schiţei şi diagramei de funcţionare din figura 9. Procesul de răcire dezvoltându-se între două izobare (p_1 şi p_2), numărul de etaje ale cascadei pentru realizarea diferenţei de temperatură între T_n şi cea a mediului ambinat T_0 este:

$$N_T = \frac{\ln \frac{T_0}{T_n}}{\ln \delta} = \frac{\ln \frac{T_0}{T_n}}{\ln \frac{T_{i-1}}{T_i}} \qquad (4)$$

mărimea adiabatei fiind constantă:

$$\delta = \frac{T_{i-1}}{T_i} = \left(\frac{p_2}{p_1} \right)^{\frac{k-1}{k}} = \text{const}. \qquad (5)$$

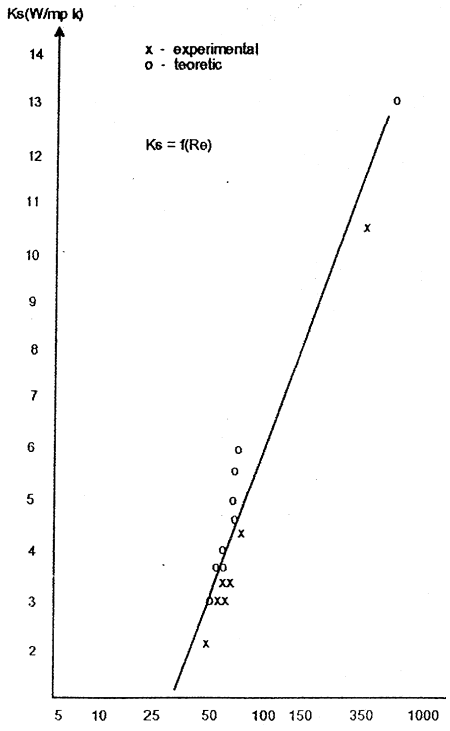

Fig. 7. Date experimentale asupra varia⇔iei coeficientului global de transfer de căldură în domeniul hidrogenului lichid

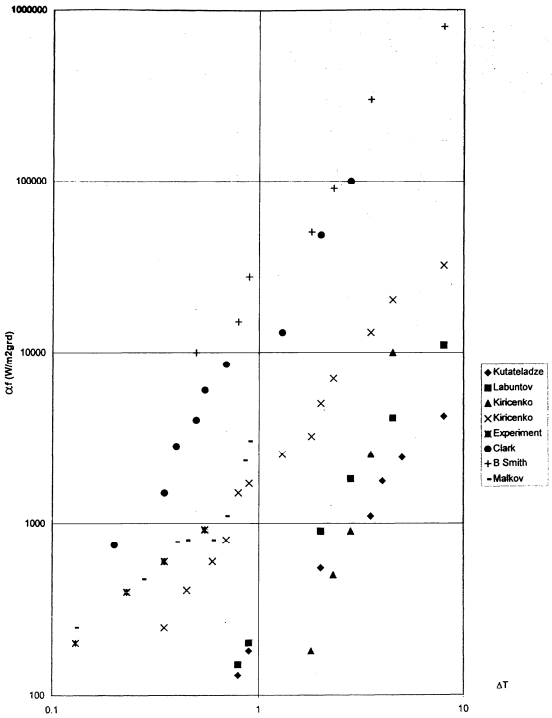

Fig. 8. Sarcina termică în func⇔ie de ΔT pentru lichide criogenice în fierbere

In practică, elementul de cascadă cu funcționare reală (cu pierderi) este prezentat în figura 10.

Numărul real de etaje al cascadei este dat de:

$$N_R = N_T \cdot \varphi \qquad (6)$$

unde

$$\varphi = \frac{\ln \varepsilon}{\ln \xi}$$

$$\xi = \frac{\beta[1-\eta_s(1-\varepsilon)]}{1-a} \qquad (7)$$

$$\varepsilon = \frac{T_{5''}}{T_3}; \beta = \frac{T_3}{T_1}; a = \frac{\Delta T_5}{T_5}$$

relațiile (7) descriu ireversibilitatea procesului şi influența recuperatorului de căldură S2.

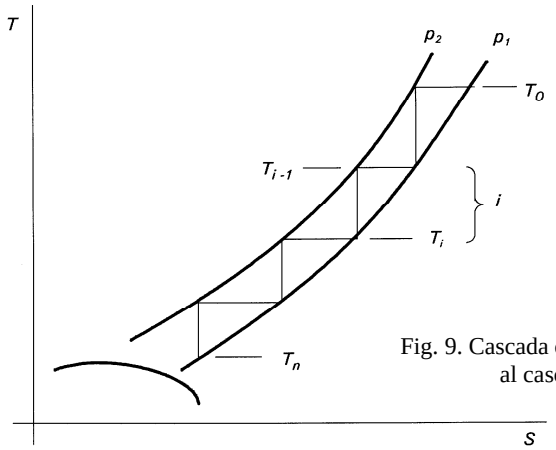

Fig. 9. Cascada criogenică ideală şi elementul (etaj) *i* al cascadei; D, G - debite de gaz

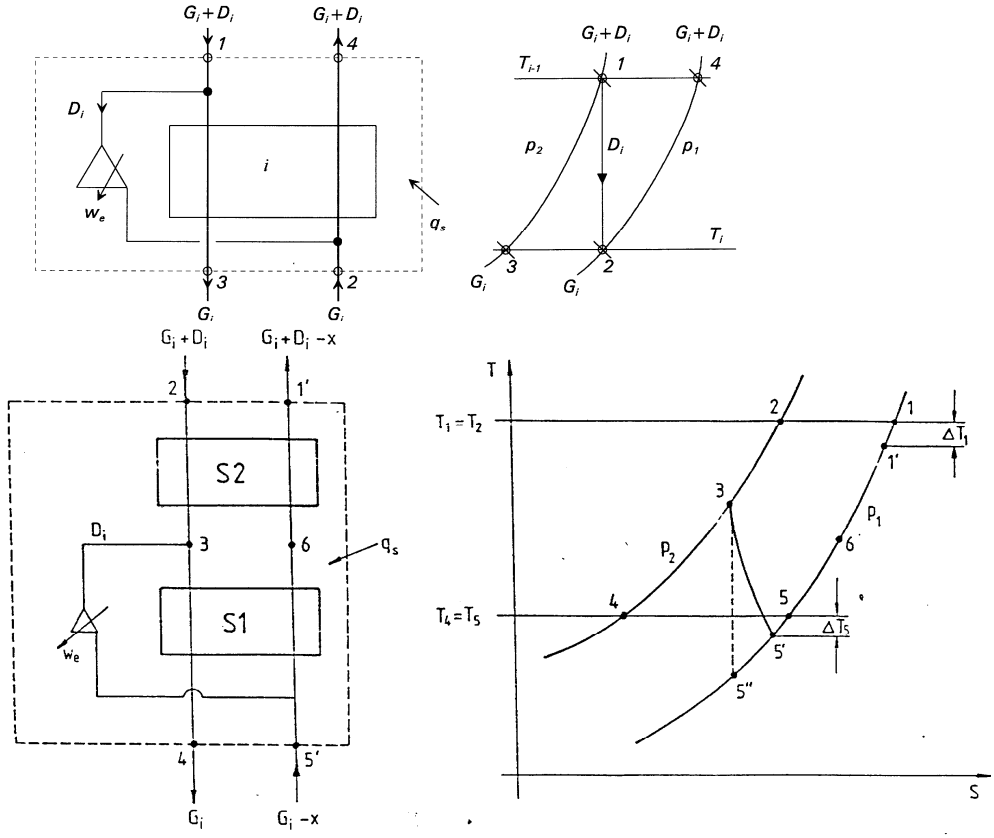

Fig. 10. Etajul *i* al unei cascade criogenice cu func⇔ionare

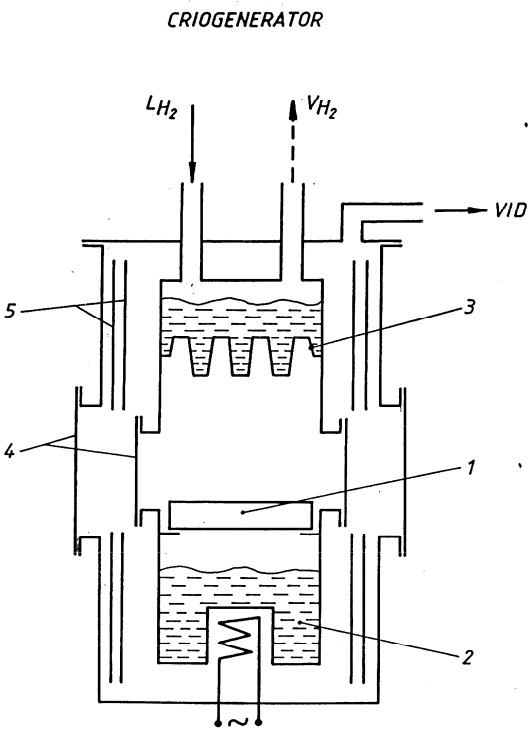

Fig. 11. Criostat pentru testarea elementului de contact la distilarea izotopică a hidrogenului lichid; 1 - element de contact lichid - vapori; 2 - fierbător; 3 - condensator; 4 - vizori; 5 - ecrane de radia⇔ie

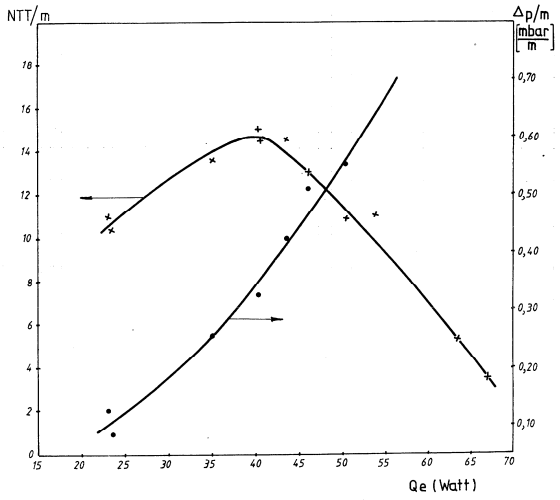

Fig. 12. Diagrama de performan⇔ă pentru o umplutură ordonată în procesul de distilare izotopică a hidrogenului lichid

Dacă la toate acestea adăugăm elaborarea de absorbanți selectivi şi testarea lor până la nivelul temperaturii hidrogenului lichid şi implicit utilizarea lor pentru separarea şi ultrapurificarea gazelor, se poate afirma că instruirea noastră în domeniul criogeniei a atins nivelul care să ne permită studiul şi elaborarea tehnologiilor de separare a deuteriului şi a tritiului prin distilarea criogenică a hidrogenului lichid [4].

Obiectivul principal al cercetărilor din domeniul criogeniei a fost elaborarea unei tehnologii de separare a izotopilor hidrogenului, respectiv a deuteriului şi tritiului, prin distilarea hidrogenului lichid.

Primul pas a fost definirea elementului de contact între fazele lichidă şi gazoasă (vapori), care să echipeze coloanele de distilare. S-au testat un taler cu clopoței, un taler perforat şi o umplutură cu geometrie ordonată realizată din plasă din sârmă de oțel inoxidabil. Testele s-au efectuat pe o coloană cu un singur taler introdusă într-o incintă vidată, protecția la radiația de căldură fiind asigurată de două ecrane concentrice. Criostatul a permis vizualizarea (fotografierea) comportării ele-mentului de contact. Schema insta-lației experimentale este prezentată în figura 11.

Circulația pe elementul de contact era asigurată prin fierberea controlată a hidrogenului lichid şi condensarea lui totală la capătul superior. Testele asupra celor trei elemente de contact au demonstrat superioritatea umpluturii ordonate, ale cărei performanțe pot fi urmărite în diagrama din figura 12 [5].

Pasul următor a fost testarea comportării umpluturii ordonate în pro-

cesul de distilare a izotopilor hidrogenului într-o coloană cu diametrul de 27 mm şi înălțimea umpluturii de 550 mm [6]. In figura 13 se poate urmări schița instalației experimentale cu sistemele de răcire (condensare) şi încălzire (vaporizare) şi în totalitate punctele de măsură pentru determinarea circulației, a stării fluidelor şi a concentrațiilor lor izotopice. Umplutura ordonată a fost astfel concepută încât lichidul să curgă sub formă peliculară (strat foarte subțire), astfel că rezistența la transferul de izotop între faze să fie preponderentă în faza de vapori. Urmărind schema din figura 14 şi ținând cont că procesul de schimb este controlat de coeficientul de transfer de masă raportat la faza de vapori, K_{ov}, se poate scrie relația de bilanț izotopic sub forma:

$$Vdy = K_{ov} \cdot a \cdot A(y - y^*)dz \qquad (8)$$

cu

$$\frac{1}{K_{ov}} = \frac{1}{k_v \cdot P} + \frac{m}{k_L \cdot \rho_m} \qquad (9)$$

descris de coeficienții parțiali de transfer şi proprietăți ale substanței. Prin integrarea relației (8) se poate determina înălțimea de umplutură, Z, care să realizeze o creştere de concentrație izotopică în faza gazoasă de la y_1 la y_2:

$$Z = \frac{V}{A \cdot a \cdot K_{ov}} \int_{y_1}^{y_2} \frac{dy}{y - y^*} = (HTU)_{ov} \cdot (NTU)_{ov} \qquad (10)$$

respectiv produsul dintre înălțimea unității de transfer, $(HTU)_{ov}$, care descrie performanța umpluturii şi numărul de unități de transfer, $(NTU)_{ov}$.

Determinarea experimentală a înălțimii unității de transfer se face în baza relației (10), respectiv:

$$(HTU)_{ov} = \frac{Z}{(NTU)_{ov}} \qquad (11)$$

unde

$$(NTU)_{ov} = \frac{2.303}{\alpha - 1} \lg \frac{(1 - y_1)y_2}{(1 - y_2)y_1} + 2.3 \lg \frac{1 - y_1}{1 - y_2} \qquad (12)$$

α fiind factorul de separare, iar y_1 şi y_2 concentrațiile izotopice măsurate la capetele coloanei.

In lipsa unor măsurători, predicția comportării unei umpluturi este riscantă, aşa că s-a căutat o asemănare cu un proces de distilare a cărui comportare poate fi determinată prin calcul şi aceasta a fost coloana de distilare cu film de lichid. Cele două tipuri de coloane sunt reprezentate în figura 15.

Comune se păstrează înălțimea coloanei, Z, şi viteza vaporilor w_v (încărcarea coloanei).

Inălțimea unității de transfer pentru coloana cu film de lichid este dată de:

$$(HTU)_{ov} = \frac{V_t}{\pi d_t K_{ov}} \qquad (13)$$

unde K_{ov} este descris de (9) şi

$$V_t = V \frac{d_t^2}{D_c^2 \cdot \varepsilon} \qquad (14)$$

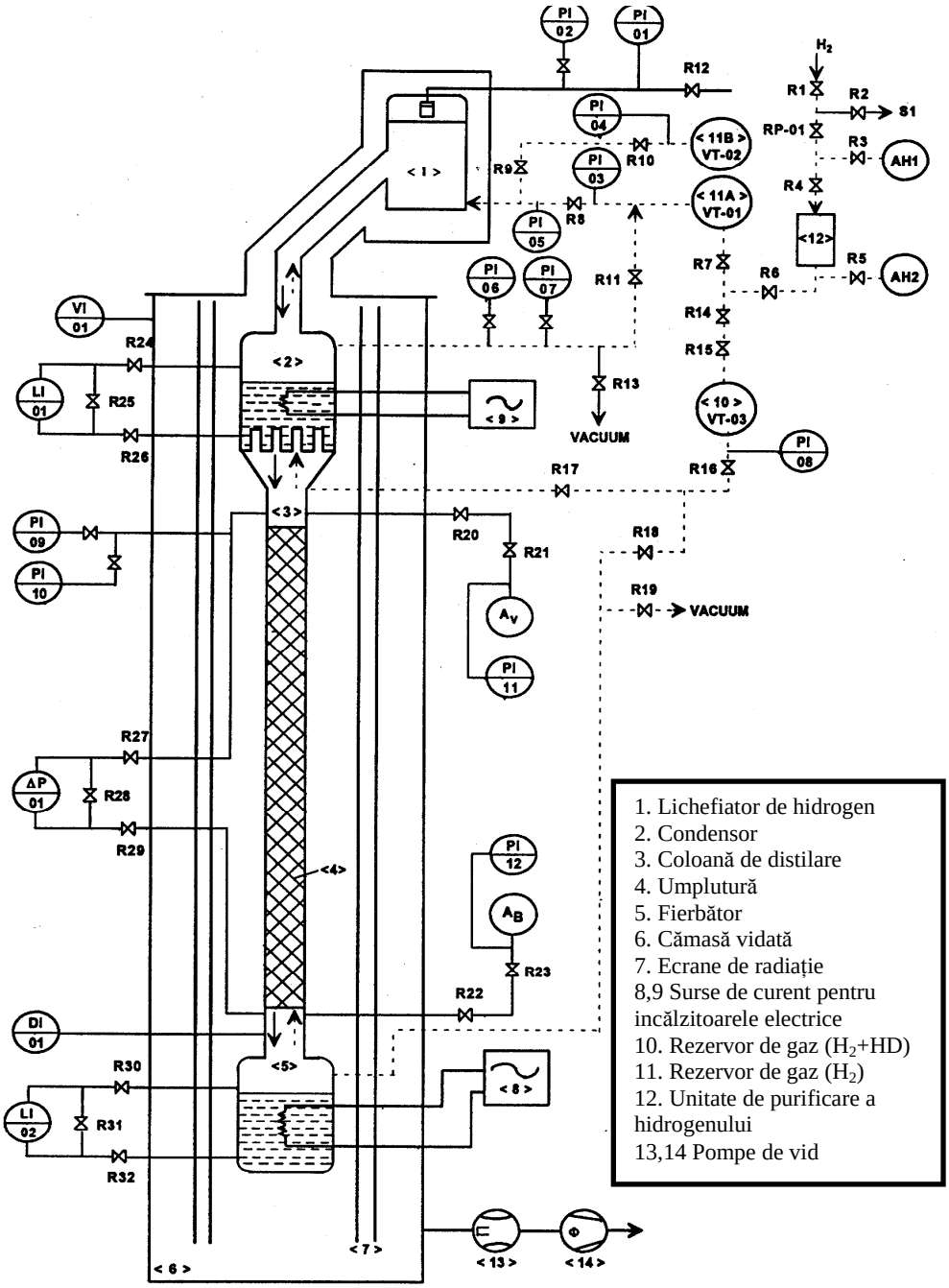

Fig. 13. Schema instala⇔iei experimentale pentru distilarea criogenică a izotopilor hidrogenului

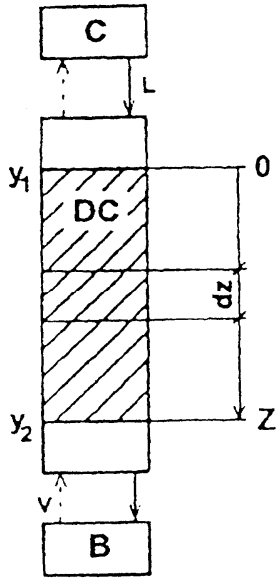

Fig. 14. Schema de calcul pentru o instala⇔ie de distilare izotopică cu coloană cu umplutură

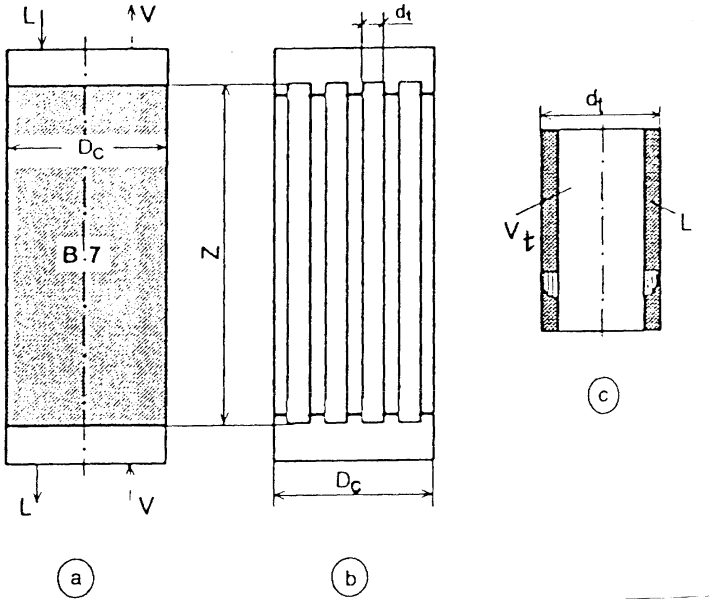

Fig. 15. Schema de calcul pentru asemănarea coloanelor de distilare cu umplutură (a) şi a coloanelor de distilare cu film de lichid (b), detaliu pentru coloana b (c)

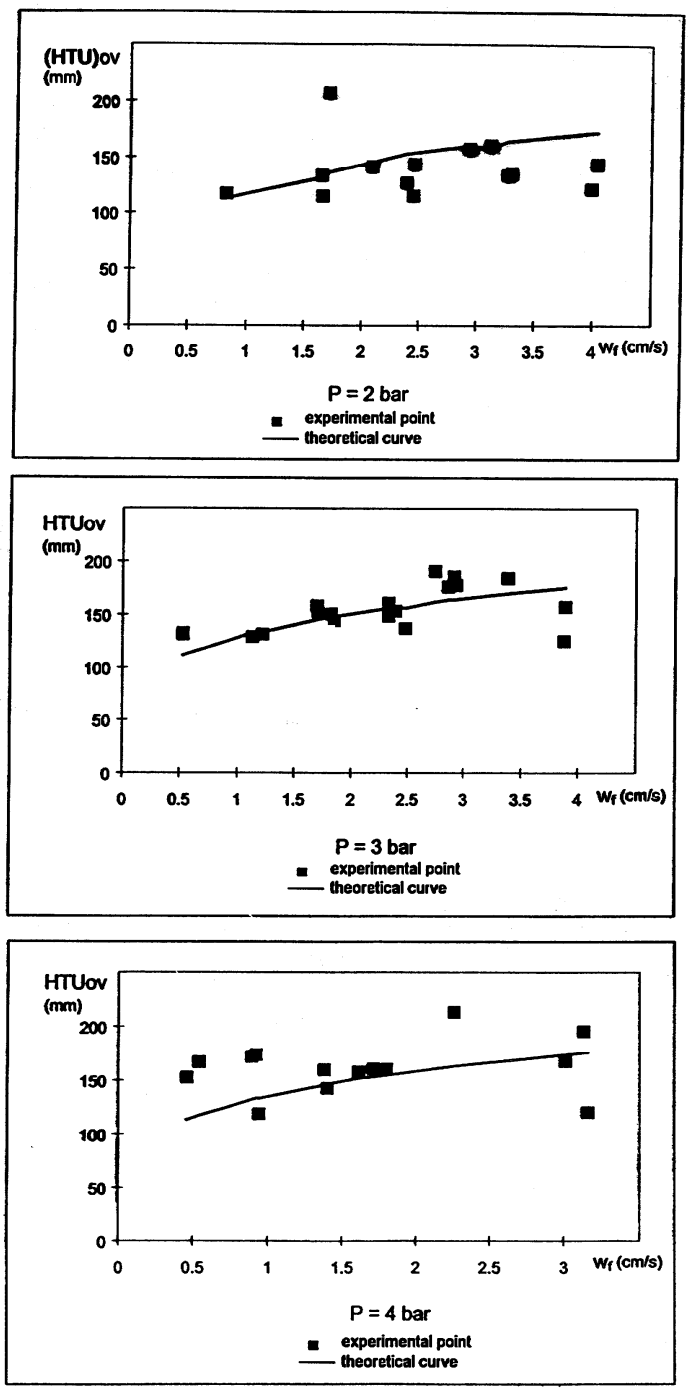

Fig. 16. Varia⇔ia $(HTU)_{ov}$ cu viteza vaporilor w_v

Din literatura de specialitate [7], K_{ov} din relația (9) poate fi calculat, astfel încât problema cheie rămânea determinarea lui d_t, diametrul coloanei (tubului) cu film de lichid. Tinând cont că pentru ambele coloane curgerea lichidului este periculoasă, iar umplutura ordonată are o formă geometrică bine determinată, practic d_t este un diametru hidraulic:

$$d_t = d_{ech} = \frac{4\varepsilon}{a} \quad (15)$$

unde a este suprafața specifică a umpluturii ($m^2 \cdot m^{-3}$), iar ε este volumul liber al umpluturii ($m^3 \cdot m^{-3}$).

Comportarea umpluturii ordonate în procesul de distilare izotopică a hidrogenului lichid a fost determinată pentru trei regimuri de operare caracterizate de presiunile 2, 3 şi 4 bari şi un domeniu de încărcare caracterizat de viteza w_v cuprinsă între 0.5÷4 $cm \cdot s^{-1}$. Rezultatele măsurătorilor sunt reprezentate în cele trei diagrame din figura 16, unde prin linie continuă este reprezentată variația funcției (13), respectiv comportarea coloanei de distilare cu film de lichid. Concordanța dintre măsurători (umplutura ordonată) şi variația funcției (13) ne permite să afirmăm că se poate face o predicție a comportării unei umpluturi ordonate – pentru procesul de distilare izotopică a hidrogenului lichid – prin intermediul coloanei cu film de lichid, atunci când determinarea diametrului hidraulic al umpluturii este posibilă.

In strânsă legătură cu lichefierea hidrogenului s-a studiat comportarea unui regenerator temic a cărui masă era formată din bile de plumb cu un diametru de 8 mm în număr de 6095, dispuse într-o coloană cu diametrul de 77 mm şi înălțime de 770 mm. Schema instalației experimentale poate fi urmărită în figura 17.

O instalație criogenică C, prin by-pass-ul R3 - R4, permite răcirea masei regeneratorului M1 până la temperatura de 80 K, după care, prin deschiderea circuitului de testare, hidrogenul de la temperatura mediului ambiant era răcit în regeneratorul M1; regeneratorul M2 era utilizat doar ca recuperator de căldură pentru a permite o funcționare normală a compresorului K. Regeneratorul M1 era prevăzut cu 11 puncte pentru măsurarea temperaturilor în lungul fluxului de hidrogen. Pentru determinarea coeficientului de transmitere a căldurii, experimentarea s-a făcut în regim nestaționar descris de sistemul:

$$\begin{aligned} \left(\frac{\partial T}{\partial f}\right)_t &= \frac{\overline{\alpha}}{C}(T_m - T) \\ \left(\frac{\partial T_m}{\partial t}\right)_f &= \frac{2 \cdot n \cdot \overline{\alpha}}{\rho_m \cdot C_m \cdot \delta}(T - T_m) \end{aligned} \quad (16)$$

în conformitate cu schema din figura 18, unde indicele *m* se referă la masa regeneratorului.

Problema cheie rămânea determinarea lui d_t, diametrul coloanei (tubului) cu film de lichid. Tinând cont că pentru ambele coloane curgerea lichidului este periculoasă, iar umplutura ordonată are o formă geometrică bine determinată, practic d_t este un diametru hidraulic:

$$d_t = d_{ech} = \frac{4\varepsilon}{a} \quad (15)$$

unde a este suprafața specifică a umpluturii ($m^2 \cdot m^{-3}$), iar ε este volumul liber al umpluturii ($m^3 \cdot m^{-3}$).

Comportarea umpluturii ordonate în procesul de distilare izotopică a hidrogenului lichid a fost determinată pentru trei regimuri de operare caracterizate de presiunile 2, 3 şi 4 bari şi un domeniu de încărcare caracterizat de viteza w_v cuprinsă între 0.5÷4 $cm \cdot s^{-1}$. Rezultatele măsurătorilor sunt reprezentate în cele trei diagrame din figura 16, unde prin linie continuă este reprezentată variația funcției (13), respectiv comportarea coloanei de distilare cu film de lichid. Concordanța dintre măsurători (umplutura ordonată) şi variația funcției (13) ne permite să afirmăm că se poate face o predicție a comportării unei umpluturi ordonate – pentru procesul de distilare izotopică a hidrogenului lichid – prin intermediul coloanei cu film de lichid, atunci când determinarea diametrului hidraulic al umpluturii este posibilă.

In strânsă legătură cu lichefierea hidrogenului s-a studiat comportarea unui regenerator temic a cărui masă era formată din bile de plumb cu un diametru de 8 mm în număr de 6095, dispuse într-o coloană cu diametrul de 77 mm şi înălțime de 770 mm. Schema instalației experimentale poate fi urmărită în figura 17.

O instalație criogenică C, prin by-pass-ul R3 - R4, permite răcirea masei regeneratorului M1 până la temperatura de 80 K, după care, prin deschiderea circuitului de testare, hidrogenul de la temperatura mediului ambiant era răcit în regeneratorul M1; regeneratorul M2 era utilizat doar ca recuperator de căldură pentru a permite o funcționare normală a compresorului K. Regeneratorul M1 era prevăzut cu 11 puncte pentru măsurarea temperaturilor în lungul fluxului de hidrogen. Pentru determinarea coeficientului de transmitere a căldurii, experimentarea s-a făcut în regim nestaționar descris de sistemul:

$$\begin{aligned} \left(\frac{\partial T}{\partial f}\right)_t &= \frac{\overline{\alpha}}{C}(T_m - T) \\ \left(\frac{\partial T_m}{\partial t}\right)_f &= \frac{2 \cdot n \cdot \overline{\alpha}}{\rho_m \cdot C_m \cdot \delta}(T - T_m) \end{aligned} \qquad (16)$$

în conformitate cu schema din figura 18, unde indicele *m* se referă la masa regeneratorului.

Cu notațiile:

$$\begin{aligned} \xi &= \frac{\overline{\alpha}}{C} f \\ \eta &= \frac{Z \cdot n \cdot \overline{\alpha}}{\rho_m \cdot C_m \cdot \delta} t \end{aligned} \qquad (17)$$

din sistemul (16) s-au obținut relațiile pentru temperaturi [8]:

$$\begin{aligned} T &= T_0 - (T_0 - T_{m0}) \int_0^{\xi} \exp[-(\xi + \eta)] J_0(2i\sqrt{\xi\eta}) d\xi \\ T_m &= T - (T_0 - T_{m0}) \exp[-(\xi + \eta)] J_0(2i\sqrt{\xi\eta}) \end{aligned} \qquad (18)$$

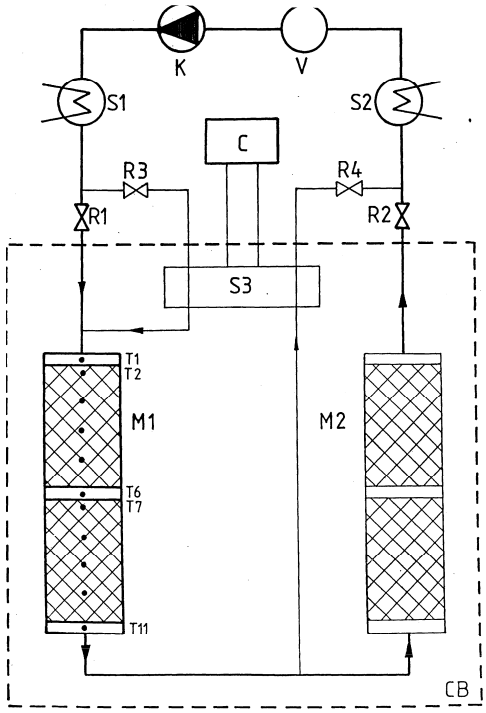

Fig. 17. Schema instala⇔iei experimentale pentru determinarea transferului de căldură al regeneratorului

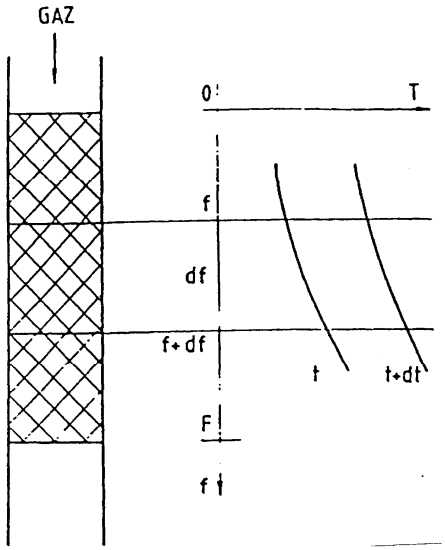

Fig. 18. Schema modelului matematic pentru procesul termic în regim nesta⇔ionar al regeneratorului

Determinările experimentale s-au făcut pentru 6 debite de hidrogen, variația temperaturilor $T_1 \div T_{11}$ fiind extinsă pentru un interval de timp de 20000 sec. Determinarea lui $\overline{\alpha}$ s-a făcut prin ajustarea profilului de temperaturi măsurat cu cel calculat, în figura 19 putându-se urmări, ca exemplu, concordarea celor două profile.

Valorile determinate pentru $\overline{\alpha}$ ($W \cdot m^{-2} \cdot K^{-1}$) în funcție de debitul de hidrogen G ($N \cdot m^3 \cdot h^{-1}$) în domeniul de temperaturi 80 - 300 K sunt date în tabelul de mai jos:

G [$N \cdot m^3 \cdot h^{-1}$]	2.6	3.9	5.19	6.49	7.79	9.74
$\overline{\alpha}$ [$W \cdot m^{-2} \cdot K^{-1}$]	16	20	23	27	28	30

şi au fost grupate în relația adimensională:

$$N_u = 0.825 \cdot Re^{0.48} \cdot Pr^{1/3} \qquad (19)$$

*

* *

Cunoștințele obținute prin experimentarea lichefierii hidrogenului şi distilării lui izotopice ne-au permis să elaborăm o tehnologie pentru separarea deuteriului şi tritiului, tehnologie adecvată extracției tritiului din moderatorul (apa grea) Centralei

Nucleare de la Cernavodă. Pentru verificarea tehnologiei, care practic reprezintă şase instalaţii înseriate, s-a construit la I.C.S.I. - Râmnicu Vâlcea, fosta Uzina G, o instalaţie pilot semiindustrială, a cărei schemă bloc poate fi urmărită în figura 20.

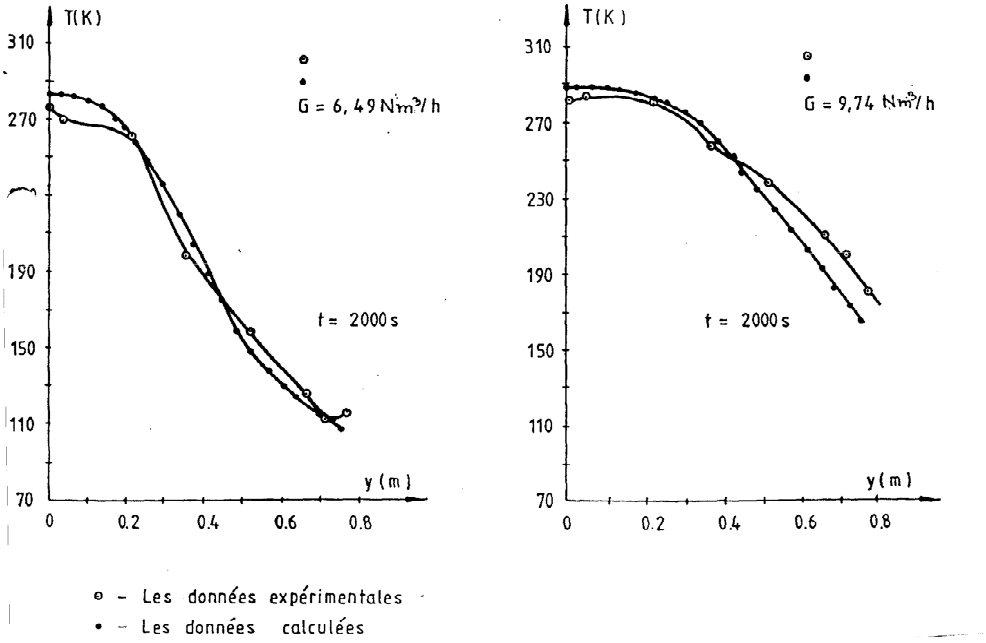

Fig. 19. Corelarea modelului matematic cu datele experimentale pentru regeneratorul termic

Intrată în teste în ultimii ani, sper să avem plăcerea de a asculta şi aprecia la viitoarea sesiune PIM rezultatele ştiinţifice şi tehnologice la valoarea cu care ne-au obişnuit până acum colegii din Râmnicu Vâlcea.

BIBLIOGRAFIE

1. M. Peculea, "Instalaţii criogenice", Ed. Conphyz, Rm. Vâlcea, 1997.
2. F. Pop, M. Peculea, *Rev. de Chimie*, **47** (6), 501 (1996).
3. E. Bologa, M. Peculea, S.D. Popa, Colocviul Naţional de Criogenie, Craiova, 1982.
4. R.G. Scurlock, "History and Origins of Cryogenics". Ed. Clarendon Press, Oxford, 1992.
5. I. Avram, I. Cristescu, M. Peculea, F. Pop, N. Smeureanu, *Cercet. Fiz.*, **41** (4) 351, (1989)
6. F. Pop, M. Peculea, C. Croitoru, *Rev. Roum. de Chim.*, **44** (2), 109 (1999).
7. W.J. Beek, K.M.K. Muttzall, "Transport Phenomena", John Wiley & Sons, Bristol, 1975.
8. M. Peculea, A. Moşteanu, *Rev. Gen. Thermique*, **35** (208) 1996.

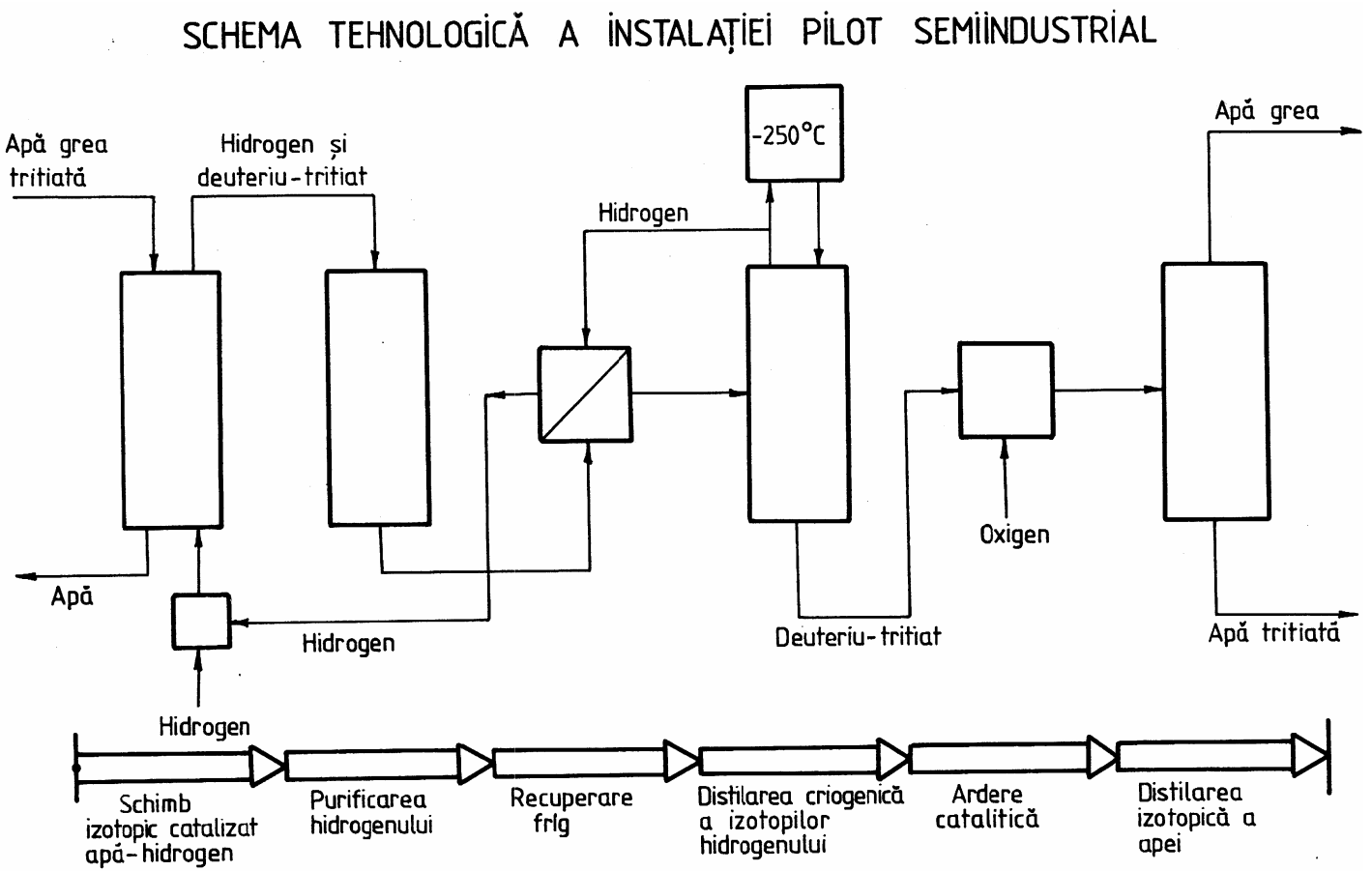

Fig. 20. Schema bloc a instala⇔iei pilot semiindustial pentru separarea deuteriului şi a tritiului

MASS INDEPENDENT ISOTOPE SEPARATION

ETIENNE ROTH

103 rue Brancas F-92310 Sèvres France.
E-mail:etienneroth@.compuserve.com

Introduction

After showing why "normal" isotope effects are expected to vary regularly with mass I will characterize mass independent effects. I shall then briefly review the discovery of variations in isotope abundances, in general, and particularly of mass independent ones. I will explain why they were discovered so late, and treat separately effects observed in nature and produced in the laboratory.

Finally interpretations of mass independent isotope effects, uses in research and eventually for separations will be discussed.

Mass dependent and mass independent isotope effects

Theoretical calculations of isotope effects in exchange reactions and equilibrium processes were made by H.C.Urey([1]), ([2]), and J.Bigeleisen and M. G. Mayer ([3]). Their dependence on masses is given here, after Weston R. ([4]).on the easily generalized example of oxygen.

Let ^{m}O be either ^{17}O or ^{18}O, and consider the exchange reaction

$$X^{m}O + Y^{16}O = X^{16}O + Y^{m}O \quad (1)$$

The isotopic fractionation of oxygen m in (1) is given by

$$\alpha_m = (Y^{m}O)/(Y^{16}O) / (X^{m}O)/(X^{16}O) \quad (2)$$

$$= (1 + 10^{-3}\delta Y^{m}O) / (1 + 10^{-3}\delta X^{m}O) \quad (3)$$

With the usual definition

$$\delta Y^{m}O = 10^{3}(RYm/Rstm - 1)., \quad RYm = [(^{m}O) / (^{16}O)]_{Y.}$$

and similar definitions for $\delta X^{m}O$, and for RXm and Rstm.

Let *m*m be the mass of isotope ^{m}O :theory leads to

$$\ln\alpha_{17}/\ln\alpha_{18} = \frac{(m16^{-1} - m17^{-1}) * \Sigma^{3}_{i=1} [aii(YO) - aii\ (XO)]}{(m16^{-1} - m18^{-1}) * \Sigma^{3}_{i=1} [aii(YO) - aii\ (XO)]} \quad (4)$$

$$= (\delta\Psi^{17}O - \delta\Xi^{17}O) / (\delta\Psi^{18}O - \delta\Xi^{18}O) = 0.529 \quad (5)$$

Using XO as reference makes all δXO zero, and (5) becomes

$$\delta Y^{17}O/\delta Y^{18}O = 0.529 \quad (6)$$

---

[1] H.C.Urey et al., *J.A.C.S.* **1935** *57* pp.321-327

[2] Urey H.C. *J.Chem. Soc.***1947,** 562

[3] Bigeleisen, J.; Mayer, M.G. *J. Chem. Phys.* **1947 ,** *15,* 261

[4] Weston R. *Chem. Reviews* **1999**, *99,* pp.2115-2136

In practice, except for hydrogen reactions, α's are always close to unity, and can be written 1 + ε thus lnα is equivalent to $\tilde{\varepsilon}$ Also aii's, force constants for three orthogonal motions of the isotopically substituted atoms, are constants, and (4) is calculated by (7)

$$\ln\alpha_{17}/\ln\alpha_{18} = (m17 - m16)/(m18 - m16) * m18/m17 \quad (7)$$

In mass dependent processes, ε's are equal per unit mass difference. When this relation is not fulfilled, one speaks of mass independent effects. They are quantised by Δ's $\Delta = \delta_{measured} - \delta_{calculated}$

Assuming equal ε's by unit mass difference, calculated δ's for all isotopes of an element are derived from ε measured for only one isotope.

Historical background

Isotope abundances variations up to 1973

In his Nobel lecture, Frédéric Joliot said that variations in isotope abundances of lead were the only ones observed in nature. Indeed, in spite of the prophesying paper by Urey and Greif (i), it took a long time before it was generally recognized that many, if not all, polyisotopic elements could be expected to ,and did, exhibit variations of their natural isotope abundances. And this was years after separation of isotopes by physical-chemical processes were achieved in the laboratory and in plants, and explained by theory based on mass differences(ii), (iii).

Of course lead isotopes are end products of separate radioactive "families" starting (now) with uranium isotopes and thorium.. Differences in initial proportions of uranium and thorium, or natural *chemical* separation of intermediate decay elements of these families, explain large variations in lead isotope proportions. They are so large that they cause readily detected atomic weight differences between lead samples of different provenance. Natural variations were discovered next in isotope abundances of light elements that are more easily altered by physical-chemical means because of their greater relative mass differences. (Only centrifugation separates isotopes on basis of absolute mass differences). Several difficulties had retarded the discovery. Firstly nature, by giving H, C, N, O one overwhelmingly preponderant isotope had made the discovery of the minor isotopes difficult, and detection of variations in abundances was not made to a precision better than a few per mil before the fifties. Consequently, by the early sixties these variations were only recognized for the four lighter elements. Now IUPAC's tables show *geochemical* ranges of isotopic compositions for isotopes of at least 12 more elements. In addition, a number of isotopes undergo nuclear decay with half lives long enough to have a stable abundance but short enough to produce daughter isotopes which alter isotopic compositions of daughter elements according to their geological age. Finally isotopically exceptional occurrences exist, the most famous being tied to the spectacular discovery of natural nuclear reactors, at Oklo, in Gabon in 1972. This discovery was a consequence of isotope abundance measurements on uranium samples. In this unique site , up to now 29 fission product elements have shown exceptional isotope compositions. Five of these are also elements having

geochemically induced isotope abundance ranges. Strontium is an element showing both, variations due to decay of rubidium 87, and exceptional values at Oklo([5]).

When natural isotopic abundances of polyisotopic elements were first studied, geochemically induced variations of isotopes were found to follow the theoretical separation laws that involve mass differences and the square of masses. Isotope separation and production using physical chemical reactions obeying these laws had long been accomplished, and it was surmised that these laws were always followed. Therefore when investigating isotope effects of reactions in nature, or even in the laboratory, *very rarely did authors bother to analyse abundances of more than one isotope. In addition inaccuracies in the use of reference samples made, and still make, interlaboratory comparisons difficult.*

Some laboratories still use "identical" standards leading to deltas differing by several units, a few neglect addition rules of δs.

And when comparing a sample to a standard, differences, expressed as *deltas (δ) are usually given only for the isotope pair which is easiest to measure.*

Mass independent isotope abundance variations of physical chemical origin in nature

In 1973 a discovery should have altered this routine. R. Clayton ([6]) found that inclusions in the Allende meteorite showed equally large negative deltas for ^{17}O and ^{18}O, of about - 40.

Later Thiemens and Heidenreich ([7]) found non mass dependent enrichments of the heavier isotopes of oxygen in atmospheric and stratospheric ozone. Mass independent isotopic composition of oxygen is also observed in atmospheric and stratospheric CO_2, N_20, CO and sulfate aerosols ([8]).

Farquhar et al ([9]) described mass independent effects of sulfur on both ^{33}S and ^{36}S. that have mass numbers of different parity and show capital deltas of opposite signs. Farquhar claims have been contested ([10]), but convincingly confirmed ([11]). A similar effect, but with reversed δ's on both isotopes, had been reported before in the laboratory([12]). Such effects can only occur on *elements having three or more isotopes. These are all elements of even atomic numbers heavier than oxygen*. No mass independent isotope effect in terrestrial samples have yet been reported that is not now assigned to reactions occuring initially in the atmosphere or stratosphere.

One may add a comment. When studying isotope effects, one must be sure of the nature of the rate determining step, and reacting species should be well identified.

---

[5] See e. g. Roth E. *J.Radioanalyt. Chem.* **1977** *37*, 1, pp. 65 -78, and *US Report NUREG/CP* - **1978**

[6] Clayton R. N. et al. *Science* **1973** *182*, p.485

[7] Thiemens M. H. et al. J. E III, **1983** *Science, 219*, p.1073

[8] Thiemens M. H.*Science* **1999** *283*, pp.341-345

[9] Farquhar J. et al. *Science* **2000** *289*, pp. 756 - 758

[10] Ohmoto H.et al. *Science* **2001,** *292*, pp 1959a

[11] Farquhar J.et al; *ibid.(Science* **2001,** *292*, pp 1959a*)*

[12] Colman J.J. et al. *Science* **1996** *273* pp. 774 -776

One should not e.g. overlook formation of S_2O ([13]) when oxidizing sulfur under low oxygen pressure.

Mass independent isotope effects and separations in the laboratory

--*Nuclear spin effect.* In 1979, Galimov ([14]) pointed out that differences between isotopes of even and odd masses could lead to chemical isotope effects. He demonstrated the validity of his hypothesis by producing, in the laboratory, a huge ^{17}O enrichment effect (+ 13%) during oxidation of ethylbenzene with molecular oxygen. At the same time, ^{18}O underwent a negligibly small depletion. He established the validity of his hypothesis in the case of ^{13}C by several experiments, especially by showing that the recombining reaction accompanying the photochemical decomposition of dibenzyl ketone produced an enrichment in ^{13}C depending on the intensity of an external magnetic field.

--*Enrichment of isotopes in stratospheric atmospheres,* Experiences have been carried out in the laboratory in order to study reactions leading to anomalous effects (see ref vii).

--*Work on isotope separations* In 1989, Y Fujii et al. described excess enrichment of ^{235}U with respect to ^{238}U over a value interpolated from enrichments of ^{234}U and ^{236}U, during ion chromatography ([15]). At that time separation of strontium by ion exchange separation did not show anomalous isotope effects. In 1993, Nishizawa et al. trying to prepare Zinc free from ^{64}Zn, by complex formation with dicyclohexano-18-crown-6, found a larger isotope effect on ^{67}Zn than on Zinc isotopes of even masses([16]). In 1994 during extraction of strontium and barium using a crown ether([17]), isotopes of odd mass number behaved differently than those of even mass number. The odd/even effects were even larger than the unit mass enrichment factors. The latter were of different magnitude and opposite signs for strontium (- O.OOO9), and for barium (+ O.OO4). These differences were related to their concentrations in the aqueous phase. During extraction of magnesium chloride into an organic phase by the same crown ether ([18]), varying concentrations in the aqueous phase modified dramatically the absolute values and even signs of the unit mass enrichment factor and of the odd/even effect which was of same order of magnitude. Various similar extraction, or chromatography processes produce analogous effects on separations of isotopes of many even numbered elements (Mg, S, Ti, Fe, Ni, Zn, Sr, Zr, Mo, Br, Nd, Sm, Gd, Hf, U) (numerous recent papers, *passim,* by Fujii Y., Nishizawa K., Fujii T, al.)

--*Dimer effect:* Joyes et al.([19]) showed that, in mass spectra of liquids produced by emission, under the action of a strong electric field, from the Au-Cu tip of an

[13] Botter R. et al. **1966** *Advances in Mass Spectrometry vol.III;* (The Institute of Petroleum)

[14] Galimov E. M. *Geokhimiya* **1979** *N°2,* pp.274-284. Translated in *Geochem. Internatl.* **1979**, pp.155 - 163

[15] Fujii Y.et al. *Z. Naturforsch.***1989** *44a,* 395

[16] Nishizawa K. et al. *Solvent Extraction and Ion Exchange* **1993,** 11 (3), 389-394

[17] Nishizawa K. et al. *Solvent Extraction and Ion Exchange* **1994,** 12 (5), 1073 - 1084

[18] Nishizawa K. et al. *Separation Sci. And Technology* **1996** 31 (5) 643 - 654

[19] Van de Walle J. et al. *Phys. Rev;B* **1996** 54 (1) pp. 261 - 265

electrode, diatomic ions of polyisotopic elements like copper or germanium were exclusively monoisotopic.

Interpretations of non mass dependent effects

In the laboratory,

-- *Nuclear spin effects.* They were not considered in early calculations of isotope effects by Urey (i), because they did not contribute to distribution (partition) functions. Galimov discovered and interpreted their role. Some chemical processes, especially those involving radicals, are associated with changes in the electron spin of the system. Interaction between electron spins and nuclear spins can influence e.g. the energy of transition from triplet to singlet state. Hence differences in reaction rates or equilibria can occur between isotopes of odd (with nuclear spin) and even (zero nuclear spin) masses. Galimov (xiv) showed that nuclear spin, making a triplet singlet transition possible during oxidation of ethylbenzene with molecular oxygen, induced selectively an enrichment in ^{17}O, observed later in oxygen after decomposition, of the intermediate tetroxide. Such effects are difficult to observe in elements having only two stable isotopes, because they superpose with normal effects. This is why Galimov had to use discrepancies between theory and experiment, and the influence of an external magnetic field to establish their existence in the case of ^{13}C.

--*Other non mass dependent behavior*. On ^{235}U it was first thought by its discoverers to be a nuclear spin effect. Calculations by J. Bigeleisen ([20]) disproved this interpretation and related quantitatively these effects to the field shift. Isotope shifts in atomic orbitals result from changes in nuclear charge distributions $<r^2>$, i. e. nuclear size and shape. They affect the ground electronic energy of an atom or molecule. Initially they were thought to produce isotope effects only in heavy elements, those with the largest volume isotope effects. Effects during extraction by a crown ether were attributed, for strontium and baryum, to the larger stability constant of the aquo-complex for odd mass numbers. For magnesium it was considered that the ion pair electrons of the ligand coordinate to a vacant 3s orbital of the magnesium ion and form a sp orbital. The resulting energy shift for individual isotopes in the $3s3p - 3s^2$ transition, was a starting point for a qualitative interpretation.

Field shifts are now considered for every element. An example of evaluation of their contribution, and of that of the nuclear spin, is found in a recent study of zinc isotope fractionation using liquid chromatography with a cryptand ([21]). The isotopic effect on charge distribution, obtained from the literature, is added to ε's derived from equation (4). Scaling factors a and b are used to quantify each term:

$$\varepsilon_{m'm} = 1/T^2\delta m/mm'*a + 1/T\delta<r^2>mm'*b \quad (5)$$

Zinc has five stable isotopes of mass numbers 64, 66, 67, 68, 70; because of possible interferences with ^{64}Ni, ^{64}Zn is not used. Isotope effects on ^{68}Zn and ^{70}Zn respective to ^{66}Zn are free of nuclear spin effects. Their measure gives a and b.

[20] Bigeleisen J. *J. Am. Chem. Soc.* **1996**, *118* pp. 3676 - 3680

[21] Fujii T. et al; *Phys; Chem. Chem. Phys.* **2001**, *3*, pp. 3125-3129

Applying equation (5), the difference between calculated and measured effect gives the nuclear spin effect. on ^{67}Zn.

--*The dimer effect:* the exclusively monoisotopic character of dimer ions, emitted from an alloyed electrode under a high electric voltage, is not fully understood. It could result from a combination of the fact: that heteronuclear ions are more fragile than homonuclear ones, and that there is a stronger surface electric field around the alloy than around pure Cu ([22])

In Nature

-- M*eteorites* All oxides of meteorites have anomalous isotope abundances (in O, Ca, Ti, etc) they are usually assigned to nuclear processes. Thus the Clayton discovery was first related to nucleosynthesis. Now, considering later findings it may be better explained by mass independent effects of physical chemical origin than by nucleosynthesis. One of the reasons is that the latter involves mixing oxygen from two separate sources, where physical chemical exchange requires only one. Some authors question as well nuclear interpretations of other observations on meteorites

-- *On terrestrial samples* Mechanisms of mass independent isotope effect have been investigated for nearly 20 years, especially on ozone formation. No other effect has yet been reported that is not *in fine* due to reactions occurring initially in the atmosphere or stratosphere.

Outstanding work has been accomplished by several teams, and progresses achieved are reviewed by several authors ([4]), ([23]). However explanations do not meet yet complete consensus. Those based on considerations of differences of reaction probabilities due to differences in symmetry of monoisotopic and substituted molecules proved finally unable to explain observations quantitatively. In the latest theoretical treatment ([24]), the principal factor affecting the enrichments is a deviation from the statistical density of states of the ozone isotopomer itself which differs for vibrationally excited symmetric (XYX) as compared with asymmetric (XYZ) ozone molecules. Rate constants, in ozone formation reactions, using a slightly modified kinetic theory, and isotope enrichments, calculated from this starting point, very well agree with experiment. However adjustment of a parameter is necessary. A theory, based on the fact that the differential reaction cross sections could be different for distinguishable and indistinguishable isotopes, in molecules, agrees also with experimental results, but also requires adjustment of a parameter. Comparison of theories is underway by the authors of the latter ([25])

[22] Joyes P. *Personnal communication*

[23] Weston R. *Chem. Reviews* **1999**, *99*, pp.2115-2136
Thiemens M. H.*Science* **1999** *283*, pp.341-345, See also xvii

[24] Gao Y. Q.and Marcus R. A. *Science* **2001** *293* pp.259, 263, Thiemens M. *ibid.* p..226

[25] Robert F; *personnal communication*

Benefits of the study of mass independent effects

Let us first recall briefly benefits of the study of mass dependent isotope effects. that have been reaped for more than half a century;.

--*Results from nuclear origin* They provide firmly established informations. Decay schemes of more than twenty isotopes have been studied and put to use as geological clocks([26]). Ion probe ^{235}U and ^{238}U images of Oklo samples established the fate of plutonium that had completely decayed more than 1.5 billion years ago.

Isotopic analysis of lunar, and later martian samples, or of samples from meteorites, enable to evaluate exposure times to solar wind, to build nucleogenesis schemes, etc..

--*Effects of physical chemical origin* -- Mass dependent isotope effects provide data on a number of subjects in nature. The less important are not data on the evolution of climates obtained by isotopic analysis of cores from polar ice caps, or paleotemperatures from carbonates.

Benefits of non mass dependent effects. They provide unique information on atmospheric and stratospheric gases, not only on the much studied ozone problem, see (viii).

--For instance, at an altitude around 30 km, CO_2 possesses a large mass independent isotopic composition. The $\delta^{18}O$ of CO_2 provides an ideal tracer of atmospheric - stratospheric mixing.

--The recent study of archean sulfides comes in confirmation of the view that studies of non mass dependent effects are of considerable potential interest for geochemistry. The first authors studying sulfur isotope abundance in the formation of archean pyrites, found a range of δ's for ^{34}S, greater in archean pyrites than in magmatic H_2S ([27].). They concluded that instead of H_2S, bacterial reduction of oceanic sulfates had produced, even 3.4 billion years ago, the sulfur for pyrites. Later the work by Farquhar that revealed mass independent effects on both ^{33}S and ^{36}S, ([9]), ruled out that mechanism, because bacterial action can not lead to such mass independent effects, and disqualified that proof of existence of bacteria.

--The influence of nuclear spins on the behavior of isotopes of odd and even mass number has been amply examplified. And the theory of isotope effects has gained in sophistication, by taking into account the influence of nuclear size and shape.

-- Finally, the study of non mass dependent effects lead to refinements of reaction rates theories when calculating effects of molecular symmetry changes due to isotope substitutions..

Conclusion

-- Much work is still required before non mass dependent phenomena are well understood

---

[26] Roth. E., Poty B.(eds.) *Nuclear Methods of dating* **1989** Kluwer, *Method. Nucl. de Datation* **1985 Masson**

[27] Ohmoto H.et al.**1993** *Science 262* pp.555 – 557

-- Considering the wealth of information that non mass dependent effects may furnish, at least laboratories engaged in isotope geochemistry should be encouraged to analyse all the isotopes of elements under study. Especially work on atmospheric and stratospheric phenomena should continue.

--It might be worthwhile to investigate odd/even effects with the purpose of finding a large effect for production of isotopes of odd mass number. These isotopes, e. g. ^{43}Ca , could be used as spikes for medical diagnostics, because, using NMR, they could be followed in vivo and in situ, even when diluted by physiological processes; but their natural abundance being very low they must first be enriched. Up to now no method does it economically.

--To allow inter laboratory comparisons, laboratory reference materials should be accurately characterized with respect to international standards, and δ's carefully calculated.

STUDIA UNIVERSITATIS BABEŞ-BOLYAI, PHYSICA, SPECIAL ISSUE, 2001

MODES OF GUEST INCLUSION IN CYCLODEXTRINS IN THE SOLID STATE

MINO R CAIRA

Department of Chemistry, University of Cape Town, Rondebosch 7701, South Africa

ABSTRACT. As part of a systematic study of the modes of inclusion of organic guests in cyclodextrins in the solid state, some observations are presented which indicate the possibility of predicting inclusion complex structure from X-ray powder diffraction patterns alone. However, the occurrence of 'unusual' modes of guest inclusion, sometimes associated with novel crystal packing arrangements, emphasises the limitations of this approach to structure prediction.

INTRODUCTION

This paper addresses aspects of solid-state modes of inclusion of organic guest molecules in native cyclodextrins (α-, β- and γ-cyclodextrin, containing 6, 7 and 8 D-glucopyranoside residues respectively) as well as in some of their common methylated derivatives (e.g. heptakis(2,3,6-tri-O-methyl)-β-cyclodextrin or TRIMEB). Such hosts are commonly used to complex drug substances in order to enhance their solubility and chemical stability.[1] Extensive research on cyclodextrin (CD) inclusion has indicated that a prerequisite for formation of a stable inclusion complex is tight fitting of the guest in the hydrophobic host cavity and that this is determined essentially by geometric and steric factors.[2] Small guest molecules containing, for example, a substituted benzene ring are common complexing partners with α- and β-CD hosts owing to compatibility between their volumes and those of the respective host CD cavities. Such guests are also known to form complexes by inclusion in the larger cavity of γ-CD, but the fit is a much looser one as indicated by molecular modelling and confirmed by X-ray crystallographic analysis. Prediction of the mode of inclusion of a given guest in a given CD molecule requires consideration of other factors in addition to that of size compatibility. For example, regioselectivity of inclusion, referring to the entry of a guest 'head-first' or 'tail-first' into the CD cavity, depends to some extent also on mutual alignment of host and guest molecular dipole moments. Lipkowitz has recently reviewed the applications of computational methods to the prediction of inclusion modes of guests in CDs,[3] pointing out that while many studies have been successful, CD molecules are deceptively simple and that molecular modelling is hampered by the large number of internal degrees of freedom associated with the inclusion process. This is especially the case if induced-fit mechanisms are postulated. A critical summary of the *status quo* by Lipkowitz highlights the inadequacies of many modelling studies in their omission of solvent (either as discrete

molecules or as a continuum) or their reliance on computed energies of single minimized structures for comparison with experimental free energies. At the same time, it is emphasized that new developments in computational hardware and software together with their responsible application should improve the success rate in predicting modes of guest inclusion in CDs.

Our interest has focused on the mode of inclusion of drug guests in solid CD inclusion complexes since these species have been pursued as candidates for incorporation into solid drug dosage forms. Recent examples of drug guests investigated include cyclizine,[4] acetaminophen,[5] and (S)-naproxen.[6] Complete structural elucidation of such complexes by X-ray analysis has been a primary goal in our laboratory, not only for the purpose of providing unequivocal structural characterization of species intended for medicinal application, but also to contribute new insights as regards complex formation. Harata has recently reviewed crystallographic studies of cyclodextrins and their inclusion complexes.[7] He has emphasised the importance of X-ray diffraction as the primary source of detailed information regarding the nature of guest inclusion. We have followed Harata's recommendation that in order to gain a better understanding of complex formation, emphasis should be placed on the systematic crystallographic investigation of as many new inclusion complexes as possible.

This paper is divided into two parts. The first relates to a previous study which described the systematic classification of CD inclusion complexes into isostructural families, based on close similarities in powder X-ray diffraction (PXRD) patterns for the members of such a series.[8] Examples are presented here showing that within selected isostructural families there may be common features associated with the guest inclusion which can be quantified by simple geometrical parameters. The point that emerges is that for a newly prepared complex containing an analogous guest, it might thus be possible to make a more informed prediction of the mode of inclusion using information from the PXRD pattern only. In the second part of this paper, instances of guest inclusion are described which suggest that predicting the mode of guest inclusion is in general a difficult problem. Examples are described where X-ray structural studies reveal unusual modes of guest inclusion arising from an unexpected factor such as direct participation of water molecules in the host-guest binding or a special geometrical feature of the guest molecule which results in unusual host-guest stoichiometry.

Crystal isostructurality and trends in guest inclusion modes

A recent study[8] described a survey of crystal structures of parent CDs and their inclusion complexes lodged in the Cambridge Structural Database.[9] The single crystal data retrieved from the Database were used to compute PXRD patterns for parent CDs (both native and O-methylated), as well as their inclusion complexes with organic guests. Visual comparison of the computed patterns enabled their systematic classification into 17 isostructural series, each corresponding to a set of complexes with nearly equal unit cell dimensions, identical space groups and close correspondence of atomic co-ordinates of common CD atoms. Details for two of these series, in which the guests contain substituted benzene rings, are listed in Table 1. A specific isostructural series is characterized by remarkably similar PXRD patterns for its members. It was consequently possible to

generate an 'average' or 'reference' PXRD pattern for each of the 17 series. The utility of these reference patterns was illustrated[8] by demonstrating how visual matching of the PXRD patterns of putative CD inclusion complexes (prepared by kneading and co-precipitation techniques) with the references led to unequivocal proof of inclusion complex formation. This method of definitive characterization of CD inclusion complexes was recommended for routine use owing to the ease of recording a PXRD pattern.

The purpose of the above study was a pragmatic one, namely to exploit the isostructurality of known CD inclusion complexes solely in order to identify new species as genuine inclusion complexes. Little reference was made to the detailed modes of guest inclusion in the various isostructural series. It was, however, pointed out that the procedure yielded also crystal unit cell data and space group information. The significance of knowing the cell data and space group is that these parameters enable an accurate reconstruction of the crystalline host 'scaffolding' which accommodates the guest molecules and hence reveal channels or cavities with well-defined topology which could be used to model guest inclusion in the solid state. This point is not discussed further in the present report but instead we draw attention to similarities of guest inclusion modes associated with their isostructurality in the solid-state. This is described for the two series listed in Table 1.

Table 1

Cell data and geometrical parameters for inclusion in two isostructural series

Isostructural series 4.[8] Host: α-CD Complex space group: $P2_12_12_1$						
Guest	**a (Å)**	**b (Å)**	**c (Å)**	**Entering group**	**φ (°)**	***d* (Å)**
p-hydroxybenzoic acid	13.356	15.342	24.896	-COOH	83.8	-1.3
p-nitrophenol	13.455	15.296	24.740	$-NO_2$	80.6	-1.4
p-iodophenol	13.477	15.373	24.573	-I	81.3	-1.2
2-fluoro-4-nitrophenol	13.431	15.299	24.780	$-NO_2$	80.8	-1.3
p-iodoaniline	13.681	15.475	24.569	-I	89.0	-1.4
Isostructural series 15.[8] Host: TRIMEB Complex space group: $P2_12_12_1$						
p-iodophenol	14.997	21.368	28.205	-I	58.0	-2.2
(R)-flurbiprofen	15.092	21.714	28.269	$-C_6H_5$	63.7	-0.6
4-biphenylacetic acid	14.890	21.407	28.540	$-C_6H_5$	65.0	-0.6
(S)-ibuprofen	15.232	21.327	27.597	$-CH_2-CH(CH_3)_2$	69.1	-3.7
(S)-naproxen	15.179	21.407	27.670	$-OCH_3$	67.4	-1.9

The two parameters φ and *d* are defined here with respect to the mean plane through the six (α-CD) or seven (β-CD, TRIMEB) glycosidic oxygen atoms linking the glucose units in the host molecules (Fig.1). The first parameter refers to the angle between this plane and the plane of the guest phenyl ring while the second is the distance from the glycosidic oxygen atom plane to the center of gravity of the guest phenyl ring. The parameter *d* is a measure of the depth of guest phenyl ring penetration into the CD cavity and is positive if the center of gravity of the phenyl ring lies above the glycosidic oxygen atom plane toward the primary side of the macrocycle.

As shown in Table 1, for one series of α-CD inclusion complexes, the angle φ spans a fairly narrow range of 80.6-89.0° indicating a preference for the guest phenyl ring plane to parallel the pseudo-sixfold axis of the host as far as possible. As pointed out by Harata,[7] the diameter and depth of the α-CD cavity (~5Å and ~8Å respectively) are ideally

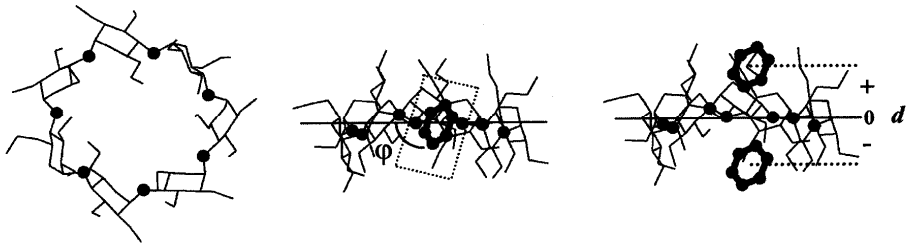

Fig.1 The geometrical parameters φ and d describing inclusion of a guest phenyl ring in TRIMEB. The left view is along the normal to the plane of the seven O atoms defining the reference plane.

suited to accommodate a benzene ring in this orientation. The centre of gravity of the phenyl ring invariably lies towards the secondary side of the host ($d < 0$) and d is fairly constant in this series despite some variation in those substituents which enter the cavity 'head-first'. In contrast, in the series of TRIMEB complexes listed, φ lies in the range 58.0-69.1°. This is again a fairly narrow angular range despite very significant variations in guest chemical structure and the nature of the entering group. The latter does however affect parameter d significantly. This parameter is close to zero only when the entering group is $-C_6H_5$. The host TRIMEB with its larger cavity size than α-CD is thus seen to allow significant tilting of the included phenyl ring. In addition, isostructurality in the above series of complexes is maintained even though there is considerable variation in the guest molecular bulk which protrudes from the host secondary side. The paucity of structural data for complexes in these isostructural series (Table 1) allows no more than indications of trends for guest inclusion. More crystal structure determinations are desirable for establishing firmer rules which could be used in a predictive fashion. Nevertheless, consideration of geometrical trends such as those indicated above may be useful and should be taken into account when attempting to predict the mode of guest inclusion using analogies based on isostructurality (i.e. using only the PXRD pattern of the complex).

An obvious limitation to the use of diffraction methods for predicting inclusion modes arises when the complex is amorphous. We recently reported the characterisation of an inclusion complex formed between a novel laurate salt of the bronchodilator albuterol (salbutamol) and hydroxypropyl-β-CD (HPBCD).[10] Due to their random degrees of substitution, CDs of this type generally do not form crystalline inclusion complexes. Inclusion of albuterol laurate within the cavity of a CD was found to be feasible by molecular modelling studies and the formation of a solid HPBCD complex was subsequently proven by a combination of techniques including thermal analysis and IR spectroscopy. Details of the mode of inclusion are, however, unknown.

'Unusual' modes of guest inclusion

Although it may be possible to derive predictive 'rules' of guest inclusion modes from trends observed for isostructural CD complexes, such rules can only be seen as guidelines. Various factors may intervene to produce a 'novel' inclusion mode (e.g. unforeseen participation of water molecules in the inclusion process). For new complexes whose PXRD patterns cannot be matched with those of established isostructural series,

prediction of the mode of guest inclusion is rendered more difficult and full X-ray analysis is necessary to settle the question. Examples in both categories are described here. The first example refers to the intervention of a water molecule as a bridge linking the host to an organic guest molecule. Water molecules are ubiquitous in crystalline cyclodextrin inclusion complexes of the native CDs. However, these water molecules are generally located outside the CD cavity and serve mainly as hydrogen bonding bridges between CD molecules. Methylated CDs and their complexes generally crystallize with few or no water molecules. Harata and co-workers reported that in the *p*-nitrophenol complex with permethylated α-CD, one water molecule is located within the CD cavity where it links the entering guest -OH group to two methoxy O atoms of the host via hydrogen bonding (Fig.2).[11]

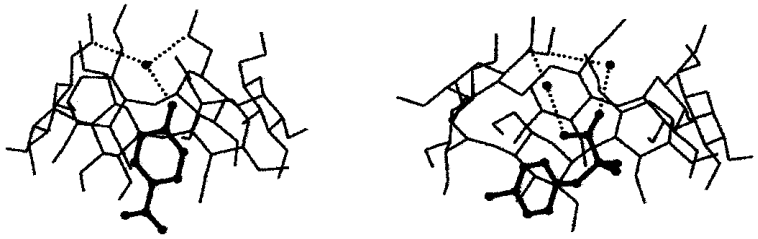

Fig.2 Left: Inclusion of p-nitrophenol in permethylated α-CD. Right: inclusion of clofibric acid in TRIMEB. Isolated circles represent water O atoms and dotted lines hydrogen bonds.

The water molecule plays a pivotal role in determining the guest inclusion mode in this case. We recently reported an analogous situation occurring in the TRIMEB complex of clofibric acid [2-(4-chlorophenoxy)-2-methylpropanoic acid].[12] This complex is isostructural with the TRIMEB-menthol complex.[13] We expected to find the more hydrophobic chlorophenyl residue inserting into the cavity and the hydrophilic -COOH group projecting from the host secondary side. (Precedents for this are e.g. the TRIMEB complexes of ibuprofen[14]and naproxen[6] where the -COOH group lies outside the secondary side of the CD molecule). Instead, for clofibric acid inclusion, the -COOH group enters 'head-first', each oxygen being hydrogen bonded to a water molecule which in turn is hydrogen bonded to a primary methoxy O atom of the host (Fig.2). These examples clearly vindicate the remarks of Lipkowitz[3] regarding the need to include water in molecular modelling of guest inclusion in cyclodextrins.

Unusual modes of inclusion may be associated with atypical host-guest stoichiometries arising from a special feature of the guest molecule. We recently reported the X-ray structure of a β-CD complex with cyclizine (1-diphenylmethyl-4-methylpiperazine, Fig.3a) which has a 4:3 host-guest (H:G) ratio[4] instead of the usual 1:1 ratio observed for β-CD complexes. PXRD showed that this complex did not belong to an established isostructural series and it was therefore necessary to determine the guest inclusion mode by full X-ray analysis. A possible explanation for a 4:3 H:G ratio is guest disorder with guest sites being partially occupied in the crystal. However, the β-CD complex with cyclizine is ordered and the guest sites are fully occupied. The structure is

based on two crystallographically distinct β-CD dimers, one of which contains two cyclizine molecules and the other only one, thus accounting for the 4:3 ratio. The guest molecule is bulky and cannot be completely encapsulated within the β-CD cavity. Invariably it is the methylpiperazine ring which inserts into the cavity leaving the bulky diphenylmethyl residue protruding from the macrocycle. Guest entry from both the primary and secondary sides characterizes the β-CD dimer containing two cyclizine molecules. The second host dimer contains only one cyclizine molecule which enters from the more favourable secondary side, leaving the other β-CD cavity empty, a most unusual structural feature. We have rationalised the formation of this 4:3 system on the basis of the known strong tendency for β-CD to form head-to-tail dimers in complexation and concluded that the resultant structure represents a compromise between an attempt to maintain a guest:cavity ratio as close to 1:1 as possible and the requirement of a stable crystal structure with the highest possible packing efficiency.[4] Cyclizine also forms a stable inclusion complex with γ-CD in which the H:G ratio is 3:1. The crystal structure has been elucidated despite the tendency for γ-CD complexes to be disordered.[7] This structure is tetragonal, space group $P42_12$, which is characteristic of all known γ-CD inclusion complexes.[8] Because the fourfold rotation axis coincides with the channel axis of the stacked γ-CD molecules, an included guest is invariably disordered unless it possesses inherent fourfold symmetry (e.g. 12-crown-4). The γ-CD complex structure was resolved by identifying the two N atoms of the methylpiperazine ring on the fourfold axis. Subsequent refienement enabled the placement of the phenyl rings in an arrangement consistent with the space group requirements. This represents a unique instance of successful crystallographic modelling of guest inclusion in γ-CD.[15] The mode of inclusion of cyclizine can be rationalised using a similar argument to that used to explain the formation of its β-CD complex.

Prediction of the mode of inclusion in a CD of a large or moderately large guest molecule is rendered difficult by the many possible degrees of guest conformational freedom. In solution, reaction of such a guest with CD molecules could yield one or more complex species with large H:G ratios associated with encapsulation of various guest hydrophobic residues in different host molecules. However, crystallization might favour one of the more common arrangements,[8] forcing the guest to fold into an unexpected conformation which can be fully encapsulated within e.g. a β-CD dimer. We recently elucidated the structure of such a complex in which the guest molecule consists of three rigid residues linked via four principal torsional degrees of freedom.[16] Initially, from PXRD it was deduced that this complex belonged to an existing isostructural series in which β-CD forms head-to-tail dimers, but it was difficult to reconcile the complexity of the guest molecule with this host arrangement. Full X-ray analysis subsequently revealed that in the complex, the guest adopts an unexpected U-shaped conformation, stabilised by intramolecular π···π interactions between the terminal residues, and in this way is fully accommodated within the β-CD dimer.

As a final illustration of sources of unusual modes of guest inclusion, we refer to complexes of acid salts, specifically those of alkali metal salts of non-steroidal anti-inflammatory drugs (e.g. diclofenac, meclofenamic acid, niflumic acid, Fig.3b,c,d). The

presence of metal ions and a carboxylate group may have profound effects on the guest inclusion mode compared with the situation involving the neutral guest. In cases we have investigated, such complexes are not isostructural with known series but instead have unique packing arrangements. For example, in the diclofenac sodium complex with β-CD,[17] strong hydrogen bonding between the carboxylate group and an oxygen atom of β-CD anchors the phenylacetate group to the host while the sodium ions link adjacent β-CD molecules by co-ordination to their respective oxygen donor atoms. This results in a complex crystalline structure with no precedent. The inclusion of the anion of niflumic acid in β-CD has recently been investigated, both in solution and in the solid state.[18] High-resolution nmr data revealed that the guest trifluoromethylphenyl residue is included in the host cavity, but no preference for entry from the primary or the secondary side could be discerned. The crystal structure of the β-CD complex with caesium niflumate shows that each β-CD cavity is simultaneously occupied by two trifluoromethylphenyl groups, one by guest entry from the primary side and the other by guest entry from the secondary side. This novel mode of inclusion is associated with a less common H:G ratio of 1:2 and a hitherto unknown crystal packing arrangement.

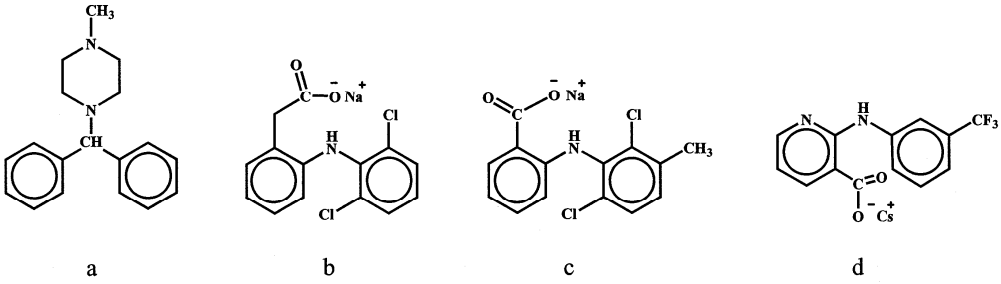

Fig.3 Chemical structures of cyclizine, and alkali metal salts of diclofenac, meclofenamic acid and niflumic acid.

Concluding remarks

Our studies on the isostructurality of CD inclusion complexes suggest that certain geometrical regularities of guest inclusion may be associated with specific isostructural series. This was illustrated with reference to complexes occurring in two such series. However a sufficient number of instances of 'unusual' modes of guest inclusion has been cited to indicate that prediction of the geometry of host-guest interaction in the crystalline state in general may be compromised by unforeseen factors. This underscores the statement of Lipkowitz that the cyclodextrins are deceptively simple molecules.[3] Our studies confirm the rich variety of structural possibilities these molecules present and with the accumulation of more X-ray structural data, we expect to encounter further novel modes of guest inclusion as well as new crystal packing arrangements.

Acknowledgements

We thank the University of Cape Town and the National Research Foundation (Pretoria) for financial assistance.

REFERENCES

1. K.-H Frömming and J. Szejtli, "Cyclodextrins in Pharmacy", Kluwer Academic Press, Dordrecht, 1998.
2. L. Szente, In "Comprehensive Supramolecular Chemistry", Eds. J. L. Atwood, J.E.D. Davies, D.D. McNicol and F. Vögtle, Pergamon Press, 1996, Vol.3, Ch.7, p.243.
3. K. B. Lipkowitz, *Chem. Rev.*, **1998**, *98*, 1829.
4. M. R. Caira, D. R. Dodds and L. R. Nassimbeni, *Supramol. Chem.*, **2001**, *13*, 61.
5. M. R. Caira and D. R. Dodds, *J. Incl. Phenom. Macro. Chem.*, **2000**, *38*, 75.
6. M. R. Caira, V. J. Griffith, L. R. Nassimbeni and B. van Oudtshoorn, *J. Incl. Phenom.*, **1995**, *20*, 277.
7. K. Harata, In "Comprehensive Supramolecular Chemistry", Eds. J. L. Atwood, J. E.D. Davies, D.D. McNicol and F. Vögtle, Pergamon Press, 1996,Vol.3, Ch.9, p.279.
8. M. R. Caira, *Rev. Roum. Chim.*, **2001**, in press.
9. Cambridge Structural Database and Cambridge Structural Database System, Version 5.18, October 1999, Cambridge Crystallographic Data Centre, University Chemical Laboratory, Cambridge, England.
10. M. R. Caira, D. R. Dodds and L. R. Nassimbeni, *J. Therm. Anal. Calorim.*, **2001**, submitted.
11. K. Harata, K, Uekama, M. Otagiri and F. Hirayama, *Bull. Chem. Soc. Jpn.*, **1982**, *55*, 3904.
12. M. R. Caira, S. A. Bourne and E. N. Mvula, *Biol. J. Armenia*, **2001**, in press.
13. M. R. Caira, V. J. Griffith, L. R. Nassimbeni and B. van Oudtshoorn, *Supramol. Chem.*,**1996**, 119.
14. G. R. Brown, M. R. Caira, L. R. Nassimbeni and B. van Oudtshoorn, **1996**, *26*, 281.
15. D. R. Dodds, PhD thesis: "Physicochemical Study of Inclusion of Drug Molecules in Cyclodextrins", 1999, University of Cape Town, South Africa.
16. M. R. Caira, E. J. de Vries and L. R Nassimbeni, **2001**, in preparation.
17. M. R. Caira, V. J. Griffith, L. R. Nassimbeni and B. van Oudtshoorn, *J. Chem. Soc., Chem. Commun.*, **1994**, 1061.
18. M. Bogdan, M. R. Caira and S.I. Farcas, **2001**, in preparation.

STUDIA UNIVERSITATIS BABEŞ-BOLYAI, PHYSICA, SPECIAL ISSUE, 2001

A GUIDED TOUR THROUGH THE SPIN DYNAMICS IN QUASI-ONE-DIMENSIONAL PLATINUM CONDUCTORS

L.V. GIURGIU

National Institute for Research and Development of Isotopic and Molecular Technologies, P.O. Box 700, R-3400 Cluj-Napoca 5, Romania, e-mail: giurgiu@L30.itim-cj.ro

ABSTRACT: We analyse the EPR linewidth in $Rb_2Pt(CN)_4(FHF)_{0,4}$ as a function of temperature. Above 60K the results are interpreted as a superposition of spin-phonon and spin-spin relaxation mechanisms.

The dominant contribution to the relaxation rate, $1/T_2$, has a dipolar origin in contrast to the spin-phonon origin observed in KCP(Br). This difference could arise from different anisotropy ratios of the transfer integrals. The influence of the inter-chain coupling is also discussed.

1.INTRODUCTION

Quasi-one-dimensional (Q1D) conductors have received much interest since the pioneering work by Krogmann [1] who suggested that mixed-valence planar d^8 metal complexes should exhibit 1D-metallic properties. The extensive research has been developed in systems containing square planar tetracyanoplatinate ion $[Pt(CN)_4]^{2-}$ which builds along the c axis of the crystal to form an infinite platinum atom chain with an overlap between the $5d_Z^2$ platinum orbitals [2]. The outstanding features associated with many Q1D molecular complexes are anisotropic physical properties, Peierls transition accompanied by a giant Kohn anomaly and a Frohlich charge density wave (CDW) [3].

Among the Q1D conductors $K_2Pt(CN)_4\ Br_{0,3}\cdot 3.2\ H_2O$,KCP(Br), is the most prominent example. The crystal structure consists of parallel linear metal strands with a Pt-Pt separation of about the same size as in Pt metal. The Coulombic inter-chain coupling takes place via the hydrogen bonded network of water molecules. Partial oxidation of the Pt ions from Pt^{2+} to $Pt^{2.3+}$ results in a partial depletion of the Q1D valence band which is characterized by an occupation number of 0.3 holes per Pt atom [4]. ^{195}Pt Mossbauer experiments suggest that all the Pt atoms are chemically equivalent and consequently the fractional valence charge is delocalized [5].

Unfortunately the platinum chains compounds family, which is very large, remains far less explored. The investigation of nearly similar compounds appears as a clue for understanding the effects of dimensionality on various physical properties. Therefore we will focus on anhydrous $Rb_2\ Pt\ (CN)_4\ (FHF)_{0,4}$,Rb CP(FHF), for the following reasons: (i) Despite a smaller inter-chain distance ($d_\perp$)than in KCP(Br), there is no coupling of adjacent chains by hydrogen bonding [6], (ii) The degree of partial oxidation, (DPO=0.40) is much larger than the characteristic one for KCP .This accounts for a shorter intra-chain

Pt-Pt separation ($d_{\|}$) compared with KCP(Br) and implies stronger Pt-Pt bonding [7]. (iii)The presumed linear bifluoride anions $(FHF)^-$ could produce a different random potential along the Pt-chains [8].

EPR spectroscopy offers the opportunity to study the magnetic interactions and to obtain informations about the spin-dynamics in Q1D conductors. Earlier EPR investigations of KCP(Br) have revealed the presence of bound d_z^2- like hole states associated with a valence band of d_z^2character [9,10].The temperature and the angular dependence of the EPR linewidth in the region above 100K were interpreted as a superposition of the spin-phonon and spin-spin relaxation component in Q1D within the framework of the mixed-valence model [10].

A theory of soliton formation in KCP(Br) and RbCP(FHF) within the one-electron approximation was proposed by us [11].Recently, we have analyzed the temperature dependence of the EPR linewidth in terms of motionally narrowed hyperfine interaction of an unpaired spin soliton delocalized over several platinum nuclei [12]. It has been shown that some of the relaxation and lineshape phenomena observed by NMR in KCP(Br) may be caused either by spin carrying solitons via hyperfine interaction or by spinless solitons via quadrupolar and chemical shift interactions [13].

In order to obtain further insight into the mechanisms responsible for the spin relaxation in Q1D platinum compounds, an EPR investigation of RbCP(FHF) single crystals was carried out. The results are compared with the previous reported ones for KCP(Br) and a discussion of the influence of inter-chain coupling is given.

2.EXPERIMENTAL

Single crystals of anhydrous RbCP(FHF) were obtained by an electrolytic procedure [14]. Lustrous metallic gold-colored crystals up to 3-4 mm in length were grown in this manner. X-ray diffraction analysis confirmed the body-centered tetragonal structure (space group I4/mcm) [7,8].

EPR measurements were carried out using a Bruker X-band spectrometer operating with a TE_{102} cavity. It is equipped with a helium gas-flow cryostat and a home-built 2-axis goniometer.

The lineshape has been found to be Lorentzian and nearly symmetric throught the investigated temperature range and for both orientations of the external field $B \| c$ and $B \perp c$, where c is the crystal axis of highest electrical conductivity). The almost symmetric shape for small single crystals proves a non-skin-depth limited lineshape.In order to evaluate the EPR-parameters the derivative spectra were fitted with the known Lorentzian lineshape, the fit parameters being the half-width at half-height (HWHH), $\delta B_{1/2}$ of the corresponding absorbtion line and the resonance field B_0 . The relaxation rate $1/T_2$ was calculated from $\delta B_{1/2}$ by means of the standard expression [15] .

3.COMPARISON BETWEEN 1D AND 3D CHARACTERISTICS OF RBCP(FHF) AND KCP(BR)

Apart from KCP(Br), no other platinum chain compound has been studied by a variety of complementary techniques. In this paper we present an EPR study of RbCP(FHF) and compare the results with the corresponding ones for KCP(Br). The

similarities and differences could be understood in terms of simple changes of the physical parameters, correlating well with expectations based on chemical arguments.

In the mean-field scenario, the Peierls instability leads to a second-orderphase transition (metal-insulator or semiconducting state) at the temperature T_P. When $T<T_P$ a fundamental instability will occcur in the sistem. A periodic lattice distorsion (PLD) results accompanied by a CDW. Also an energy gap, $2\Delta_0$ will appear in the electronic spectrum at the Fermi-vector k_F corresponding to a Fermi energy $E_F = \hbar^2 k_F^2 / 2m$,where m is a effective mass of the charge carriers [4].The Peierls gap gives rise to an activated electrical conductivity $\sigma_{\parallel}(T)$ along the Pt-chains.At high temperatures the lattice is undistorted and $\sigma_{\parallel}(T)$ appears to be rather temperature independent. The metallic conductivity, σ_m is shown in Table 1, together with the other relevant 1-D parameters for both RbCP(FHF) and KCP(Br).

Table 1.

One-dimensional parameters for the Q1D compounds RbCP(FHF) and KCP(Br)

Parameter	Unit	RbCP(FHF)	KCP(Br)
d_{II}	Å	2.798[7]	2.888[28]
$d_{\perp}$	Å	8.972[7]	9.906[28]
DPO	-	0.10[7]	0.30[28]
T_P	K	118[28]	400[3]
Δ_0	eV	0.018[28]	0.072[28]
k_F	(π/d_{II})	0.80[28]	0.85[28]
E_p	eV	2.80[28]	3.29[28]
σ_{max}	$\Omega^{-1}cm^{-1}$	1600-2300[24]	300-350[18,29]

In the real Q1D compounds the chains are not completely separated from one another but are present in a crystal lattice and there is, therefore, finite transverse electronic coupling between conducting chains. The 1D fluctuations at low temperatures will create correlated domains over fairly long parts of uncoupled chains. This introduce a 3D character into the system which suppresses fluctuations and leads to a phase transition at T_{3D}, often referred to as the transition temperature at which the Peierls instability manifests itself [3].Introducing a relative electronic transverse coupling constant η the dependence of T_{3D} on η has been computed by Horowitz et al.[16]

In principle one can determine η from the ratio T_{3D}/T_P and for smal η the following expression was derived [16]:

$$\eta = \frac{2.5(T_P / T_F)}{\ln(T_P / T_{3D})} \qquad \text{for } \eta \leq 4(T_P/T_F) \tag{1.}$$

The alternative way of deriving η comes from work of Soda et al. [17] where, assuming the electron transport by hopping, the ratio of the conductivity perpendicular and parallel to the c axis is given by:

$$\frac{\sigma_{\perp}}{\sigma_{\parallel}} = \eta^2 \left(\frac{d_{\perp}}{d_{\parallel}} \right)^2 \qquad (2.)$$

with interchain spacing $d_{\perp}$ and intrachain distance $d_{\parallel}$. The interchain coupling may occurs either through static coulombic coupling or by electron hopping from chain to chain depending on the chemical nature of the crystal lattice. The results concerning 3D characteristics are summarized in Table 2.

Table 2.

Three-dimensional parameters for RbCP(FHF) and KCP(Br).The upper and lower parts relate to the teoretical analysis [16] and conductivity data [17], respectively.

	RbCP(FHF)	KCP(Br)
T_{3D}	80 K [24]	100 K [24]
T_P/T_F	0.004 [24]	0.007 [18]
η	0.020 [18]	0.017 [18]
$\sigma_{\|\|}/\sigma_{\perp}$	—	10^4 [2]
$(d_{\perp}/d_{\|\|})^2$	10.28 [18]	11.77 [18]
η	—	0.003 [18]

The high DPO in RbCP(FHF) will result in a different degree of band filling and hence a different value of E_F and of the wavelenght of the associated lattice distorsion compared with KCP(Br) (Table 1). The much smaller value of the activation energy determined for RbCP(FHF) could indicate a weaker electron-phonon coupling. As one can see from Table 2, T_{3D} for the bifluoride complex will occur at lower temperature than in KCP(Br) because of the diminished coupling between the adjacent chains. In RbCP(FHF) $d_{\parallel}$ is ≅0,1A less in KCP(Br) and no hydrogen bonded network of water molecules exists between the platinum atom chains. Thus, the observed lowering of T_{3D} could confirm the suggestion that Coulombic inter-chain coupling is enhanced by the presence of a hydrogen bonding accros the conducting chains [18].Because of the lower T_{3D} value for RbCP(FHF) there is only a very limited temperature range available for studying the semiconductor region below T_{3D}.

One has to consider the above differences between RbCP(FHF) and KCP(Br) in determining the characteristic behaviour of the spin dynamics in Q1D platinum compounds.

4.SPIN RELAXATIONS IN Q1D PLATINUM COMPOUNDS

It is well established that the relative magnitude of the dominant processes causing spin relaxation, the spin-phonon and the spin-spin interactions, depends strongly on the dimensionality of the band structure [19,20].One can summarize the theoretical results in the following way.

The EPR linewidth is in principle a superposition of a spin-phonon and spin-spin contributions:

$$\frac{1}{T_2} = \frac{1}{T_2^{s-ph}} + \frac{1}{T_2^{s-s}} \tag{3.}$$

In isotropic metals, the former is caused by the spin-flip scattering of conduction electrons by acoustical phonons, Elliot mechanism, and the spin resonance is determined by the electron-phonon scattering rate [21].It was also shown that for a given scattering rate as determined from the transport properties and for a given spin-orbit coupling, the rate of spin-flip will be much smaller in 1D metals than in 3D systems [19].For systems with flat energy surfaces, it arises from the sharp reduction in one-dimension of the forward ($k \cong k'$) and backward ($k \cong - k$)scatterings. Deviations from this very small linewidth are allowed by the introduction of 3D character due to the interchain hopping motions of electrons.

The high anisotropy of the conductivity in Q1D compounds has an opposite effect on the spin-spin dipolar component of the linewidth. The effects of dimensionality on motional narrowing of dipolar broadening were investigated for magnetic insulators [22] and organic conductors [19].The result is the following: the anisotropy can significantly increase the dipolar linewidth i.e. 1D narrowing by spin diffusion is much less effective than 3D spin diffusion having the same correlation time.

The Q1D nature of platinum chain compounds has, therefore, two opposing effects on the effective linewidth: reduction of the rate of spin-phonon relaxation and enhancement of the dipolar contribution. Which mechanism dominates the linewidth will depend on the deviation of the Fermi surface from planarity and on the magnitude of the spin-orbit coupling.

In what follows we examine the spin-phonon and spin-spin relaxation rates in terms of the discussions given in [10,19].

4.1 SPIN - PHONON RELAXATION

A strong spin-orbit coupling, as evidenced in platinum compounds by the large anisotropy of g factor [9],contributes to the 3D spin-relaxation through the Elliot mechanism and the corresponding spin-phonon relaxation rate is given by

$$\frac{1}{T_2^{s-ph}} = a(\Delta g)^2 \tau_R^{-1} \tag{4.}$$

where Δg is the isotropic g - shift, a is a constant of the order of 1 or 30 in 3D metals and τ_R is the 3D scaterring time. Δg was evaluated to be of the order .$\Delta g \cong \lambda / \Delta E$ where λ is the spin-orbit coupling constant and ΔE the separation to the nearest band with the same transformation properties.

In Q1D case one could assume that τ_R^{-1} can be expressed [23] by

$$\tau_R^{-1} = \left(\frac{\nu_\perp}{\nu_\parallel} \right) \tau_\nu^{-1} \tag{5.}$$

where τ_ν is the scattering time which contributes to 1D conduction along the chains and $\nu_\perp$ and $\nu_\parallel$ are the inter and intra-chain hopping rates, respectively. If the golden rule applies [17], then

$$\nu_\perp = \frac{2\pi}{\hbar}\left|t_\perp\right|^2 N(E_F); \quad \nu_\parallel = \frac{2\pi}{\hbar}\left|t_\parallel\right|^2 N(E_F) \tag{6}$$

where $t_\perp$ and $t_\parallel$ are the transverse and longitudinal transfer integrals, respectively and $N(E_F)$ is the density of states at the Fermi surface. We would like to mention that due to the highly anisotropic nature of the d_{z^2} platinum orbitals, the overlap integral in the c axis direction, is $t_\parallel$ much bigger than $t_\perp$.

In terms of the above discussion, Eq. (4) becomes

$$\frac{1}{T_2^{s-ph}} = a\left(\frac{t_\perp}{t_\parallel}\right)^2\left(\frac{\lambda}{\Delta E}\right)^2 \tau_\nu^{-1} \tag{7.}$$

where

$$\frac{\nu_\perp}{\nu_\parallel} = \left(\frac{t_\perp}{t_\parallel}\right)^2 \tag{8.}$$

can be considered as the reduction factor of the parameter a due to the one-dimensionality.

The temperature dependence of $1/T_2^{s-ph}$ is attributed to that of τ_ν which can be derived from the longitudinal conductivity [17]:

$$\sigma_\parallel = \left(\frac{ne^2}{m^*}\right)\tau_\nu \tag{9.}$$

where n, e and m^* are the density of carriers, the electron charge and the effective mass, respectively. In the Peierls regime n is expressed by

$$n = n_0 \exp\left(-\frac{\Delta}{T}\right) \tag{10.}$$

where $n_0 = 0.4$ per Pt-ion corresponds toRbCP(FHF) and Δ is the activation energy.

In the metal-insulator transition regime of KCP(Br) it was found that $\sigma_\parallel(T)$ can be well approximated by an equation given as

$$\sigma_\parallel(T) \propto \frac{\exp(-\Delta/T)}{T^3} \tag{11}$$

Combining Eqs. (9) - (11) it results that τ_ν is proportional to T^{-3}.

The same behaviour holds for RbCP(FHF) in the temperature range 60 - 100K. A fit to Eq. (11) of the corresponding $\sigma_\parallel(T)$ data [24] results in $\tau_\nu = 4.5 \cdot 10^{-7}$ sec $\cdot K^3/T^3$

and Δ= 664 K ($\sigma_{\|max}$ = 2300 Ω^{-1} cm^{-1} and free electron mass were considered). It could be compared with the value of $3.2 \cdot 10^{-7}$ sec $\cdot K^3/T^3$ which was evaluated for KCP(Br) [10].

Therefore, the temperature dependence of the isotropic spin-phonon contribution to the linewidth, $1/T_2^{s-ph}$, can be rewritten as:

$$\frac{1}{T_2^{s-ph}} = C_1 T^3 \tag{12.}$$

where

$$C_1 = a\left(\frac{t_\perp}{t_\|}\right)^2 \left(\frac{\lambda}{\Delta E}\right)^2 (\tau_v T^3)^{-1} \tag{13}$$

4.2 SPIN - SPIN RELAXATION

It case of 3D conductors, the spin-spin correlation function decays exponentially with a correlation time τ_c and when the condition $\langle \Delta\omega^2 \rangle^{1/2} \tau_c << 1$ ($\langle \Delta\omega^2 \rangle$ is the second moment of the resonance line) is met, the lineshape is Lorentzian and the motionally narrowed linewidth is given by [25]

$$\gamma_{3D} = \langle \Delta\omega^2 \rangle \tau_c \tag{14}$$

Considering 1D systems in which the spin-spin correlation function obeys a diffusion equation, the narrowing process leads to a non-Lorentzian lineshape with a halfwidth of [22]:

$$\gamma_{1D} = \left(\frac{4}{3}\right)^{2/3} \langle \Delta\omega^2 \rangle^{2/3} \tau_c^{1/3} \tag{15}$$

Since the ratio γ_{1D}/γ_{3D} >>1 (where the same τ_c is considered), the narrowing mechanism is less effective in 1D than in 3D resulting in the enhacement of the dipolar contribution to the effective linewidth.

The influence of the inter-chain hopping rate on γ_{1D} has been investigated for Q1D conductors [19,20]. Depending on the magnitude of both γ_{1D} and $\nu_\perp$,three different regimes exist.Appropriate for our investigations is the case $\gamma_{1D}/\nu_\perp \approx 1$ (it will be justified a posteriori) which leads to a Lorentzian lineshape and the spin-spin relaxation rate expressed by [19]

$$\frac{1}{T_2^{s-s}} = \langle \Delta\omega^2 \rangle \bar{\tau}_c , \tag{16}$$

where $\bar{\tau}_c = (\tau_c/\nu_\perp)^{1/2}$ is the effective spin correlation time.

If the dominant contribution to the dipolar interaction is consideed totake place only along the Pt-chains and considering an axial symmetry for the g-tensor, the angular dependence of $\left\langle \Delta\omega^2 \right\rangle$ reads [10]

$$\left\langle \Delta\omega^2 \right\rangle = \frac{1}{\hbar}\frac{S(S+1)}{3}\left(\frac{2g_{\parallel}^2 + g_{\perp}^2}{2}\beta^2\right)\sum_j r_{ij}^{-6}\left(3\frac{g_{\parallel}^2}{g^2}\cos^2\nu - 1\right)^2 , \quad (17)$$

where

$$g^2 = g_{\parallel}^2\cos^2\nu + g_{\perp}^2\sin^2\nu \quad (18)$$

S is the spin of the magnetic ions, r_{ij} are the vectors connecting spins i and j and ν is the angle between the chain axis c and the magnetic field.

Within the framework of the mixed valence model where thermally excited carriers through a finite energy gap contributed to the magnetic properties, the temperature dependence of the mean distance of spins, $\bar{r}$ could be written as [10]:

$$\bar{r} = \frac{1}{n} = \left[\frac{0,4}{d_{\parallel}}\frac{\exp(-\Delta/T}{1+\exp(-\Delta/T)}\right]^{-1} \quad (19)$$

with n derived from Eq. 10.

Considering Eqs.(16)-(19) ,one arrives at the following expression for the temperature dependence of $1/T_2^{s-s}$

$$\frac{1}{T_2^{s-s}} = C_2\left[3\left(\frac{g_{\parallel}}{g}\right)^2\cos^2\nu - 1\right]^2\frac{\exp(-\Delta/T)}{1+\exp(-\Delta/T)} \quad (20)$$

where

$$C_2 = \frac{1}{\hbar^2}\frac{S(S+1)}{3}\left(\frac{2g_{\parallel}^2 + g_{\perp}^2}{2}\beta^2\right)^2\frac{0,8}{d_{\parallel}^6}\bar{\tau}_c \quad (21)$$

and $\bar{\tau}$ is assumed to be temperature independent.

Finally, the effective relaxation rate as a superposition of the two mechanisms of relaxation reads

$$\frac{1}{T_2} = C_1T^3 + C_2\left[3\left(\frac{g_{\parallel}}{g}\right)^2\cos^2\nu - 1\right]^2\frac{\exp(-\Delta/T)}{1+\exp(-\Delta/T)} \quad (22)$$

5. RESULTS AND DISCUSSIONS

EPR spectra were observed in the 30 - 90 K temperature range and can be interpreted by an axial-spin Hamiltonian with spin S = 1/2. At the lowest temperatures all electrons are expected to be in the CDW condesate and this could be the reason of the

complete vanishing of the electronic paramagnetism below 30 K. At high temperatures close to T_P = 118 K, the EPR signal fades out and its detection became difficult.

As in the case of KCP(Br) the anisotropic g - factor has an axial-symmetry with the major axis parallel to the c-axis. The principal g-values are consistent with those expected for the d_z^2 - like hole states mixed due to the spin-orbit coupling with the degenerate d_{xz} , d_{yz} states and are expressed by [26].

$$g_{\parallel} = 2N^2 - 3N^2(\lambda/\Delta E)^2$$

$$g_{\perp} = 2N^2 + 6N(\lambda/\Delta E) - 6N^2(\lambda/\Delta E)^2 \qquad (23)$$

where N is the normalization coefficient of the zero-order wave function following spin-orbit interaction λ is the spin-orbit coupling constant and ΔE is the energy separation between $a_{2u}(d_z^2)$ and the degenerate e_u (d_{xz}, d_{yz}) states.

The measured g values for RbCP(FHF) together with N and $\lambda/\Delta E$ parameters deduced by means of Eq.(23) are given in Table 3 and compared with corresponding KCP(Br) data [10].The results show that in both compounds the carriers are holes in d_z^2-like states. Since no temperature dependence of the g - factor can be observed in the limits of experimental accuracy (±0.002) the energy difference ΔE is temperature independent. It could means that the atomic displacements are not affected by the presence of localized anharmonic vibration modes, described by a generalized Morse potential [27].

Table 3.

Comparison between principal g values, N and $\lambda/\Delta E$ parameters (Eq.(22)) for Q1D platinum compounds

	RbCP(FHF)	KCP(Br)
$g_{\parallel}$	1.951	1.945
$g_{\perp}$	2.313	2.341
N	0.99	0.99
$\lambda/\Delta E$	0.063	0.068

The temperature dependence of the spin susceptibility, χ_s could be evaluated from the corresponding dependence of the EPR integral intensity I, as determined by double integration of spectra. In Fig.1, ln(I ×T) is plotted as a function of 1/T above 60 K. The fit of the data to the following equation

$$I = \text{const.}\frac{\exp(-\Delta/T)}{T} \qquad (24)$$

gives an activation energy of Δ= 305 K. It is smaller than the value obtained from $\sigma_{\parallel}(T)$ analysis (see Sec.4.1). The reason could be that one expects the conductivity to decrease as fast or faster than the spin susceptibility because any electron that can conduct can flip its spin but not vice versa. However the values of the activation energies should be treated with some reservation because of the narrow temperature range of the fits and the possible sample dependence.

We would like to mention that the experimentally observed trend of Δ decreasing from KCP(Br) ($\Delta \approx 501$ K) to RbCP(FHF) is a consequence of the increasing DPO and decreasing $d_{\|}$ in this series [24,28].

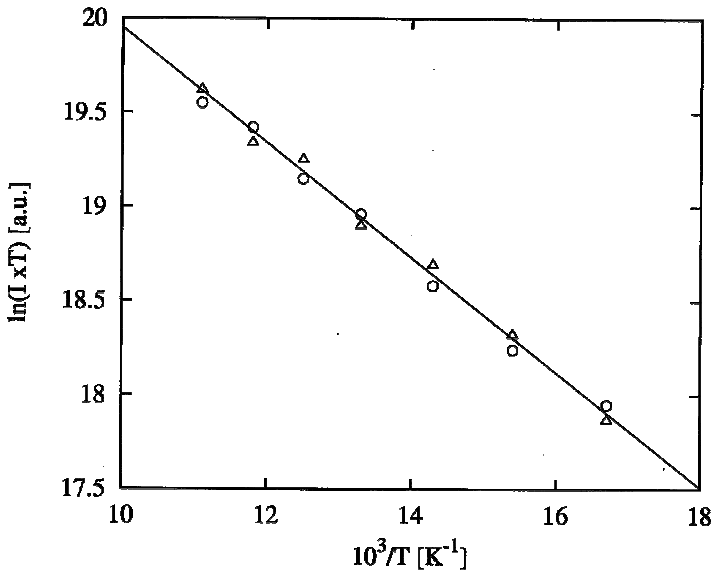

Fig. 1*. Temperature dependence of the EPR integral intensity.The straight line shows the best fit to Eq.(24).The relative intensity $I_{\perp}$ was normalised to the ratio $g_{\|}/g_{\perp}$ in order to compare with $I_{\|}$.*

With decreasing temperature the EPR linewidth in RbCP(FHF) decreases rapidly, goes through a minimum at $T_{min} \approx 55$K and than starts increasing. Such a behaviour was also observed for KCP(Br) where $T_{min} \approx$ 85K [9,10]. A comparison of the linewidths $\delta B_{1/2}$ as a function of temperature for RbCP(FHF) and KCP(Br) is shown in Fig.2.

As one can see, the temperature range where the resonances are observed for RbCP(FHF) is narrower than the corresponding one for KCP(Br) in accordance with the previously mentioned difference in the characteristic T_{3D} and T_P values between these compounds (Sec.3).

The temperature dependence of the linewidth in KCP(Br) was assumed to arrise from two competing processes which determine the linewidth minimum: a hole-phonon collision broadening and a motional narrowing at high and low temperatures, respectively [9].

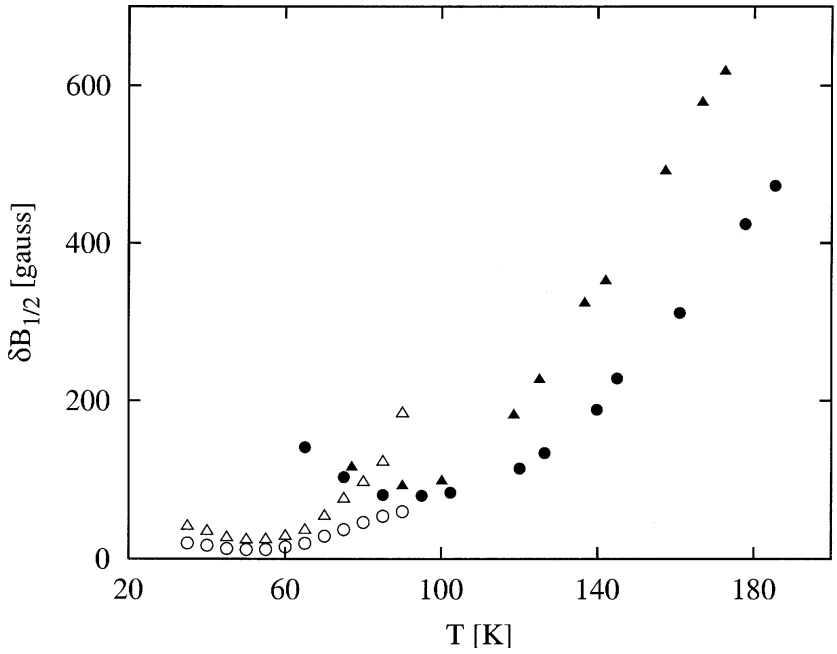

Fig.2 *Comparison of the temperature dependence of the experimental linewidths* $\delta B_{1/2}$ *with B || c (Δ) and B ⊥ c (o) for RbCP(FHF) (open symbols) and KCP(Br) (full symbols).The KCP(Br) data were taken from [9,10]*

In the following analysis we restrict ourselves to the high temperature regime above 60 K where EPR linewidth could be interpreted as a superposition of the isotropic spin-phonon and anisotropic spin-spin relaxation mechanisms as discussed in Sec.4. The temperature dependence of the effective relaxation rate, $1/T_2$, is shown in Fig.3 for both orientations of the external magnetic field. The fits to the data (solid lines) using Eq.(22) are consistent with the following parameters: $C_1 = (250 \pm 14)$ sec^{-1} K^3 and $C_2 = (18.8 \pm 0.9)$ $10^9 sec^{-1}$. Here we have taken $\Delta \approx 305K$ as resulting from the temperature dependence of the EPR integral intensity. These could be compared with the corresponding values of $800 sec^{-1}$ K^{-3} and 5.6 10^9 sec^{-1} reported for KCP(Br) [10].

Considering our results and making contact with Eq.(12) and (16), one has to conclude that the dominant contribution to the linewidth is of spin-spin origin (≈85%)

By using C_1 -value, $\lambda / \Delta E$ shown in Table 3, a ≈ 30 appropriate for alkali metals and τ_ν as evaluated before, one gets $\nu_\perp / \nu_\parallel = 0.945 \cdot 10^{-3}$ for the reduction factor due to the one-dimensionality. We estimate for the effective correlation time, $\bar{\tau}_c = (\tau_c \tau_\perp)^{1/2}$ a value of $1.6 \cdot 10^{-10}$ sec by means of Eq.(21) and C_2. Since τ_c is the correlation time of the dipolar field acting on an individual spin, one could consider τ_c as the intra-chain hopping time. This leads to $\bar{\tau} = (\nu_\parallel \nu_\perp)^{-1/2}$ which allows us to determine $\nu_\parallel$ and $\nu_\perp$ separately. The anisotropy ratio of the transfer integrals derived from Eq.(8) together with the inter and intra-chain hopping rates as resulting from the above analysis are given in Table 4 in comparison with KCP(Br) values [10] .

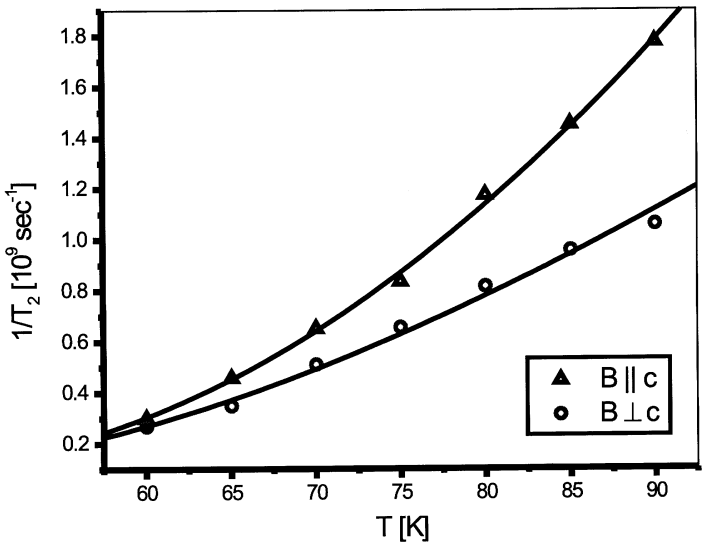

Fig.3 Temperature dependence of the experimental $1/T_2$ relaxation rates with B || c (Δ) and B ⊥ c (o) for RbCP(FHF).The solid lines represent the best fit to Eq.(22)

The finding that the spin-phonon relaxation mechanism does not dominate the relaxation rate, as it was the case for KCP(Br), is quite surprising. Since the spin orbit coupling and the scattering times are comparable the only justification for this difference is a reduced anisotropy ratio of the transfer integrals, $t_\perp / t_\parallel$ in RbCP(FHF) (Table 4). It could arise from two processes.

One might immediately think of a smaller $t_\perp$ - value because there is no coupling of adjacent Pt-chains by hydrogen bonded network of water molecules. A weaker interchain interaction in RbCP(FHF) than in KCP(Br) should result in a smaller hopping rate, $\nu_\perp$,

and exactly such a behaviour can be seen from Table 4. This will not only reduce the spin-phonon interaction but will increase the dipolar contribution. Next one has to consider that the shorter $d_{\|}$ (Table 1) implies a stronger Pt-Pt bonding which could increase $t_{\|}$.

Undoubtedly, our results are in agreement with the theoretical model of the linewidth dependence on dimensionality which for small $t_{\perp}/t_{\|}$ precludes the possibility that the spin-phonon contribution to the relaxation rate to be dominant . The significant increase of the dipolar linewidth can be related to a higher anisotropy in the band structure. It could imply that the band structure of RbCP(FHF) is more one-dimensional than the corresponding one for KCP(Br).

Tabel 4.

Experimentaly determined $t_{\perp} / t_{\|}$, $\nu_{\perp}$ and $\nu_{\|}$ values for RbCP(FHF) and KCP(Br) as discussed in the text.

	RbCP(FHF)	KCP(Br)
$t_{\perp}/t_{\|}$	0.030	0.043
$\nu_{\perp}$ $[\mathrm{sec}^{-1}]$	$1.9 \cdot 10^{8}$	$5.5 \cdot 10^{8}$
$\nu_{\|}$ $[\mathrm{sec}^{-1}]$	$2.1 \cdot 10^{11}$	$3.1 \cdot 10^{11}$

We would like to mention that a similar behaviour was found in organic conductors. Here, the spin-relaxation mechanism in TTF - halides and pseudohalides was shown to have a dipolar origin in contrast to the spin-phonon dominated linewidth in TTF-TCNQ [19]. The one-dimensionality of TTF-TCNQ is of the same order ($t_{\perp} / t_{\|} \approx 0.042$) as that of KCP(Br) [17].

We are ready now for justifying *a posteriori* the condition $\gamma_{1D} / \nu_{\perp} \approx 1$ used to derive the expression of the motionally narrowed dipolar line in the presence of the interchain coupling Eq.(11). Considering the estimated value of $\nu_{\perp}$ (Table 4) one gets $\gamma_{1D} / \gamma_{\perp} \approx 0.25$ and 1.4 at 60 K and 90 K, respectively. The condition $\left\langle \left(\Delta\omega^{2}\right) \right\rangle^{1/2} \tau_{c} << 1$ is also fulfilled in the measured temperature range.

6. CONCLUSIONS

The spin-relaxation mechanism and the influence of the inter-chain coupling were investigated by EPR in the anhydrous Q1D compound RbCP(FHF) and compared with KCP(Br). The g factor analysis shows that the carriers are holes in d_{z^2}- like states mixed with the degenerate d_{xz}, d_{yz} states through the spin-orbit coupling.

EPR linewidth can be measured in the temperature range between 30 and 90K and goes through a minimum at $T_{min} \approx 55K$ The temperature dependence of the effective relaxation rates, $1/T_2$ in the high temperature regime above 60K could be understood as a superposition of the isotropic spin-phonon and anisotropic spin-spin relaxation mechanisms. Taking into consideration the experimental results and theoretical analysis, the dominant contribution to the relaxation rate was found to have a spin-spin origin (≈85 %)

in contrast to the spin-phonon dominated linewidth observed in KCP(Br).This difference between the mechanisms of the relaxation could arise from different anisotropy ratios of the transfer integrals, $t_{\perp} / t_{\parallel}$, the one-dimensionality of RbCP(FHF) being higher than that of KCP(Br). A weaker interchain interaction (smaller hopping rate) due to the absence of coupling between Pt-chains by hydrogen bonding in RbCP(FHF) will reduce the spin-phonon interaction and increase the spin-spin contribution.

ACKNOWLEDGEMENT

L.V. Giurgiu gratefully acknowleges the financial support by the joint visiting scientist program of the Max-Planck-Institute and the University of Stuttgart.

REFERENCES

[1] Krogmann K.: Angew. Chem. Int. Ed. Engl. **8**, 35-42(1969)

[2] Zeller H.R.: Festkorperprobleme **13**, 31-58 (1973)

[3] Toombs G.A.: Phys. Rep**. 40**, 181-240 (1978)

[4] Krogmann K., Hausen H.D.: Z. Anorg. Allgem. Chem. **358**, 67-81 (1968)

[5] Ruegg W., Kuse D., Zeller H.R.: Phys. Rev. **B8**, 952-955 (1973)

[6] Williams J.M., Schultz A.J.: Molecular Metals, p.337-368, Hatfield W.E. eds, New York: Plenum Press 1979

[7] Williams J.M., Gerrity D.P., Schultz A.J.: J. Am. Chem. Soc**. 99**, 1668-1669 (1977)

[8] Schultz A.J., Coffey C.C., Lee G.C., Williams J.M.: Inorg. Chem. **16**, 2129-2131 (1997)

[9] Mehran F., Scott B.A.: Phys. Rev. Lett. **31**, 1347-1349 (1973)

[10] Takahashi T., Doi H., Nagasawa H.: J. Phys. Soc. Jpn. **48**, 423-429 (1980)

[11] Pana O., Giurgiu L.V., Mehring M.: Solid State Commun. **84**, 651-655 (1992) **; 119**, 553-557 (2001)

[12] Pana O., Kessler C., Filip C., Giurgiu L.V., Ursu I., Mehring M.: Appl. Magn. Reson. **12**, 247-253 (1997)

[13] Mehring M. in: Proc. VII AMPERE Summer School, p.211-215 , Portoroz, Slovenia 1992; Mehring M., Kanert O. Mali M., Brinkmann D.: Solid State Commun. **33**, 225-228 (1980)

[14] Coffey C.C., Williams J.M.:Inorg. Synth. **20**, 25-26 (1979)

[15] Poole C.P. Jr.: ESR - A Comprehensive Treatise on Experimental Techniques, 2nd edn., p.592, John Willey & Sons 1983

[16] Horovitz B., Gutfreund H., Weger M.: Phys. Rev. **B12**, 3174-3185 (1975)

[17] Soda G., Jerome D., Weger M., Alizon J., Gallice J., Robert H. Fabre J.M., Giral L.: J. Phys. **38**, 933-948 (1977)

[18] Karneiro K., Peterson A.S., Underhill A.E., Wood D.J., Watkins D.M., Mackensie G.A.: Phys. Rev. **B19**, 6279-6287 (1979)

[19] Tomkiewicz Y., Taranko A.R.: Phys. Rev. **B18**, 733-742 (1978)

[20] Tomkiewicz Y.: Phys. Rev. **B19**, 4038-4048 (1979)

[21] Elliott R.J.: Phys. Rev. **96**, 266-279 (1954)

[22] Hennessy M.J., McElwee C.D., Richards P.M.: Phys. Rev. **B7,** 930-947 (1973)

[23] Bloch A.N., Carruthers T.F., Poehler T.O., Cowan D.O.: Chemistry and Physics of One-Dimensional Metals, p.47-86, Keller H.J. eds., 1976

[24] Wood D.J., Underhill A.E., Schultz A.J., Williams J.M.: Solid State Commun. **30**, 501-504 (1979)

[25] Kubo R., Tomita K.: J. Phys. Soc. Jpn. **9**, 888-919 (1954)

[26] Krigas T., Rogers M.T.: J. Chem. Phys.**55**, 3035-3044 (1971); Giurgiu L.V., Nicula A. Studia Univ. Physica **2**, 63-67 (1978)

[27] DeAbreu C.D., Pinhal N.M., Vugman N.V.: J. Mag. Reson.**100**, 588-592, 1992

[28] Underhill A.E., Wood D.J., Carneiro K.: Synth. Met. **1**, 395-405 (1979/80)

[29] Bereblyum A.S., Buranov L.I., Khidekel M.D., Schegolev I.F., Yakimov E.B.: JETP Lett. **13**, 440-442 (1971)

COMPARISON BETWEEN WATER DISTILLATION PROCESS AND HYDROGEN ISOTOPE EXCHANGE PROCESS FOR DEPLETION AND ENRICHMENT OF TRITIUM IN LIGHT WATER

MASAMI SHIMIZU[*] and KENJI TAKESHITA[**]

[*] *Isotope Science Laboratory 1198 Issiki, Hayama, Kanagawa-ken 240-0111, Japan*
[**] *Dept. of Environmental Chemistry and Engineering, Tokyo Institute of Technology, 4259 Nagatsuda, Midori-ku, Yokohama 226-8502, Japan*

ABSTRACT. The dimensions of typical tritium separation processes, water distillation process and the hydrogen-isotope exchange process with hydrophobic Pt-catalyst, were evaluated numerically for the recovery of tritium from wastewater generated by the decommissioning of Magnox reactor. Both the column diameter and the column height required for the hydrogen-isotope exchange process were much smaller than these for the water distillation process. The application of hydrogen-isotope exchange process to the treatment of the tritiated wastewater is effective for not only the reduction of process dimensions but also the depression of energy consumption.

1. Introduction

When a 165-MWe Magnox reactor is decommissioned, a large amount of tritiated wastewater is generated by cutting the concrete and the steel structure of reactor [(1)]. Then, the quantity of tritiated wastewater and the content of tritium in the wastewater are given as 7600 m^3 and 2.2×10^{11} Bq, respectively [(1)]. If tritium is recovered by operating an appropriate separation process for 5 yrs and then the operating time of separation process per year is given as 8000 h/y, the waste water flow rate, F, and the tritium concentration of the waste water, x_F, are evaluated as

$$F = \frac{7600\times10^{3}\,\mathrm{kg}}{5\mathrm{y}\times8000\mathrm{h/y}}\times\frac{1}{18\mathrm{kg/kmol}} = 10.56\mathrm{kmol/h} \tag{1-1}$$

$$x_F = \frac{(2.2\times10^{11}\,\mathrm{Bq})(3.12\times10^{-10}\,\mathrm{m^3/Ci})}{(7600\mathrm{m^3})(3.7\times10^{10}\,\mathrm{Bq/Ci})} = 2.44\times10^{-13}\,\mathrm{T-atom\ fraction} \tag{1-2}$$

respectively. In this study, typical separation processes, the water distillation process and the hydrogen-isotope exchange process using Pt-catalyst, were applied for the recovery of tritium in the wastewater. The dimensions of these processes were evaluated numerically under the following same initial conditions,

- tritium concentration of T-enriched waste water : $x_p = 10^4 x_F = 2.44 \times 10^{-9}$ T-atom fraction

- tritium concentration of T-depleted waste water : $x_D \leq 1 \times 10^{-14}$ T-atom fraction.

Namely, the ratio of $(x_P / x_F) = 10^4$ and that of $(x_D / x_F) \leq (10^{-14}) / (2.44 \times 10^{-13}) = 0.041$. When tritium concentration of the waste water x_D is less than 10^{-14} T-atom fraction, the wastewater is dischargeable directly to the atmosphere. When either the water distillation process or the hydrogen isotope exchange process is applied for the recovery of tritium from the wastewater, it is necessary to remove the impurities in the wastewater as a pretreatment of the wastewater. In this study, the process dimensions will be evaluated for the wastewater without impurities.

2. Isotope Separation factors

Two isotope exchange reactions between hydrogen and tritium,

$$H_2O(g) + HT(g) \leftrightarrow HTO(g) + H_2(g) \tag{2-1}$$

$$H_2O(l) + HTO(g) \leftrightarrow HTO(l) + H_2O(g) \tag{2-2}$$

have to be considered for the numerical evaluation of proposed processes. In the previous papers [2),(3)], the isotope separation factor for Reaction (2-1), $\alpha_g^{H/T}$, is given as

$$\alpha_g^{H/T} = \frac{[HTO(g)][H_2(g)]}{[H2O(g)][HT(g)]} = \exp\{0.292 \cdot \log(t + 273) + \frac{336.5}{t + 273} - 1.055\} \tag{2-3}$$

and that for Reaction (2-2), $\alpha_l^{H/T}$, as

$$\alpha_l^{H/T} = \frac{[HTO(l)]}{[H_2O(l)]} \frac{[H_2O(g)]}{[HTO(g)]} = \frac{P_{H2O}}{P_{HTO}} = \exp\{-0.00791 - \frac{47.98}{t + 273} + \frac{23122}{(t + 273)^2}\} \tag{2-4}$$

where t denotes Celsius temperature. From Eqs.(2-2) and (2-4), the separation factors of $\alpha_g^{H/T}$ and $\alpha_l^{H/T}$ can be calculated as the function of temperature.

3. Water distillation process

Fig.3-1 shows the schematic description of water distillation process. Tritium is enriched at the bottom of column. The separation performance of tritium in water distillation column was described mathematically in the previous paper[4]. The ratios of tritium fraction between bottom and feed, (x_P/x_F) and that between top and feed, (x_D/x_F), are given as

$$\left(\frac{\chi_P}{\chi_F}\right) = \frac{(P/V) + (1 - \alpha_1)}{(P/V) + (1 - \alpha_1)(\alpha_1 / \gamma)^{M+1}} \tag{3-1}$$

$$\left(\frac{\chi_D}{\chi_F}\right) = \frac{(\alpha_1 / \gamma')\alpha_1(1 - 1/\gamma') + (\alpha_1 / \gamma')^{N+1}(1 - \alpha_1)}{(\alpha_1 / \gamma')^N \alpha_1(1 - 1/\gamma') + (\alpha_1 / \gamma')(1 - \alpha_1)} \tag{3-2}$$

respectively.

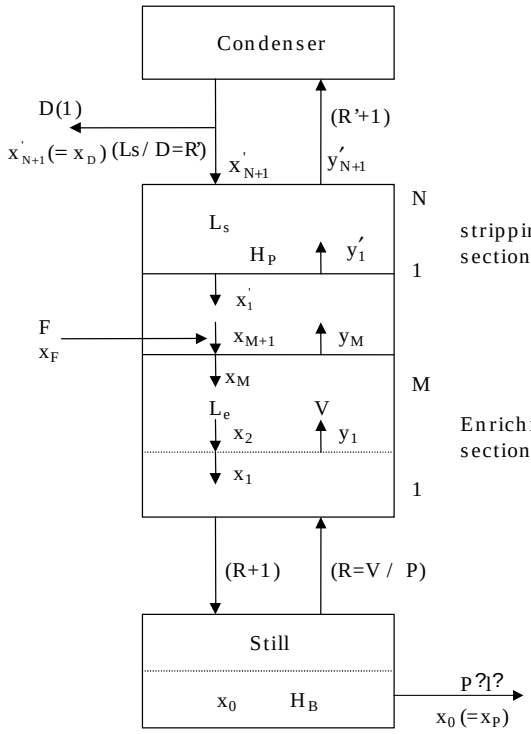

Fig. 3-1 Schematic description of water distillation column

In the conditions that the process is operated at 70°C, the separation factors are calculated as

$$\alpha_1^{H/T} = 1.062$$

and

$$\alpha_1 = 1/\alpha_1^{H/T} = 1/1.062 = 0.942$$

As shown in Eq.(1-2), the atom fraction of tritium in the feed solution is estimated as $x_F = 2.44\text{x}10^{-13}$. When the overall separation factor for the enrichment of tritium is given as10^4, the atom fraction of tritium in the production and the fraction ratio of (x_D/x_F) are given as $x_P = 2.44\times10^{-9}$ and 0.041, respectively, from the mass balance equations of tritium, $Fx_F=Px_P+Dx_D$ and F=P+D. Therefore, the molar flow rates of product water and stripped water are calculated as

$$P = F\frac{(x_F - x_D)}{(x_P - x_D)} = 10.56\text{x}(9.59\text{x}10^{-5}) = 1.013\text{x}10^{-3} \quad \text{kmol/h}$$

$$D = F - P = 10.56 - 1.013\text{x}10^{-3} = 10.559 \quad \text{kmol/h}$$

The molar ratio of the production flow to the vapor flow, (P/V), is given as

$$(P/V) = \frac{P}{D(1+R')}$$

where R' denotes the reflux ratio at the top of distillation column. The molar ratio of the production flow to the depletion flow is described as

$$(P/D) = \frac{1-(x_D/x_F)}{(x_P/x_F)-1}$$

from the overall mass balance equation of tritium. From (x_D/x_F)=0.041 and (x_P/x_F)=10^4,

$$(P/V) = \frac{1-0.041}{(10^4-1)}\frac{1}{(1+R')} = (9.591\times10^{-5})\frac{1}{(1+R')}$$

As shown in Appendix (A), the reflux ratio at the top of the distillation column, R', has to be given as more than 23.2. **Table 3-1** shows the relations among the reflux ratio (R'), the number of theoretical plates of the enriching section (M), the vapor flow rate (V) and the measure of process dimension (M·V), which were calculated from Eq.(3-1). The optimum reflux ratio, R', and the optimum number of theoretical plates of the enriching section, M, are evaluated as 24 and 170, respectively. Then, the number of theoretical plates of the stripping section, N, is given as 111 from Eq.(3-2) substituting γ ', which was calculated by the relation of $\gamma' = L_s / V = (D \cdot R') / [D(R'+1)]$.

When a commercial pack-ing, Sulzer Packing, was used in the distillation column, the HETP of distilltion column was reported to be 0.1m at the operating conditions that the column temperature is 70°C and the linear velocity of vapor is 1.0 m/s (op.c) [5]. Therefore, the heights of the enriching section and the stripping section are evaluated as 17m and 11.1m, respectively. As shown in Appendix (B), the cross-sectional area of the distillaion column, A, is calculated as 2.06 m^2 in the conditions of π=233.7 mmHg and V=264 kmol/h, as shown in Ref. (5). Thus, the column diameter, Di, is given as 1.62 m.. As the latent heat of evaporation, L, is given as 1.0×10^4 kcal/kmol at 70°C, the energy consumption for the phase conversion between liquid and vapor, C_{EV}, is calculated as 3062 kW from the relation of $C_{EV} = V \cdot L/860$ (1kw=860 kcal/h). The operating conditions and the calculation results were summarized in

Table3-1 The relations among the reflux ratio (R'), the number of theoretical plates of the enriching section (M), the vapor flow rate (V) and the measure of process dimension (M·V)

R' [-]	24	25	26
M [-]	170	169	168
V [kmol/h]	264	275	285
M·V [kmol/h]	4.49×10^4	4.65×10^4	4.79×10^4

Table 3-2 Summary of water distillation process

Operating temperature	70 °C	Remarks
Vapor pressure	233.7 mmHg	
$\sim^{H/T}$	1.062	
No.of Theor .. Plates M N (M+N)	 170 111 281	
H=(0.1)(M+N) [m]	28.1	HETP=0.1m [5]
u [m / s (op.c.)] F [kmol / h] V / F V [kmol / h] A [m²] D: [m] C_{EV} [kw]	1.0 10.56 25.0 264 2.06 1.62 3062	 Appendix(B) Appendix(B) Appendix(B)

Table3-2.

4. Hydrogen isotope exchange process

4-1 Separation system

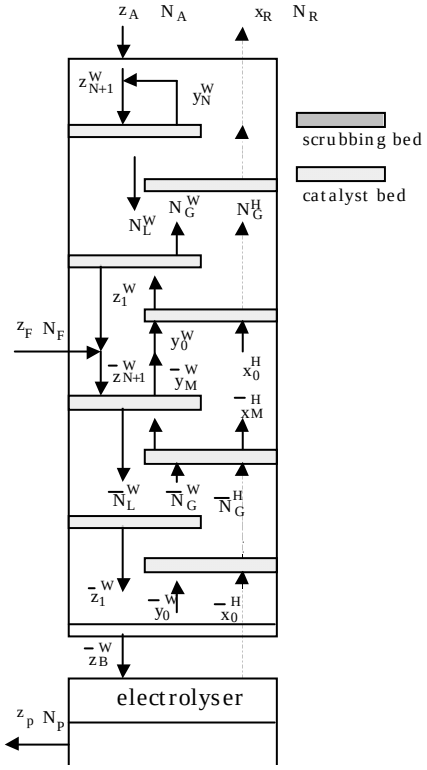

Fig.4-1 Schematic description of hydrogen-isotope exchange process

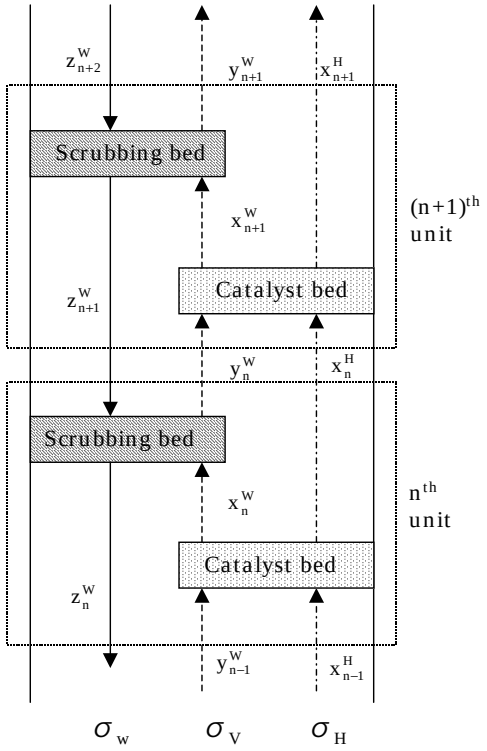

Fig.4-2 Schematic description of exchange column

Figures 4-1 and **4-2** show the hydrogen-isotope exchange process using Pt-catalyst, which consists of an exchange column with Pt-catalyst and an electrolyser. It should be noted that the process does not have a phase converter, H_2/O_2-recombiner at the top of column. Natural water is fed to the top of the exchange column and the tritium-depleted hydrogen gas is discharged to the atmosphere. The electrolyser plays a role as a phase converter, in which H_2O is decomposed electrochemically to H_2 and O_2. The hydrogen gas obtained is transferred to the bottom of exchange column. The exchange column has many units, which consists of a packed bed with a hydrophobic Pt catalyst and a scrubbing bed with a commercial packing, Dixon packing. The hydrophobic Pt-catalyst is a porous stylene-divinylbenzene copolymer impregnated with 0.5 wt% Pt (0.5wt% Pt/SDBC) and is 4 mm in diameter. Tritium is transferred from $H_2(g)$ to $H_2O(l)$ in the exchange column. The overall exchange reaction of hydrogen isotope can be described as

$$HT(g) + H_2O(l) \leftrightarrow H_2(g) + HTO(l) \tag{4-1}$$

The hydrogen-isotope exchange reaction between $H_2(g)$ and H_2O (v),

$$HT(g) + H_2O(v) \leftrightarrow H_2(g) + HTO(v) \tag{4-2}$$

takes place in the Pt-catalyst bed and that between H_2O (l) and H_2O (v),

$$HTO(v) + H_2O(l) \leftrightarrow H_2O(v) + HTO(l) \tag{4-3}$$

in the scrubbing bed. Tritium is enriched at the bottom of exchange column.

4-2 Numerical calculation of hydrogen-isotope exchange process

In the n-th unit, the exchange efficiency η_c of Pt-catalyst bed and the scrubbing efficiency η_b of scrubbing bed are defined as

$$\text{and} \qquad \eta_b = \frac{\chi_n^W - y_n^W}{\chi_n^W - (y_n^W)_e} \qquad\qquad \eta_C = \frac{\chi_{n-1}^H - \chi_n^H}{\chi_{n-1}^H - (\chi_n^H)_e} \tag{4-4}$$

respectively, where the suffix, e, denotes equilibrium. As seen in Figs.4-1 and 4-2, the relationships among x^H, y^W and z^W are obtained as follows,

$$\begin{aligned} x_n^H &= Ax_{n-1}^H + By_{n-1}^W \\ x_n^W &= Cx_{n-1}^H + Dy_{n-1}^W \\ y_n^W &= Ez_n^W + Fx_n^W \\ z_{n+1}^W &= Gz_n^W + Hx_n^W \end{aligned} \tag{4-5}$$

where the coefficients of A to H are defined as follows,

$$A = 1 - \frac{\alpha_g \eta_c}{\alpha_g + \gamma_g}, \quad B = \frac{\eta_c}{\alpha_g + \gamma_g}, \quad C = \frac{\alpha_g \gamma_g \eta_c}{\alpha_g + \gamma_g}, \quad D = 1 - \frac{\gamma_g \eta_c}{\alpha_g + \gamma_g}, \quad E = \frac{\eta_b}{\alpha_1 - \gamma_1 \eta_b},$$

$$F = (1 - \eta_b) - \frac{\gamma_1 \eta_b^2}{\alpha_1 - \gamma_1 \eta_b}, \quad G = \frac{\alpha_1}{\alpha_1 - \gamma_1 \eta_b} \quad \text{and} \quad H = \frac{-\alpha_1 \gamma_1 \eta_b}{\alpha_1 - \gamma_1 \eta_b}$$

Eqs.(4-5) are transformed to the following finite difference equation concerning x^H.

$$x_{n+3}^H + px_{n+2}^H + qx_{n+1}^H + r\,x_n^H = 0 \tag{4-6}$$

where, the coeficients of p, q and r deonte as p = – (A + DF + G), q = (ADF – BDF + AG + DFG + DEH) and r = (BC – AD)(FG – EH). The solution of Eq.(4-6) is given as follows,

$$x_n^H = K_1 g_1^n + K_2 g_2^n + K_3 g_3^n \ (n=0) \tag{4-7}$$

where, g_1, g_2 and g_3 denote the real roots of the following characteristic equation,

$$g^3+pg^2+qg+r=0 \tag{4-8}$$

K_1, K_2 and K_3 mean constants to determine the boundary conditions shown in the Section 4-3. By Combining Eqs.(4-5) with Eq.(4-7), the atom fractions of tritium in hydrogen gas, water vapor and water are given as

$$x_n^W = \sum_{i=1}^{3} Ki[C + \frac{D}{B}(g_i - A)]g_i^{n-1} \qquad (n\geq 1) \tag{4-9}$$

$$y_n^W = \sum_{i=1}^{3} Ki(\frac{g_i - A}{B})g_i^n \qquad (n\geq 0) \tag{4-10}$$

$$z_n^W = \sum_{i=1}^{3} \frac{Ki}{BE}\{(g_i - A)g_i - F[BC + D(g_i - A)]\}g_i^{n-1} \qquad (n\varepsilon 1) \tag{4-11}$$

The concentration profiles of tritium in hydrogen gas, water vapor and water of the stripping section of the multiunit hydrogen isotope exchange column are calculated by Eqs.(4-7) to (4-11). Similarly, these of the enriching section are calculated by the following equations,

$$\bar{x}_n^H = \sum_{i=1}^{3} \bar{K}_i \bar{g}_i^n \qquad (n\geq 0) \tag{4-12}$$

$$\bar{x}_n^W = \sum_{i=1}^{3} \bar{K}_i[\bar{C} + \frac{\bar{D}}{\bar{B}}(\bar{g}_i - \bar{A})]\bar{g}_i^{n-1} \qquad (n\geq 1) \tag{4-13}$$

$$\bar{y}_n^W = \sum_{i=1}^{3} \bar{K}_i(\frac{\bar{g}_i - \bar{A}}{\bar{B}})\bar{g}_i^n \qquad (n\geq 0) \tag{4-14}$$

$$\bar{z}_n^W = \sum_{i=1}^{3} \frac{\bar{K}_i}{\bar{B}\bar{E}}\{(\bar{g}_i - \bar{A})\bar{g}_i - \bar{F}[\bar{B}\bar{C} + \bar{D}(\bar{g}_i - \bar{A})]\}\bar{g}_i^{n-1} \tag{4-15}$$

where the bars on these symbols denote the enriching section.

4-3. Boundary conditions for calculation

The boundary conditions for the exchange column of Fig.4-1 were given as

$$(1) \quad \bar{z}_B^W(N_A + N_F) = z_P N_P + \bar{x}_0^H \bar{N}_G^H \tag{4-16}$$

$$(2) \quad \bar{z}_1^W = \bar{\gamma}_1 \bar{y}_0^W + (1 - \bar{\gamma}_1)\alpha_1 \bar{y}_0^W \tag{4-17}$$

$$(3) \quad \bar{x}_0^H = (1/\alpha_{El})z_P \tag{4-18}$$

for the enriching section and

(4) $$x_0^H = \bar{x}_M^H \quad (4\text{-}19)$$

(5) $$y_0^W = \bar{y}_M^W \quad (4\text{-}20)$$

(6) $$z_l^W N_L^W + z_F N_F = \bar{z}_{M+1}^W (N_L^W + N_F) \quad (4\text{-}21)$$

(7) $$x_F = \bar{z}_{M+1}^W \quad (4\text{-}22)$$

(8) $$z_{N+1}^W \cdot N_L^W = z_A \cdot N_A + y_N^W \cdot N_G^W \quad (4\text{-}23)$$

for the stripping section. Then, the separation factor of tritium in the water electrolysis, α_{El}, is 5.6 at 30℃[7]. The values of K_1, K_2, K_3, $\overline{K}_1$, $\overline{K}_2$ and $\overline{K}_3$ are calculated by way of the above boundary conditions and Eqs.(4-4) to (4-15).

4-4 Summery of calculation conditions and results

The calculation conditions and results were summarized in **Table 4-1**. The flow rate of natural water from the top of column, N_A, was assumed as a half of feed rate. Namely, the molar flow ratio, (N_A/N_F), was given as 0.5 instead of the minimum flow ratio, 0.183, which is required to

Table 4-1 Summery of calculation results

Item	Calculation conditions&results	Remarks
N_F[kmol/h]	10.56	
Z_F[T atom-fraction]	$2.44*10^{-13}$	$2.895*10^7$ Bq/m^3 water
N_A[kmol/h]	5.26	Assumed as half of feed rate
Z_A[T atom-fraction]	$2*10^{-17}$	Concentration of tritium in natural water
N_R[kmol/h]	15.84	
X_R[T atom-fraction]	$\leq 1*10^{-14}$	Dischargeable directly to the atmosphere
N_p[kmol/h]	$1.03*10^{-3}$	
Z_p/Z_F	$1*10^4$	Enrichment factor of tritium
P[mmHg]	760	Operating preasure
t°C	70	Operating temperature
U_g(H+V)[Nm/s]	0.6	(H_2+vap.) gas velocity
η_c[-]	0.9	Ref.(8)
η_b[-]	0.9	Ref.(8)
H_g[m]	0.1	Height of catalyst bed
H_l[m]	0.15	Height of scrubbing bed
n_E	13.8	No. of unit in enriching section
n_S	7.7	No. of unit in stripping section
H_E[m]	4.14	Height of enriching section. Height of unit is assumed as 0.3 m/unit.
Hs[m]	2.31	Height of stripping section. Height of unit is assumed as 0.3 m/unit
D_{ex}[m]	0.55	Eq.(4-24)
V_{cat}[m^3]	0.57	Eq.(4-25)
C_{EL}[kw]	1774	Eq.(4-26)

obtain the enrichment factor of 10^4. The column diameter (D_{EX}), the total volume of Pt-catalyst (V_{cat}) and the energy consumption of electrolyser (C_{EL}) were evaluated as

$$D_{EX} = \left\{ \frac{(N_F + N_A - N_P)(22.4)(\frac{\pi}{\pi - p_{H2O}})}{3600 \cdot u_{g(H+V)}(\frac{3.14}{4})} \right\} \quad [m] \quad (4\text{-}24)$$

$$V_{cat} = H_g(n_E + n_S)(D_{EX}^2)(3.14/4) \quad [m^3] \quad (4\text{-}25)$$

$$C_{EL} = N_R \cdot 22.4 \cdot \kappa \quad (\kappa = 5kwh/Nm^3 - H_2) \quad [kW] \quad (4\text{-}26)$$

5. Conclusion

Table 5-1 shows the comparison of calculation results between the hydrogen-isotope exchange process and the water distillation process. It is found that the diameter and height of hydrogen-isotope exchange process are much smaller than those of water distillation process and the energy consumption of elecrolyser is reduced to about 55% of that of still of water distillation process. It is concluded that the hydrogen-isotope exchange process is suitable for the treatment of tritiated wastewater generated by the decommissioning of Magnox reactor.

Table 5-1. Comparison between hydrogen-isotope exchange process and water distillation process

F or NF [kmol/h]	10.56		Feed flow
XF or ZF [T atom fraction]	$2.44*10^{-13}$		Tritium in feed
R' or γ_A[-]	R'=L_S/D=24	γ_A =N_A/N_F=0.5	Reflux ratio
D or N_R [kmol/h]	D=10.559	N_R=15.839	Depleted flow
x_D or x_R [T-atom fraction]	x_D 10^{-14}	x_R 10^{-14}	Release to atmosphere
N_A [kmol/h]		5.28	
z_A [T-atom fraction]		$2*10^{-17}$	Tritium in Natural water
P or N_P [kmol/h]	P=$1.01* 10^{-3}$	N_P=$1.03\ 10^{-3}$	Production
x_P/x_F or z_P/z_F	$1*10^4$		Enrichment factor
(Operating conditions)			
Pressure [mmHg]	233.7	760	
Temperature (°C)	70	70	
u_V or $u_{g(H+V)}$	u_V=1.0 m/s (op.c)	$u_{g(H+V)}$=0.6 Nm/s	
(Operating constants)			
HETP [m]	0.1		
η_c [-]		0.9	Sulzer packing (Ref.5)
η_b [-]		0.9	Ref.8
Hg [m]		0.1	Ref.8
Hl [m]		0.15	Ref.8
(Results of calculation)			
No of theor. plates	281		M=170 N=111
No of units		22	n_e=14 n_s=8 units
Height of Colum [m]	28.1	6.6	Height of unit=0.3 m
Diameter of Column [m]	1.62	0.55	App.(B), Eq(4-24)
V_{cat} [m3]		0.57	Eq(4-25)
C_{EV} or C_{EL} [kw]	3062	1774	App(B), Eq(4-26)

Appendix (A) Reflux ratio, R', at the top of the water distillation column

From Eq.(3-1), the following equation

$$\left(\frac{\alpha_1}{\gamma}\right)^{M+1} = \frac{\left(P/V\right)\left(1-x_P/x_F\right)+\left(1-\alpha_1\right)}{\left(x_P/x_F\right)\left(1-\alpha_1\right)} \qquad \text{(A-1)}$$

is obtained. As $(\alpha_1/\gamma)^{M+1}$ is positive, the numerator of Eq.(A-2)

$$\left(\frac{P}{V}\right)\left(1-\frac{x_P}{x_F}\right)+\left(1-\alpha_1\right)>0 \qquad \text{(A-2)}$$

has to be positive. From the mass balance equation, (P/V) is expressed by

and $(1-\alpha_1)$ is $\left(1-\alpha_1\right)=\left(1-\frac{1}{1.062}\right)=0.058$

$$\left(\frac{P}{V}\right)=\frac{1-\left(x_D/x_F\right)}{\left(x_P/x_F\right)-1}\bullet\frac{1}{\left(1+R'\right)}$$

From these results, the limitation of reflux ratio, R', is given as

$$R'>23.17 \qquad \text{(A-3)}$$

Appendix (B) Cross-sectional area of distillation column

The cross-sectional area of distillation column can be calculated by

$$A=\frac{(V)(22.4)\left(\frac{P_{H2O}}{\pi}\right)\left(\frac{273+t}{273}\right)}{(3600)\cdot u_v} \qquad [m^2] \qquad \text{(B-1)}$$

When u_V = 1.0 m / s (op.c)[5] for Sulzer Packing (op.c) ,

$$A\approx\left(\frac{V}{u}\right)\left(\frac{P_{H_2O}}{\pi}\right)(273+t)\left(2.27920\times10^5\right) \quad [m^2] \qquad \text{(B-2)}$$

The column diameter calculated from Eq.(B-1) was shown in **Table B-1**.

Operating pressure π [mmHg]	233.7	Remarks
Operating Temperature t [°C]	70	
Vapor flow rate V [kmol/h]	264	
Vapor superficial velocity uV [m/s (op.c)]	1.0	Reference (4)
Sectional area A [m^2]	2.06	Eq. (B-1)
Diameter of column Di [m]	1.62	

Table.B-1 Evaluation of column diameter, Di, by Eq.(B-1)

SYMBOLS

P : T-enriched water flow rate [kmol / h]
V : Vapor flow rate [kmol / h]

γ : flow ratio = Le / V

γ ':flow ratio = Ls / V

Le, Ls : Flow rates of water in the enriching section and stripping one [kmol /h]
M, N : Numbers of theoretical plate in enriching section and stripping one [-]

x_n^H, x_n^W, y_n^H and z_n^W : T-atom fractions of hydrogen and water vapor leaving the n^{th} catalytic bed and those of water vapor and liquid leaving the n^{th} scrubbing bed respectively [-]

$\gamma_g = \sigma_H / \sigma_V = (\pi - P_{H2O}) / P_{H2O} \quad \gamma_l = \sigma_V / \sigma_W$

$\alpha_g = \alpha_g^{H/T} \quad \alpha_l = \alpha_l^{H/T}$

σ_H, σ_V and σ_W : Hydrogen, water vapor and water liquid flow rate [kmol / m^2h]

REFERENCES

(1) Proposal of Fuji Electric Co.Ltd (1997)

(2) J.F.Black : J.Chem.Phys , 11 , 395 (1943)

(3) M.M.Popov : Atom Energ. SSSR , 8 , 420 (1960)

(4) M.Shimizu and S.Hibino : Some Analyses on the Operation of Water Distillation Column , Nippon Genshiryoku Gakkaishi (Japanese) 4 , 313 (1962)

(5) M.Asahara : Hydrogen Isotope Separation by Water Distillation , “Separation of Deuterium and Tritium “ ed.by Nakane , Isomura and Shimizu (in Japanese) , Gakujyutsu – Shuppan Centre (Japan) , 1982.

(6) M.Shimizu , T.Doi , A.Kitamoto , and Y. Takashima : Numerical Analysis on Heavy Water Separation Characteristics for a pair of Dual Temperature Multistage-Type H_2/H_2O-Exchange Columns , J. of Nucl. Sci. Technol. 17 , 448 (1980)

(7) K.Takeshita, Y.Wei, M.Shimizu, M.Kumagai and Y.Takashima: Application of H_2/HTO-Isotopic Exchange Method to Recovery of Tritium from Waste Water generated in Spent Nuclear Fuel Reprocessing Plant , Fusion Technol. 28 , 1572 (1995)

(8) Private communications on the design data and the operating performance of the IPCR-PNC type tritiated D_2O upgrader in the Fugen site.

STUDIA UNIVERSITATIS BABEŞ-BOLYAI, PHYSICA, SPECIAL ISSUE, 2001

THE IMPORTANCE OF HAVING DIFFERENT ISOTOPES IN NMR/NQR STUDIES

DETLEF BRINKMANN

Physik-Institut, University of Zuerich, CH-8057 Zuerich, Switzerland

ABSTRACT. The paper reviews some less known but representative examples where the NMR study of two isotopes of the same element yields important information on very different characteristic features of the compound. We will discuss the following examples: (i) Determination of the type of molecular movements of a transient Xe molecule in the gas phase (by using the Xe isotopes ^{129}Xe and ^{131}Xe). (ii) Classical nature of the isotope effect of the Li diffusion coefficient in Li metal (^{7}Li and ^{6}Li in solid Li). (iii) Dynamics of Cu-O chains in a high-temperature supercon-ductors (^{63}Cu and ^{65}Cu). (iv) Isotope shift of the opening temperature of the spin gap in the superconductor $YBa_2Cu_4O_8$ using ^{16}O and ^{18}O exchanged samples; in this example only one NMR isotope, ^{63}Cu, is studied.

1. Introduction

Nuclear Magnetic Resonance (NMR) is essentially a nuclear Zeeman effect, *i.e.* the splitting of the magnetic energy levels of magnetic nuclei in a static magnetic field. Applying a radio-frequency field at the proper frequency induces transitions between these levels and gives rise to an NMR signal. Each stable element of the periodic table (except for Ar and Tc) has at least one isotope which possesses a nuclear magnetic dipole moment and hence can be employed in an NMR experiment. This fact gives rise to the power of NMR as a spectroscopic tool which allows one to study static and dynamical aspects of materials in all phases (gas, liquid, solid) at the atomic level.

As an additional "gift by nature", 36 chemical elements have even several magnetic isotopes, *e.g.* H, Li, B, N, Cl, K, Cu, Xe, Ba. Furthermore, there are 62 elements which posses at least one isotope having a nuclear quadrupole moment and thus, in addition to NMR, allow Nuclear Quadrupole Resonance (NQR) experiments.

Given this rich supply of isotopes, no wonder that chemical compounds with different isotopes of the same element, for instance H_2O and D_2O , play an important role in NMR studies. Well known are the structural investigations in liquids by NMR (high-resolution NMR) where, *e.g.*, hydrogen is replaced by deuterium if a certain bond is of special interest. The hydrogen bond studies in ferroelectrics using also deuterium substitution are a typical example from solid state physics.

In our review, we will present less known but representative examples where the NMR study of two isotopes of the same element yields important information on very different characteristic features of the compound (structure, dynamics *etc*.).

2. Transient Xe molecules in Xe gas

Xenon has two nuclear magnetic isotopes, ^{129}Xe with nuclear spin I = 1/2 and ^{131}Xe with I = 3/2. If xenon gas can be regarded as an one-atomic and diamagnetic gas, the interaction between the nuclear moments is the only mechanism for spin-lattice relaxation. This is the process which brings the spin system into thermal equilibrium with its surroundings, the "lattice"'. In other words, this relaxation changes the nuclear magnetization that is *parallel* to the external magnetic field. The process is brought about by local magnetic fields which fluctuate at the Larmor frequency; the time constant of the process is called spin-lattice relaxation time, T_1.

In the case of the simple xenon gas, one calculates a relaxation rate of

$$\frac{1}{T_1} = \frac{2\gamma^4 \hbar^2 n}{R^4 < v^2 >}$$

where γ is the gyromagnetic ratio, R is the atomic diameter, n is the number of atomic collisions per time unit, and $< v^2 >$ is the mean quadratic molecular velocity. For the ^{131}Xe isotope in xenon gas with a pressure of about 8 MPa, one calculates $T_1 = 10^7$ s compared to an experimental value of about 10^{-2} s [1,2].

The discrepancy is resolved if one considers an additional and very powerful relaxation mechanism: the interaction between the ^{131}Xe nuclear electric quadrupole moment and the fluctuating electric field gradients created during a molecular collision and being present at the nucleus. But what about the ^{129}Xe isotope which lacks a quadrupole moment because of its I = 1/2 and where one measures T_1 values of the order 10^3 s [2]? The solution had been found by [3]. He employed for his calculation a density-proportional "chemical shift" of the Xe resonance found by Carr and his associates [4,5]. Torrey used this shift as a means of calibrating the spin-rotational coupling which exists in a *diatomic* xenon system during *collisions* of xenon atoms. Torrey showed that diatomic xenon molecules are less effective than atomic collisions in producing relaxation.

3. Isotope effect of the Li diffusion coefficient in Li metal

Due to the lack of a suitable isotope, self-diffusion in lithium cannot be studied by the common radioactive tracer technique, hence measurements so far of the tracer self-diffusion coefficient D^T have been carried out only by mass spectroscopy of the stable isotopes ^{6}Li and ^{7}Li. There are, however, several determinations of the macroscopic self-diffusion coefficient D^{SD} from measurements of the NMR spin-lattice relaxation times. In all these studies one primarily obtains the Li hopping rates and determines D^{SD} via the Einstein diffusion equation. D^{SD} does not include the effect of spatial correlation of successive jumps and differs from D^T by the correlation factor f.

We have performed the first direct measurement of Li diffusion coefficients D^{NMR} in solid Li [5] by the NMR pulsed magnetic field gradient (PMG) technique [6]. The PMG method differs from the tracer technique with respect to the following points: (i) In the PMG method, it is the nuclear magnetic moment rather than radioactivity or mass that labels those atoms whose diffusion is studied; (ii) the labelled atoms are "natural" constituents of the solid and are not artificially introduced; (iii) the

energies dissipated on the atomic scale during the PMG experiment are totally negligible; (iv) the experiment itself is non-destructive. The PMG method therefore allows one to measure either the true self-diffusion coefficient, *i.e*. the isotope under observation has the same mass as the atoms of the crystal (for instance the diffusion of ^{7}Li in pure ^{7}Li metal), or impurity diffusion where a solute species such as ^{7}Li diffuses in a ^{6}Li matrix. The PMG method which we have employed in several diffusion studies of superionic conductors [7] yields the diffusion coefficient in a straightforward way without any *apriori* knowledge of the diffusion mechanism. Since the PMG method and tracer techniques essentially measure the same physical quantity defined via Fick's first law, we do not distinguish between D^{NMR} and D^{T} any more and denote both by D for short.

We have measured D for both ^{6}Li and ^{7}Li in three samples differing by their isotopic composition. This allows us to check the isotopic dependence of the diffusion coefficient and to settle the long-standing question of the possible existence of a non-classical isotope effect in Li diffusion. Furthermore, by combining our D data with results for D^{SD} from spin-lattice rela-xation measurements, the spatial correlation factor f could be extracted.

The NMR signals of both lithium isotopes were observed with pulse spectrometers. The conventional $\pi/2 - \pi$ radio-frequency (rf) pulse sequence yields the spin echo. The magnetic field gradient pulses of amplitude G and width δ, separated by a time Δ, are applied between the rf pulses and the echo. By performing the experiment once with and once without the gradient pulses, yielding the echo amplitudes A_D and A, respectively, the diffusion coefficient D can be inferred from the equation

$$\ln\left(A_D / A\right) = -D\left(\gamma\,\delta\,G\right)^2\left[\Delta - (1/3)\,\delta\right] \qquad (1)$$

The equation is valid if the steady background gradient G_0 is much smaller than G. Typical values for G_0 and G are 8 T/m and 0.01 T/m, respectively, and Δ is of the order of 10 ms. Δ defines the time during which diffusion is observed.

Fig.1 shows part of the results, for details see the figure caption. The errors quoted for an individual D value result from a fit of Eq. (1) to the echo amplitudes at a particular temperature. Thus, the error bars reflect short term fluctuations occurring during the measurement of a single D value which takes about one day. Within the limited temperature range of our measurements the data suggest an Arrhenius behavior of the diffusion coefficient for each of the five sets of D values: $D = D_0^{'}\exp\left(-E/kT\right)$, where E is the activation energy. Fur further details of the data evaluation see Ref. [5], which, among others, yields new prefactors, D_0.

To discuss our results in view of the isotope effect, we use the short-hand notation $^m D(n)$ which denotes the diffusion coefficient of the isotope ^{m}Li in a matrix consisting principally of ^{n}Li. Among others, we got the result

$$^6 D_0(7) / {}^7 D_0(6) = 1.02 \pm 0.12$$

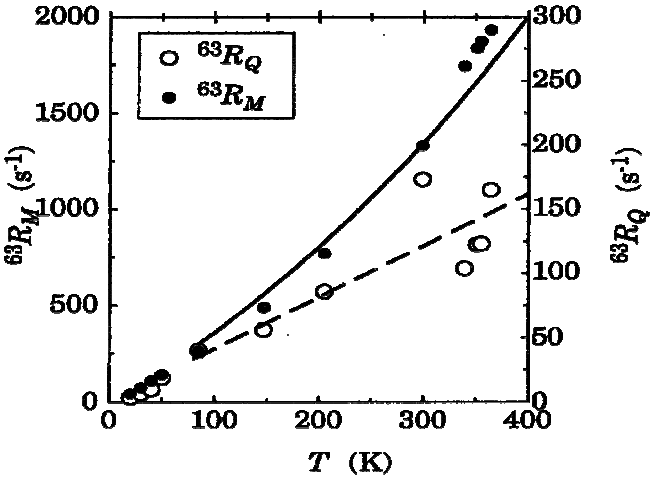

Figure 1: Temperature dependence of the diffusion coefficients of ^{7}Li in natural Li (open and full circles, sample I: 92.6 % ^{7}Li, 7.4 % ^{6}Li) and in enriched ^{7}Li (triangles, sample II: 99.97 % ^{7}Li) and of ^{6}Li in enriched ^{6}Li (crosses, sample III: 95.5 % ^{6}Li, 4.5 % ^{7}Li). The open circles refer to a magnetic field of 2.11 T, all other symbols to 5.17 T. The lines are fits of an Arrhenius law to the ^{7}Li data in natural Li and to the ^{6}Li data in enriched ^{6}Li, respectively, using a constant E = 0.561 eV. The data around 400 K are shown enlarged to better disclose the error bars. From Ref. 5.

The corresponding results from mass spectroscopy [8] are 1.27 ± 0.03 (above 383 K) and 1.35 ± 0.03 (below 383 K) which exhibit a striking isotope effect and which do not overlap with our result.

On the other side, one obtains, according to classical statistics, prefactors $D_0 \propto m^{-1/2}$. For instance: $^6D_0$ (6) / $^7D_0$ (6) = 1.08 which agrees very well with our experimental value 1.07 ± 0.008. We therefore concluded that the isotope effect can be explained in terms of classical statistics.

4. Spin and charge dynamics in the Cu-O chains of $YBa_2Cu_4O_8$

The high-temperature superconductor (HTSC) compounds $YBa_2Cu_3O_7$ (Y123 for short) and $YBa_2Cu_4O_8$ (Y124) contain single and double Cu-O chains, respectively. Even though these compounds are among the most widely studied of the HTSC, no established consensus has been reached for the ground state and the low energy excitations of the single and double chains. Because of the anisotropy of the electronic properties suggested by the crystalline structure and confirmed experimentally, the Cu-O chains present a good example of a quasi one-dimensional (1D) electronic conductor.

If probed by NMR or NQR, the chains of Y123 and Y124 do not exhibit simple metallic behavior. For instance, the Cu Knight shift varies linearly with temperature, and the spin-lattice relaxation rate, $1/T_1$, increases approximately with the temperature cubed, while, in a simple metal, the Knight shift is temperature independent and $1/T_1$ increases linearly with temperature.

We have performed new studies of the Cu-O chains in Y124 [9]. Among others, we have measured the ^{63}Cu and ^{65}Cu NQR spin-lattice relaxation rates, $1/T_1$, as a function of temperature. Experience tells us that $1/T_1$, can be written as a sum of two contributions:

$$1/T_1 = R_M + R_Q \tag{2}$$

The "magnetic relaxation rate", R_M, is related to magnetic field fluctuations at the nuclear site induced by the valence electron spins, while the "quadrupolar relaxation rate", R_Q, is associated with electric field gradient (EFG) fluctuations which can arise from valence electron and/or ionic charges. In general, in NQR, the magnetic contribution, R_M, is given by the expression [10]:

$$R_M = 3\,k_B T(\gamma^2 / 2\mu_B^2)\sum_q F(q)\,\chi''(q,\omega_Q)/\omega_Q,$$

where $F(q)$, called the form factor, is the square of the Fourier-transformed hyperfine coupling constant, and $\chi''(q,\omega_Q)$ is the imaginary part of the dynamic spin susceptibility.

First, we decompose the Cu $1/T_1$ raw data into the magnetic and quadrupolar contribution. This can be accomplished since R_M is proportional to the gyromagnetic ratio squared, γ^2, and R_Q is proportional to the quadrupole moment squared, $(eQ)^2$. Writing Eq. (2) for both Cu isotopes, the following ratio can be formed

$$\frac{^{65}T_1}{^{63}T_1} = \frac{^{63}R_M + {}^{63}R_Q}{^{65}R_M + {}^{65}R_Q} = \frac{1+y}{a+by}$$

where the quotients $a = {}^{65}R_M / {}^{63}R_M = ({}^{65}\gamma / {}^{63}\gamma)^2 = 1.1477$ and $b = {}^{65}R_Q / {}^{63}R_Q = ({}^{65}Q / {}^{63}Q)^2 = 0.8562$ are known. Hence, $y = {}^{63}R_Q / {}^{63}R_M$ can be calculated. The results of the decomposition are shown in Fig. 2. Note that R_Q is about one order of magnitude smaller than R_M. The dashed line is a guide to the eye while the solid curve represents a fit to be discussed later.

In view of the 1D character of the band and of the sizable electronic correlations, we consider the 1D electron gas model [11] as most appropriate to analyze our data. In this model, the direct electron-electron interaction is parameterized in terms of four coupling constants g_i for left and right moving fermions. In the limit of the Hubbard model, these coupling constants all reduce to a single interaction parameter, U. A peculiar characteristic of this model is the complete separation of long wavelength charge and spin excitations, a phenomenon commonly called spin-charge separation.

In a 1D metal, there are only two channels of magnetic relaxation: those induced by quasiparticles with $q \cong 0$ and $q \cong 2k_F$. We thus write $R_M = R_M\,(q \cong 0) + R_M\,(q \cong 2k_F)$. We have shown that the $q \cong 0$ channel is dominating; it is related to the uniform spin susceptibility, $\chi_0(T)$, by the following equations:

$$R_M[q \cong 0] = \frac{3\pi\, H_{hf}^2\; k_B\; T}{4\,\hbar\,\mu_B^2}\,\chi_0^2(T) \tag{3}$$

where H_{hf} is the hyperfine field at the Cu nucleus. We stress that Eq. (3) is a consequence of the dimensionality and electronic correlation of the system, and it should not be confused with the Korringa relation.

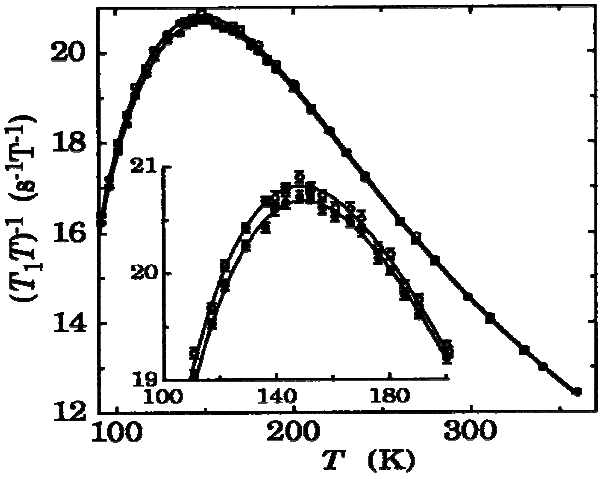

Figure 2.Temperature dependence of the magnetic (R_M) and quadrupolar (R_Q) spin-lattice relaxation rate. The solid line is a fit to the data, the dashed line is a guide to the eye.From Ref. 9.

We have fitted the Cu relaxation and Knight shift (not shown here) data to our theoretical expressions [see Ref. 9], the result is the solid curve in Fig. 2 whose fit parameters agree very well with data obtained elsewhere; for details see Ref. 9. The quadrupolar contribution, R_Q, is relatively small compared to the total Cu relaxation rate. We can safely exclude the phononic origin of the quadrupolar relaxation. We believe that R_Q is due to the charge carriers. R_M and R_Q have different temperature dependences which is not expected for a simple metal. This difference is an indication for the separation of spin and charge excitations expected in the framework of the 1D electron gas model.

5. Isotope shift of the opening temperature of the the spin gap

One of the central and heavily debated questions in high-temperature superconductivity research concerns the origin of the so-called pseudogap occurring in the normal state of underdoped superconductors. The pseudogap refers to the transfer to higher energy of the density of low-energy excited states. In NMR and neutron scattering experiments, the pseudogap reveals itself as a spin gap. For instance, the Cu spin-lattice "relaxation rate per temperature unit", $(T_1T)^{-1}$, increases with falling temperature and reaches a maximum at T^*, which is a proper scale for the temperature dependence of the spin gap. For $YBa_2Cu_4O_8$ (Y124), the corresponding values are T_c = 81 K and $T^* \approx 150$ K.

We detected anomalies in the temperature dependence of several NMR and NQR quantities measured in the normal state of Y124, for instance in NQR frequencies, Knight shifts, line widths, and relaxation times [12]. These anomalies, which occur around $T^\dagger$ = 180 K, are the signature of an electronic crossover which

involves enhanced charge fluctuations in planes and chains. Because of the proximity of $T^{\dagger}$ and T^{*}, we have argued that the spin gap effect in Y124 is caused by a transition due to a charge density wave (CDW) instability [13]. Among others, we predicted a dependence of T^{*} on the isotope mass. Thus, corresponding measurements allow one to check the consistency of the CDW model.

We reported a high-accuracy NQR study [14] of the planar ^{63}Cu nuclei in Y124, supplemented by susceptibility measurements, on ^{16}O and ^{18}O exchanged Y124 samples which revealed the presence of an isotope effect on both T_c and T^{*}. Both isotope exponents, defined as $\alpha = -\Delta \ln(T^{*}) / \Delta \ln(m)$ and correspondingly for T_c, are finite and have, within the experimental error, the same value. This result is contrary to a study [15] which reported the absence of an isotope effect in the pseudogap of Y124 as determined by ^{89}Y NMR.

Fig. 3 presents our $(T_1T)^{-1}$ results whose general behavior is consistent with earlier measurements. However, we were able to reduce the errors on the $(T_1T)^{-1}$ data to the extremely low values of approximately 0.3 %. The maximum of the $(T_1T)^{-1}$ data of the ^{18}O sample is higher than that of the ^{16}O sample and it is shifted to lower temperature.

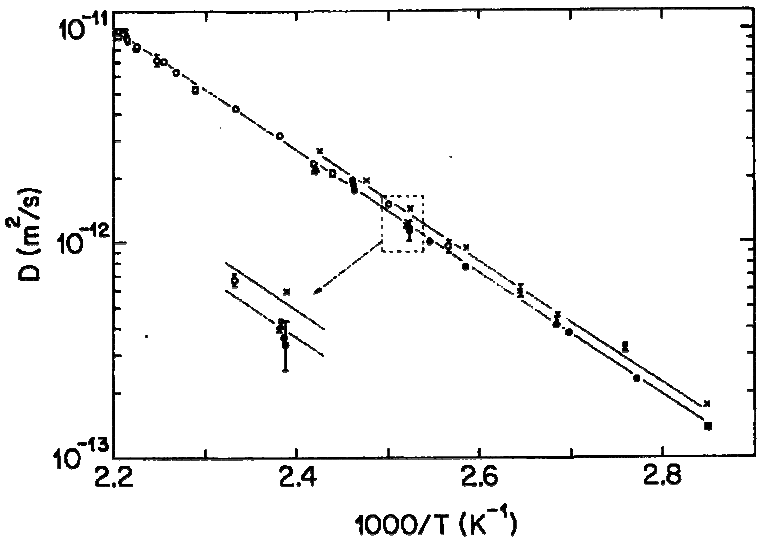

Figure 3: ^{63}Cu spin-lattice "relaxation rate per temperature unit", $(T_1T)^{-1}$, of ^{16}O (•) and ^{18}O (○) exchanged Y124 samples. The data is fitted to Eq.(4). Insert: Zoom of the $(T_1T)^{-1}$ data around T^{*} From Ref. 14.

Since at present no theoretical derivation of T_1 exists which takes into account the presence of the spin gap and its isotope effect, one must analyze the $(T_1T)^{-1}$ data with the help of a phenomenological function. We used the relation

$$(T_1\,T)^{-1} = CT^{-a}\left[1-\tanh^2\left(\frac{\Delta}{2T}\right)\right] \qquad (4)$$

which is frequently used in describing T_1 data [16] and which is based on a function used to describe properly the dynamic susceptibility data in the presence of a spin gap, as determined by neutron scattering measurements. The factor CT^{-a}, with $a \cong 1$, takes into account the high-temperature Curie-like divergence of $(T_1T)^{-1}$, and the hyperbolic tangent describes the temperature dependent gap. Δ is a measure for the gap and it is the only parameter allowed to differ for the two sets of data. To improve the confidence level, we have replaced T by the expression $T' = T + a_0 + a_1/T + a_2/T^2$ where each of these three parameters is required to have the same value for the two data sets, i.e. Δ, which is a measure for the gap, is the only parameter allowed to differ for the two sets. It is important to stress that T^*, defined as the maximum of Eq. (4) , and Δ are strictly proportional, so that also T^* can be used as a proper parameter for the temperature scale of the gap.

The best value of the T^* shift is 0.96 K resulting in an isotope exponent $\alpha_{T^*} = 0.061(8)$ which agrees quite well with the corresponding exponent $\alpha_{Tc} = 0.056(12)$ for T_c as determined by SQUID magnetization measurements. This fact seems to confirm the growing evidence for a common origin of the superconductivity and the pseudo gaps.

REFERENCES

[1] E. Brun, J. Oeser, H.H. Staub, C.G. Telschow, Phys. Rev. 93, 904 (1954).

[2] D. Brinkmann, E. Brun, H.H. Staub, Helv. Phys. Acta 35, 431 (1962).

[3] H.C. Torrey, Phys. Rev. 130, 2306 (1963).

[4] R.I. Streever and H.Y. Carr, Phys. Rev. 121, 20 (1961); E.R. Hunt and H.Y. Carr, Bull. Am. Phys. Soc. 7, 293 (1962).

[5] M. Mali, J. Roos, M. Sonderegger, D. Brinkmann, and P. Heitjans, J. Phys. F: Met. Phys. 18, 403 (1988).

[6] E.O. Stejskal and J.E. Tanner, J. Chem. Phys. 42, 288 (1965).

[7] D. Brinkmann, Progress in NMR Spectroscopy 24, 527 (1992).

[8] A. Lodding, J.N. Mundy, and A. Ott, Phys. Status Solidi 38, 559 (1970).

[9] F. Raffa, M. Mali, A. Suter, A.Yu. Zavidonov, J. Roos, D. Brinkmann, and K. Conder, Phys. Rev. B 60, 3636 (1999).

[10] T. Moriya, J. Phys. Soc. Jpn. 18, 516 (1963).

[11] J. Solyom, Adv. Phys. 28, 201 (1979); V. J. Emery, in *Highly Conducting One-Dimensional Solids*, edited by J.T. Devreese, R.P. Evrard and V.E. van Doren (Plenum, New York and London, 1979) Chap. 6.

[12] A. Suter, M. Mali, J. Roos, D. Brinkmann, J. Karpinski, and E. Kaldis, Phys. Rev. B 56, 5542 (1997).

[13] I. Eremin, M. Eremin, S. Varlamov, D. Brinkmann, M. Mali, and J. Roos, Phys. Rev. B 56, 11305 (1997).

[14] F. Raffa, T. Ohno, M. Mali, J. Roos, D. Brinkmann, L. Conder,and M. Eremin, Phys. Rev. Lett. 81, 5912 (1998).

[15] G.V.M. Williams *et al*., Phys. Rev. Lett. 80, 377 (1998).

[16] For instance: D. Brinkmann and M. Mali, in *NMR -- Basic Principles and Progress*, edited by P. Diehl, E. Fluck, H. Günter, R. Kosfeld, and J. Seelig (Springer, Berlin, 1994), Vol. 31, p.171.

STUDIA UNIVERSITATIS BABEŞ-BOLYAI, PHYSICA, SPECIAL ISSUE, 2001

NITROGEN ISOTOPE EXCHANGE BETWEEN NITRIC OXIDE AND NITRIC ACID

D. AXENTE

National Institute for Research and Development of Isotopic and Molecular Technology, 3400 Cluj-Napoca, P.O.Box 700,ROMANIA

The exchange rate law experimentally observed for $^{15}N/^{14}N$ exchange in NO - HNO_3 system at low nitric acid concentration, both at atmospheric pressure [1] and at low pressure of NO [2]: $R = k[H^+][NO_3^-][HNO_2]$, is identical with the rate law for the reaction between NO and HNO_3, when HNO_2 is formed.

The rate of nitrogen isotope exchange between NO and HNO_3 has been measured as a function of nitric acid concentration of $1.5 \div 4$ M.l^{-1}. The exchange rate law is shown to be $R = k[HNO_3]^2[N_2O_3]$ and the measured activation energy is $E = 67.78$ kJ.M^{-1} [3]. It is concluded that N_2O_3 participates in $^{15}N/^{14}N$ exchange between NO and HNO_3 at nitric acid concentration higher than 1.5 M.l^{-1}.

The rate of the same isotope exchange in NO - HNO_3 system has been also measured as function of nitric oxide pressure $0.1 \div 0.4$ M.Pa for 1 and 2 M.l^{-1} HNO_3. It is demonstrated that $^{15}N/^{14}N$ exchange in this system has a linear dependence of NO pressure as indicated by rate measurements at different NO partial pressures and constant overall pressure, by adding helium in reactor. Using the rate law presented above the nitrogen isotope exchange rate for nitric acid concentration $1.5 \div 10$ M.l^{-1} were calculated [4]

Nitrogen isotope exchange between nitric oxide and concentrated nitric acid with a single stage separation factor $\alpha = 1.055$, for 10 M.l^{-1} nitric acid, at 25^o C, provides the bases for ^{15}N separation process that is most widely used at the present time, i.e. the method of Spindel and Taylor [5].

In order to know what happens in ^{15}N separation at higher pressure, when the isotopic transport is improved, a stainless steel laboratory experimental plant with a 1000 mm long and 18 mm i.d. column, packed with triangular wire springs $1.8 \times 1.8 \times 0.2$ mm, was utilised. At 1.5 atm (absolute) and 2.36 ml.cm^{-2}.min^{-1} flow rate, HETP was 7% smaller than at atmospheric pressure and 1.5 times smaller flow rate. The operation of ^{15}N separation plant at 1.8 atm (absolute), instead atmospheric pressure, will permit doubling of the 10 M.l^{-1} nitric acid flow rate and ^{15}N production of the given column [6].

Chemical exchange of nitrogen between nitric oxide and nitric acid provides the bases for nitrogen separation process that is most widely used at the present time:

$$^{15}NO + H^{14}NO_3 \leftrightarrow {}^{14}NO + H^{15}NO_3 \quad (1)$$

The exchange rate law experimentally observed for isotopic exchange (1) at low nitric acid concentration, both at atmospheric pressure and at low pressure of NO:

$$R = k[H^+][NO_3][HNO_2] \quad (2)$$

is identical with the rate law for the reaction between NO and HNO_3, when HNO_2 is formed.

On the basis of the experimental data [7] the following mechanism for $^{15}N/^{14}N$ exchange was proposed:

$$NO + NO_2 \leftrightarrow N_2O_3 \text{ (rapid reversible)} \quad (3)$$

$$N_2O_3 + H_2O \leftrightarrow 2HNO_2 \text{ (rapid reversible)} \quad (4)$$

$$HNO_2 + H^+ + {}^{15}NO_3^- \leftrightarrow {}^{15}NNO_4 + H_2O \text{ (rate determining)} \quad (5)$$

$$^{15}NNO_4 \leftrightarrow {}^{15}NO_2 + NO_2 \text{ (rapid reversible)} \quad (6)$$

$$^{15}NO_2 + NO \leftrightarrow {}^{15}NNO_3 \text{ (rapid reversible)} \quad (7)$$

$$^{15}NNO_3 + H_2O \leftrightarrow H^{15}NO_2 + HNO_2 \text{ (rapid reversible)} \quad (8)$$

$$H^{15}NO_2 + 2HNO_2 \leftrightarrow {}^{15}NO + NO + H^+ + {}^{15}NO_3^- + H_2O \text{ (rapid)} \quad (9)$$

$$NO + H^{15}NO_3 \leftrightarrow HNO_3 + {}^{15}NO \quad (10)$$

The rate determining stage is reaction (5), as is also the case for the formation of nitrous acid in solution [8]. The others (6), (7), (8), (9) are reversible reactions taking place more rapidly, as well as reaction (10). According to this mechanism the dinitrogen tetroxide, dinitrogen dioxide and nitrous acid are intermediates in nitrogen exchange between NO and HNO_3 (10). Returning to Eqn.(5), it may be written in another form:

$$HNO_2 + H^{15}NO_3 \rightarrow {}^{15}NNO_4 + H_2O \quad (11)$$

implying the participation of undissociated molecule of nitric acid. This reaction may also be written as:

$$NO^+.H_2O + {}^{15}NO_3^- \rightarrow {}^{15}NNO_4 + H_2O \quad (12)$$

in which the hydrated nitrosyl cation, easily formed in solution from HNO_2 and H^+, appears. The last reaction (Eqn.12) indicates the possible role of an assymetric molecule N_2O_4 (nitrosyl nitrate $NONO_3$) which should be rapidly isomerised to the symmetrical stable form N_2O_4.

When nitric oxide and nitric acid are mixed a number of reactions occur, resulting in several chemical species in both the liquid and gas phases. At low nitric acid concentration HNO_2 is formed in the liquid according to:

$$2NO + HNO_3 + H_2O \leftrightarrow 3HNO_2 \quad (13)$$

At acid concentration above 1 ÷ 1,5 $M.l^{-1}$, HNO_2 rapidly decomposes, via several reactions such as [9]:

$$2HNO_2 \leftrightarrow N_2O_3 + H_2O \leftrightarrow NO + NO_2 + H_2O \quad (14)$$

$$HNO_2 + HNO_3 \leftrightarrow N_2O_4 + H_2O \quad (15)$$

The NO is relatively insoluble and goes into the gas phase and NO_2 (N_2O_4) is continually hydrated and thus removed from the equilibria. The concentration of HNO_2 decreases as the nitric acid concentration increases so the Eqn.(13) is no longer a true equilibrium and the secondary species formed in the liquid at high acid concentration is N_2O_3 rather than HNO_2. As the nitric acid concentration is further increased above $11M.l^{-1}$, N_2O_3 decomposes according to:

$$N_2O_3 + 2HNO_3 \leftrightarrow 2N_2O_4 + H_2O \quad (16)$$

In the kinetic measurements HNO_3 solution was preequilibrated chemically with NO gas, and the system was then desequilibrated by addition of a small quantity of $H^{15}NO_3$ solution of 18.55 at.% ^{15}N. In order to eliminate the possibility that phase mixing imposes a rate limitation, aqueous solutions of nitric acid were brought into contact with NO gas by vibration of reaction cell and the exchange of nitrogen was followed by sampling the gas phase for mass spectrometric analysis. The exchange data were treated by use of McKay law in the form:

$$-\frac{d\ln(1-F)}{dt} = \frac{A+B}{A \cdot B}R \quad (17)$$

where R is the nitrogen isotope exchange rate ($M.l^{-1}.s^{-1}$) and F is the exchange fraction at time t:

$$F = \frac{X_t - X_0}{X_\infty - X_0} \quad (18)$$

the values of X represent the ^{15}N content of NO at time 0,t and ∞,isotopic equilibrium, A is the initial nitric acid concentration ($M.l^{-1}$) and B is the total moles of nitric oxide in the gas phase (NO_G) and in the liquid (NO_L) divided by solution volume ($M.l^{-1}$).Using these definitions for A and B we assume that nitrogen exchange is limited by the rate of NO_3^- - HNO_3 exchange, this being reasonable for nitric acid solution under 1 $M.l^{-1}$, when the liquid may be considered as consisting of nitrate (NO_3^- and HNO_3),HNO_2 and gas of NO. Above this concentration N_2O_3 presence in liquid is considered and A and B values undergo some changes.

If all NO absorbed in liquid is transformed in N_2O_3 [Eqns.(2),(3)], according to equilibrium:

$$4NO + 2HNO_3 \leftrightarrow 3N_2O_3 + H_2O \quad (19)$$

the NO consumed to give N_2O_3 was calculated by taking ¾ of the nitric oxide absorbed in nitric acid solution (NO_L).

The equilibrium N_2O_3 concentrations were calculated from nitric oxide concentrations in liquid,[NO_L], at 730 torr pressure and 25°C, and are given in column 4 of Table 1 and Fig.1. [N_2O_3] determined by chemical analysis and calculated from thermodynamic data [9] are given in column 5, respectively column 6 of Table 1.

Table 1

T = 25° C; p_{NO} = 730 torr
*** (9.9 M.l^{-1}) ; ** (11.8 M.l^{-1})**

$[HNO_3]_i$, M.l^{-1}	NO (absorbed at equilibrium,$[NO]_L$) M.l^{-1}	NO (absorbed at equilibrium,$[NO]_L$) g.l^{-1}	$[N_2O_3]$ (calculated from $[NO]_L$), M.l^{-1}	$[N_2O_3]$ (chemical analysis) M.l^{-1}	$[N_2O_3]$ (calculated,[4]) M.l^{-1}
1	**0.139**	**4.17**	**0.104**	**0.063**	**-**
2	**0.230**	**6.90**	**0.172**	**0.124**	**-**
4	**0.340**	**10.20**	**0.255**	**0.221**	**-**
6	**0.420**	**12.60**	**0.315**	**0.263**	**0.360**
8	**0.520**	**15.60**	**0.390**	**0.290**	**-**
10	**0.630**	**18.90**	**0.470**	**0.350**	**0.430** *
12	**0.760**	**22.80**	**0.570**	**-**	**0.520****

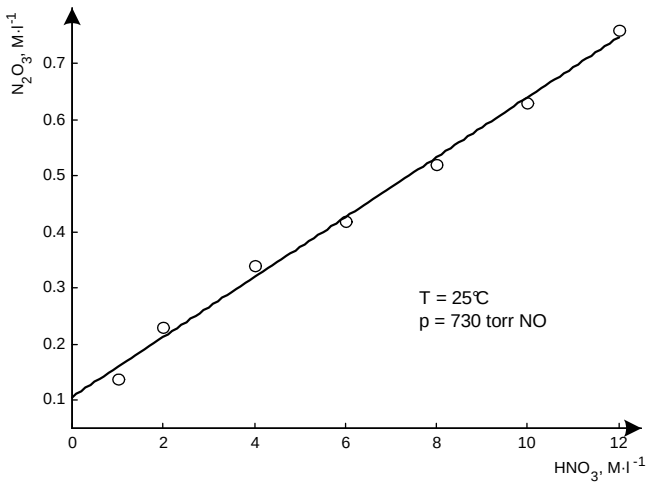

Fig.1. Equilibrium N_2O_3 concentrations

[NO]L, measured at 91.25 torr NO pressure and 25o C, [N2O3] calculated from it and determined by chemical analysis are presented in Table 2; [N2O3], calculated from [NO]L is also given in Fig.2.

Table 2

T = 25°C ; p_{NO} = 91.25 torr

$[HNO_3]_i$, M.l^{-1}	NO absorbed, $[NO]_L$, M.l^{-1}	$[N_2O_3]$, calculated from $[NO]_L$, M.l^{-1}	$[N_2O_3]$, (chemical analysis) M.l^{-1}
1	**0.0320**	**0.0240**	**0.020**
2	**0.0422**	**0.0316**	**0.038**
3	**0.0646**	**0.0485**	**0.042**
4	**0.0770**	**0.0578**	**0.054**

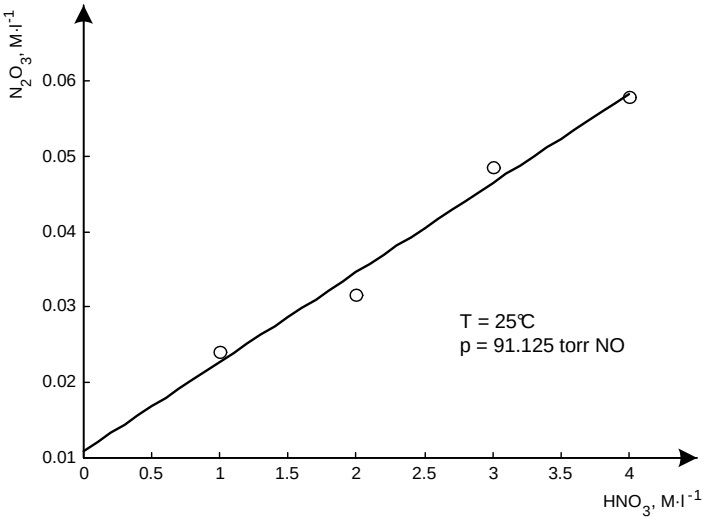

Fig. 2. Calculated N_2O_3 concentrations

For chemical analysis of N_2O_3 a known quantity of 0.5 N $KMnO_4$ solution, and 10 ml of 25 % sulphuric acid solution were introduced in the reaction cell then the excess of permanganate was titrated by 0.1 N $FeSO_4$ solutions. The permanganate consumed by NO from the gas phase was also determined.

In $[N_2O_3]$ calculus the liquid was assumed to consist only of nitrate (NO_3^-, HNO_3) and N_2O_3, the presence of small amounts of other species: NO,NO_2 and N_2O_4 was neglected.

There is a good agreement between $[N_2O_3]$, calculated from $[NO]_L$ and those determined by chemical analysis especially at a pressure of 91.25 torr NO.

The results of the kinetic measurements of nitrogen exchange are summarized in Table 3; for $[HNO_3]_i$: 1.5 ÷ 2.5 $M.l^{-1}$ R was determined at 730 torr NO and for $[HNO_3]_i$: 3 ÷ 4 $M.l^{-1}$ at 91.25 torr NO pressure.

Table 3

T = 25° C

$[HNO_3]_i$ $M.l^{-1}$	R $M.l^{-1}.s^{-1}$	$[HNO_3]_e$ $M.l^{-1}$	$[N_2O_3]$ $M.l^{-1}$	R / $[HNO_3]_e^2.[N_2O_3$	p_{NO} torr
1.5	**$6.21.10^{-3}$**	**1.400**	**0.1500**	**0.021**	**730**
2.0	**$1.49.10^{-2}$**	**1.885**	**0.1725**	**0.024**	**730**
2.5	**$2.31.10^{-2}$**	**2.370**	**0.1850**	**0.022**	**730**
3.0	**$8.83.10^{-3}$**	**2.968**	**0.0485**	**0.021**	**91.25**
4.0	**$2.03.10^{-2}$**	**3.961**	**0.0578**	**0.023**	**91.25**

We note the approximate constancy of the R/ $([HNO_3]_e^2$. $[N_2O_3]$ as shown in column 5,Table 3, which would imply the rate law:

$$R = k\,[HNO_3]^2\,[N_2O_3] \qquad (20)$$

for $^{15}N/^{14}N$ isotopic exchange in NO - HNO_3 system, in the concentration range1.5 ÷ 4 $M.l^{-1}$ nitric acid.

From Eqn.(18) the role of N_2O_3 in nitrogen isotopic exchange at nitric acid concentration higher than 1.5 $M.l^{-1}$ is obvious when N_2O_3 appears in the liquid instead of HNO_2.

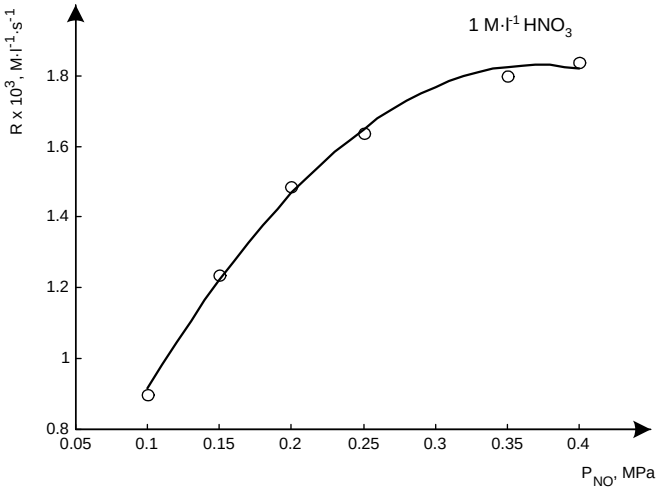

Fig. 3. Nitrogen isotope exchange rate versus nitric oxide pressure

The rate of $^{15}N/^{14}N$ exchange between NO and HNO_3 at different nitric oxide pressure [4] was measured using a stainless steel reactor designed to work at pressure up to 0.5 MPa.

The nitrogen exchange rate (R) for $1M.l^{-1}$ initial nitric acid concentration versus nitric oxide pressure is presented in Fig. 3 and R dependence of NO partial pressure, the measurements done at the same overall pressure (0.4 MPa) by adding helium or nitrogen in the reactor, are presented in Fig 4 (a), respectively (b) for $1M.l^{-1}$ HNO_3 and Fig 5 (a) and (b) for $2\ M.l^{-1}$ HNO_3.

We conclude that the $^{15}N/^{14}N$ exchange rate in NO - HNO_3 system has a linear dependence of NO pressure as indicated by rate measurements at different NO partial pressures and constant overall pressure, by adding helium in reactor, (Fig 4 and Fig 5).

We did not obtain a linear dependence of nitrogen exchange rate of NO pressure (Fig. 3) because the measurements have been done at different overall pressures in reactor (0.1 ÷ 0.4), when diffusion rate in the gas phase (which diminishes with pressure increasing) influenced the kinetic data. This assumption was confirmed by measurements at the same overall pressure by adding helium in reactor, when isotopic exchange rate limitation by diffusion in gas was diminished.

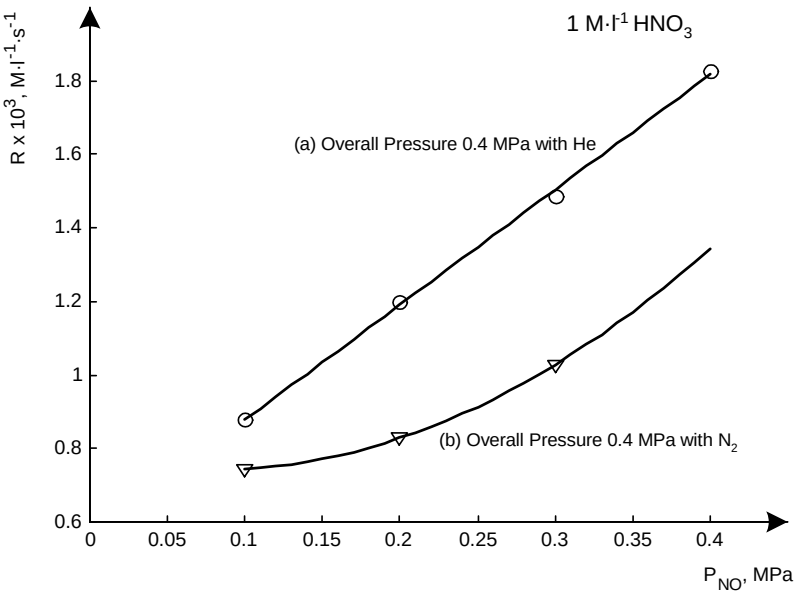

Fig. 4. Nitrogen isotope exchange rate versus partial nitric oxide pressure for $1\ M\cdot l^{-1}$ HNO_3: (a) overall pressure 0.4 MPa with helium; (b) overall pressure 0.4MPa with N_2

By adding nitrogen in reactor $^{15}N/^{14}N$ exchange rate was diminished (Fig 4 and Fig 5) according to the smaller diffusion rate in gas phase N_2 + NO) which is similar to that in pure NO.

The linear dependence of nitrogen exchange rate in studied system of NO pressure is a new argument for exchange rate law (20), because absorbed NO quantity in the liquid phase (HNO_3 solution) has a linear dependence of NO pressure [4] and between absorbed nitric oxide concentration there is the same dependence. Using Eqn.(20) the $^{15}N/^{14}N$ exchange rate (R) in NO - HNO_3 system, at 25°C and 730 torr NO pressure were calculated for nitric acid concentration 1.5 ÷ 10 $M.l^{-1}$ (Table 4), considering $[HNO_3]_e$, $[N_2O_3]$ and k = 0.022 $M^{-2}.l^2.s^{-1}$ [4].

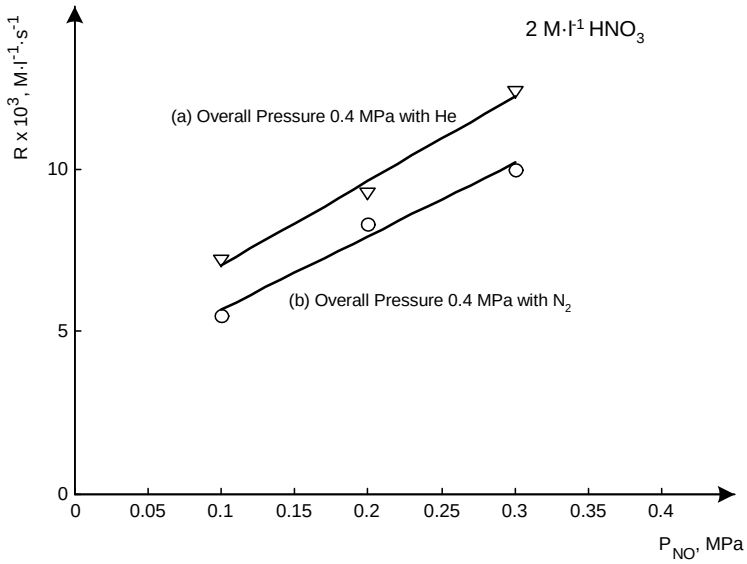

Fig. 5. Nitrogen isotope exchange rate versus partial nitric oxide pressure for 2 $M \cdot l^{-1}$ HNO_3: (a) overall pressure 0.4 MPa with helium; (b) overall pressure 0.4MPa with N_2

Table 4

Rate of nitrogen isotope exchange in NO - HNO_3 system

$[HNO_3]_i$ $M.l^{-1}$	$[HNO_3]_e$, [3] $M.l^{-1}$	$[N_2O_3]$, [3] $M.l^{-1}$	R $M.l^{-1}.s^{-1}$
1.5	**1.40**	**0.150**	**$6.47.10^{-3}$**
2.0	**1.90**	**0.170**	**$1.36.10^{-2}$**
3.0	**2.89**	**0.210**	**$3.86.10^{-2}$**
4.0	**3.68**	**0.245**	**$7.30.10^{-2}$**
5.0	**4.85**	**0.280**	**$1.45.10^{-1}$**
6.0	**5.90**	**0.320**	**$2.45.10^{-1}$**
8.0	**7.77**	**0.395**	**$5.25.10^{-1}$**
10.0	**9.72**	**0.470**	**$9.77.10^{-1}$**

The kinetic data presented above are of interest in ^{15}N separation by chemical exchange in NO - HNO_3 system.

At the Institute of Isotopic and Molecular Technology, Cluj-Napoca, Romania a ^{15}N production plant using the method of isotopic exchange in NO, NO_2 - HNO_3 system began to operate in 1968 at atmospheric pressure. Tacking into account that recent kinetic data presented above showed that $^{15}N/^{14}N$ exchange rate in this system has a linear dependence on NO pressure, it is important to know what happens during the ^{15}N separation process at higher pressure than atmospheric one, when the isotopic transport between the two phases is improved.

The schematic diagram of the laboratory experimental plant for the determination of ^{15}N separation process at different pressure is presented in Fig.6. On the top of the stainless steel column (1),(1000 mm long, 18 mm i.d., packed with triangular wire springs 1.8×1.8×0.2 mm, thermostated at 25 ^oC), 10M nitric acid solution was supplied. In the hastelloy refluxer (2) (700 mm long, 52 mm i.d., with 3 - 4 mm ceramic packing) nitric acid is quantitatively converted into nitrogen oxides:

$$2HNO_3 + 3SO_2 + 2H_2O \rightarrow 2NO + 3H_2SO_4 \quad (21)$$

$$2HNO_3 + SO_2 \rightarrow 2NO_2 + H_2SO_4 \quad (22)$$

The ratio between nitric oxide and nitrogen dioxide concentrations in the gaseous mixture depends on the water flow rate in the top of refluxer (2) (3) [10]. The increase of nitric oxide concentration leads to the increase of the effective overall single stage separation factor [9], while the nitrogen dioxide concentration decreases under a certain value [10],diminishes the chemical exchange rate in the separation column.

The exothermic reactions (2) and (3) take place in the refluxer (2) Fig.6, on the ceramic packing, the height of the reaction zone is 5 to 10 cm; the refluxer wall temperature, which attains 40 to 80^oC, is continuously registered using platinum thermoelement (T) connected to the recorder (R), Fig.6.

The plant pressure was fixed by a regulator (3) connected to a SO_2 cylinder and measured with a gauge (4). At the bottom of the column the gas samples are taken off in evacuated glass ampoules for nitrogen isotopic analysis.

After the nitrogen oxides leave the top of the column (1), they enter into flowmeters (5) and (6), each of them have regulating valves, which allow the plant to operate at desired pressure. The main nitrogen oxide flow (about 90 %) passes through the flowmeter (5) and the rest through the solenoid valve (7), automatically control by means of recorder (R) and controller (C). By proper adjustment of the main and by - pass flows of nitrogen oxides, a fair control of the plant can be achieved. Finally the NO,NO_2 gaseous mixture is converted into nitric acid solution in an oxidation and absorption tower.

Before starting operation of the exchange system, column (1) was flooded with 10M nitric acid to ensure proper wetting of the packing. Then the column was drained slowly with a flow of 10M HNO_3. When the column was free of excess nitric acid solution, SO_2 was introduced into refluxer (2). For all experimental measurements

presented in this paper a water flow, representing 30% of the nitric acid flow rate flow, was fed to the top of the refluxer.

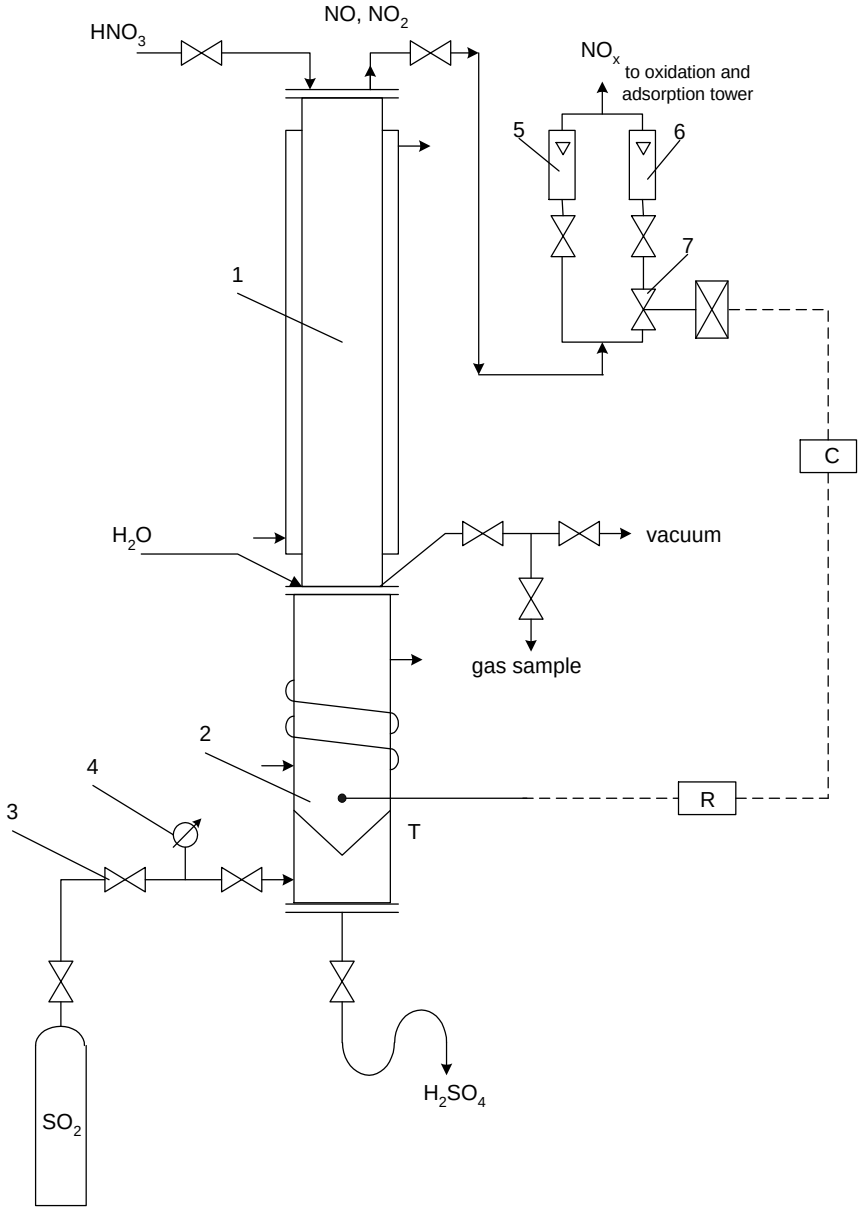

Fig. 6. Schematic diagram of the experimental plant: 1 – stainless steel column, 2 – hastelloy refluxer, 3 – pressure regulator, 4 – pressure gauge, 5,6 – flowmeters, 7 – solenoid valve, C – controller, R – recorder, T – platinum thermoelement

In Table 5 the experimental data are presented the separation carried out at atmospheric pressure in the plant (Runs 1, 2, 3, Table 5) allowed the determination of steady -state overall separation (S_∞) and that of the height equivalent to a theoretical plate (HETP),which were calculated from the following relations, valid for total reflux:

$$S_\infty = \frac{N_b}{0.365} \qquad (23)$$

$$S_\infty = \square^n \qquad (24)$$

$$HETP = \frac{H}{n} \qquad (25)$$

where N_b is the ^{15}N concentration at the bottom of the column, (at.% ^{15}N); 0.365 is the isotopic concentration of the nitric acid fed on the top of the column; H is the height of the packed column,1000 mm; n is the number of the stages.

Table 5.

Experimental data for ^{15}N separation

Run No.	10M HNO_3 flow $ml.h^{-1}$	10M HNO_3 flow rate $ml.cm^{-2}.min^{-1}$	H_2O flow $ml.h^{-1}$	Pressure atm.abs.	Isotopic Conc. at.% ^{15}N	Overall separation (S_∞)	HETP cm
1	**240**	**1.57**	**80**	**1**	**1.338**	**3.665**	**4.13**
2	**380**	**2.49**	**100**	**1**	**1.024**	**2.80**	**5.20**
3	**480**	**3.14**	**150**	**1**	**0.919**	**2.52**	**5.79**
4	**360**	**2.36**	**110**	**1.5**	**1.470**	**4.02**	**3.85**
5	**480**	**3.14**	**145**	**1.8**	**1.320**	**3.61**	**4.17**
6	**600**	**3.93**	**200**	**2.5**	**1.007**	**2.76**	**5.27**

It is considered that for pressure range utilised in this paper the single stage separation factor, $\propto$, is constant[11].

At atmospheric pressure and 2.49 $ml.cm^{-2}.min^{-1}$ 10M HNO_3 flow rate, HETP increased 25 % in comparison with the value measured at 1.57 $ml.cm^{-2}.min^{-1}$ (Table 5), optimum flow rate determined for the same packing was 1.86 $ml.cm^{-2}.min^{-1}$ [12]. At 1.5 atm. (absolute), (Run 4) and 2.36 $ml.cm^{-2}.min^{-1}$ flow rates HETP was 7% smaller than at atmospheric pressure and 1.5 times smaller flow rate (Run 1).

HETP at 3.14 $ml.cm^{-2}.min^{-1}$ flow rate and at 1.8 atm.(absolute), (Run 5) is practically equal with that obtained at atmospheric pressure and two times smaller flow rate (Run 1).

At 2.5 atm.absolute and 3.93 $ml.cm^{-2}.min^{-1}$ there is a 26 % increase of HETP in comparison with that obtained at 1.8 atm.absolute and 3.14 $ml.cm^{-2}.min^{-1}$ flow rate.

For all pressures and nitric acid flow rates utilised in this paper the nitrogen oxides refluxer did operate well with a stable reaction zone, the sulphuric acid was free of nitrogen losses and SO_2 did not enter in the separation column.

The pressure increase in the ^{15}N separation plant using chemical exchange in the system NO, NO_2 - HNO_3 improved the isotopic transport between the two phases circulated in countercourrent in a packed column. This was possible owing to chemical exchange rate increase at higher nitrogen oxide pressure.

The operation of the ^{15}N separation plant at a pressure of 1.8 atm. (absolute) instead of an atmospheric one, will permit doubling of the 10M nitric acid flow rate and of the ^{15}N production of a given column.

The improved performance at higher pressure is significant for a large scale ^{15}N separation, which would be utilised for production of nitride fuels for FBRs.

An experimental plant with hastelloy refluxer, instead of a glass unit, does operate well, the reaction zone position being automatically controlled at higher pressure.

REFERENCES

[1] D.Axente, O.Piringer, J.Inorg. Nucl.Chem., 33, 665 (1971)

[2] S.Jordan, F.T.Bonner, Inorg.Chem.12, 1369 (1973)

[3] D.Axente, M.Abrudean, A.Bâldea, J.Radioanal.Nucl.Chem. 207, 1, 163 (1996)

[4] D.Axente, M.Abrudean, A.Bâldea, J.Radioanal.Nucl.Chem. 222, 1-2, 149 (1997)

[5] a W.Spindel, T.I.Taylor, J.Chem.Phys., 33, 981 (1955)

b W.Spindel, T.I.Taylor, Trans.N.Y.Acad.Sci.Ser.I., 19, 3 (1958)

c T.I.Taylor, W.Spindel, Proc.Symp.on Isotope Separation, Amsterdam 1957, North Holland Publ.Co., Amsterdam, p.158 (1959)

[6] D.Axente, A.Bâldea, C.Teacă, M.Abrudean,R.Horga, J.Radioanal.Nucl.Chem., 240, 3, 987 (1999)

[7] D.Axente, G.Lacoste, J.Mahenc, J.Inorg.Nucl.Chem., 36, 2057 (1974)

[8] H.Abel and H.Schmid, Z.Physik 132, 55 (1928); 134, 279 (1928); 136, 135 (1928)

[9] M.J.Stern, Lois Nash Kauder, W.Spindel, J.Chem.Phys., 36, 3, 764 (1962)

[10] D.Axente, T.Fodor, Isotopenpraxis, 5, 273 (1969)

[11] T.Ishida, W.Spindel, "Separation of ^{15}N", Annual Progress Report to U.S.Atomic Energy Commission for Contract AT (30-1)-3462, NYO-3462-4, (1968)

[12] D.Axente, A.Bâldea, M.Abrudean, Proc.Symp.on Isotope Separation and Chemical Exchange Uranium Enrichment, Tokyo 1990, Buletin of the Res.Lab.for Nuclear Reactor, Tokyo Institute of Technology, Tokyo, p.357 (1992)

STUDIA UNIVERSITATIS BABEŞ-BOLYAI, PHYSICA, SPECIAL ISSUE, 2001

DATA EVALUATION LINKING BASIC AND APPLIED RESEARCH AMONG EUROPEAN CENTERS OF EXCELLENCE*

VLAD AVRIGEANU, MARILENA AVRIGEANU and TUDOR GLODARIU

"Horia Hulubei" National Institute for Physics and Nuclear Engineering (IFIN-HH), P.O. Box MG-6, 76900 Bucharest, Romania

ABSTRACT. Review of the atomic and nuclear data evaluation at IFIN-HH is carried out along with research priorities of European Commission (EC) Fifth Framework Programme (FP5). Integration of basic research and objectives of nuclear safety and environmental protection is thus ensured as well that of scientists from Central and Eastern Europe (CEE) into the EC research programmes, e.g. EURATOM and EC Joint Research Center (JRC) projects. Recent experience of IFIN-HH receiving EC/FP5 Support for CEE Centres of Excellence, is discussed with the aim of further increase of the above-mentioned integration.

1. Introduction

The objective of consolidation of the scientific basis for, e.g., atomic and nuclear data is a research priority of the EURATOM/Fifth Framework Programme (FP5). Thus, advanced low-activation and radiation-resistant materials, as well as the precise definition of a reference material with reduced activation are main lines of *FP5 Key Actions*. However, since it is costly and virtually impossible to measure all atomic and nuclear data required by these applications, the development of the corresponding computing methods are essential. On the other hand, specific experimental data do not impose sufficient constraints on the theoretical nuclear reaction models. Most of them could be equally well reproduced in terms of different approaches by adjustment of parameters always involved even in the "parameter free" models. In order to increase the predictable power of model calculations, compensation of opposite effects due to various less accurate parameter values can be avoided by means of[1]: (a) unitary use of common model parameters for different mechanisms, (b) use of consistent sets of input parameters determined by various independent data analysis, and (c) unitary account of a whole body of related experimental for isotope chains of neighboring elements.

Improved nuclear model calculation methods for nuclear activation data have been carried out at IFIN-HH by using the exciton and the Geometry-Dependent Hybrid (GDH) semi-classical models for the pre-equilibrium emission (PE) and Hauser-

*Lecture at *The 2-nd Conference on Isotopic and Molecular Processes*, Cluj-Napoca, September 27-29, 2001. Work supported in part under the MEC Grant No. 1366/2001.

[1] M. Avrigeanu, M. Ivascu, and V. Avrigeanu, Z. Phys. A **329** , 177 (1988); ibid. **335**, 299 (1990); Atomkernenergie-Kerntechnik **49**, 133 (1987)

Feshbach statistical model within the computer code STAPRE-H95[2]. Since PE models have been recently proved[3] not able to reproduce the decrease of the *(n,p)* reaction excitation function in the energy range above the common 15 MeV value, additional work has had to be devoted to this objective. Further advance is possible by the development in the meantime within IFIN-HH of the novel partial level-density formalism[4] of the recent IAEA Reference Input Parameter Library (RIPL)[5] as well as an improved version of the corresponding computer code PLD[6].

It should be noted that the statistical-model parameters are involved beyond the reaction cross-section calculations also in various studies of nuclear phenomena from, e.g., elastic scattering to cold fission, which may be used for their analysis too[7,8]. Moreover, since completion of the EURATOM-FUSION objectives has recently requested nuclear-data evaluation for D incident on ^{6,7}Li, for D energies up to 50 MeV, we have analyzed the possibility to work on it at IFIN-HH. The previous IFIN-HH results concerning both the realistic effective nucleon-nucleon (NN) interaction[9] and the use of the double-folding (DF) model for microscopic optical-potential calculation[10,11] may be helpful in this respect.

We have thus looked for the integration of basic research and objectives of nuclear safety and environmental protection within the EC research programmes such as EURATOM and EC *Joint Research Center* (JRC). A fruitful cooperation is established in this respect between IFIN-HH and the EC/JRC *Institute for Reference Materials and Measurements* (IRMM) based on previous IFIN results[3,4,6-9], our group working now under the following projects:

- Association EURATOM - NASTI-Romania (2000-2002),
- EC/JRC/IRMM project *"Neutron Data Measurement and Evaluation Activities"*, (two senior scientists and two open positions as PhD-student), and
- EC/FP5/INCO2 *Support for Centres of Excellence* under Contract ICA1-CT-2000-70023 with IFIN-HH**.**

The last action was initiated and largely guided by EC/JRC/IRMM-Geel, leading finally to the only one successful atomic-physics proposal from EEC under the corresponding FP5 call. Basic points of our group contributions to these projects are given in the following.

---

[2] M. Avrigeanu and V. Avrigeanu, *STAPRE-H95 Computer Code*, IPNE Report NP-86, Bucharest,1995; in E. Sartori (Ed.), *Nuclear Model Codes*, OECD NEA Data Bank, Saclay, 1992, p. 102; News NEA Data Bank 17 (1995) 22, 25.

[3] A. Fessler, E. Wattecamps, D.L. Smith, and S.M. Qaim, Phys. Rev. C **58**, 996 (1998).

[4] A. Harangozo, I. Stetcu, M. Avrigeanu, and V. Avrigeanu, Phys. Rev. C **58**, 295 (1998).

[5] P. Oblozinsky, *"Development of Reference Input Parameter Library (RIPL) for Nuclear Model Calculations of Nuclear Data"*, Report INDC(NDS)-335, IAEA, Vienna, 1995; Report IAEA-TECDOC-1034, IAEA, Vienna, 1998 [http://www-nds.iaea.or.at/ripl/].

[6] M. Avrigeanu and V. Avrigeanu, Comp. Phys. Comm. **112**, 191 (1998).

[7] V. Avrigeanu, P.E. Hodgson, and M. Avrigeanu., Phys. Rev. C **49**, 2136 (1994).

[8] V. Avrigeanu, A. Florescu, A. Sandulescu, and W. Greiner, Phys. Rev. C **52**, R1765 (1995).

[9] M. Avrigeanu *et al.*, Phys. Rev. C **54**, 2538 (1996); ibid. **56**, 1633 (1997).

[10] M. Avrigeanu, G.S. Anagnostatos, A.N. Antonov, J. Giapitzakis, Phys. Rev. C **62**, 017001 (2000).

[11] M. Avrigeanu, A.N. Antonov, H. Lenske, and I. Stetcu, Nucl. Phys. **A693**, 616 (2001).

2. Double-folding method for calculation of nuclear potential

In order to establish the correctness of various assumptions considered within the DF method[11] for the few-nucleon systems, the large density effects on the elastic scattering of ^{6,8}He on ^{4}He within microscopic optical potential have been analyzed. The comparative analysis of the experimental and microscopic elastic scattering angular distributions of ^{6,8}He on ^{4}He has been carried out. The calculated angular distributions have been obtained employing a microscopic real optical potential based on (a) Tanihata and COSMA models (see[11] for references) for the density distributions of Helium isotopes (Fig. 1), and (b) the M3Y, BDM3Y, and DDM3Y Paris effective NN interactions (Fig. 2). The sensitivity of the calculated cross sections with respect to both density distributions and effective NN interactions have been analyzed on this basis.

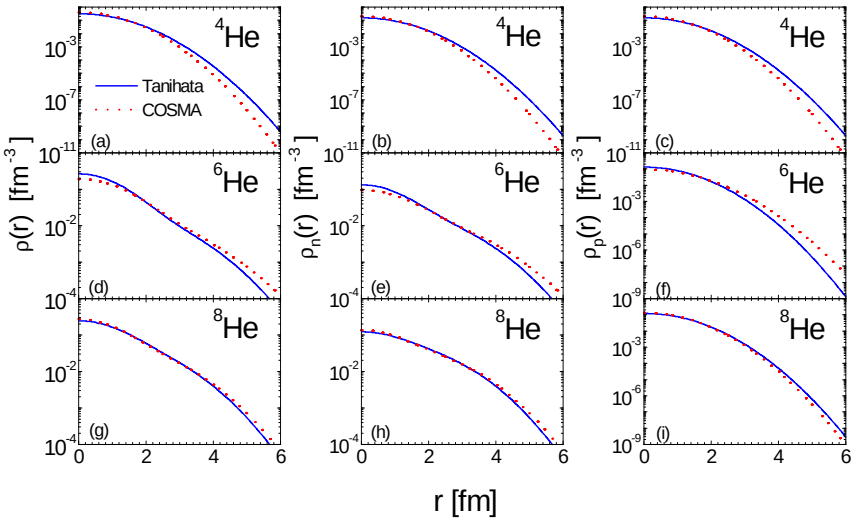

Fig. 1. Neutron and proton density distributions for ^{4,6,8}He nuclei by Tanihata and COSMA models.

Finally, it results that Tanihata's density distributions and the density dependent DDM3Y Paris effective NN interaction led to better agreement with the experimental data (Fig. 3). Based on these results it becomes possible the use of DF method for calculation of the nuclear potential for complex particles (e.g. ^{2,3}H, ^{3,4}He) emitted in fast-neutron induced reactions on medium nuclei, as well as for evaluation of the nuclear data for D incident on ^{6,7}Li.

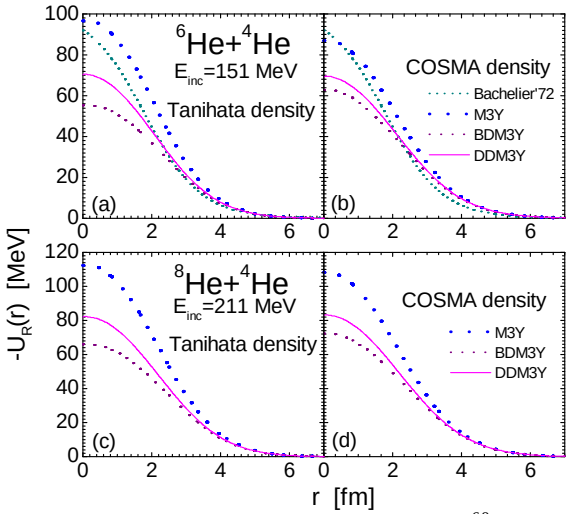

Fig. 2. Comparative analysis of the microscopic real optical potentials, for ^{6,8}He scattered on ^{4}He calculated with Tanihata and COSMA densities, and M3Y, BDM3Y, DDM3Y effective NN interactions.

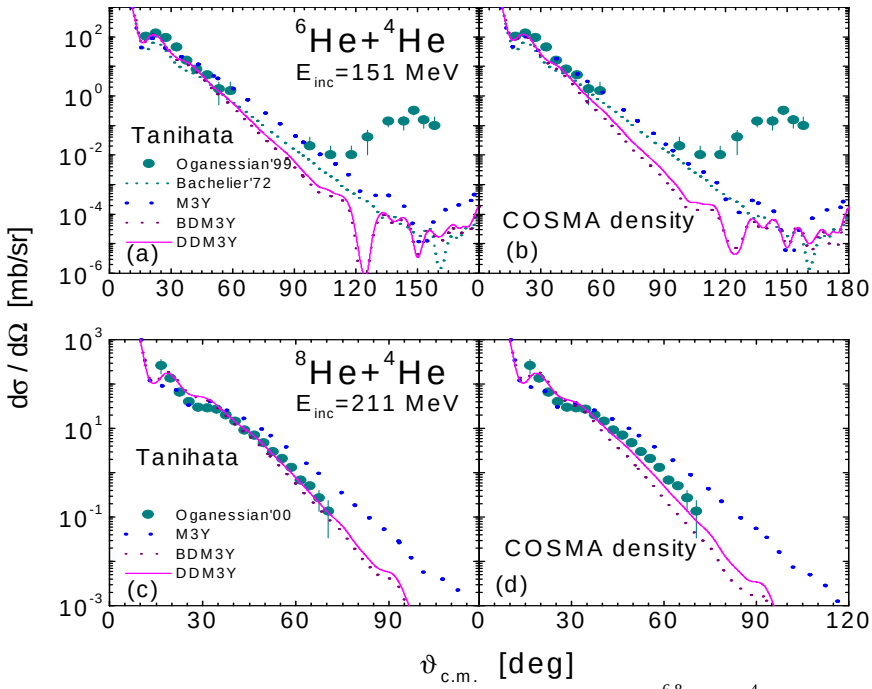

Fig. 3. Comparison of the elastic scattering differential cross sections of ^{6,8}He on ^{4}He, calculated with Tanihata and COSMA parametrization and with M3Y, BDM3Y and DDM3Y-Paris effective NN interaction, and the experimental data of Oganessian *et al*. (1999).

3. Improved model calculation of nuclear activation data

In the frame of the cooperation between IFIN-HH (Bucharest) and EC/JRC/IRMM (Geel) it was carried out recently the analysis of new IRMM accurate measurements, being established[12] that an improper consideration of the normalization method was involved by all recent international evaluated nuclear-data files in the case of the reaction $^{51}V(n,n'\alpha)^{47}Sc$. Work on new evaluated file for fast-neutron reactions on vanadium, of further interest for EAF-99 become thus necessary.

Next, during the *Workshop on Activation Data – EAF-2001* (6-7 Nov. 2000, CE de Cadarache) it was stated that extension of the model calculations, requested by the development of the next library version EAF-2003, is conditioned by their validation in various mass regions. It is why the above-mentioned consistent model calculations have been carried on also for the Mo isotopes. The first step of this work has been the study of the activation cross sections for reactions induced on ^{92}Mo, namely, $^{92}Mo(n,p)^{92}Nb^{m}$, $^{92}Mo(n,\alpha)^{89}Zr^{g,m}$, $^{92}Mo(n,2n)^{91}Mo^{g,m}$, and $^{92}Mo(n,n'p)^{91}Nb^{m}$, for which there is also a large amount of measured data. However, there are yet many discrepancies between even recent data sets, while three basic evaluations performed in the last decade at well-known laboratories show wide differences, e.g. up to ~50% for the (n,p) reaction[13,14] and ~65% for the (n,α) reaction[13,15]. In order to obtain confident calculated cross sections under these conditions, we have had to enlarge the parameter analysis carried out already in this respect concerning the following quantities which are most important for calculation of the isomeric cross section ratios:

3.1. Ratio between the *nuclear moment of inertia I* - the third parameter of the back-shifted Fermi gas (BSFG) model for the nuclear level density - and the rigid-body value I_r has been obtained[16] by using the method of Weigmann[17] *et al.* and the corresponding recent experimental neutron and proton-resonance spacings (RIPL), as shown in Fig. 4.

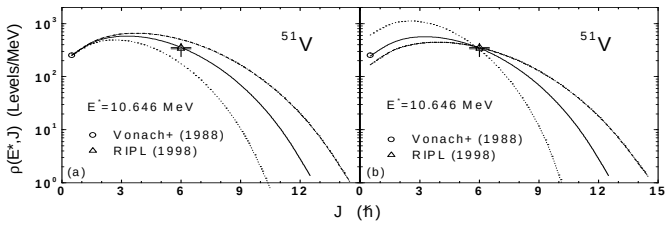

Fig. 4. Comparison[16] of the spin-dependent level densities of the nucleus ^{51}V.

[12] P. Reimer, V. Avrigeanu, A.J.M. Plompen, and S.M. Qaim, Phys. Rev. C (in press).
[13] S.M. Qaim, R. Wolfle, and B. Strohmaier, Phys. Rev. C **40**, 1993 (1989).
[14] P.E. Garret, L.A. Bernstein, J.A. Baker, K. Hauschild, C.A. McGrath, D.P. McNabb, W. Younes, M.B. Chadwick *et al*, Phys. Rev. C **62**, 054608 (2000).
[15] N. Yamamuro, Nucl. Sci. Eng. **109**, 128 (1991).
[16] V. Avrigeau, T. Glodariu, A.J.M. Plompen, H. Weigmann, J. Nucl. Sci. Eng. (to be published).
[17] H. Weigmann, C. Wagemans, A. Emsallem, and M. Asghar, Nucl. Phys. **A368**, 117 (1981).

3.2. The analysis of the *nuclear-level density* parameters ***a*** and **Δ** of the back-shifted Fermi gas (BSFG) model was carried out for 70 isotopes in the atomic-mass range A=79-111. The fit of the most recent experimental low-lying discrete levels (ENSDF file on the BNL-Brookhaven web site) and the *s*-wave nucleon resonance spacings (the corresponding RIPL file on the NDS/IAEA-Vienna web site) was done in this respect, corresponding to the values 0.5, 0.75, and 1 for the ratio I/I_r (Fig. 5).

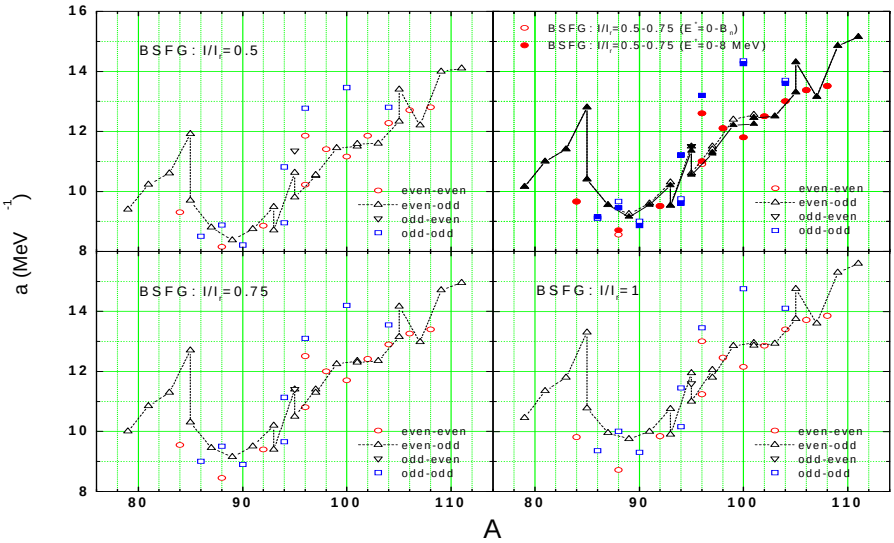

Fig. 5. Values of the level-density parameter *a* obtained by fit of the ENSDF and RIPL data

3.3. The BSFG model has been used for the *nuclear level density* at excitation energies lower than 12 MeV, which is the excitation region in which the corresponding parameters are obtained by fit of experimental data. At higher excitation it has been adopted the realistic analytical formula of Schmidt *et al.*[18]. This approach has been revised on the basis of all available data for the level density at excitation energies above the binding energy[16] (Fig. 6).

3.4. The *optical model potential* (OMP) for calculation of proton transmission coefficients on the residual nucleus ^{92}Nb, for energies up to 20 MeV, has been established through the analysis of the available ^{93}Nb*(p,n)*^{93}Mo reaction cross sections up to E_p=5.5 MeV, and total proton reaction cross sections around E_p=10 MeV (Fig. 7).

3.5. The systematics of the correction factor of the γ-ray strength functions shown in Fig. 8(a), used for the *γ-ray transmission coefficients* calculation in the framework of a modified energy-dependent Breit-Wigner model, has been established by analyzing the RIPL average radiative widths of the *s*-wave neutron resonance. At the same time the *γ-ray* decay schemes have been considered most carefully as shown, e.g., in Fig. 8(b).

[18] K.-H. Schmidt, H. Delagrange, J.P. Dufour, N. Carjan, and A. Fleury, Z. Phys. A **308**, 215 (1982).

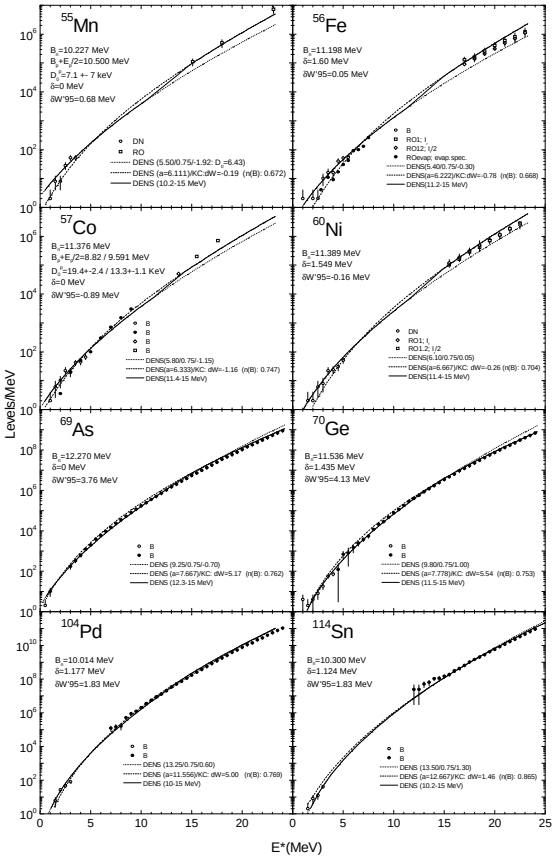

Fig. 6. Experimental and calculated observable total level densities[16].

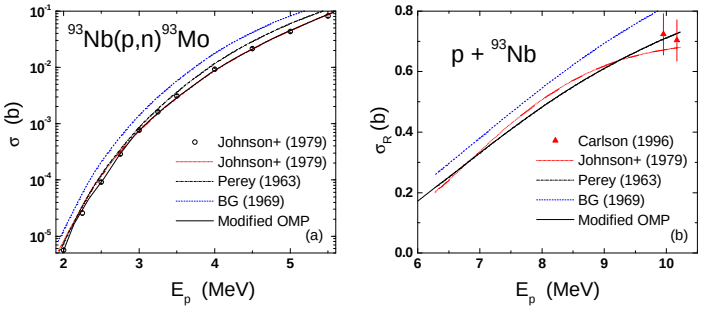

Fig. 7. Comparison of experimental and calculated *(p,n)* and proton total reaction cross sections[19].

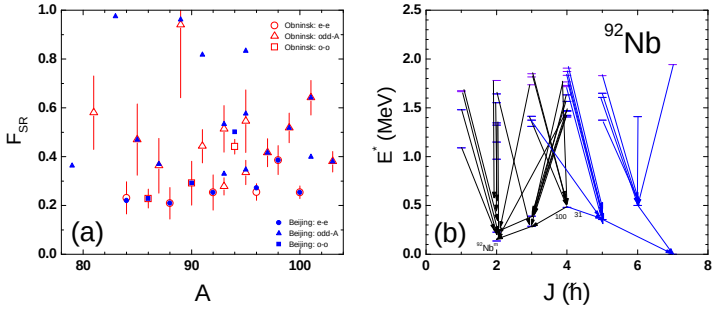

Fig. 8.(a) Systematics of the EDBW γ-ray strength functions, and (b) γ-ray decay scheme of ^{92}Nb.

Finally, the calculated[19] *excitation functions* for activation reactions ^{92}Mo*(n,p)*^{92}Nb^{m}, ^{92}Mo*(n,α)*^{89}Zr^{g,m}, ^{92}Mo*(n,2n)*^{91}Mo^{g,m}, and ^{92}Mo*(n,n'p)*^{91}Nb^{m} are shown in Figs. 9-11.

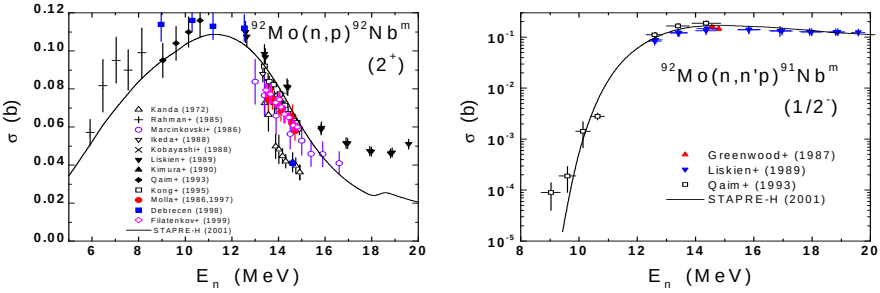

Fig. 9. Comparison[19] of experimental and calculated *(n,p)* and *(n,n'p)* cross sections of ^{92}Mo.

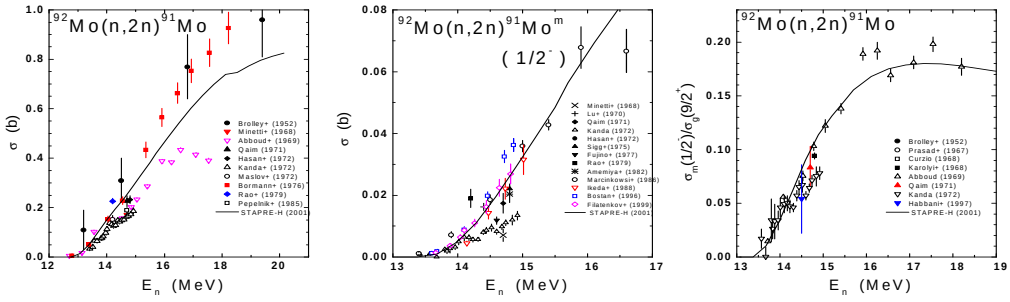

Fig. 10. Comparison[19] of experimental and calculated *(n,2n)* reaction cross sections of ^{92}Mo.

[19] M. Avrigeanu, V. Avrigeanu, and A.J.M. Plompen, J. Nucl. Sci. Eng. (to be published).

The agreement between calculated and the available experimental data could be considered good in the limit of experimental errors. It is thus proved the GDH specific account of the nuclear-density distribution. Moreover, one of the main assumptions of the model is intra-nuclear transition rate based on average imaginary OMP, so that no free parameter comes in and the corresponding results become more confident.

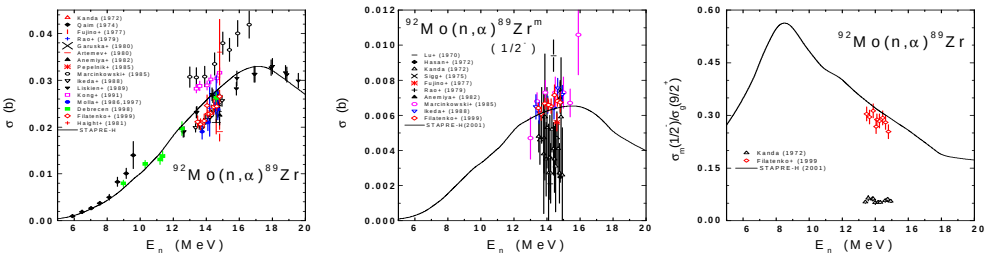

Fig. 11. Comparison[19] of experimental and calculated *(n,α)* reaction cross sections of ^{92}Mo.

4. International collaboration by networking and twinning

Civil nuclear power is a major component of the energy production in Europe and in the world. The scarcity of R&D funds and markets compels to co-ordination of the nuclear research undertaken by the various actors, countries and organisations. A "durable" European structure in this respect is proposed to be a network of "centres of excellence", of technical topics that, each one in his turn, will be organized in networks[20]. The strategic orientation should be given by a Steering Committee of the network, which will be assisted by a more operational structure (an operating agent, e.g. EC/JRC).

Reliable theoretical models and their associated parameters are needed for computation of physical quantities that cannot be easily measured but are essential for the design of advanced nuclear energy production systems (e.g. fusion reactors and accelerator-driven systems) as well as for analysis of the performance of systems intended to reduce the inventory of long-lived radioisotopes in nuclear waste. Therefore it is important to harmonise the policies and standards of safety and environmental protection of EEC countries and EU member states and to integrate all activities in the domain of nuclear energy.

The IFIN-HH successful project *"Inter-Disciplinary Research and Applications based on Nuclear and Atomic Physics"* (IDRANAP) under the EC/FP5/INCO2 *"Support for Centres of Excellence"* [21] is actually a useful experience in this respect. This proposal, largely guided by EC/JRC/IRMM-Geel and being finally the only one successful atomic-

[20] MICHELANGELO Network: R&D needs of nuclear-energy industry and also long-term planning, EC, Brussels, October 2000.

[21] EC/FP5/INCO2 (Confirming the international role of Community research, 1998-2002) *"Support for Centres of Excellence"*, Call identifier: ICFP599A1AM03, 1999-06-15 (deadline: 1999-10-15).

physics project from EEC under this FP5 call, has had the following scientific, social and economical main objectives:

- promotion in Romania of applications deriving from atomic and nuclear physics research;
- interdisciplinary research in fields such as ecology, health, biology, science of materials;
- to ensure conditions for scientific activities where students from Romanian or regional universities may find PhD programmes and an inspiring scientific climate to improve their training that counteract their tendency of migration in the West.

However, negotiation of the actual contract did not take into account that the "excellence" does not characterize the work conditions of the unit submitting the proposal IDRANAP but the results of the staff obtained even in such conditions. Therefore, real helpful assistance should be provided firstly for improvement of the work conditions at the own site.

Nevertheless, development of international collaboration by networking and twinning is decisive in order to enhance the expertise of our researchers as well as our research infrastructure so that we may be able to participate in European programmes.

STUDIA UNIVERSITATIS BABEŞ-BOLYAI, PHYSICA, SPECIAL ISSUE, 2001

ASPECTS REGARDING COMPUTER CONTROL OF ^{15}N SEPARATION PLANT

KAUCSÁR M., V.COSMA, D.AXENTE, A. BÂLDEA, H. BENDEA, V. BUNEA

National Institute for Research and Development
of Isotopic and Molecular Technologies
P. O. Box 700, 3400 Cluj-Napoca 5, ROMANIA

In order to improve the efficiency of a separation plant the whole process must be automatically controlled. A computerized control system is imposed by the high complexity of the isotopic separation process. The role of the data acquisition and control system is to keep automatically the separation process at an optimal level in all external conditions, eliminating the influence of the perturbing parameters. Regarding the separation plant from the point of view of the control engineering, the plant has one single useful output - the isotopic product. This output is characterized by a complex function, which involves qualitative (isotopic concentration) or/and quantitative (amount) properties of the product. There are two important inputs into the system: one is the amount of the substances and compounds, which supplies the plant, and the other is the electric power energy. Our first aim is to reduce to minimum the input/output ratio of the separation plant. On the other hand, applying this automatic control system we can reduce to minimum the operating personnel also. The hardware of the developed data acquisition and control system can be adapted to other separation plants, too, by the appropriate change of the sensors and the actuators. In this case the control software must be rewritten.

The isotopic product is sampled and analyzed using a dedicated mass spectrometer. An overall closed loop through the separation plant including this mass spectrometer could be very efficient, but the theoretical analysis is too complex and it is very difficult to realize in practice. Therefore multiple local control loops are preferred to apply for each important and with product strongly correlated parameter. Between these parameters there are complex interdependencies, governed by differential equations.

The simplified block diagram of the computer controlled ^{15}N separation plant is shown in figure 1. The process is based on the well-known Spindel-Taylor isotopic exchange:

$$^{15}NO+H^{14}NO_3 \leftrightarrow {}^{14}NO+H^{15}NO_3$$

with a single stage separation factor $\alpha = 1.055$ for 10M HNO_3, atmospheric pressure and room temperature [1], [2].

In chemical processes the temperature is one of the most important parameters. Thus, the temperature θ_{C1} and θ_{C2} of the separation columns must be maintained at constant level. Therefore the columns are surrounded by auxiliary water with controlled temperature at $26\pm0,5\ ^0C$, using a three positional control system. In

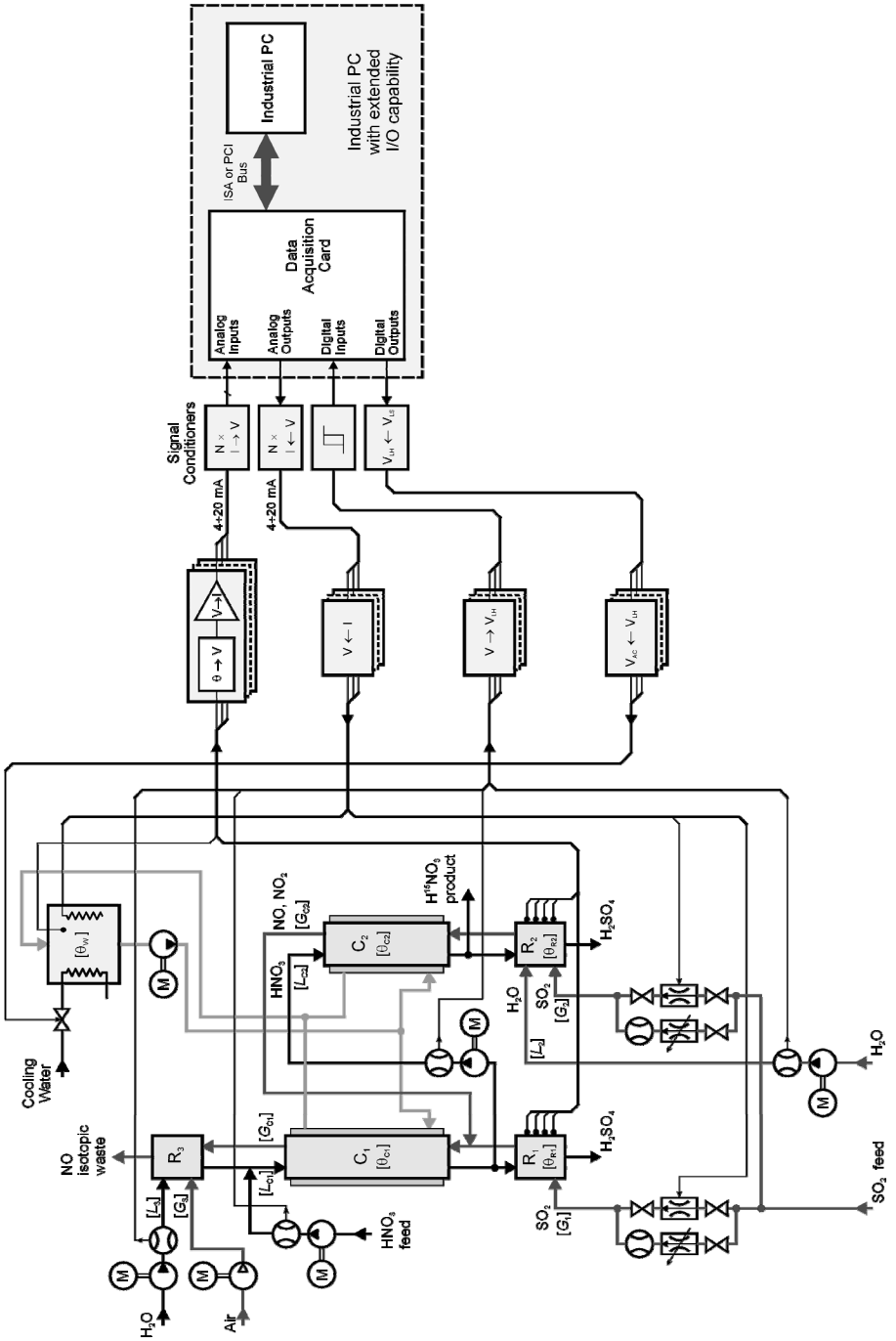

Fig. 1 Simplified block diagram of the computer controlled ^{15}N separation plant

refluxors R_1 and R_2 the exothermal chemical reactions take place in about 10 to 20 cm zone. These zones must be maintained at a given optimal height, and are localized measuring the temperature gradient over the height of the refluxors. Therefore each refluxor is provided by a temperature sensor array based on LM335, integrated circuit precise temperature sensor with easily calibration. This sensor operates as a 2-terminal zener with the breakdown voltage directly proportional to absolute temperature. The developed temperature measuring circuit (fig. 2) is 4–20 mA current transmitter and measures the temperature between 0 and 100 ^{0}C. The current transmitted to the computer is linearly proportional with the temperature:

$$I_\theta = I_0 + I_\theta \cdot \theta$$

where θ is the measured temperature expressed in degrees Celsius, $I_0 = 4\ \text{mA}$ is the output current at 0 ^{0}C and $I_\theta = 0.16\ \text{mA} / {}^0\text{C}$ is the measuring slope.

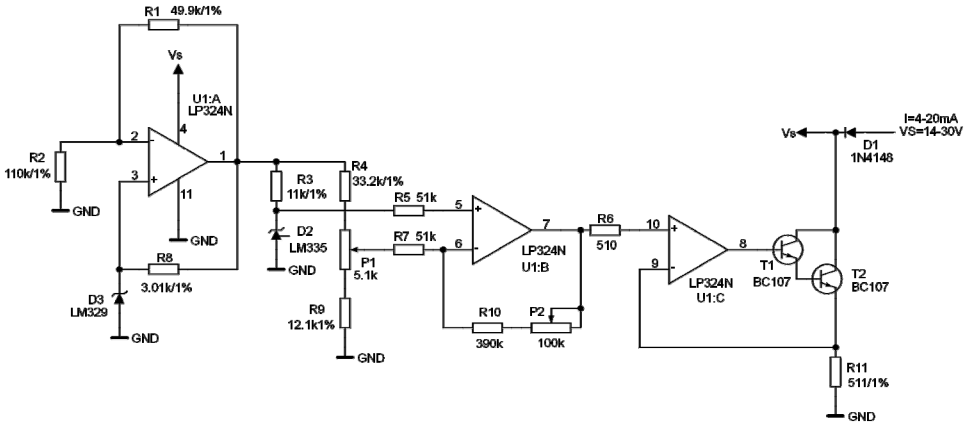

Fig. 2 Detailed circuit diagram of the temperature transmitter circuit

The position of the reaction zone is controlled by means of two main parameters: the flow of the nitric acid (L_{C1} and L_{C2}) and the flow of the sulfur dioxide (G_1 and G_2). The flows L_{C1} and L_{C2} are maintained at an optimal level using two constant flow rate feeding pumps. Two precision flow regulators control the flows G_1 and G_2 in such a manner that the height of the reaction zones falls in the predefined zone for optimal isotopic exchange [3], [4]. For this purpose the computer uses the thermal information obtained across the height of the refluxors by the mean of the sensor array.

The flow regulator delivers a flow, which depends only from its control input and is independent from its load resistance. The block diagram of the developed flow regulator is represented schematically in figure 3. For this purpose a valve (type VMC from Jouvenel & Cordier SA), developed for corrosive gases with fine and very reproducible flow setting capability is used. The output flow is measured with DM-100 thermal mass flowmeter, developed and manufactured in our institution (maximum

measured flow: 100 ml/min sensibility: 0.05 V/ml/min, response time: 10 sec). The driver of the servomotor of the valve is a phase controlled thyristor circuit. In order to improve the overall performance of the entire flow regulator system the nonlinear transfer characteristics from servomotor to flow is linearized using a nonlinear circuit with inverse nonlinear transfer characteristics [5], [6]. The detailed regulator circuit is presented in figure 3.

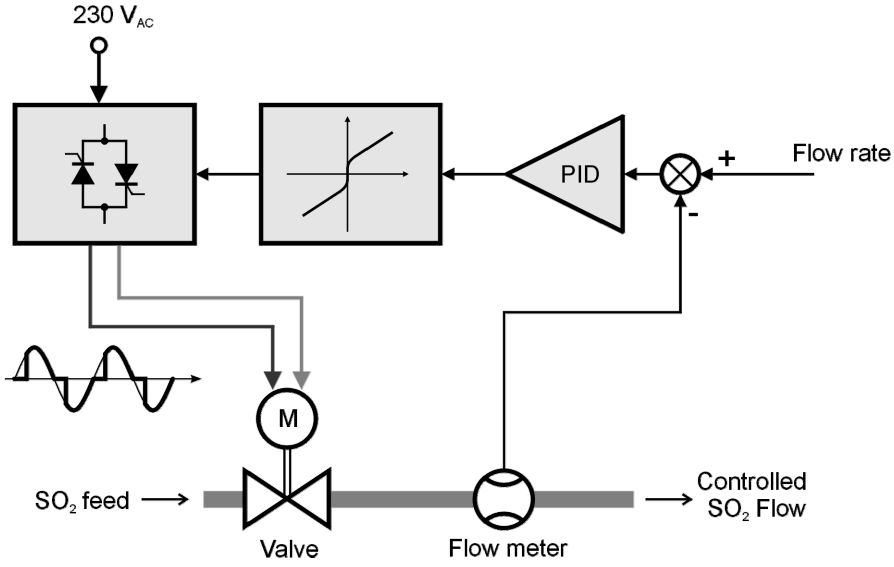

Fig. 3 Block diagram of the precision flow regulator

The industrial PC controls the separation plant through the input/output hardware. The PC is equipped with standard input/output ports, but in order to use it in the complex feedback loops, extra input/output hardware – dedicated input/output module cards – must be added to it. The structure of a single closed loop serving the automatic control of one single parameter of the separation plant is shown in figure 5. The whole control system is a complex combination of such simple control loops. Between the individually controlled parameters there are complex interdependencies, which must be taken into consideration.

Depending on the operating principle of the detectors and actuators the signals involved in the whole system are analog and digital. The majority of the sensors and transducers generate analog signals and only a few of them have digital output. The last case is typical for transducers specialized mainly in the detection of the level of a parameter. Actuators also need analog or digital control signals, corresponding to their operating principles. The analog signal is transmitted using the industrial standard 4–20 mA current. Where possible, digital data transmission is preferred. The separation process is relatively slow, thus instead of parallel digital data transfer the serial digital data transfer is preferred.

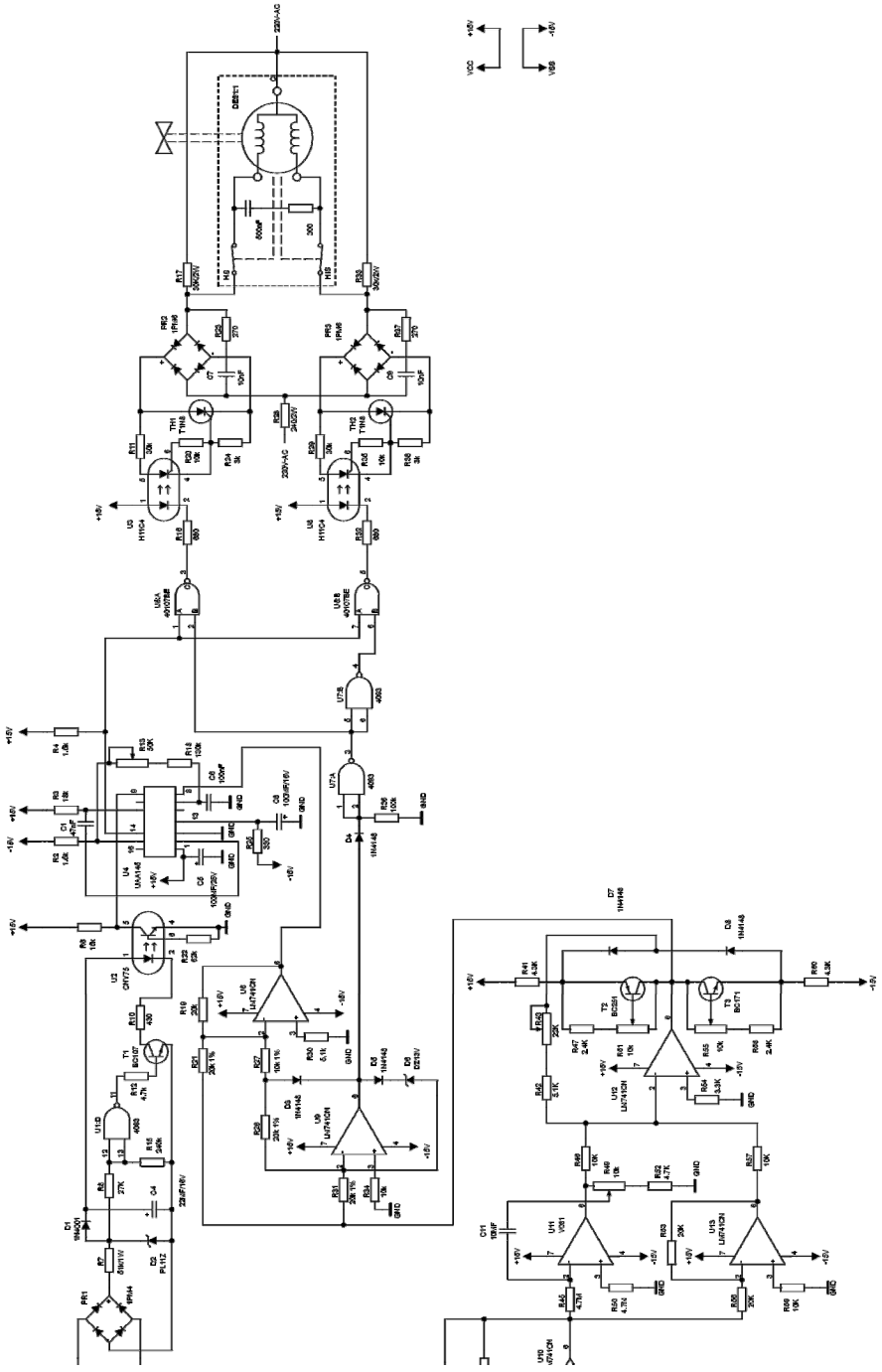

Fig. 4 Detailed circuit diagram of the flow regulator

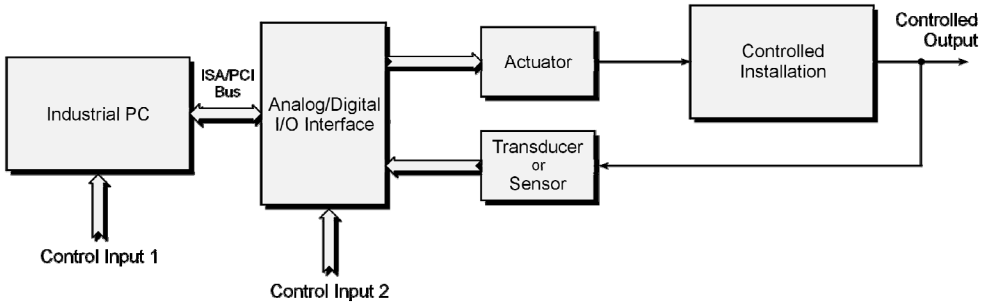

Fig.5 Controlling one of the multitude of significant parameters with a PC

The computer control of isotopic plant has a great advantage being very flexible in implementing all adequate control software with operator friendly interfacing routines. In the development of the control software one of the RAD systems is taken under consideration. A Rapid Application Development (RAD) system allows the programmer to produce a stable Windows program (application) relatively quickly and without a detailed knowledge of the inner workings of Windows itself [7]. Common RAD packages include Visual Basic, Visual C++ and Delphi. For this application we use Delphi. Delphi generates fast compiled code without sacrifying the execution speed. In creating with Delphi Win32 console applications or Win32 graphical user interface (GUI) programs we have all the power of a true compiled programming language (Object Pascal).

BIBLIOGRAPHY

1. *Spindel, W., Taylor, T.I.* – J.Chem.Phys. 23,981, (1955)
2. *Spindel, W., Taylor, T.I.* – Trans. New-York Acad.Sci., Ser.I, 19, 3 (1956)
3. *Benedict, M., Pigford, T.H.* – Nuclear Chemical Engineering, McGraw-Hill Book Co.
4. *Axente, D.* – Metodica separării pe coloane a izotopului ^{15}N, Studii cercetări chimie, tom.19, nr.4, p.395-415
5. *Thailer, G.J.; Pastel, M.P.* – Analysis and Design of Nonlinear Feedback Control Systems; McGraw-Hill Book Co., Inc. New-York 1962
6. *Călin, S.* – Regulatoare automate; Ed.Didactică şi Pedagogică, Bucureşti 1976
7. *** – Computing with Delphi. The University of Science and Technology in Manchester, 1996, http://www.me.umist.ac.uk/delphi.htm
8. *Young, A., Podgoretsky, A.* – How to Write To Hardware Ports in Windows Using Delphi. The Delphi Hardware Programmers's Archive, 1997, Johvi, Estonia

EXTENDING THE APPLICATION AREA OF A TIME-OF-FLIGHT MASS SPECTROMETER TO DETECT FRAGMENTS RESULTING FROM MULTIPLY CHARGED ION COLLISIONS

DANA DUMITRIU[*], D. IOANOVICIU[**], C-TIN CIORTEA[*], N. GLIGAN[**], GH. BACIU[**]

** "Horea Hulubei" National Institute for Physics and Nuclear Engineering, P. O. Box Ro MG-6, Bucharest-M¾gurele ROMANIA*
*** National Institute for Research & Development of Isotopic and Molecular Technologies, P. O. Box 700 Ro 3400 Cluj-Napoca, ROMANIA*

Introduction

The detection of the fragments resulted from collisions of high energy multiply charged ions is connected with the extraction of the analysed charged particles from an increased volume. This implies some specific conditions concerning the time-focusing conditions. Therefore some modifications can be included in the design of the time-of-flight mass spectrometer constructed for fullerene ion detection. The ion source (Fig. 1) was adapted to accomodate the high energy ion beam. The structure of the ion extracting electrode system was redesigned with this purpose. Appropriate diameter openings were provided to obtain the desired reacting gas throughput. The eflectron was adapted to the deeper analysed ion forming region. With this purpose the system was recalculated for second order focusing conditions. A solution was found accounting for the insertion of an additional grid in the former reflectron design. To obtain the best configuration, with a minimal modification of the field free spaces and ato locate the detector closely to its initial position a detailed ion optical study of the time focusing conditions was worked out. Other possible improvements are outlined.

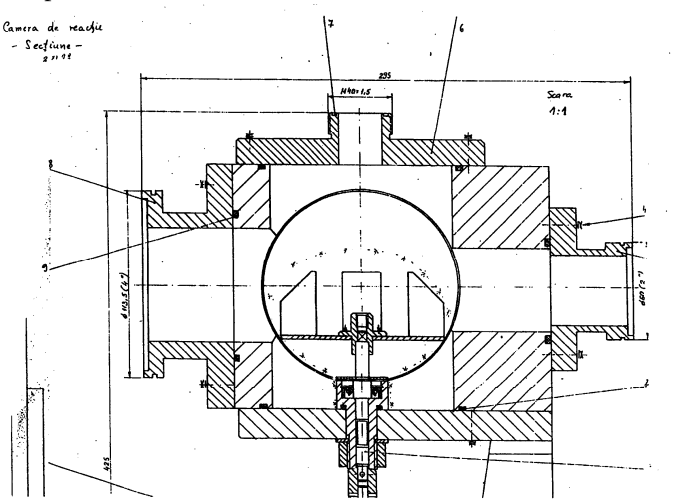

Figure 1. The ion source

The time-of-flight mass spectrometer for fullerene and recoil ions was already described briefly in the preceding of the PIM conference series [1]. The basic geometric parameters to remember are:

- The extracting field is established in a region of 16.7 mm depth.
- The incidence angle of the ion packet axis to the electric field limit is of 2 degrees.
- The total length of the field-free path is 2360 mm. This distance was established for the original design intended to ensure an energy focusing in time of first order. The use of this instrument to detect fragments from multicharged ion collisions implies more harsh focusing conditions for the ions of different energies as the space region producing ions to be analyzed is deeper.

This kind of focusing problems are solved by including two stage mirrors inside the time-of-flight mass spectrometer. The second order focusing in time for ions gaining different energies inside the source is obtained if a number of conditions, geometric as well as electric, are satisfied. The ratio of the electric fields inside the second stage E_2 and inside the first stage E_1 respectively must satisfy the following relationship:

$$E_2/E_1 = (1 - 3p^2)/\{(1-p^2)(1-p + p^3 ds/d_1)\}$$

Here besides E_2 and E_1 the following symbols were used:
$p = (U_r/U)^{1/2}$ is a parameter connecting the ion energy in the field free space U to its energy at the boundary of the second stage U_r, with $U_r = U - eE_1d_1$ where the ion of charge e penetrated through the first stage of depth d_1. d_s is the depth of the ion extracting region, identical in this case of a single stage ion source, with the accelerating field extent.

The field free space of length L, needed to ensure second order energy focusing in time is given by the expression:

$$L = 2[2d_1 + d_s(1 - p^2)]/(1 - 3p^2)$$

The mass dispersion in time of the mass spectrometer D_g, is given by the formula:

$$D_g = (L/v)(1 - p^2)$$

while the third order aberration can be written as:

$$A_b = (1 - p^2)/(8p^2)(L/v)(eE_s s + mv_{zo}^2/2)^3/U^3$$

Based on the knowledge of the above quoted parameters and these formulas a solution to switch from first ordr energy focusing in time to second order focusing of this kind was devised.

The first criterion in searching the appropriate solution was to be so selected to need the smallest number of changes in design. So it was decided to try the position of the ion source and of the detector, both unchanged, keeping in this way the field free space length also unmodified.

To determine the position where a second grid must be inserted calculations were made:

The second grid can be inserted between two consecutive rings of the mirror (Fig. 2) As the width of a ring is 20 mm, this is the step we can increase the distance of the first stage depth.

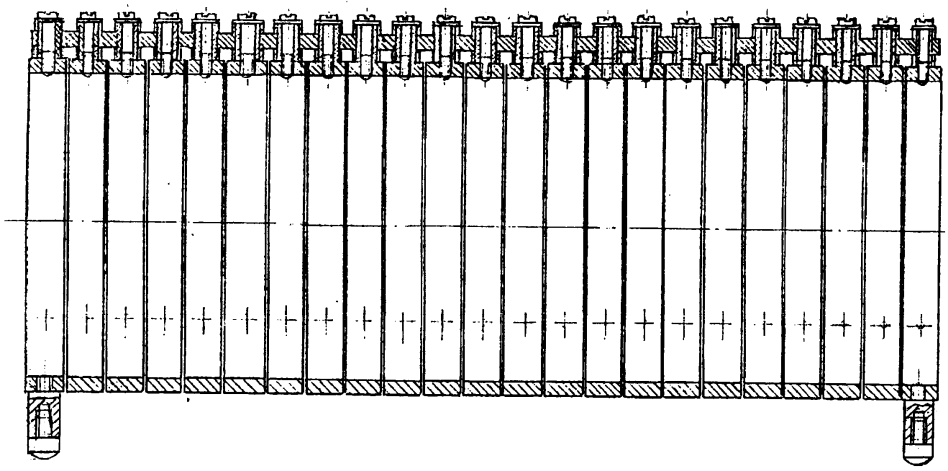

Assuming d_s = 16.7 mm and L = 2360 mm, the other parameters were calculated for various positions of the intermediate grid. To see the depth where the second grid must be located inside the 640 mm long (32 ring) original mirror, the second stage depth was calculated for each case. The second stage depth d_r was calculated with the expression:

$$d_r/d_1 = p^2/(E_2/E_1)$$

which results from the definition of p.

The variation of the first stage depth as function of the parameter p ensuring the second order energy focusing in time, keeping the old value for L, is represented in Fig. 3.

As function of the same parameter is given the reference ion velocity-flight time product in another figure (Fig. 4).

The third order aberration coefficient variation is presented in Fig. 5.

The depth of the second stage is illustrated in Fig. 6.

The third order aberration coefficient increases monotonically with the depth of the first stage. Accounting for this reason the grid must be placed closer to the mirror's entry limit.

To not allow field penetration through meshes to deformate the stage structure itself, the second grid must be inserted not to close to the entry limit. So it was decided to insert it at 120 mm from the entry face of the mirror. For this geometry the value of the parameter p is 0.511914, the aberration coefficient 831 and the depth of the second stage 17.976 mm.

1. Dana Dumitriu, D. Ioanoviciu, C-tin Ciortea, Z. Szilagyi, Gh. Baciu, N. Gligan Conference on Isotopic and Molecular Processes 23-25 September 1999 Cluj-Napoca.

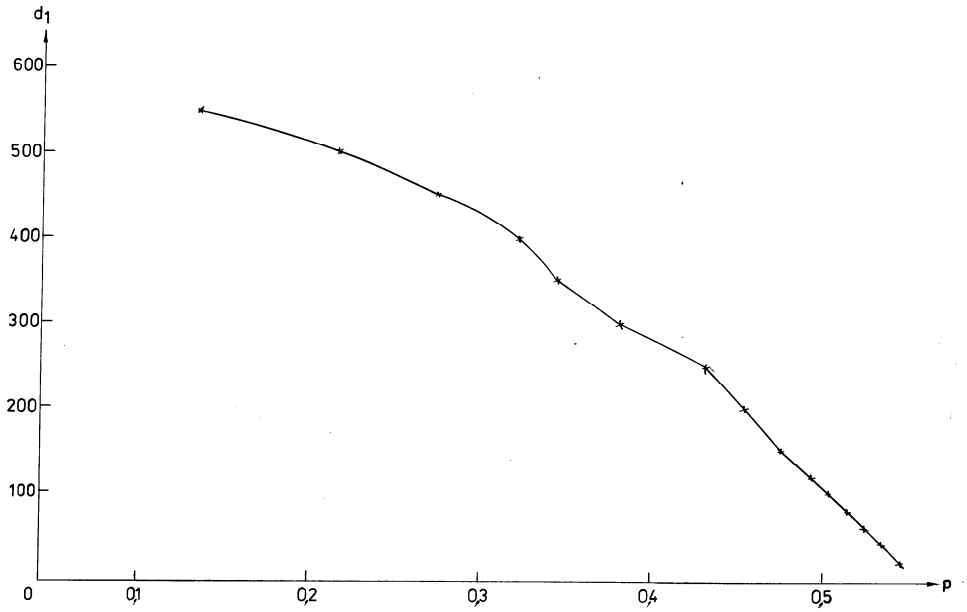

Figure 3.

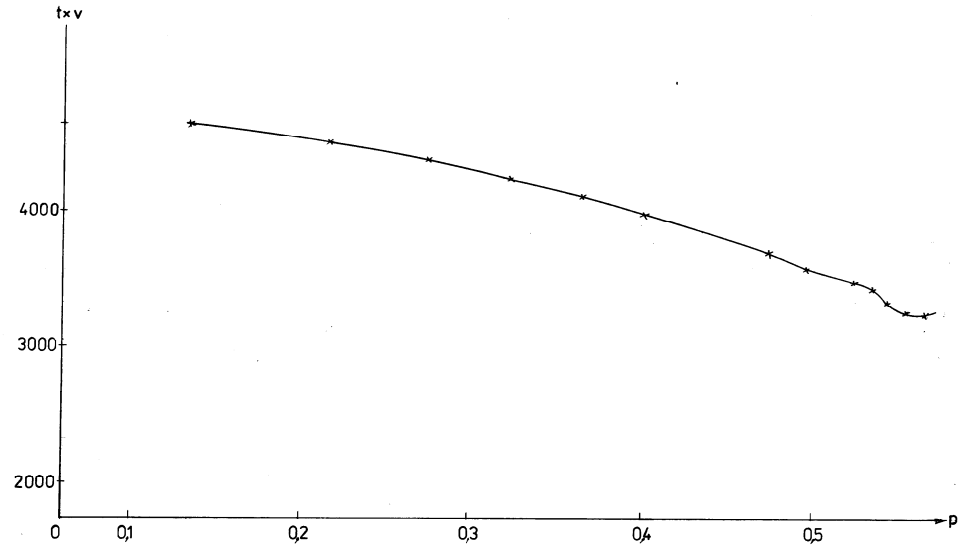

Figure 4.

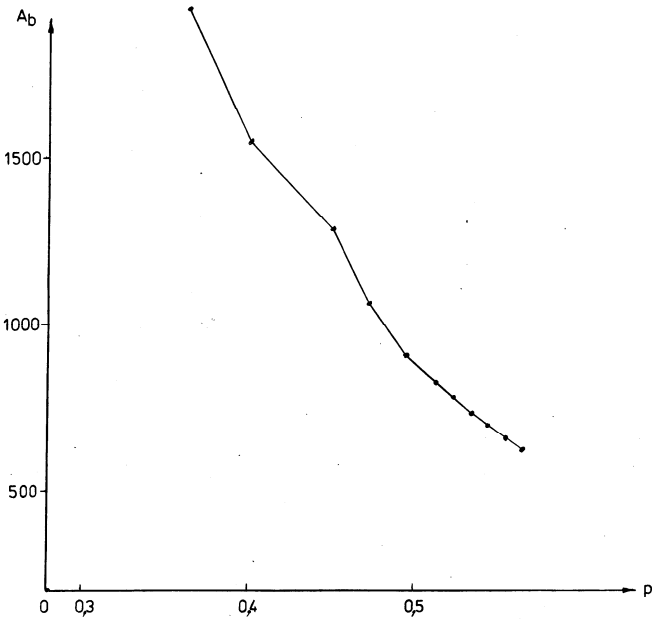

Figure 5

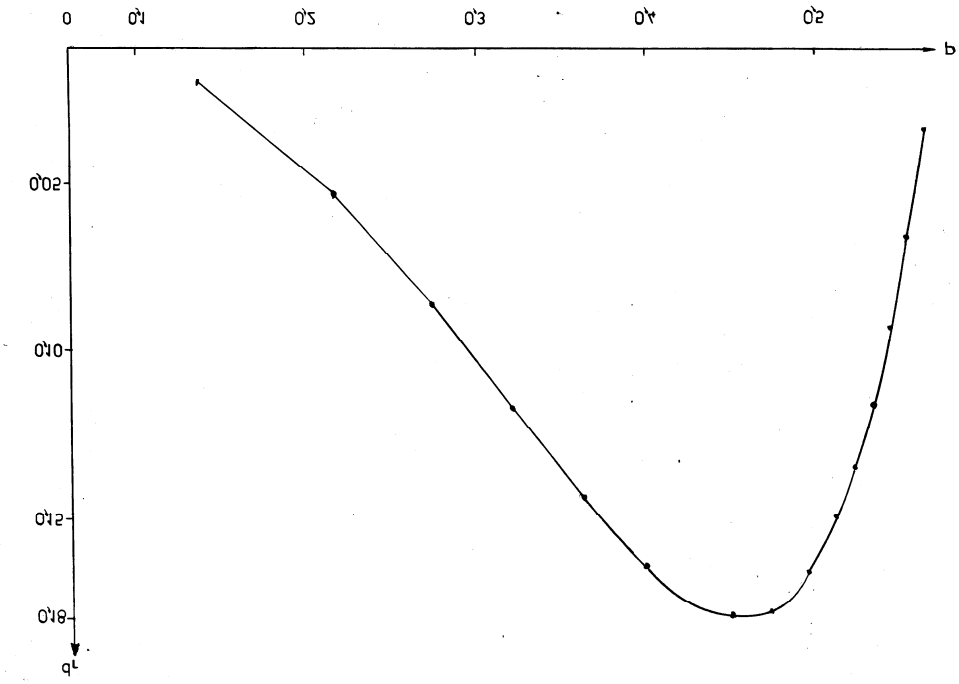

Figure 6

STUDIA UNIVERSITATIS BABEŞ-BOLYAI, PHYSICA, SPECIAL ISSUE, 2001

APPLICATION OF CARBON ISOTOPE ANALYSIS IN FOOD TECHNOLOGY

ZS. SZÁNTÓ, É. SVINGOR, I. FUTÓ, L. PALCSU, M. MOLNÁR

Inst. of Nucl. Res. of the Hung. Acad. of Sci., 4032 Debrecen, Bem tér 18/c.

SUMMARY. SIRA of carbon has developed rapidly into a powerful analytical technique in food industry. An isotopic analysis of $\delta^{13}C$ frequently will provide valuable information about the source (sources) of the carbon.

Carbon SIRA has found broad applications in the fruit juice industry where isotopic standards of identity are firmly established for apple juice and orange juice, and guard against the addition of sugars from corn or cane sources. Isotopic standards to assure the quality of honey and pure maple syrup are also well established. Governmental agencies use the standards for detecting fraudulent products, while industry uses the isotopic method for quality assurance.

Introduction

The purpose of the paper is to present through some examples the practical applications of carbon isotope analysis in food industry. Carbon isotope analysis is a powerful tool in monitoring the identity, origin or purity of foodstuff of various types [1]. Most of the isotopic analysis are performed for quality control in the food technology.

Measurement of stable isotopic composition of the lighter elements allows evaluation of food adulteration of natural sweeteners with high fructose corn syrup (HFCS). Is that the product really honey, maple syrup, orange juice, apple juice…etc.? SIRA will tell you.

What`s SIRA? SIRA is the abbreviation of stable carbon isotope ratio analysis. The overall process of carbon SIRA consists of three stages. The first stage is the selection of the sample or the isolation of the particular compound to be analyzed. The second stage involves the conversion of this compound into CO_2 gas. The third stage is the analysis of the CO_2 by mass spectrometry [2].

Carbon SIRA is performed on carbon converted to CO_2 form for mass spectrometry. All types of compounds therefore must be converted quantitatively to carbon dioxide for analysis. There has been quite a lot of research related to the different techniques used in the last decade for conversion [1-3]. In our laboratory CO_2 was obtained by a microcombustion technique. The samples were loaded into Sn capsules and moved into the quartz tube of an elemental analyzer (NA1500 NCS, Carlo Erba Instruments) where the samples were combusted in a stream of oxygen at 1200°C. The quartz tube was filled with tungstic oxide and CuO where the excess of oxygen was reduced. On the PORAPAQ column the resulting mixture of combustion gases were separated (due to the different retention on the column). The CO_2 obtained was trapped in an ampoule at liquid nitrogen temperature. The water resulting from the

combustion reaction was absorbed by a $MgClO_4$ trap. CO_2 was purified and before connecting the ampoule containing the sample to the mass spectrometer a gas pressure adjustment was made.

^{13}C to ^{12}C ratio was measured in a McKinney-Nier type mass spectrometer developed in the INR-HAS. The spectrometer has a dual inlet system and triple ion collector (the ion signals are measured simultaneously). The carbon SIRA values are customarily reported with respect to the PDB standard. However the lab utilize our own working standard gas in daily operations.

Generally speaking, the isotopic content of natural molecules is the result of:

- climatic and geographical conditions
- the photosynthetic metabolism of plants

The ranges of $\delta^{13}C$ values for the major carbon reservoirs of importance to the food sciences are shown in Fig. 1.:

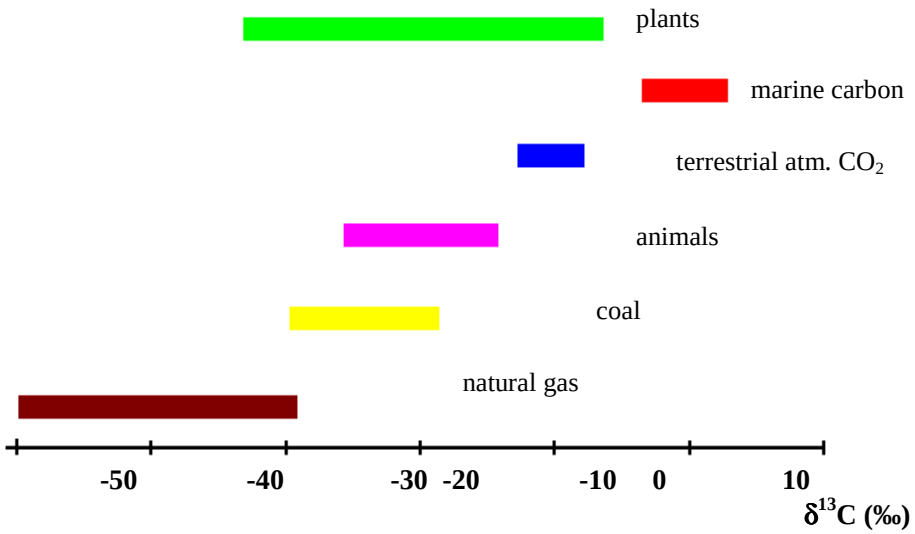

Fig.1. *Range of carbon isotope variations in selected carbon cycle reservoirs*

The largest reservoir of carbon is the ocean, where it occurs primarily as dissolved carbonate and bicarbonate. The average $\delta^{13}C$ value of the total carbon in the ocean is about 0 ‰ on the PDB scale.

The isotopic ratio ($^{13}C/^{12}C$), measured by the isotopic ratio mass spectrometry, can be used to discriminate between plants of different photosynthetic metabolism of CO_2. Each metabolic group can be characterised by a different isotopic deviation of $\delta^{13}C$. The following metabolic groups can be differentiated: C3, C4 and CAM [4].

The $\delta^{13}C$ values found in C3 plants range from about –22 ‰ to about –35 ‰, while carbon from C4 plants are somewhat heavier, ranging from about –8 ‰ to about –20 ‰ [3-5]. Values for CAM plants, which use features of both the C3 and C4 pathways,

spread throughout most of the ranges of values found for C3 and C4 plants. Pineapples and cactus are notable examples of CAM plants.

Avoiding the biochemical fractionation of carbon isotopes during photosynthesis, one thing has to be mentioned: depending on the different ways of fixing CO_2 green plants are using more or less energy and are more or less efficient in its utilization of the available atmospheric carbon dioxide [5-6].

Carbon SIRA in food technology

The vast economic size of the market for food offers great temptations for the production and sale of fraudulent products, adulterated products and synthetic products that are labeled as natural ones. Conventional techniques of chemical analysis have served the food industry well for many years but are limited in their ability to detect certain types of fraudulent or mislabeled products. The aversion to added sugar and the demand for "all natural" food products among consumers has led to a great deal of mislabeling on the part of food processors in order to achieve greater economic gain.

The nature of deceptions detectable by carbon SIRA in food technology falls into three broad categories. The most common is the **adulteration of an expensive natural product**, such as apple juice, with a much cheaper natural product such as cane sugar or high fructose corn syrup (HFCS). The second is **outright falsification of a food**. An example is maple syrup produced by simple addition of maple flavoring to a sugar syrup or HFCS. The third general category is **the sale of synthetic materials as natural ones** or the addition of synthetic materials to natural ones in order to increase the volume of the product. The procedure for using carbon SIRA in monitoring food products involves two stages. It must first be established that the product to be analyzed, or some specific component of it, has a particular isotopic composition that can be distinguished from that of the materials that might be used to adulterate it. Potential adulterating components are then analyzed to establish their isotopic identity. The carbon SIRA method cannot, in general, be used to establish purity unequivocally but it can be used to establish impurity or adulteration with a high degree of success.

Most of the well-established carbon SIRA procedures, which have found application in food science, are related to the substantial isotopic difference between products formed by C3 or C4 photosynthesis. An increase in the isotopic deviation of the $\delta^{13}C$ of the ethanol produced by the fermentation of sugars from a fruit juice (C3), leads to the conclusion that cane or corn sugar (C4) has been added.

In Table 1. some products of the food industry are presented together with their source, number of analysis performed and the carbon isotope composition found:

For regulatory purposes the official Association of Official Analytical Chemists (AOAC) set a conservative limit of carbon isotope composition as a proof of adulteration [7].

The clear-cut isotopic standard of identity for 100% pure maple syrup was traced at –24 ‰ with a standard deviation of less than ± 1 ‰.

The standard of identity of apple juice with respect to carbon isotope composition was set at the value of –25.4 ‰ ± 1.2 ‰ (adulteration limit accepted –23.5 ‰)

Table 1.

Carbon isotopic analysis of different food products

Material	Source (plant type)	No. of analysis	Average $\delta^{13}C$ (‰)	Standard deviation (‰)
C3				
Maple syrup		20	-24.0	±0.2
Apple juice		20	-25.4	±0.2
Orange juice		10	-25.7	±0.2
Grape juice		10	-27.0	±0.4
Cellulose		5	-24.9	±0.1
Cane sugar or HFCS		10	-9.8	±0.2
Subfossilic wood		5	-23.96	±0.2
Vanillin **(CAM)**	Madagascar	10	-20.4	±0.2
	Java	6	-18.7	±0.4
	Mexico	3	-20.3	±0.1
	Tahiti	3	-16.8	±0.2
	Synthetic (lignin)	14	-27.4	±0.7
	Synthetic (eugenol)	4	-30.8	±0.2
	Synthetic (guaiacol)	3	-32.7	±0.4
Citral **(C4)**	Lemon grass	3	-11.6	±0.7
	Synthetic citral	3	-27.6	±0.5

In case of orange juice (orange which is a C3 fruit and its juice consists almost entirely of fruit sugars with minor amounts of other components) the standard of identity for the isotopic composition was set at –25.7‰ ±1 ‰ (the limit for quality assurance purposes is –24.5 ‰).

The isotopic composition of grape juice is of special interest because of the large amount of such juice used in the production of wine and other spirits. The grape juice shows a larger spread of the $\delta^{13}C$ values than that of most fruit juices, but provide an isotopic standard of identity of –27 ‰ ± 2 ‰. The reason for the somewhat less negative $\delta^{13}C$ values for grapes is not clear but may relate to the presence of other organic compounds in the juice.

Natural vanillin is derived from a genus of plants using the CAM pathway. Is obtained by solvent extraction from the vanilla beans and is traded as an extract. The synthetic vanillin of identical character to natural can be made from lignin, eugenol (clove oil) or guaiacol (a coal tar distillate) at a much lower price that of natural vanillin. Natural vanillin ranges in $\delta^{13}C$ from –16.8 ‰ to –20.4 ‰, which is typical for CAM plants, while synthetic vanillins gives values more negative than –26.8 ‰- -32.7 ‰. Any vanillin, which gives a $\delta^{13}C$ value more negative than –21 ‰ must be considered to have synthetic additives. The different species, growing in different geographical places can be easily distinguished, based upon the different isotopic ratio found [8].

Citral derived from lemon grass was found to have a C4 composition of –11.6 ‰, while synthetic citral had an isotopic composition of –27.6 ‰.

Honey

HFCS became in the early seventies a widespread used cheap sweetener commonly used in liquid form for honey adulteration because it could not be detected reliably by conventional chemical techniques.

Normally honey is derived from flowering plants, which are almost exclusively C3 in their photosynthetic behavior. HFCS is derived from corn, which is a C4 photosynthetic plant.

In Table 2. the result of carbon isotope ratio analysis of 30 honey samples originating from different parts of Hungary were presented:

Table 2.

Carbon isotopic analysis of honey samples from Hungary

Material	No. of analysis	Average $\delta^{13}C$ (‰)	Standard deviation (‰)
C3			
Honey	30	-24.4	±0.1
Cane sugar or HFCS	10	-9.7	±0.2

The samples represent all commercially important honey sources and all geographical regions in Hungary. We analyzed 10 HFCS samples, as well. Statistical analysis of the pure honey data indicated that the $\delta^{13}C$ of honey showed a coefficient of variation of only 3.86 %, which was the smallest variability yet encountered for any constituent or physical property of honey.

A histogram of $\delta^{13}C$ analysis of commercial honey samples submitted to our laboratory is presented in Fig.2.:

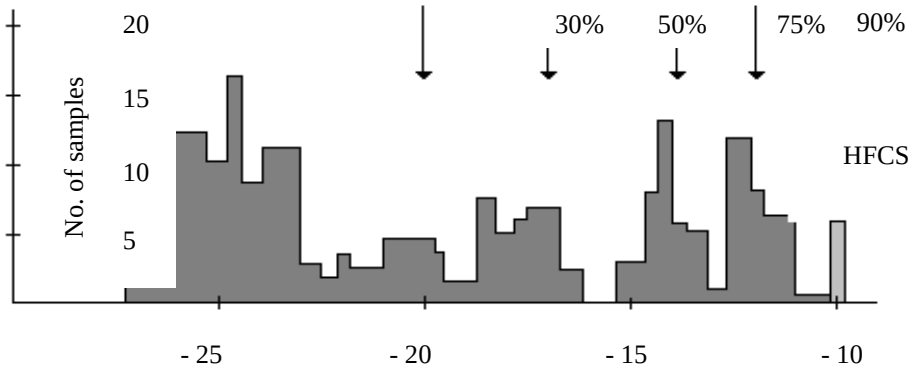

Fig.2. *Carbon isotopic analysis of pure honey and HFCS*

It is especially interesting that the distribution of data suggests fixed levels of adulteration. The histogram shows pronounced abundance peaks at 30, 50, 75, 90% adulteration. It seems reasonable that fraudulent addition of HFCS would be done according to a simple mathematical formula and such indeed seems to be the case.

Although this procedure of detecting corn or cane sugar adulteration of honey was validated and adopted in 1977 as an official method, the wide range of values found for pure honey (mean –25.4 ‰ range –22.5 ‰ to –27.4 ‰) produces a considerable area of uncertainty within which no positive judgment can be made about purity without other testing.

For regulatory purposes the method for detecting HFCS in honey set a conservative limit of $\delta^{13}C$ = -21.5 ‰ as a proof of adulteration.

The need for improved testing became apparent. To eliminate these difficulties a new procedure was developed in which each of the honey samples provided its own natural internal standard. The purity of the honey sample is judged by the difference between the isotope ratio value of the whole honey sample and the isotope ratio value of its separately prepared protein fraction. This principle was proposed by Parker and was further examined by Bricout and Koziet [9-10].

A candidate component for this approach should be a normal constituent, present in sufficient quantity and easily isolated. The most abundant constituent in honey after the sugar, oligosaccharides and gluconic acid is the protein, which averages 169 mg/100 g and ranges from 58 to 786 mg/100 g [11]. It originates largely from the honeybee.

The procedure consists in diluting a known amount of honey in distilled water adding sodium tungstate solution and sulphuric acid to precipitate proteins. The centrifuge tube is immersed in a 80°C water bath until visible flocculates form (10-15 min). The sample is centrifuged 5 min at 1500 rpm, decant the supernate and wash pellet 5 times with water. After drying the protein at 75°C for 24 h, the protein samples are weighted into Sn boats, combusted and measured the $\delta^{13}C$ by the same method used for honey.

The apparent corn/cane sugar content might be calculated as follows:

$$\textbf{Adulteration (\%)} = 100 * (\delta^{13}C_{\text{protein}} - \delta^{13}C_{\text{honey}}) / \delta^{13}C_{\text{protein}} - (-9.7)$$

reporting negative values for % adulteration as 0%. –9.7 ‰ is considered the mean $\delta^{13}C$ value of HFCS. The method permits the objective evaluation of possible adulteration especially in case of small quantities of corn/cane sugar (7-20%).

Whether the apparent corn/cane content of samples are result of their deliberated addition by the producers or is resulted from feeding sugar in the absence of a nectar flow is not addressed here.

REFERENCES

[1] Winkler F., Schmidt H. L., Z. Lebensm. Unters. Forsch., 1980, 171, 85-94.

[2] Tieszen L., Nature, 1978, 276, 97.

[3] White J.W., Doner L., J. Assoc. Off. Anal. Chem., 1978, 61, 746-750.

[4] Smith B., Epstein S., Plant Physiol., 1971, 47, 380-384.

[5] Gregory R., Biochemistry of Photosynthesis, Wiley: C.O. Chichester, Academic Press, New York, 1977, 52, 427-430.

[6] Crews C., Williams S., Vines H, Black C., CO_2 metabolism and plant productivity, Univ. Park P.: Baltimore, 1976, pp. 235-250.

[7] AOAC standards, 16th edition, section 44., 1995.

[8] Hoffman P., Salb M., J. Agric. Food Chem., 1979, 27, 352-355.

[9] Bricout J., Fontes J., Merlivat L., J. Assoc. Off. Anal. Chem., 1981, 64, 85-90.

[10] Bricout J., Koziet J., Ann. Falsif. Expert. Chim., 1975, 69, 245.

[11] White J.W., Honey. In: Advances in Food Research, eds. C.O. Chichester, E. M. Mrak and G.F. Stewart, Academic Press, New York, 1978, pp. 288-374.

STUDIA UNIVERSITATIS BABEŞ-BOLYAI, PHYSICA, SPECIAL ISSUE, 2001

DIFFERENT GEOMETRIES FOR MINIATURAL MASS SPECTROMETERS

C. CUNA, B. TUZSON, D. IOANOVICIU

National Institute for Research and Development of Isotopic and Molecular Technologies Cluj-Napoca, Romania

Introduction

Mass spectrometers are among the most precise and sensitive tools for chemical and isotopic analysis but the laboratory instruments are very expensive and bulky.

Our paper is aiming to develop mass analyzers as a mini system with reduced size, rugged and transportable. These analyzers are being designed for applications that include in-situ environmental monitoring and inspection. Therefore, it allows the rapid detection of hazardous chemical compounds in air, soil and water.

This paper presents the concept of a few mass analyzers, which were specifically designed for the small dimensions, instruments in such a way that they would be able to detect with sufficient sensitivity and accuracy all type of environmental pollutants.

Theory

There are many publications dealing with the focusing of charged particles in magnetic sector analyzers. The methodology used here is that of Cotte (1938) and Penner (1961), i.e., the matrix representation (the advantage of the matrix formulation is that the total transfer matrices for a complete magnet system can be computed as products of individual matrices for each component including the spaces of free flight between the magnets). However, our starting point is the ideal focusing field, determined from the simple geometry. In practice, magnetic fields of the ideal shapes may not be achieved, for various reasons, including difficulty of machining the pole pieces, field inhomogeneities, and fringing-field effects. We accept the straight-line approximation (because of the low resolution required by our purpose) and the asymmetric case (Fig.1). There are obviously a very great number of asymmetric lenses with linear boundaries, which might be considered. Three parameters were selected to make a design criterion suitable to help overcome the problems rises on the case of the miniaturized magnetic sector.

1) Sensitivity: in order to maximize transmission of ions through the analyzer, only geometries with simultaneous focusing (double direction focusing) in horizontal and vertical planes were considered.

The condition of point focusing is:

$$\tan(\phi - \psi) - 2\tan\varepsilon'' = (\cot\eta - \phi)^{-1}$$

where $tan\ \eta = tan\ \varepsilon' - R/l'$

$tan\ \psi = tan\ \varepsilon' + R/l'$

2) The path length of the ions from the ion source to the collector. Any reduction in path length that the ions take will result in a proportional decrease in the probability of collision with a molecule and corresponding decrease in ion beam broadening. In addition, a short ion pathway is necessary for the compactibility of the instrument

3) The mass resolving power (RP).

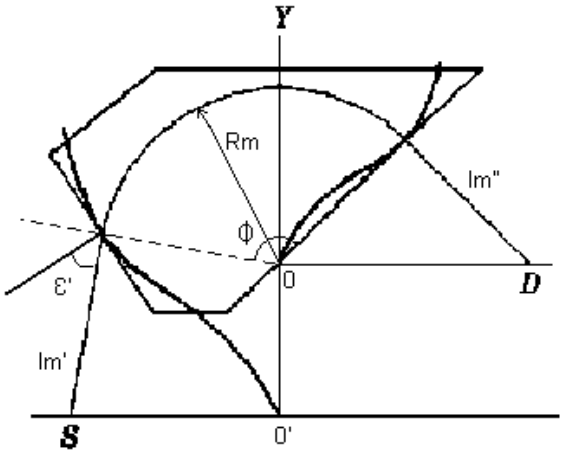

Fig.1 Geometry of asymmetric case

Many mass spectrometers use simple, symmetrical geometry where $l' = l''$ and the ion beam enters and exits the magnetic field normal to the pole faces ($\varepsilon' = \varepsilon'' = 0$). However, the dispersion of such instruments is fixed by the radius of the sector so that high dispersion requires a large instrument with long pathway; they are also unable to perform double direction focusing. In order to satisfy the above criteria, it is necessary to use asymmetrical geometry where the optic axis is non-normal to the magnetic boundaries and entrance and exit angles are not necessarily equivalent. These geometries allow double direction focusing and much greater dispersion than a normal geometry instrument of the same radius sector.

Using just simple geometrical relationships made the first optimization. We fixed $\varepsilon'' = 0$; $l''/R = 0.75$ and we searched the optimal values for ε' and ϕ, taking into account our criteria.

The next step was to consider the case of $\varepsilon'' \neq 0$. The equations describing the focusing properties of a magnetic sector are extensive, so solving them manually is a tedious, laborious task. Using the Matlab programming language, we wrote some programs that allow the calculations to be performed by computer and facilitate a systematic search for favorable solutions.

Three parameters ϕ , l' and ε' were varied systematically and the program yielded solutions for l'', ε'' , M_y and M_z . The search area was $\phi = 60°$ to $140°$, $\varepsilon' = -45°$ to $+45°$ and l' from $0.5R$ to $1.5R$. However, we already knew that the optimal area was $\phi = 120°$ and $\varepsilon' = 20°$ to $+45°$ which was then investigated on a finer scale.

A final solution, picked from an optimum compromise for the criteria discussed above, yielded a geometry of $\phi = 120°$, $l' = 1.326R$, $l'' = 0.971R$, $\varepsilon' = 34.1°$ and $\varepsilon'' = 47.8°$.

The design and theoretical performance is compared in Table 1 with a known geometry (reported by Cross) for stable isotope mass spectrometers. The Cross-geometry has an upper magnification coefficient; the path length of our analyzer is considerably shorter than in the case of the Cross. Both extended geometries have double direction focusing.

Table 1

Parameter	*As (opt.)*	*Cross*	*As (trig.)*
ϕ(deg)	120	90	120
$l'(R)$	1.326	2.0	0.67
$l''(R)$	0.971	2.0	0.75
ε'(deg)	34.1	26.57	40.0
ε''(deg)	47.8	26.57	0.0
Radial angular coeff. at $l''(\alpha)$	0.00	0.00	0.00
Axial angular coeff. at $l''(\tau)$	0.00	0.00	3.77
Dispersion	3.94	4.00	2.15
Magnification	0.99	1.00	0.73

We also investigated another geometrical arrangement, namely, a double focusing analyzer with an electric deflector and a magnetic deflector in a reverse-geometry (Fig.2).

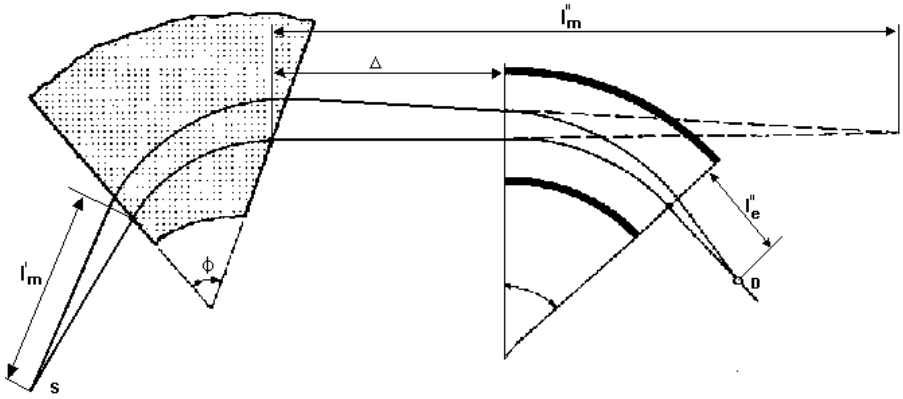

Fig. 2

To calculate the ion-optical properties of this kind of analyzers the following transfer matrices are to be used: the source-analyzer field-free space, the electric and magnetic fields, the field free space between the sectors and the last field-free space and the fringing fields at the entrance, respectively at the exit side of each sector.

The over-all transfer matrix [T] of this system is expressed as follows:

$$[T] = [L_e]\cdot[F_{re,34}]\cdot[E]\cdot[F_{re,12}]\cdot[\Delta]\cdot[F_{rm,34}]\cdot[M]\cdot[F_{rm,12}]\cdot[\ [L_m]$$

The condition of the first-order focusing is given by $T_{12} = T_{13},= 0$.

Assuming the electric field is homogeneous and straight effective boundaries a computer exploration gives the following combinations:

Nr	l_m' (R_m)	ε' (deg)	ε" (deg)	ϕ_m (deg)	Δ (R_m)	ϕ_e (deg)	R_e (R_m)	l_e'' (R_m)
1.	0.833	0	- 24	120	0.155	104.85	1.50	0.469
2.	0.632	0	- 28.6	65	0.75	129.6	1.166	0.24
3.	0.121	10	28.6	103	0.10	147.3	1.50	0.25
4.	1.10	17	- 24.77	119.5	0.25	81.36	1.50	0.97

where: R_m= 6 *cm.*

We already construct a double focusing analyzer with Wien filter and magnetic deflector (both located in the same pole-gap). Part of the homogeneous magnetic sector is transformed in a Wien filter when two plane condenser plates are immersed into the gap. The entry and exit pole boundaries are to be cut in such a way that the beam enters and exits at the same angle. (see Fig.3)

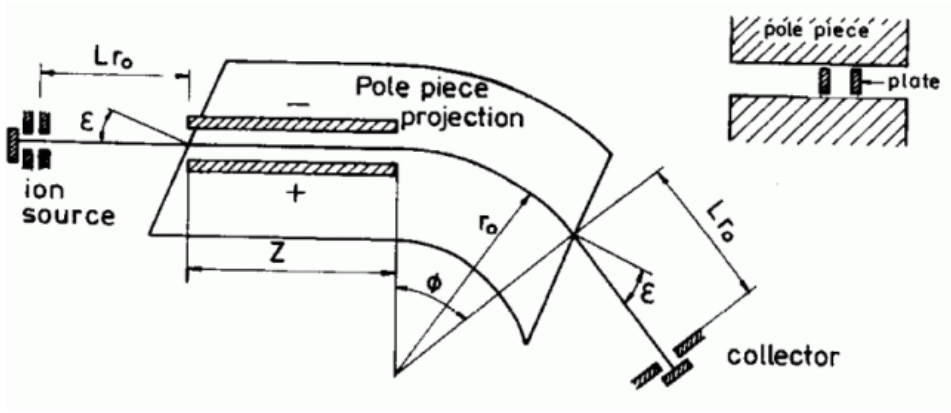

Fig.3

To calculate the ion-optical properties of this kind of analyzers the following transfer matrices are to be used: of the source-analyzer field-free space, of both the electric and magnetic fringing fields at the Wien filter's entry, including oblique incidence, for the Wien filter unperturbed crossed-fields, the exit electric fringing field of the filter, for the homogeneous magnetic sector part, for the exit magnetic fringing fields, oblique incidence, and for the last field-free space.

The first-order radial angular and energy focusing conditions give:

$$L = 1/(\tan \phi - \tan \varepsilon') \, , \; z = \phi'$$
$$M_x = -1, \; D_\gamma = L \tan \phi,$$

where L is the length of first and last field-free space, D_γ the mass dispersion coefficient, z the Wien filter effective length, all in units of the main path radius r_0.

Stigmatic focusing is obtained if the following additional condition is fulfilled:

$$\tan \varepsilon = (1/\phi + \tan \phi)/2 \qquad \text{for } M_y = +1$$

or

$$\tan \varepsilon = (\tan \phi)/2 \qquad \text{if } \; M_y = -1$$

Assuming the electric field is homogeneous and straight effective boundaries, a computer exploration gives the following basic parameters for a particular geometry with $My = +1$:

$$\phi = 88°, \; \varepsilon = 86.09°, \; L = 0.071$$

and for another with $M_y = -1$:

$$\phi = 60°, \; \varepsilon = 40.89°, \; L = 1.1547$$

This design ensures stigmatic focusing enhancing sensitivity by an order of magnitude, additionally, it ensures energy focusing making the instrument's resolution insensitive to increased energy spread. While the resolution increase by energy focusing is not always spectacular for such small instruments, this kind of focusing offers a dramatic sensitivity improvement by using a thick ionizing electron beam and increasing the ion extraction from the ionization chamber.

Conclusion

The new analyzers have shown improved performances to develop mass spectrometer as a mini system, i.e. portable, over conventional designs. The ion optical design (short ion pathway and high dispersion) is important here. A substantial sensitivity and resolution increase were obtained. It is also possible to build compact double focusing mass spectrometers, by using a Wien filter and a magnetic deflection sector, both included in a common pole-gap.

REFERENCES

1. H. Wollnik, *Nucl. Instr. And Meth.* 34 (1965) 213
2. H. Wollnik, *Nucl. Instr. And Meth.* 52 (1967) 250
3. H. Matsuda, T. Matsuo, *J. Mass Spectrom. Ion Phys*. 6(1971) 385
4. H. Matsuda, *J. Mass Spectrom. Ion Phys.* 14 (1974) 219
5. C. Cuna, D. Ioanoviciu, *Studii şi Cerc. Fiz* 2, 27 (1975) 153
6. H. Matsuda, *Nucl. Instr. Meth*. 187 (1981) 127
7. P. W. Hawkes, E. Kasper, *Principle of Electron Optics*, Academic Press, 1989, London
8. D. Ioanoviciu, C. Cuna, *Rapid. Com. Mass Spectrom*. 9 (1995) 512
9. P. Siebert, G. Petzold, A. Hellenbart, J. Muller, *Appl. Phys*. (1998) 155

STUDIA UNIVERSITATIS BABEŞ-BOLYAI, PHYSICA, SPECIAL ISSUE, 2001

EFFECT OF DEUTRATION ON THE VIBRATIONAL SPECTRA OF ORGANIC MOLECULES

FERENC BILLES, HENRIETTA ENDRÉDI and BALÁZS VÁRADY

Department of Physical Chemistry, Budapest University of Technology and Economics, H-1025 Budapest, Budafoki út 8, Hungary. E-mail: billes.fkt@chem.bme.hu

ABSTRACT. The deuteration of organic molecules is a very important tool for the assignment of their vibrational spectra. This article deals with the theoretical and experimental problems of the effect of deuteration on the vibrational spectra. The authors introduce several examples, the results of their own measurements and calculations and interpret the effects observable these vibrational spectra.

1. Introduction

The *deuteration of organic compounds* means the change of ^{1}H atom for ^{2}H ones. From the point of view of deuteration of the H atoms of organic molecules can be divided into two groups.

The *hydrogens belonging to the first group* are easily changed. Simply, one have to shake the solution of the compound in heavy water for a longer time or boiling the solution with reflux for a longer time. These hydrogen atoms participate in very polar bonds and therefore they are „mobile". On can find such kind hydrogens e.g. in OH, NH or COOH groups.

The deuteration with heavy water has a great drawback: the result is an equilibrium between the hydrogenated and the deuterated compounds.

The mentioned process does not act on the *second type hydrogens* that are „stable" in comparison of the first type ones. The hydrogen atoms of these type take part in slightly polar bonds. The hydrogen atoms in the CH groups are representatives of these group. The deuteration of these H atoms is more complicate. One have to synthesize the deuterated compound starting the preparation with simpler deuterated compounds. This method is more complicate than that with heavy water, however, it yields a compound deuterated theoretically perfectly, practically near to 100 %.

The hydrogens are very stable in the C-H bonds. However, sometimes the electronic effect of the neighbouring N atoms act on these bonds and the C-H hydrogen can be changed for deuterium through shaking with heavy water.

This article deals with our own results in this field.

2. Vibrational spectroscopy and deuteration

The deuteration redouble the atomic mass of ^{1}H and this has a very large effect on the vibrational spectra of the molecule.

According to the *theory* of the vibrational spectra [1] the calculation of the fundamental frequencies of a molecule can carried out according to the equation for the matrix eigenvalues

$$\left|\mathbf{GF} - \lambda\mathbf{E}\right| = 0$$

where **G** is the so-called inverse kinetic energy matrix, depending on the atomic masses and the geometric parameters of the molecule. **F** denotes the force constant

matrix representing the intramolecular forces. Its estimation is difficult. The best way for the determination of **F** is the calculation applying quantum chemical methods [2]. Besides, the equilibrium geometry of the molecules is also calculable in this way. **E** is a unit matrix. λ: containing the vibrational frequencies,

$$\lambda = 4\pi^2 c^2 \tilde{\nu}^2$$

where c stands for velocity of light in vacuum and the vibrational wavenumbers are denoted with $\tilde{\nu}$.

In the case of isotopomers very good approximations are widely applied: the intramolecular forces (matrix **F**) and the molecular geometry are independent of the isotopic change. Of course, this is applicable also for the deuteration, too. That means, during the calculation of the vibrational frequencies of isotopomers only the changes in the atomic masses in the matrix **G** are considered.

The most important methods of the *experimental* vibrational spectroscopy are the infrared and the Raman ones.

How does act the deuteration on the experimental spectra?

Compounds with „mobile" hydrogens build often *intermolecular hydrogen bonds*. This self-association is reflected in the energy levels of the molecule. The hydrogen bond building causes electronic shifts in the molecules. This effect decreases the energy levels of the molecule and in this way weakens the XH bonds.

The environments of the XH (X=O,N) bonds are very different, i.e. the energy levels of molecules in the molecular ensemble differ slightly each from the other. The result is a nearly normal distribution of the molecular energy levels.

The effect of association on the infrared and Raman spectra is different.

The characteristic XH stretching bands shift to lower frequencies in both infrared and Raman spectra.

The intensities of *infrared* spectral bands depend on the changes in dipole moments during the vibration of the vibrational mode where the XH stretching motion dominates. The association increases the dipole moments. As a result of the hydrogen bond building the XH stretching bands shift to lower frequencies and broaden. Very strong, sometimes very broad association bands are observed, sometimes they cover other weaker bands.

The intensities of the *Raman* bands depend on the changes in the molecular polarizability during the vibration of the vibrational mode where the XH stretching motion dominates. The XH stretching bands shifted and broaden similarly like in the infrared spectrum but he bands are less intense. The association structure is hardly observable, the bands covered in the infrared spectrum by association bands are here quite well observable.

The *deuteration* changes the **G** matrix , some of its diagonal elements decrease. Therefore *the characteristic wavenumbers* of the XD stretching bands are in good approximation $\sqrt{1/2}$ fold the wavenumbers of the XH stretching bands.

The *deuteration of „mobile" hydrogen* atoms decreases the self-association. Since, however, the deuteration results in an equilibrium this is useful only in the cases if the equilibrium is shifted to a large manner to the deuterated compound and/or the association is not very strong. Otherwise, this method is not very effective.

The deuteration of the stable hydrogen atoms can help in the assignment of the spectral bands, with its shift and intensity changes. The deuteration ceases also Fermi resonance and so the Fermi bands disappear and therefore it helps in the elucidation of the Fermi resonance.

3. Examples

The next figures illustrate the mentioned effects of the deuteration. The effects are introduced on the vibrational spectra of five molecules. The structure of furan, phenol, pyrrole and tetrazole are presented in Fig. 1, while the same of bilirubin is shown in Fig. 2.

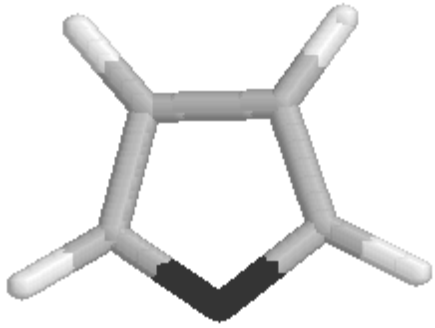

Furan

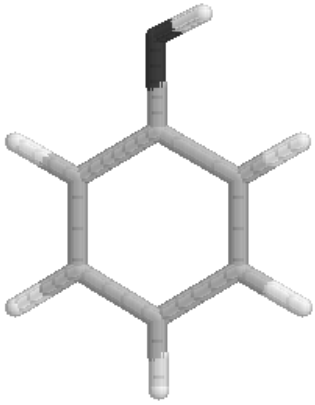

Phenol

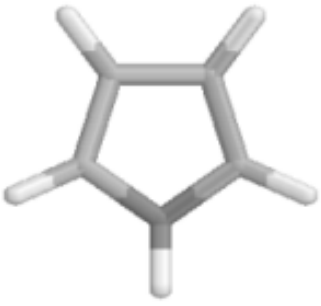

Pyrrole

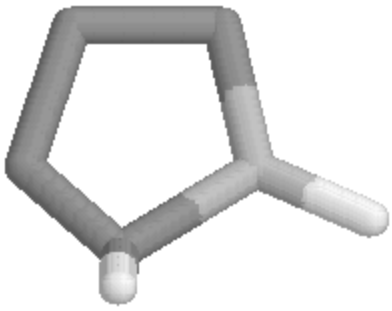

Tetrazole

Fig. 1. The molecular structure of furan, phenol, pyrrole and tetrazole.

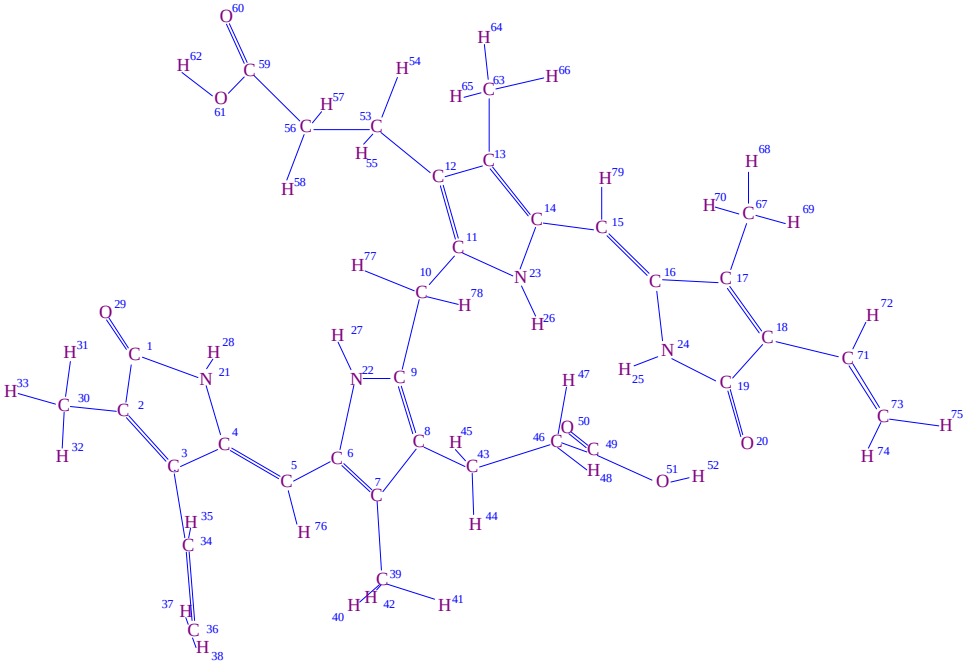

Fig. 2. The molecular structure of bilirubin.

Fig 3 gives the vapour infrared spectra of phenol, phenol-d5 and phenol-d6 in the 3700 to 2100 cm^{-1} region [3]. The spectrum of phenol-d6 shows the mixture of phenol-d5 and phenol-d6, the OH stretching band about 3650 cm^{-1} is more intense than the OD stretching band at 2700 cm^{-1}: the equilibrium is shifted to the ^{1}H isotopomer. However, the deuteration of the CH hydrogens is perfect: the broad band of the CH stretching shifts from about 3150 to about 2250 cm^{-1}.

Fig. 4 contains the neat infrared spectra of pyrrole, pyrrole-ND and pyrrole-D5 [4]. The N-deuteration shifts the NH stretch band from 3400 cm^{-1} to 2520 cm^{-1}. The equilibrium is shifted to the ^{2}H isotopomer. It is interesting, the last band in the spectrum of the D5 compound shifts to 2560 cm^{-1}. At the same time the decrease of the intensity of the NH stretch band indicates the shift of the equilibrium to ND. This fact proofs that the deuteration of the CH hydrogens affect on the equilibrium of the isotopomers.

Fig. 5 introduces the infrared and Raman spectra of tetrazole-d0 and tetrazole-ND [5]. The ND deuteration was carried out with heavy water. The infrared spectrum of the non-deuterated tetrazole reflects the very strong intermolecular interactions. The deuteration of the „mobile" hydrogens decreases a little the intensity of the association band but shows that the equilibrium is shifted to tetrazole-NH isotopomer. However, with this deuteration the CH stretching band is shifted from the position about 3150 cm^{-1} to about 2300 cm^{-1} indicating the perfect deuteration of the CH group of tetrazole. The deuteration of the CH group is observable similarly in the Raman spectrum. Comparing

the infrared and the Raman spectra one can conclude that the Raman spectrum is hardly sensitive to the association.

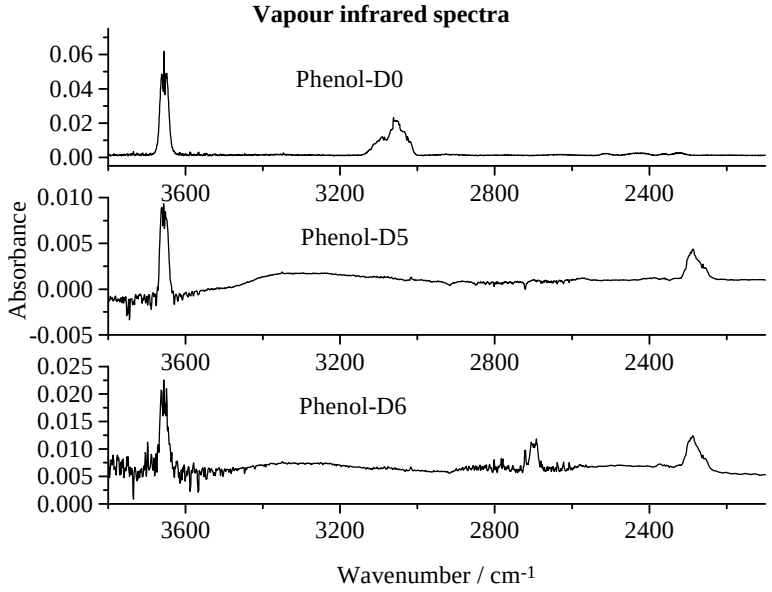

Fig. 3. Infrared spectra of vapour phase phenol, phenol-D5 and phenol-D6 in the 3700 - 2100 cm^{-1} region.

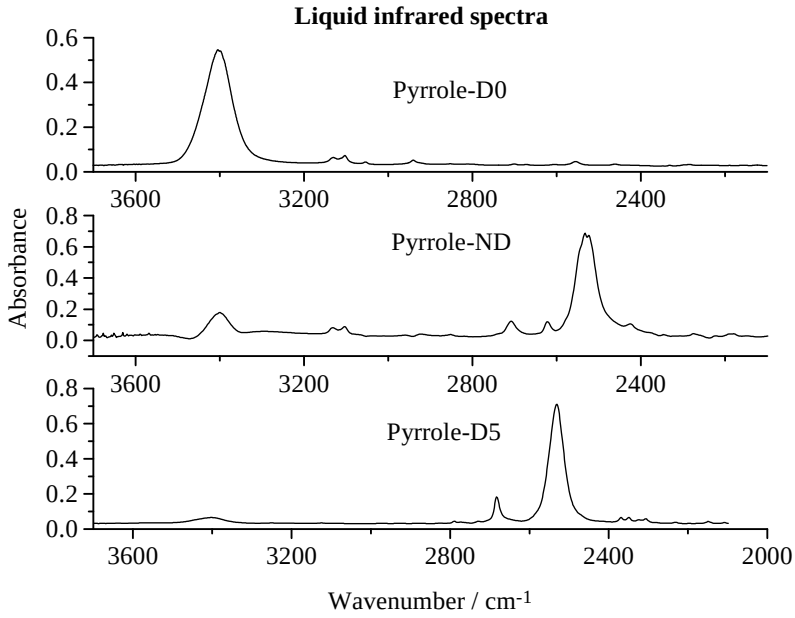

Fig. 4. Infrared spectra of liquid pyrrole, pyrrole-ND and pyrrole-D5 in the 3650 - 2000 cm^{-1} region.

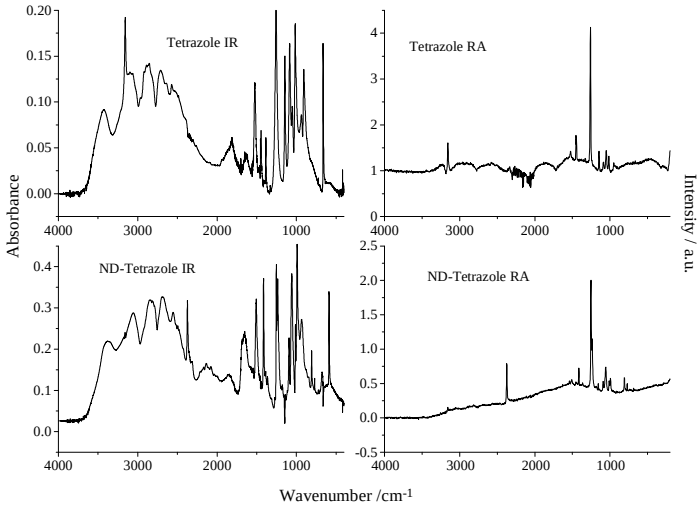

Fig. 5. Infrared (4000 - 400 cm^{-1}) and Raman spectra (4000 - 200 cm^{-1}) spectra of tetrazole and deuterated tetrazole.

Fig. 6 presents the infrared and Raman spectra of a large molecule, the bilirubin [6], see Fig. 1. The molecule contains NH and COOH groups as proton donors and acceptors and C=O groups as proton acceptors. The deuteration of the „mobile" hydrogens decreases the intensity of the stretching band of the non-associated NH groups (about 3400 cm^{-1}) and a new band appears about 2500 cm^{-1} belonging to the stretching of the non-associated ND groups. The building of intermolecular hydrogen bonds by the NH and COOH groups is spatially hindered. The NH and OH stretching band region of the Raman spectrum is practically insensitive to the deuteration.

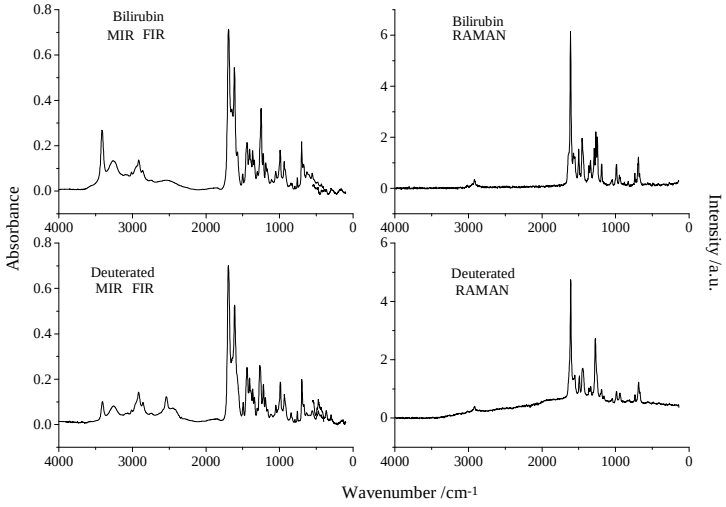

Fig. 6. Infrared (4000 - 100 cm^{-1}) and Raman spectra (4000 - 200 cm^{-1}) of bilirubin.

Figs. 7 and 8 show the infrared and Raman spectra of furan, respectively [7]. The effect of deuteration is introduced on both experimental and calculated (simulated) spectra. Since the molecule contains only „stable" hydrogen atoms the efficiency of the deuteration is practically perfect, as it was awaited. The calculated band positions are very close to the measured ones both in infrared and Raman spectra but the calculated intensities differ sometimes from the measured ones. Namely, the approximation used for the band intensities by the quantum chemical methods is weak. However, better method does not exist so far.

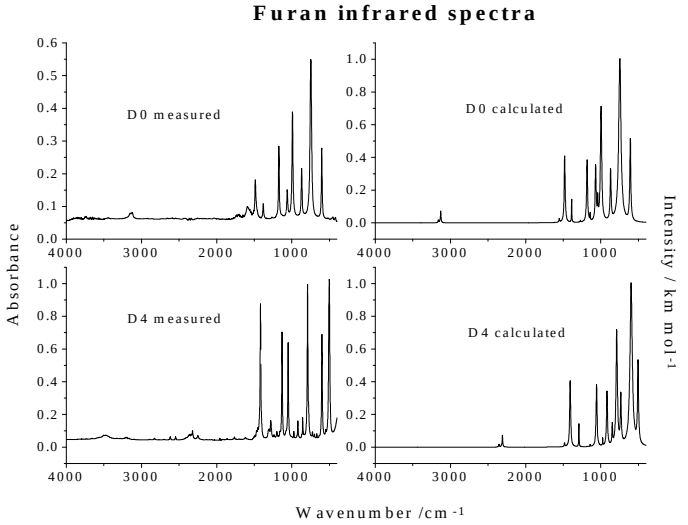

Fig. 7. Experimental and calculated infrared spectra of furan and furan-D4 in the 4000 - 400 cm^{-1} region.

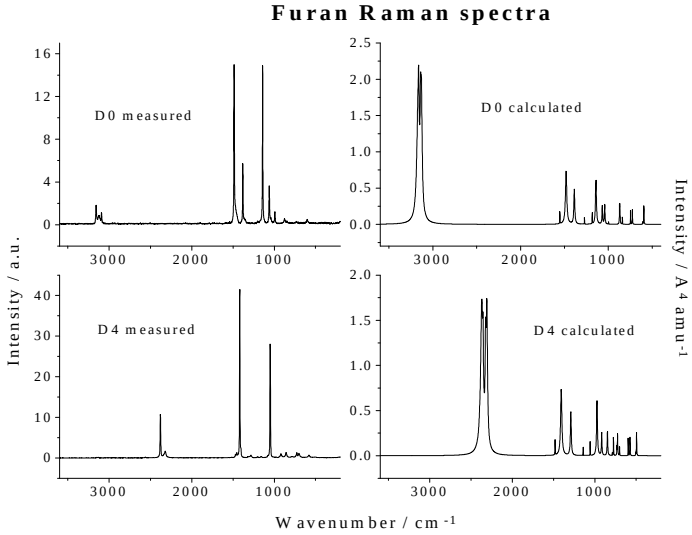

Fig. 8. Experimental and calculated Raman spectra of furan and furan-D4 in the 4000 - 200 cm^{-1} region.

With Fig. 9 we return to the spectra of phenol [3]. The infrared spectra of the CCl_4 solutions of the parent molecule and its full deuterated derivative were recorded and the corresponding spectra of the isolated molecule were calculated. The calculations cannot consider the existence of the equilibrium and the association. Of course, these are also absent in the spectra calculated for isolated molecules. The diluted solutions show very weak association bands. The equilibrium is shifted to the direction of the deuterated isotopomer, in contrary to the vapour phase (see Fig. 3).

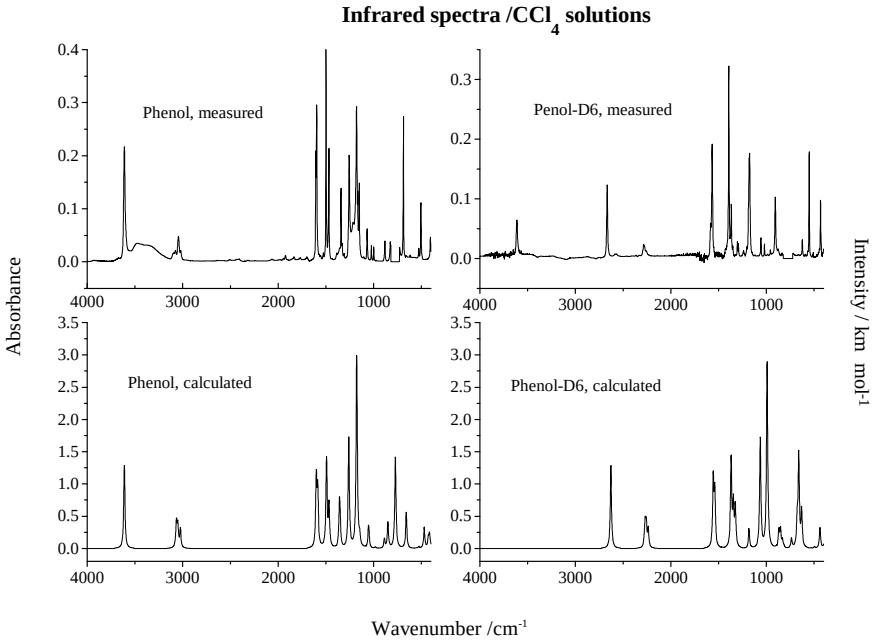

Fig. 9. Experimental (in CCl_4 solution) and calculated infrared spectra of phenol in the 4000 - 400 cm^{-1} region.

4. Conclusions

The examples tried to support the effects explained in the theoretical part. The deuteration of „mobile" hydrogens are in close connection with the investigation of hydrogen bonds. The deuteration of the „stable" hydrogens can help in the assignment of the vibrational spectra. Calculated (simulated) infrared and Raman spectra show the spectrum of the isolated molecule. The calculated frequencies are close to the experimental ones, while the intensities are sometimes far from the measured ones. The calculations cannot reflect the association bands and the isotopic equilibria but can help in the assignment of the spectra.

REFERENCES

1. Wilson, E.B., Decius, J.C., Cross, P.C.:Molecular vibrations (McGraw-Hill, New York, 1953).
2. Gribov, L.A., Orville-Thomas, J.W.: Theory and methods of calculation of molecular spectra (J. Wiley and Sons, Chichester, 1988).
3. Keresztury, G., Billes, F., Kubinyi, M., Sundius, T.: J. Phys. Chem., **A102,** 1371-1380 (1998).
4. Geidel, E., Billes, F.: J. Mol. Structure THEOCHEM **507**, 75-87 (2000).
5. Billes, F., Endrédi, H., Keresztury, G.: J. Mol. Structure (THEOCHEM), **530,** 183-200 (2000).
6. Billes, F,. Várady, B.: article in preparation.
7. Billes, F., Böhlig, H., Ackerman, M.: article in preparation.

SYNTHESIS OF [1, 3 - $^{15}N_2$] URACIL

MARIA CHIRIAC, DAMIAN AXENTE

National Institute for Reasearch and Development of Isotopic and Molecular Technologies, 3400 Cluj-Napoca, P. O. Box 700, Romania

The synthesis of ^{15}N labelled uracil, using $CO(^{15}NH_2)_2$ as starting isotopically labelled material, is presented.

The experimental procedure is an adaptation of the synthesis methods for the corresponding unlabelled compounds.

Urea - $^{15}N_2$ used as starting material was obtained from $H^{15}NO_3$ (99 at. % ^{15}N) produced at the National Institute for Reasearch and Development of Isotopic and Molecular Technologies.

The uracil structure was confirmed using the mass spectrometry method and the isotopic label was determined by mass spectrometry on the molecular compound.

Experimental

[1, 3 - $^{15}N_2$] uracil synthesis is presented in next scheme:

$$KCN + Cl - CH_2 - COOH \xrightarrow[40\text{-}50^0C]{Na_2CO_3} NC - CH_2 - COOH + KCl$$

$$NC - CH_2 - COOH + {}^{15}NH_2 - CO - {}^{15}NH_2 \longrightarrow {}^{15}NH_2 - CO - {}^{15}NH_2 - CO - CH_2 - CN \quad (1)$$

$$(1) + \xrightarrow[\text{Raney Ni} : H_2]{C_6H_4 - NH_3^+Cl^-} C_6H_4 - NH - CH = CH - CO - {}^{15}NH_2 - CO - {}^{15}NH_2 \quad (2)$$

$$(2) + \xrightarrow[4^0C]{\text{ethanolic HCl}} C_6H_4O_2{}^{15}N_2 \quad (3)$$

(1) = [1, 3 - $^{15}N_2$] cyanoacetylurea
(2) = [1, 3 - $^{15}N_2$] β-phenylaminoacryloylurea
(3) = [1, 3 - $^{15}N_2$] uracil

Synthesis of [1, 3 - $^{15}N_2$] uracil (3)

Chloroacetic acid (3.46 g) was dissolved in a minimum amount of water and neutralised by addition of anhydrous sodium carbonate. 1.96 g KCN in 10 ml of water

were added to the sodium chloroacetate solution and the temperature allowed to rise to 60^0C.

The reaction continued until the temperature ceased to rise, then the mixture was allowed to stand for twelve hours at room temperature. The resultant pale yellow solution was acidified and the excess of HCN, water and HCl were removed under reduced pressure at 50^0C. The residue was taken up in absolute alcohol and the solvent removed.

A suspension of urea - $^{15}N_2$ (1.86 g) in freshly distilled acetic anhydride was added to the dried residue and the mixture was heated at 100^0C for 30 minutes. Water was then added to the solution and upon cooling a crystalline solid was isolated, that proved to be (1) in 82% yield relative to urea. The melting point of the product is 211 - 2^0C.

Cyanoacetylurea [1, 3 - $^{15}N_2$] (2.92 g) and activated Raney Nickel (approximatelly 1.0 g) were suspended in water (115 ml) containing aniline·HCl (3.5 g). The suspension was exposed to hydrogen (1.5 atm.) and agitated for ten hours at room temperature. The resultant paste was extracted with alcohol several times. The filtrates were combined and the volume reduced on a rotary evaporator. Upon cooling a crystaline solid was isolated and identified as product (2) (1.86 g, 40% yield). M.P. = 208^0C. This product was dissolved in absolute alcohol which has been saturated with HCl gas at room temperature. The suspension was stored at 4^0C for four days, filtered, and the solid washed with cold ethanol (3 ml), then with NH_4OH. The filtrates was combined and the pH was adjusted to 3 with conc. H_2SO_4. The precipitate that resulted was identified as [1,3 - $^{15}N_2$] uracil (3); (0.480 g, 48% yield).M.P. = 309-315.

The uracyl structure and purity was confirmed using the mass spectrometry method and the isotopic label wass determined by MS analysis.

REFERENCES

[1] TRIPLET, J.W., MACK, S.W., SMITH, L.S., J. of Labelled Compounds and Radiopharm., Vol. XIV, No. 1, p. 35 (1978).

[2] SAFONOVA, T.A. and NESTEROV, V.M., Khimiya Geterotsiklicheskikh Soedinenii, 6:6, 847 (1970). (C.A.73:109395r, 1970).

[3] LIPNICK, R.L., FISSEKIS, J.D., J. of Labelled Compounds and Radiopharm., Vol. XVII, No. 2, p. 247 (1980).

STUDIA UNIVERSITATIS BABEŞ-BOLYAI, PHYSICA, SPECIAL ISSUE, 2001

ETHYLAMINE – D_7 FROM ACETONITRILE – D_3 BY CATALYTIC REDUCTION

V. ALMASAN, MIHAELA LAZAR, EVA LAURA GANEA, ANDREEA GLUHOI, P. MARGINEAN

National Institute for Research and Development of Isotopic and Molecular Technologies, Cluj Napoca

By replacing the high natural isotopic abundance atom with one of its isotopes one can obtain isotopic isomer molecules. The importance of these isotopic isomers consists in their structure and chemical properties, which are identical. The differences between molecules are: molecular mass and magnetic nuclear properties. Our work is relating to hydrogen and its stable isotope – deuterium. The isotopic isomers are deuterated molecules, which have one or more hydrogen atoms replaced by deuterium atoms. Deuterated compounds are helpful in molecular structural investigations by Nuclear Magnetic Resonance (NMR) and Mass Spectrometry (MS), or reaction mechanism studies. Thus isotopically labeled molecules become indispensable because the chemical disturbances are lower in the studies of chemical processes.

The synthesis of these labeled compounds it can be made by one of two paths:

- the molecules with simple structures will be obtained by isotopic exchange with heavy water or deuterium gas in homogenous or heterogeneous catalyzed reactions;
- the more complex molecules, are usually obtained by chemical synthesis. In these techniques, deuterated chemical reagents have to be used, depending on the place and the number of hydrogen atoms, which will be replaced.

Some classes of deuterated substances are more or less interesting, depending on their reactivity in chemical synthesis.

Many drugs are in the class of superior amines. In the process of chemical drug syntheses it is important to establish an optimal technique for the intermediate and the final products analyses.

For the successful use of NMR and MS methods, internal standards are needed. The deuterated compounds with a well-known number and molecular position of deuterium atoms are suitable for such internal standards.

Generally the primary amines are actives and valuables precursors in the synthesis of other more complexes compounds. The ethylamine D_7 corresponds to this purpose. The synthesis of ethylamine can be made by ammonium alkylation with Et-X or by catalytic reduction of acetonitrile. For our purpose the most suitable method is the acetonitrile D_3 reduction with D_2.

There are two methods to obtain the deuterated ethylamine by acetonitrile reduction:

1. Natural acetonitrile catalytic reduction by D_2. Two kind of reactions take places over the same catalyst, the CN group reduction and the H/D isotopic exchange of hydrogen atoms from the methyl radical.
2. Acetonitrile D_3 catalytic reduction by D_2 .

The first method has a disadvantage: the rate of catalyzed H/D isotopic exchange reaction is lower than the reduction rate of CN group. Thus, the methyl hydrogen is not totally replaced by deuterium. For this reason, the second method was chosen. [1]

The process steps are:

I. The obtaining of acetonitrile D_3

II. The catalytic reduction of acetonitrile with D_2.

I The obtainining of acetonitrile D_3

The molecular structure of acetonitrile (CH_3CN), indicates that a good method for the deuteration is the catalysed isotopic exchange H/D between the natural acetonitrile and a deuterium supply. The chosen donor is heavy water and the reaction is:

$$2CH_3CN + 3D_2O \xrightarrow{OD^-} {}_3CN + 3H_2O \quad (1)$$

The CN group is strongly attractive for electrons and mobilizes the CH bonds from the CH_3 group. The consequence is an increasing H/D exchange rate for the reaction between acetonitrile and heavy water.

If we note with X, Y the numbers of acetonitrile and heavy water moles respectively, and with x, y the isotopic concentration (in % at. D), the isotopic balance equation is [1]:

$$1{,}5X_1x_1 + Y_1y_1 = 1{,}5X_2x_2 + Y_2y_2 \quad (2)$$

The ratio of the numbers of exchangeable atoms between the two reagent molecules is 3/2 = 1.5

At the equilibrium $x_2 = x_e$ and $y_2 = y_e = x_e$, and:

$$\frac{X_e}{1-X_e} = \alpha \frac{1-Y_e}{Y_e} \quad (3)$$

The isotopic exchange constant α is roughly 1, and may be used as such in mathematical modeling. In this assumption, " γ " which is the initial molar ratio of reagents necessary for obtaining of x_e, can be calculated: [2]

$$\gamma = \frac{Y_1}{X_1} = 1.5 \frac{x_e - x_1}{y_1 - x_e} \quad (4)$$

Two kinds of H/D isotopic exchange process will be presented:

1. Each isotopic equilibration stage uses 99.8% at. D heavy water
2. Different concentrations of waste heavy water are used in earlier stages of the process and in the final stage 99,8% at. D heavy water.

1. The isotopic exchange process can be assimilated with a countercurrent cascade where the product of the first stage is the reagent for the second stage.

Experimental results are shown in tabel 1.

In this case we have a little number of stages but the heavy water consume is high. Thus, waste heavy water, with isotopic concentration between 50%D – 95%D, with low economical value, results for every stage.

Tabel 1.

Acetonitrile deuteration using natural acetonitrile and 99,7% at. D heavy water

	Concentration (% at.D)						
	I	II	III	IV	V	VI	VII
Ac-r	Nat.	50	80	90	95	97	99
Ac-p	50	80	90	95	97	99	99.5
γ	1.51	2.28	1.55	1.60	1.11	4.29	3.75

2. In the same experimental arrangement the process is started with different deuterium concentration of waste heavy water samples. The deuterium concentration of the heavy water used in the first step is 65% at. D. In the next steps the deuterium concentration of the used heavy water is rised up to 99,8% at.D.

Table 2

Acetonitrile deuteration using waste heavy water

	Concentration (% at.D)								
	I	II	III	IV	V	VI	VII	VIII	IX
D_2O	65	65	80	90	95	98	99	99.7	99.7
Ac-r	Nat	50	60	75	85	92	96	98	99
Ac-p	-	60	75	85	92	96	98	99	99.5
γ	50	6	4.5	6	3.5	3	3	2.14	3.75

When the isotopic exchange equilibrium is reached on every stage, the reaction mixture must be separated. The separation by distillation is not adequate because, the water and the acetonitrile make an azeotrope.

Increasing the natrium deuteroxide content in the reaction mixture, the solubility of acetonitrile is diminished until the separation of the mixture in two layers. The upper layer is acetonitrile. In this way, the chemical degradation remains insignificant.

II Catalytic reduction of acetonitrile D_3 to ethylamine D_7.

The ethylamine D_7 is a useful intermediate in the synthesis of some organic compounds specifically deuterium labeled (as mebamine) with five deuterium atoms in well-known positions.

The reaction of catalytic reduction of acetonitrile D_3 to ethylamine D_7 is:

$$CD_3CN + 2\,D_2 \xrightarrow{Ni/Cr_2O_3} CD_3{-}CD_2{-}ND_2 \qquad (5)$$

The catalytic reduction of acetonitrile can be done even in liquid phase on metal catalyst e.g. – Ni Raney – or in gaseous phase on metal / support catalyst. In this work we present the reduction in liquid phase on metal / support catalyst, more precisely Ni / oxide support catalyst.

The reaction products are: monoethylamine, diethylamine and triethylamine. So, it is very important for the catalyst to have a good activity and a good selectivity too. A good selectivity for the primary amine gives a less complicate separation process of the reaction mixture.

The catalysts were prepared by coprecipitation. The method consists in coprecipitation in aqueous solution of nitrate mixtures of nickel and support metal with natrium carbonate (or natrium hydroxide). The precipitate was washed, dried, calcinated in N_2 flow at 350˚C and then passivated by reduction in H_2 flow at 350˚C.

The catalysts were characterized by total and active surface measurement. The active surface, respectively the Ni surface, was measured by hydrogen chemosorption at room temperature. Assuming that each metal atom link a hydrogen atom and the Ni cross section area is 6,5Å^2 the nickel surface can be calculated from the amount of adsorbed hydrogen.

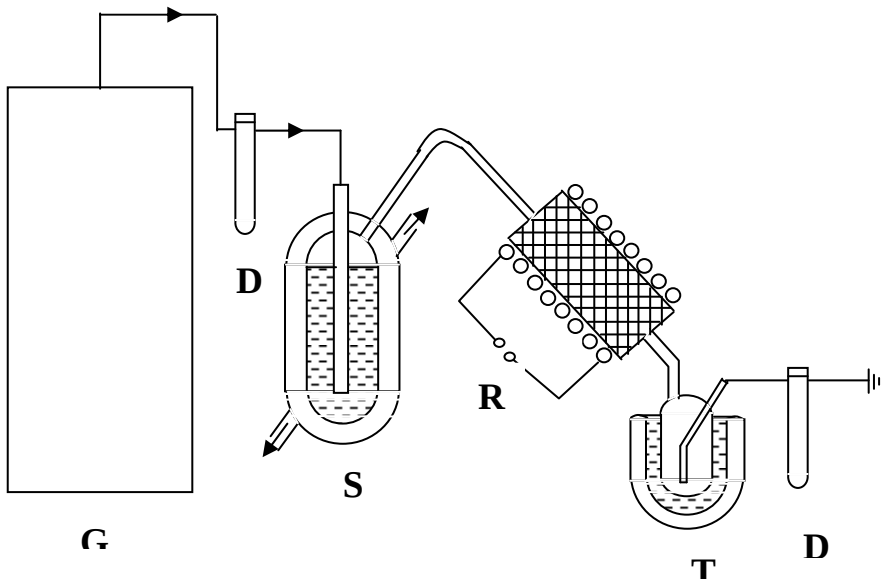

Figure 1. The experimental set up for the catalytic reduction of acetonitrile

G – deuterium supply, D – flowmeter, S – CD_3CN vapors saturator,
R – catalytic reactor, T – freezing trap

The catalysts were tested into the experimental set-up shown in figure 1. The hydrogen flow is saturated with acetonitrile vapors at 0˚C. The hydrogen and acetonitrile mixture passing through the catalyst bed in the reactor at 70 ˚C. The catalytic reactor is on line with a gas chromatograph with flame ionization detector, to analyze the reaction products.

The most appropriate catalyst for our purpose in Ni/Cr_2O_3, which combine the activity and selectivity requested.

The practical conditions to obtain ethylamine – D_7 from deuterated acetonitrile were studied for this catalyst. The reduction was made in the same experimental setup (figure 1). The deuterium gas was supplyed by heavy water electrolysis. A deuterium flow of 6-8 l/h was saturated in deuterated acetonitrile at known temperature (stabilized with a thermostat). The deuterium and acetonitrile mixture was passed through Ni/Cr_2O_3 catalysts (≈3.6g) at 80 – 100˚C. The reduction reaction was strongly exoterme, so the catalyst temperature was difficult to control.

In these conditions the acetonitrile was totally transformed in products. Selectivity in monoethylamine was strongly dependent of the saturation temperature.

The results concerning the dependence of the selectivity versus the saturation temperature are presented in table 3.

Table 3

The dependence of the selectivity versus the saturation temperature

Saturation temperature	MEA %	DEA%	TEA%
18	93.8	4.95	1.25
20	90.7	7.2	2.1
25	84.4	12.5	3.1
30	78.2	16.7	5.1
[a]25	62.4	23.5	14.1

[a] – after 400 hours

The reaction selectivity for ethylamine – D_7 is lower when the acetonitrile vapor pressure is high. The reaction takes place on the catalyst surface between the adsorbed species of acetonitrile and deuterium. When the catalyst surface is covered with acetonitrile (high vapor pressure) multiple collisions take place and the results are DEA and TEA.

The aim of our activity is to produce relative big amount of ethylamine – D_7 in a reasonable time. Working at low saturation temperature is not indicated – even if it provides a good concentration of EA – because the reaction rate is very low. In practice we are led to a compromise solution of 25˚C saturation temperature- which provides a big amount of EA in short time and a good selectivity for EA.

An interesting experimental result is presented in the last row of table 3. The catalyst selectivity for EA is lower after a few weeks. We don't have yet an explication for this behavior.

BIBLIOGRAPHY

1. V. Almasan – Ph.D Thesis- Babes Bolyai University, Cluj Napoca, 1997
2. R. Roghinsky – Theoretical consideration of isotop utilization in chemical reaction, Moscow, 1956

STUDIA UNIVERSITATIS BABEŞ-BOLYAI, PHYSICA, SPECIAL ISSUE, 2001

HIGH-ORDER HARMONICS IN THE FEW-OPTICAL-CYCLE REGIME

C. ALTUCCI[1,3], R. BRUZZESE[3], C. DE LISIO[3], V. TOSA[2], M. NISOLI[4], S. STAGIRA[4], G. CERULLO[4], S. DE SILVESTRI[4], O. SVELTO[4], P. BARBIERO[4], L. POLETTO[5], G. TONDELLO[5], P. VILLORESI[5]

[1]Dipartimento di Chimica, Università della Basilicata (Italy), INFM Unità di Napoli (Italy)
[2]National Institute for Isotopic and Molecular Technology, Cluj-Napoca (Romania)
[3]Dipartimento di Scienze Fisiche, Università di Napoli (Italy), INFM Unità di Napoli (Italy)
[4]Centro di Elettronica Quantistica – CNR, Dipartimento di Fisica, Politecnico di Milano (Italy), INFM Unità di Milano (Italy)
[5]Università di Padova (Italy), INFM Unità di Padova (Italy)

ABSTRACT. The beam divergence of high-order harmonics generated in Helium by an ultra-short Ti:sapphire laser (7 fs and 30 fs) is experimentally characterized by means of a flat-field, high-resolution spectrometer. The harmonic beam divergence is also analysed as a function of the gas-jet position relative to the laser beam waist. Results, which are partly different from previous measurements performed at longer laser pulse duration, are discussed.

1. INTRODUCTION

High-order harmonics as a coherent XUV radiation source exhibit unique properties, such as high brightness, due to good temporal and spatial coherence [1,2], and extremely short pulse duration [3]. Thanks to these unique features, high-order harmonic sources lend themselves as interesting candidates for applications in physics, chemistry, and biochemistry.

The availability of extremely short pulse duration solid state lasers [4,5] has allowed efficient generation of harmonic pulses with duration in the range 30-5 fs, and the emission of coherent radiation down to the *water window* spectral region (4.4-2.3 nm) [6,7].

Moreover, the advent of the above mentioned laser sources makes two exciting perspectives much closer: *i*) the use of sub-10 fs laser pulses opens the way to single attosecond x-ray pulses; *ii*) the availability of intense soft-x-ray pulses in a near-diffraction-limited beam, which should be focusable to peak intensities of the order of 10^{13} Wcm^{-2}, promises to speed up the field of x-ray nonlinear optics [8].

In the present paper we concentrate on the characterisation of the spatial mode of harmonic radiation generated, in the spectral region 30-8 nm, both in Neon and Helium by Ti:sapphire laser pulses with duration of 30 fs or ≈ 7 fs. In particular, we show the measured harmonic beam divergence as a function of the harmonic order and of the distance, *z*, of the gas jet relative to the laser beam waist. One of the most relevant features of our observations is that the harmonic beam divergence generally increases with harmonic order. This behaviour is somehow different from that of previous measurements performed at longer laser pulse duration [9].

It is worth stressing that, in spite of the relatively small number of photons per harmonic pulse (typically $\approx 10^5$ at 31.8 nm which corresponds to the 25th harmonic of the fundamental), the spectral brightness of harmonic radiation can be very high, due to the extremely short pulse duration and to the good spatial coherence. Correspondingly, an estimate of the spectral brightness for the 25th harmonic leads to 10^{22}-10^{23} photons/(Å·s·srad).

2. DESCRIPTION OF THE EXPERIMENT AND RESULTS

The Ti:sapphire laser system used for the experiment delivers 30 fs, up to 1 mJ laser pulses (centred at 795 nm) at a 1 kHz repetition rate. Sub-10-fs pulses are generated by the hollow fiber compression technique [4]. In our set-up, the laser pulse duration can be set to 30 fs or to 5-7 fs, depending on whether the hollow fiber is filled in with Argon or not Amplitude and phase of the compressed pulses have been monitored by Spectral Phase Interferometry for Direct Electric field Reconstruction (SPIDER) [10]. Typical pulses have duration of 5-7 fs and energy of 0.3 mJ, while the spectral phase is generally constant over the pulse spectrum. Laser pulses are focussed onto the gas jet by a 25 cm focal length silver mirror, which leads to a confocal parameter of about 6 mm. The laser-gas interaction length is ~1 mm, with a gas pressure of ~50 Torr. The position *z* of the gas jet along the propagation axis can be easily varied by translating the electromagnetic valve. The harmonic radiation is spectrally dispersed by a grazing incidence, flat field spectrometer (Fig.1) consisting of a toroidal mirror (incidence angle 86°, and radii of 6500 mm in the tangential plane and 14.7 mm in the sagittal plane) followed by a Pt-coated spherical grating (radius of 5649 mm, average groove density of 1200 mm^{-1}). Harmonics are finally detected by means of an intensified microchannel plate (MCP), followed by a charge coupled device (CCD) camera. The sensitive element of the MCP is located 235 mm far from the grating.

A typical spectrum, obtained in He for 7 fs laser pulses and at laser peak intensity at focus of $\approx 10^{15}$ Wcm^{-2}, is shown in Fig.2. The harmonic spectrum develops along the horizontal direction, and harmonics from the 23rd (rightmost) up to the 67th are clearly observable. The vertical direction contains information on the spatial profile of the harmonic beams. The spectrum of Fig.2 is measured when the gas-jet is placed about 1 mm *before* the laser focus in the converging beam: in these conditions a good compromise between conversion efficiency and harmonic beam divergence is reached, in order to maximize the harmonic spectral brightness. As Fig.2 clearly depicts, the harmonic beam divergence increases almost linearly with the harmonic order. The corresponding quantitative analysis is reported in the insert of Fig.2, where the harmonic beam divergence angle (FWHM) is plotted against the harmonic order. The harmonic beam divergence increases, in this case, almost three times, from ≈1.2 mrad for the lowest order harmonic observed, namely H23, up to more than 3 mrad for harmonics at the end of the plateau, as H65. A similar behaviour is observed also for 30 fs laser pulses, though, in this second case, the harmonic beam divergence is generally larger, increasing by a factor of two, from ≈2.3 mrad for the lowest order harmonics up to ≈4.6 mrad for harmonics at the end of the plateau.

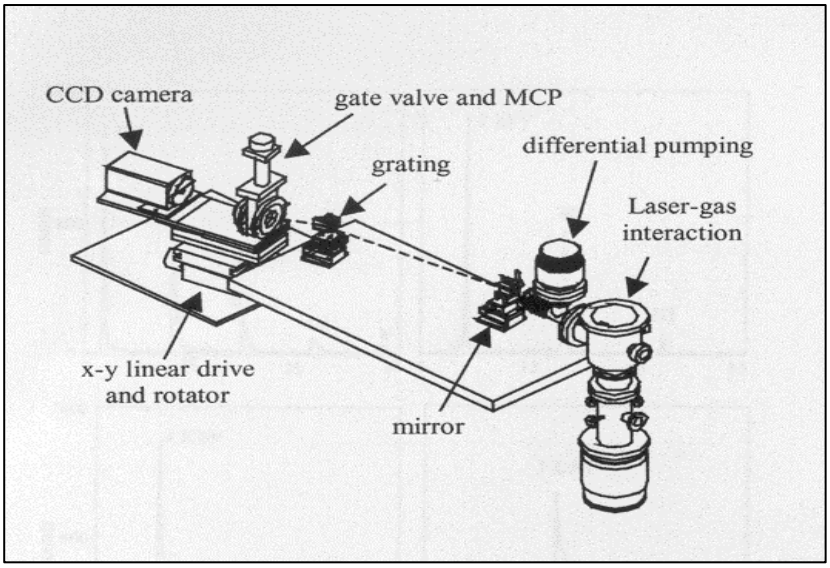

Figure 1. Layout of the experimental apparatus: detail of the interaction chamber, the XUV flat-field spectrometer, and the detector.

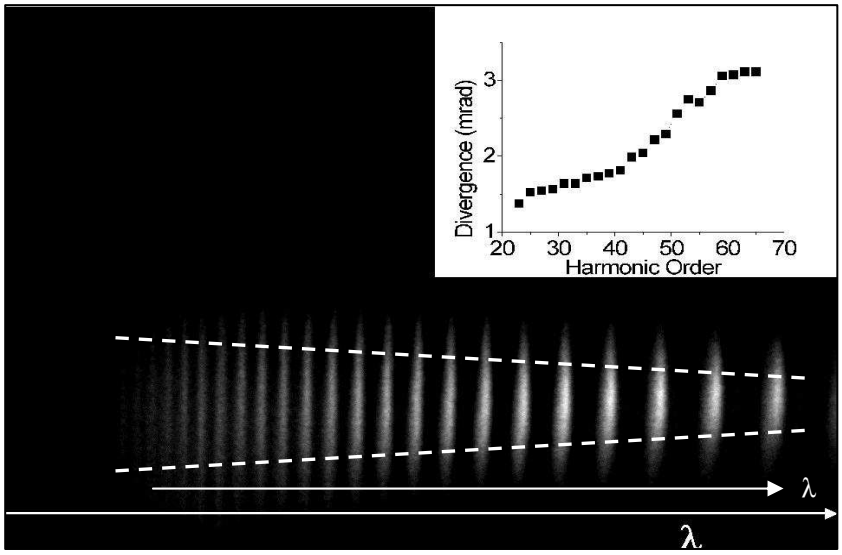

Figure 2. Spectrum obteained in 30 Torr of He for 7 fs laser pulses and for a laser peak intensity of $\approx 10^{15}$ Wcm^{-2} at focus. The gas jet is placed, in this case, about 1 mm before the laser focus, in the converging beam. The insert shows the harmonic divergence, evaluated as FWHM of the spatial profile, vs the harmonic order.

In figure 3 we report the spatial profiles of harmonics belonging to different regions of the spectrum, namely H25 and H43, respectively in the central and final part of the plateau, and H61 in the cutoff region. Apart from the increasing divergence

angle, it is worth stressing that they present a bell-shape without any structure. This is a general behaviour, observed for all the investigated ranges of the experimental parameters.

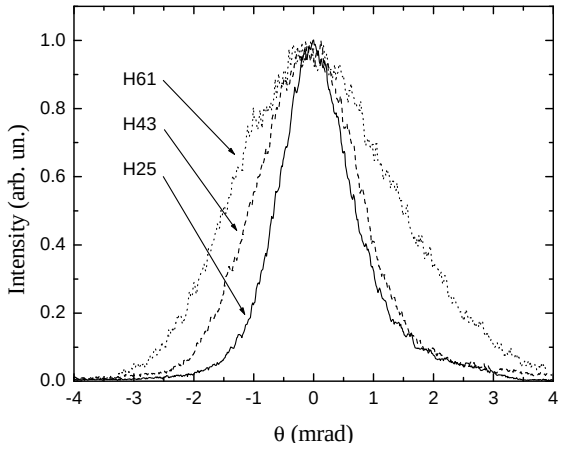

Figure 3. Spatial intensity profile of h25, H43, H61 in the same conditions as Fig.2

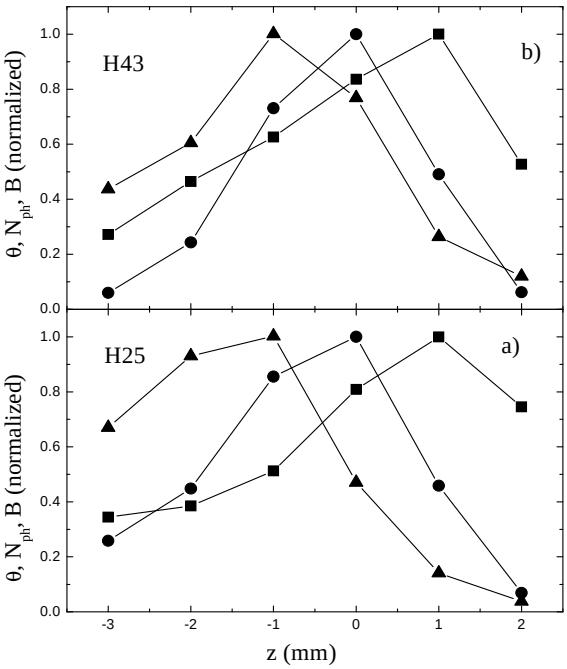

Figure 4. Beam divergence, θ (squares), number of photons, N_{ph} (circles), and spectral brightness, B (up triangles), all normalized, vs the gas jet position, z, along the propagation axis, for H25 (a) and H43 (b) in 30 Torr of He for a laser pulse duration of 7 fs.

The harmonic beam divergence has also been investigated as a function of, *z*. In general, the largest harmonic beam divergence has been observed about 1 mm after the laser focus, in the diverging beam, while the highest conversion efficiency has been obtained just around the laser focus. Such a surprising feature, widely reproducible and observed in a large number of experimental conditions (both for 30 fs and 7 fs pulses and for various gases), is in contrast with previous measurements performed at longer laser pulse duration [9] and is still under study.

Figure 4 illustrates the above mentioned behaviour. Beam divergence, photon number, and spectral brightness are plotted, each one normalized to its maximum value, as a function of z, for H25 (31.8 nm), case a), and H43 (18.5 nm), case b), in He. In the figure, the value $z = 0$ corresponds to the gas jet at focus, and the laser propagates from $z<0$ to $z>0$. Both harmonics exhibit the same characteristics: the highest conversion efficiency, i.e. the largest photon number N_{ph}, is obtained approximately at the laser focus, whereas the beam divergence, θ, is maximal about 1 mm *after* the laser focus (z=1 mm). Thus, the spectral brightness, $B \propto N_{ph}/\theta^2$, is maximal at z=-1 mm, namely about 1 mm *before* the laser focus, in the

converging beam. No satisfactory explanation has been found yet for such a behaviour: additional experimental investigations and theoretical analysis, based on a 3-D propagation model [11] which also accounts for the nonadiabatic single atom response, are planned in order to understand this feature.

We remark that in our experimental conditions the maximum brightness is generally obtained at $z \approx$ -1 mm, *i.e.* in the converging laser beam. It is worth noticing that the peak value of the brightness, *B*, of Fig.4 is 10^{22}-10^{23} photons/Å·s·srad. It has been estimated by the formula:

$$B = \frac{N_{ph}^{meas} \cdot \eta_{TOT}}{\Delta\Omega \cdot \delta\lambda \cdot \tau_h},$$

where N_{ph}^{meas} is the measured number of harmonic photons, η_{TOT} is the overall conversion efficiency of the whole apparatus, $\Delta\Omega$ is the solid angle subtended by the harmonic beam, $\delta\lambda$ the harmonic bandwidth, and τ_h the harmonic pulse duration. All the above quantities but τ_h, have been measured, whereas τ_h has been assumed to be 3 fs. However, this estimate is reasonable only if nondispersive elements are employed for harmonic selection or if harmonic pulse recompression is implemented. In our case, the use of a diffraction grating introduces pulse lengthening.

3. A PHYSICAL MODEL FOR THE GENERATION AND PROPAGATION OF THE HIGH ORDER HARMONICS

To understand better the above experimental results we developed a computer code based on a physical model [11] for the generation and the propagation of high order harmonics. It includes a physical model for the single atom response in intense electric field, and the propagation equations for both the laser field and for the generated radiation.

a) Single atom response:

The nonlinear dipole moment $d_{nl}(t)$ in the Strong Field Approximation formalism is:

$$d_{nl}(t) = 2\,\mathrm{Re}\left\{ i \int_{-\infty}^{t} dt' \left(\frac{\pi}{\varepsilon + i(t-t')/2} \right)^{3/2} d^{*}\left[p_{st}(t',t) - A(t) \right] d\left[p_{st}(t',t) - A(t') \right] \times \right.$$

$$\left. \times \exp[-iS_{st}(t',t)] E_1(t') \right\} \exp\left[-\int_{-\infty}^{t} w(t')dt' \right]$$

where the stationary value of momentum and action are

$$p_{st}(t',t) = \frac{1}{t-t'} \int_{t'}^{t} A(t'')dt''$$

$$S(t',t) = (t-t')I_p - \frac{1}{2}p_{st}^2(t',t)(t-t') + \frac{1}{2}\int_{t'}^{t} A^2(t'')dt''$$

and the dipole matrix element for transitions from the ground state to a continuum state characterized by a momentum p is:

$$d(p) = i\frac{2^{7/2}(2I_p)^{5/4}}{\pi}\frac{p}{(p^2+2I_p)^3}$$

The tunnel ionization rate from the ground state is written in Amosov Delone Krainov (ADK) model as:

$$w(t) = \frac{I_p}{\hbar}\left|C_{n*}\right|^2\left(\frac{4I_p}{\hbar w_t}\right)^{2n*-1}\exp\left(-\frac{4I_p}{3\hbar w_t}\right)$$

b) Propagation of the fundamental field E_1:

The 3-D wave equation for the propagation of the fundamental field, takes into account the presence of a plasma generated by the laser in the gas. If n_e is the electron density one can write an equation of the form:

$$\nabla^2 E_1(r,z,t) - \frac{1}{c^2}\frac{\partial^2 E_1(r,z,t)}{\partial t^2} = \frac{e^2 n_e(r,z,t)}{c^2}E_1(r,z,t)$$

which eventually can be written in the moving frame ($z'=z$, $t'=t-z/c$) as:

$$\nabla_\perp^2 E_1(r,z',t') - \frac{2}{c}\frac{\partial^2 E_1(r,z',t')}{\partial t'\partial z'} = \frac{e^2 n_e(r,z',t')}{c^2}E_1(r,z',t')$$

where the paraxial approximation ($\frac{\partial^2 E_1}{\partial z^2} \approx 0$) has been used. The temporal derivative can be eliminated by performing a Fourier transform (FT), yielding the parabolic type equation:

$$\nabla_\perp^2 E_1(r,z',\omega) - \frac{2i\omega}{c}\frac{\partial E_1(r,z',\omega)}{\partial z'} = FT\left[\frac{e^2 n_e(r,z',t')}{c^2}E_1(r,z',t')\right]$$

Due to the complex nature of the quantities involved, this is in fact a system of two equations which has been solved numerically using the Cranck-Nicolson method.

c) Propagation of the harmonic field E_h:

Harmonic field (E_h) propagation obeys the 3-D wave equation similar to that written for the harmonic field. A spatial polarisation $P_{nl}(r,z,t)$ is present, due to the laser induced dipoles of the atoms which did not ionise, and plays the role of the source:

$$\nabla^2 E_h(r,z,t) - \frac{1}{c^2}\frac{\partial^2 E_h(r,z,t)}{\partial t^2} = \mu_0 \frac{\partial^2 P_{nl}(r,z,t)}{\partial t^2}$$

As above, it can be written in the moving frame ($z'=z$, $t'=t-z/c$) as:

$$\nabla_\perp^2 E_h(r,z',t') - \frac{2}{c}\frac{\partial^2 E_h(r,z',t')}{\partial t'\partial z'} = \mu_0 \frac{\partial^2 P_{nl}(r,z',t')}{\partial t^2}$$

By performing a Fourier transform (FT), the above equation is transformed in system of two parabolic type equations:

$$\nabla_\perp^2 E_h(r,z',\omega) - \frac{2i\omega}{c}\frac{\partial E_h(r,z',\omega)}{\partial z'} = -\omega_0^2 \mu_0 P_{nl}(r,z',\omega)$$

which can be soved numerically. Note that equations were derived without performing the slowly varying envelope approximation in time.

After solving numerically the equations for E_1 and E_h, the program compute the power spectrum of the harmonics.

3. CONCLUSIONS

The beam divergence of high-order harmonics generated in He by a ≈7fs Ti:sapphire laser has been extensively investigated. The main and somehow unexpected features of our results are: the harmonic beam divergence generally increases with the harmonic order, and, its trend as a function of *z*, presents a maximum when the gas jet is positioned in the diverging beam, whereas in previous measurements at rather longer laser pulse duration (≥100 fs) [9] the maximum of the harmonic divergence angle occurred in the converging laser beam. This result, very well reproducible and observed also for 30 fs laser pulses, seems to indicate that different phase-matching conditions for the harmonic propagation process occur in the case of very short laser pulse duration. The dipole phase, which could be very much affected by nonadiabatic effects due to the extremely short laser pulse duration, might play a different role in the phase-matching conditions when compared to harmonic generation by longer laser pulses.

REFERENCES

[1] Bellini M., Lyngå C., Gaarde M.B., Hänsch T.W., L'Huillier A., and Wahlström C.-G., *Phys. Rev. Lett.* **81** (1998) 297.

[2] Zerne R., Altucci C., Bellini M., Gaarde M.B., Hänsch T.W., L'Huillier A., Lyngå C., and Wahlström C.-G., *Phys. Rev. Lett.* **79** (1997) 1006.

[3] Sartania S., Cheng Z., Lenzner M., Tempea G., Spielmann C., Krausz F., and Ferencz K., *Opt. Lett.* **22** (1997) 1562.

[4] Nisoli M., De Silvestri S., Svelto O., Szipöcs R., Ferencz K., Spielmann C., Sartania S., and Krausz F., *Opt. Lett*. **22** (1997) 522.

[5] Spielmann C., Burnett N.H., Sartania S., Koppitsch R., Schnürer M., Kan C., Lenzner M., Wobrauschek P., Krausz F., *Science* **78** (1997) 661.

[6] Chang Z., Rundquist A., Wang H., Murnane M.M.. Kapteyn H.C., *Phys. Rev. Lett*. **79** (1997) 2967.

[7] Villoresi P., Ceccherini P., Poletto L., Tondello G., Altucci C., Bruzzese R., de Lisio C., Nisoli M., Stagira S., Cerullo G., De Silvestri S., Svelto O., *Phys. Rev. Lett*. **85** (2000) 2494.

[8] Salières P., Le Dèroff L., Auguste T., Monot P., d'Oliveira P., Campo D., Hergott J.-F., Merdji H., Carrè B., *Phys. Rev. Lett* **83** (1999) 5483.

[9] Salières P., Ditmire T., Perry M.D., L'Huillier A., and Lewenstein M., *J. Phys. B* **29** (1996) 4771.

[10] Iaconis C. and Walmsley I.A., *IEEE J. Quantum Electron.* **35** (1999) 501.

[11] Priori E., Cerulllo G., Nisoli M. Stagira S., De Silvestri S., Villoresi P., Poletto L., Ceccherini P., Altucci C., Bruzzese R., and de Lisio C., *Phys. Rev. A* **61** (2000) 063801.

STUDIA UNIVERSITATIS BABEŞ-BOLYAI, PHYSICA, SPECIAL ISSUE, 2001

SOLITON SIGNATURE IN THE INFRARED SPECTRA OF NONLINEAR QUASI-ONEDIMENSIONAL MOLECULAR CRYSTALS

D. GRECU, ANCA VIŞNESCU

Institute of Physics and Nuclear Engineering "Horia Hulubei"
Bucharest, Romania, e-mail: dgrecu@theor1.theory.nipne.ro

ABSTRACT. Davydov's soliton remains an attractive and possible mechanism for the energy transport in proteins. Discussed initially in the context of alpha-helix structure, it was applied later in several situations. An interesting system is the acetanilide (ACN), which has many features in common with other hydrogen bonded polypeptide structures. An unconventional amide I band was disovered in infrared and Raman spectra at low temperatures, which was interpreted as a manifestation of the existence of soliton in this structure. The theory of the infrared spectra is reviewed, with emphasize on the resonant interaction between short waves (amide I excitations) and long waves (phonons), interaction responsible for the soliton generation.

1. INTRODUCTION

The mechanism for energy transport in proteins has been an active area of research for over 30 years, but still is not yet elucidated. Many years ago, an attractive model was proposed by Davydov. In this model the amide I oscillations act as baskets for the storage of biological energy released in the adenosine triphosphate hydrolysis. The nonlinear interaction of these intramolecular excitations with the acoustic field, describing the oscillations of the molecule along the α-helix chain, provides the mechanism for generation of self-trapped excitations along the chain. In this way the energy can travel over considerable molecular distances without being thermally dissipated. Many authors have discussed and tried to improve this model, and in spite of many controversial arguments it still remains in actuality [1], [2] (and references therein).

2. DAVYDOV'S MODEL

The model represents a very drastic approximation of the real situation, and in spite of its simplicity it can not be solved exactly. Usually the quantum model is discussed in a kind of coherent state approximation and a system of coupled nonlinear equations for the classical field variables is found, namely

$$i\hbar \dot{a}_n = Ea_n - \sum_{p=1} J_p (a_{n+p} + a_{n-p}) + \chi \rho_n a_n \tag{1}$$

$$M\ddot{\rho}_n - w(\rho_{n+1} - 2\rho_n + \rho_{n-1}) = \chi(|a_{n+1}|^2 - 2|a_n|^2 + |a_{n-1}|^2) .$$

Here a_n is the classical amplitude of the amide I oscillation in the n-th molecule, $E=E_0-D$, where E_0 is the oscillation energy and D a static shift due to lattice effects, J_p is the dipole-dipole interaction energy between C=O dipoles (usually only nearest neighbours interaction is considered), ρ_n is the relative displacement of two adjacent molecules, M and w are the mass and the elastic spring, and χ is the coupling constant for the mode-lattice interaction.

In studying this system we have to make distinction between two regimes of space-time variations. The first corresponds to some fast motions described by space and time variables of order of the distance between molecules and the inverse of a characteristic frequency. These motions are described mainly by the linearized equations and correspond to a decoupled system of intramolecular excitations (A-system) of frequencies

$$\hbar\omega(k) = E - 2\sum_{p=1} J_p \cos klp \tag{2}$$

and a system of acoustical phonons (P-system) with the dispersion relation

$$\Omega(k) = 2\Omega_0 \left|\sin\frac{kl}{2}\right| \quad , \qquad \Omega_0 = \sqrt{\frac{w}{M}} \ . \tag{3}$$

When no kind of resonance condition exists (this will be discussed latter) the inclusion of the nonlinear coupling terms in the equations of motion will affect a little these rapid motions, an effect which can be discussed perturbatively.

But there is also an another regime, characterized by some kind of slow space and time variables, where the small cumulative effects of nonlinearity manifest and lead to a modulation of the amplitude of the propagating excitation (Benjamin-Feir or modulation instability) and the creation of a spatially localized excitation – the soliton. In the present paper we are interested in this regime, and to discuss it we need an adequate mathematical formalism. This is given by the asymptotic method of multiple scales (or reductive perturbative) method [3].

If ε is a small parameter the slow variables are defined as

$$\xi = \varepsilon(nl - v_g t), \quad t_2 = \varepsilon^2 t, \ldots \tag{4}$$

where v_g is a group velocity to be specified latter. Then the separation of fast and slow variables in the A-system is achieved assuming the following asymptotic expansion for a_n

$$a_n = e^{i(knl-\omega t)} \sum_{j=1} \varepsilon^j A_j(\xi, t_2, \ldots) . \tag{5}$$

As concerns the P-system one assumes that it depends only on the slow variable (4) (the acoustical branch is assumed to be "slaved" to the optical branch). As the right hand side of the second equation (1) is of ε^4 order, an asymptotic expansion for ρ starting with the ε^2 term has to be used

$$\rho = \sum_{j=2} \varepsilon^j P_j(\xi, t_2, \ldots) \tag{6}$$

All these expansions are now introduced in (1) which has to be satisfied in any order of ε. For the A-system in order ε^1 the equation is satisfied if $\omega(k)$ is given by the dispersion relation (3) and in order ε^2 if the group velocity is given by

$$v_g = d\omega/dk = \omega_1 \qquad (\omega_n = 1/n!\, d^n \omega(k)/dk^n).$$

In order ε^3 the first amplitude A_1 has to satisfy the equation

$$i\frac{\partial A_1}{\partial t_2} + \omega_2 \frac{\partial^2 A_1}{\partial \xi^2} + \frac{\chi}{\hbar} P_2 A_1 = 0 \qquad \textbf{(7)}$$

coupling the A and P systems.

Turning now our attention to the P-system the discussion starts with the ε^4 order. With the notation $c_p = \Omega_0 l$ for the phase velocity of the acoustical phonons one obtains

$$(v_g^2 - c_p^2)\frac{\partial^2 P_2}{\partial \xi^2} = \frac{\chi}{M} l^2 \frac{\partial^2 |A_1|^2}{\partial \xi^2} \qquad (8)$$

If $v_g \neq c_p$ (no resonance condition) from (1) one gets

$$P_2 = -\frac{\chi}{w}\frac{1}{1 - \frac{v_g^2}{c_p^2}}|A_1|^2 \qquad (9)$$

which introduced in (7) gives

$$i\frac{\partial A_1}{\partial t_2} + \omega_2 \frac{\partial^2 A_1}{\partial \xi^2} + q|A_1|^2 A_1 = 0 \qquad (10)$$

$$q = \frac{\chi^2}{\hbar w}\frac{1}{1 - \frac{v_g^2}{c_g^2}}.$$

This is the complete integrable nonlinear Schrödinger equation (NLS). When $\omega_2 q > 0$ (focusing case) the NLS equation admits soliton solutions [4], [5].

In the next order, ε^4, for the A-system one obtains

$$i\frac{\partial A_2}{\partial t_2} + \omega_2 \frac{\partial^2 A_2}{\partial \xi^2} + q(A_1^2 A_2^* + 2|A_1|^2 A_2) =$$

$$-i\frac{\partial A_1}{\partial t_3} + i\omega_3 \frac{\partial^3 A_1}{\partial \xi^3} - i\lambda\left(A_1^2 \frac{\partial A_1^*}{\partial \xi} - |A_1|^2 \frac{\partial A_1}{\partial \xi}\right) \qquad (11)$$

$$\lambda = 2q\omega_2 v_g / (c_p^2 - v_g^2)$$

This is an inhomogeneous linear equation for A_1. In the left hand side (lhs) one recognizes the linearized NLS equation (around a solution A_1 of the NLS equation), and the inhomogeneity in the right side (rhs) depends only on A_1. Possible secular behaviours appear any time if in the rhs of (11) are identified solutions of the linearized NLS equation (the symmetries of the NLS equation). They can be eliminated if the t_3 dependence of A_1 is determined from the next equation in the NLS hierarchy (the complex mKdV equation), namely

$$-\frac{\partial A_1}{\partial t_3}+\omega_3\left(\frac{\partial^3 A_1}{\partial \xi^3}+6c\left|A_1\right|^2\frac{\partial A_1}{\partial \xi}\right)=0 \tag{12}$$

$$c=\frac{\chi^2}{2\hbar w\omega_2}\,\frac{1}{1-v_g^{\,2}/c_g^{\,2}}$$

The remaining inhomogeneous linear equation for A_2 will be now free of secularities and if A_1 is the one soliton solution it can be exactly integrated by a suitable transformation [6].

The previous discussion is valid if $v_g \neq c_p$. Now let us discuss the case when $v_g = c_p$ and show that this corresponds to a long wave – short wave resonance situation. Let us consider the resonance of a triad

$$k_1 = k_2 + k_3$$
$$\omega_1 = \omega_2 + \omega_\varepsilon \tag{13}$$

and suppose that k_1 and k_2 are very close, $k_1 = k+\varepsilon k$, $k_2 = k-\varepsilon k$. Then the wave number triad is automatically satisfied if $k_3 = 2\varepsilon k$, while the frequency triad is satisfied if

$$\omega_\varepsilon = \omega(k+\varepsilon k) - \omega(k-\varepsilon k) \approx 2\varepsilon k\, d\omega/dk = k_3\, d\omega/dk \tag{14}$$

But $\omega_3/k_3 = c_p$ is the phase velocity of the long wave, while $d\omega/dk = v_g$ is the group velocity of the short one. Then this kind of resonance takes place any time when $c_p = v_g$, a condition which is easily achieved if the short waves belong to an optical branch, and the long waves to an acoustical one. When this situation happens the equations (8) is no longer valid as the ε^4 order is automatically satisfied. The lhs is different of zero starting with the ε^5 order, and this can be achieved if the asymptotic expansion (5) is modified, namely

$$a_n = \mathrm{e}^{i(knl-\omega t)}\sqrt{\varepsilon}\sum_{j=1}\varepsilon^j A_j(\xi, t_2, \ldots) \tag{15}$$

the definition of the slow variables remaining unchanged. Then it is easily seen that in the order ε^5 the P-system has to satisfy the equation

$$i\frac{\partial P_2}{\partial t_2} = -\frac{\chi}{2Mv_g} l^2 \frac{\partial |A_1|^2}{\partial \xi} \tag{16}$$

The equations (7) and (16) constitute an integrable system know as Zakharov-Benney equations. [5], [7], [8]. Its soliton solution is only slightly modified from the soliton solution of the NLS equation. Higher order approximations can be worked as before; more details will be presented elsewhere.

3. CRYSTALINE ACETANILIDE CASE

Different types of collective excitations in quasi 1-D molecular crystals consisting of weakly interacting molecules (groups of atoms) can exist. The most studied are the excitons. They can be generated by light and characterize many processes of absorbtion and luminiscence. In the beginning part of this paper a discussion of another kind of collective excitation – the soliton – was given. It is supposed that they can be excited in chemical reactions and by other local actions, playing an important role in biological processes. But they cannot be excited directly by light.

But there is a very notable exception, namely the crystalline acetanelide ($CH_3CONHC_6H_5$) (ACN), an organic quasi-one-dimensional crystal, whose structure is very similar with the structure of typical polypeptide chain in protein. In the early seventies Careri et al. found an unconventional amide I band at 1650 cm^{-1} (shifted by about 15 wave numbers from the primary band) at low temperature and assigned it to a soliton type excitation in this system [1], [9], [10]. To explain the experimental results a Davydov type model was used, in which the amide I oscillations are interacting nonlinearly with a low frequency optical mode (describing the hydrogen bonded proton motion). Treating the low frequency optical mode as an Einstein oscillator the Hamiltonian is given by

$$H = \sum h_n - JV \tag{17}$$

$$h_0 = [E_0 + \lambda_0 (b_n + b_n^+)] B_n^+ B_n + \hbar\omega_0 b_n^+ b_n \tag{18}$$

$$V = \sum (B_n^+ B_{n+1} + B_n^+ B_{n-1}) \tag{19}$$

Here B_n^+ (B_n) is the creation (annihilation) operator for an amide I oscillation b_n^+ (b_n) the creation (annihilation) operator of the Einstein oscillator of frequency ω_0, λ_0 the coupling constant of the mode-mode interaction and J the dipole-dipole interaction energy between two amide I oscillations. In the ACN case J is small compared with λ_0, so the problem can be solved by using a perturbation theory in J. The unperturbed problem is described by the energy operator of the "displaced harmonic oscillator" for which exact eigenvalues and eigenfunctions are known [11]. A Bloch function can be now written for the perturbed problem and a first order estimate of the energy gives

$$E(k) = E_0 - \frac{\lambda_0^{\,2}}{\hbar\omega_0} - 2J\cos k\, e^{-(\frac{\lambda_0}{\hbar\omega_0})^2}. \quad (20)$$

In an infrared experiment only k=0 states are observed. The peak of 1650 cm^{-1} corresponds to a k=0 soliton type excitation (the name "soliton" is used in a wider sense of a spatially localized solution) having the binding energy

$$E_B = \frac{\lambda_0^{\,2}}{\hbar\omega} - 2J\,[1 - e^{-(\frac{\lambda_0}{\hbar\omega_0})^2}] \quad (21)$$

One of the striking property of this peak is its strong temperature dependence, the absorbtion strength varying as $exp(-\beta T^2)$. This fact is due to the interaction with the acoustic phonon bath [1], [11]-[13]. In conclusion the appearance and the temperature dependence of the experimentally observed amide I band at 1650 cm^{-1} in ACN can be explained along the lines proposed by Davydov.

Acknowledgments *Helpful discussions with Dr. A.S. Cârstea are kindly acknowledged. This work was supported by the Ministry of Education ads Research under the grant nr. 5194/6008.*

REFERENCES

1. A. Scott – Phys. Reports **217,** 1(1992)
2. P.L. Christiansen, A.C. Scott, eds.- "*Davydov's Soliton Revisited. Self-Trapping of Vibrational Energy in Protein" (*NATO ASI Series, Ser. B **243**; Plenum Press, New York, 1990)
3. S. Taniuti – Suppl. Prog. Theor. Phys. **55,** 1(1974)
4. M.J. Ablowitz, H. Segur – "*Solitons and the Inverse Scattering Transform"* (SIAM, Philadelphia, 1981)
5. R.K. Dodd, J.C. Eilbeck, J.D. Gibbon, H.C. Morris "*Solitons and Nonlinear Wave Equations"* (Acad. Press, London, 1982)
6. D. Grecu, Anca Vişinescu, A.S. Cârstea – J. Nonlinear Math. Phys. Suppl. **8,** 139(2001)
   D. Grecu, Anca Vişinescu – "*Multiscale analysis of a Davydov model with an harmonic long range interaction."* (to be published)
7. D. J. Benney – Stud. Appl. Math. **56**, 81(1977)
8. N. Yajima, M. Oikawa – Prog. Theor. Phys. **56**, 1719 (1976)
9. G. Careri, U. Buontempo, E. Galluzzi, A.C. Scott, E. Graton, E. Shyamsunder – Phys. Rev. B **30**, 4689(1984)
10. J.C. Eilbeck, P.S. Lomdahl, A.C. Scott – Phys. Rev. B **30**, 4703(1984)
11. A.C. Scott, I.J. Bigio, C.T. Johnston – Phys. Rev. B **39**, 517(1989)
12. S. Takeno – Prog. Theor. Phys. **75**, 1(1986)
13. D.M. Alexander, J.A. Krumhansl – Phys. Rev. B **33**, 7172(1986)

ULTRASOUND PROPAGATION THROUGH BIOLOGICAL TISSUES

FERRIDE SEVERCAN[1], DANA DOROHOI[2], DORINA CREANGA[2]

[1] *Middle East University, Department of Biological Sciences, Ankara, Turkey*
[2] *Al. I. Cuza University, Department of Biophysics and Medical Physics, 11A Blvd. Carol, Iasi- 6600, Romania*

ABSTRACT. Important information about anatomic functionality of biological tissues, as well as the presence of the tumors or of the foreign bodies can be obtained using physical parameters characterizing the ultrasound propagation in the tissues.

The velocity and the absorption coefficient of ultrasound in biological tissues were measured using a pulse method. The pulse generator had a frequency of 10^3 Hz and the high frequency generator had a variable frequency in the range (1-4) MHz. Ceramic plates were used as generator and receiver of the ultrasounds.

The measured parameters were used to estimate the adiabatic compressibility and the internal pressure in the studied tissues.

Introduction

Ultrasound action on complex molecular media may result in various modifications such as: stimulation of chemical reaction, water decomposition in H and OH radicals - which is followed by hydrogen peroxide generation-polymerization and de-polymerization, cell membrane disorganization due to proteins damages (especially enzymes), lipids and vitamins damage. Protein molecule modifications are dependent on the side chain and lateral chain nature as well as on the gases dissolved in protein suspension. Protein de-polymerization could be related to the cavitation phenomena, precisely on the implosion forces acting on cavitation bubbles. De-polymerization was noticed only when the dissolved gas was oxygen. Enzymatic activity of various proteins is diminished, vanishes or it is not affected by ultrasound action. When enzyme activity is affected, then a mass transfer under ultrasound waves occurs. Glucose, fructose and saccharine may be hydrolyzed under ultrasound action and new compounds may be generated in the initial liquid matrix. Some vitamins such as C vitamin are destroyed while the biosynthesis of other vitamin, such as D_2, is stimulated by ultrasound waves.

Energy absorption in animal tissue is given by:

$$P = I_1 S[1 - \exp(-2d\alpha)] \tag{1}$$

where **P** is absorbed power, $\mathbf{I_1}$ is the ultrasound intensity, **S** is the tissue surface, **d** is the tissue width and a $\boldsymbol{\alpha}$ is the absorption coefficient.

In the Table II the absorption coefficient is given for different tissues.

Physical quantities that are able to describe ultrasound propagation are velocity and acoustic impedance (see formulas and Tables II and III):

$$v^2 = \frac{1}{\rho\beta} \quad (2) \qquad \beta = -\frac{1}{V}\frac{\partial V}{\partial P} \quad (3) \qquad Z = v.\rho \quad (4)$$

where **v** is ultrasound velocity, ρ is tissue density, **V** and **P** have the meaning of volume and pressure and β is the adiabatic compressibility coefficient.

Table I.

Absorption coefficient in biological media (C. C. Tudose, 1997)

Frequency (MHz)	Tissue	Absorption coefficient (cm^{-1})
0.800	Muscle and grease	0.141
0.800	Grease tissue	0.102
800	Muscle	0.192
2.400	Muscle and grease	0.472
1.000	Water	0.0003
1.000	Sanguine plasma	0.007
1.000	Blood	0.02
1.000	Muscle	0.2-0.5
1.000	Liver	0.17
1.000	Kidney	0.22
1.000	Grease	0.13
1.000	Bone	3.2

Table II.

Ultrasound velocity and impedance in some biological media at 24 ^{0}C

(Schmitt &Brown, 1970)

No	Propagation medium	Acoustic impedance ($g/cm^2/s$)	Propagation velocity(m/s)
1	Water	1.48	1480
2	Blood	1.64	1547
3	Brain	1.56	1514
4	Muscle	1.63	1567
5	Collagen	1.68	1680
6	Soft tissue	1.55	1550
7	Bone	6.9	3550
8	Dentine	8.0±0.4	3600±200

Ultrasound velocity in biological media is dependent both on the protein concentration of biological liquids composing the biological tissue and on the external pressure - factors that are influencing tissue density.

But the influence of these factors is depending on temperature so that, in the present study, we carried out measurements on the ultrasound velocity in biological tissue for different temperatures.

Materials and methods

An ultrasound pulse method was utilized to measure acoustic wave velocity. A laboratory device designed and assembled in our labs was used for the biological tissue exposure.

Pulse generator had a frequency of 10^3 Hz while the high frequency had a variable frequency in the range 1-4 MHz. Three adiabatic rooms, having an ultrasound generator and receptor ceramic plates with the frequencies of 1, 2 and 4 MHz, were used in our experiments. The cells containing tissue samples had different lengths and are bounded to the generator and receptor of ultrasound through two acoustical adapters, in which ultrasonic damages are negligible (fig. 1).

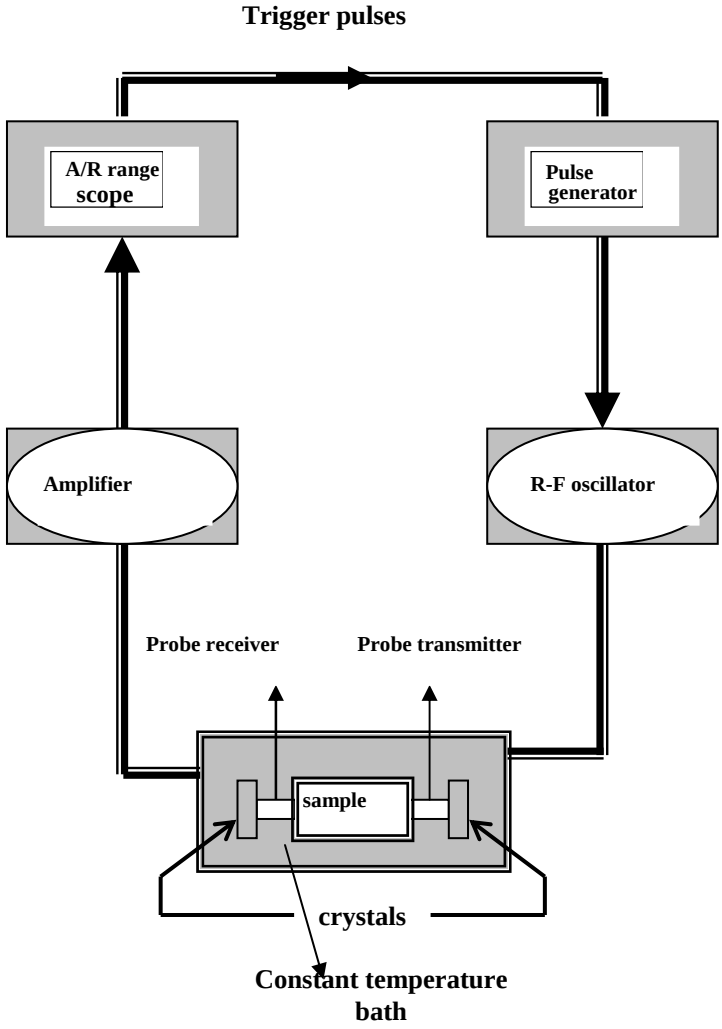

Figure 1. Block schema for determination of the velocity and absorption coefficient of ultrasound in mammalian tissues

Water, rabbit blood and beef liver, were the biological materials that we tested. Temperature was varied between 24 ^{0}C and 39.5 ^{0}C using a Unicam Specac Digital Temperature Controller Unit.

Results and discussion

Ultrasound velocity recorded for every tested temperature is given in the graphics below. In all three cases there is a decreasing of ultrasound velocity to the temperature increasing, a second order polynomial being the mathematical function that fits better the experimental points (according with literature data - Naghy, I., 1984).

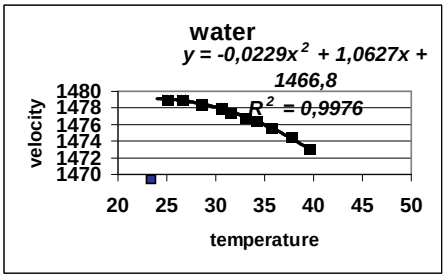

Figure 2a. Ultrasound velocity (m/s) in water (R^2-square correlation coefficient). Temperature in ^{0}C.

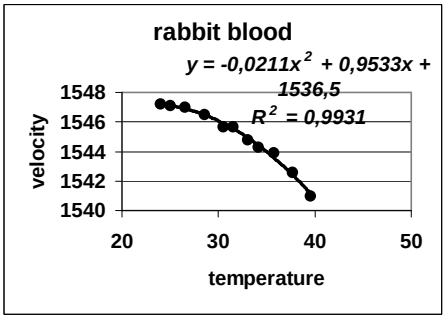

Figure 2b. Ultrasound velocity (m/s) in rabbit blood (R^2-square correlation coefficient). Temperature in ^{0}C

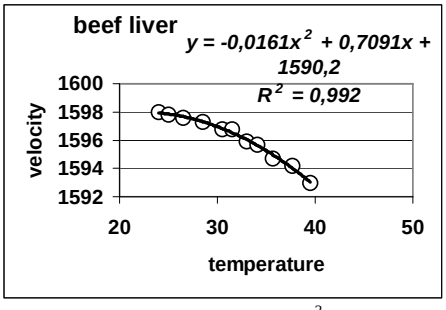

Figure 2c. Ultrasound velocity (m/s) in beef liver (R^2-square correlation coefficient). Temperature in ^{0}C

In the Table III the coordinates for maximum points of the polynomial approximation functions are given.

Table III.

Ultrasound maximum velocity values as computed by polynomial approximation

No.	Sample	$\mathbf{t_{(max)}}$ (^{0}Celsius)	$\mathbf{v_{max}}$ (m/s)
1	Water	23.20	1479.13
2	Rabbit blood	22.59	1547.27
3	Beef liver	22.02	1598.08

It results that velocity is reaching a maximum value for a certain temperature that is very closed to the 24 ^{0}Celsius, i.e. the lowest temperature considered in our experiments. Some unavoidable error sources affected results in Table III, so that in the case of water experiments the velocity obtained experimentally for 24 ^{0}Celsius is lower than the maximum velocity.

In Figs. 3 a-c some mathematical correlations were revealed between the three investigated media. It is obvious that linear functions fit experimental data. From line slopes, one may observe the same order relation for every temperature:

$$\mathbf{v_{water} < v_{blood} < v_{liver}} \tag{5}$$

To get an interpretation on this relation we combine the relations (2) and (4):

$$\mathbf{v = \frac{1}{Z\beta}} \tag{6}$$

and look to the Table II, where is obvious that:

$$\mathbf{Z_{water} < Z_{blood} < Z_{soft-tissue}} \tag{7}$$

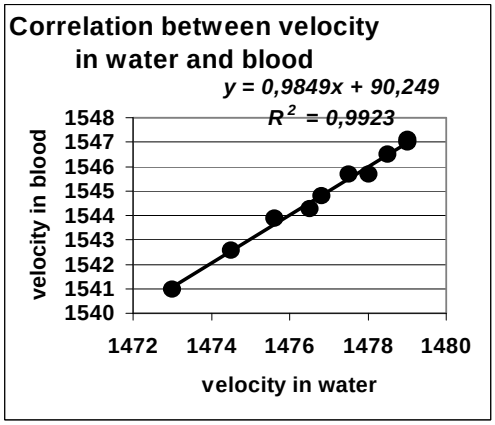

Figure 3a. Linear dependence of ultrasound velocity (m/s) in water on the ultrasound velocity (m/s) in blood

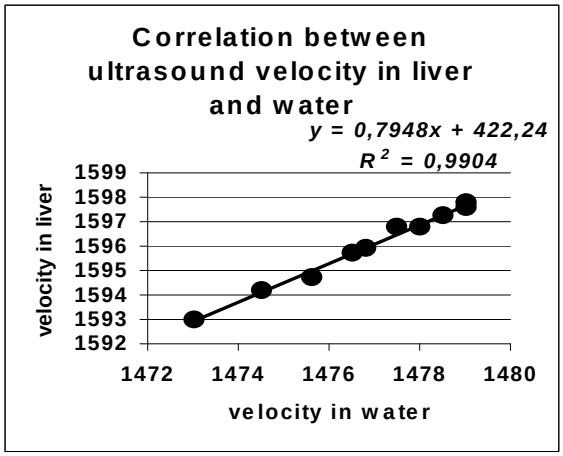

Figure 3b. Linear dependence of ultrasound velocity (m/s) in water on the ultrasound velocity (m/s) in liver

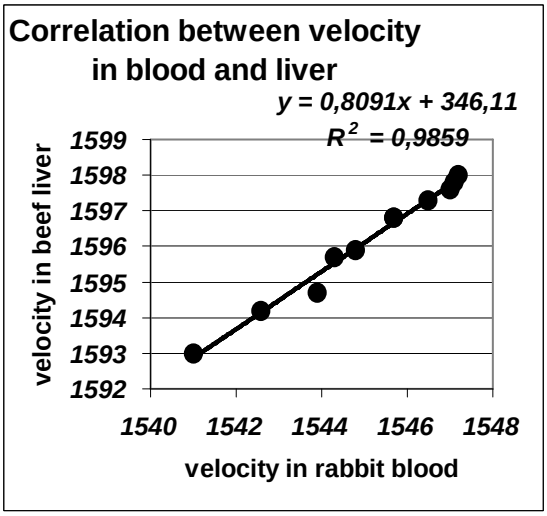

Figure 3c. Linear dependence of ultrasound velocity in blood on the ultrasound velocity in liver

So, we may say that coefficient β is the one that need to take adequate values to assure the inequality (5). Further experiments are designed to get this coefficient. One can see that linear correlation coefficients are high, but distinct from the unit, revealing direct proportionality relationships but also peculiar behavior of the tissue couples considered in the above graphs. This may be related to the different values of tissue impedance and adiabatic coefficient.

Conclusion

1. Ultrasound velocity in the tested biological media decreases to the temperature enhancing, in the temperature range tested inhere, following a second order polynomial.

2. For any tested temperature value, ultrasound velocity is higher when the protein concentration is higher

3. Linear correlation between pairs of biological media was obtained, slope values reflecting various differences in protein, oxygen and glucose concentration.

Further investigations are designed in order to evaluate adiabatic compressibility coefficient and absorption rate, since medical applications (diagnosis and therapy) are requiring such information in order to compute ultrasound energy doses.

REFERENCES

[1] I. I. Nagy, *Efectele biologice ale ultrasunetelor in medii biologice*, Ed. Medicala 1984;

[2] H.P. Schwan (Ed), *Absorption and Dispersion of Ultrasound in Biological Media*, Mc. Graw Hill;

[3] C. C. Tudose, *Ultrasunetele*, Ed. Stiintifica 1997;

[4] W. Schmitt and H. Brown, *Ultrashalkardiographie*, Stuttgart 1970;

[5] A. Suryavanaschi and R. Singh, *Acustica* **76** (1992), 86;

[6] F. Takemura and Y. Matsumoto, *Acustica* **76** (1992), 112;

[7] D. P. Edmonds (Ed.), *Ultrasonics*, Academic Press 1981;

[8] B. Brown and E. J. Goodman, *Ultrasons de haute intensite*, Ed. Dunod, 1959;

[9] D. E. Goldmann and T. F. Hueter, *J. Acoust. Amer. Soc.* **28** (1956), 35-37.

STUDIA UNIVERSITATIS BABEŞ-BOLYAI, PHYSICA, SPECIAL ISSUE, 2001

X AND W ESR STUDIES OF TRANSITION METAL CLUSTERS ENCAPSULATED IN SANDWICH-TYPE POLYOXOMETALATES

O. COZAR, L. DAVID, C. CRĂCIUN, V. CHIŞ

Dept. of Physics, "Babeş-Bolyai" University, 3400 Cluj-Napoca, Romania

ABSTRACT. The series of sodium/potassium salts of the sandwich-type heteropolyanions $[M^{n+}{}_3(H_2O)_x(BiW_9O_{33})_2]^{(18-3n)-}$ (M^{n+} = $(VO)^{II}$, x = 0 and M^{n+} = Cr^{III}, Mn^{II}, Fe^{III}, Co^{II}, Ni^{II}, Cu^{II}, x = 3) was investigated by X and W bands ESR spectroscopy. In the complex with vanadium(IV) the unpaired electrons are trapped on the parent ions (g_{II} = 1.899, $g_{\perp}$ = 1.974, $|A_{II}|$= 184 G, $|A_{\perp}|$= 69 G) and the V^{IV} ions are prevalently dipolar coupled. In the case of the other trinuclear clusters, the metallic coupling is based on the superexchange mechanism realized through the heteropolyoxometalate frame. The isotropic exchange constants were estimated for the Cr^{III} (J = –4.116 cm^{-1}) and Mn^{II} (J = –2.074 cm^{-1}) clusters from the temperature dependance of the linewidths of the HF-EPR signals. The **g** tensor is isotropic for the complexes with Cr^{III}, Mn^{II} and Fe^{III} ($g \approx 2.0$), axial for the Cu^{II} cluster (g_{II} = 2.080, $g_{\perp}$ = 2.237) and rhombic for the Ni^{II} complex (g_x = 2.201, g_y = 2.211, g_z = 2.292). The zero field splitting tensor is rhombic for the clusters of Mn^{II} (D = –0.381 cm^{-1}, E = 0.054 cm^{-1} for the spin state S = 7/2) and Ni^{II} (D = 1.66 cm^{-1}, E = 0.18 cm^{-1} for the spin state S = 1). Two species with different degrees of the rhombical distortion have been identified in case of the Fe^{III} (D_1 = 1.5 cm^{-1}, E_1 = 0.12 cm^{-1} and D_2 = 1.5 cm^{-1}, E_2 = 0.5 cm^{-1}) and Co^{II} ($g_x{}^1$ = 5.021, $g_y{}^1$ = 3.561, $g_z{}^1$ = 2.401 and $g_x{}^2$ = 5.776, $g_y{}^2$ = 3.813, $g_z{}^2$ = 2.850) samples.

Introduction

During the last years, sandwich-type heteropolyoxometalates (HPOM) encapsulating clusters of early transition metals have received much attention both from applied (in material science, medicine, catalysis) and fundamental research perspectives [1,2]. The metallic clusters are usually encapsulated between two Keggin or Dawson-Wells trilacunary fragments. In this context, our research focuses on the ESR and HF-ESR investigation of Bi^{III} based sandwich-type HPOM with three 3d transition metals $[M^{n+}{}_3(H_2O)_x(BiW_9O_{33})_2]^{(18-3n)-}$ (M^{n+} = $(VO)^{II}$, x = 0 and M^{n+} = Cr^{III}, Mn^{II}, Fe^{III}, Co^{II}, Ni^{II}, Cu^{II}, x = 3).

Experimental

ESR spectra on powdered solids have been recorded at room temperature and 80 K at *ca.* 9.6 GHz (X-band) using a Bruker ESP 380 spectrometer. W-band ESR spectra were recorded on the HF-ESR Grenoble spectrometer at 190 GHz frequency. Powder samples were pressed in pellets to avoid preferential orientation of the crystallites in the strong magnetic field.

Results and discussion

The powder ESR spectrum of the complex with vanadyl (Fig.1), obtained in the X-band at room temperature was simulated as a superposition of two Gaussian components, an axial and an isotropic one. The axial component exhibit the signals due to the hyperfine coupling of the unpaired electron spin with the nuclear spin of the ^{51}V isotope (I = 7/2) (g_{II} = 1.899, $g_{\perp}$ = 1.974, $|A_{II}|$ = 184 G, $|A_{\perp}|$ = 69 G). The unpaired electrons are predominantly trapped on the parent ions. The degree of covalency of the in-plane V–O π bonds β_2^2 = 0.876 evaluated using the LCAO-MO method for V^{IV} ion in a C_{4v} local symmetry indicates a dominant ionic character of the in-plane π bonds. The broad component of the spectrum could be interpreted in therms of the presence of very weak extended exchange interactions within the vanadyl triangular cluster. The excited state S = 3/2 could be responsible for the appearance of the broad component of the spectrum, because of the unsolved hyperfine structure and possible g and A tensors anisotropies [3].

HF-ESR spectra of the polycrystalline complex with three Cr^{III} ions, obtained in W-band (190 GHz) and 5–200 K temperature range (Fig.2), contain a broad line at g ≈ 2.0. By raising the temperature, the linewidth of the signal decreases because of small Cr^{III}–Cr^{III} superexchange interactions. The temperature dependence of the inverse of the linewidth was fitted (Fig.3) taking into account the proportionality $(\Delta B(p\text{-}p))^{-1} \sim \chi_M T$, with χ_M being the molar susceptibility, and in the frame of a HDVV model for three exchange-coupled high-spin Cr^{III} ions ($S_1 = S_2 = S_3 = 3/2$) [4,5]:

$$\chi_M T = (N\mu_B{}^2 g^2/3k)(3x^{3/8} + 60x^{15/8} + 157.5x^{35/8} + 252x^{63/8} + 247.5x^{99/8})/$$
$$(4x^{3/8} + 16x^{15/8} + 18x^{35/8} + 16x^{63/8} + 10x^{99/8})$$

where x = exp(J/kT) and all other parameters have their usual meanings. The best fit was obtained with J = –4.116 cm^{-1} and considering the g = 1.995 mean value in the temperature range of 5–85 K. The three Cr^{III} ions are antiferromagnetically coupled as arises from the negative value of the exchange coupling constant. A large signal ($\Delta B(p\text{-}p)$ ≈ 2800 G) assigned to coupled Cr^{III} ions was obtained in the X-band powder ESR spectra, at room temperature. The supplementary signal appearing in the spectrum obtained at T = 80 K at g_2 = 4.047 is due to $\Delta M_S = \pm 2$ transitions.

ESR spectra of the powder complex with Mn^{II} performed in the X-band at room and nitrogen liquid temperatures show an isotropic signal at g_1 = 2.013 typical for coupled Mn^{II} ions and a small signal at half-field (g_2 = 4.264) due to $\Delta M_S = \pm 2$ transitions (Fig.4). The HF-ESR spectra (190 GHz) of the polycrystalline sample pressed in a pellet of the Mn^{II}complex in the temperature range 5–80 K exhibits an asymmetric signal at about g = 2.0. The exchange coupling constant J = –2.074 cm^{-1} was estimated following the same procedure as for the Cr^{III} cluster, but for a system with three antiferromagnetic coupled high-spin Mn^{II} ions with $S_1 = S_2 = S_3 = 5/2$ [6]. ESR spectrum obtained at T = 5 K was simulated using the following parameters: S = 7/2, g = 2.027, D = –0.381 cm^{-1}, E = 0.054 cm^{-1}.

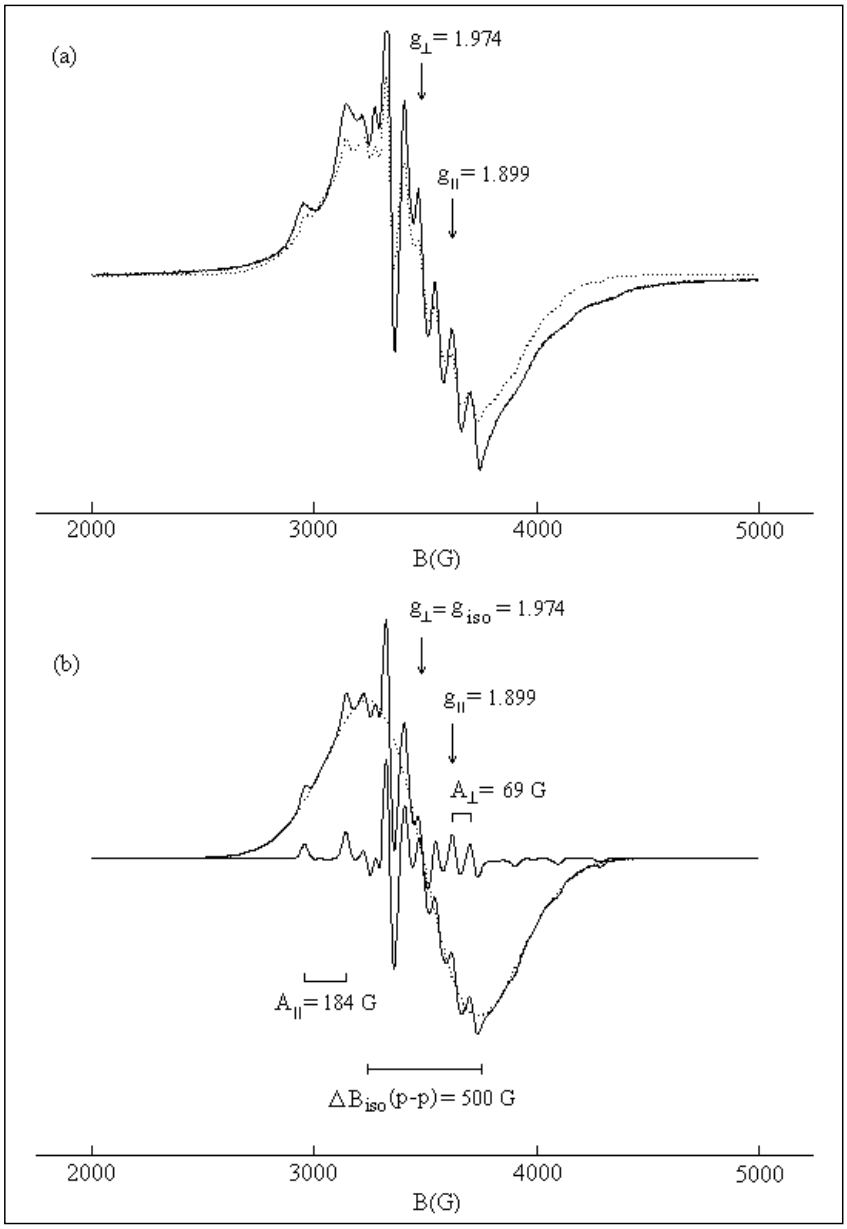

Fig.1. *(a) The experimental powder ESR spectrum of the complex with vanadyl, obtained in the X-band at room temperature (normal line) and its simulated spectrum (dotted line) (b) The components of the simulated spectrum of the complex.*

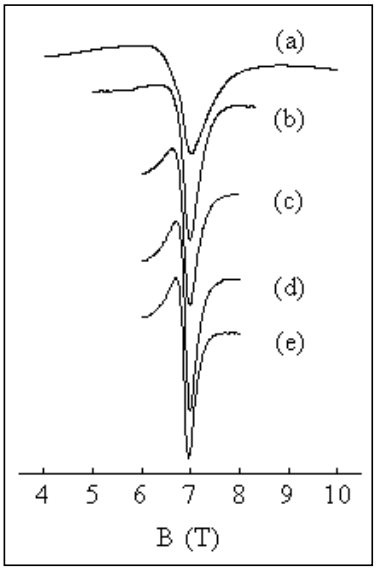

Fig.2 *HF-ESR spectra (190 GHz) of the poly-crystalline complex with Cr^{III} pressed in a pellet, recorded at temperatures: (a) 5 K, (b) 15 K, (c) 25 K, (d) 50 K, (e) 85 K*

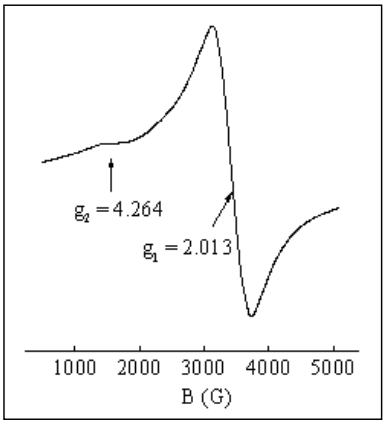

Fig.4 *Powder ESR spectra of the complex with Mn^{II} recorded in the X-band at T = 293 K temperature*

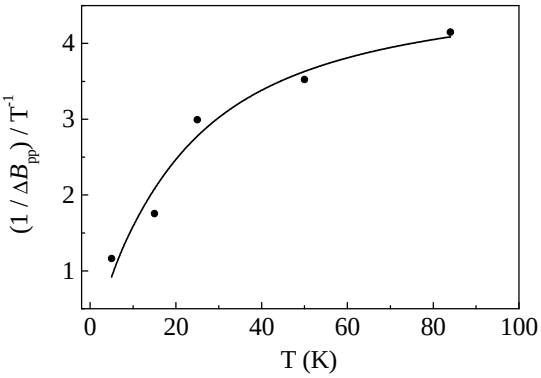

Fig.3 *Temperature dependence of the inverse of the linewidth $(\Delta B(p\text{-}p))^{-1}$ for the HF-ESR signal of the complex with Cr^{III}. The solid line is the best fit of the data.*

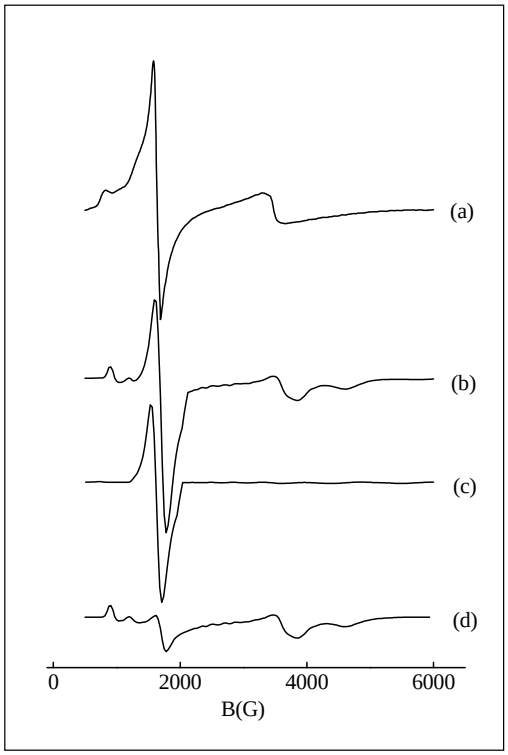

Fig.5 *(a) Powder ESR spectrum of the complex with Fe^{III} obtained in the X-band at T = 80 K.*
(b) The total simulated spectrum as sum of the spectra (c) and (d), assuming S = 5/2 spin state

The powder ESR spectrum obtained in the X-band at T = 80 K for the complex with Fe^{III} contains three main features at the effective g values 8.493, 4.289 and 2.000 and a shoulder at 5.498 (Fig.5a). The ESR spectrum was interpreted using one S = 5/2 spin state. The positions of the main signals were reproduced by simulation with an isotropic **g** tensor, ($g_x = g_y = g_z = 2.0$) and a rhombic fine structure tensor (D = 1.5 cm^{-1}, E = 0.12 cm^{-1}) (Fig.5d). For reproducing the intensities of the signals at $g_{eff} \approx$ 4.289 for transitions in $M_S = \pm 3/2$ doublet and $g_{eff} \approx 8.493$ for transitions in $M_S = \pm 1/2$ doublet, the above spectrum was superposed with another component with a stronger signal at $g_{eff} \approx 4.289$. This component (Fig.5c), present in the 4:1 ratio with the first component, is characterised by an isotropic g tensor ($g_x = g_y = g_z = 2.0$) but a zero field splitting tensor with a greater rhombicity (D = 1.5 cm^{-1}, E = 0.5 cm^{-1}).

The powder ESR spectrum of the complex with Co^{II}, recorded in the X-band (9.7 GHz) at T = 80 K, exhibits a very broad signal (ΔB(p-p) ≈ 2160 G) centered at g = 3.582 and a small signal at $g \approx 2.00$. Only the last signal remains in the spectrum when increasing the temperature. The observation of this signal even at room temperature is in good agreement with the presence of coupled Co^{II} ions, with square pyramidal local environments. HF-ESR spectra (190 GHz) of the pollycrystaline complex pressed in a pellet exhibit at least four signals (Fig.6). The ratio of the intensities for the two signals at lower magnetic fields is almost constant in the temperature range 5–50 K, which indicates that they originate in the same spin state. The HF-ESR spectrum at T = 5 K was simulated by superposing in 2:1 ratio the spectra of two distinct species (g_{x1} = 5.021, g_{y1} = 3.561, g_{z1} = 2.401 and g_{x2} = 5.776, g_{y2} = 3.813, g_{z2} = 2.850), characterised by the same effective spin S_{eff} = 1/2 for three antiferromagnetic coupled Co^{II} ions.

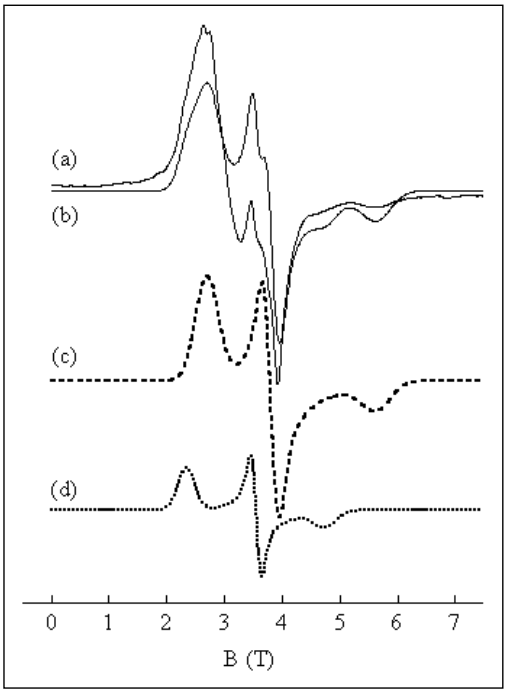

***Fig.6** (a) HF-ESR spectrum (190 GHz) at T = 5 K of a polycrystalline sample of the complex with Co^{II} pressed in a pellet and (b) the simulated spectrum as sum of the spectra (c) and (d) assuming S = 1/2 spin state*

HF-ESR spectra of the polycrystalline sample with Ni^{II} pressed in a pellet (Fig.7) contain the most intense signals in the 2–8 T magnetic field region. The intensity of the signals varies with temperature so that at 25 K three sharp signals and two broader ones are observed. The obtained spectra were interpreted in terms of one S = 1 spin state for three antiferromagnetic coupled Ni^{II} ions. The magnetic fields for $\Delta M_S = \pm 1$ transitions estimated

from the spectrum at 5 K were used for supplying the ESR parameters by means of Chasteen procedure [10,11]. The cluster presents a small rhombic distortion both in **g** (g_x = 2.201, g_y = 2.211 and g_z = 2.292) and **D** tensors (D = 1.66 cm^{-1} and E = 0.18 cm^{-1}).

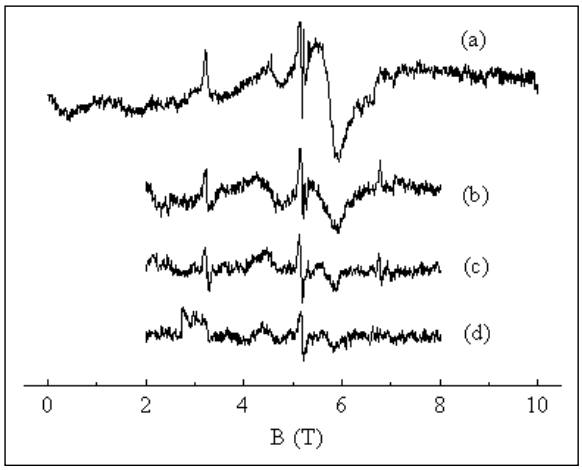

Fig.7 *Temperature dependence of the HF-ESR spectra (190 GHz) of the polycrystalline sample of the complex with Ni^{II} pressed in a pellet (a0 T = 5 K, (b) T = 15 K, (c) T = 25 K, (d) T = 50 K*

In the case of the complex with Cu^{II}, the anti-ferromagnetic coupling between the Cu^{II} ions, favorised by the geometry of the cluster and the spin frustration, leads to a double degenerate S = 1/2 ground state, which is ESR inactive, and one. ESR active S = 3/2 excited state The best fit of the spectrum was obtained with an axial spin Hamiltonian with S = 3/2, principal g values g_{II} = 2.080 and $g_{\perp}$ = 2.237, the axial zero field splitting parameter D = 0.0214 cm^{-1}. The parallel direction is along the C_3 axis of the trinuclear copper cluster and also along the perpendicular direction of the individual **g** tensors.

Conclusion

ESR and HF-ESR investigation of the sodium/potassium salts of the $[M^{n+}{}_3(H_2O)_x(BiW_9O_{33})_2]^{(18-3n)-}$ (M^{n+} = $(VO)^{II}$, x = 0 and M^{n+} = Cr^{III}, Mn^{II}, Fe^{III}, Co^{II}, Ni^{II}, Cu^{II}, x = 3) heteropolyanions lead to the estimation of the type of the metal-metal interaction, of the ESR parameters and the ground spin states of the metallic clusters.

Vandium ions have a C_{4v} local symmetry and are prevalently dipolar coupled. The weak superexchange ineraction lead to the S = 1/2 ground state and the excited S = 3/2 state. Trinuclear Cr^{III} cluster has an isotropic g = 1.995 factor and the Cr^{III} ions are antiferromagneticaly coupled (J = –4.116 cm^{-1}). In the case of the Mn^{II} cluster, where the metallic ions are antiferromagnetically coupled (J = –2.074 cm^{-1}), one S = 7/2 state was identified (D = –0.381 cm^{-1}, E = 0.054 cm^{-1}, g = 2.0). Two distinct species have been identified at 80 K in the sample of the complex with Fe^{III}, characterised by the S = 5/2 spin state and D_1 = 1.5 cm^{-1}, E_1 = 0.12 cm^{-1} and D_2 = 1.5 cm^{-1}, E_2 = 0.5 cm^{-1} zero field splitting parameters, respectively. Co^{II} cluster is characterised by the effective spin S = 1/2 and the sample is a mixture of two nonequivalent species (g_x^1 = 5.021, g_y^1 = 3.561, g_z^1 = 2.401 and g_x^2 = 5.776, g_y^2 = 3.813, g_z^2 = 2.850). Ni^{II} cluster has one S = 1 ground state and **g** (g_x = 2.201, g_y = 2.211, g_z = 2.292) and **D** (D = 1.66 cm^{-1}, E = 0.18 cm^{-1}) rhombic tensors. Trinuclear Cu^{II} cluster has an ESR inactive S = 1/2 doublet as ground state and an excited state S = 3/2 (g_{II} = 2.080, $g_{\perp}$ = 2.237, D = 0.0214 cm^{-1}).

REFERENCES

1. H. Andres, J. M. Clemente-Juan, R. Basler, M. Aebersold, H.-V. Güdel, J. J. Borrás-Almenar, A. Gaita, E. Coronado, H. Büttuer, S. Janssen, *Inorg. Chem.*, **40**, 1943 (2001)
2. A. Müller, F. Peters, M. T. Pope, D. Gatteschi, *Chem. Rev.*, **98**, 239 (1998)
3. B. Botar, T. Yamase, E. Ishikawa, *Inorg. Chem. Comm.*, **3**, 579 (2000)
4. V. Tangoulis, D. A. Malamatari, K. Soulti, V. Stergiou, C. P. Raptopoulou, A. Terzis, T. A. Kabanos, D. P. Kessissoglou, *Inorg. Chem.*, **35**, 4974 (1996)
5. O. Kahn, in *Molecular Magnetism*, VCH Publishers, Inc., New York, 1993, pp. 212.
6. D. M. L. Goodgame, M. Goodgame, P. J. Hayward, *J. Chem. Soc., A*, 1352 (1970)
7. C. R. Staples, I. K. Dhawan, M. G. Finnegan, D. A. Dwinell, Z. H. Zhou, H. Huang, M. F. J. M. Verhagen, M. W. W. Adams, M. K. Johnson, *Inorg. Chem.*, **36**, 5740 (1997)
8. J. J. Girerd, G. C. Papaefthymiou, A. D. Watson, E. Gamp, K. S. Hagen, N. Edelstein, R. B. Frankel and R. H. Holm, *J. Am. Chem. Soc.*, **106**, 5941 (1984)
9. R. S. Drago, in *Physical Methods for Chemists*, Saunders, Phyladelphya, 2nd edn., 1977, pp. 587.
10. L. A. Pardi, A. K. Hassan, F. B. Hulsbergen, J. Reedijk, A. L. Spek and L.-C. Brunel, *Inorg. Chem.*, **39**, 159 (2000)
11. N. D. Chasteen, *Inorg. Chem.*, **10**, 2339 (1971)

STUDIA UNIVERSITATIS BABEŞ-BOLYAI, PHYSICA, SPECIAL ISSUE, 2001

COORDINATION OF URANIUM(IV) IONS TO MONOLACUNAR AND TRILACUNAR KEGGIN-TYPE HETEROPOLYOXOMETALATES. SPECTROSCOPIC AND MAGNETIC INVESTIGATION

L. DAVID*, C. CRĂCIUN*, O. COZAR*, D. RUSU**

**Dept. of Physics, "Babeş-Bolyai" University, 3400 Cluj-Napoca, Romania*
***Department of Chemical-Physics, Medical and Pharmaceutical University, 3400 Cluj-Napoca, Romania*

ABSTRACT. Eight complexes with different numbers of uranium ions $K_{12}[U(BW_{11}O_{39}H)_2]\cdot 23H_2O$, $K_{19}[U_2KAs_4W_{40}O_{140}]\cdot 42H_2O$, $Na_m[(UO)_3(H_2O)_6(XW_9O_{34})_2]\cdot nH_2O$ (X = P, m = 12, n = 21; X = Si, m = 14, n = 19; X = Ge, m = 14, n = 17) and $Na_m[U_3(XW_9O_{33})_2]\cdot nH_2O$ (X = As, m = 6, n = 15; X = Bi, m = 6, n = 18; X = Sb, m = 6, n = 16) have been investigated by spectroscopic (IR, UV-VIS, ESR) and magnetic susceptibility methods. In all complexes the U^{IV} ions are coordinated by eight oxygen atoms in a cvasicubic local environment. The ground state of the $^3H_4$ multiplet is Γ_1 for the complex with one U^{IV} ion, but Γ_5 for that with two uranium ions. Uranium(IV) complexation intensifies the charge transfer in the tricentric W–$O_{b,c}$–W bonds. In the complexes with two and three uranium ions, the actinides are antiferromagneticaly coupled.

Introduction

Heteropolyoxometalates (HPOM) are molecular blocks of metal oxide formed by WO_6 and/or MoO_6 octahedra sharing vertices or edges. In the last years, polyoxometalates and their metallic complexes have been intensely studied for the important applications in catalysis, medicine and materials science. Different ions can coordinate the polyoxometalates by occupying their lacunary sites. This is an advantage because of the possibility of stocking the radioactive waste into the HPOM complexes.

Experimental

IR spectra have been performed on a Specord IR-75 Spectrophotometer and FT-IR spectra on an Equinox 55 Bruker Spectrophotometer in the 4000–400 cm^{-1} range, using KBr pellets. Electronic spectra were performed in aqueous solutions within a range of λ = 200–800 nm using an ATI Unicam-UV-Visible Vision Software V 3.20. The magnetic susceptibility measurements were performed using a Faraday type balance in the temperature range of 77–290 K.

Results and discussion

The $K_{14}[U(BW_{11}O_{39})_2]\cdot 25\ H_2O$ heteropolyanion

The $K_{14}[U(BW_{11}O_{39})_2]\cdot 25H_2O$ heteropolyoxometalate contains two monolacunary Keggin units linked by one uranium ion.

(a) FT-IR data. The bands of the $\nu_{as}(W–O_c–W)$ and $\nu_{as}(W–O_b–W)$ vibrations for bonds of the edge and corner sharing WO_6 octahedra respectively are the most shifted bands in the IR spectrum of the complex compared to the ligand spectrum (Table 1). This fact corelated with the change of the relative intensities of corresponding bands indicate the uranium ion coordination at the O_b and O_c atoms in the lacunary regions of the Keggin fragments.

Table 1

The heteropolyoxometalate frame IR bands of the $K_9[BW_{11}O_{39}]\cdot 14H_2O$ ligand and $K_{14}[U(BW_{11}O_{39})_2]\cdot 25H_2O$ complex

Band	Ligand (cm^{-1})	Complex (cm^{-1})
$\nu_{as}(B–O_a)$	993 (m,sp)	1000 (m,sp)
$\nu_{as}(W=O_d)$	950 (s,sp)	950 (s,sp)
$\nu_{as}(W–O_c–W)$	920 (s,sp); 890 (s,b); 873 (s,b)	890 (s,sp)
$\nu_{as}(W–O_b–W)$	840 (s,sp); 818 (s,sp)	835 (s,b); 820 (s,b)
$\nu_{as}(W–O_a)$	790 (s,sp); 753 (s,sp)	770 (s,b); 750 (s,b)

w-weak, m-medium, s-strong, sh-shoulder, b-broad, sp-sharp, vs-very strong, vw-very weak

(b) UV-spectra. The UV electronic spectra (Fig.1) exhibit two characteristic bands at ≈210 nm and ≈246 nm for the ligand and ≈210 nm and ≈252 nm for the complex assigned to the $d_\pi–p_\pi$ electronic transition in $W=O_d$ and $W–O_{b,c}–W$ bonds respectively [1,2]. The shape of the spectra indicates the increasing of the charge transfer in the tricentric bonds after the uranium complexation.

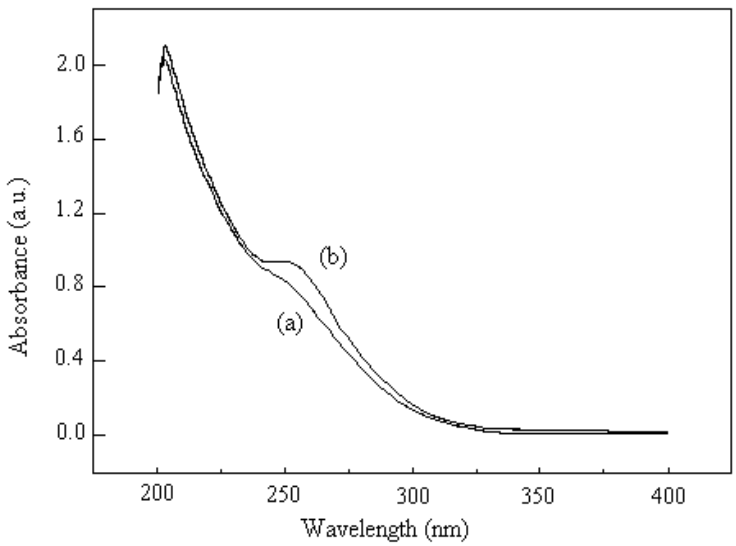

Fig.1 UV spectra of the (a) $K_{27}[KAs_4W_{40}O_{140}]\cdot 45H_2O$ ligand and (b) $K_{14}[U(BW_{11}O_{39})_2].25H_2O$ complex obtained in 5×10^{-5} mol l^{-1} aqueous solution

(c) Visible spectra. The visible electronic absorbtion spectrum of the complex is typical for the uranium(IV) ions into a cvasicubic configuration with $^3H_4$ ground state. The absorbtions are due to internal transitions between the f orbitals of uranium: $^3H_4 \rightarrow {}^3P_0$ at 676, 691 nm, $^3H_4 \rightarrow {}^1D_2$ (646 nm) and $^3H_4 \rightarrow {}^1G_4$ (625 nm) and $^3H_4 \rightarrow {}^3H_6$ (930 nm) [3]. The last band was used for the estimation of the spin-orbit coupling parameter (λ = 978 cm^{-1}) which confirm the presence of the U^{IV} ion.

(d) Magnetic susceptibility measurements. The monomeric character of the complex is indicated by the Curie-Weiss behaviour of the magnetic susceptibility in the temperature range 135–290 K [4]. The magnetic moment $\mu_{eff} = 2.83\ \mu_B$ corresponds to the oxidation state +4 of the uranium ion. The relatively high temperature independent paramagnetism ($\chi_0 = 2.73 \cdot 10^{-3}$ emu/mol) is due to the Γ_1 ground level of the $^3H_4$ multiplet.

The polyoxotungstate $K_{19}[U_2KAs_4W_{40}O_{140}] \cdot 42H_2O$

The $[KAs_4W_{40}O_{140}]^{27-}$ cryptand contains four trilacunary $\{AsW_9\}$ Keggin fragments bound by four WO_6 octahedra.

(a) ***Infrared Spectra.*** The representative frequency range of the IR spectra for the $K_{27}[KAs_4W_{40}O_{140}] \cdot 45H_2O$ ligand and $K_{19}[U_2KAs_4W_{40}O_{140}] \cdot 42H_2O$ complex is given in Fig.2. The coordination of the uranium ions to the cryptand is indicated by the appearance in the IR spectrum of the complex of the $\nu_{as}(U–O) \approx 1133\ cm^{-1}$ vibration and by the shift of the $\nu_{as}(W–O_b–W)$ (805, 785 cm^{-1} for the ligand and 810, 770 cm^{-1} for the complex) and $\nu_{as}(W–O_d)$ (950, 970 cm^{-1} for the ligand and 960 cm^{-1} for

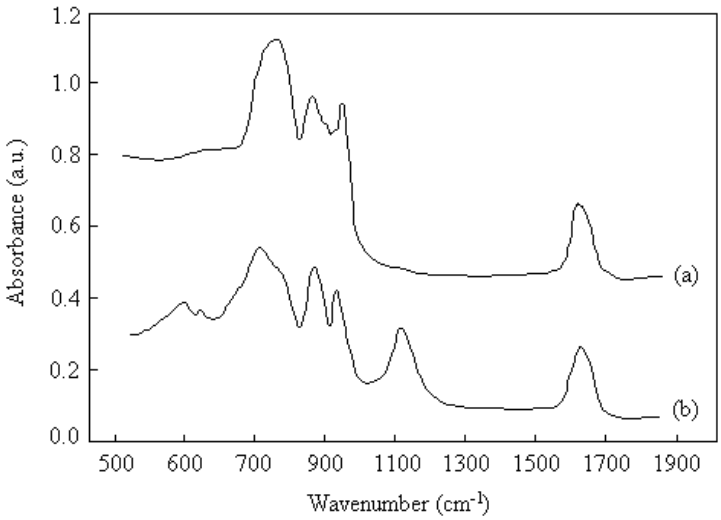

Fig.2 IR spectra of the (a) $K_{27}[KAs_4W_{40}O_{140}]\ 45H_2O$ ligand and (b) $K_{19}[U_2KAs_4W_{40}O_{140}]\ 42H_2O$ complex

the complex) vibration bands in the IR spectrum of the complex compared to the ligand spectrum [5]. The analysis of the IR spectra indicates the coordination of the uranium ions to the oxygen atoms from the lacunary region of the Keggin fragmnts and to the O_d oxygen atoms of WO_6 binding octahedra.

(b) Electronic Spectra. The UV absorption bands centered at ≈ 47390 cm^{-1} for the free ligand and at ≈ 45040 cm^{-1} for the complex are assigned to $p_\pi(O_d)–d_{\pi^*}(W)$ transitions into the terminal bonds and the broad bands at 41700–38400 cm^{-1} for the ligand and 43500–40000 cm^{-1} for the uranium complex are assigned to $p_\pi(O_{b,c})–d_{\pi^*}(W)$ transitions in the tricentric bonds. The presence of two shoulders on the absorption band indicates that the trilacunary Keggin anions have nonequivalent $W–O_{b,c}–W$ bonds [6]. The visible absorption spectra of the complex (Fig.3), performed in aqueous solutions at different concentrations contain the f → f transitions of the uranium ions situated in a cubic configuration (Table 3) and presents the ground state $^3H_4$.

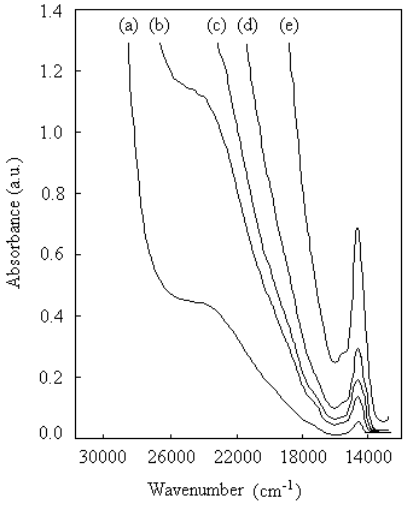

Fig.3 Visible electronic spectra of the $K_{19}[U_2KAs_4W_{40}O_{140}]·42H_2O$ complex in aqueous solution at different concentrations (a)10^{-3} mol l^{-1}, (b) $2.5·10^{-3}$ mol l^{-1}, (c) $5·10^{-3}$ mol l^{-1}, (d) $7.5·10^{-3}$ mol l^{-1}, (e) 10^{-2} mol l^{-1})

Table 3

Electronic transitions of the $K_{19}[U_2KAs_4W_{40}O_{140}]·42H_2O$ complex

Band	ν (cm^{-1})	Assignment
L	14 720	$^3H_4 \rightarrow {}^3P_0$
O	15 440	$^3H_4 \rightarrow {}^1D_2(^1G_4)$
R	17 670	$^3H_4 \rightarrow {}^3P_1$
V	20 160	$^3H_4 \rightarrow {}^1I_6$
W	23 600	$^3H_4 \rightarrow {}^3P_2$

(c) ESR Spectra. The powder ESR spectrum of the complex obtained at room temperature exhibits the most intense signals in the 3250–3400 G region. The fine structure of the ESR spectrum can be interpreted by considering one S_{eff} = 1 effective spin for the uranium(IV) ion and a Γ_5 sublevel of the $^3H_4$ multiplet as ground state. The principal values of the gyromagnetic tensor **g** of the complex are g_x = 2.045, g_y = 2.050 and g_z = 2.085 and the zero-field splitting parameters D = $18.31 \cdot 10^{-4}$ cm^{-1} and E = $5.99 \cdot 10^{-4}$ cm^{-1}.

Sandwich-type uranium(IV)–polyoxometalates with three uranium ions

Sandwich-type uranium(IV)-polyoxometalates: $Na_m[(UO)_3(H_2O)_6(XW_9O_{34})_2] \cdot nH_2O$ (X = P, m = 12, n = 21; X = Si, m = 14, n = 19; X = Ge, m = 14, n = 17) and $Na_m[U_3(XW_9O_{33})_2] \cdot nH_2O$ (X = As, m = 6, n = 15; X = Bi, m = 6, n = 18; X = Sb, m = 6, n = 16) were investigated by FT-IR and UV-VIS spectroscopy. Complexes with P, Si and Ge derives from α-A trilacunary Keggin anions, the complex with As from α-B-type and complexes with Bi and Sb from β-B-type anions. The corresponding ligands are $Na_8H[PW_9O_{34}] \cdot 14H_2O$, $Na_{10}[SiW_9O_{34}] \cdot 15H_2O$, $Na_{10}[GeW_9O_{34}] \cdot 14H_2O$, $Na_9[AsW_9O_{33}] \cdot 12H_2O$, $Na_9[BiW_9O_{33}] \cdot 13H_2O$, $Na_9[SbW_9O_{33}] \cdot 12H_2O$.

(a) FT-IR spectra. The complexes FT-IR spectra contain two supplementary bands for ν(U–O) vibrations which indicate the presence of non-equivalent U–O bonds (except for the complex with P which has a single band) (Fig.4) [7]. For the complexes with P, Si, Ge and As, ν_{as}(W–O_c–W) bands shift towards higher frequencies and ν_{as}(W–O_b–W) towards lower frequencies compared to the ligands bands. These indicate the coordination of every uranium ion to terminal oxygens of edge-sharing octahedra. For the complex with Bi, all tricentric frequencies are red-shifted in the complex spectrum compared to the ligand spectrum. The ν_{as}(W–O_c–W) frequency band, singular in the spectrum of the ligand with Sb, is splitted in the spectrum of the uranium complex with Sb because of the presence of nonequivalent W–O_c–W bonds.

(b) UV-VIS spectra. The UV spectra of the U^{IV}–POM complexes and of the ligands obtained in aqueous solutions present the charge transfer bands for $p_\pi(O_d) \rightarrow d_{\pi^*}(W)$ and $p_\pi(O_{b,c}) \rightarrow d_\pi(W)$ electronic transitions (Table 4). The bicentric bands are shifted towards higher wavenumbers after the complexation by uranium of trivacant Keggin units with P, Si and Sb and lower wavenumbers for the others [8,9]. The enhancement of $p_\pi(O_{b,c}) \rightarrow d_\pi(W)$ transition bands intensities compared to those of the ligands and the decrease of their corresponding wavenumbers show that the stability of the lacunary Keggin frameworks increases in all complexes compared to the ligands. The visible electronic spectra of the U^{IV}–POM complexes performed in aqueous solutions indicate that the local symmetry around the uranium ions is quasicubic, with $^3H_4$ ground level. The L band is splitted (except for germanium complex) because of some distortions of the cubic ligand field around the uranium ions [10].

Table 4

UV transition bands (cm^{-1}) of the ligands (**L1**–**L6**) and the complexes (**1**–**6**)

Band	**L1 / 1**[a]	**L2 / 2**	**L3 / 3**	**L4 / 4**	**L5 / 5**	**L6 / 6**
$\nu(p_\pi \rightarrow d_{\pi^*})$ (W=O_d)	47120 s,b 47280 s,b	46480 s,b 46800 s,b	46000 s,b 45760 s,b	46640 s,b 46480 s,b	47280 s,b 46720 s,b	46640 s,b 47280 s,b
$\nu(p_\pi \rightarrow d_{\pi^*})$ (W–$O_{b,c}$–W)	41040 m,sh 39640 m,vb	41360 m,sh 39000 m,vb	41600 m,sh 38800 m,vb	40880 m,sh 39120 m,vb	41520 m,sh 40720 m,sh	40880 m,sh 39920 m,sh

[a]s-strong, m-medium, b-broad, vb-very broad, sh-shoulder

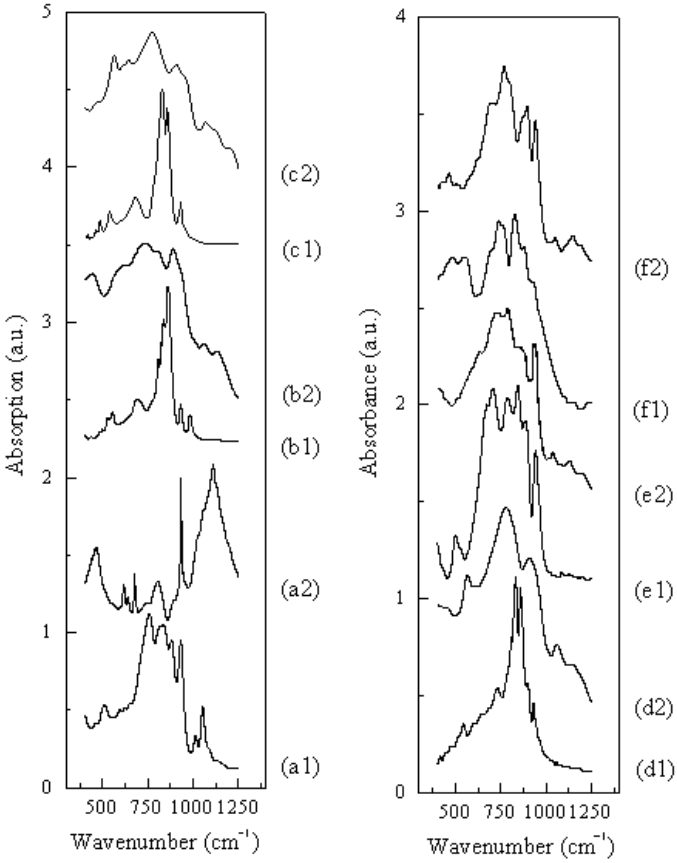

Fig.4 *FT-IR spectra of the ligands with (a1) P, (b1) Si, (c1) Ge, (d1) As, (e1) Bi, (f1) Sb and uranium complexes with (a2) P, (b2) Si, (c2) Ge, (d2) As, (e2) Bi, (f2) Sb*

(c) Magnetic susceptibility

Temperature dependance of the magnetic susceptibility data for the complex with germanium is presented in Fig.5. The obtained effective magnetic moment is μ_{eff}=4.40 μ_B and the Curie temperature is θ=–73 K. The magnetic moment value and the negative θ correspond to a system with S=1 ground state, obtained through antiferromagnetic exchange between the uranium(IV) spins.

Conclusions

Spectroscopic investigations of $K_{14}[U(BW_{11}O_{39})_2]\cdot 25\ H_2O$ complex indicate the coordination of the uranium(IV) ion at two monolacunary Keggin fragments, by the substitution of $W{=}O_d$ units. The uranium(IV) ion is eight coordinated by oxygen atoms in a cvasicubic local environment, with a $^3H_4$ electronic ground state. The magnetic susceptibility measurements show the absence of any exchange or dipolar interactions between the uranium ions and one Γ_1 ground state into the $^3H_4$ multiplet.

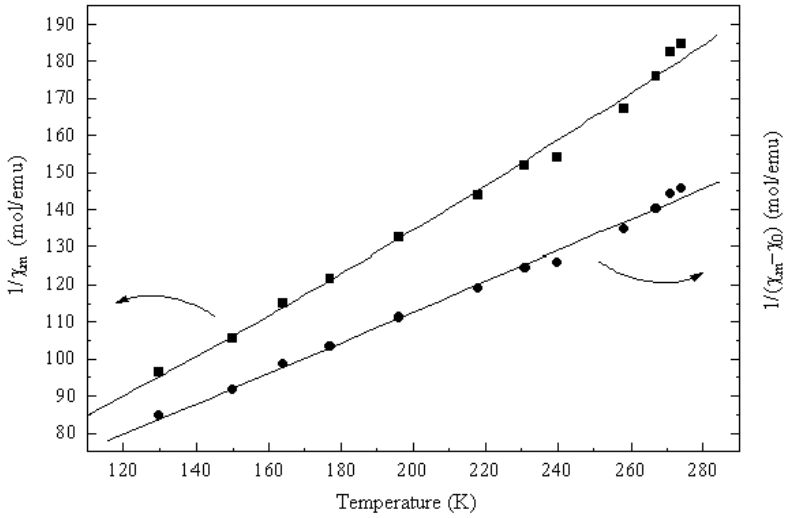

Fig.5 Temperature dependence of the reciprocal molar magnetic susceptibility of the $Na_{14}[(UO)_3(GeW_9O_{34})0_2]\cdot 23H_2O$ complex. Lines are the best fit of the temperature dependence of the measured (€) data and diamagnetic corrected (●) values respectively.

The IR spectrum of the $K_{19}[U_2KAs_4W_{40}O_{140}]\cdot 42H_2O$ complex contains an additional band (ν_{as}(U–O)) compared to the ligand spectrum, a proof of the coordination of the uranium ions to the oxygen atoms of the polyanion. The vibration bands of the polyoxometalate are shifted in the complex spectrum compared to the ligand spectrum due to the coordination of the uranium ions at oxygen atoms from lacunary regions of the $\{AsW_9\}$ units and binding WO_6 octahedra. VIS and ESR spectra indicate the presence of cubic environments around the uranium ions with Γ_5 ground state into the $^3H_4$ multiplet.

FT-IR investigation of the series of uranium(IV)–polyoxometalates containing three uranium(IV) ions indicates the coordination of the uranium into the lacunary regions of two trivacant Keggin units. The UV spectra show the increased stability of the lacunary Keggin frameworks after complexation. All uranium ions are octacoordinated into a quasicubic local symmetry.

REFERENCES

1. J. H. Kenedy, Analyt. Chem. 32 (1960) 150.
2. G. M. Varga Jr., E. Papaconstantinou, M. T. Pope, Inorg. Chem. 9 (1970) 662.
3. R. Papaalardo, B. C. Jorgensen, Helv. Phys. Acta. 37 (1964) 79.

4. O. Vogt, k. Mattenberger, j. Löhle, j. Rebizant, journ of alloys and Compounds, 271-273 (1998) 508.
5. R.A. Satten, D. Young, D.M. Gruen, J. Chem. Phys., 33 (1960) 1140.
6. M. Mickelon, g. Hervé, m. Leyrie, j. Inorg. Nucl. Chem., 42 (1980) 583.
7. R.A. Gazarov, G.A. Gardeeva, I.D. Koli and V.I. Spitsyn, Dokl. Nauk SSSR, 255(2) (1980) 373.
8. T. Yamase, Chem. Rev. 98 (1998) 307.
9. H. So and M.T. Pope, Inorg. Chem., 11 (1972) 1441.
10. I. Creaser, M.C. Heckel, R.J. Neitz and M.T. Pope, Inorg. Chem., 32 (1993) 1573.

^{1}H-NMR METHODOLOGY APPLIED TO ELUCIDATE THE ADDITION REACTION OF PYRIDINE AND IMIDAZOLE COMPOUNDS WITH α,β-UNSATURATED CARBOXYLIC ACIDS

VIRGIL BARBOIU

"Petru Poni" Institute of Macromolecular Chemistry, Aleea Grigore Ghica Voda 41A, Iasi-6600, e-mail: vbarboiu@ichpp.tuiasi.ro

In a series of recent papers [1-5] we reported the synthesis of carboxybetaines by the addition reaction[1] of tertiary amines with α, β - unsaturated carboxylic acids. Previously, some macromolecular carboxybetaine compounds have been obtained by one of the following reaction: alkylation of pendant tertiary amine group containing polymers with halogenated acetic acids or their esters, and polymerization of betaine group containing monomers. The former chemistry was applied using poly(4-vinylpyridine) and poly(styrene-co-vinylbenzyldimethylamine) [6] and the latter using vinylimidazole.[7]

The present article described how the ^{1}H-NMR methodology was used to establish the reaction mechanisms the kinetic of carboxybetaine formation.

Experimented Data and Observations

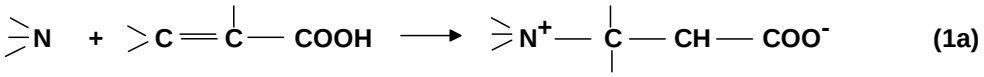

(1a)

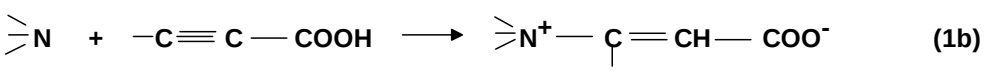

(1b)

Reaction between amines and acids were carried out at 50^{o}C with amine concentration of 1 mol/L. Water, methanol and acetonitrile were used like solvents. It was found that the reaction yield (or transformation degree for polymers) can be conveniently determined as a function of the reaction time by using ^{1}H-NMR spectra of the reaction mixture. For this, reactions were performed directly in NMR tubes using deuterated solvents.

The following amines were found to give significant output of betaine products when are reacted with acrylic, maleic, fumaric, itaconic and propiolic acids: 4 –methylpyridine, N-methylimidazole, poly(4-vinylpyridine) and poly(N-vinylimidazole). Low amounts of betaine products resulted from 2-methyl and 2,4-dimethylpyridine with acrylic acid and from 4-methyl-pyridine with methacrylic and crotonic acids. No reaction products were obtained with 2-methylpyridine and poly(2-vinylpyridine).

The shortenings for other reactants are obtained changing 4MP and AA with corresponding shortenings. The notations remain the same.

Reaction products. The notations for reactants and reaction products are given in Table 1. Because the structures obtained from different reactants are analogous, only those forms resulting from 4-methylpyridine and acrylic acid will be presented.

Table I.

Notations for reactants and reaction products.

Chemical Name / Structure	Shortening	Notation
4 – Methylpyridine	4MP	A
Acrylic acid	AA	B
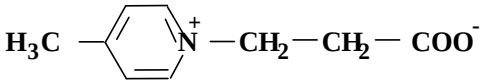		$4MP^+$ - $\underline{AA}^-$ $X^\pm$
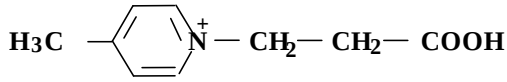		$4MP^+$ - $\underline{AA}^-$ X^+
		AA^- B^-
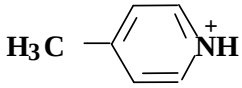		A^+
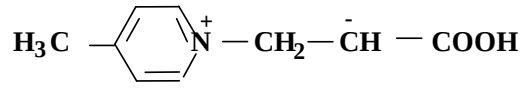		$C^\pm$

The following types of reactions products were evidenced: one zwitterionic, as betaine, another one with structure of cation-anion pair, and the common salt. The content of these products was highly dependent on the solvent and the purification method used. The zwitterionic ($X^\pm$) and ions pair (X^+ B^-) products were isolated as pure compounds. They were differentiated by spectrometric methods, especially from ^{1}H-NMR spectra (Figure 1). The salt products were observed in protic reaction mixtures but their isolation was not possible.

Table II.

Reaction products in protic and aprotic solvents

Solvent	Species present in the reaction mixture	Products isolated from the reaction mixture
CD_3CN	A and B	X^+B^-
CD_3OD or D_2O	A, A^+, B, B^-	X^+B^- and / or $X^\pm$
or their mixture	X^+ and $X^\pm$	

Experimental observations. The species present in the reaction mixture and the reaction products are presented in Table II. It was observed that the reaction product precipitates and shows an X^+B^- structure when the reactions are carried out in

acetonitrile, i.e. in an aprotic solvent. This fact leads to the hypothesis of the reaction 2. Another observation of interest is that, when acetone or ethyl ether is added to a methanol or water solution of an X^+B^- compound, the corresponding $X'S^\pm$ compound precipitates instantaneously. This leads to the assumption that in solution the products X^+B^- are involved in the equilibrium reaction 3.

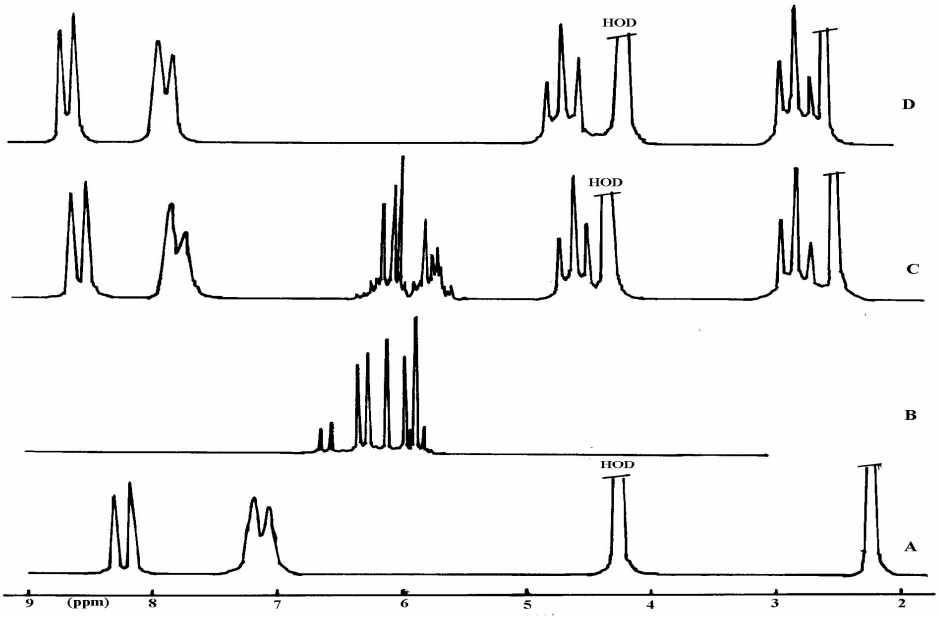

Figure 1. [1]H-NMR spectra in D_2O from 4-methylpyridine (A), acrylic acid (B), and their corresponding products X^+B^- (C), and $X^\pm$ (D).

$$\mathbf{A + 2\,B \rightleftharpoons X^+ + B^-} \qquad \mathbf{(2)}$$

$$\mathbf{X^+ + B^- \rightleftharpoons X^\pm + B} \qquad \mathbf{(3)}$$

$$\mathbf{A + B \rightleftharpoons A^+ + B^-} \qquad \mathbf{(4)}$$

The reactions 2 and 3 happen also in protic solvents like water and methanol, therefore the reaction product is generally a mixture of X^+B^- and $X^\pm$ compounds, in this case. Such reaction mixtures are homogeneous and their [1]H-NMR spectra can be used to evaluate the concentration of the species which are present at any reaction time.

The following difference was observed between the NMR spectra of alcoholic and aqueous reaction mixtures.: the formers show distinct aromatic proton signals from the species A and A^+ or X^+ or $X^\pm$ while the latter display on a broad signal for all these structures. This fact shows that the equilibrium of reaction 4 is much more right-shifted in water than in alcohol.

Two methods were used to isolate the reaction products from protic reaction mixtures: vacuum drying and precipitation with acetone. The first method allowed to obtain X^+B^- compounds and the precipitation gave only $X^\pm$ compounds.

Reaction Mechanism and Kinetics of the Betaine Formation

Reaction mechanism. It is generally accepted that the addition reaction between a tertiary amine and an α, β-unsaturated carboxylic acid takes place by a nuleophilic attack of the nitrogen atom at the β-carbon of the acid double bond, and a dipolar ion $C^{\pm}$ with structure given in Table I appears.[8] Protonation of this carbanion is probably an intermolecular process involving a new acid molecule rather than a solvent molecule because the compounds X^+B^- and $X^{\pm}$ were obtained in both protic and aprotic solvents. The carbanion state is confirmed by α-carbon atom deuteration occurring when the reaction was carried out in the protic deuterated solvents. Taking into account the above experimental findings, the following reactions seem to be generally implied for the formation of betaine products:

$$\mathbf{A + B} \rightleftharpoons \mathbf{A^+ + B^-} \qquad \mathbf{(5)}$$

$$\mathbf{A + B} \rightleftharpoons \mathbf{C^{\pm}} \qquad \mathbf{(6)}$$

$$\mathbf{C^{\pm} + B} \rightleftharpoons \mathbf{X^+ + B^-} \qquad \mathbf{(7)}$$

$$\mathbf{X^+ + B^-} \rightleftharpoons \mathbf{X^{\pm} + B^-} \qquad \mathbf{(8)}$$

The neutralization reaction 5 is expectable for both protic and aprotic solvents. Conforming to the experimental observations, its equilibrium is dependent on solvent, in acetonitrile and methanol being left-shifted, and odds with in water. Reaction 6 excludes a direct transformation of the salt structures A^+B^- into $X^{\pm}$ zwitterionic structures. The carbanion $C^{\pm}$ is an unstable intermediary which can not be evidenced in NMR spectra. **Kinetic model of betaine formation in aprotic solvents**. Previously we reported the kinetic model applicable for protic reaction mixtures.[3,5] Here the process performed in an aprotic solvent will be considered. As in this case the reaction product precipitates with an ions pair structure and the reaction mixture contains only the reactants. (Table II), the reactions 6 and 7 can be only considered. Moreover, because it is accepted that the constant rate of reaction 7 is much higher than the rate constant of the decomposition of $C^{\pm}$,[9] the reversibility of reaction 6 can be neglected. In such conditions, the reactions 6 and 7 can be condensed in the trimolecular reaction 9 with $\mathbf{k_a}$ the rate constant of the addition reaction.

$$\mathbf{A + 2\,B \rightarrow X^+ + B^-} \qquad \mathbf{(9)}$$

By using the notations $a = [A]_o$, $b = [B]_o$, and $x = [X^+] = [B^-]$, the reaction 9 is described by the equation 10.

$$\mathbf{dx / dt = k_a (a - x) (b - 2 x)^2} \qquad \mathbf{(10)}$$

Determinations of addition rate. To find $\mathbf{k_a}$ it was necessary to measure either the quantity of precipitate or the concentration of reactants for different values of the reaction time. It was found that the measurements of reactant concentrations are easy-doing and more accurate that those of precipitate. Such measurements can be performed from IR, UV or NMR spectra. We used the ^{1}H-NMR spectra recorded on deuterated acetonitrile reaction mixtures respecting the condition **b = 2 a**. In this particular case the solution of the equation 10 takes the easy-handling form 11 where $\mathbf{a_t = [A] = a - x.}$

Obviously the equation 11 is also valuable for protic reaction mixtures. It has been previously used for reactions performed in CD_3OD and CD_3OD – D_2O mixtures.[3,5]

The fact that this kinetic model is really applicable is illustrated in Figure 2 for the reactions of 4-methylpyridine and N-methylimidazole with acrylic acid.

$$(a / a_t)^2 = 1 + 8\, k_a\, a^2\, t \qquad (11)$$

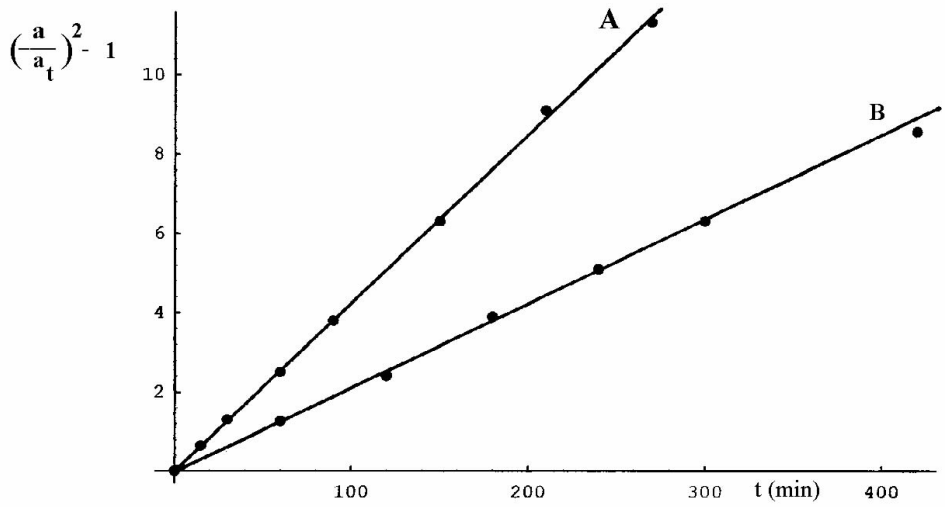

Figure 2. Experimental plot of equation 11 for 4-methylpyridine (A) and N-methylimidazole (B) reacted with acrylic acid in acetonitrile.

Table III.

The values of k_a determined for reactions carried out in CD_3CN at 50°C

Reactants	k_a ($mol^{-2}\ L^2\ min^{-1}$)
4-methylpyridine + acrylic acid	0.0053
N-methylimidazole + acrylic acid	0.0009
4-methylpyridine + crotonic acid	0.00002
N-methylimidazole + crotonic acid	0.00003
4-methylpyridine + methacrylic acid	0.000003
N-methylimidazole + methacrylic acid	0.000004
poly (4-vinylpyridine) + acrylic acid	0.0018
poly (N-vinylimidazole) + acrylic acid	0.0053

The values of k_a obtained for several systems are given in Table III. One observes that, indifferently of amine reactant, the reactivity of acids decreases drastically in the order acrylic acid crotonic acid methacrylic acid what evidences the influence of

substitution and substitute site. Relating to the amine reactant, the reactivity changes in the order 4MP ≅ PNVI > P4VP > NVI. It is rather strange that the accepted rule "that the reactivity of a functional group is lower in macromolecular compounds than in corresponding low molecular models" is not respected for imidazole compounds. It is as if a reacted imidazole group promotes reaction of its neighbors, i.e. the addition reaction would be of "zipper" type. This fact might be explained by the acidity of the $N–CH–N^+$ group which is much higher for polymer than for its model.

Conclusions

The reaction between pyridine and N–substituted imidazole compounds with α, β-unsaturated carboxylic acids could offer ions pair products as well is betaines. The salts structures were observed (but not isolated) only in aqueous reaction mixtures.

The synthesis of betaine compounds consists of two reactions: the addition, which implies two molecules of acid and leading to a pair of ions X^+B^-, and an equilibrium reaction between the product X^+B^- and the zwitterionic (betaine) product $X^\pm$. In protic solvent, the equilibrium reaction is coupled to addition, to which supplies acid, so that there is a global accumulation of zwitterionic structures. The addition is the only one to take place into aprotic (polar) solvents.

The process of betaine formation was experimentally confirmed. Its kinetic model was proved for aprotic solvents and the addition rate constant was determined for several systems.

REFERENCES

1. V. Barboiu, E. Streba, C. Luca, C. I. Simionescu, *J. Polym. Sci., Polym. Chem. Ed.*, **33**, 389 (1995).
2. V. Barboiu, E. Streba, M. N. Holerca, C. Luca, *J. Macronol. Sci., Chem*., **A32**, 1385 (1995).
3. V. Barboiu, M. N. Holerca, E. Streba, C. Luca, *J. Polym. Sci., Polym. Chem. Ed*., **34**, 261 (1996).
4. E. Streba, C. Luca, M. N. Holerca, V. Barboiu, C. I. Simionescu, *Rev. Roum. Chim.*, **42**, 413 (1997).
5. V. Barboiu, E. Streba, C. Luca, I. Radu, G. E. Grigoriu, *J. Polym. Sci., Polym. Ed*., **36**, 1615 (1998).
6. (a) H. Ladenheim, H. Morawetz, *J. Polym. Sci.*, **26**, 251 (1957); (b) T. Hamaide, M. Guambodoe, A. Guyot, *Polymer*, **31**, 286 (1990).
7. T. H. Wielema, J. B. F. N. Engerbets, *Eur. Polym. J*., **26**, 415 (1990).
8. S. Patai, Ed., *The Chemistry of the Amido Group*, Interscience, New York, 1968.
9. T. Taghizadeh, C. Caze, C. Loucheux, *Polym. Bull.*, **4**, 429 (1981), and *Eur. Polym. J*., **18**, 907 (1982).

ADSORPTION ON SILVER SURFACE OF 5-(3-NITRO-4-METHYL-PHENYL)-FURAN-2 CARBALDEHIDE

T. ILIESCU[A*], F. D. IRIMIE[B], M. BOLBOACA[C] ,CS. PAIZS[B], W. KIEFER[C]

[a] *Babes-Bolyai University, Physics Faculty, 3400 Cluj-Napoca, Romania.*
[b] *Babes-Bolyai University, Chemistry Faculty, 3400 Cluj-Napoca Romania.*
[c] *Institut für Physikaliche Chemie, Universität Würzburg, D-97074,Würzburg, Germany*

ABSTRACT. FT Raman and SER spectra of 5-(3-nitro-4-methyl-phenyl)-furan-2 carbaldehide at different pH values were recorded. A theoretical vibrational analysis was made and compared with FT Raman spectra. At low pH values both samples present a good SER spectra. The shift to red of SERS bands by 10-15 cm^{-1} is an indication of chemisorption of these species, which are bonded to the silver surface via nonbonding electrons of ring oxygen.

Keywords: Raman spectroscopy; SERS; 5 substituted-furan-2 carbaldehide

Introduction

Furan-2 carbaldehide derivatives are very important intermediates in organic synthesis. The bacteriostatic effects of these compounds were checked up with good results.

Surface Enhanced Raman Scattering (SERS) was observed for many molecular species. Because of suppression the of fluorescence, this nonradiativ transfer being determined by the roughness of the silver surface, this technique is very useful for molecules that present this phenomenon, especially for molecules of biological interest [1,2].

In this paper we present the investigation of 5-(3-nitro-4 methyl-phenyl)-furan-2 carbaldehide (5-(3-N-4MP)-F-2C) from analytical (FT-Raman spectroscopy) and theoretical (DFT calculation) point of view. We recorded SER spectra of this specie adsorbed on silver particles at different pH values in order to elucidate the form in which the adsorbed molecules may exist in adsorbed state. To our knowledge these data are not yet present in literature.

Experimental

The compounds were obtained from the corresponding diassonium salt and furfural in aqueous medium using $CuCl_2$ catalyst. [3] The products were purified with column chromatography on silica gel.

The FT Raman spectra were recorded using a Brucker IFS 120HR spectrometer with an integrated FRA 106 Raman module and a resolution of 2 cm^{-1}. Radiation of 1064 nm from Nd-YAG laser was employed for excitation. A Ge detector, cooled with liquid nitrogen, was used. SER spectra were recorded with a Spex 1404 double spectrometer using 514.5 nm and 300W output of Spectra physics argon ion laser. The detection of Raman signal was carried out with a Photometrics model 9000 CCD camera. Spectral resolution was 2 cm^{-1}. A citrate reduced Ag colloid was employed as SERS substrate. Ag citrate was prepared according to the literature [4]. Small amounts of 10 μL of sample 10^{-1}mol L^{-1} ethyl alcohol solution were added to 3-ml colloid. 0.1 ml 10^{-1}mol L^{-1} NaCl solution was also added for producing a stabilization of the colloidal dispersion and a

**Corresponding author. Tel.: +40-64-405300; fax: +40-64-191906. E-mail address: ilitra@phs.ubbcluj.ro*

considerable enhancement of the SER spectra. The final concentration of the sample were approximately 3.2 10^{-4} mol.l^{-1}. NaOH and H_2SO_4 were used to obtain different pH values.

The density functional theory (DFT) calculations were performed using GAUSSIAN98 [5]. Using a fully optimized geometry as reference geometry performed all calculation of harmonic wavenumber. The DFT geometry optimization was carried out with the combination of Becke's 1988 exchange functional [6] and the Perdew-Wang 91 gradient-corrected correlation functional [7] (BPW91). The 6-31+G* basis sets for all atoms has been employed in the geometry optimization and the vibrations calculations.

Results and Discussion

By rotation of the (CHO) group in 5-(3-N-4MP)-F-2C, two rotational isomers, *syn*-form and *anti*-form, were obtained. Theoretical calculations at the BPW91/6-31+G* level of theory were performed for both isomers. The optimized geometry of these rotamers with the labeling of their atoms are shown in Fig.1.

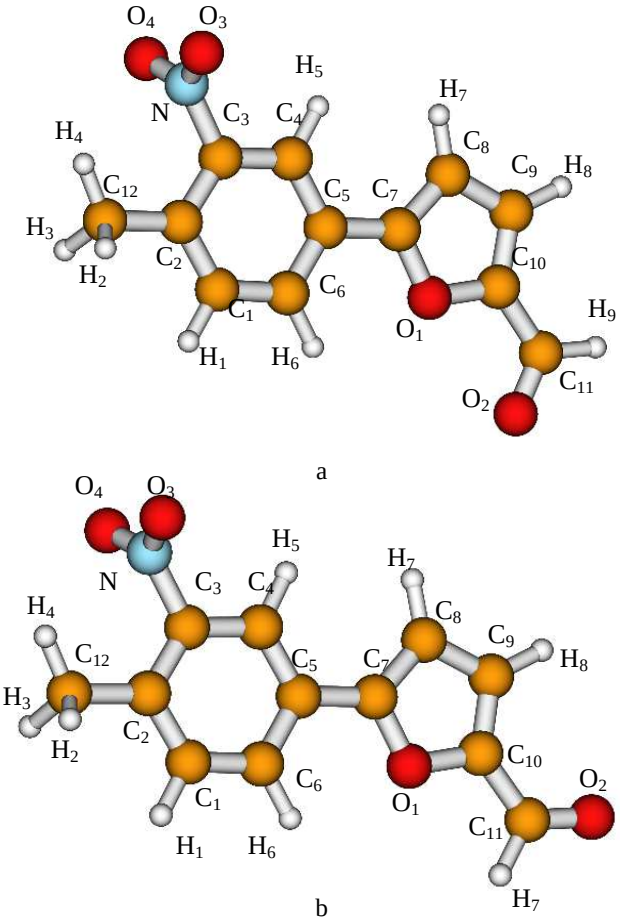

Fig.1. Structural formula for the two isomers of 5-(3-nitro-4-methyl-phenyl)-furan2 carbaldehide. (a) syn-form isomer, (b) anti-form isomer

The optimized structure of both conformers is not planar. Thus the C3NO3 and C4NO4 angles have 117^o while the dihedral angle C4C3NO3 and C4C3NO4 have -86^{o}and 93^o respectively. Further, the analytical harmonic vibrational modes have been calculated in order to ensure that the optimized structure correspond to minima on the potential energy surface. The total energy for the *syn*-form isomer, including zero-point correction, are found to be –817.825627 and –817.826568 hartree at the BPW91/6-31+G* level of theory. Therefore, at this level of calculation, the *anti*-form isomer was found to be more stable than *syn*-form by 2.995 KJ.mol^{-1}.

The observed bands in IR, FT-Raman and SER spectra at pH 1 of 5-(3-N-4MP)-F-2C together with theoretical calculation of both isomers are summarized in Table 1.

Table 1

Experimental (infrared, FT-Raman) and calculated wavenumbers (cm^{-1}) (anti/syn forms) of 5-(3-nitro-4-methyl-phenyl)-furan-2 carbaldehide.

IR	Raman	Calc.[1] anti/syn	SERS pH 1	Assignment
	179m	170/180		$\delta(C_{4,5,7}) + \delta(C_{9,10,11})$
	267w	246/285		$\omega(C_2C_{12}) + \omega(C_{10}C_{11})$
	386m	378/378		ring 1[b] out of plane def.
505m	505m	500/496		
551sh	558sh	560/559		ring 1 + ring 2[c] out of plane def
560vw	567w	598/608		
619w	620w	635/629		
672m	675m	670/681		
757m	756sh	741/757	724w	$\omega(C_3N)$
768sh	771m	779/772		ω(CH) (ring 2)
801m	800m	784/784	796w	$\delta(O_3NO_4) + \delta(C_{1,2,3}) + \delta(C_{4,5,6})$
810sh	811m	817/822		ω(CH) (ring 1)
934m	932m	937/937	903w	ν(CN) + $\delta(O_1C_{7,8}) + \delta(C_{4,5,6})$
967m	967m	964/961		ω(CH) (COH)
1039m	1040m	1031/1039	1032m	ω(CH) (ring 2) + ω(CH) (CH_3)
1048sh				
1096w	1106w	1081/1081		$\delta(C_{1,2,3}) + \delta(C_{4,5,6}) + \nu(C_{8,7}O_1)$
1211m	1212m	1205/1201	1211vw	τ(CH) (ring 1 + ring 2) + $\nu(C_{2,12}) + \nu(C_{5,7}) + \nu(C_{10,11})$
1217sh	1218sh	1220/1244		
1250m	1251w	1264/1270	1224w-m	ρ(CH) (ring 1)
1278sh	1278sh	1278/1292		$\nu(C_{5,7}) + \rho$(CH) (ring 1)
1294m	1295m	1313/1313	1294w-m	$\nu(O_3NO_4)$
1355m	1355s	1334/1331	1331s	ring 1 stretching + $\nu(C_{8,9})$
1391m	1392m	1392/1391	1375s	ring 1 + ring 2 stretching
1405sh	1402sh	1413/1415		ρ(CH) (ring 2 + CH_3)
1469m	1470s	1469/1471	1453w-m	ρ(CH) (CH_3)
1524s	1524vs	1514/1514	1519s	ring 1 + ring 2 stretching
1533s	1533s	1533/1531		$\nu(O_3NO_4) + \nu(C_{9,10,11}) + \nu(C_{1,6,5})$
1579m	1579m	1571/1568	1573s	ring 1 + ring 2 stretching
1620s	1621vs	1619/1619	1603s	

IR	Raman	Calc.[1] anti/syn	SERS pH 1	Assignment
			1634sh	
1664sh 1674s	1665m 1674vs	1687/1690		ν(CO) (COH) *anti*-isomer ν(CO) (COH) *syn*-isomer
2820m 2916sh	2820m	2862/2844		ν(CH) (COH)
2928m	2928m	2999/2999		ν(CH) (CH_3)
3066m 3078sh	3058sh 3069m	3066/3067 3076/3077		ν(CH) (ring 1)
3114w	3112w	3204/3199		ν(CH) (ring 2)

[*]Abbreviation: w-weak, m-medium, s-strong, ν-very, sh-shoulder, ν-stretching, δ-bending, ρ-rocking, τ-twist, ω-wagging,.

Calc[1]: BPW91/6-31+G[*], ring 1[b]-phenyl ring, ring 2[c]-furan ring.

The assignment of the normal modes of vibration for the molecules was accomplished mainly by comparison with related molecules [8-11] and using the wavenumber (unscaled values) and intensities as obtained by BPW91 method. The theoretical results obtained with the 6-31+G* basis set reproduce closest the experimental values. A strict comparison between the experimental and calculated wavenumbers and intensities is not possible in this case because the experimental data were obtained for the solid state, whereas the theoretical results are for gas phase. It is well known that the calculated wavenumbers are obtained by using the harmonic approximation, whereas the experimental wavenumber are anharmonic by nature. Nevertheless, the quality of quantum chemical results at the presented theoretical level is sufficient to be useful for the assignment of the experimental data.

From solid state sample only strong fluorescence could be obtained for visible excitation, therefore IR excitation was necessary. F T Raman (Ordinary Raman Spectrum-ORS) of solid 5-(3-N-4MP)-F-2C is presented in Fig.2a. SER spectra in silver sol at different pH values (1and 13) are indicated in Fig.2b and 2c (to simplify the figure only spectra at two pH values was chosen).

Low concentration ($3.2\ 10^{-4}$ $molL^{-1}$) of utilized 5-(3-N-4MP)-F-2C to obtain SERS is a proof that we have an enhancement of Raman signal (ORS from solutions of such concentration cannot be obtained)

In the spectrum of 5-(3-N-4MP)-F-2C bands that appear in the 1600-1500 cm^{-1} region are broad and split in two components (1524-1533, 1664-1674 cm^{-1}). This splitting can be explained by the presence of two rotational isomers. Same splitting is present in the Raman spectrum of furfural [8]. In the ORS of 5-(3-N-4MP)-F-2C the bands at 1664 and 1674 cm^{-1} were attributed to the ν(C=O) stretching vibration of anti-form and syn-form isomers respectvely determined by the substituent group. presented in Fig.1.

The significant differences between FT Raman and SER spectra concerning the relative intensities and the bandwidth indicate a strong interaction between metal and adsorbate, this causing a quite different derivative of molecule's polarizability tensor.

There are two possibilities of molecule adsorption on metal surface, namely physisorption and chemisorption. The spectrum of physisorbed molecules is practically the same as that of free molecules, small change being observed only for the bandwidths. This situation corresponds to a relative large distance between metal surface and adsorbed molecules [12].

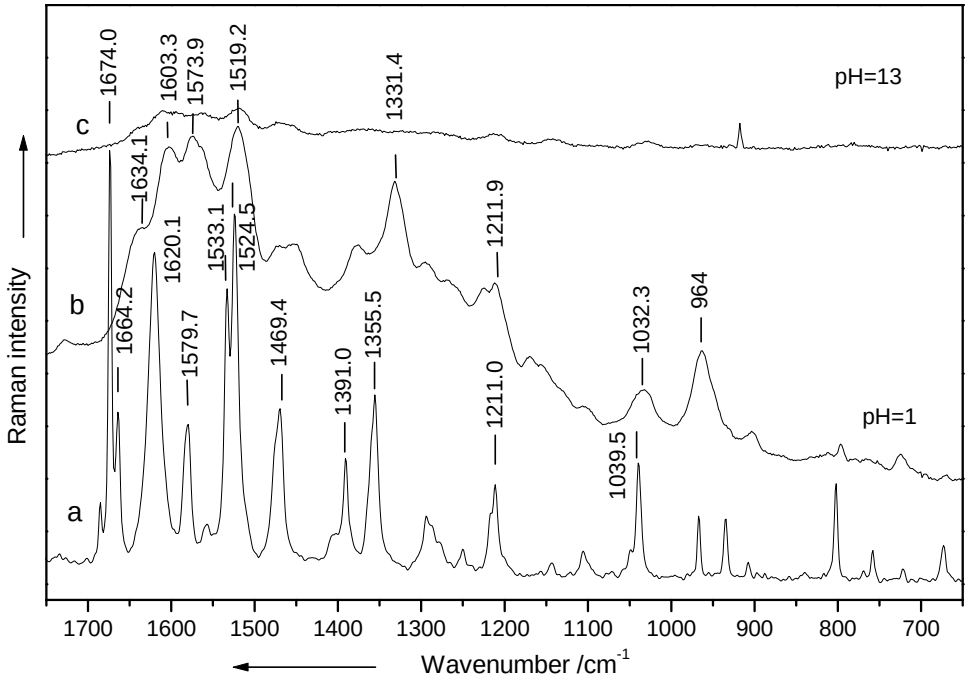

Fig. 2. FT Raman (a) and SER spectra at pH 1 (b) and 13 (c) of 5-(3-nitro-4-methyl-phenyl)-furan-2 carbaldehide

When the molecules are chemisorbed, there is an overlapping of the molecular and metal orbital, the molecular structure being modified and in consequence, the position of the bands and their intensities are dramatically changed [13].

Comparing the SER spectrum of 5-(3-N-4MP)-F-2C to the corresponding ORS (Fig.2) a shift to the lower wavenumber could be observed. Therefore, we conclude that there is a chemisorption of 5-(3-N-4MP)-F-2C molecules on the silver surface.

The enhancement of Raman signal in SERS can be explained through the two main mechanisms [13,14], the electromagnetic one, which implies the increase of the electric field near the silver surface through the resonance plasmon excitation. This mechanism explains the enhancement of the physisorbed molecules.

The chemical mechanism supposes the binding of the molecules on the silver surface, when the charge transfer between molecule and metal can occur. In this case a new specie metal-molecule SERS complex is formed. This can explain the band shift and the change in the relative intensities of the SER spectra compared to the corresponding ORS.

In our case is very difficult to separate these two mechanisms, both contributing to the enhancement of the Raman signal. Additionally, is possible to have some resonance Raman contribution to the total enhancement because the excitation wavelength 514.5 nm falls in the wing of the absorption band of both samples.

For 5-(3-N-4MP)-F-2C (Fig.2a) the split of the bands (1533.1-1524.5; 1664.2-1674 cm $^{-1}$) suggests that both isomers are Raman active. In SER spectrum of this sample, at pH 1 (Fig.2b) the broadening of the bands and dramatically changes of the relative intensities are accompanied by the shift to the lower wavenumber by 10-15 cm $^{-1}$, especially for the bands in the 1450-1650 cm $^{-1}$.region. These spectral changes can be explained by the adsorption on silver surface and by the presence of two Raman active isomers, the bands specific to each isomer being not resolved after adsorption.

The absence of the bands due to the C=O stretching mode corresponding to the both isomers in SER spectra can be a consequence of the hydration of the C=O bond according to the reaction

$$(CH_3\text{-}NO_2\text{-}C_6H_4\text{-}C_4H_2O)\text{-}CHO \underset{}{\overset{H_2O}{\rightleftharpoons}} (CH_3\text{-}NO_2\text{-}C_6H_4\text{-}C_4H_2O)\text{-}CH(OH)_2$$

The shoulder at 1634.1 cm^{-1}, present in SER spectrum has no correspondence in the bulk spectrum and is probably given by surface complex formed by adsorption.

In alkaline medium SER spectrum of 5-(3-N-4MP)-F-2C (Fig.2c) presents a very broad bands.

Spectral modification at alkaline pH can be explained by transformation of the aldehides according to reaction (Cannizzaro reaction)

$$2\,R\text{–}CHO \xrightarrow{[OH^-]} R - CH_2OH + R - COOH$$

SER spectra being probably a superposition of both species, namely, R-CH_2OH and R-COOH.

The orientation of the adsorbed 5-(3-N-4MP)-F-2C molecules can be determined with the help of surface selection rules for Raman scattering. These rules for roughened surface have been described by Creighton [15] and by Moskovitz and DiLella [16]. If the molecular z-axis is normal to the surface, then vibration of the adsorbed molecules, which have a polarizability tensor component along this axis, will be preferentially enhanced. Gao and Weaver [17] observed significant (~25 cm^{-1}) red shift relative to the bulk spectra in the ring band of the flat adsorbed substituted benzene derivatives, due to backdonation of electron density from the metal to the π^*antibonding orbital. A similar phenomenon was observed in the case of pyridine derivative [18]. These conclusions could be extended to the furan ring.

The 5-(3-N-4MP)-F-2C molecule has low symmetry and all vibrations will have a polarizability tensor component along the z-axis. .

In SER spectrum of 5-(3-N-4MP)-F-2C, at low values of the pH, the stretching modes of the furan and phenyl rings (see Table 1) are more enhanced than other modes and red shifted by 10-13 cm^{-1} comparing to the bulk spectrum. The out of plane modes of the adsorbed molecules are weak enhanced. If the molecular plane would be vertical to the metal surface then a blue shift of the ring breathing modes is expected [19]. In our case the ring plane of the 5-(3-N-4MP)-F-2C molecule is probably not perfectly vertical but rather inclined to the silver surface, the molecules being bonded on the metal surface through the nonbonding electrons of the ring oxygen.

Because of the broadening of the bands at alkaline pH for both samples is very difficult to tell which of the species R, R'-CH_2OH or R,R'-COOH are adsorbed and which are the orientation of these species to the silver surface.

Conclusions

A vibrational analysis was performed on 5-(3-nitro-4-methyl-phenyl)-furan-2 carbaldehide. Both isomers, *syn* and *anti*-form of 5-(3-nitro-4-methyl-phenyl)-furan-2 carbaldehide are Raman active. The sample presents good SER spectra at low pH values but at large pH the enhancement is very weak and bands are more broadened. The red shift by 10-15 cm^{-1} of the SERS bands, comparing to the ordinary Raman spectrum, indicates the chemisorption to the silver surface. The absence of band due to the C=O stretching mode corresponding to the both isomers in SER spectrum was explained by hydration of C=O bond. The molecular species are tilted oriented to the metal surface and bonded to it *via* nonbonding electrons of the ring.

Acknowledgements

The authors wish to thank Professor Dr. I. A. Silberg from Chemistry Institute Cluj-Napoca for fruitful discussion.

REFERENCES

1. T. M. Cotton, J-H. Kim, G. D. Chumanov, *J. Raman Spectrosc*. **22** (1991) 729.
2. I. R. Nabiev, K. K. Sokolov, M. Manfait, *Biomolecular Spectroscopy*, R. J. H. Clark and R. E. Hester, Eds., John Wiley and Sons, Chichester, 1993, p.287.
3. F. D. Irimie, Cs. Poizs, M. Tosa, C. Majdak, P. Moldovan, R. Misca, M. Caprioara, *Sudia Univ. Babes-Bolyai, Chemia, in press.*
4. T. K. Lee. D. Meisel, *J. Phys. Chem*. **87** (1982) 3391.
5. Gaussian 98, Revision A 7, Gaussian, Inc., Pittsburgh PA, 1998
6. A. D. Becke , *Phys. Rev.* A 38 (1988) 3098.
7. J. P. Perdew, Y. Wang, *Phys. Rev.*, B 45 (1992) 13244
8. E. V. Sobolev, V.T. Alexanean, R. A. Karahanov, I. F. Belinskii, V. A. Ovoboda, *J. Structurnoi Himii*, **4** (1963) 358.
9. F. R. Dollish, W. G. Fately, F. F. Bentley, *Characteristic Raman Frequencies of organic compounds*, Jon Wiley and Sons, New York, 1974, p. 220-224.
10. A. R. Katritzky Ed., *Physical Methods in Hrterocyclic Chemistry* , Vol. II, 1963, Academic Press, New York, p.201-208.
11. K. Mukherjee, D. Bhattacharjee, T. N. Misra, *J. of Colloid and Interface Science*, **193** (1997) 286.
12. T.Vo-Din, *Trends in Analyt. Chem*.,**17** (1998) 557
13. A. Campion. P. Kambhampati. *Chem. Soc. Rev*., **27**, (1998) 241.
14. M. Moskovitz, *Rev. Mod. Phys*. **57,** (1985), 783.
15. J. A. Creighton, *Surf. Sci*.,**124**, (1983) 209.
16. M. Moskovitz, D. P. Lella, *J. Chem. Phys*., **73 (**1980) 6068.
17. P. Gao, M. J. Weaver, *J. Phys. Chem*., **89** (1985) 5040.
18. S. M. Park, K. Kim, M. S. Kim, *J. Mol. Struct*., **328** (1994) 169.
19. J. F. Arenas, J. L. Castro, J. C. Otero, J. I. Marcos, J. *Raman Spectrosc*. **23** (1992) 249.

STUDIA UNIVERSITATIS BABEŞ-BOLYAI, PHYSICA, SPECIAL ISSUE, 2001

MAGNETIC AND STRUCTURAL PROPERTIES OF SOME GLASSES CONTAINING RARE EARTH IONS WITH APPLICATIONS IN TELECOMMUNICATIONS

CULEA EUGEN and GOG LIDIA

Physics.Dept., Technical University of Cluj-Napoca,
Str.C.Daicoviciu nr.15, 3400 Cluj-Napoca, Romania

The $xR_2O_3(1-x)[(1-y)Na_2B_4O_7 \cdot yMO]$ vitreous system with R=Nd, Gd, Dy and Ho, MO= Al_2O_3 or PbO, y=0 or 0.05 and x = 0.01÷0.25 were prepared and studied magnetic susceptibility and density measurements. Magnetic susceptibility data indicate a Curie-Weiss type magnetic behaviour of the samples. Density data suggest that the rare earth ions play a network modifier role in the studied glass matrices. Al_2O_3 shows an anticlustering effect in the case of glasses containing holmium ions.

1.Introduction

Glasses containing rare earth (RE) ions constitute the ideal material for obtaining the main elements of the equipment used in telecommunications (lasers, amplifiers, and optical fibers) [1-3]. One of the most important requirements concerning the laser active elements is to contain a high level of RE ions in order to ensure a high level of the laser power. However, the increase of the RE ion concentration is limited by the clustering tendency of these ions, which occurs at relatively low concentration. To follow the evolution of the clustering mechanism with respect to the RE ion concentration and the possible anticlustering effects of some additives, we studied some borate glasses containing Nd, Gd, Dy and Ho ions and two additives, namely Al_2O_3 and PbO, using magnetic susceptibility and density measurements. The mentioned rare earth ions were choosen because previous reports (Nd [4, 6], Gd [7-11], Dy [12] and Ho [13, 14]) show that they appear in the oxide glass matrices in a single valence state, namely RE^{3+}.

2.Experimental

Samples of the $xR_2O_3(1-x)[(1-y)Na_2B_4O_7 \cdot yMO]$ vitreous system (noted xRNM) where R=Nd, Gd, Dy and Ho, MO= Al_2O_3 or PbO, y=0 or 0.05 and x = 0.01, 0.05, 0.10, 0.15, 0.20 and 0.25 were obtained using reagent grade $Na_2B_4O_7 \cdot 10H_2O$, PbO and Nd_2O_3. Appropriate amounts of $Na_2B_4O_7$ glass powder, Al_2O_3 or PbO and RE oxide were mixed and melted at 1000^oC for 15 minutes. The melts were quenched on a refractory steel block.

Magnetic susceptibility measurements were performed on a Faraday type balance in the 80-300K temperature range. Density measurements were performed using the picnometric method with water as the reference immersion liquid.

3.Results and discussion

The magnetic behaviour of the xRNM glasses was assumed to be due to the presence of the RE ions. The experimental magnetic susceptibility data obtained for the xRNM glasses were corrected taking into account the diamagnetic contribution of the host glass matrices.

The thermal variation of the inverse magnetic susceptibility was linear for all the samples. Fig.1 presents the thermal variation of the inverse molar magnetic susceptibility, χ_m^{-1}, of xRNM glasses, where R=Nd. This figure is representative for all the samples of the xRNM vitreous system and indicate a Curie type behaviour for the samples with $x \leq x_{cr}$ and a Curie-Weiss type behaviour for $x > x_{cr}$, described by

$$\chi_m^{-1} = (T-\theta_p)/C_m \quad (1)$$

where C_m is the molar Curie , θ_p is the paramagnetic Curie temperature and x_{cr}=0.03-0.10 depending on the rare earth ion type.

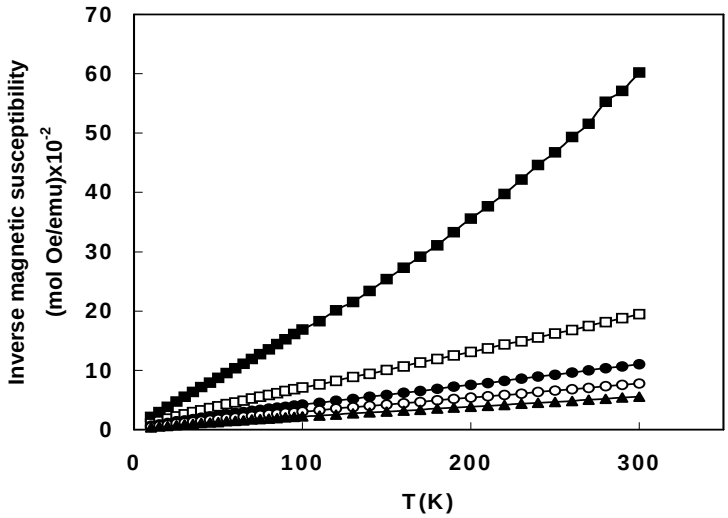

Fig.1: Temperature dependence of the inverse magnetic susceptibility of xRNM glasses with R=Nd, MO=PbO, y=0.05 and x=0.05(■), 0.10( ), 0.15(●), 0.20(○) and 0.25(▲).

Fig.2 presents the composition dependence of the paramagnetic Curie temperatures,θ_p, of the xRNM glasses. Note the small and negative values obtained for θ_p.

The analysis of magnetic data for xRNM glasses suggests that for the glasses containing small amount of RE oxide ($x \leq x_{cr}$) the magnetic RE^{3+} ions are isolated and no magnetic order is present. The glasses with $x > x_{cr}$ present a mictomagnetic type behaviour [15], where both isolated and exchange coupled RE magnetic ions are present in the glass matrix. As suggested by the small negative θ_p values, the exchange interactions between the RE^{3+} ions are weak and predominantly antiferromagnetic.

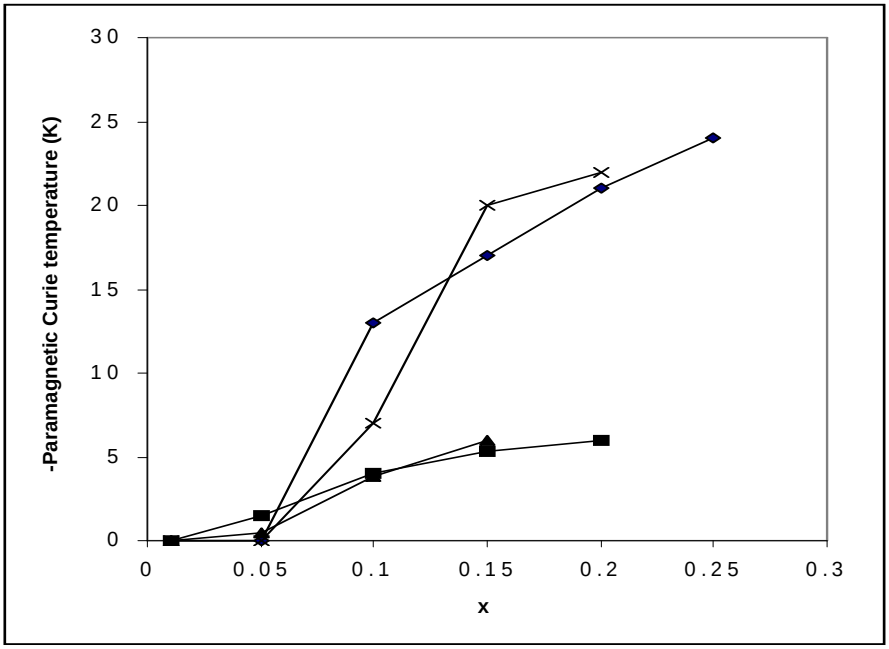

Fig.2: Composition dependence of the paramagnetic Curie constant, θ_p, of the xRNM glasses with y=0, R=Nd (◊), Gd(■), Dy(▲) and Ho (**x**).

The magnetic data obtained for the xRNM glasses are in agreement with the data previously reported for other oxide glasses containing the same RE ions [5-14] and were summerized in Tabel 1.

Table 1:

Magnetic data of xRNM glasses.

R (RE ion)	**x**	**Electronic configuration**	**Magnetic behaviour**	**Paramagnetic Curie temperature Θ_p**
Nd^{3+}	0.01-0.25	$4f^3$	Curie-Weiss x_{cr}=0.10	$0< /\Theta_p/ \leq 26$ K
Gd^{3+}	0.01-0.20	$4f^7$	Curie-Weiss x_{cr}=0.05	$0< /\Theta_p/ \leq 6$ K
Dy^{3+}	0.01-0.15	$4f^9$	Curie-Weiss x_{cr}=0.03	$0< /\Theta_p/ \leq 6$ K
Ho^{3+}	0.01-0.20	$4f^{10}$	Curie-Weiss x_{cr}=0.10	$0< /\Theta_p/ \leq 22$ K

Fig.3 shows the compositional variation of the density for the xRNM glasses. A simple inspection of the data presented in this figure suggests that all the studied RE ions exerted a network modifier role in the host glass matrices.

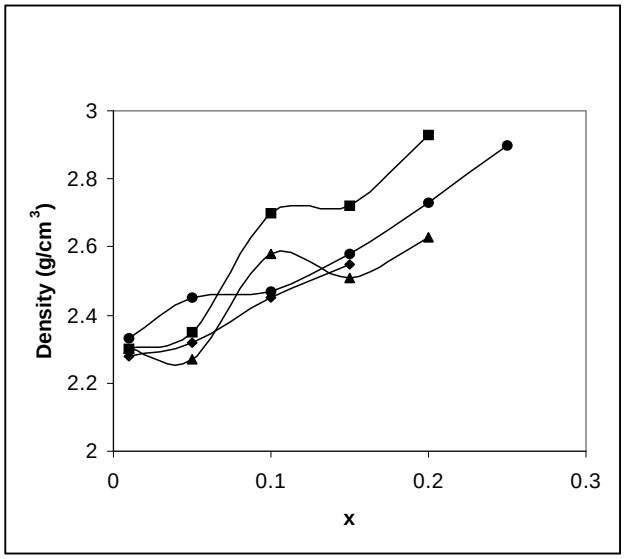

Fig.3: Composition dependence of the density of xRNM glasses with y=0, R=Nd(●), Gd(▲), Dy(◆) and Ho(■).

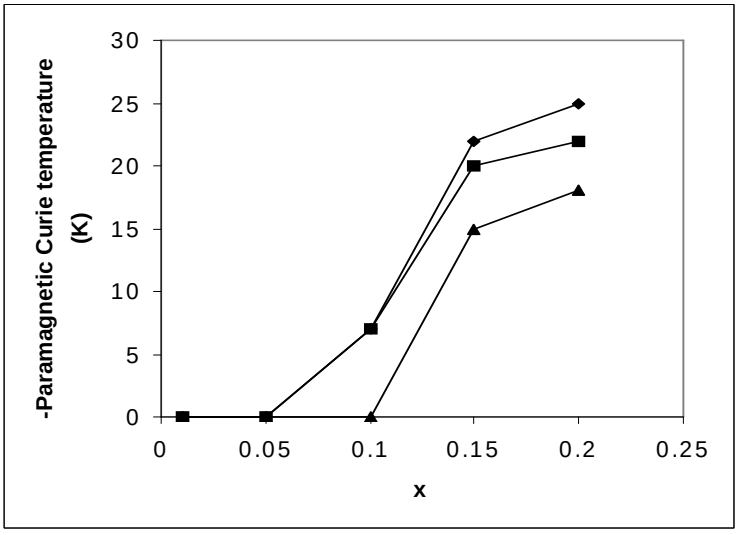

Fig.4: Influence of the additives on the composition dependence of the paramagnetic Curie constant, θ_p, for the xRNM glasses with R=Ho, y=0(◆), y=0.05 and MO=PbO(■), and y=0.05 and MO=Al_2O_3(▲).

Fig.4 presents the compositional variation of the paramagnetic Curie temperature xRNM glasses with R=Ho and M=0, Pb and Al. The data from this figure suggests a weak anticlustering effect of the aluminium oxide in the case of the holmium ions. For all the other samples the influence of the additives was neglectible.

Conclusions

Magnetic data indicate that the magnetic behaviour of xRNM glasses is of a Curie-Weiss type. For samples with small amounts of RE ions ($x \leq x_{cr}$) they appear as isolated species, while for higher amounts of RE ions ($x > x_{cr}$) a mictomagnetic behaviour, due to the presence of both isolated and coupled species, was observed. Al_2O_3 shows an anticlustering effect in the case of glasses containing holmium ions.

REFERENCES

1. CLARE A., in *Rare Elements in Glasses*, Key Engineering Materials, edited by J.E.SHELBY, Vol.**94-95** (Trans. Tech. Publications) 1994, pp.161-181.
2. PARADIS P.F., BABIN F., GAGNE J.M. and LEVESQUE S., *J.Opt.Soc.America*, **B14** (1997) 1009.
3. DAWAR A.L., MEHTA V. MANSINGH A. and RUP R., *Optical Mater.* **22** (1997) 33.
4. MOORJANI K. and COEY J.M.D, *Magnetic Glasses*, Elsevier Publishers, Amsterdam, 1984.
5. ARDELEAN I., ILONCA GH. and SEVIANU V., *J.Less-Comm.Met.***111** (1985) 113.
6. CULEA E. and BRATU I., *Acta Materialia* **49** (2001) 123-125.
7. NICKLIN R.C., JOHNSTONE J.K., BARNES R.G. and WILDER D.R., *J.Chem.Phys.*, 59 (1973) 1652.
8. ARDELEAN I., BURZO E.,MITULESCU-UNGUR D. and SIMON S.,*J.Non-Cryst.Solids* **146** (1992) 256.
9. VALENTE M.A. and MENDIRATTA S.K., *Phys.Chem.Glasses*, **33**, 4 (1992) 149.
10. ILIESCU T., SIMON S., MANIU D. and ARDELEAN I., *J.Mol.Structure* **294** (1993) 201.
11. CULEA E.,POPA. and COSMA I.,*J.Magn.Magn.Mat.* **157/158** (1996)163-164.
12. CULEA E. and BRATU I., *J.Non-Cryst.Solids* **262** (2000) 287-290.
13. BURZO E., ARDELEAN I.and MITULESCU D, *J.Mater.Sci.Let.* **11** (1992) 1496-1497.
14. CULEA E., RISTOIU T. and BRATU I., *Mat.Sci.& Engn.*, **B57** (1999) 259.
15. BECK P.A., *Metall.Trans*, **2** (1971) 2015.
16. EVERSTEIN F.C., STEVELS J.M. and WATERMAN H.I.,

STUDIA UNIVERSITATIS BABEŞ-BOLYAI, PHYSICA, SPECIAL ISSUE, 2001

SCALING IN THE TEMPERATURE FACTOR OF PROTEINS

VASILE V. MORARIU*

[*]National Institute for R&D of Isotopic and Molecular Technologies
POBox 700, 3400 Cluj-Napoca, Romania, e-mail: vvm@L40.itim-cj.ro

1.INTRODUCTION

Many spatial and temporal processes and phenomena in Nature have fractal characteristics. They have been noticed from molecular to Universe levels and represents a face of the complexity.

A closely investigated subject was the fractal aspects of protein structure (1). Proteins are three dimensional structures of which is dictated by their aminoacid sequence. Because of the compact structure of most proteins amino acid residues that are at distant points in the sequence can be in close proximity in the folded state. They may interact by various type of physical forces which cause long-range interactions and finally the 3D structure of the molecule. Proteins have an intrinsic self-similarity with regard to the compactness and packing of their structures and this results in a simple form of fractal behavior.

The fractal characteristics of the proteins have been revealed in terms of *mass, length* and *surface*. That is all proteins form a certain pattern in respect to their *mass, length* and *surface* versus some unit of structure. This pattern is a fractal or, in other words represents a long range correlation. For example the *mass* fractality is expressed in terms of the radius of giration R_g as $M \sim R^D$ where D is fractal dimension. As the mass will be proportional to the number of the units, N, in the chain, $N \sim M \sim R^D$. This can be represented as the simple power law $R_g \sim N^\nu$ where ν is a fractional exponent. Its value calculated for 90 proteins was found to be 0.35 ± 0.05 or 1/3 similar to clasically colapsed polymer (1). One may further look at the *length scaling* of the protein backbone measured as by the stepwise connection of straight lines between the α carbon atoms. the relationship is $L \sim m^\nu$ where L is the total length of the protein backbone and *m* is the length for different intervals of m residues. This scaling revaled that classical polymers are quasi ideal with the exponent being 1/2 while proteins have a value of 1/3 therefore proteins behave differently from classical collapsed polymers. Another fractal property refers to the protein *surfaces*. For example $A \sim M^\nu$ where A is the surface area and M is the molecular weight and $\nu = 0.72$ for 14 different proteins (1). Scaling laws were also established for membrane proteins (1).

We can notice that the fractal aspects of proteins reflect either the internal structure of proteins but also the interprotein relationship.

Scaling in the protein dynamics is however a subject which has very little been touched (1). Our own work revealed fractal dynamics from experiments of totally unrelated fields such as cell biology and cognitive psychology (2-3).

The aim of the present work is to look at the inside correlation of the fluctuations in a protein. The question is whether the amplitude of the fluctutions, in other words, the mobility inside the protein chain has a random or some kind of order or correlation. We may *a priori* suspect that due to the fact that the structure of the proteins are correlated in a fractal manner, the fluctuations or mobility might show a similar fractal character. What kind of information we may further expect from such an analysis ? The basic idea is that fractal structures are generally regarded as optimum designed structures and according to the fractal characteristics we may check up for some models of the protein organization as functionally organized structures (2).

It has been previously suggested that the temperature factor T_f of some proteins has a long-range character as found from the linear charactersitic of the double log plot of the spectrum (4-7). The mobility at atomic level can be characterized in terms of the temperature factor T_f which is: $T_f = 8\pi^2 < u^2 >$, where $< u^2 >$ is the mean square of the amplitude of vibrations. T_f is determined by X ray diffraction. The mobility of protein structure is presently regarded as a key feature for undertaking the function.

We have used in our analysis series of T_f for calmodulin, an ubiquitous calcium binding protein and searched for the correlation properties in the series.

2.MATERIALS AND METHODS OF ANALYSIS

The temperature factor T_f of calmodulin for various species was extracted from the Protein Data Bank. We found available data for frog calmodulin as revealed by NMR in solution and for all the rest of the species from X ray diffraction of the crystal form. The difference beteen the two sets of data is that NMR offer information for the hidrogen atom while crystal data not include this atom. Another problem is to choose the data in the series as the data for the atoms in the side chain of aminoacid residues are somewhat arbitrary placed in the series. In order to avoid this problem we choose for our investigation only the protein backbone atoms or the main chain where the natural order is kept in the series. Therefore the following chain is considered all along the primary structure:

$$N — C_\alpha — C — N — C_\alpha — C — N...$$

The series of data were subjected to Fast Fourier Form (FFT) and to Detrended Fluctuation Analysis (DFA). FFT offers the simplest and the traditional way to check for presence of scaling in the data by fitting with a line the double log plot of the spectrum. If the fitting line well approximated the spectrum, the slope of the fitting line represents the scaling exponent denominated as β. However if nonstationary behavior is present in the series the spectral analysis of the fluctuations introduce suplimentary correlations which alter the β exponent. DFA on the other hand removes nonstationarity and results in a "pure" exponent α (8). Its value is 0.5 for random series, 1 for the so called 1/f noise (f is for frequency) and 2 for brownian noise (i.e. integrated random series or random walk). According to this method the fluctuations are first integrated:

$$y(k) = \sum_{i=1}^{k} (x_i - x_{mean})$$

where x_i is the the *i*th number and x_{mean} is the mean value of the numbers in the series. Further a function F(n) is calculated for increasing box size n where local nonstationarities are removed if exist.

$$F(n) = \sqrt{1/N \sum_{k=1}^{N} [y(k) - y_n(k)]^2}$$

A plot of F(n) vs. n gives a line whose slope represents the scaling exponent α.

3.RESULTS

An example of the temperature factor series for the main chain of the bovine calmodulin is shown in fig.1. It can be seen that there are fluctuations along the chain which jump in several places, i.e. nonstationarity is present in the series. The amplitude spectral appearence of the series following FFT is presented in fig.2. The spectrum is of the power law type although some slight periodicities might be superposed on the power law background. This is clearly illustrated in Figure 3 as a

Fig.1 Temperature factor series of bovine calmodulin for the main chain

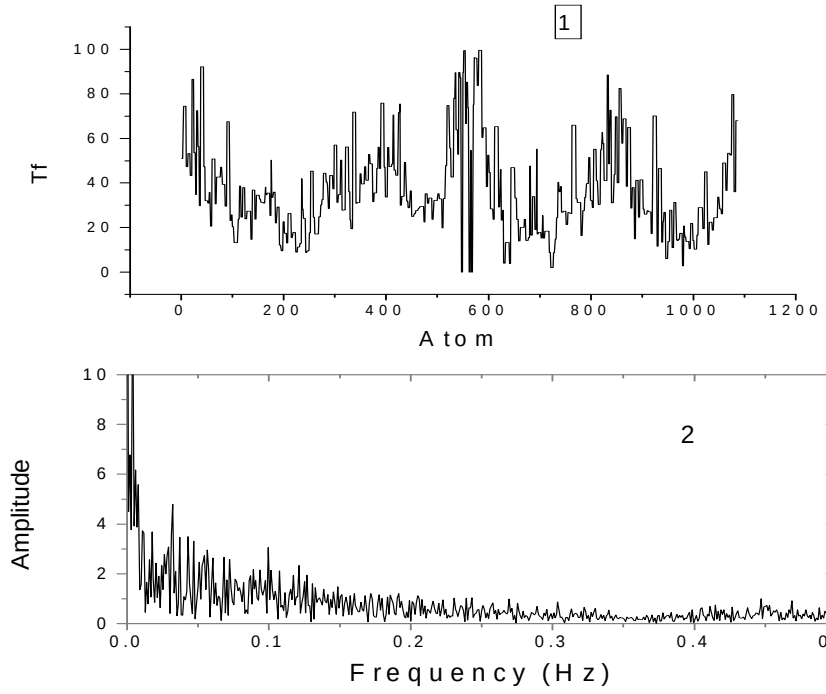

Fig.2 The amplitude spectrum of the temperature factor series for bovine calmodulin

double logarithmic plot of the power spectrum. The spectrum can be fitted by a line which has a slope $\beta = -1.39$. Therefore the series presents a fractal characteristic or scaling over a three order of magnitudes. Further the DFA plot is shown in fig.3 for the same case. The plot can be fitted by a straight line characterized by a slope $\alpha=1.39$ which means that the series fall into the category of fractal behavior or long range correlation.

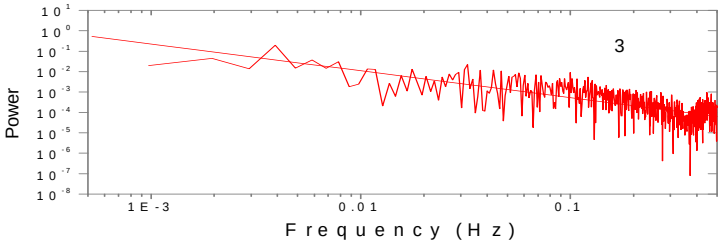

Fig.3 The power spectrum of the temperature factor series for bovine calmodulin on a double log plot. The linear fit has a slope $\beta = -1.31$.

The relationship between α and β scaling exponents is $\beta = 2\alpha - 1$. Therefore we may calculate a $\beta_{calculated}$ value from the value of α. In the case illustrated in fig.4, $\alpha = 1.39$, therefore $\beta_{calculated} = 1.78$. At the same time the value of β resulting from the spectral analysis is 1.31. As $\beta_{calculated} \neq \beta$, it clearly shows that there are nonstatioarities in the original series which are counted by the FFT procedure. Such a situation is common for practical all protein series and it would possibly seem of some interest when comparing various proteins in terms of nonstationarities. Their significance has not until now been considered and it will be discussed elsewhere.

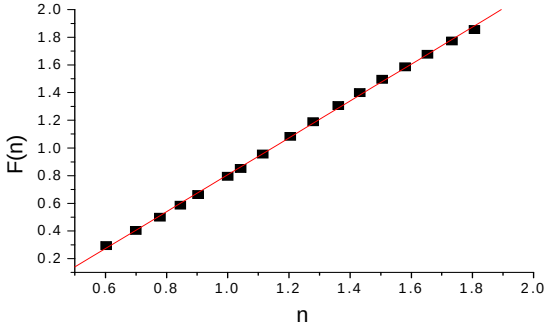

Fig.4 DFA plot of the temperature factor series of bovine calmodulin. The slope of the fitting line is the scaling exponent $\alpha = 1.39$

The results of the DFA analysis for the calmodulin protein belonging to various species and in various binding forms are illustrated in table 1. Only the frog calmodulin is in solution, all the other data correspond to crystal form. Some forms have 4 calcium ions bound to the protein which involves preliminary activation of the

protein prior to interaction to the substrate. One protein is a mutant form and other is in complexed form with trifluorperazine (TFA). The mutant form and the calmodulin complexed with TFA seems to present extrem value compared to the other data although the value for rat appears unusualy high. In any case the average value for all the data in table 1 is 1.31±0.05. This value is very close to 4/3 = 1.33. In order to Table 1. The α scaling exponents for calmodulin of different species and in various binding combinations further check if this figure is close to 4/3, more DFA analysis was performed on a few other proteins. The results for the α cscaling exponent are as follows: bovine cythocrome c, 1.34; human cytochrome c, 1.35; hemoglobine chain A. 1.36. If we add these few figures to the calmodulin statistics we get an average value of 1.315±0.036. It is quite clear that according to this result, the average value for proteins falls within the range of 4/3.

No	Protein code in Protein Data Bank	Species	Binding complex	Method of analysis	α scaling exponent
1	1cfc	Frog	apo form	NMR in solution	1.14
2	4cln	Drosophila	4 Ca	X ray crystal	1.35
3	1osa	Paramecium	4 Ca	X ray crystal	1.31
4	1cdl	Bovine	4 Ca and light chain kinase	X ray crystal	1.33
5	1cll	Bovine	4 Ca and kinase II	X ray crystal	1.39
6	3cln	Bovine	4 Ca and 1 eq trifluorperazine	X ray crystal	1.25
7	1cdm	Bovine	4Ca and 2 eq trifluorperazine	X ray crystal	0.97
8	1ctr	Rat	4 Ca	X ray crystal	1.53
9	1a29	Gallus (mutant)	4 Ca	X ray crystal	1.46
10	1ahr	Homo	4 Ca	X ray crystal	1.32
11	Average value				1.31±0.05

4.DISCUSSION

As this is the first time that a DFA analysis is reported on the protein temperature factor series, there is no term of comparative analysis with other data, and most important for interpretation. (Further data on the same line is published in this volume in the papers by V.V.Morariu & L.Gheorghe, and A.Coza & V.V.Morariu, see ref. 9-10). As mentioned in the introduction, proteins were found to have a fractal structure in terms of mass, surface and length. We might possibly suspect that they have some bearings to the present findings. Ratio of the surface to the mass (or volume) can be expressed in terms of the ratio L^2/L^3 which as a logarithmic plot gives a straight line with a slope of 2/3. We can further notice that our value of 4/3 is a multiple of 2/3. This represents a possible clue for the interpretation of the present findings as other types of scaling such as the quarter power scaling presents various forms of 1/4 and multiples of 1/4. The fact that the value of 4/3 is proportional to

[A/V]A where A is area and V is volume, it might suggest, the long range correlations into the series is controlled by these parameters.

What would be the fundamental significance of these findings ? We might quote from Gregory Dewey's book a sensitive question: "..A protein crystalographer might well ask: What has the fractal approach told us that we do not already know?" (1). I think that the answer can be found in some recent models for the quarter power scaling or other types of scaling (cited in ref.2). All these models point out to the fact that such scalings reflect optimization of the system. For example the fractal structure of the lungs, the channels in a leaf, or a river drainage system represent optimal structures for the transportation and therefore feeding or draining the system. As always, optimization means the best choice of conflicting parameters. Talking in terms of "optimization" also means that we talk in anthropic terms but also in biological terms as the evolution brings a system to the optimum design. A river drainage area can be regarded as an optimum design of the mother Nature. However in physical terms and for physical processes, there must be acting a sort of a minimum action physical principle. For example cracking a window glass by knocking with a stome results in a nice fractal. Why ? Because this must the most efficient way to disipate the energy. A colleague scientist made the point: "What is the use of fractals when we find everywhere fractals?" The answer might be very simple and it is surprising what simple it is: where ever we found a fractal, it tells us that we deal with an optimum design for the particular structure or phenomenon. After all we know that Nature is a great oportunist.

As far as the problem of proteins is concerned we may say that such structures are optimally designed to perform their task As temperature factors are related to mobility or the flexibility, and in turn these properties are regarded as crucial to functioning, it is no wonder the present findings.

Therefore if we want to answer Dewey's question we might say: a crystal structure tells us how the protein is organized whereas if the protein is a fractal it tells us why the protein is organized so.

Finally, the preliminary result of the present work is totally new: 1) The temperature factor series of the protein main chain is fractal, that is long range correlation prevails over a three orders of magnitude. 2) The scaling exponent is around 4/3 for the investigated proteins.

The present work as well as the work presented in ref.9-10 is intended to be continued by the following steps: a)Gathering of more data for other proteins in order to firmly establish that the α scaling exponent is around 4/3; b) The distribution of the scaling exponent willd be evaluated. We suspect that the distribution is gaussian with a median value centred at 4/3. c) The rationale for 4/3 scaling of the protein main chain should be further developed.

Acknowledgements: I thank Aurel Coza for calculations and helpful discussions.

REFERENCES

1. T.Gregory Dewey, Fractals in Molecular Physics, Oxford University Press, Oxford, 1997.

2. V.V.Morariu and A.Coza, Quarter power scaling in dynamics: experimental evidence from cell biology and cognitive psychology, Fluctuation and Noise Letters vol. 1, No.3, L111-L117

3.V.V.Morariu, A.Coza, A.M.Chis, A.Isvoran and L.C.Morariu, Scaling in cognition, Fractals, to appear in December 2001.

4. A.Isvoran, V.V.Morariu, A.Negreanu-Maior, Int.J.Chaos Theory and Apllications, vol4, Attractor control of the changes in the molecular vibrations of human lysozyme upon substrate binding. no.1, 13-22, 1999

5. A.Isvoran, D.Dolha and V.V.Morariu, Attractor control of the stability of the lysozymes, Int.J.Chaos Theory and Aplications, vol 5 no.1. 2000

6. A.Isvoran, V.V.Morariu, Comparison of the behavior of sea hare myoglobin when it forms two different complexes, Chaos, Solitons and Fractals, vol.12 1041-1045, 2001

7. A.Isvoran, V.V.Morariu, Analysis of the nonlinear behavior of ascaris trypsin inhibitor from NMR data, Chaos, Solitons and Fractals, vol.12, 1485-1488, 2001

8. C..-K.Peng, S.Havlin,,H.E.Stanley and A.L.Goldberger, Detrended Fluctuation Analysis, Chaos vol.5, 82-87, 1995

9. V.V.Morariu and Lavinia Gheorghe, Scaling in the temperature factor series of cytoskeleton proteins, in Proceedings of the Second Conference "Isotopic and Molecular Processes" PIM 2001, Sept.27-29, 2001, Studia Universitatis Babes-Bolyai, Special Issue 2001

10. A.Coza, V.V.Morariu, Scaling characteristics of the structure of human hemoglobin, Proceedings of the Second Conference "Isotopic and Molecular Processes" PIM 2001, Sept.27-29, 2001, Studia Universitatis Babes-Bolyai, Special Issue 2001

STUDIA UNIVERSITATIS BABEŞ-BOLYAI, PHYSICA, SPECIAL ISSUE, 2001

SPECTROSCOPIC INVESTIGATION OF THE ELECTRON DELOCALIZATION AND MOLECULAR CONFORMATIONAL CHANGES IN POLYPYRROLE INDUCED BY DIFFERENT DOPING IONS

R. TURCU*, R. GRECU, M. BRIE**, I. PETER*, A. BOT*, W. GRAUPNER*****

** National Institute of R & D for Isotopic and Molecular Technologies, P.O. Box 700, 3400 Cluj-Napoca, Romania*
*** Institute of Chemistry "Raluca Ripan", 3400 Cluj-Napoca, Romania*
**** Institut fur Festkorperphysik, Technische University Graz, A-8010 Graz, Austria*

ABSTRACT. We report a comparative study of the optical properties of polypyrrole (PPY) synthesized by two methods: electrochemical and chemical oxidation of the monomer (pyrrole) in the presence of different doping ions (p-toluensulfonate, dodecylsulfate, dodecylbenzenesulfonate, perchlorate, tetrafluoroborate). By using FTIR and UV-Vis spectroscopy we investigated the changes of the molecular and electronic structure of polypyrrole induced by the preparation conditions. Our main goal was to find out the relevant synthesis parameters, which have a strong influence on the electron delocalization length and the molecular architecture of polypyrrole.

1. Introduction

Conducting polymers are new materials that combine the mechanical and chemical properties of isolator polymers with the electrical and optical properties of inorganic semiconductors and metals.

Polypyrrole is one of the most used conducting polymers for applications due to the good stability of his properties and because it can be easy synthesised as a homopolymer and also as a composite. The success of PPY applications depends on the improvement of the properties and the processability of this material. Therefore one of the main research goal is the correlation between the synthesis parameters and the molecular architecture of PPY in order to obtain the required properties for a specific application [1].

In this paper we report a comparative study of the optical properties of polypyrrole (PPY) synthesized by two methods: electrochemical and chemical oxidation of the monomer (pyrrole) in the presence of different doping ions (p-toluensulfonate, dodecylbenzenesulfonate, perchlorate, tetrafluoroborate). By using FTIR, UV-Vis spectroscopy we investigated the changes of the molecular and electronic structure of polypyrrole induced by the preparation conditions. Our main goal was to find out the relevant synthesis parameters, which have a strong influence on the electron delocalization length and the molecular architecture of polypyrrole.

2. Experimental

2.1 Samples preparation

a) Electrochemical synthesis of polypyrrole

The electrochemical synthesis of polypyrrole was carried out with different electrolyte types: p-toluenesulfonic acid (HTSO), sodium toluenesulfonate (NaTSO), lithium perchlorate ($LiClO_4$) and tetrabutyl-ammonium-tetrafluoroborat (Bu_4 NBF_4), sodium dodecylbenzenesulfonate (DBSNa). The electrolyte concentration, c_e was varied in the range 0.01-0.15 M. The polymerization was carried out in galvanostatic conditions at room temperature using different current densities: $0.25 \leq j \leq 1.25$ mA/cm^2. Polypyrrole films with thickness h in the range 10-25 μm were obtained.

b) Chemical synthesis of polypyrrole

The monomer pyrrole and the dopant DBSNa were mixed vigorously with distilled water. The water solution of the oxidant ammonium persulfate (APS) was added by dropping to the pyrrole-DBSNa solution. The polymerization was performed by using the oxidant/monomer (O/M) molar ratio 0.2 and dopant/monomer (D/M) molar ratio 0.5 or 0.8. The mixture was stirred out at 15°C for 24 hours and adding excess methanol to the reaction flask terminated the polymerisation of pyrrole. PPY was formed as a black powder, which was filtered and washed successively with distilled water, methanol and acetone, followed by filtering and drying in a vacuum oven at 30°C for 14 hours. PPY chemically synthesised using large-size protonic acid dopants such as DBS is soluble in organic solvents like m-cresol and chloroform.

The polypyrrole fine black powder (100 mg) was dissolved in 2 ml of chloroform or m-cresol. As was previously reported by J.Y. Lee et al., PPY(DBS) has a lower solubility in chloroform than in m-cresol [2]. To improve the solubility of PPY powder DBSNa (100 mg) was added to the solution. The solutions were stirred for 18 hours and then filtered through a Millipore filter paper. Thin films of polypyrrole were cast from these solutions on glass or ITO (indium tin oxide) covered polycarbonate supports for UV-Vis transmission measurements.

2.2 Optical measurements

Specular reflectance measurements in the range 200 - 6000 cm^{-1} were performed on free-standing PPY films by FTIR spectroscopy on a BOMEM MB-102 spectrophotometer. The absolute value of sample reflectivity was determined relative to the reflectivity of an aluminium mirror. The optical constants for PPY films were calculated from the reflectance spectra with Kramers-Kronig (K-K) technique [3].

Infrared transmission spectra in the range 400-4000 cm^{-1} were recorded by a spectrophotometer JASCO FTIR-610, on pressed pellet prepared from the chemically prepared PPY(DBS) powder embedded in KBr or on thin film cast on KBr crystal from the filtered solution of PPY in chloroform.

UV-Vis transmission spectra of the as-prepared thin polymer films on glass support were recorded by a Lambda 9 spectrophotometer.

3. Results and discussion

3.1 Reflectance spectra of the electrochemically prepared PPY

The reflection spectra of polypyrrole samples, shown in Fig.1 are sensitive to the nature of the electrolyte and to the d.c. conductivity values. The higher reflectivity was obtained for TSO doped PPY samples. Significantly lower reflectivity was obtained for sample 4, with the lower σ_{dc}. These results demonstrate that the surface morphology of the sample has a significant contribution to the reflectance. We consider that the roughness of the film surface depends on the nature and concentration of the electrolyte. The surface roughness is lower for TSO^- doped film as compared with ClO_4^- doped one and decreases with the decrease of the electrolyte concentration.

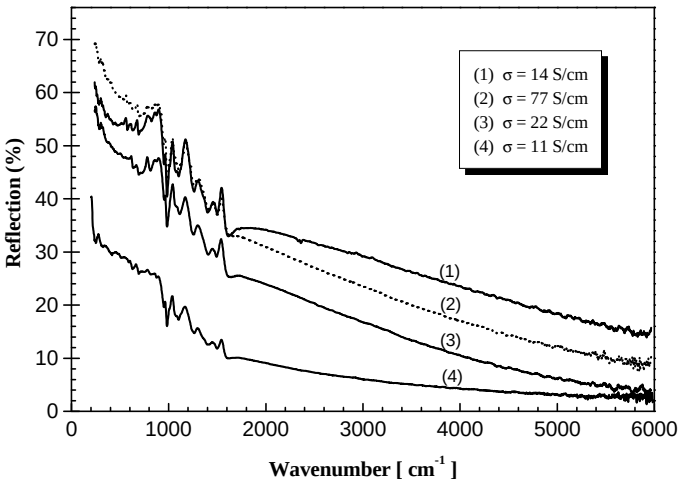

Fig.1 Reflection spectra of PPY films electrochemically prepared with different electrolytes: 1- NaTSO ; 2-HTSO ; 3- $LiClO_4$; 4-NaDBS

The increase of the reflectance at lower frequencies indicates a metal-like behavior. But to find out if the electrons are indeed delocalized in our samples we have to determine the behavior of the dielectric function in the investigated spectral range.

The real and imaginary parts of the refractive index, $n(\omega)$ and $k(\omega)$ were calculated from the reflection spectra with the Kramers-Kronig technique [3], where first the phase angle θ is determined using the following relationship:

$$\theta(\omega_0) = -\frac{1}{2\pi}\int_0^{\infty} \log\left(\frac{\omega+\omega_0}{\omega-\omega_0}\right)\frac{d\log\sqrt{R(\omega)}}{d\omega}\,d\omega \qquad (1)$$

Then we can determine n and k :

$$n = \frac{1-R}{1+R-2\sqrt{R}\cos\theta} \qquad k = \frac{2\sqrt{R}\sin\theta}{1+R-2\sqrt{R}\cos\theta} \tag{2}$$

For this purpose we have to extrapolate the experimental data to zero and infinite energies (wavenumbers). For the low energies a Hagens-Rubens function was used [3, 4], as the reflectance increases to low energies for all films investigated. To high energies the data were extrapolated by a decay function (ω^{-s}).

The spectral dependencies of n and k for TSO^- doped polypyrrole sample 2 are shown in Fig.2. Similar behaviour for n and k was obtained for the other polypyrrole samples investigated [4]. Several peaks located at 850, 1018, 1150, 1300, 1450 and 1530 cm^{-1}, which correspond to the characteristic absorption peaks of the pyrrole ring, can be observed in the spectral dependence of k (Fig.2). The values of k(ω) increase with the increasing of the d.c. conductivity values of the samples. The band located at 1530 cm^{-1} is attributed to the collective vibration of C=C/C-C inter and intra-rings. The characteristic frequency of this band is related to the conjugation length on the chains: the lower is the frequency, the higher is the conjugation length. We can estimate a conjugation length of 9-10 rings for our electrochemically prepared PPY [1,4].

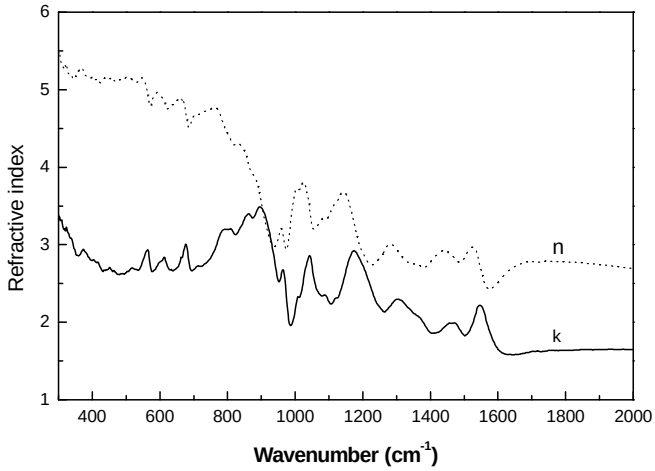

Fig.2 Real part (n) and imaginary part (k) of the refractive index for PPY (sample 2 from Fig.1)

The complex dielectric function, ε is defined by:

$$\varepsilon = \varepsilon_1 + i\varepsilon_2 = \varepsilon_1 + i\frac{\sigma}{\omega\varepsilon_0} \tag{3}$$

The real and imaginary part of the dielectric function were calculated from n and k values, using the relations:

$$\varepsilon_1 = n^2 - k^2 \quad ; \quad \varepsilon_2 = 2nk = \frac{\sigma}{\omega\varepsilon_0} \tag{4}$$

From Fig.3 one can observe that the real part of the dielectric function ε_1 is positive in all the spectral range. This behavior indicates that most charge carriers are localized in our PPY samples.

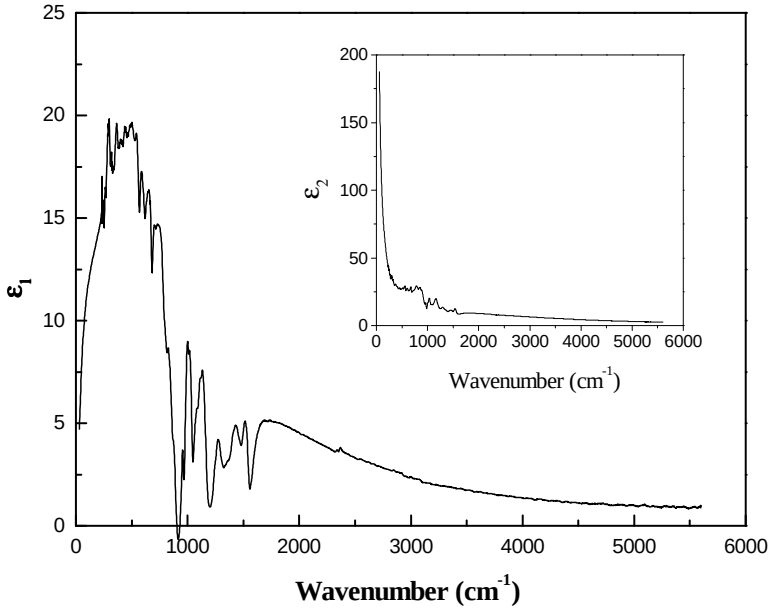

Fig.3 Real and imaginary parts of the complex dielectric function for PPY (sample 2 from Fig.1)

3.2 Optical properties of the chemically prepared PPY

UV-vis absorption spectra

The absorption spectra of PPY(DBS) thin films cast from chloroform and m-cresol filtered solutions (100 mg PPY_1 (DBS) powder in 2 ml of solvent) are presented in the Fig 4. It is well know that two characteristic bipolaronic absorption bands located at ~ 1 eV and ~ 2.6 eV appears in the optical spectra of doped PPY [6]. A shift of these bipolaronic bands could appear as a function of the doping level.

From the Fig. 4 one can see that the bipolaronic absorption band located at 2.6eV for PPY(DBS) obtained from chloroform solution is shifted to higher energies for the sample obtained from m-cresol solution. The shift of the absorption band could be attributed to the polymer-solvent interaction. The nature of the solvent molecule influences the polymer chains conformation and the length of the conjugated segments leading to a difference in the energy gaps. We consider that PPY(DBS) cast from m-cresol solution contain shorter conjugated segments as compared with PPY(DBS) cast from chloroform solution [7].

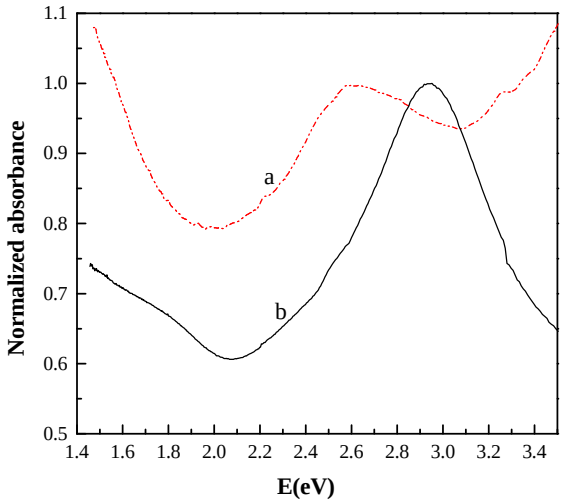

Fig.4 Normalized absorbance of PPY(DBS) films cast from: a- chloroform solution; b- m-cresol solution

IR spectra

In Fig. 5 we can compare the infrared spectra for the as-synthesised PPY(DBS), spectrum A and for the soluble fraction, spectrum B obtained by the filtration of PPY(DBS) chloroform solution. Both spectra show an increase of the absorbance in the range 1700-4000 cm^{-1} , which is attributed to the tail of the electronic transition located in the near infrared. The absorbance increases more slowly in this region for the soluble fraction PPY(DBS) as compared to the as-synthesised sample. This behaviour could be due to a lower oxidation degree or to a decrease of the π electrons delocalization along the chains of the soluble fraction. The lower contribution of the electronic transitions involving charge carriers make a clear evidence possible in the spectrum B of the absorption bands located near 2900 cm^{-1} attributed to the vibrations of C-H groups in the dopant DBS. Moreover, the stretching vibrations of the N-H group in PPY can be observed as a shoulder near 3300 cm^{-1} in the spectrum B.

The significant differences between the spectra A and B appear for the bands located around 900 cm^{-1}, 1200 cm^{-1} and 1550 cm^{-1}, see the inset in the Fig. 5. These absorption bands characteristic for the oxidized PPY have been associated by Zerbi with the effective conjugation coordination and show sensitivity to the oxidation level and to the conjugation length of the chain [9].

The band located at 1550 cm^{-1} in the spectrum A is attributed to C=C/C-C stretching vibrations of the PPY chain [9]. The shift of this band to a higher frequency, 1569 cm^{-1} in the spectrum B indicate that soluble PPY(DBS) contain mainly shorter conjugated chains as compared with the as-prepared PPY .

The absorption band located at 1198 cm^{-1} in the spectrum A are ascribed to ring breathing vibrations and its shift to higher frequency in the spectrum B support the idea of the lower oxidation level for the soluble fraction as compared to the as-synthesised PPY.

From the inset in the Fig. 5 one can observe that the intense band located at 914 cm^{-1} in the spectrum A has a significant shift to higher frequency (by 26 cm^{-1}) in the spectrum B. This band could be attributed to a PPY ring vibration mode in the oxidation state. This assignment is based on the fact that ring vibrations are much more sensitive to the oxidation level and to the conjugation length of the chains as compared to C-H vibrations [9].

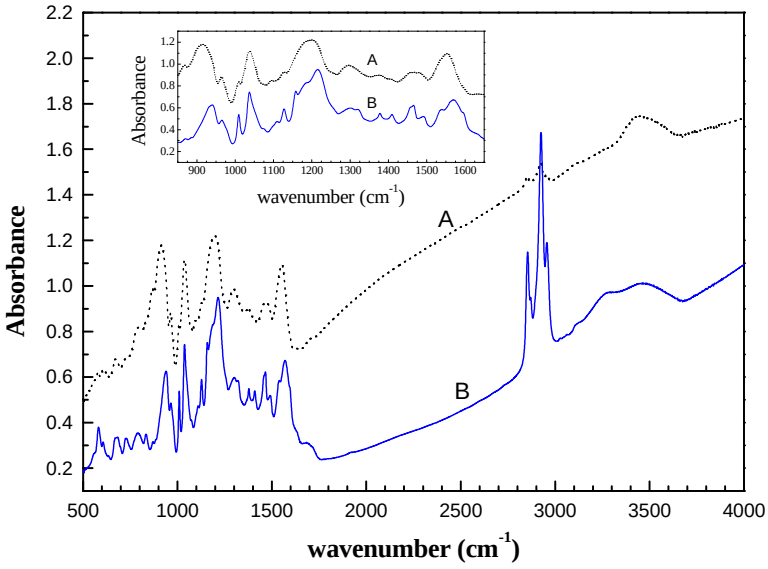

Fig.5 IR spectra of PPY(DBS): A-as-synthesised sample; B-soluble fraction in chloroform

The comparison of the IR spectra for the chemically prepared soluble PPY(DBS) and the electrochemically prepared PPY doped with different ions (TSO, ClO_4, BF_4, DBS) shows that the former contains mainly shorter conjugation lengths and has a lower degree of oxidation.

REFERENCES

1. J. Rodriquez, H. J. Grande, T.F. Otero, "Polypyrroles: from Basic Research to Technological Applications", in: *Handbook of Organic Conductive Molecules and Polymers*, ed. H.S. Nalwa, John Wiley & Sons, 1997, Vol.2, p.415
2. J.Y. Lee, D.Y. Kim, C.Y. Kim, *Synth. Met.* 74, (**1995**), 103
3. G. Leising, in "*Organic Materials for Photonics"*, ed.G.Zerbi, Elsevier, Amsterdam 1993.p.173
4. R.Turcu, M.Brie, G.Leising, V.Tosa, A.Mihut, A.Niko, A.Bot, *Appl. Phys.* A67, (**1998**), 283
5. R.S. Kohlman, T.Ishiguro, H.Kaneko, A.J. Epstein, *Synth. Met.* 69, (**1995**), 325
6. O. Chauvet, S. Paschen, L. Forro, L. Zuppiroli, *Synth. Met.* (**1994**) *63*, 115
7. R.Turcu, W.Graupner, C.Filip, A.Bot, M.Brie, R.Grecu, *Adv.Mater. Opt. Electron.***(1999)**, 9, 157
8. G.Zerbi, M. Gussoni, C. Castiglioni, *Conjugated Polymers*; Ed. J.L.Bredas, R.Silbey, Kluwer Academic Publishers, 1991; 435-507

SECONDARY AMINES SPECIFIC LABELED WITH DEUTERIUM

V. ALMASAN, MIHAELA LAZAR, EVA LAURA GANEA

National Institute for Research and Development of Isotopic and Molecular Technologies, P.O. Box 700, R-3400 Cluj – Napoca 5, Romania

1. Introduction

The analyses of structures and qualities of chemical substances is a modern problematic with implications in many research areas. The analysis accuracy is influenced by the utilization of some standard molecules. The specific deuterium labeled molecules have a great advantage because they have the same chemical potential like the natural molecules, but in addition, they differ only by their molecular masses. These kinds of molecules can be used like internal standards, into the MS and NMR analyses. Using these internal standards, the MS research becomes more efficient. Thus, the research laboratories, which undertake chemical synthesis of new drugs, ask for these isotopically labeled molecules for the establishment of analytical methods and the certification of drugs molecular structure and properties.

2. Theoretical aspects

Deuterium labeling, generally, can be done either by H/D isotopic exchange or by chemical synthesis. For H/D isotopic exchange heavy water is used and D_2 is used and for the synthesis some smaller molecules with deuterium content. To synthesize big molecules containing deuterium in well-known positions, it is necessary to establish those reaction conditions, which doesn't allow the reverse D/H isotopic exchange.

The aim of our work is to offer a sure synthesis way to obtain an asymmetrical amine, which contains deuterated ethyl - D5 radical. This amine has the possibility to be further transformed in other bigger molecules, without any risk of losing the deuterium atoms from the molecule.

The mebamine (4-methoxy (2-aminoethyl) propylbenzene) is a reagent from the class of complexe secondary amines, used as intermediary reagent in the synthesis process of a possible drug, called 'mebeverine'. To monitor the synthesis process of this possible drug, internal standards are necessary in MS and NMR analyses, to establish the certification methods of the final product. If the method for structural analyses is the mass spectrometry, the introduction of deuterium atoms in molecule is necessary because these give a difference by a few mass units to the resulting ions into the spectrometer ion source. This reveals the importance of the partially specific deuterium labeling of some molecules.

In the next scheme we will present a method for the synthesis of this possible drug, and also, the role and the stage in which the partially deuterated compound (which is the subject of this work) is involved.

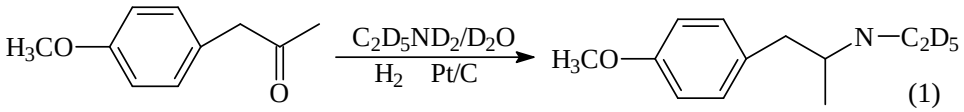

p-methoxyphenilacetone — Mebamine (1)

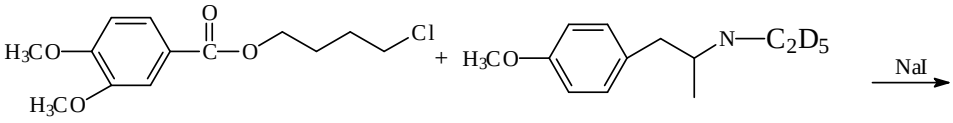

Veratric acid, 4-chlorobutylester Mebamine-D5 (2)

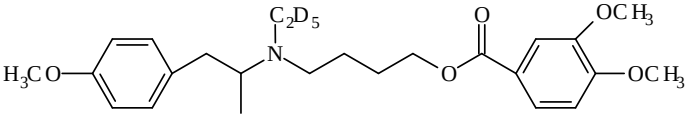

Mebeverine base

In accordance with these reactions, the process starts from a commercial reagent (p-methoxy phenilacetone) to obtain partially deuterated mebamine, and in the last stage it is coupled with veratric acid,4-chlorobutylester and finally, a partially deuterated drug, named "mebeverine – D5" is obtained.

The chemical procedure for the obtaining of mebamine-D5 is led conformingly with the following reactions:

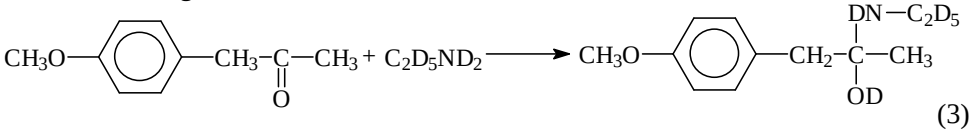

(3)

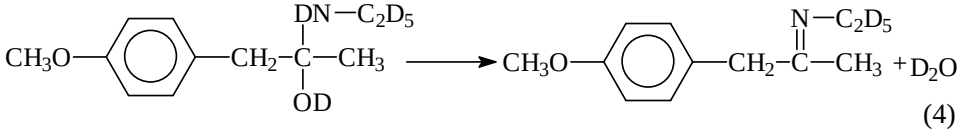

(4)

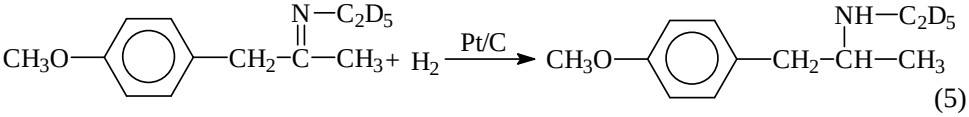

(5)

These reactions take place simultaneously, into an autoclave, to 10-atmosphere pressure, at 90˚C, in the presence of a Pt/C catalyst and under hydrogen atmosphere. Thus a global equation can be written:

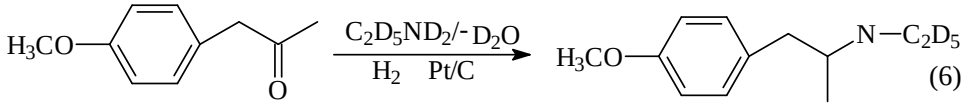

p-methoxy phenilacetone Mebamine (6)

3. Experimental, results and discussions

An appropriate method to obtain molecules, like mebamine, is the chemical synthesis. Generally, it can be considered that a big molecule is build from another molecular rests, which are coming from the reactants.

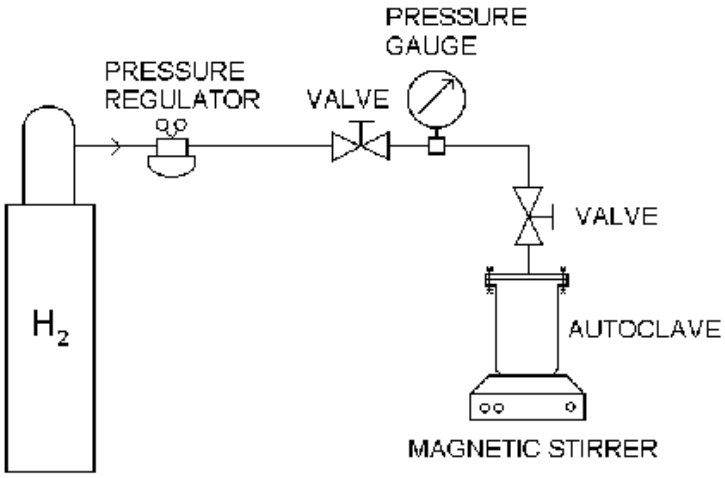

Figure 1. Mebamine – D5 experimental setup

In the particular case of specific deuterium labeled molecule, it is very important to choose the deuterated reagent molecule, which is the supply of the deuterated molecule rest that must have a good chemical stability in the next stages of the chemical synthesis. This synthesis takes place into the experimental setup, presented in figure 1.

Into an autoclave from a nonmagnetic steel was brought slurry of 155 ml (1.01 mol) p-methoxy phenilacetone, 125 ml of 70% m/m solution of ethylamine in water (this is about 102 g, 1.59 mol) and 0.5g of 10% m/m platinum on carbon paste (this contain about 40% m/m dry catalyst and about 60% m/m water).

The slurry was stirred and the air was removed from the autoclave. The vacuum was replaced by nitrogen. This procedure was repeated three times. The autoclave was brought under vacuum and the vacuum was removed three times by hydrogen. The fourth time the vacuum was replaced by hydrogen until the hydrogen pressure rose to 10 atm.

The stirring was started and the reaction mixture was heated at 90˚C and stirred with a linear speed of at least 1400 cycles/minute. The hydrogenation was started. A drastic stirring is necessary because the mixture is heterogeneous and there are three phases: a solid one (the Pt/C catalyst), a liquid one (the reaction mixture) and a gaseous phase (the hydrogen). The global reaction (6) is composed from three elementary chemical reactions. The first one is the coupling of carbonyl group of p-methoxyphenylacetone with the amine group of ethylamine-D7 forming a hydroxiamine, as it can be seen in reaction (3). The second stage is a water elimination (D_2O) shown in reaction (4), and the third stage, as it can be seen from reaction (5), is the hydrogenation of the double bond C=N by a heterogeneous catalyzed reaction. The final result was partially deuterated mebamine- D5. The synthesis time was 10-12 hours and the end of the reaction was reached when the hydrogen pressure remained constant. In this moment, the heating

was stopped and the reaction mixture was put out from the autoclave. The reaction mixture was filtered and washed with 50 ml of water. 475 ml of water, 160 ml of toluene and 129 ml of 50% m/m sulfuric acid were added to the filtrate. The mixture was very well mixed and the layers were separated. The toluene layer was washed with 30 ml of water. To the combined water layers was added 125 ml of 50% m/m sodium hydroxide and 390 ml of water. The pH was higher than 12. The water layer was extracted twice with toluene, the toluene extracts were washed with water, and then the toluene was removed by distillation in vacuum. The yield of mebeverinamine was 220 ml with a purity of about 85-90% g/g.

M.S spectroscopy and NMR were used to control the isotopic and chemical quality. An example is the electron impact ionization MS spectrum of our compound (fig. 2).

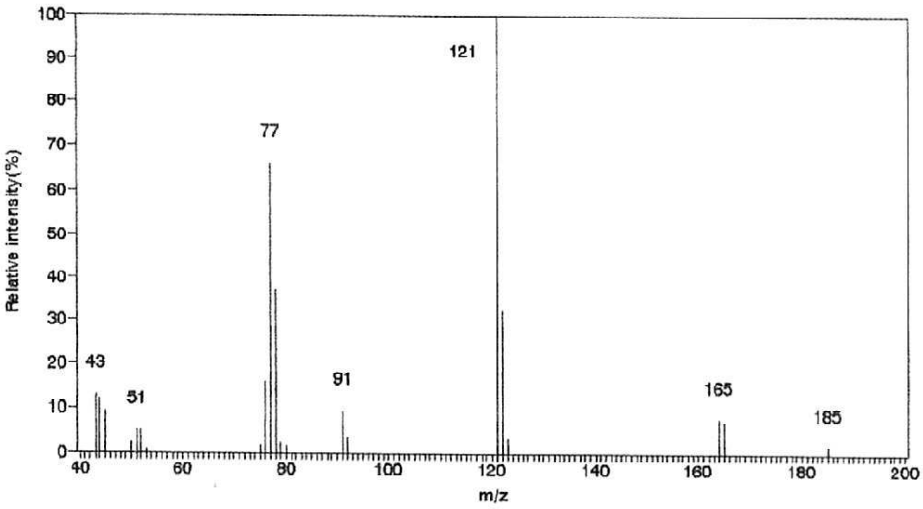

Figure 2. The electron impact ionization MS spectrum for mebamine-D5

Into the experimental setup shown in figure 1, the hydrogen pressure decay inside of autoclave was monitored. The hydrogen consumption vs. time is a measure of the global reaction evolution. This kinetic approach for the reaction (5) is presented bellow:

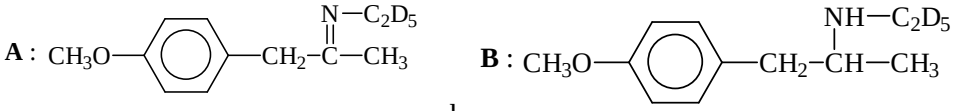

$$H_2 + Pt \underset{k_2}{\overset{k_1}{\rightleftharpoons}} 2H_{ads}$$

$$A + Pt \underset{k_4}{\overset{k_3}{\rightleftharpoons}} A_{ads}$$

$$2H_{ads} + A_{ads} \xrightarrow{k_5} B$$

The reaction rate has the expression:

$$r = \frac{k_1 k_4 k_5}{k_2 k_3} p_{H_2} \cdot \theta$$

Where: θ = platinum surface coverage degree

p_{H_2} = hydrogen partial pressure

$$k = \frac{k_1 k_4 k_5}{k_2 k_3}$$

Because at 9 atm, the platinum surface area is full covered, $\theta \approx 1$. In these circumstances, the reaction rate becomes:

$$r = k \cdot p_{H_2}$$

If we plot the experimental variation of hydrogen pressure vs. time, we obtain the kinetic curve from figure 3 and figure 4 shows the variation of log p vs. time.

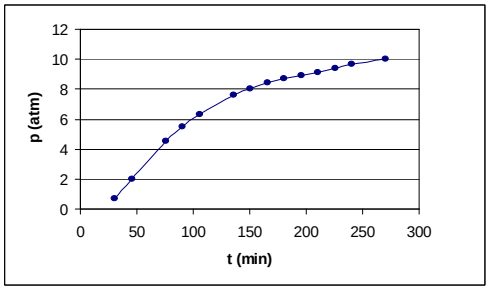

Figure 3. hydrogen pressure vs. time

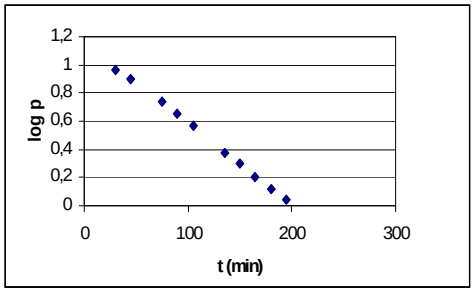

Figure 4. log p vs. time

$k = 1.5*10^{-2}$ atm/min

In this work the kinetics of the total reaction was studied and also the practical reaction conditions were established in order be able to propose a method to get specifically asymmetrically deuterated secondary amines.

STUDIA UNIVERSITATIS BABEŞ-BOLYAI, PHYSICA, SPECIAL ISSUE, 2001

STUDIES OF ADSORPTION METHODS FOR HYDROGEN ISOTOPES STORAGE ON ZEOLITIC SIEVES

FELICIA VASUT, IOANA CRISTESCU, ION CRISTESCU, SEBASTIAN BRAD

National Institute of Cryogenics and Isotopic Separations, Ramnicu Valcea, Romania
Feliciavasut@yahoo.com

ABSTRACT. Molecular sieves and active carbon were used for the hydrogen isotope adsorption. The adsorption process occurred at liquid nitrogen temperature. The commercial zeolites have the same properties as natural zeolites, but they have a regular pore structure. They also have affinity for molecules with different size and defined shapes. Experimental results obtained at liquid nitrogen (77.4K) revealed the efficiency of the active carbon and zeolitic sieves for temporary storage of hydrogen isotopes. The storage of hydrogen isotopes in hydride form is considered being very practical from the point of view of a large storage capacity. The reason for this is that the reaction between hydrogen isotopes and many hydrides forming metals is spontaneous at room temperature yielding hydrides of low dissociation pressure at the ambient temperature.

Key words: storage, hydrogen isotopes, intermetallic compounds, zeolitic sieves, adsorption, gases.

Adsorption of hydrogen isotopes on zeolitic sieves and active carbon

For the transportation without losses of hydrogen isotopes the necessity of their storage occures. It is necessary to take into account a series of special requirements in the case of the transportation of radioactive mixtures of hydrogen isotopes.

Zeolites are important materials used for the adsorption of hydrogen isotopes because they have a high adsorption capacity, are stable to radiolysis under the tritium radiation and they are more accessible than metals and intermetallic compounds.

We study the adsorption propereties of synthetic zeolites in a wide range of temperature and pressure. We used molecular sieves 4A, 5A and active carbon. The 4A and 5A zeolites have a tridimensional structure with 11.4Å diameter. When the hydration water is eliminated, the material has a porous structure. The porous volume represents 45% of the overall zeolite volume for 4A and 5A. The activation temperature of the zeolite and carbon is very important to obtain a high adsorption capacity. If the temperature used for the activation is small, the structural water will not be eliminated and the adsorption capacity will be low. The excessive temperature will destroy the porous structure.

Physical adsorption process of hydrogen isotopes was obtained at the liquid nitrogen temperature (77.4K). The entrance flux gas in the adsorption system is composed of dry deuterium and protium. This mixture is cooled in liquid nitrogen and then is passed on the adsorbent getter at the same temperature (77.4K). The flux of the gas in the adsorbent getter is 5 and 72 l/h (witch correspond 0.008 and 0.134 velocity of discharge).

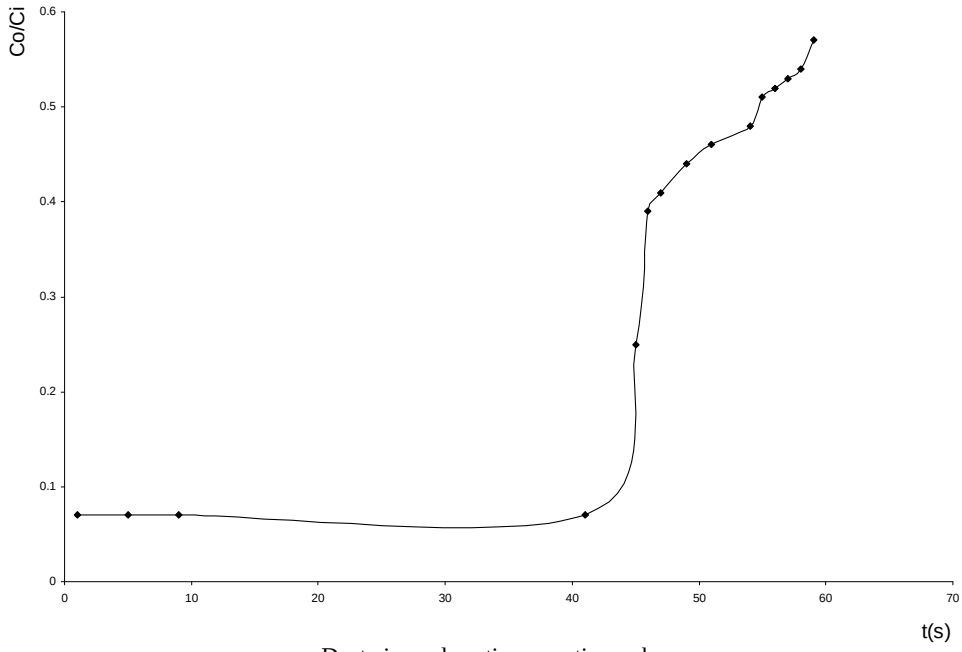

Deuterium adsorption on active carbon

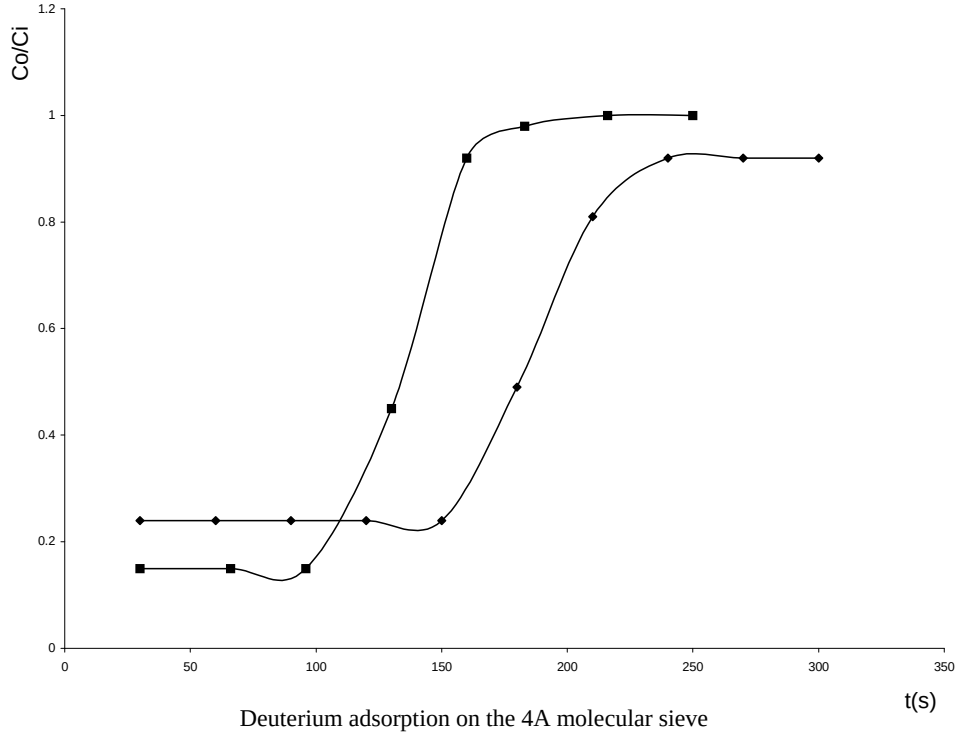

Deuterium adsorption on the 4A molecular sieve

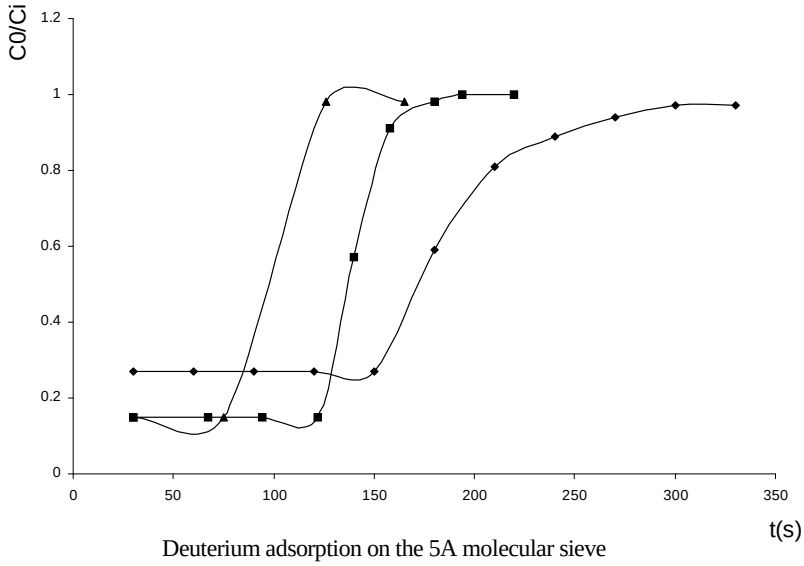

Deuterium adsorption on the 5A molecular sieve

The adsorption capacity for hydrogen isotopes was calculated with the relation:

$$A = V_{ads}/m \ \ (cm^3/g)$$

In the next table, the adsorption capacity and efficiency for different materials used in ours experiments are presented:

Adsorbent	T (K)	Q (l/h)	A (cm^3/g)
Active carbon (IPMP Buzau, Romania)	77.4	5.90	79.443
Molecular sieve 4A	77.4	8.18	1.315
	77.4	10.28	1.615
Molecular sieve 5A	77.4	8.00	1.226
	77.4	9.47	1.456
	77.4	11.25	1.340

REFERENCES

[1] I.A. Alekxeev, S.P. Karpov, V.D. Trenin - "Zeolite cryopumps for hydrogen isotopes transportation" Fusion Technology, (Oct. 1995)

[2] I.A. Alekseev – "Isotope and phase equilibrium of hydrogen on zeolite NaA", J.Appl.Chem. URSS (1985)

MASS AND HEAT TRANSFER ON B7 STRUCTURED PACKING AT SEPARATION OF HYDROGEN ISOTOPES BY DISTILLATION

CORNELIA CROITORU, FLOAREA POP, GHEORGHE TITESCU, IOAN STEFANESCU and MARIUS PECULEA*

National Institute of Research-Development for Cryogenic and Isotopic Technologies ICSI RM. VALCEA, Str. Uzinei nr. 4, Tel. 0040-050-732744, Fax 0040-050-732746, Romania
**Technical University of Civil Engineering of Bucharest, Bd. Lacul Tei, nr. 124, Sector 2, Tel. 0040-1-2421208, Fax 0040-1-2420781, Romania*

1. INTRODUCTION

The paper presents theoretical and experimental data about mass and heat transfer on B7 type structured packing, in the deuterium separation by distillation. The first part of the paper is reserved to the mass transfer study in the isotopic distillation of hydrogen, and the second part is reserved to the mass and heat transfer in the case of water isotopic distillation.

2. MASS TRANSFER STUDIES

2.1 Multi-tubular column model

The height of the transfer unit, efficiency measure of the liquid-vapour contact element, is based on the two film theory. It is assumed that at liquid-vapour interface, equilibrium is snapshot established and the resistance to the mass transfer in liquid and vapour bulk is negligible, all the resistance to the transfer being concentrated in vapour and liquid boundary-layers.

At the packed distillation columns the liquid flow is pellicular. If the void space of packing $\left(\frac{\pi \cdot D_c^2}{4} \cdot Z \cdot \varepsilon\right)$ is divided in *N* parallel tubes with d_t diameter and height equal with the packed bed height *(Z)*, one obtains a multi-tubular column. Each tube simulates the distillation in a wetted-wall column. The calculus relationship for HTU in wetted-wall column is the following [1,2,3]:

$$(\mathrm{HTU})_y = \frac{V \cdot d_{ech}}{D_c^2 \cdot \varepsilon \cdot \pi \cdot K_y'} \tag{1}$$

where the characteristic parameter for the structured packing is $d_{ech} = d_t = 4 \cdot \varepsilon / a$ d_{ech}. The over-all mass-transfer coefficient is reported to the vapour phase, because this phase opposes the greatest resistance. K_{OV} is calculated by the individual coefficients and slope of the equilibrium curve:

$$\frac{1}{K_y'} = \frac{1}{k_V \cdot P} + \frac{m}{k_L \cdot \rho_m} \tag{2}$$

The mass transfer coefficient in vapour phase was calculated with Johnstone and Pigford relation (3), and in liquid phase with V.G. Levici correlation for Sherwood number, relations (4).

$$\left(k_V \cdot P\right) \cdot \frac{A}{V} \cdot \left(\frac{\eta_V}{\rho_V \cdot D_V}\right)^{2/3} = 0.033 \cdot \mathrm{Re}_V^{-0.23} \tag{3}$$

$$\mathrm{k_L} = \frac{\mathrm{Sh_L} \cdot \mathrm{D_L}}{\delta_\mathrm{L}^\mathrm{c}} = \frac{\mathrm{c} \cdot \mathrm{Re_L^{1/2}} \cdot \mathrm{Sc_L^{1/2}} \cdot \mathrm{D_L}}{\delta_\mathrm{L}^\mathrm{c}} \tag{4}$$

2.2 The multi-tubular column model verification

Verification of the multi-tubular column model with experimental data was done. Figure 1 presents schematiclly an experimental plant for hydrogen isotopes separation by cryogenic distillation. The distillation column for H_2-HD mixture, with inner diameter of 27 mm, is equipped on a height of 550 mm with B7 type structured packing. Experimental data are shown in table 1 and figure 2. For $(NTU)_y$ calculation the Colburn formula was used [4]:

Table 1.

Experimental data

Q_F (W)	P_{col} (bar)	T_{col} (K)	P_{cond} (bar)	T_{cond} (K)	w_f (cm/s)	y_1 (ppm)	y_2 (ppm)
4.6	3.01	24.7	2.88	22.7	0.53	88	703
4.6	3.01	24.7	2.91	24.53	0.53	93.7	759
10.2	3.07	24.79	2.95	24.6	1.13	89.5	742
10.4	2.82	24.4	2.72	24.24	1.22	82	696
14.82	3.02	24.71	2.86	24.46	1.7	126.2	713
14.82	3.01	24.7	2.86	24.46	1.71	119	718
15.6	2.98	24.65	2.8	24.37	1.82	88.6	550
16	3	24.68	2.8	24.37	1.85	84	563
20.15	3	24.68	2.85	24.4	2.33	131	723
20.15	3	24.68	2.85	24.45	2.33	115.5	733.6
20.7	3	24.68	2.8	24.37	2.39	89.9	539
20.15	2.78	24.33	2.6	24.04	2.48	70.9	558.2
23.52	2.98	24.65	2.78	24.33	2.74	133	563.5
24.99	3.04	24.74	2.85	24.45	2.86	150	708.5
24.99	2.98	24.65	2.81	24.38	2.91	168	740.7
24.99	2.96	24.62	2.8	24.37	2.93	152	718.5
29.25	3	24.68	2.8	24.37	3.38	160	710.8
33.28	2.97	24.63	1.69	22.25	3.88	56	508.9
33.63	3	24.68	2.78	24.33	3.89	117	670.8

In the case of hydrogen distillation, the theoretical values of the height of the transfer unit, calculated by means of equivalent diameter of packing, are closed to those experimentally determined.

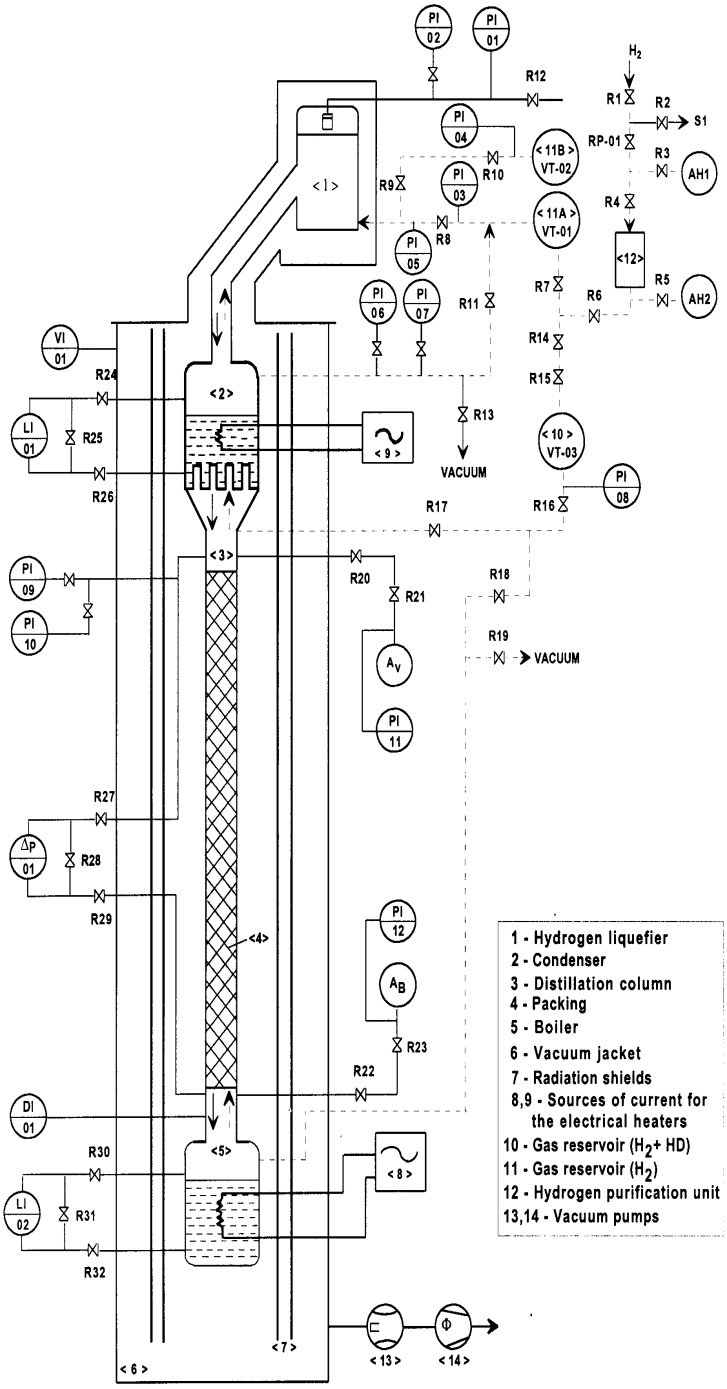

Figure 1. Schematic diagram of the experimental cryogenic plant

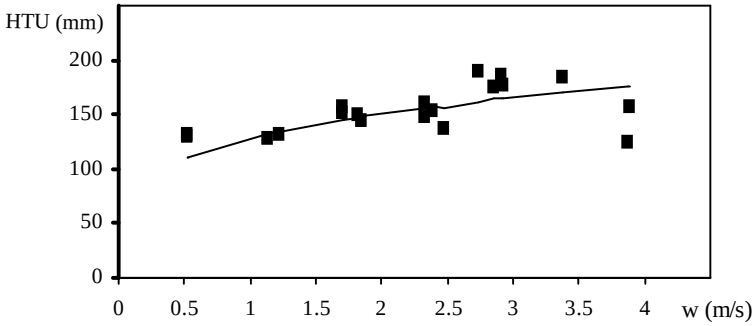

Figure 2. HTU variation with the vapour velocity
P = 3 bar
■ experimental date
▬ calculated date

3. MASS AND HEAT TRANSFER STUDIES

3.1. Mathematical model

A more complex study, for the mass and heat transfer, was performed on water isotopic distillation, also considering the packing bed a multi-tubular wetted-wall column [5]. The steady-state mathematical model for the mass and heat transfer includes the following equations: overall mass balance, isotopic balance over the liquid or vapour volume element, the mass transfer between vapour and liquid phases, the heat balance over the liquid or vapour volume element, the heat transfer between vapour and liquid phases

$$\frac{dL}{dz} = \frac{dV}{dz} \tag{6}$$

$$N = \frac{1}{A_l} \cdot \frac{d(L \cdot x)}{dz} = \frac{1}{A_v} \cdot \frac{d(V \cdot y)}{dz} \cdot \frac{A_v}{A_l} = K_y \cdot a_{l-v} \cdot (y - y^*) = K_y' \cdot (y - y^*) \tag{7}$$

$$\begin{aligned} Q + Q_f &= \frac{1}{A_l} \cdot c_{pl} \cdot \frac{d(L' \cdot t_l)}{dz} = \frac{1}{A_l} \cdot c_{pv} \cdot \frac{d(V' \cdot t_v)}{dz} = \\ &= K_t' \cdot (t_v - t_l) + \frac{dL}{dz} \cdot c_{p_l} \cdot t_l \end{aligned} \tag{8}$$

The mathematical model has been completed with relations for the estimation of the mass and heat transfer coeficients.

3.2. Experimental data

The experimental plant for water distillation is represented schematically in figure 3. The distillation column has an inner diameter of 108 mm and it is equipped with B7 type structured packing on 14 m height. The column has 12 points for temperature and concentration measurement, which allowed us to determine the locale values of the mass and heat transfer coefficients, presented in figure 4 and 5. It can be noticed, at the column top, the influence of subcooled reflux and between stratum 4 and stratum 5 imperfections of the column insulation.

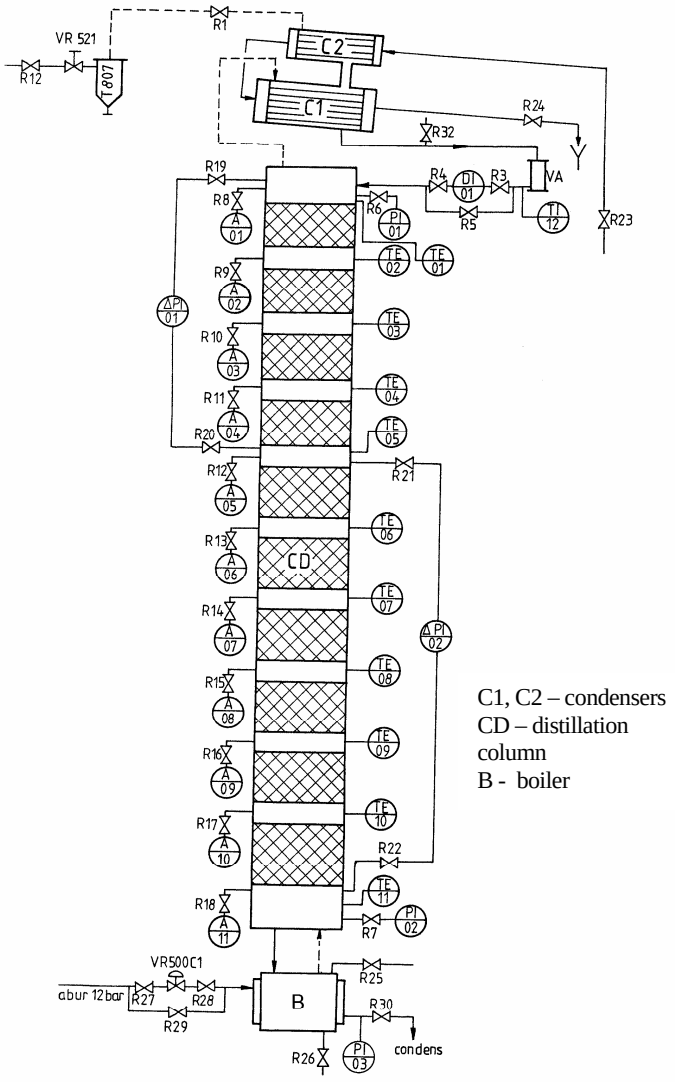

Figure 3. Schematic diagram of the experimental water distillation plant

In water distillation the values of the height of the mass transfer unit range within 50-150 mm domain. Between the theoretical estimation of a distillation column functioning and the measured values one can observe a relative error ranging within 8 - 19% domaine. This fact requires correction, by means of the experimental data, for the coefficients used in the criterion relations.

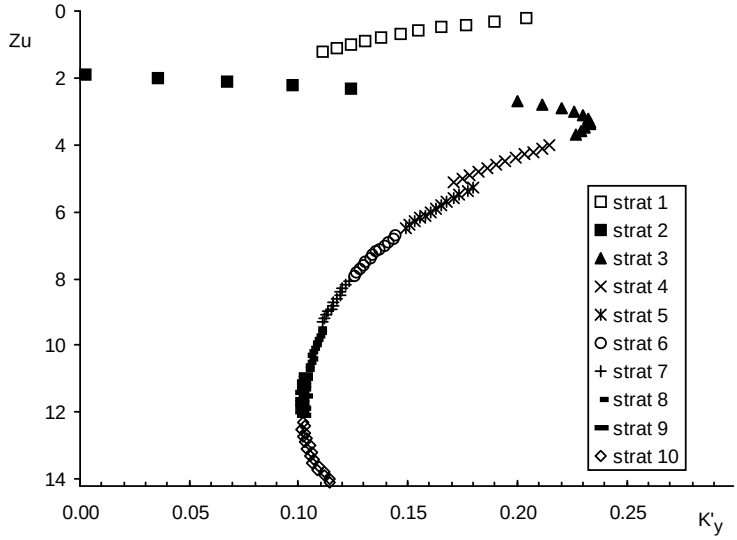

Fig. 4 Mass transfer coeficents, experimental determined
f = 1.6
Zu [=] m, K'_y [=] kmol/(m^3.s)

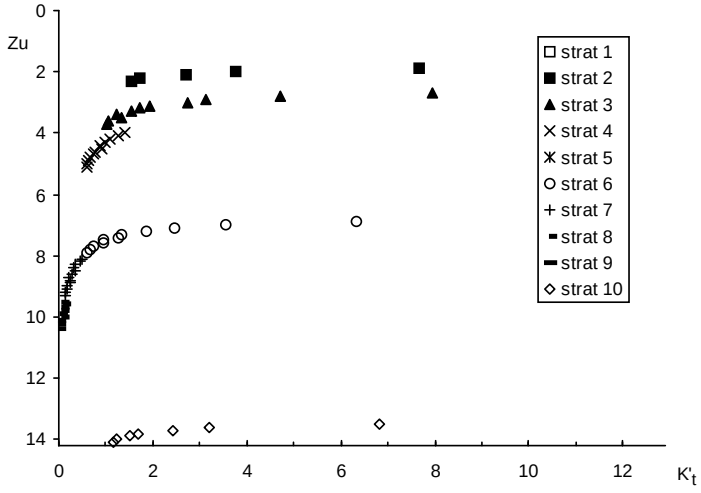

Fig. 5 Heat transfer coeficents, experimental determined
f = 1.6
Zu [=] m, K'_t [=] kW/(m^3.grd)

4. Conclusions

The HTU mean value at water distillation (~0.1 m) is closed of the HTU mean value at hydrogen distillation (~0.2 m).

The HTU values, experimentally or theoretically obtained, constitute designing data for the hydrogen and heavy water plants. Determined values of HTU for the H_2 - HD and H_2O – HDO – D_2O isotopic mixture distillation enter thus in practice.

The level of the mass and heat transfer coefficient, evaluated theoretically and verified experimentally, are comparable with other separation processes from the chemical industry. This fact justifies the use of the multi-tubular wetted-wall model for the description of the transfer processes in distillation columns equipped with B7 ordered packing.

BIBLIOGRAPHY

1. Floarea Pop, Marius Peculea and Cornelia Croitoru - Experimental Determination of the Height of Transfer Unit at the Hydrogen Isotopic Distillation on Ordered Packing, B7 Type", Revue Roumaine de Chimie, nr. 2, 1999
2. A. Paris - "Les procédés de rectification dans l'industrie chimique", Dunod - Paris, 1959
3. T. Yamanishi, K. Okuno, Y. Naruse, E. Sada - "Analysis of Characteristics of Cryogenic Distillation Column in Separation of Hydrogen Isotopes", Journal of Chemical Engineering of Japan, vol. 26 nr. 1 (1993)
4. E. P. Dutkai - "Coloane cu umplutur` [n tehnologia chimic`", Editura Tehnic` Bucuresti, 1977
5. C. Croitoru, F. Pop, Gh. Ti\escu, M. Culcer, M. Iliescu].a. - Experimentari asupra transferului de masa si caldura in coloane echipate cu umplutura ordonata tip B7, raport de cercetare, C43/14.06.2001, ICSI Rm. Valcea

SYMBOLS

$(HTU)_y$ – height of transfer unit reported to vapour phase
L, L', V, V' – liquid, vapour flow rate
d_{ech} – equivalent diameter
D_c – column diameter
ε - voidage of packing
K'_y, K'_t, k_L, k_V - global mass and heat transfer coefficient; liquid, vapour partial film mass heat transfer coefficient
m - slope of equilibrium curve
P - total pressure
ρ_m, ρ_V - molar liquid density, vapour density
δ_L^c - thickness of mass transfer boundary layer of liquid phase
A, A_l, A_v, a_{l-v} – area of free column section, liquid , vapour flow section area , interfacial area
D_L, D_V – Diffusion coeficient
Sh, Re, Sc - Sherwood, Reynolds, Schmidt number
z -height
x, y - liquid, vapour phase isotopic concentration
c_p - heat capacity
t_L, t_V - liquid, vapour temperature

THE EVALUATION OF SOME THERMODYNAMIC PARAMETERS BY RIA METHOD

I.I. DOROBANTU, DELIA-IRINA CUCU

National Institute of C&D for Physics and Nuclear Engineering "Horia Hulubei", Life and Environmental Physics Department, Bucharest-Magurele, Romania, 407 Atomistilor St., PO BOX MG 6, E-mail: cdelia@ifin.nipne.ro

ABSTRACT. Intrinsic association constant characterises the binding of an antibody with a monovalent antigen or hapten. The binding forces between antibody and the respective hapten are relatively weak and consist mainly of Van der Vaals forces, electrostatic forces and hydrophobic forces. Thus, it is important to know the thermodynamic parameters as enthalpy, Gibbs energy and the entropy involved in the formation of an antigen-antibody complex in order to characterise a certain antigen-antibody complex. The present paper evaluates some of thermodynamic parameters by using RIA (radioimmunoassay) method.

Introduction

According to Le Chatelier's principle, a bimolecular reversible reaction for the antiprogesterone antibody-progesterone system at chemical equilibrum is represented by the ecuation:

$$Ab + Pr \underset{K_{-1}}{\overset{K_{+1}}{\rightleftharpoons}} AbPr$$

The rate of the forming (v) of the immune complex (AbPr) will be:

$$v = \frac{d[AbPr]}{dt} = K_{+1}[Ab][Pr] - K_{-1}[AbPr]$$

where [AbPr] – the concentration of the immune complex;

[Ab] – the concentration of the antibodies;

[Pr] – the concentration of the progesterone of a given time;

K_{+1} – the forming constant of the immune complex;

K_{-1} – the dissociation constant of the immune complex.

After the reaching of the chemical equilibrum (v=0), will results:

$$\frac{K_{+1}}{K_{-1}} = K = \frac{[AbPr]_e}{[Ab]_e[Pr]_e}$$

where $[AbPr]_e$, $[Ab]_e$, $[Pr]_e$ – the concentrations system components at equilibrum, K beeing equilibrum constant (the affinity constant).

In the case of antibody- labeled antigene system (Pr^*), the equilibrum constant will be:

$$K^* = \frac{[AbPr^*]_e}{[Ab]_e[Pr^*]_e}$$

The labeled antigene Pr – ^3H is not structural different against unlabeled antigene Pr, so one can consider that the affinities of the antibodies against the labeled and unlabeled steroids are the same and therefore, $K=K^*$, this fact beeing the reason of using of tritiate marker for antisera titre determination.

In the case of indirect labeling of the steroid (the coupling of steroid with a carrier), the marker will be structural different from steroid, $K \neq K^*$. This can be a disadvantage between labeled and unlabeled steroid for bonding situs of antibodies.

The determination of equilibrum constant k of antiprogesterone antibody-progesterone system using As antigene radioactive progesterone

At equilibrum,

$$K^* = \frac{[AbPr^*]_e}{[Ab]_e[Pr^*]_e}$$

where $$\frac{[AbPr^*]_e}{[Pr^*]_e} = \frac{B}{F} = \frac{\text{i.p.m...in..precipitate}}{\text{i.p.m...in..supernatant}}$$

B = radioactive activity of the immune complex;

F = the free radioactivity in solution.

If one note: $[Ab]_e = a - [AbPr^*]_e$, a = initial concentration of the antibody;

$[Pr]_e = p - [AbPr^*]_e$, p = initial concentration of the progesterone.

$$[AbPr^*]_e = \frac{B}{B+F} \times p$$

If one note $B_s+F = T_0$ (the total activity), then:

$$[AbPr^*]_e = \frac{B_S}{T_0} \times p$$

$$E = \frac{B}{F} \cdot \frac{1}{a - \frac{B}{T_0} \cdot p} = \frac{\frac{B_S}{T_0}}{1 - \frac{B_S}{T_0}} \cdot \frac{1}{a - \frac{B_S}{T_0} \cdot p}$$

This relation permits the calculation of the equilibrum constant K when the concentration of the substances are known as well the B/T_0 value.

Ab-Pr-^3H system

$$K = \frac{[AbPr - H]_e}{[Ab]_e \cdot [Pr - H]_e} = \frac{B_S}{F_S} \cdot \frac{1}{a - \frac{B_S}{T_0} \cdot p}$$

where $B_s = B - B_{nesp}$

$F = T_0 - B_s$

B = specific bonding of the radioactivity;

F = free radioactivity in supernatant;

B_{nesp} = nonspecific bonding.

Table 1.

Experimental data for Ab - Pr^{3}H system;
a = 1.7x10^{-8} M; dilution of antiserum (1/400); T = 296 K (23^{0}C); T_0 = 17 500 ipm

Pr-^{3}H (pg)	Total radio-activity (ipm)	Pr (ng)	Bonding radioactivity in immune complex (B) (ipm)	Calculated specific radioactivity B-B_{nesp} (ipm)	$\frac{(B-B_{nesp})}{T_0}$	$\frac{(B-B_{nesp})}{F}$	Kx10^7 (lxmol^{-1})
200	17 500	0	10 350	8054	0.46	0.85	5.00
200	17 500	0.5	10 009	7713	0.44	0.78	5.77
200	17 500	1	9919	7623	0.43	0.75	5.53
200	17 500	2	8792	6496	0.37	0.59	4.92
200	17 500	3	7705	5409	0.31	0.45	4.7
200	17 500	5	6081	3785	0.22	0.28	3.41
200	17 500	10	5211	2915	0.17	0.20	5.88
200	17 500	20	3507	1211	0.07	0.07	-
200	17 500	50	2665	369	0.02	0.02	-
200	17 500	200	2249	-	-	-	-
200	17 500	normal serum + 0 ng Pr	2307	-	-	-	-
200	17 500	normal serum + 200 ng Pr	2285	-	-	-	-

Average equilibrum constant K = 5.03x10^7 litri x mol^{-1}

Table 2.

Experimental data for Ab - Pr^{3}H system
a = 1.7x10^{-8} M; dilution of antiserum (1/400); T = 277 K (4^{0}C); T_0 = 17 500 ipm

Pr-^{3}H (pg)	Total radio-activity (ipm)	Pr (ng)	Bonding radioactivity in immune complex (B) (ipm)	Calculated specific radioactivity B-B_{nesp} (ipm)	$\frac{(B-B_{nesp})}{T_0}$	$\frac{(B-B_{nesp})}{F}$	Kx10^7 (lxmol^{-1})
200	17 500	0	14 200	11119	0.64	1.74	1.74
200	17 500	1	13860	10779	0.62	1.60	1.3
200	17 500	2	11836	8755	0.50	1.00	1.1
200	17 500	5	6988	3907	0.28	0.28	0.5
200	17 500	normal serum + 0 ng Pr	3081	-	-	-	-

Average equilibrum constant K = 1.16x10^8 litri x mol^{-1}

Ab-Pr-6-S-CH_2-CO-Histamin ^{125}I (Pr^{125}) SYSTEM

Table 3.

Experimental data for Ac – Pr^{125}I system; a = 3.4x10^{-8} M; dilution of antiserum (1/200); T = 296 K (23^{0}C)

Pr-^{125}I (pg)	Total radio-activity (ipm)	Pr (ng)	Bonding radioactivity in immune complex (B) (ipm)	Calculated specific radioactivity B-B_{nesp} (ipm)	$\frac{(B-B_{nesp})}{T_0}$	$\frac{(B-B_{nesp})}{F}$	Kx10^7 (lxmol^{-1})
500	149783	0	22083	9283	0.062	0.079	2.32
500	147549	1	22169	9309	0.063	0.075	2.20
500	148697	2	21869	9069	0.061	0.072	2.25
500	150237	3	19720	6920	0.046	0.053	1.7

Pr-^{125}I (pg)	Total radio-activity (ipm)	Pr (ng)	Bonding radioactivity in immune complex (B) (ipm)	Calculated specific radioactivity B-B_{nesp} (ipm)	$\frac{(B-B_{nesp})}{T_0}$	$\frac{(B-B_{nesp})}{F}$	Kx10^7 (lxmol^{-1})
500	149003	5	18211	5411	0.036	0.041	1.4
500	148256	10	16544	3744	0.025	0.028	1.27
500	149274	20	14696	1896	0.013	0.014	0.7
500	147356	50	13114	314	0.002	0.002	-
500	148290	200	12896	96	-	-	-
500	148376	serum N + 0 ng Pr	12817	-	-	-	-
500	151200	serum N +200 ng Pr	12781	-	-	-	-

Average equilibrum constant K = 1,69X10^6 litrixmol^{-1}

Table 4.

Experimental data for Ac – Pr^{125}I system; a = 3.4x10^{-8} M; dilution antiserum (1/200); T = 277 K (4^{0}C)

Pr-^{125}I (pg)	Total radio-activity (ipm)	Pr (ng)	Bonding radioactivity in immune complex (B) (ipm)	Calculated specific radioactivity B-B_{nesp} (ipm)	$\frac{(B-B_{nesp})}{T_0}$	$\frac{(B-B_{nesp})}{F}$	Kx10^7 (lxmol^{-1})
500	149324	0	32476	15606	0.103	0.132	3.88
500	149288	0.5	32153	15283	0.102	0.132	3.8
500	148976	1	32032	15162	0.102	0.130	3.8
500	149763	2	31710	14840	0.101	0.126	3.9
500	150544	5	26588	9718	0.064	0.078	3.2
500	148054	ser N + 0 ng Pr	16870	-	-	-	-

Average equilibrum constant K = 3.72X10^6 litrixmol^{-1}

Gibbs energy of Ab – Pr system

For a chemical reaction, the variation of the free energy (ΔG) is:

$$\Delta G = \Delta G^S + RT \ln K$$

where ΔG^S = variation of standard free energy;
R = constant (1.98 cal/molxgrad);
K = equilibrum constant of the chemical reaction;
T = absolute temperature of the system (grade Kelvin).

At equilibrum $\Delta G = 0 \Rightarrow \Delta G^S = -RT \ln K$ sau $\Delta G^S = -2.3\ RT \lg K$

Ac-Pr^{3}H				
T_1	T_2	a	K	ΔG^S
296K	-	1.7x10^{-8} M	5.3x10^7 litri x mol^{-1}	- 10.412 Kcal/mol
-	277K	1.7x10^{-8} M	1.16x10^8 litri x mol^{-1}	- 10.172 Kcal/mol
Ac-Pr^{125}I				
T_1	T_2	a	K	ΔG^S
296K	-	3.4x10^{-8} M	1.86x10^6 litri x mol^{-1}	- 8.45 Kcal/mol
-	277K	3.4x10^{-8} M	3.72x10^6 litri x mol^{-1}	- 8.29 Kcal/mol

The reaction enthalpy

For a chemical reaction at equilibrum,

$$H^S = \frac{2.3RT_2T_1}{T_2 - T_1} \cdot \lg \frac{K_2}{K_1}$$

where: K_1, K_2 are the equilibrum constants at T_1 and T_2 ;
ΔH^S – the variation of the standard enthalpy.

Ac-Pr^{3}H					
a	K_1	K_2	T_1	T_2	ΔH^S
$1.7x10^{-8}$ M	$5.3x10^7$ litrixmol^{-1}	$1.16x10^8$ litrixmol^{-1}	296 K	277 K	-6.68 Kcal/mol
Ac-Pr^{125}I					
a	K_1	K_2	T_1	T_2	ΔH^S
$3.4x10^{-8}$ M	$1.86x10^6$ litrixmol^{-1}	$3.72x10^8$ litrixmol^{-1}	296 K	277 K	-5.954 Kcal/mol

The enthropy of the reaction system

The variation of standard enthropy is:

$$S^S = \frac{H^S - G^S}{T}$$

where ΔS^S = the variation of standard enthropy of the system; T = absolute temperature (Kelvin degrees).

AC-Pr^{3}H			
T	ΔH^S	ΔG^S	ΔS^S
296 K	-6.68 Kcal/mol	-10.41 Kcal/mol	12.6 cal x mol^{-1} x grad^{-1}
AC-Pr^{125}I			
T	ΔH^S	ΔG^S	ΔS^S
296 K	-5.95 Kcal/mol	-8.45 Kcal/mol	8.4 cal x mol^{-1} x grad^{-1}

REFERENCES

1. Fleeker J; J Assoc Off Anal Chem 1987 Sep-Oct 70:5 874-8

2. Knopp D, Nuhn P, Dobberkau HJ; Arch Toxicol 1985 Oct 58:1 27-32

3. Flanagan RJ, Ruprah M; Clin Chem 1989 Jul 35:7 1342-7

4. Yamada H, Kuroda A, Yatabe T, Inaba T, Chiba K, Iio M; Radioisotopes 1981 Jun 30:6 311-7

5. Agasan AL, Stewart BJ, Watson TG; J Immunol Methods 1994 Dec 28 177:1-2 251-60

STUDIA UNIVERSITATIS BABEŞ-BOLYAI, PHYSICA, SPECIAL ISSUE, 2001

THE ASSESSMENT OF THE QUALITY OF THE FOOD BY ^{13}C ISOTOPE RATIO MASS SPECTROMETRY

STELA CUNA[*], C. CUNA[*], GABRIELA BALAS[*], FILOFTEIA GAFTOI[**]

[*]*INCDTIM Cluj-Napoca*
[**]*Geological Institute of Romania, Bucuresti*

Introduction

Natural abundance of stable isotopes is an important source of information on each chemical species because, the isotopic content of a given molecule depends on its origin and the history of the processes involved. The isotopic fractionation of those elements in the environment, follows complex patterns which allow correlation to be established between the final products (juice, wine, honey) and raw materials (water and CO_2) from which they have been biosynthesized [1]. Low cost sweeteners, artificial or natural flavorings, citric acid and water can be added to fruit concentrates simulating natural juices. Pure honey is also a relatively expensive food that can be adulterated by mixing it with the much cheaper high fructose corn syrup. Adulterants such as simple sugar solutions can be detected by chemical analysis. More sophisticated sweeteners like high fructose corn syrup are difficult to detect by chemical analysis or by chromatographic tests. Isotope ratio mass spectrometry of carbon and, to a lesser extent of hydrogen and oxygen is a technique for the detection of adulteration or establishment of authenticity in food products [2].

The theoretical base of the method

The method is based on different isotopic fractionations that appear in two cases:

1.) A molecule may result from a natural or an artificial process. The rate of the natural process is different from the artificial one and this results in different isotopic fractionation. The molecule resulted from a natural process will have an isotopic composition of the ^{13}C and the molecule resulted from a synthetic process will have a different isotopic composition of the ^{13}C.

2.) The natural abundance of ^{13}C in foods is also related to how plant fixes carbon during photosynthesis [3]. Plants using the Calvin cycle are called C_3 plants and plants that use the Hatch-Slack cycle are called C_4 plants. About 80-90 % of agriculturally cultivated plants belong to the C_3 group. Plants that use a Calvin cycle discriminate against ^{13}C more than plants with a Hatch-Slach cycle. The ^{13}C content of the C_3 plants varies between -35‰ and -22‰ while the same parameter of the C_4 plants varies between -20‰ and -8‰. Targets of adulterations (honey, fruit juices, high commodity oils) use the C_3 plants. The adulterators such as high fructose corn syrup, cane sugar and corn oil use the C_4 plant product.

Analytical technique and results

Carbon must be converted to CO_2 for stable $^{13}C/^{12}C$ isotope ratio measurements [4]. The organic carbon in a sample was converted to CO_2 gas through the dry combustion method.

The materials required were: quartz tube, CuO wire, Cu wire, Ag foil, Pt wire, Cajon metal fittings, muffle furnance and vacuum manifold for separation of CO_2 gas (Fig.1)

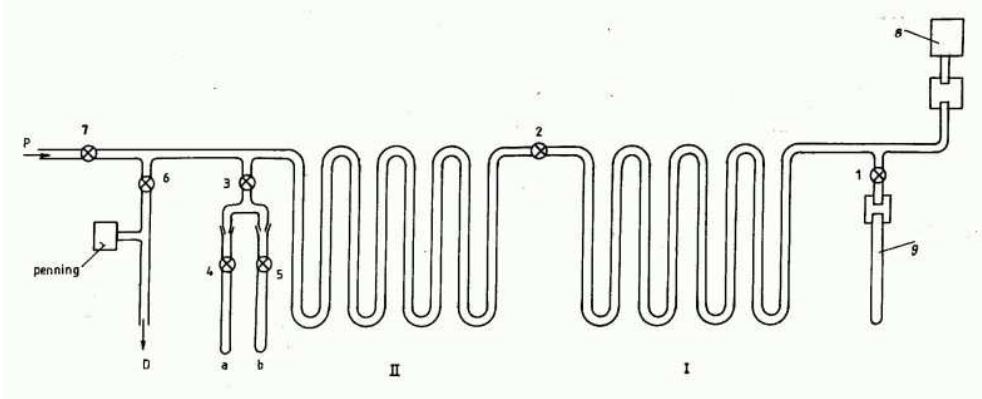

Fig. 1 Vacuum system for isolation and purification of CO_2

P - preliminary pump
D - diffusion pump
1-7 - valves
a,b - sample bulls
I, II - traps
8 - vacuum gauge
9 - quartz tube

The organic material are placed in the quartz tube with the CuO wire, Ag foil, Cu wire and Pt wire. The tube is attached to the vacuum manifold via a Cajon fitting and evacuated to remove air and water from the sample and then sealed it. The sample tube is then combusted in a muffle furnance to 500º C for 1/2 hour and then heated to 850 ºC for 2 hours. After combustion, the tube is attached to a vacuum manifold and cracked to release the combustion gases. The CO_2 gas is cryogenically separated and purified and then collected in a sample bulb.

The CO_2 gas was analysed with a mass spectrometer for isotope ratio analysis. The method was used for the detection of a synthetic flavor from a natural one, namely the bitter almond natural oil and the synthetic benzaldehide (C_7H_6O), the natural bergamot mint oil (linalyl acetate-$C_{12}H_{20}O_2$), the natural acetic acid and the synthetic acetic acid ($C_2H_4O_2$).

There is a great difference between the C_3 plant (-25,92 ‰ and - 29.62 ‰) and the C_4 plant (- 13.68 ‰). There is also, a difference between the natural and synthetic molecules (-23.13 ‰ versus - 13.68 ‰).

The precision of the methode was ±0.4 ‰. For sample sizes ranging between 3 µl and 8µl, the linearity was very good.

The results are show in the Table 1:

Sample	$\delta^{13}C$ ‰	
	synthetic	natural
benzaldehide	-23,24	-25.92
acetic acid	-23.13	-13.68
linalyl acetate	-	-29.62

Conclusions

^{13}C analysis is a key analytical technique used to detect undeclared addition of low cost adulterants to high value foods. We developed a method for the analysis of the ^{13}C isotope content in organic samples. The organic samples conversion to CO_2 was accomplished by combustion in an oxygen excess and the isotopic content of ^{13}C in CO_2 was measured by mass spectrometry. The precision and linearity of the method were tested was used for the detection of a synthetic flavour from a natural one.

REFERENCES

1. Kevin Robards, Michael Antolovich, Analyst, vol 120, pp 1-28, 1995
2. Modern Isotope Ratio Mass Spectrometry, ed. J.D. Winefordner, Jhon Wiley &Sons, New York, 1995
3. G. Edwards and D.A. Walker, C_3, C_4: Mechanisms and Cellular and Environmental Regulation of Photosynthesis, Blackwell Scientific, Oxford, 1983
4. Carbon Isotope Techniques, ed. David C. Coleman and Brian Fry, Academic Press Inc., New York, 1991

STUDIA UNIVERSITATIS BABEŞ-BOLYAI, PHYSICA, SPECIAL ISSUE, 2001

ISOTOPIC INVESTIGATIONS ON THE MINERAL WATERS FROM SOMESENI – CLUJ, ROMANIA

STELA CUNA[1], PETRE BERDEA[1], CALIN BACIU[2]

[1] National Institute of Research- Development for Isotopic and Molecular Technologies Cluj-Napoca
[2]Babes-Bolyai University of Cluj-Napoca, Faculty of Biology and Geology

1. INTRODUCTION

The best conceivable stable tracers of water are represented by the isotopes of the constitutive atoms of the water molecule ^{18}O and D (1,2). If the isotope content changes along ground water path, it will reflect the history of the water. On the contrary, if the isotope content does not change within the aquifer, it will reflect the origin of the water. Origin deals with location, period and processes of recharge and history deals with mixing, salinity and discharge processes (1).

The Someseni mineral water spring area is located in the eastern part of Cluj-Napoca, Romania at the contact between the alluvial plane and the first terrace of the Somesul Mic River (3). The therapeutical qualities of this water were known since the early 1920's. The spa was established in 1927.

Detailed physical and chemical analyses were performed by the Institute of Balneology and Physiotherapy (4). The radon contents of these waters were also measured (5-7). Theirs chemical composition is dominated by sodium and chloride. Higher values of radon content were noticed for some of them.

From a geological point of view, the mineral aquifer is located on the western border of Neogene Transylvanian Basin. The Someseni spring area is situated on an anticline with salt core. Marls with frequent intercalation of sandstone and volcanic tuffs dominate the lithology of these deposits. The alluvial deposits of the river generally cover the Neogene formations.

From the hydrological point of view, a relative recent research admits the existence of two distinct circuits: a deep one which is following the Neogene formation with salt contents, and a shallow one located within the alluvial deposits which is touching only the upper part of the salt body (8).

We believe after the hydrogen and oxygen isotopes analyses of this waters that there is a single circuit of these mineral waters.

2. MATERIALS AND METHODS

The water samples for the spring No. 1, 2, 3, 8, 15, Becas river and Someseni well were collected monthly from July 2000 to May 2001 at Someseni spring area. Prior to deuterium analyses the waters were vacuum distilled.

For the determination of the oxygen isotopic composition of waters, the waters was equilibrated with CO_2 and then the isotopic composition of the CO_2 gas was measured. The equilibration time was reduced to a few hours by shaking the samples. When isotopic equilibration has been atteined, the CO_2 was extracted from the container, separated from the water vapour by means of a dry ice trap and analysed with a mass spectrometer versus a given reference. We used as reference the same CO_2 tank used in equilibration.

The deuterium analyses of water are carried out on the hydrogen gas obtained by quantitative reduction of water sample (9). The water sample (about 1 μl) is introduced in a heated glass reservoir and a small portion of the sample is introduced in the mass spectrometer at a constant rate through a glass capillary and a quartz tube containing uranium ribbon at 650^0C connected directly to mass spectrometer ion source.

The isotopic content is expressed as δ value in part per thousand:

$$\delta=(R/R_S-1)1000$$

where R is the isotopic ratio of the probe and R_S is the isotopic ratio of the internal standard, SMOW (Standard Mean Ocean Water) (1, 2).

3. RESULTS AND DISCUSSION

The results of the deuterium and oxygen-18 measurements of waters from springs, Becas river and well at Someseni Spa are presented in Fig.1 and Table1.

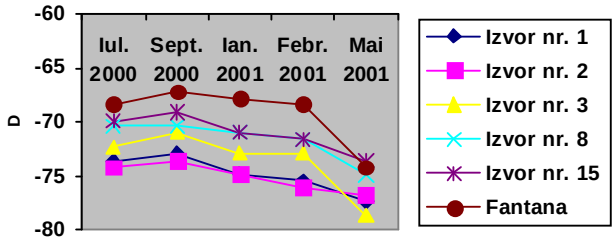

Figure 1. Comparison of D and ^{18}O content in Someseni springs

Table 1. Temporal variation of D and ^{18}O content

Data	Ianuarie 2001		Februarie 2001	
Proba	δD‰	δ^{18}O‰	δD‰	δ^{18}O‰
Izvor nr.1	-74.9±1.5	-8.90±0.4	-75.5±2	-9.27±0.4
Izvor nr.2	-74.9±2	-8.73±0.3	-76.1±1,5	-6.85±0.7
Izvor nr.3	-72.9±1.5	-8.65±0.7	-72.9±2.5	-8.95±0.5
Izvor nr.8	-71.0±1.7	-8.08±0.7	-71.6±2.4	-7.71±0,4
Izvor nr.15	-71.0±2	-8.28±0.5	-71.6±2	-8.52±0,4
Fantana	-67.9±1.5	-8.61±0.6	-68.4±1.5	-7.47±0.3
Becas	-73.6±1	-8.65±0.5	-68.4±2	-8.77±0.4

The time period investigated by us was a dried one with insignificant precipitations. A good stability in time and correlation of the deuterium and oxygen

contents for the five investigated springs, Becas river and well was shown by the measurements.

In such a way it is more convenient to assume that all the spring are related to a unique aquifer. The ground water trajectory is probably, following the previous layers (sandstone, volcanic tuffs) intercalated in the Neogene pile of sediments. The anticline structure interrupted the continuity of these formations, facilitating the water ascension. Water found different ways to reach the surface in the salt brecia zone. The so called "deep waters" are not always concentrated brines.

This assumption can be sustained by the hydrogen and oxygen isotopes measurements of the waters from this area.

The measurements also confirmed the results of some studies (2), showing that seasonal variations in the isotopic content are largely attenuated over the water mass, and that the shallow ground waters like the water studied in our case, present the mean annual deuterium content of the precipitation (-66 ‰ the Cluj-Napoca mean deuterium content).

4. CONCLUSIONS

In our opinion, the mineral aquifer of Someseni water spring area is a single circuit of mineral waters. The infiltration is occurring through previous layers, as volcanic tuffs and sandstones in a unidentified recharging zone generating a confined aquifer. This assumption can be sustained by the hydrogen and oxygen isotopes of the waters from this area.

REFERENCES

1. Fontes I.Ch., Environmental isotopes in ground water hydrology, in: P.Fritz and I.Ch. Fontes (eds.), Handbook of Environmental Isotope Geochemistry, vol. 1, Elsevior Sci. Publ.Comp., Amsterdam-Oxford-New York (1980), pp. 75-134
2. Clark I., Frit P., Environmental Isotopes in Hydrology, Lewis Publ., Boca Raton-New York (1997)
3. Baciu C., Cosma C., Berdea P., An approach to the dynamics of mineral waters from Someseni Spa
4. IBF, Apele minerale si namolurile terapeutice din Republica Socialista Romania, vol II, Bucuresti (1965), pp. 186-209
5. Atanasiu G., Radioactivite des sources d'eau de Roumanie-III, An. I.G.R., XVI (1931), 935-943
6. Szadecky K.G., A szamosfalvi sosfurdo geologiaja, Erd. Muz. (1933), 4-6, 10
7. Cosma C., Baciu C, Ristoiu D., Some aspects of radon potential in soil and underground waters in the Somesul Mic hydrographic basin (North-western Romania) (In press)
8. Pricajan A., Apele minerale si termale din Romania, Ed. Tehnica, Bucuresti (1972)
9. Berdea P., Cuna C., Feurdean V., Buza A, Bot A, Pirtoc N., Spectrometrul de masa SMAD-2A pentru analiza izotopica a apei, ST. Cere.Fiz. 44 (1992), 407-417

STUDIA UNIVERSITATIS BABEŞ-BOLYAI, PHYSICA, SPECIAL ISSUE, 2001

RADIATION - INDUCED DEGRADATION OF DNA IN PHOTODYNAMIC THERAPY OF CANCER

RODICA M. ION*, F. SCARLAT, KERIMAN GUNAYDIN***, V.I.R. NICULESCU**, FL. SCARLAT****

** Institute for Chemical Research, Dept. Chemical Analysis, Splaiul Independentei 202,Bucharest-79611, Romania; E-mail: irma@pcnet.ro*
*** National Institute of Physics for Lasers, Plasma and Radiation, Bucurest-Magurele, P.O.Box MG-36, Romania;E-mail: scarlat@pcnet.ro*
**** Mustafa Kemal University, Faculty of Science and Letters, Chemistry Department, Antakya-Hatay,Turkey; E-mail: gunaydin@mku.edu.tr*

ABSTRACT. DNA is a critical cellular target for oxidative processes induced by physical and chemical stresses. It is known that the direct effect of ionizing radiation on DNA results mainly in base ionization and may lead to mutation, carcinogenesis and cell death. The degradation of DNA induced by laser and ionizing radiation (photon beam), is analyzed in this paper. **The laser degradation of DNA is a singlet oxygen process, while the ionizing radiation degradation is a radicalic one.** A series of lesions among the major bases degradation product has been measured in isolated DNA (8-OxodGuo) exposed to gamma radiation in aerated aqueous solution. Degradation can be accounted for by the formation of hydroxyl radicals upon radiolysis of water (indirect effect). The relative contribution of the two mechanisms in damaging DNA depends on the type of radiation. Single strand breaks and base damage seem to be mainly produced by the attack of hydroxyl radicals on DNA, whereas double strand breaks result predominantly of direct energy deposition. The four bases are degraded in high yield. When DNA is irradiated in solution, single strand breaks are mainly due to the abstraction of an H atom from the 4' position of 2'-deoxyribose by the attack of OH radicals produced by water radiolysis. Quantification of the modified bases showed the guanine is the preferential target. Ionizing radiation produces very low quantities of degradation products of DNA if compared with photochemical pathway. When absorb the light, the photosensitizers reach an excited state able to abstract one electron from the DNA bases, producing the related radical cation, guanine being the preferential target. Ionizing radiation induce several types of DNA modifications, including chain breaks, DNA-protein cross-links, oxidized DNA bases. A high value for 8-OxodGuo degradation observed in control cells treated with either MB or AO by comparison with the others conditions. Ionizing radiation produces very low quantities of 8-OxodGuo, if compared with photosensitizers.

1. INTRODUCTION

The photodynamic therapy of cancer is a fascinating method for cancer diagnosis and treatment of various types of tumors by the combined action of oxygen, light and sensitizer [1].

Under irradiation with light (laser) and/or ionizing radiation, in the presence of a photosensitizer (porphyrinic type), DNA support several modifications including chain breaks, DNA-protein cross-links, abasic sites and oxidized DNA bases, which have been shown to be able to induce point mutations [2-5].

The production of DNA damage by ionizing radiation involves two mechanisms, direct and indirect effects. Direct effect lead to ionization and excitation of DNA molecules, while indirect effect is due to the interaction of reactive species, in particular of OH. radicals produced by water radiolysis, with targets in DNA. Single strand breaks and base damage seems to be mainly produced by the attack of hydroxyl radicals on DNA, whereas double strand breaks result predominantly of direct energy deposition [6,7]. Base damage may also occur from the formation of radical cation of purine and pyrimidine components when DNA is irradiated with photon beam in solution, single strand breaks are mainly due to the abstraction of an H atom from the 4' position of 2'-deoxyribose by the attack of OH. radicals produced by water radiolysis.

Ionizing radiation produces very low quantities of degradation products of DNA if compared with photochemical pathway. When absorb the light, the photosensitizers reach an excited state able to abstract one electron from the DNA bases, producing the related radical cation, guanine being the preferential target.

2. EXPERIMENTAL PART

A solution of calf thymus DNA was either exposed to the photon beam of a 7 MeV accelerator, or photosensitized in a photoreactor irradiated with an wavelength greater than 350 nm in the presence of few sensitizers: riboflavin (RB), benzophenone (BF), acridine orange (AO), methylene blue (MB) and tetra-p-sulpho-phenyl-porphyrin (TSPP).

Except TSPP which was synthesized in tha lab, the other sensitizers have been used as delivered from Fluka. Continuous air bubbling was mentained during all experiments. Then, DNA was digested into nucleosides and 8-OxodGuo and 5-OHdCyt were analyzed by reverse phase HPLC associated with an UV detector and also by IR spectroscopy.

The electron and photon radiation beams were supplied by the 7.0 Mv Linear Accelerator of the National Instituted for Laser, Plasma and Radiation Physics, Romania.

All the irradiation processes with light were achieved with a medium-pressure 250-W mercury lamp (Romlux-Romania).

The visible absorption spectra were recorded on a SPECORD M400 Carl Zeiss Jena spectrophotometer. All spectroscopic studies were performed in the porphyrin concentration range of 8×10^{-5} to 1×10^{-8} M.

IR spectra (for KBr pellets) were run on a SPECORD M80 Carl Zeiss Jena spectrometer with a computer command.

3. RESULTS AND DISCUSSION

The five photosensitizers were found to degrade DNA bases with different efficiencies for each type of irradiation. This was explained first of all by the difference in the UV-Vis absorption spectra of each photosensitizers and by their

variation in electron abstraction quantum yield. The yields were expressed with respect to that of 8-OxodGuo which was normalized to 100 (Table 1).

Table 1.

Relative yield of formtion of modified bases within DNA either exposed to photon beam (800 R) in aerated solution or photosentized by light in the presence of different photosensitizers [a]

Lesion	photon beam	BF	RB	MB	AO	TSPP
8-OxodGuo	100	100	100	100	100	100
5-OHCyt	26.2	0.7	1.3	75.6	71	80

[a] Yields expressed in % with respect to 8-OxodGuo

Also, by measuring the tail moment (through the alkaline single-cell gel electrophoresis) was possible to detect in a.u. (arbitrary units of tail moment)/ Gy for 8-OxodGuo, Table2.

Table 2.

DNA lesions by photon or light exposure, measured by means of 8-OxodGuo degradation

Lesion	photon beam	BF	RB	MB	AO	TSPP
8-OxodGuo	0.26	0.7	0.65	0.60	0.6	0.5

It's difficult to explain the high value of the tail moment observed in control cells treated with either MB or AO. Ionizing radiation produces very low quantities of 8-OxodGuo, if compared with photosensitizers.

The processes involving DNA are affected by photodynamic therapy. The damage is mediated by singlet oxygen and this specie can travel only about 0.1 □m in a cell before it is deactivated. The capacity for singlet oxygen generation is different for different kind of photosensitizers used in this paper, Table 3.

Table 3.

The quantum yields for singlet oxygen generation for the sensitizers used [8]

Photosensitizer	□($^1O_2$)
MB	~ □□
AO	~ □□
TSPP	~ □□
RB	~ □1
BF	~ □□

The SSB (single strand breaks) are mainly formed through the attack of OH radicals. OH radicals react with DNA to remove an H atom, most often the H4' or the H5' of the 2'-deoxyribose located in the minor groove, leading to strand rupture. The kinetics for DNA degradation was observed by means of A 270 nm (absorption of DNA extracted from mice as previously reported), Fig.1.

Porphyrins and/or metalloporphyrins mediated cleavage of nuclei acids occurs via oxidative attack on the sugar moiety, nucleobase modifications which lead to strand scission or by photoinduced mechanism involving either the porphyrin excited state or

singlet oxygen [9,10]. Further, porphyrin-induced changes of DNA conformation could allow for the specific probing of DNA structure. The contribution of the radicalic species and of the singlet oxygen is under work and will reported subsequently.

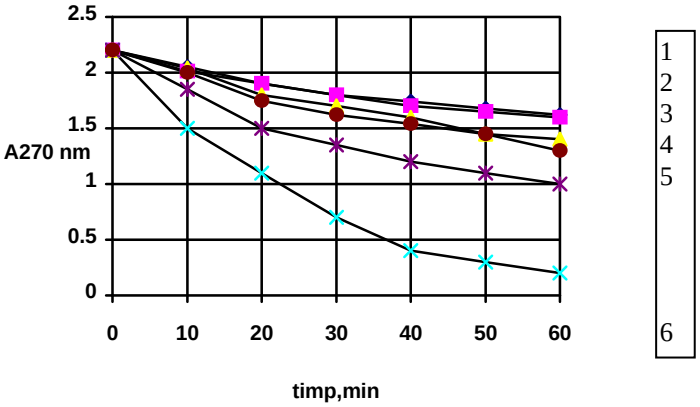

Fig.1. The kinetic of DNA degradation in different conditions
1 - BF; 2 - AO; 3-RB; 4 - AO; 5 - photon beam; 6 - TSPP

It's difficult to explain the high value for 8-OxodGuo degradation observed in control cells treated with either MB or AO by comparison with the others conditions. Ionizing radiation produces very low quantities of 8-OxodGuo, if compared with photosensitizers.

Selective degradation of the guanine residues might be the primary damage responsible for the formation of both alkali-labile bounds and strand scission. Acridine produces not only thymine dimers but also other lessions. DNA synthesis is inhibited by AO or MB in the presence of light. In the light, MB, RB, AO all decreased the melting temperature of DNA, suggesting that the DNA had been degraded [9]. Photosensitization has been shown to destroy deoxyguanosine and deoxyadenosine. Kinds of DNA damage that happens under the influence of light include altered or missing bases, single-strand breaks, and cross-linking.

When the DNA backbone is broken by PDT by the ionizing radiation, the ends contain 3' terminal phosphoglycolaldehydes or 3' terminal phosphates which cannot act as substrates for DNA polymerase I or DNA ligase.

4. CONCLUSIONS

Studies on the photodynamic effect coupled with ionizing radiation have concentrated on singlet oxygen. A major target attacked by toxic oxygen species is likely to be DNA. Also, the attack of singlet oxygen on DNA will give rise to either single stranded breaks or alkali-labile bonds. Kinds of DNA damage that happens under the influence of light include altered or missing bases, single-strand breaks, and cross-linking.

From this paper a high value for 8-OxodGuo degradation was observed in control cells treated with either MB or AO by comparison with the others conditions. Ionizing radiation produces very low quantities of 8-OxodGuo, if compared with photosensitizers and with TSPP especially.

REFERENCES

1. R.M.Ion, *Progr.Catal., 6(1),55(1997);*
2. Q.M.Zhang, H.Sugiyama, I.Miyabe, S.Matsuda, I.Saito, S.Yonei, *Nucleic Acids Res., 25, 3969(1997);*
3. A.A. Purmal, Y.Wahkow, S.S. Wallace, *Nucleic Acids Res., 22,72(1994);*
4. K.C.Cheng, D.S.Cahill, H.Kasai, S.Nishima, L.A. Loeb, *J.Biol.Chem., 267, 166(1992);*
5. R.M.Ion, *Proc.Int.Symp.DNA conformations, modifications, recognision in biomedicine, Brno, 62(2000);*
6. R.E. Krish, M.B.Flick, C.N.Trumbore, *Rad.Res., 126, 251(1991);*
7. A.Chaterjee, W.R. Holley, *Int.J.Quant. Chem., 39,709(1999);*
8. R.M.Ion, M.Grogorescu, F.Scarlat, VIR.Niculescu, Fl.Scarlat, *Rom.Rep.Phys., submitted, 2001;*
9. R.M.Ion, M.Grogorescu, F.Scarlat, VIR.Niculescu, Fl.Scarlat, *Studia Universitatis Babes-Bolyai, Physica, 321 (2000);*
10. R.M.Ion, M.Grogorescu, F.Scarlat, VIR.Niculescu, Fl.Scarlat, *Studia Universitatis Babes-Bolyai, Physica, 331 (2000);*

STUDIA UNIVERSITATIS BABEŞ-BOLYAI, PHYSICA, SPECIAL ISSUE, 2001

DEUTERIUM VARIATION OF HUMAN BLOOD SERUM

P. BERDEA[*], STELA CUNA[*], M.CAZACU[**], M.TUDOSE[**]

[*] *INCDTIM, P.O. BOX 700, R3400 Cluj-Napoca*
[**] *Spitalul Universitar CFR, Cluj-Napoca*

The deuterium content of healthy human blood plasma is about 149-150 ppm. Some variations of deuterium content with age and sex were observed in blood plasma.

We report for the first time the variation of deuterium content of blood plasma of the patients with cancer disease. The deuterium content of blood plasma of cancerous human is diminished by about 5-7 ppm compared with the healthy one. The tumors cell have a higher speed of growth than the normal cell and this results in consuming a greater quantity of deuterium. The replacement of tap water with deuterium depleted water in a drinking water for the mice diminishes the growth rate of the tumors, and the slight increase in the deuterium concentration stimulates this growth.

1. INTRODUCTION

Some studies reveal that naturally occurring deuterium is essential for maintains the normal cell growth rate of humans (1), animals (1,2) or plants (3).The course of deuteration in mice is documented (4).

Deuteration equilibrium in the body fluids is 95% attained in ten days. The incorporation of deuterium into liver, kidney and spleen reachs equilibrium by the third week.

Similarly, variations of deuterium human fluids as blood serum or urine depending on deuterium contents of drinking water and diet are also expected.

Compared with drinking water, in Central Europe, the human blood plasma is enriched by $30^0/_{00}$ in the deuterium content. Change of location frequently induces a change in the isotopic content of the blood (5). Some variations of deuterium content of healthy human blood with age and sex were observed (6).

We report another variation of deuterium content of blood serum for patients with different cancer diseases. The deuterium content of blood serum of cancerous human patients is depleted by about 5-7 ppm in comparison with healthy one.

2. MATERIALS AND METHODS

The results reported here are based on the analyses of the human blood serum for 9 patients with different cancer diseases.

The serum was separated by centrifugation and was distilled in vacuum.

The deuterium analyses of water are carried out on the hydrogen gas obtained by quantitative reduction of water sample. The water sample (about 1 μl) is introduced in a heated glass reservoir and a small portion of the sample is introduced in the mass

spectrometer at a constant rate through a glass capillary and a quartz tube containing a uranium ribbon at 650^0C, connected directly to mass spectrometer ion source.

The deuterium content is expressed:

-as deuterium ratio R=D/H in ppm units

where D is the number of deuterium atoms

H is the number of hydrogen atoms.

-as δ values in "part per thousand"

$$\delta=(R/R_S-1)\ 1000$$

where R is the deuterium ratio of sample

R_S is the ratio of international VSMOW standard (Vienna standard Mean Ocean Water)

The precision of the determination of δD values was $\pm 2^0/_{00}$.

3. RESULTS AND DISSCUTIONS

The Table1 presents the deuterium content of blood serum for nine patients with different cancer diseases.

Table1.

Deuterium contents of blood plasma for the patients with cancer diseases

Sample nr.	Code name	Sampling date	Neoplasm location	R (ppm)	δ ($^0/_{00}$)
1	HOR.	23.03.2001	colon	140.3±0.14	-99.4±1.4
2	BAN.	23.03.2001	pancreas	134.4±0.15	-137.1±1.5
3	HOI.	23.03.2001	pancreas	143.3±0.17	-80.0±1.7
4	RAD.	23.03.2001	stomach	142.2±0.14	-87.1±1.4
5	BAT.	23.03.2001	stomach	145.6±0.2	-65.2±2.0
6	COL.	23.03.2001	colon	144.6±0.16	-72.0±1.6
7	FIL.	23.03.2001	rectal	143.0±0.1	-82.0±1.0
8	PET.	23.03.2001	pancreas	144.9±0.12	-69.7±1.2
9	MIS.	23.03.2001	colon	143.6±0.15	-78.1±1.5
			Mean value	142.4±3.4	-85.6±3.4

The human serum in Central Europe is enriched with 30 ‰ compared with drinking water mean deuterium content. The deuterium contents of the blood serum of healthy humans (about -37 ‰) was higher compared with mean deuterium content of the mean drinking water deuterium content (about -69 ‰) by about 32 ‰ (5,6).

On the contrary, the deuterium content of blood serum for patients with cancer disease is lower or very close to the mean deuterium content of the drinking water. Our result is in concordance with some studies (1,2,3,4). Such a study, using deuterium depleted water, shows that naturally occurring deuterium is essential for maintaining the normal cell growth rate in animals, humans or plants. Deuterium depleted water

proved an inhibitory effect in plant growth or in proliferation of tumors cells bath for animal and human.

The tumor cells are deuterium consuming. As a consequence the deuterium content of blood serum of tumors patients is depleted in deuterium compared with healthy one.

4. CONCLUSIONS

The blood plasma for healthy human is enriched in deuterium compared with mean local deuterium content of the drinking water. For the human patients heaving different cancer diseases the deuterium content of blood plasma is diminished or close to mean deuterium content of drinking water and more depleted compared with healthy humans. Such a variation of deuterium content of human blood serum is correlated with the cancer disease .

REFERENCES

1. G. Somlyai, G. Jancso, G. Jakli, K. Vass, B. Barna, V. Lakics and T. Gaal, Naturally occurring deuterium is essential for the normal growth rate of cells, FEBS **317**, (1993), 1-4
2. D. Ieremia, Rodica Dumitrescu, Elena Nes, Restriction of cellular growth by deuterium deprivation, IV-th Nat.Conf. of Biophys., 16-18 Oct. Cluj-Napoca , (1997)
3. P. Berdea, Cristina Dobrota, C. Cosma, Stela Cuna, Growing rate decrease of the maize embryos sprouted in deuterium-deplated water (20 ppm), Colloqvium Spectroscopicum Internationale XXXI, Ankara, Turkey, Sept. 5-10, (1999)
4. J.J. Katz and H.L. Crespi, Isotope effects in biological systems in: C.J. Collins and N.S. Bowman (eds.), Isotope effects in Chemical Reactions, Van Nostrand Reinhold Company, New York (1970), pp. 286-353.
5. U.Zimermann, and U. Cegla, Der Deuterium-und Sauerstoff-18-Gehalt der Korperflussigkeit des Menschen und seine Anderung bei Ortswechsel, Natur wissenschaften, **60**, (1973), 243-246.
6. L. Blaga, Lucia Blaga, The deuterium content of human metabolic fluids in relation with human metabolic processes (in Romania), IFA-Bucuresti, Scientific Report (1978), 1-4

AUTOMATION OF A THERMAL IONISATION MASS SPECTROMETER

A. PAMULA, M. LEUCĂ, S. ALBERT, ADRIANA BENȚA

National Institute for Research and Development of Isotopic and Molecular Technologies, P.O.Box 700, 3400 Cluj-Napoca 5, Romania

Introduction

In the Mass spectrometry, chromatography and ion physics laboratory, a thermal ionization mass spectrometer was designed and built. It is a single focussing instrument with a stigmatic magnetic sector analyzer. The block diagram of the apparatus is shown below:

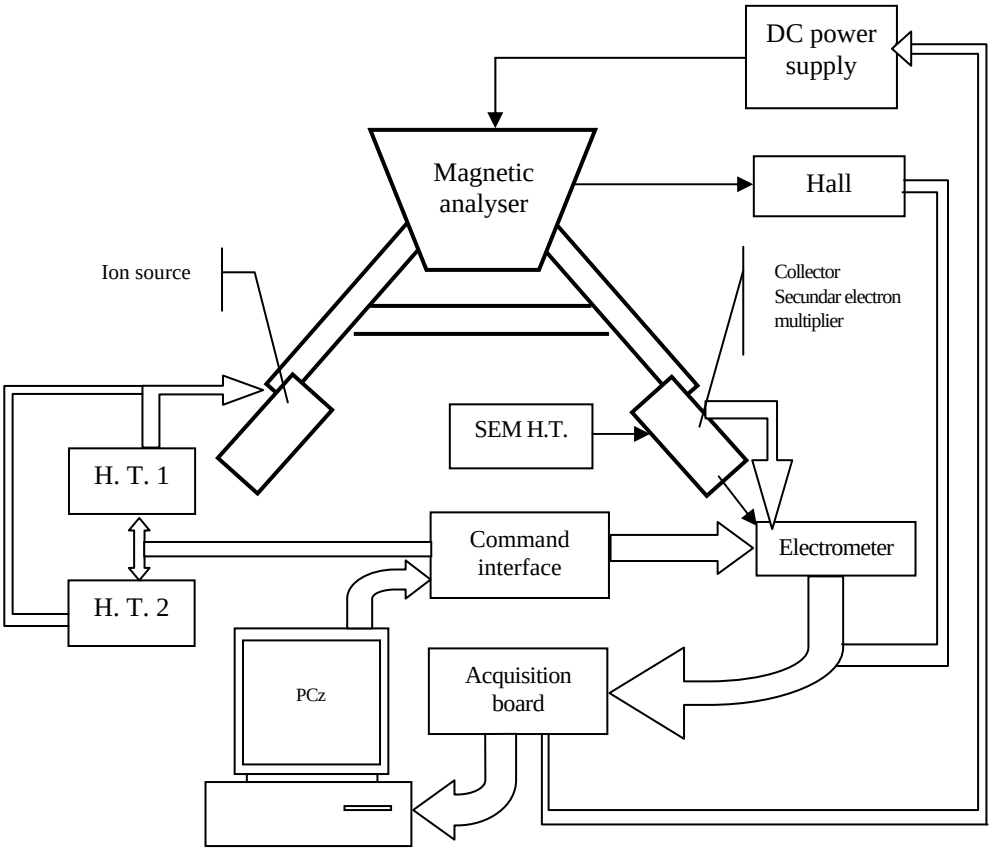

Figure 1: Block diagram of the mass spectrometer

The automation of the instrument concerns the scanning of the mass spectrum, commands for the range and gain of the electrometer, data acquisition, and data processing.

The spectrometer was built with a single collector system and a secondary electron multiplier. As we have to perform isotopic analysis of uranium, the masses we are interested in are 235 and 238. If we would use a continuous scan of the mass spectrum, we should scan a large mass interval 234.5 .. 238.5. This means that there should be an important delay between the collection of the ^{235}U isotope and the collection of the ^{238}U isotope. Fluctuations of the electric parameters, and/or of the thermal conditions in the ion source could appear in this interval and produce important alteration of the analysis accuracy. To minimize these inconvenients, we perform a magnetic scanning only over a mass peak, afterwards we realize a "jump" to the other peak modifying the energy of the ions in the ion source and perform a magnetic scanning between the same limits but in the reverse direction. The electrometer gain is commuted to the right value to ensure detection sensitivity. The "zero level" and the amplitude of the ion signal are detected and the amplitude of the ion peak is registered.

The entire process is monitored by a PC computer equipped with an acquisition board. An interface was designed and realized, to control the electrometer gain and sensitivity and to commute the high voltage supplied to the ion source.

The command interface

The parallel port LPT1 is used to transmit commands from the PC to the mass spectrometer. A "data" octet is used on this purpose. The bits 1 .. 3 are acting on the electrometer "range", the bits 4 ..6 are used to set the electrometer gain and the 7^{th} bit commutes the high tension supplied to the ion source. Table 1 shows the signification of each bit in the data octet.

Setting the bit 0 .. 5 on "0" makes its significance active. "1" of the bit D6 sets the high tension supplied to the ion source to the value fitted for the collection of the ^{238}U ion current. "0" on this bit brings the ^{235}U ion to the collector.

The electrometer was designed as a modular structure in what concerns the measuring range and gain command. The command schema is a three states bistable corresponding to the three measuring ranges, respectively gains. It is made-up with a MOS 40107 circuit, gate and NOT, with two entries, open collector type.

Table 1.

The command byte

Bit	Pin		
D0	1	$10^{-6}A$	Electrometer range
D1	2	$10^{-8}A$	
D2	3	$10^{-10}A$	
D3	4	x 1	Electrometer gain
D4	5	x 10	
D5	6	x 100	
D6	7	selection of the high tension	
D7	8	not used	

The activation is achieved by a push button from the front panel. The circuit commutes in the new state, which remains memorized and is shown by a LED on the front panel. The command from the PC is connected in parallel with the push button. The command interface is made-up also with the MOS 40107 circuit. Thus, it is possible to send commands for the commutation of the range and/or the gain either manually from the front panel or from the computer.

The high voltage unit of the mass spectrometer contains two independent high voltage supplies. These allow preselecting two independent values for the ion accelerating voltage. A set of relays commutes one or the other preselected voltage to the output of the high voltage unit.

The electrical schema of the command interface is shown in figure 2 and figure 3.

The scanning of the magnetic field in the analyzer is performed via a 12 bits digital analog converter placed on the acquisition board. One command digit corresponds approximately to 2 Gs. As this scanning resolution is too rough, the two excitation coils of the analyzer magnet were separated. One coil is supplied with 10 A. constant CC, the other one is excited by a CC power supply controlled by the digital analog converter. Thus, the scanning resolution is better then 1Gs/digit

The software interface

A software application, which controls the analytical process, was written. It offers dialog boxes to supply the main parameters like the sample name, the electrometer gain for each ion current, the magnetic induction in the analyzer. A very friendly graphical interface allows the focusing of the spectrometer. During the analysis, the peak amplitude is graphically represented on the display. The program takes into account the fluctuation influence of the ion current intensity, the mass discrimination in the ion source and achieves a statistical treatment of the measured isotopic ratios.

Conclusions

With very few hard modifications, it was possible to achieve a quasi-complete automation of the thermal ionization mass spectrometer.

Many other "old generation" mass spectrometers with high ion optics characteristics could be updated in this way.

The scanning method allow peak acquisition in a relatively sort time, improving thus the accuracy of the apparatus.

STUDIA UNIVERSITATIS BABEŞ-BOLYAI, PHYSICA, SPECIAL ISSUE, 2001

UPGRADING OF THE HP-5985A QUADRUPOLE MASS SPECTROMETER

N. LUPŞA, V. MIREL, A. PAMULA, N. PALIBRODA, ALINA N. NICA

National Institute for Research and Development of Isotopic and Molecular Technologies, P.O.Box 700, 3400 Cluj-Napoca, ROMANIA

The Hewlett - Packard 5985A instrument is a quadrupole mass spectrometer.

Features

- mass range 10 to 1000 amu
- gas chromatograph coupling
- direct introduction probe system (DIP)
- ion source with electronic impact ionization and chemical ionization
- ions detection with secondary electrons multiplier
- electrometer logarithmic amplifier
- HP 21 MX-E minicomputer (with 64 kB RAM) coupling

Hardware description of the designed interface

The HP 5985A mass spectrometer is designed to communicate with the HP 21 MX-E minicomputer through a bi-directional 16 bit parallel interface with separated lines for the two directions. TTL integrated circuits are used. There is no galvanic separation between the TTL and analog circuits in the electronic units of the spectrometer.

This upgrade aims the replacement of the old HP 21 MX-E computer by an IBM compatible PC. For this purpose, a new interface had to be built.

This interface stays of two parts: an electronic block placed alongside of the other original electronic units of the spectrometer and an interface board, which is placed the computer. The data are transmitted between the spectrometer and the electronic block in parallel on 16 bit and between the electronic block and the interface board there is a serial transmission of data, entirely controlled by the electronic block. The data transfer rate of 1 Mbytes/ sec. is much higher than the transfer rate of a standard serial interface RS232C.

The electronic block ensures galvanic insulation between the spectrometer and the computer circuits by optocouplers. These are placed on the routes of the serial communication signals. The galvanic insulation is necessary in order to avoid the possible perturbation of the analog circuits of the spectrometer by the disturbing signals.

The electronic block and the interface board realise two communication lines (one in each direction) between the spectrometer and the internal bus of the computer.

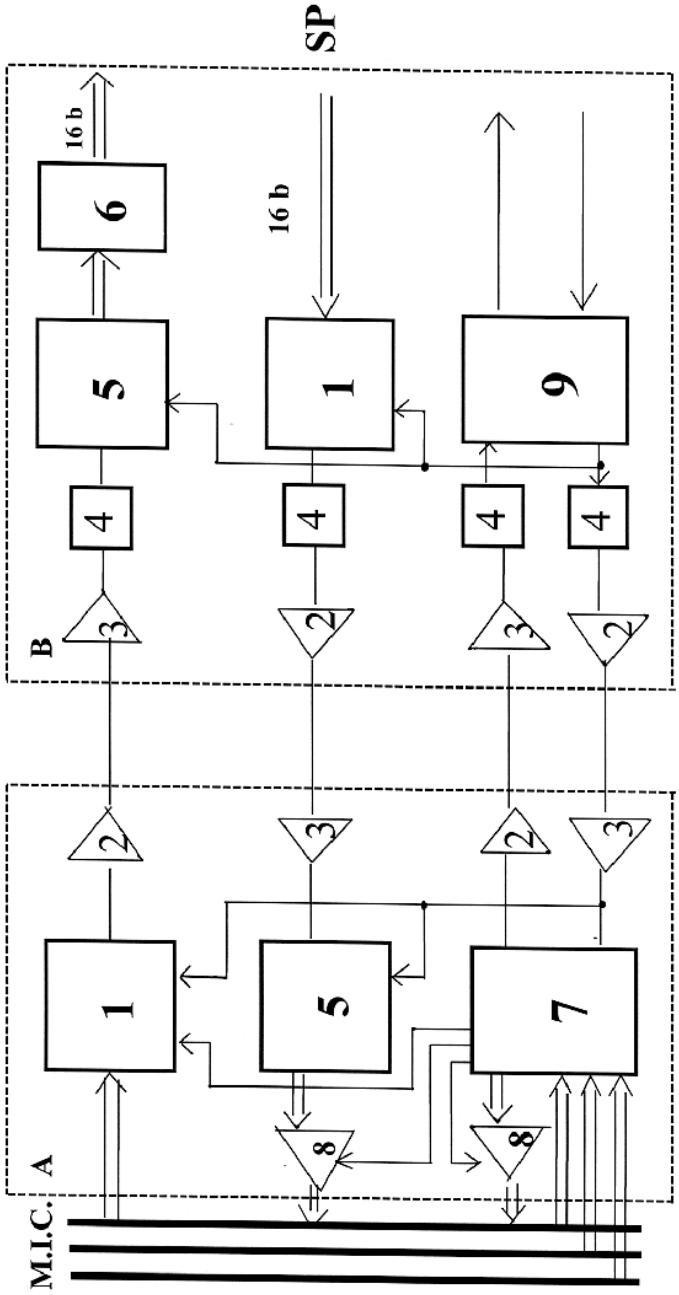

Fig.1 The block diagram of the interface

A. INTERFACE BOARD **B. ELECTRONIC BLOCK**

1. parallel / serial converter 2. transmitter cable 3. receiver cable 4. optocoupler 5. serial / parallel converter 6. buffer register
7. command circuit 8. bus driver 9. command signals generator
M.I.C. - computer internal bus SP - connection with the mass spectrometer

The transmission of the information from the computer to the spectrometer is realized via a 16 bit data register connected with a shift register for the parallel / serial conversion, an amplifier for the signals transmission by cable (the registers and the amplifier are placed on the interface board) and the amplifier for the signals reception, the optocoupler, the 16 bit shift register for the serial / parallel conversion and the 16 bit buffer register (all these placed in the electronic block).

The transmission of the information from the spectrometer to the computer is realized via a 16 bit shift register for the parallel / serial conversion, the optocoupler, an amplifier for the signals transmission by cable (all are placed in the electronic block) and the amplifier for the signals reception, the 16 bit shift register for the serial / parallel conversion (all placed on the interface board).

The electronic block, contains also - sequential circuits which generate the necessary command signals for the serial data transmission in both direction. The interface board contains circuits for the connection with the internal bus of the computer (register addresses decoder, the bus connection, the initiation of data transfer and status reading).

Software description

Computer programs were written for the:

- acquisition of spectra,
- calibration and
- tests.

The acquisition program is the main program which controls the analytical process. The user can select the spectrometer parameters: the potential supplyed to the ion source electrodes, the electron-emission current, the ion source temperature, the secondary electron multiplier voltage, the mass range to be scanned. Once the electrical parameters set up, the spectra acquisition can be performed. The program monitors the scanning of the preselected mass range, the reading of the ionic current values and their storage.The computer display is divded in two registers. The total ion current versus time and the last mass spectrum are plotted.

The tunning program allows the adjustment of the electrical parameters, in order to obtain a correct peak shape and the a right relative peak height in a known mass spectrum of a calibration compound.

The calibration program updates the mass scale of the quadrupole filter

The structure of the programs. The software described above is integrated as a turbo-vision application. The object oriented programing led to a friendly interface based on menus and commands accessible via the status line.

Test programs are used to chek the functionality of the spectrometer and of the interface components.

Conclusions

- the minicomputer HP 21 MX-E, which is physicaly and moral worn out, was eliminated from the spectrometer configuration
- The interface hard and soft, has requirements fulfilled by most IBM-compatible PC.
- The data acqusition procedures generates files wich are processed by the software packet "CROMA". This program is used to process all the GC-MS coupling data form the Mass Spectrometry Laboratory of INCDTIM.

REFERENCES

1. HP 5988A Mass Spectrometer Hardware Manual, Hewlett Packard Company, 1985
2. A. Lesea, R. Zaks, Microprocessor interface techniques, Sybex Inc., 1978
3. V. Mercea, P. Ardelean, D. Ioanoviciu, A. Pamula, D. Ursu, Introducere în spectrometriea de masă, Ed. Tehnică, Bucureşti, 1978
4. J. H. Jansen, Handboek digitale electronica deel 1 - Bouwstenen in TTL en CMOS, Kluwer Technische Boeken, 1982
5. Gh. Săndulescu, Protecția la perturbații în electronică industrială şi automatizări, Ed. Tehnică, Bucureşti, 1985
6. V.Căprariu, A. Enyedi, M. Muntean, M. Chiorean, Sistemul de operare DOS - Ghidul Programatorului, microInformatica, Cluj-Napoca, 1991
7. T. Bălănescu, Ş. Gavrilă, H.Georgescu, M. Gheorghe, L.Sofonea, I.Văduva, Programarea în limbajele Pascal şi Turbo Pascal, vol. 1, vol. 2, Ed. Tehnică, Bucureşti, 1992

STUDIA UNIVERSITATIS BABEŞ-BOLYAI, PHYSICA, SPECIAL ISSUE, 2001

POTENTIOSTATIC SYSTEM WITH DATA ACQUISITION FOR ELECTROCHEMICAL MEASUREMENTS

N. LUPŞA, GH. MIHĂILESCU, V. MIREL, ALINA NICA, A. PAMULA, STELA PRUNEANU

National Institute for Research and Development of Isotopic and Molecular Technologies P.O.Box 700, 3400 Cluj-Napoca, ROMANIA

Introduction

We have designed and built a potentiostatic system which is connected to a computer from the PC family, in the same way as any other equipment (e.g. scanner, printer).

The potentiostatic control is realized through the computer, and the obtained data are stored in the computer memory, plotted on the screen and recorded on the disk as a file .The file data are available for late offline processing.

The voltage value lays between -5V and +5V with a speed which can be chosen between 2.5 mV/s and 1000 mV/s. For the current measurement there are five levels with the following maximum values: 10 µA, 100 µA, 1mA, 10 mA, 100 mA.

The main parts of the potetiostatic system are:

- the electrochemical cell interface
- the electronic block
- the interface board from the computer.

A control and data acquisition program ensures the potentiostatic system function.

Hardware description of the potentiostatic system

The interface with the electrochemical cell contains the following electronic circuits: the electrometer amplifier for the reference electrode and the current amplifier for the current measurement through the cell. These circuits work at low - level signal.

The electrical connections from the electrochemical cell to the cell interface are made through shielded cables, and if it is necessary, even the cell can be shielded inside the interface box. The shields are made in order to extend the measurement range to lower current values (nanoamper).

The electronic block has the following component parts:

- a d.c. amplifier for the electrochemical cell excitation
- the circuits for automatic adjustment of the current loop
- a 12 bit digital / analog converter for numeric scan
- logic circuits for the selection of the current measurement range
- a 12 bit analog / digital converter for current measurement
- circuits for data transmission to the computer

- supply sources

In the electronic block there are also circuits for galvanic isolation (realized with optocouplers) between the potentiostat circuits and the computer. The galvanic isolation was made in order to interrupt a direct way of transmission of the possible disturbing signals to the electrochemical cell (within the electrochemical cell there are low level signals).

The transmission of information (data and commands) through the cable, between the electronic block and the interface board of the computer is serial. Data transfer rate of 125 Kbytes/s is higher than the data transfer rate of the standard serial interface RS232C. Specific circuits placed in the electronic block assure the serial transmission.

The logic circuits used in the electronic block are CMOS type (so the supply current is reduced). The interface board inside the computer achieves the connection between the internal bus of the computer and the electronic block. On the interface board there are circuits for the serial transmission and circuits for the data transmission between data registers and computer bus.

Software description

The control and data acquisition program allows to:

- adjust the values of the operation parameters (voltage range, scanning speed, scanning mode: singular or repeatedly, current range)
- the scanning start and stop
- data record on the disc, in a file

When the scanning is performed, the spectra are also plotted on the screen. Test programs are used to verify the functionality of the potentiostatic components (interface board, the scanner, analog - numeric converter etc.).

The programs were created using specific subprograms for the control of the potentiostatic components (data transmission line, the scanner, analog / digital converter, the circuits for the selection of the current measurement range).

Electrochemical deposition of thin chalcogenide layer for copper cation detection

A thin chalcogenide layer was deposited by cyclic voltammetry on the surface of a metallic electrode. An aqueous combination of $AgNO_3$, $CuSO_4$, H_2SO_4 and Se IV was used as electrolyte /7/. The potential was varied between 50…72 mV/SCE, at a speed rate of 24mV/s. In order to test the response of chalcogenide layer, three electrodes were prepared (I, II and III). A number of 50 cycles were performed on the first two electrodes (I and II) while on electrode number III were performed 100 cycles. Typical cyclic voltammograms obtained during chalcogenide layer deposition are presented in fig.1

After preparation of the chalcogenide layer, the electrodes were conditioned for 15 min in 10^{-6} M $CuSO_4$ with ionic strength j=0.01 (KNO_3) and following they

standard solutions were prepared from a stock standard solution (1 M $CuSO_4$) by sequential dilution.

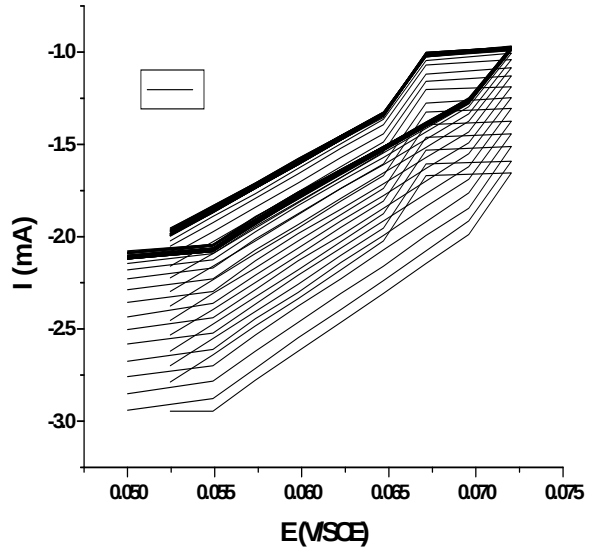

Fig.1 Cyclic voltammograms obtained during deposition of a thin chalcogenide layer (potential range: 50…72 mV/SCE; speed rate: 24 mV/s)

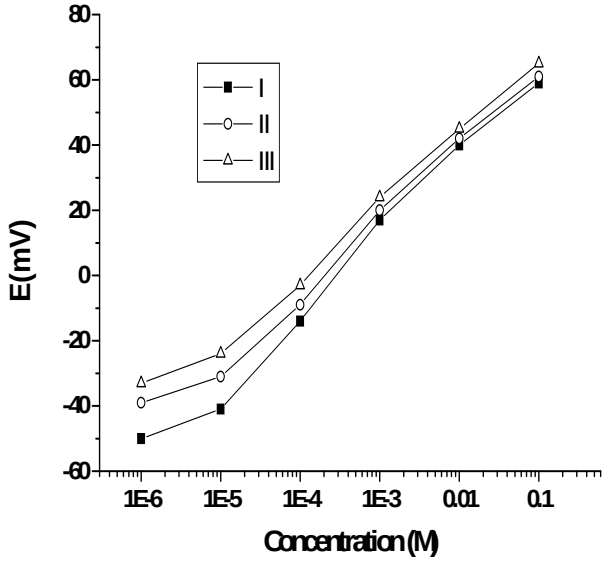

Fig.2 Calibration functions for the thin chalcogenide layer electrodes (I, II and III) in Cu^{2+} solutions

In fig. 2 are represented the calibration functions of the three electrodes. One can see that the electrodes have linear response in the range of $10^{-1}…10^{-5}$ M, so the layer is suitable for copper cation detection.

Conclusions

The potentiostat coupled to the computer has the following advantages:

- the data processing time is reduced
- it allows a much higher data record
- it is easier to work with it

The build apparatus is open to some improvement:

- analog scanning (the elimination of the numeric scanning levels)
- the current range should be extended to lower levels (nanoamper)

REFERENCES

1. R. Greef, R. Peat, L. M. Peter, D. Pletcher, J. Robinson, Instrumental methods in electrochemistry , Ellis Horwood Limited , 1985
2. Electroscan™ 30 - Electroanalitical System, Beckman Instruments, Inc., Scientific Instruments Division, Fullerton, California 92634, January 1967
3. Bulletin 7079, An introduction to electroanalysis, Beckman Instruments, Inc., Scientific and Process Instruments Division, Fullerton, California 92634
4. Gh. Sandulescu, Protectia la perturbatii în electronica industriala si automatizari, Ed. Tehnica, Bucuresti, 1985
5. V.Caprariu, A. Enyedi, M. Muntean, M. Chiorean, Sistemul de operare DOS - Ghidul Programatorului, microInformatica, Cluj-Napoca, 1991
6. T. Balanescu, S. Gavrila, H.Georgescu, M. Gheorghe, L.Sofonea, I.Vaduva, Programarea în limbajele Pascal si Turbo Pascal, vol. 1, vol. 2, Ed. Tehnica, Bucuresti, 1992
7. M.T.Neshkova, Laboratory Robotics and Automation, 4 (2000)216, vol.12

STUDIA UNIVERSITATIS BABEŞ-BOLYAI, PHYSICA, SPECIAL ISSUE, 2001

IMPROVEMENT OF ISOTOPE RATIO MASS SPECTROMETRY ANALYSIS BY CHANGING THE AMPLIFIER CHANNEL AND BY AUTOMATIC DATA ACQUISITION

N. LUPŞA, V. MIREL, STELA CUNA, ALINA N. NICA, A. CHIŞ

National Institute for Research and Development of Isotopic and Molecular Technologies, P.O.Box 700, 3400 Cluj-Napoca, ROMANIA

Introduction

The goal of our work was to modernize the ATLAS M - 86 mass spectrometer in order to perform much accurate and precise isotopic ratio analyses. The improvement was realized by changing the old electronic units and by coupling the mass spectrometer to a personal computer (PC) - with the purpose to allow all of the spectrometer components to be controlled by the computer.

Our research was focused on the ionic current measurement. The electronic components realizing this are the following:

- the spectrometer interface
- the control block of the spectrometer
- the ionic currents measurement block

Hardware description of the electronic components

1.Spectrometer interface

The spectrometer interface is a board pluged inside the computer and it assures the data transfer between the computer and the spectrometer. The data are transmitted byte by byte (the bits of one byte are transmitted in parallel). In fact the transmission is realized between the interface board and the control block of the spectrometer.

Through the interface view, the control block of the spectrometer is an ensemble of 8 bits addressable registers.

In the control block, besides the registers, there are components controlled through similar operations with the register writing, but without providing the writing information. The control block uses only the pulse which trigers the writing in a register.

2. The control block of the spectrometer

The control block enssures the data transmission between the computer and each electronic block of the spectrometer.

It consists of the following electronic blocks:

- for the control of the vacuum system
- for the control of the sample introduction system
- the supply block of the ions source
- for the scanning control
- the ionic currents measurement block

The data transmission between the control block of the spectrometer and each block enumerated above is serial, in order to be realized with less wires and to reduce the number of circuits which make the necessary galvanic insulation of the analog circuits (they are sensible to perturbations). For the measurement of ionic currents were used:

- voltage - frequency conversion to determine the isotopic ratios
- direct conversion, with successive approximation in order to obtain the spectra

The measurement block contains voltage - frequency converter with successive approximation with serial outputs. The control block of the spectrometer contains the counters and the time base, respectively the logic of the control and the data register with serial input.

- **Serial transmission control**

Between the control block of the spectrometer and the electronic blocks there is a serial data transmission. The serial transmission control (realized on two boards) generates the necessary sequence commands for a byte transmission, from the data register of a board interface of a block to the corresponding register of that block.

- **The counters**

There are two 24 bits binary counters. For reading, they are distributed in three registers of 8 bits each.

3. The ionic currents measurement block

The ionic currents measurement block realizes the measurement of the ionic currents on two collectors (Faraday cup type collectors): CF1 and CF2.

There are the following measurement possibilities:

- simultaneous measurement of the two currents for high accuracy determination of their ratio ;

- the measurement of one of the two currents (any of them) to obtain a spectra.

The ionic currents measurement block contains:

- two channels electrometer
- the interface for the two channels electrometer
- two voltage - frequency converter for the simultaneously measurement of the ionic currents of the two collectors (CTFA and CTFB)
- analog / digital converter for the measurement of one current in order to obtain a spectra (CAN)
- multiplexers for the connection to the converters inputs the proper signals (measurement and calibration signals)
- scale switches
- circuits for galvanic isolation and for the signals transmission through the connection cable with the control block of the spectrometer

- **The two channels electrometer**

The two channels electrometer contains current / voltage converter designed with electrometer amplifiers. There are two signal channels: A and B. Because most of the time the ionic currents values are much different between them (ratios of 1 to 10,...., 1 to 100) we chose different transfer factors for the two channels. The channel B is more sensible. For this channel there is the possibility to make the zero adjustment of the electrometer amplifier; in order to achieve this we used an analog / digital converter. To each amplifier the resistor from reaction can be chosen with a relay. Another relay allows to switch the connection of the two collectors to the amplifier inputs (CF1 to channel A and CF2 to channel B, respectively CF1 to channel B and CF2 to channel A).

- **The interface for the two channels electrometer**

The interface for the two channels electrometer has the following components: digital / analog converter for the zero adjustment, the circuits which drives the relays and provides their status, and the necessary registers.

REFERENCES

1. MAT - Mass Spectrometer M 86 - Description, operation, service, Atlas Mess - und Analysen Technik, GMBH, Bremen, 1962
2. C. Iliescu, C. Ionescu - Golovanov, W. Szabo, I. Szekely, D. Bărbulescu, Măsurări electrice şi electronice, Ed. Didactică şi Pedagogică, 1983

3. I.Ardeleanu, H. Giuroiu, L.L. Petrescu, Circuite Integrate CMOS - Manual de utilizare, Ed. Tehnică, Bucureşti, 1986
4. A. Vătăşescu, s.a.m.d., Circuite integrate liniare - Manual de utilizare, vol.3, Ed. Tehnică, Bucureti, 1984
5. Gh. Săndulescu, Protecția la perturbații în electronică industrială şi automatizări, Ed. Tehnică, Bucureşti, 1985
6. V.Căprariu, A. Enyedi, M. Muntean, M. Chiorean, Sistemul de operare DOS - Ghidul Programatorului, microInformatica, Cluj-Napoca, 1991
7. T. Bălănescu, Ş. Gavrilă, H.Georgescu, M. Gheorghe, L.Sofonea, I.Văduva, Programarea în limbajele Pascal şi Turbo Pascal, vol. 1, vol. 2, Ed. Tehnică, Bucureşti, 1992
8. V. Mercea, P. Ardeleanu, D. Ursu, Introducere în studiul spectrometriei de masă, Ed. Tehnică, Bucureşti, 1978

STUDIA UNIVERSITATIS BABEŞ-BOLYAI, PHYSICA, SPECIAL ISSUE, 2001

SYSTEMS FOR HPLC SAMPLE INJECTION

GABRIEL POPENECIU

National Institute for Research and Development of Isotopic and Molecular Technologies, P.O.BOX700, 3400, Cluj-Napoca 5, Romania

ABSTRACT. The design characteristics and techniques of using HPLC sample injectors differ markedly. These differences affect a chromatograph's ability to provide accurate analitycal results. The HPLC sample injectors discussed in this paper are the types currently used in high performance liquid chromatography techniques. All of them transfer atmospheric pressure sample from a syringe or vial to a sample loop. The loop is then connected by valving action to the high pressure pump-to-column stream, which carries the sample onto column.

1. INTRODUCTION

Early liquid chromatography injectors were similar to those used in gas chromatography. A tee connected the source of mobile phase to column and one port of the tee contained an elastomeric septum. Sample was transferred from syringe to column by piercing the septum with the syringe needle. This insertion of sample directly into flowing mobile phase exposed both syringe and septum to high pressure solvent, compromising precision and reliability. Modern designs avoid these problems, because the sample is transferred from syringe to a sample lop at atmospheric pressure and the loop is then connected by valuing action to the high-pressure pump-to-column stream, which carries the sample onto the column.

Flow of liquid through the sample, and indeed through all tubing of the chromatograph, has a laminar flow pattern. The fluid velocity is maximum on the axis of the tube and decrease to zero at the wall, so the front end of the sample becomes diluted. This phenomenon manifests itself in different ways in the various types of injectors discussed below.

The design characteristics divided HPLC injectors into four types. Figure 1. presents the injector flow diagram for each type.

Type 1 Injectors - use a completely filled sample loop to determine the injected volume. These simple, reliable devices are six-port rotary valves. A syringe is used to push or suck an excess of sample into a sample loop, filling it completely. Highly precise injections are achieved because the loop volume determines the injected volume.

Type 2 Injectors - use a microsyringe to transfer sample into the loop. The sample size is always smaller than the loop volume, so it is the syringe which determines the injected volume. No sample is trapped or wasted, but the precision is not as high as type 1.

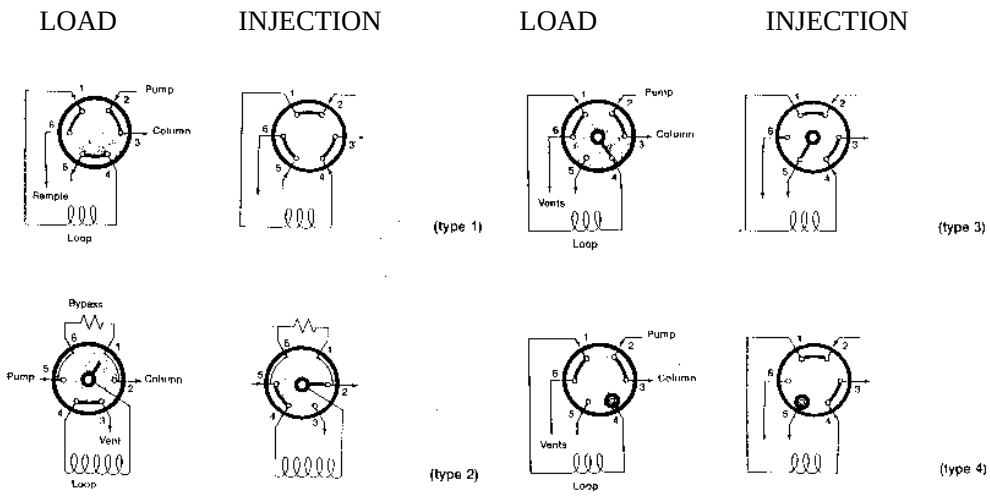

Figure 1. Injector Flow Diagrams. I - Load; II - Injection. The view is from the stator -rotor interface, where the flow switching takes place, as seen from the front of the injector. The small circles represent the ports in the valve stator. The bold arcs and radial lines represent the connecting passages in the rotor, which turn 60^0 clockwise when the injector is moved from the load position to inject position. The large circles represent the needle port.

Type 3 Injectors - use both complete and partial filling methods, but trap some sample. The loop is loaded by inserting the syringe into the needle port and dispensing the contents. The syringe is left inserted in the port until after the valve is switched. The switching action inserts the loop into the stream without exposing the syringe to high pressure. In the injection position the syringe is removed and some sample remains trapped in a connecting passage of the injector. There are three consequences of this trapped volume: sample is wasted, the injector must be flushed after each injection and the syringe reading is in error by the amount of trapped volume.

Type 4 Injectors - also uses both methods, but does not trap sample. This type is similar to type 3 injector but it does not contain a connecting passage between syringe needle tip and sample loop. It therefore not trap sample and there is no sample waste, no syringe reading error and no need to flush between injections, except in trace analysis.

2. TECHNICAL SOLUTIONS

We had realise the design and the development of the **Syringe Loading Sample Injector *Model SIA100***, belongs to type 4 mentioned above. It is a six ports rotary valve in which loading of the sample loop is accomplished with the syringe through a needle port built into the valve shaft.

2.1 Theory of operation

Figure 1. (diagrams for type 4) shows the flow diagram: in the load position the high pressure eluting solvent flows to the column directly via ports 2 and 3. The loop is loaded at the atmospheric pressure from a syringe via the needle port, which aligns with stator port 4. Excess solvent or sample exits the loop via vent port 6. Rotation of the shaft clockwise through 60^0 switches to the inject position. The eluting solvent flows to the column via the sample loop, forcing the sample ahead of it. Note that the sample now travels in a direction opposite to that when it was loaded, flowing to the column with minimum delay.

Figure 2. shows the needle port geometry. When the syringe needle is fully inserted, the flat tip of the needle touches the flat face of the stator so that the entire volume of sample discharged from the syringe enters the stator passage which is part of the sample loop. Therefore is no sample loss. The flat stator face is polished alumina ceramic, a hard surface which cannot be damaged by syringe needle.

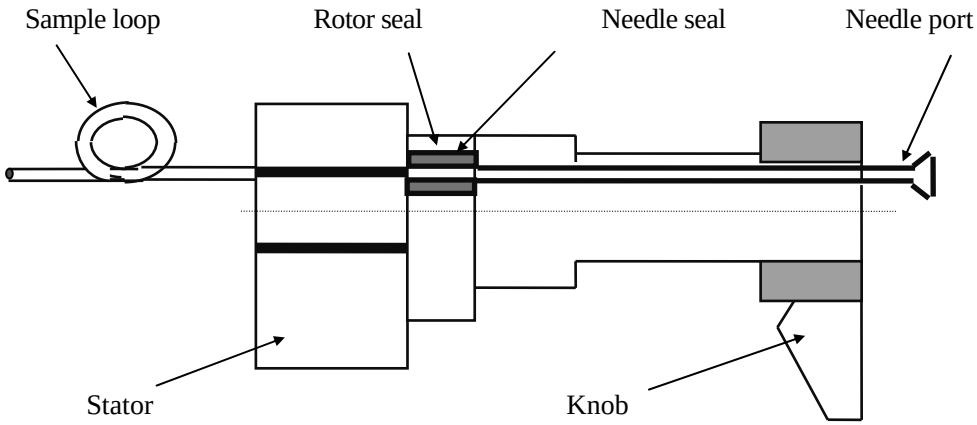

Figure 2. Model SIA100 Needle Port Geometry

2.2 Sample loading methods

Two methods of loading the sample can be used: the complete loop filling method and the partial filling method. So the great advantage to the user of the Model SIA100 is that it can be used as a conventional fixed loop injector, which is known to give the best volumetric precision, or as a variable volume injector with zero sample loss.

3. DESCRIPTION

Figure 3. is a general view of Model SIA100. The stator (13) is 10TiMoNiCr175 stainless steel and contains six ports for 1,6 mm tubing. The stator face (11) is a polished alumina ceramic disc mounted in a stainless steel ring (16) which in turn is held in proper alignment on stator by two pins. Sandwiched between the stator and the alumina face stator is a seal disc (14) which form a high pressure seal between the two

parts and joins the six ports to the six mating holes in the stator face. The rotor face (10) is a Teflon rotor seal. Slots in the rotor seal make flow paths between the adjacent stator ports and turning the rotor 60^0 switches the flow paths as shown in Figure 1. Two stop pins (17) and the rotor pin (18) limit the rotation to 60^0. A thrust bear (5) and four conical spring washers (6) push the rotor (7) and rotor seal against the stator face with sufficient force to hold the operating pressure.

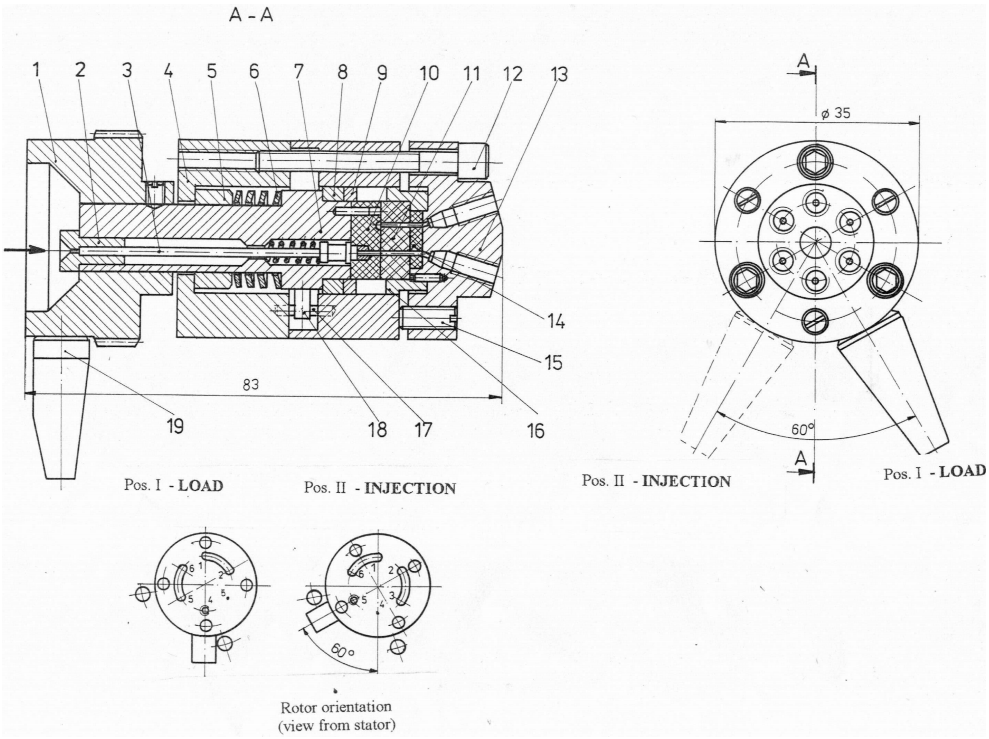

Figure 3. Model SIA100 General View: 1- action gear; 2-needle guide; 3-needle port tube; 4-body; 5-thrust bearing; 6- spring washers; 7-rotor; 8-bearing ring; 9-isolating seal; 10-rotor face; 11-stator face; 12-stator screws; 13-stator; 14-seal disc; 15-set screws; 16-stator ring; 17-stop pins; 18-rotor pin; 19-knob.

There is an off-axis hole through the rotor which is in line with the needle port hole in the rotor seal. This is the hole through which the sample loading syringe needle passes. A Teflon sleeve is embedded in the rotor seal and the needle port tube (3) pushes against the outer edge of this sleeve with spring tension just sufficient to compress the Teflon around the needle. This forms the needle seal which insures that all of the sample liquid passes into the stator passage. The needle guide (2) is tight fit over the needle port tube and holds it in place inside the rotor shaft.

Model SIA100 allows two operating modes: manual injection with handle and automatic injection with an electromagnetic actuator built around it.

Figure 4. shows SIA100 actuator, this is a rotary double-acting electromagnetic actuator with two electromagnets (A;B), A for load position and B for inject position. Piston (3) motion is converted to shaft rotation by a rack and pinion gear (4). The state of the model SIA100 Injector, is indicated by two optic sensors (4) . These can signal an integrator to start or keep a microprocessor informed of valve position.

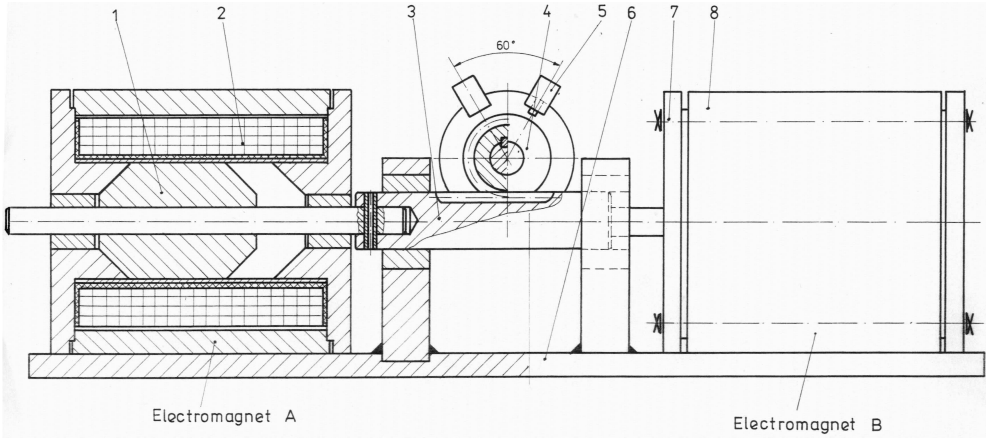

Figure 4. Model SIA100 Actuator View: 1-plunger; 2-solenoid; 3-rack; 4-gear drive; 5-photosensors; 6-support; 7-electromagnet body; 8-electromagnet lids.

4. EXPERIMENTAL MEASUREMENTS

The HPLC sample injector, model SIA100 was submitted to some experimental measurements to find the answers to the following questions:

a) What precision can be expected from an injector?
b) What volumetric accuracy do injectors provide ?
c) How can the design solutions eliminate the cross contamination ?

a) Injector volumetric variance affects analitycal precision of the system HPLC and it depends by the method of injection:

- partial filling: the volumetric precision depends on the syringe - the observed system precision which we achieved using the Model SIA100 Injector with 10µl partial loop loading via 10µl syringe was 0.35% relative standard deviation (RSD).
- complete filling: the precision depends on the density stability of the sample liquid - the observed system precision which we achieved using the Model SIA100 Injector with 20µl loop, completely filled was 0.06% RSD.

In summary, complete loop filling is the method of choice when highest analitycal precision is required and it contributes only about 0.03% RSD, compared to 0.3% contribution with partial filling method.

b) The volume of sample that is actually injected onto column does not always correspond with the syringe reading in the partial loading technique, or with the loop volume in the complete loading technique. The magnitude of this error depends on the type of injector and manner in which the loop is loaded.

The accuracy characteristics of the Model SIA100 were investigated using the following method: different sample volumes were loaded into the loop from a syringe, and the resulting peak areas or peak heights were plotted, as in Figure 5. These data indicate that the offset error is essentially zero, and that a volume of 0.1µl can be accurately injected.

In summary, we can state that the volume of sample delivered from a syringe in a partial filling method should be less than the actual loop volume: 50% is a safe value. The volume of sample transferred into a loop in the complete filling method should be more then the actual loop volume: five times the loop volume is usually enough and this can be reduced by segmentation.

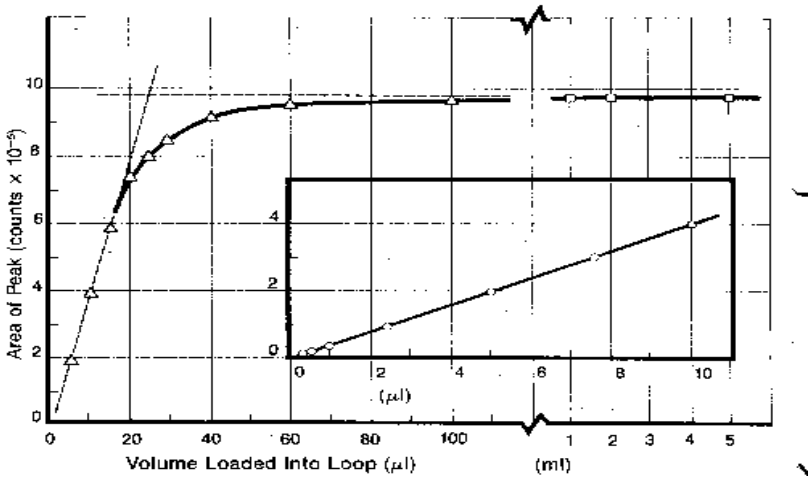

Figure 5. Accuracy of Model SIA100 sample injector. Data were obtained using three syringe size: 10 µl (o), 100µl (Δ) and 5 ml (□). The straight line correlation coefficient is 1.000. Departure from linearity starts around 15µl , i.e., at about 60% of actual sample loop volume.

c) Even thought the Model SIA100 sample injector has been design to eliminate the trapped volume, we would expect there to bee a very small amount of cross contamination if the injector is not flushed between injections. This is because of sample traces left on the surface of the needle seal and rotor seal, and in the liquid left the needle port. After a lot of measurements we can say that the contamination is less than 0.1% for a 10 µl injection.

5. CONCLUSIONS

Model SIA100, presented in this paper, is an automatic syringe loading sampler injector with an electromagnetic actuator built around it in a compact package. This combination provides an injector which can be applied to every liquid chromatographic task.

In manual operating mode it can be used with a partial loop loading for maximum volumetric versatility, allowing accurate injection volume of 1 µl to 1 ml. And it can be used with complete loop loading for maximum volumetric precision, achieving absolute area precision as little as 0.05 RSD.

The primary application of Model SIA100 is as a component of automatic injection systems . When connected to a autosampler it is used for unattended routine analysis of different samples. When connected to a single sample reservoir it is used for automatic repetitive injection of the same sample for different purpose: automated methods development, precision studies, preparative separations.

The features of Model SIA100 are listed bellow:

- Maximum versatility in HPLC sample injection.
- Two operating modes:
  - Automatic injection with electromagnetics.
  - Manual injection with handle.
- Manual injection capabilities:
  - Complete loop filling for precision.
  - Partial loop filling for flexibility.
  - Zero sample loss/no flushing.
- Automatic applications:
  - Analysis using an autosampler.
  - Methods development on same sample.
  - Prep runs via repetitive injections.
  - Precision studies under fixed conditions.
- 5 µl to 2 ml removable sample loops.
- $450 \cdot 10^5$ Pa maximum operating pressure.
- 0.4 mm diameter flow passages.
- 15 daN-cm operating torque.

REFERENCES

1. Snyder, L.R. and Dolan, J.W., Getting Started in HPLC, User's Manual, LC Resources, Lafayette, CA, 1985.
2. Harvey, M.C. and Stearns, S.D., J. Chromatogr. Sci. **21**, 473, 1983.
3. Harvey, M.C., Stearns, S.D. and Averette, LC Liquid Chromatogr. HPLC Mag. **3**, 434, 1985.
4. Majors, R.E., LC Liquid Chromatogr. HPLC Mag. **2**, 358, 1984.
5. Dolan, J.W., LC Liquid Chromatogr. HPLC Mag. **2**, 834, 1984.
6. Dolan, J.W., and Snyder, L.R., Troubleshooting HPLC Systems, User's Manual, LC Resources, Lafayette, CA, 1986.
7. Technical Notes 5, Rheodyne, December, 1983.
8. Technical Notes 1, Rheodyne, September, 1994.

STUDIA UNIVERSITATIS BABEŞ-BOLYAI, PHYSICA, SPECIAL ISSUE, 2001

"LC 100" AN ANALITYCAL SYSTEM FOR HIGH PERFORMANCE LIQUID CHROMATOGRAPHY

GABRIEL POPENECIU[1], HORIA BENDEA[2]

[1] *National Institute for Research and Development of Isotopic and Molecular Technologies, P.O.Box 700, 3400, Cluj-Napoca 5, Romania*
[2] *Technical University, Faculty of Electronics, 3400, Cluj-Napoca, Romania*

ABSTRACT. To elaborate a HPLC system is a challenge for each engineer in the lab: on one hand, there are complex mechanical components like the solvent delivery system, the injector system and the detector; on the other hand, an intelligent control system is necessary to co-ordinate these various modules. Recent advances in instrument hardware and software technology are of particular importance for anyone who is involved in the development and optimisation of HPLC methods. The paper describes the "LC100" system with particular attention given to the main components of the HPLC system.

1. INTRODUCTION

High-Performance Liquid Chromatography (HPLC), as a separation technique for non-volatile substances in mixtures, has a wide range of applications in the industrial world today. Over the last decade, instrumentation for liquid chromatography has evolved towards higher flexibility, greater ease of use and higher reliability.

Designing an HPLC system requires a high degree of interaction between various disciplines, including mechanics, materials science, chemical physics, optics, electronics, firmware and software. Problems that must be solved include the handling of liquid having a wide range of solvent properties at flow rate from 1µl/min to 10,000µl/min and pressures up to $400x10^5$ Pa, control of mechanical components, detection of chemical substances and data handling.

2. SYSTEM DESIGN OBJECTIVES

To get a cost-effective, easily upgradable, and flexible system, some key objectives were decided for our "LC100" system:

- To provide the chromatographer with the necessary hardware and software tools for the methods development process in a wide range of application areas, and to allow the user to choice various approaches to the methods development problem;
- To provide the user with single-point control system through a uniform, intuitive operator interface. With this system of integrated modules, the user and system communicate using the personal computer screen and keyboard;
- Distribute the functions of the system into hardware control, data acquisition, data processing, and a user interface;
- Use a hierarchical structure that is easily understandable;
- Use a LC-IB as the communication link to a standard personal computer (PC).

3. SYSTEM OVERVIEW

Figure 1. shows the general architecture of the "LC100" System. It is a typical hierarchical structure with the PC as the head. The PC serves two purposes: the human interface and the management of automatic multiple analyses with variable parameters. The separation part of LC100" System consists of the solvent delivery system, the column compartment with heated oven and the injector system. The detector part is a spectrophotometric detector in ultraviolet domain. All this independent modules are connected to the LC controller.

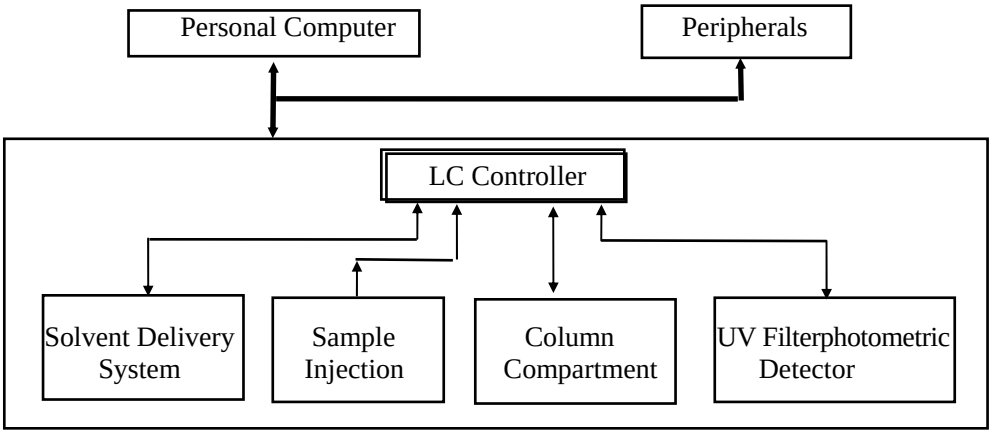

Figure 1. The Architecture of LC100 System.

Figure 2. presents the system communication in the LC100 System. The distribution of the system into modules is done on three levels. Level 1 can be seen by the user. It is represented by the physical devices, like PC or the plotter, and is connected via LC-IB. Level 2 is created by the hardware design of the LC devices, which is based on several single-processor computers located on different boards inside the mainframe and connected by special hardware. Level 3 is implemented by software within a single-processor computer.The applications software is based on a multitasking operating system. It is designed as a collection of tasks, each performing a particular function and interacting through a communications mechanism.

The different components at any distribution level within the system are relatively independent. Each level can be characterised by the usable resources for coupling the components. For level 1 it is the message communication over the LC-IB by cables and standard hardware interfaces. The level 2 environment consists of hardware designed specifically for liquid chromatography. The coupling of components at level 3 is done by the operating system, which provides an intertask communications mechanism.

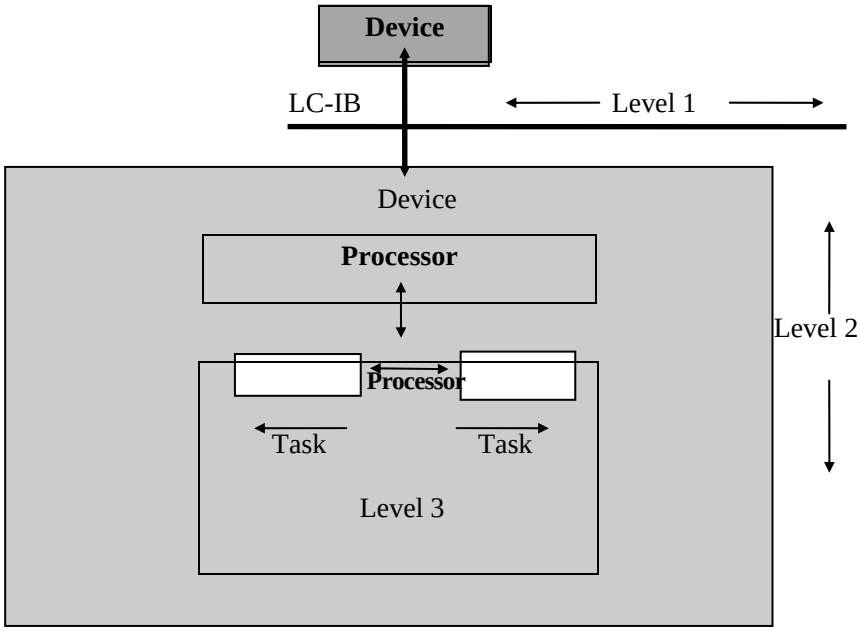

Figure 2. Communication in the LC100 System.

4. TECHNICAL SOLUTIONS

Contained within the LC100 System mainframe are component modules designed to perform as one integrated system, so the user can configure the system for a particular type of application and each module can be easy removed and exchanged.

4.1 SLS100 Solvent Delivery System

Because the parameters for solvent delivery have a major influence on resolution in HPLC, great care was taken to provide flexibility and programmability in solvent delivery while increasing the level of reliability and precision essential for the HPLC method development chemist. The programmable solvent module as a high-performance pump is characterised by pumping a constant flow of solvent at working pressures up to $400x10^5$ Pa. Constant flow, in the range 0.1 – 10 ml/min, is achieved with a pair of specially-driven positive-displacement pumping chambers. Each pumping chamber consists of a pump head cavity in which a small, accurately machined plunger slides back and forth. The two pistons are driven such that their reciprocating directions are opposing resulting in one plunger drawing in solvent while the other is expelling solvent. By this arrangement, the pumping chambers alternately supply the solvent.

Figure 3. graphically illustrates how the flow from each pumping chamber may be combined to obtain a steady flow is achieved by complex piston displacements. Noncircular gears are utilised to drive the pistons so that their forward motion in expelling solvent takes more time than their reserve motion in drawing solvent.

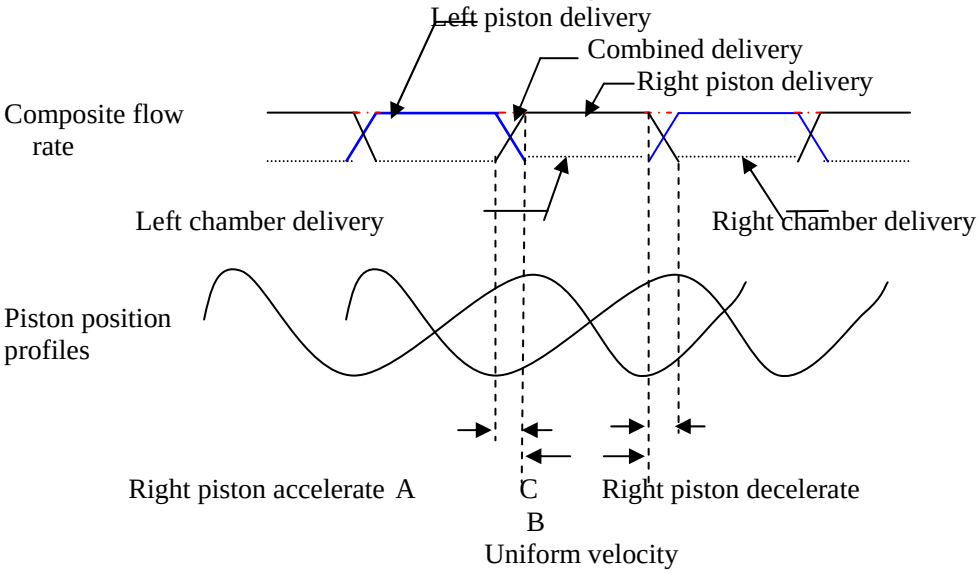

Figure 3. Combined Delivery of Pumping Chambers.

The minor fluctuations which remain as a result of the crossover intervals of the pumping cycles are smoothed by a pulse damper. This unit is a small flow-through device in which fluid is accumulated and discharged and it provides a flow rate accuracy about ± 0.005 ml/min. The smooth solvent flow from the high pressure pulse damper is piped to the transducer unit, which is a flow-through Bourdon type pressure sensor with a very low dead volume, that detects the magnitude of the solvent back-pressure.

The electronic module of SLS100 provides the following functions: the flow rate control, detect and indicate the solvent back-pressure, limit pumping operation to pre-set overpressure level and compensate for solvent compressibility to maintain constant flow rate.

We realised a prototype of the SLS100 System delivery system which is presented in figure 4.

4.2 Model SIA100 Sample Injector

Model SIA100 is an automatic syringe loading sample injector with an electromagnetic actuator built it in a compact package an it can be applied to every chromatographic task. This injector provides maximum versatility in both methods of loading the sample: complete loop filling and partial filling. The great advantage is that it can be used as a conventional fixed loop injector , which is known to give the best volumetric precision, or as a variable injector with zero sample loss. The injection

volume can be chosen in the range 5 µl – 2 ml and the sampling time is compatible with high-speed LC.

The prototype of Model SIA100 Sample injector was submitted to some experimental measurements, and those confirmed its features.

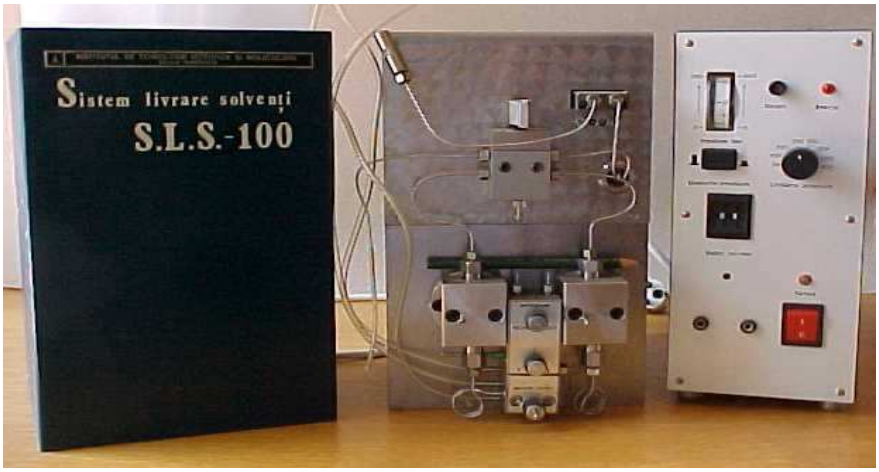

Figure 4. SLS 100 System Delivery System

4.3 DUV100 Absorbance Detector

The model DUV100 is an UV filter-photometric detector and consists of an optics unit and an electronics unit. The schematic diagram of the DUV100 detector is shown in figure 5. Light from the mercury lamp which is transmitted through the cell assembly is converted into electrical signals by a photo-detector. The electrical signals are transmitted to the amplifiers, components of the electronics unit .

An important problem in absorbance detection is distinguishing between genuine absorbance and a change in energy reaching the detector because of refractive index changes in the sample cell. As the refractive index in the cell varies, the fraction of light which strikes the cell wall varies. Since reflection of UV light from the cell wall is negligible, the deflected light which strikes the cell is absorbed and appears as an absorbance, change on the detector even in the absence of any sample, so the fraction of deflected light absorbed by the cell wall will vary with changes in refractive index within the cell. This problem is solved, using a taper-cell which insures that all the light which enters the cell will leave it if there is no true absorbance. As shown in figure 6.a taper-cell walls diverge to a greater extent than the worst possible case of light beam bending due to some of the light strikes the wall of the cell thus resulting in false absorbance readings.

The taper-cell of DUV100 Detector is especially useful where RI effects pronounced such as in gradient elution work in which many solvent pairs produce RI curves with maximum in mid range, and RI correction is especially significant for work requiring high sensitivity due to low sample concentrations.

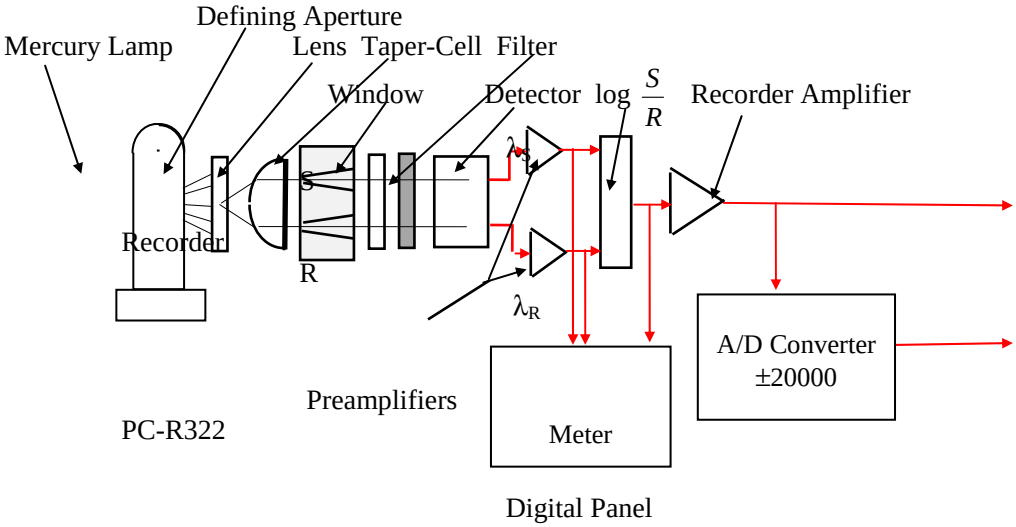

S = Sample; R= Reference; λ = Wavelength.

Figure5. **DUV 100** Detector Optics and Electronics Diagram

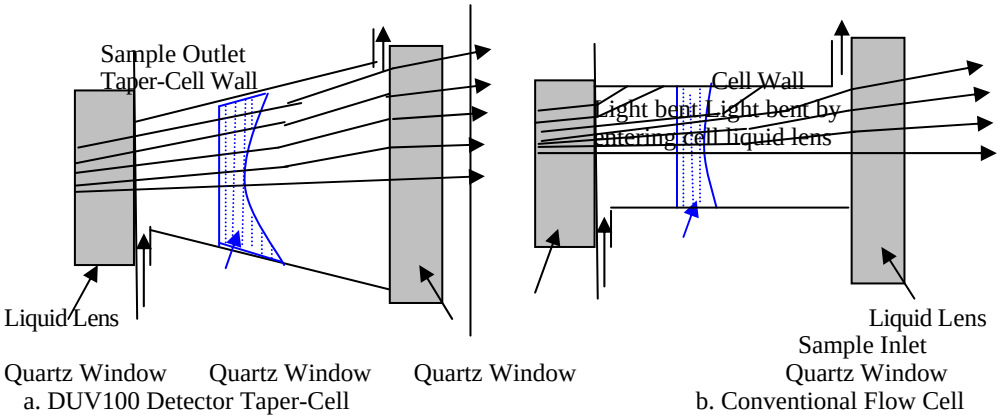

Figure 6. Taper-Cell Versus Conventional Cell

In the designs of the flow cell we used the "Iron Rule" of chromatography, which says that no more than 10% of the original resolution must be lost in the detection system. This means that the volume of the flow cell, V_{cell}, must be:

$$\mathbf{V_{cell}} < 0.5\ V_r / N$$

where V_r = retention volume; N = number of theoretical plates.

For this reasons, the DUV10 Detector designs is a trade-offs between path length, cell volume, and total photon flux, which is controlled by the element with the smallest light conductivity, the flow cell.

4.4 Column Compartment

This unit must ensure temperature homogeneity within the column by means of an airbath thermostat, which maintains a temperature precision of $\pm 0.5^0$ C.

4.5 LC Controller

The system controller provides centralized menu, driven control of all LC100 HPLC System components mention above. The controller controls the parameters for: solvent selection, solvent delivery, stream switching, column temperature, detection, integration, peak identification, calibration, results format, plot format, and file translation.

5. CONCLUSIONS

Our **LC100 HPLC System** is designed in a modular conception, each module can be easily removed and exchanged. The main specifications of each component module are presented bellow.

5.1 Solvent Delivery System SLS100:

Pump type	- dual-piston pump; piston displacement volume 100µl, each head.
Solvent delivery modes	- constant flow rate and constant pressure delivery.
Constant flow rate delivery	- flow rate setting range: 0.1 to 10 ml/min, incr. of 0.1 ml/min. - flow rate accuracy: ± 2% or ±0.005 ml/min whichever is higher. - flow rate precision: within ±0.3%.
Constant pressure delivery	- pressure setting range: 10 – 400x10^5 Pa. - pressure accuracy: ± 10% or 10x10^5 Pa whichever is higher.
Overpressure limits	- continuously adjustable between 10 – 400x10^5 Pa.
Pressure sensor	- zero dead volume flow-through Bourdon-type tube.
Liquid contact surface materials	- stainless steel, ruby, sapphire, Teflon, kel-F.

5.2 Sampler Injector Model SIA100:

Operating modes	- automatic injection with electromagnetics; - manual injection with handle.
Manual injection capabilities	- complete loop filling for precision; - partial loop filling for flexibility; - zero sample loss/no flushing.
Automatic applications	- analysis using an autosampler; - methods development on same sample; - prep runs via repetitive injections; - precision studies under fixed conditions.
Injection volume	- 5 µl to 2 ml removable sample loops.
Operating pressure	- maximum 450·10^5 Pa maximum.
Liquid contact surface materials	- stainless steel, ceramic, Teflon.

5.3 Absorbance Detector DUV100:

Detector type	- absorbance detector in ultraviolet region; - detection element – double Si – photodiode.
Wavelength range	- 195 – 350 nm.
Light source	- mercury lamp.
Bandwidth	- 10 nm.
Wavelength accuracy	- ± 2 nm.
Noise level	- below ± $1{,}5 \times 10^{-5}$ AU nm.
Drift	- below ± 1×10^{-3} AU nm.
Cell volume	- 12,5 µl (10 mm x 1.2 mm I.D.).
Liquid contact surface materials	- stainless steel, quartz Teflon.
Recorder output/Integrator output	- 1 mV, 10 mV/ 0.4 V/AU, 0.8 V/AU.

5.4 LC Controller:

Multitasking operating system	- editing of a background parameter file or pretreatment file while another file is running in the foreground is provided for.
Operation panel	- display 6" monochromatic CRT, character and graphic display.
Standard input/output terminals	- start signal input terminal for sample injector: 1; - alarm signal input terminal: 1; - star/stop signal output terminal for external units: 2;
Control of LC100	- all the control is made by the control program, in each step (102).
Control of SLS100	- setting items: flow rate, upper pressure limit, monitor nominal pressure, select the solvent (max 3 solvents accessible).
Control of DUV100	- setting items: automating zeroing and polarity switching.
Control of column oven	- setting items: oven temperature and upper limit temperature, nominal temperature is monitored.
R 232 interface	- for data transmission to and from external computers.
Other functions	- backup protection of memory in case of power failure; - self-diagnostics.

REFERENCES

1. Snyder, L.R. and Dolan, J.W., Getting Started in HPLC, User's Manual, LC Resources, Lafayette, CA, 1985.
2. Schwartz, H.E. and Kucera, P., Anal. Chem. 55, 1752-1760, 1983.

3. Harvey, M.C., Stearns, S.D. and Averette, LC Liquid Chromatogr. HPLC Mag. **3**, 434, 1985.
4. Majors, R.E., LC Liquid Chromatogr. HPLC Mag. **2**, 358, 1984.
5. Dolan, J.W., LC Liquid Chromatogr. HPLC Mag. **2**, 834, 1984.
6. Dolan, J.W., and Snyder, L.R., Troubleshooting HPLC Systems, User's Manual, LC Resources, Lafayette, CA, 1986.
7. Maeder, M, Anal. Chem., 59, 527-530, 1987.
8. Technical Notes 1, Rheodyne, September, 1994.
9. Hewlett-Packard Journal, Vol. 35, April 1990, entire issue.
10. Byrne, S.H., Modern Practice of Liquid Chromatography, J.J Kirkland, ED., 1991.
11. Technical Notes, Waters Associates, 1996.

STUDIA UNIVERSITATIS BABEŞ-BOLYAI, PHYSICA, SPECIAL ISSUE, 2001

HOW ALTERATION OF ELECTRIC PARAMETERS CAN DETERIORATE TIME-OF-FLIGHT MASS SPECTROMETER PERFORMANCE

D. IOANOVICIU, V. COSMA, C. CUNA, M. KAUCSAR, A. PAMULA, B. TUZSON

National Institute for Research & Development of Isotopic and Molecular Technologies, P. O. Box 700, Ro 3400 Cluj-Napoca, ROMANIA

INTRODUCTORY

Some general considerations are available from the literature about the stabilities of the electronic units of the time-of-flight mass spectrometers [1]. There are many possible alterations of the voltages and pulses applied to the electrodes of the ion source as well as of the electrostatic mirror and of the postaccelerating electrodes. The possible alterations of the electric parameters were examined and their effect on the mass resolution estimated. A first class of such parameters were those regarding the ion source. First the effect of a deviation from the correct value of the ratio of the extracting voltage to the total acceleration voltage in a space focusing instrument was determined. The influence of the instabilities of the voltage applied to such a reflectron on the instrument resolution was calculated. Based on these results the performances of the instruments were correlated with those of the electronic units. Also some improvements are suggested.

PARABOLIC POTENTIAL TIME-OF-FLIGHT MASS SPECTROMETERS THE ION EXTRACTING FIELD IN THE ION SOURCE

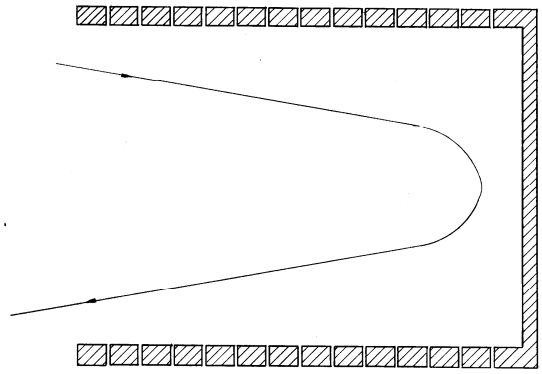

(Figure 1)

Generally the ion sources are working in a uniform field regime during the accumulation of the ions. When the fields inside the extracting region becomes

different from that in the accelerating part the temporal space focusing point a defocusing will be induced for the ions created at different depth inside the ionization region. The resulted flight time difference must be added to that of the initial length of the ion packet. The additional length dt of the ion packet depends on the ratio of the fields inside the two regions E_2/E_1 (assumed to be constant during ion extraction) as well as the spatial extent according to the formula:

$$dt = s(E_2/E_1-1)[d_2/d + (d/d_1)^{1/2}-1]/v$$

where s is the depth of the extraction region while v is the final velocity of the ions of mass m,

$$d = d_1+d_2$$

This formula allows us also to determine the effect of the ondulations of the voltage applied to the extracting electrode. Therefore, if the broom voltage period is smaller than the extraction time length for E_1 we must use the average value.

THE FRONTS OF THE EXTRACTING POTENTIAL PULSE

During the central ion source electrode voltage increase till the nominal extracting potential value, the ions will be submited to fields differing from that which ensures the correct longitudinal focusing in the longitudinal space focus. If T is the time of the extracting field increase from zero to the correct value, E, then the flight time t_t of an ion extracted in this manner to the longitudinal focusing point results to be:

$$t_t = [T + (T^2 + 4F)^{1/2}]/2 + (4md)/(T^2+4F)^{1/2}$$

where $F = (2m/eE)(d + s) - T^2/3$

In this way the ion packet will be lengthened with respect to the ideal value by dt:

$$dt = sT^2(eE/2md)^{1/2}/(24d)$$

FOCUSING LENS

The instability of the voltage applied to the transversal focusing lens located on the entry aperture of the analyzer changes the ion packet final dimensions by the radial transversal extension at the entry, normally to the flight direction. Let consider an unipotential lens of focal length f, located in such a manner that the focus coincides with the longitudinal focusing point. The increase of the transversal dimension dD is proportional to the initial diaqmeter s_o:

$$dD = s_o df/f = s_o\, dV/V$$

then proportional to the relative variations of the voltage applied to the focusing lens.

ELECTROSTATIC MIRROR POTENTIAL

A stable voltage, having a wrong value, between some limits can act on the packet lenth only by the mixt terms resulting by combining the effect of the incorrect field with the position with respect the axis at the entry into the mirror.

If the voltage applied to the mirror electrodes has a sinusoidal component of small amplitude:

$$E= E_{exact}(1 + a \cos pt)$$

then finally it results a time difference for the ions formed at different distances inside the ion source and which enter at different phases in the mirror:

$dt = 4Na(2q^2-p^2)/[p(4q^2-p^2)]\sin(p/2q)$ where the following symbols were used:

N number of double relections inside the mirror, $q = (eG/m)^{1/2}$, G the gradient of the mirror gradient.

NUMERICAL ESTIMATIONS

The following numerical values refer to an instrument of parabolic potential type of 1400 mm length. If the ionization region extends over s = 1.5 mm depth, the extracting field over d_1 = 3 mm, while the acceleration happens over the distance d_2 = 19 mm, for ions of 1 keV energie and mass 100 u, for an imprecision of 1% for the ratio of the two fields it results an aditional scattering of the ion packet of about 1 ns, which reduces the resolution to 2440 (if in the absence of this error the resolution would be 2700).

For a 10 ns impulse increasing time an additional lenghtenning of 0.284 ns results the influence on the resolution being small, reduced to 2610.

An 1 % instability of the focusing lens voltage, for an ion packet lenth of 5 mm transversal extension at the limit of the analyzer will induce a transversal dimension increase of the packet of 0.05 mm involving a resolution decrease to 2376.

If on the mirror electrodes we apply a voltage with a sinusoidal component superimposed over the continuous voltage, having a frequency of $1.6x10^4$ Hz the resulted lengthenning of the packet will be of $4.6x10^{-5}$ a, that is for a = 10^{-3} of $4.6x10^{-8}$s, inducing a resolution decrease to 415.

HOMOGENEOUS ELECTRIC FIELD MIRROR TIME OF FLIGHT MASS SPECTROMETERS

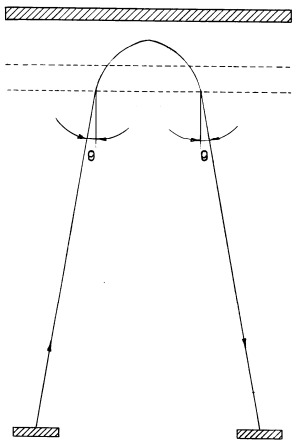

(Figure 2)

For the homogeneous electric field mirror time of flight mass spectrometers the tolerances to be enforced on electronic supplies can be correlated with the mass resolution. Variations in the ion accelerating voltages of δV_{ac}, induce an additional ion packet energy spread of $e\delta V_{ac}/U$ which is however compensated in a first order approximation. For single stage mirror mass spectrometers the stability must be better than $1/(2R)^{1/2}$ where R is the expected instrument mass resolution. Then for a desired resolution of 500 a stability of the accelerating voltage of better than $3.2x10^{-2}$ is already satisfactory. However for second order energy focusing time of flight mass spectrometers results from the ratio $1/(2R)^{3/2}$ which indicates a stability of $1.1x10^{-5}$ for a 1000 mass resolution.

The mirror must be fed by a voltage of stability better than 1/(2R) that means 10^{-3} for the first, $5x10^{-4}$ for the second case. Other calculations state more rigurous conditions for stability: two orders of magnitude better than the inverse of resolution, or $2x10^{-5}$ for the first and 10^{-5} for the second case.

CONCLUSIONS

Based on the above presented formulas and calculations the stabilities of the electronic units of the time of flight mass spectrometers can be predicted.

REFERENCES

1. B. A. Mamyrin, Int. J. Mass Spectrom. Ion Processes **131** (1994) 1.

STUDIA UNIVERSITATIS BABEŞ-BOLYAI, PHYSICA, SPECIAL ISSUE, 2001

MICROCONTROLLER BASED INTERFACE UNIT FOR 5KW MICROWAVE OVEN

VASILE SURDUCAN, EMANOIL SURDUCAN, CAMELIA NEAMTU

National Institute for Research and Development of Isotopic and Molecular Technologies, P.O.Box 700, 3400 Cluj Napoca 5, ROMANIA.

1. Introduction

Microwaves are, maybe, one of the greatest discoveries of the 20'th century. With a vavelenght between 30 cm and 3 mm and a power between 1 mW and 500 KW they are used practically in all fields from medicine to industry. Microwave thermal and chemical tratments are well known for his high efficiency, 3 to 1000 times greater then the conventional processes because of the ***direct energy transfer*** into materials and the ***selective compounds heating*** following dielectric permittivity parameters of the materials involved in reaction or in the treatment (equation 1):

$$\varepsilon = \varepsilon' - i\varepsilon''_{eff} \tag{1}$$

where: - ε' is the real part of the permittivity, which characterize the amount of microwave reactive power changed with material (without absorption);

- ε''_{eff} is the imaginary part of the permittivity, which characterize the microwave global absorption in the material.

The permittivity is a function of the material temperature and of the microwave frequency. In the general case, the permittivity is a tensor which depends on the homogeneity and anisotropy of the materials. The microwave power absorbed in the material, assuming that all microwave power is transformed in warmth, is (equation 2):

$$P = \omega\varepsilon_o K_i \int_{vi} [\varepsilon_i F_i (\varepsilon_i) E_i^2] dV \tag{2}$$

where: $\omega = 2\pi f$,

f - microwave frequency,

E_i - microwave E field in "i" point;

K_i - coupling coefficient for "i" point ;

F_i - filling factor;

ε_i - absorber mixture relative permittivity in point "i";

ε_o - free space permittivity;

vi - is the local volume in "i " point;

Any microwave oven is a multimodal microwave cavity in which the incident power (usual 700W to 70KW at 2.45 GHz) has a particular distribution . If the probe to be treated has a great volume (like drying foods in foodstuff industry or ceramic materials microwave drier), this multimodal cavity is suitable for a treatment because

many parts of the local power distribution are intersecting the probe volume. The user must have a total control of the microwave radiation like: modifying continuously the output power in a large range (not only the output energy used in almost all home-appliance ovens) and controlling precisely the treatment period.

We present here, briefly, our design concerning a 5KW magnetron oven with an effective volume of 1 cubic meter, based on continuous wave CK 101 magnetron and driven by a flash microcontroller PIC16F877.

2. The concept

In fig.1 is shown the typical structure for our high power microwave oven:

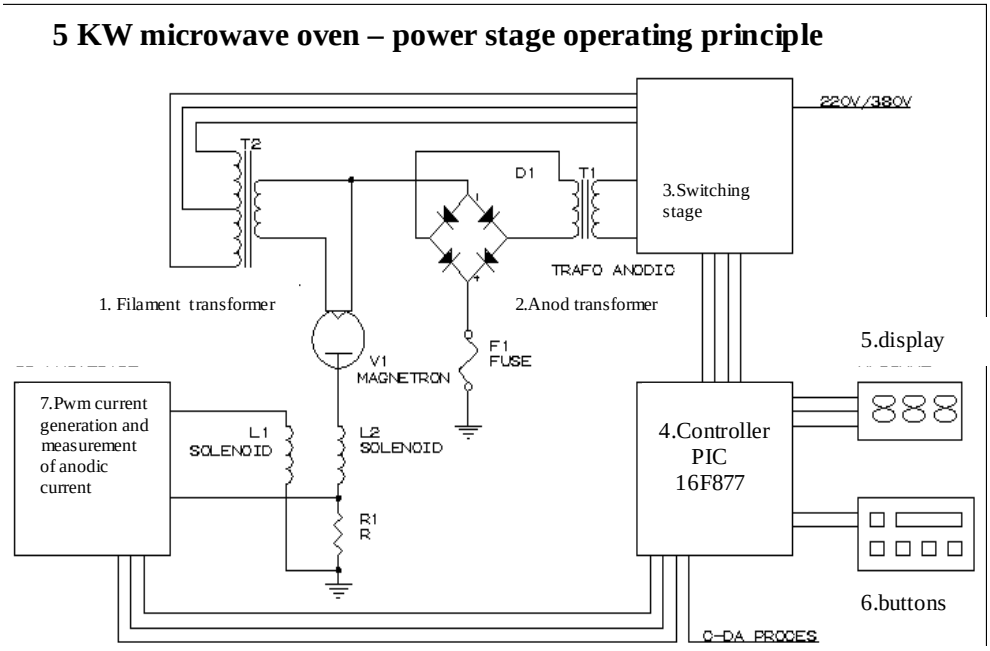

The magnetron (microwave power generator) is supplied through an anodic transformer (T1-6KV/1A) and a two steps filament transformer (T2-7.5V/42A and 5.5V/36A). The magnetic field of the magnetron is produced in two coils (L1 supplied from a PWM based constant current source, with max.10A and 20V voltage swing and L2 supplied by a feedback anodic current). All supplying algorithm are supervised by microcontroller board (4) with a simple interface user (6) consisting in four functional buttons (the same buttons have different functions displayed on the second line of the LCD as the program flow chart required) and a large LCD display. Because the high anodic temperature (150 C), a cooling system (with cold water and air flow) is required. Both the water flow command and air flow presence are supervised by the microcontroller board using an anodic temperature measurement. All other parameters like door status (open or closed), cooling water pressure, treatment period and output microwave power are also under microcontroller control.

3. The firmware

The firmware is a software translated into a hex code by a compiler [3] or an assembler and stored in the microcontroller's [1] memory by a programming sequence, assisted by the PC and by a hardware programmer [5] board. A bootloader [2] will allow fast low voltage programming as many time as the firmware development is requiring. For our oven, there are 14 different LCD screens, (the starting screen is presented in fig.2) distributed in four working modes of the oven's "brain":

Fig.2 – The starting screen

a ***programming mode*** (fig.3)in which the user can specify the output power and the treatment period:

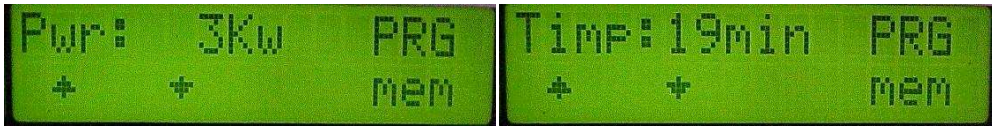

Fig.3 – Programming mode screens

a ***treatment mode*** where some specific information are displayed, like treatment time in progress, microwave output power and current status (**on** – shut on the microwave radiation inside the oven, by initiating first a 3 minutes filament heating procedure and a priority test door status and cooling parameters of the magnetron; **standby** - the user may open the door unit and change the probe while the magnetron filament is still heated but anodic current is shutdown,
off – the current process is finished and the magnetron filament is also shutdown),

Fig.4 – The ON screen (treatment mode)

a ***measuring mode*** where the user may check some important plant parameters like magnetron anodic current and temperature (measuring mode is active only from inside of treatment mode),

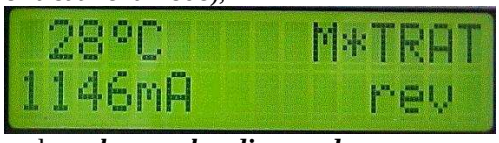

Fig.5–The measuring screen (treatment mode)

and an ***abnormal ending mode*** ,

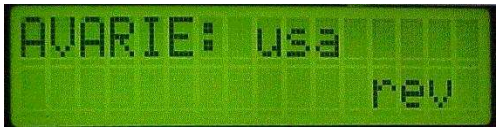

Fig.6 – Error screen (door open in treatment mode)

for extremely situation, like ***door open*** when treatment is in progress (situation with maximum priority considering operator biological protection, solved using microcontroller interrupts), anod ***temperature exceeded***, anod ***current out of limits*** or ***low*** water ***pressure***.

3. The microcontroller board design

A simple configuration with PIC16F877 microcontroller (fig.7), running at 4MHz

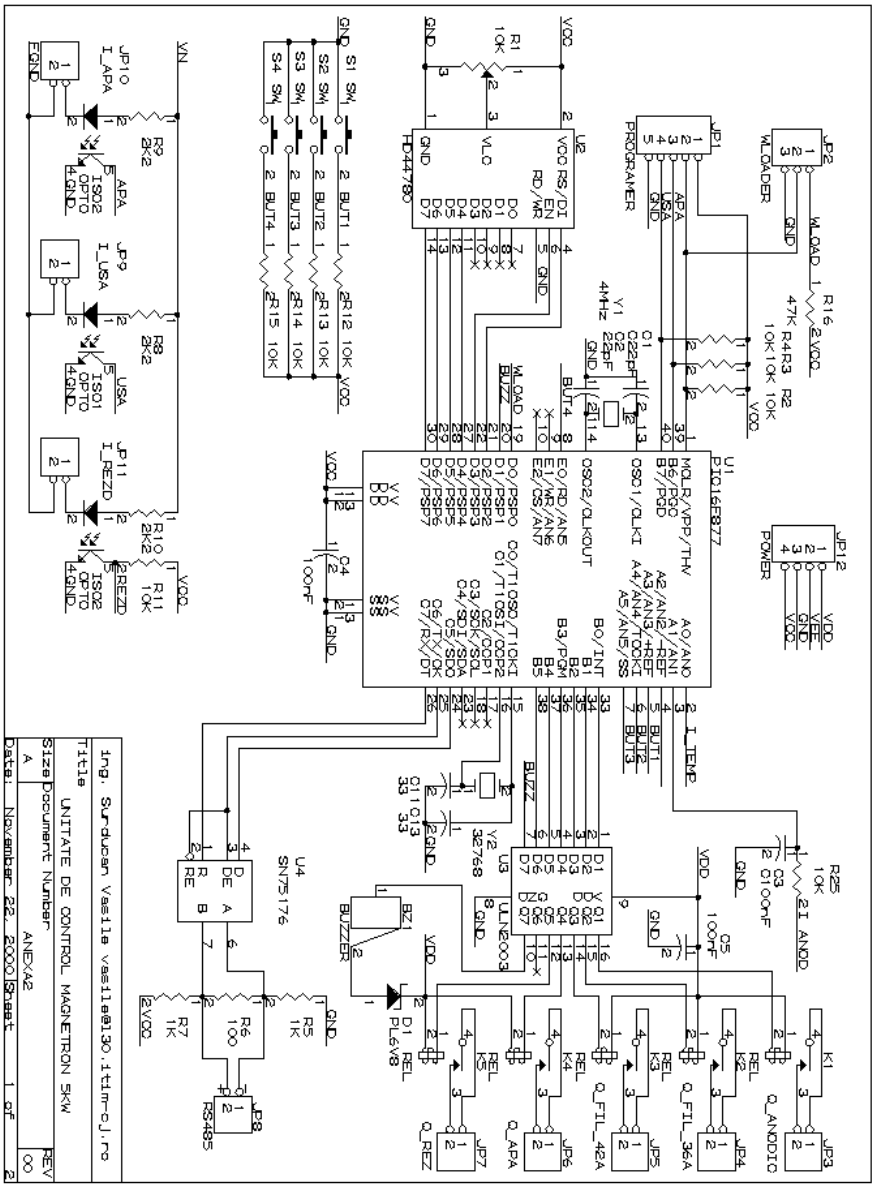

Fig.7 Microcontroller board schematic

clock speed and 32768 Hz real time clock was chosen. Hd44780 display (U2) is connected using nibble mode transfer on PORT_D. Two "in circuit programming" connectors are used , one for HVP (JP1) and another for bootloader LVP (JP2). All inputs and outputs to plant are isolated using optocouplers or relays driven by a specialized driver (U3), except the analogic inputs which are measuring voltage signals near ground. The temperature sensor measuring the anodic temperature and the sense resistor which convert the anodic current into voltage are carefully configured to avoid noise interference and high voltage leackage. A PWM signal from CCP1 filtered with a RC network is used for reference to generate the magnetization constant current for magnetron coil. A piezo-buzzer is also used to mark all important events with user interface (pressing buttons or signalizing the process end). A RS-485 or an optional RS-232 interface will be provided for long distance measurements and programming.

4. Conclusions:

Our microwave oven has the following characteristics:

- output power: 3-5KW continuous mode
- output frequency: 2.45 GHz
- effective treatment volume: 1 cubic meter
- supply 220Vca/30A or 3x380V/10A

- gauge (height x width x deep): 1350x1450x1120 mm
- weight: less then 250 kg
- moveable oven

Destination:

- ceramic materials fast drying
- foodstuff industry drier

BIBLIOGRAPHY

1. PIC16F877 data sheet: http://www.microchip.com/10/lit/picmicro/16f87x/index.html
2. Bootloader: http://www.xs4all.nl/~wf/wouter/pic/wloader/index.html
3. Compiler: http://www.come.to/jal
4. Working group: http://www.egroups.com/list/jallist/info.html, http://www.piclist.com
5. Programmer: http://www.propic2.com

DEVELOPMENT SYSTEM FOR MICROCONTROLLER BASED DATA ACQUISITION SYSTEM

ST.POPESCU, M.KAUCSAR, H.BENDEA, T.SIMPLĂCEANU, C.BINDEA

National Institute of Research and Development for Isotopic and Molecular Technology, PO Box 700, 3.400 Cluj-Napoca, Romania

The development system designed for microcontroller applications is formed of four subensanbles:

1. The basic Kernel.
2. The microcontroller programmer.
3. The development modules kit
4. The development software.

1.The basic Kernel

This is a functional construction set up of four parts:

a) Development module for computing units based on the microcontroller from Intel, Atmel, Philips families, accordingly the following block diagram (fig. 1).

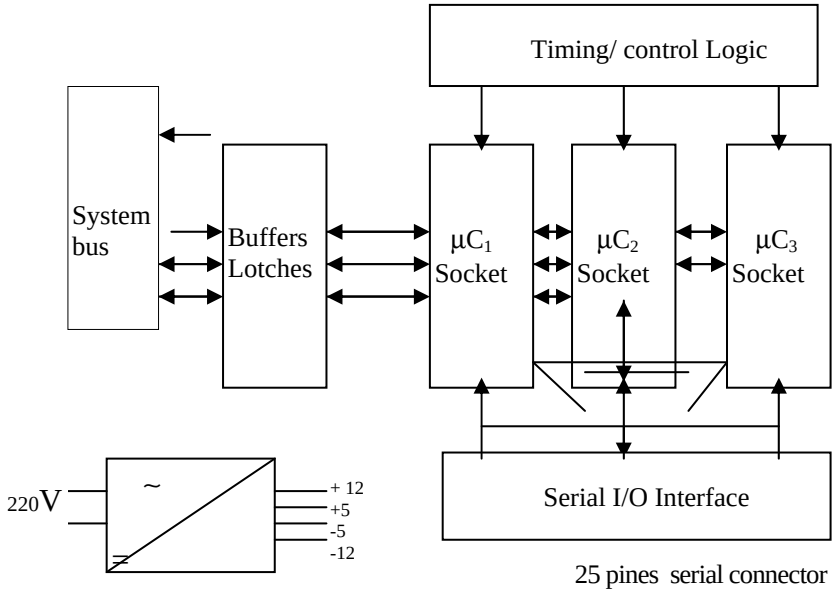

Fig. 1 The development madule for computing

One of the buffers and lotteries role is to protect the microcontroller from the manipulation and load adaptation errors, in contact with other modules.

In the some time these devices ensure the direction: data input / data onput

b) System BUS

To ensure the parallel interconnection to ports level with external world, a system BUS was built for: DATA, ADDRESES, CONTROLS and POWER SUPLYES lines. This system BUS is built up of five connectors, each wits 2x32 pines.

The connection has been made with wire wrapping technology.

When needed they can join other types of connectors.

c) The serial interface

To ensure the serial interconection with the operation console (data display system) a serial interface was built up , wich ends up with a 25 pines connector .

This interface alows the connection with the master PC computer (master - slave connection).

The Boud-rate of the serial comunications is programmed inside the driver interface.

d) The power supply

This delivers the stabilised voltages of ± 5V, ± 12V, required both by the central computer module and by the developing modules existing on the system bus.

2.The microcontroller programmer

The user's code machine programms are developed on a PC computer and are stocked under a file**.exe** or file**.com** form.

These files have to be transferred into the microcontroller flash memory.

The transfer operation is achieved by a memory writer. Its functional diagram is the folowing (fig. 2).

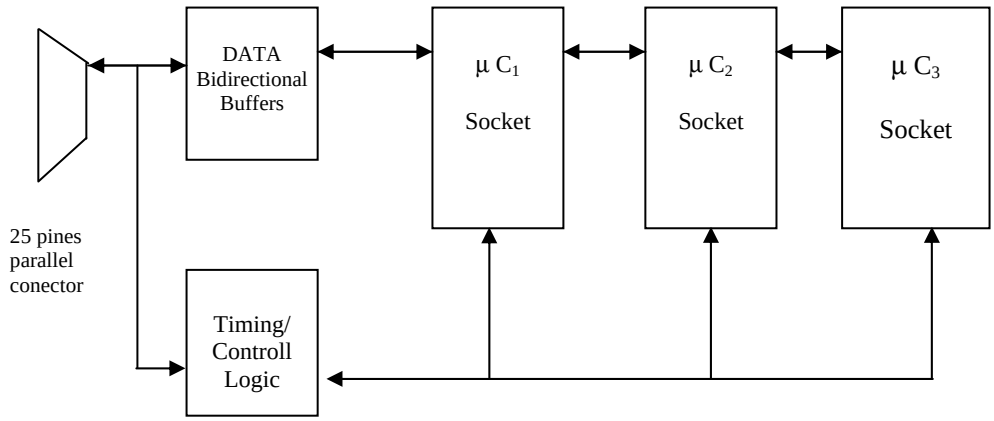

Fig. 2 The microcontroller programmer

The memory programmer is connected to a PC parallel port.

The DATA, already written in the flash memory, are readable in order to be compared with the initial file.

Sockets for the three types of microcontrollers ATMEL: AT89C2051, AT89C51, AT89C52 are provided on the programmer module.

For other types of microcontrollers, additional sockets may be attached..

3.Development modules Kit

For developing and testing user applications, three types of modules were implemented:

1. Parallel outputs module.
   This is made up by bus buffers, CI selection logic, wire-wraped sockets and line analogy amplifiers. For example we used a 12 bits Digital to Analogy Converter. It is possible to connect through wire-wrapping procedure many other 8 ÷ 16 bits DAC-s.
2. Parallel imput module.
   These modules are built up in the same way as the parallel output modules; the only thing that differ is the communications sense. We used a 12 bits ADC converter.
   The ADC socket can be connected in different maners, depending on its terminals.
3. The external memory module.
   This consists of 4K static RAM and 4K EPROM.
   The external memory module is used in user applications where the extension of the internal microcontroller memory is required.

4.The development SOFTWARE resources

We used the ATMEL, Intel and FRAMKLIM software kits (editors assemblers, debugers). These utility packages are set up either as separated programmes in DOS operation system, or integrated in Windows developing environment. In this last case we can write C language subprogrammes, (or Pascal) which, through the processing procedures, are mixed with that subprogrammes coming from the assembler language.

In this way we achieved communication drivers for the serial interface, and developed working programmes for the parallel I/0 interfaces.

ANALOG SIGNAL ACQUISITION AND PROCESSING BY VIRTUAL INSTRUMENTATION

ROMAN BAICAN, DAN NECSULESCU*

Adam Opel AG, Germany
**University of Ottawa, Canada*

Product research, development and manufacturing as well as experimental work in laboratories rely on data acquisition solutions for system monitoring, control and instrument characterization. A complete data solution usually consists of sensing, signal conditioning, data acquisition and processing, analyzing, visualization, report generation and actuating, as shown in figure 1.

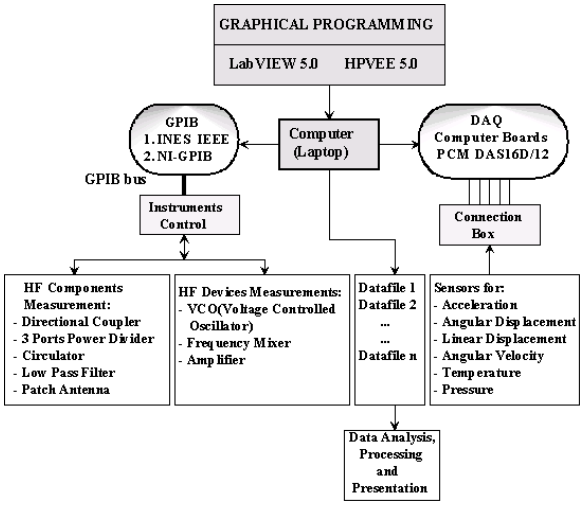

Fig.1 The generic structure of virtual instrumentation

The direct link to an evolutionary process is accomplished by the sensors which deliver for each parameter an electric signal (normally analog). After conditioning (amplified, filtered, smoothed, formation, etc.) the signal will be acquired by a DAQ (Data Acquisition Card), converted by a A/D (Analog to Digital Converter) and transmitted to the main computer. With an appropriate software, the signal will be analyzed and processed. To create complete and optimum data acquisition solution within a minimum time, dedicated hardware and software tools are needed such that not the development time is reduced but also the complex functionality required for carrying out all data acquisition tasks concurrently is available.

Most important is now to find a suitable software to drive the process. Until recently, to visualize process parameter and to connect system component, software based on the standard text programming languages was used.

However, on account of these language complexity, such programs require computer specialists which normally do not have sufficient knowledge about process automation. System monitoring and control has today new, more complex, requirements resulting from the need for integrating numerous instruments, tele-monitoring and tele-operation, fast and complex signal processing and signal analyzing, fusing signals from various instruments etc. The fulfillment of these new requirements is greatly facilitated by the availability of cheaper and more versatile computing facilities. Monitoring and control is an integral part of computerized production and follows the trend towards tighter system integration, increased productivity and cost reduction. Hardware evolution from minicomputers to PC (Personal Computers), embedded micro-controllers and computer networks as well as programming evolution from assembly languages, high-level languages, visual programming to graphical programming languages enabled new computerized instrumentation solutions.

A major change occurred, with the appearance of virtual instrumentation which replaced part of signal acquisition, processing and display, in traditional instruments, by personal computer based counterparts. As a result of graphical programming based solutions, the computer monitor was turned into a replacement of the front panel of the traditional instruments and, in fact, with enhanced features. Plug-in data acquisition boards transform personal computers into digital device capable to collect signals from sensors and to send commands to actuators.

Virtual instrumentation supports a variety of computer based monitoring and control systems which, besides plug-in Data Acquisition boards (DAQ) include General Purpose Instrument Bus (GPIB) and VXI mainframes.

The presentation of this application covers the fundamental knowledge needed for interfacing sensors with a PC using the new framework of virtual instrumentation.

This application focuses on the knowledge needed to a non specialist in computers to develop a modern monitoring system i.e. to connect sensors to a PC (or a Laptop), condition their signals when required as well as to store and process the data using digital signal processing subroutines available in commercial virtual instrumentation packages.

The principal features of this application are: a) Using the HP VEE and LabVIEW, the two most important virtual programming language, to control the instruments, to acquire the signals and to process them; b) Signal acquisition based on DAQ Card; c) Execution of signal acquisition from various sensors. The applications contains numerous programming and numerical examples how to measure the temperature, angular and linear displacement and vibrations and are organized in the following modules:

Module 1 PCM-DAS16D/12DAQ Card-Pulse and DC Voltage Response

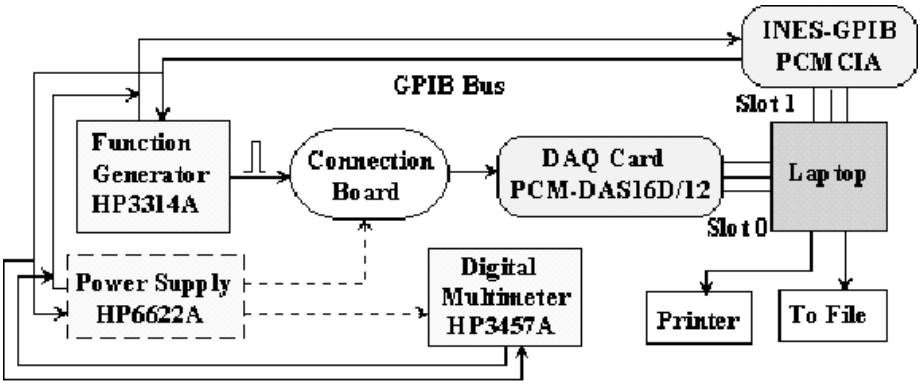

Fig.2 Experimental set-up for obtaining DAQ Card pulse and DC voltage response

In figure 3 is shown the DAQ Card response signals for the inputs signals 1KHz and 100KHz, and in figure 4 the DC voltage response of the DAQ Card.

The Work area of the Das2.vee program for card DC voltage response, presented in figure 5, contains the virtual front panel of the instruments, the dialog boxes, the visualizing charts, the file name and data numeric display.

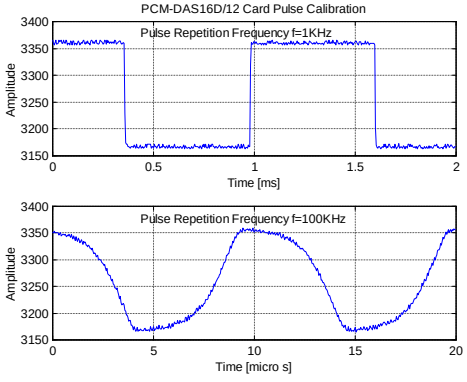

Fig.3 Card Pulse Calibration

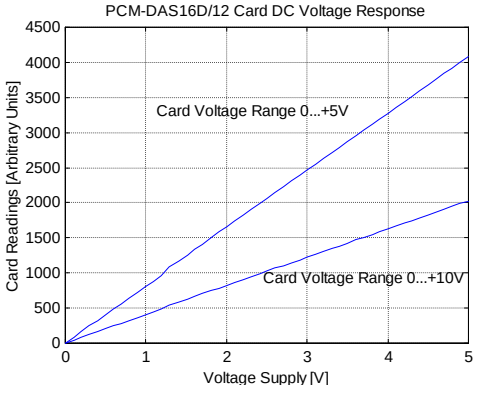

Fig.4 Card DC Voltage Response

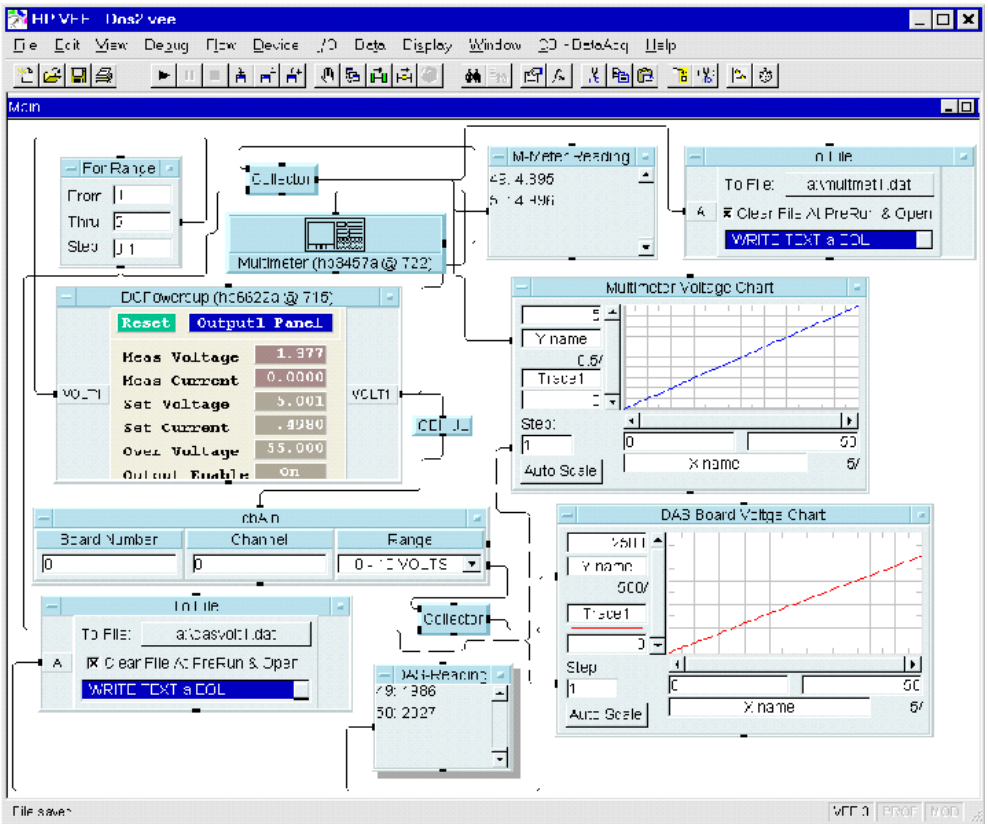

Fig.5 Work area of the Das2.vee program for card DC voltage response.

Module 2 Signal Acquisition from Various Sensors

2.1 Angular Potentiometer

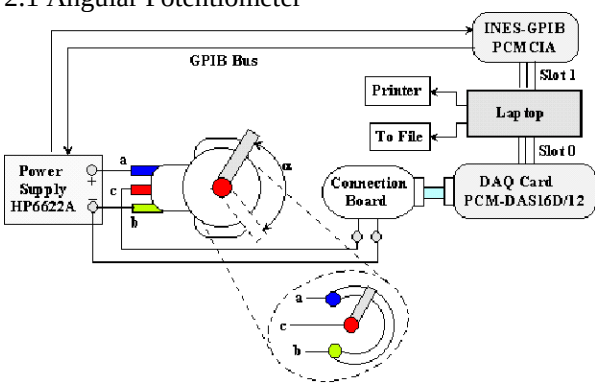

Fig.6 The measurement block diagram

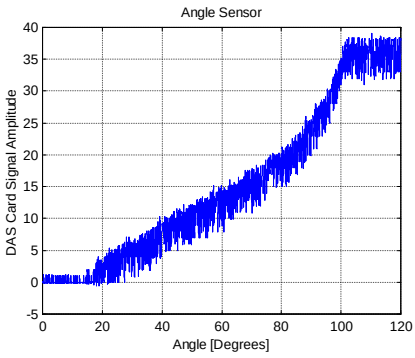

Fig.7 The Voltage response vs. Angle

This potentiometer type used as a sensor, converts angular displacement into voltage.

The block diagram presented in figure 6, contains the measurement scheme of the Angular Potentiometer whose angular displacement α is a result of turning manually its wiper.

The Power Supply control is achieved by the INES-GPIB Card.

2.2 Inductive Sensor

The inductive sensor uses variable magnetic interaction to convert motion into time varying voltage. The block diagram presented in figure 8 contains the measurement scheme of an inductive sensor excited by a vibrating membrane.

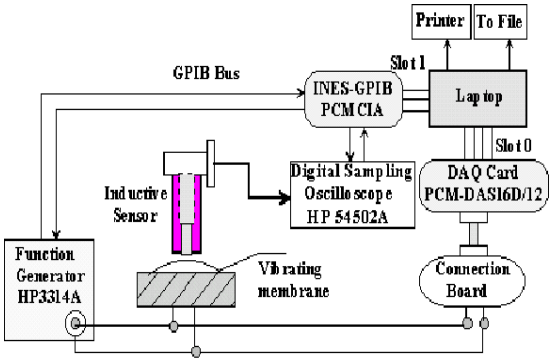

Fig.8 The block diagram

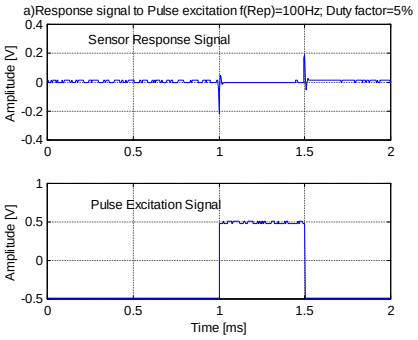

Fig.9 The response signal and the pulse excitation signal

The Function Generator control is achieved by the INES-GPIB Card. The inductive sensor response is measured with the GPIB Digital Sampling Oscilloscope. The vibrating membrane excitation signal from the Function Generator is measured by the DAQ Card.

2.3 Thermocouple

The thermocouple convert temperature variations into a voltage signal. In figure 10 is shown the block diagram to measure the temperature variations of a Heat Source with a thermocouple.

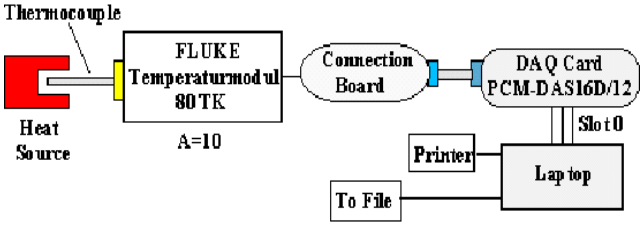

Fig.10 The block diagram

The HP VEE Work Area shown in figure 11, contains the virtual instruments. The top part shows the dialog boxes which permit the selection of the acquisition and analyzing parameters of the DAQ Card. The bottom part shows the graph of the thermocouple output signal in an unspecified units, the file name, data collector and numerical display.

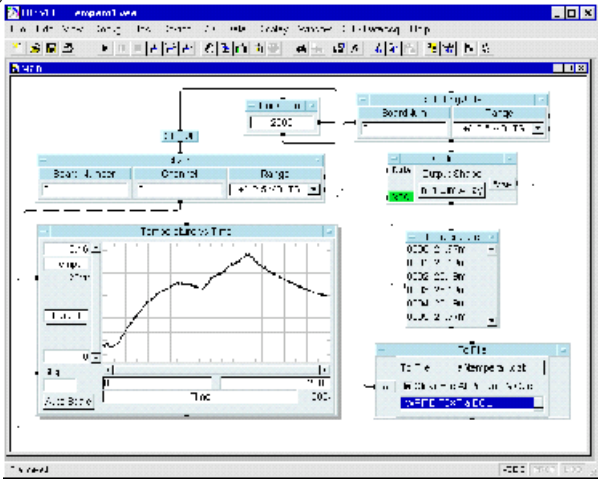

Fig.11 HP VEE work area for temperature measurement with a thermocouple

Module 3 Measuring Control for HF Components Characterization

3.1 HF Passive Components: Low-Pass Filter

An ideal Low-Pass Filter is a passive electric network that allow to pass without attenuation input signals below a desired frequency value, called cut-off frequency. The signals with the frequencies greater than the cut-off frequency are attenuated.

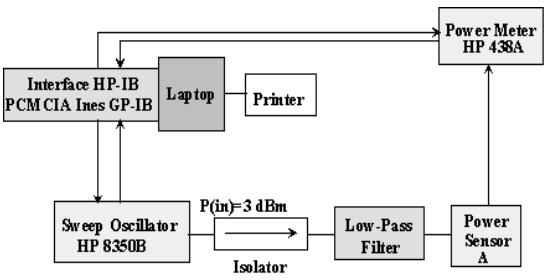

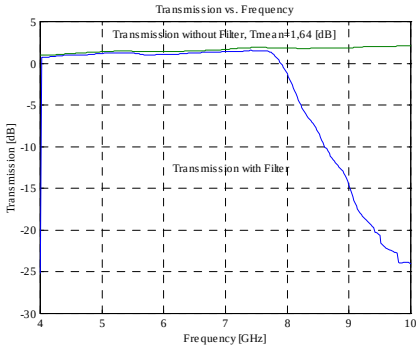

Fig.12 The block diagram

Fig.13 Transmission signal vs. frequency

INES-GPIB Card is used in this measurement and control scheme (figure 12) for the instrument control of the Sweep Oscillator and for the data acquisition with the Power Meter.

Only transmission is measured with and without filter. In the figure 14 is presented the HP VEE Work Area with the virtual instruments. The top parts shows the dialog box of the instrument control of the Sweep Generator for the frequency range from 4 to 10 GHz in steps of 20 MHz. The bottom part shows the dialog box of the Power Meter with input from Power sensor. The right hand side of the figure contains the data collectors, numerical and graphical display.

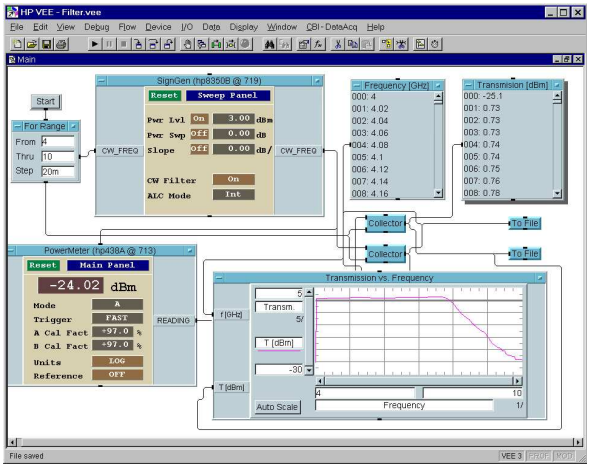

Fig.14 The HPVEE Work Area with the virtual instruments

3.2 HF Active Components: VCO (Voltage Controlled Oscillator)

VCO produce signals of variable frequency, due to a non-linear component (for example a varactor diode) whose capacitance is modified by an input voltage. Consequently, the VCO frequency is modified in a desired range.

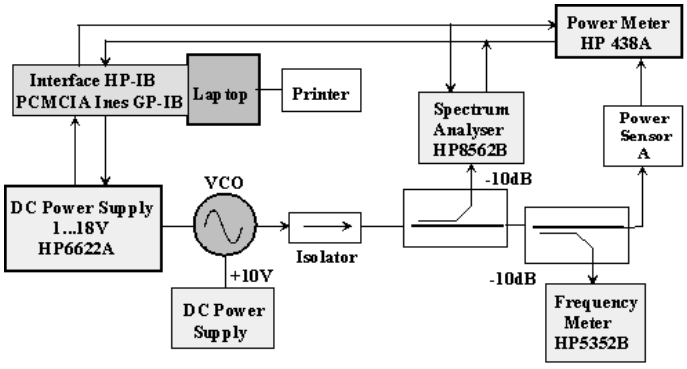

Fig.15 The block diagram to measure the characteristics of a VCO

INES-GPIB Card is used in this measurement and control scheme, shown in figure 15 for the instrument control of the DC Power Supply and for the data acquisition and analysis with the Power Meter, Frequency Meter and Spectrum Analyzer.

The process under measurement and control is a VCO supplied by a constant 10V DC Power Supply an a variable from 1 to 18V GPIB controlled DC Power Supply. The test consists in the measurement of VCO power and frequency output versus variable input voltage.

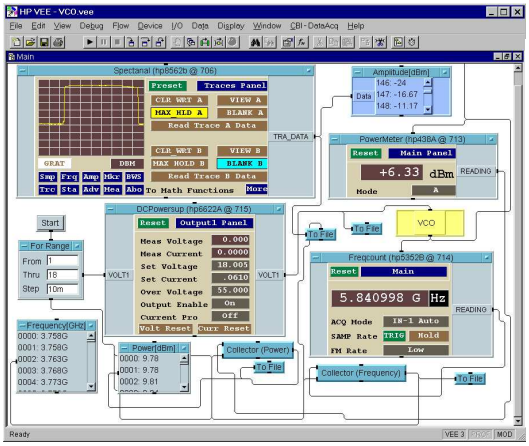

Fig.16 The HP VEE Work Area

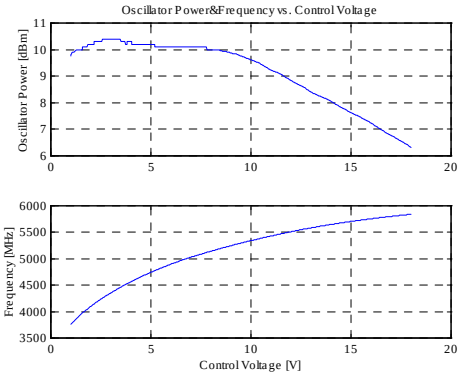

Fig.17 The VCO Power & Frequency vs. voltage

The HP VEE Work Area (figure 16) contains the display of the results of the Spectrum Analyzer, Power Meter and Frequency Meter as well as a control block, For Range, for variable voltage DC Power Supply from 1 to 18V in steps of 10 mV.

Module 4 Signal Processing

4.1 Signal Generation–Ramp Pattern

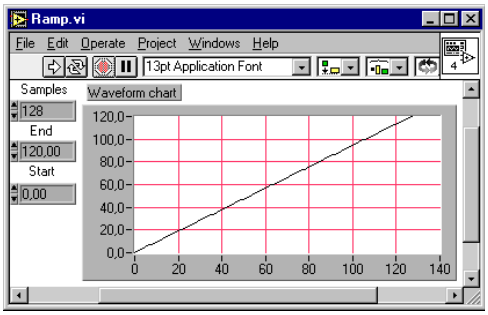

Fig.18 Front Panel

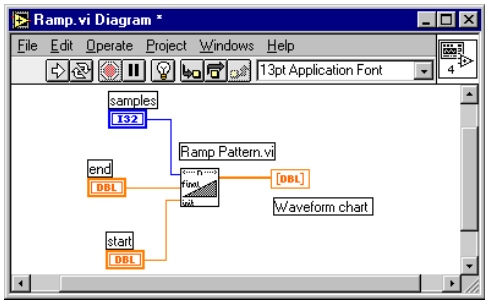

Fig.19 The Block Diagram

The LabVIEW Front Panel (figure 18) for the Ramp Pattern program Ramp.vi contains controls for Samples, End and Start as well as an indicator for displaying graphically the Ramp Pattern. The block diagram (figure 19) is centered around the Ramp Pattern.vi Virtual Instrument and the corresponding icons for the controls and indicators.

4.2 Mathematical Operation of Signals – Differentiation & Integration of a function

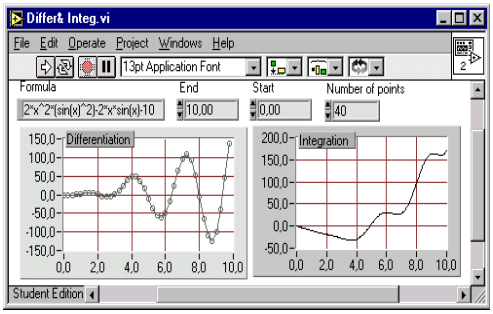

Fig.20 The Front Panel

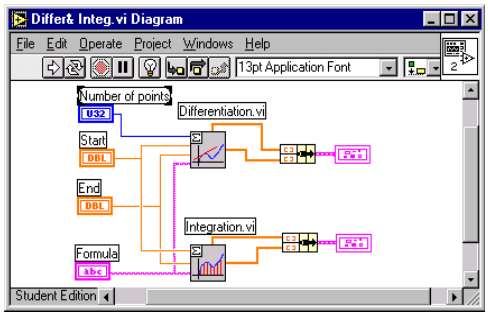

Fig.21 The Block Diagram

The Front Panel (figure 20) shows the graphical results of the differentiation and integration of a function given in Formula for the values between Start=0 to End=10 with Number of points=40. The block diagram (figure 21) is centered around Differentiation.vi and Integration.vi Virtual Instruments and contains the icons corresponding to the controls and indicators from the Front Panel.

4.3 Filtering – Smoothing

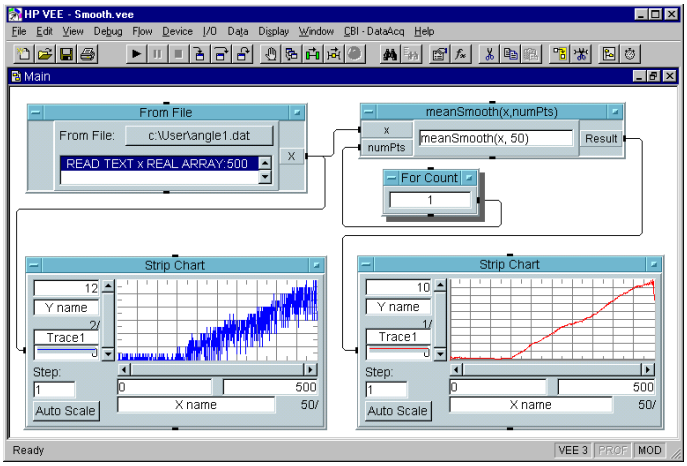

Fig.22 The HP VEE Work Area of the smooth.vee program

Another example of Signal Processing is a smooth.vee program for filtering the noisy output of the previously presented angular potentiometer signal.

The Work Area (figure 22) contains the From File block with data address, the mean Smooth block of the Filter (with the sliding windows of 50 samples) and two Strip Charts to represents the noisy and filtered signals.

The application is specifically addressed to senior undergraduate students in engineering and science as well as for practicing engineers and researchers with interest in using computer based instrumentation. This application is an introduction by illustrative examples to the use of Virtual Instrumentation based on HP VEE and LabVIEW.

A complete presentation of HPVEE and LabVIEW can be found in the references [1-5].

REFERENCES

1. HP VEE Graphical Programming Tool, Hewlett-Packard
2. R.Helsel, Visual Programming with HP VEE, Prentice Hall, 1996
3. LabVIEW, Data Acquisition Basics Manual, National Instruments, 1998
4. R.Bishop, Learning with LabVIEW, Addison Wesley, 1998
5. R.Baican, D.Necsulescu, Applied Virtual Instrumentation, WIT Press, 2000

STUDIA UNIVERSITATIS BABEŞ-BOLYAI, PHYSICA, SPECIAL ISSUE, 2001

SPECTROSCOPIC INVESTIGATION OF SOME POLYMORPHIC DRUGS. PART I. *INDOMETHACINE*

I. BRATU[1], RODICA GRECU[2], GH. BORODI[1], FELICIA GOZMAN-POP[3], M. BOJITA[3]

[1]National Institute for Research and Development of Isotopic and Molecular Technologies, P.O. Box 700, R-3400 Cluj-Napoca 5, ROMANIA, E-mail: ibratu@L30.itim-cj.ro
[2]"Raluca Ripan" Institute of Chemistry, Fantanele 30, R-3400 Cluj-Napoca
[3]"Iuliu Hatieganu" University of Medicine and Pharmacy, Pasteur 6, R-3400 Cluj-Napoca

ABSTRACT. The polimorphism of *Indomethacine*, an antiphlogistic drug, was investigated by X-ray diffraction and FTIR spectral methods. The recrystallization from various solvents has as effect the formation of two polymorphs and different solvates.

Keywords: polymorphism; *Indomethacine*; FTIR spectroscopy, X-ray diffraction

Introduction

An adequate selection of the drugs crystalline structure is a major task of the pharmacists. They should include in their investigations the thermodynamical and stability aspects and also the behavior of these drugs in living organisms.

In a crystalline material the constituent molecules are part of an orderly three-dimensional structure. Often, depending on the particular crystallization conditions, the molecules arrange themselves in various forms (crystal lattices). This type of crystalline material is said to be polymorphic and each of its crystal ordering is called a polymorph. In other words the polymorphs are substances with the same chemical composition but presenting different crystalline forms (various crystallographic systems, lattice parameters and position of the atoms in the elementary cell). When the crystal lattice include solvent molecules in its structure, the recrystallization leads to the formation of solvates or ″pseudo-polymorphs″.

The significance of polymorphism to the pharmaceutical industry lies in the different properties (e.g. solubility, dissolution rate, chemical reactivity, melting point, resistance to degradation, bioavailability) of various polymorphs, which dictate the biodisponibility of the active substance.

The *Indomethacin*e *i.e.* 1-(p-chlorobenzoil)-5-methoxy-2-methylindol-3-acetic acid is a drug that presents antiphlogistic, analgesic and antipiretic activities. There exist discussion in the literature concerning the polymorphism of the *Indomethacine* [1]. In order to study the polymorphism of this drug, the X-ray diffraction patterns and infrared spectra are used in the present paper.

Experimental

*Indomethacin*e was prepared in accordance to literature [2]. By recrystallization from toluene and methanol two polymorphic forms, named I (m.p. 153–154°) and respectively II (m.p. 159–164°), were obtained. Other samples were prepared by recrystallization from benzene, chloroform, ethanol and ethyl ether.

X-ray diffraction spectra were obtained with a DRON-2 powder diffractometer using the CuK_α radiation and a Ni filter. Infrared spectra were registered in the 400–4000 cm^{-1} spectral range with a JASCO-610 FTIR spectrometer using KBr pellet and chloroform solution techniques.

Results and Discussion

There are some questions concerning the number of the polymorphs of *Indomethacine*: three (α with m.p. 154.5–155.5°, β with m.p. 158-160°° and γ with m.p. 160-161.5°) [1] or only two (form II with m.p. 160°, form I with m.p. 154°) [3,4]. It is known only the fact that *Indomethacine* with therapeutic efficiency, named here form I, is a crystalline powder (triclinic crystallographic form [1]), m.p. 153–154°.

A polymorphic transformation is characterized by a change in which a reorganization of ions appears, atoms or molecules that occupy the nodes of the lattice. For different polymorphs one can modify the crystallographic system, the parameters of the elementary cell and the mode of the distributions of the atoms in the elementary cell. The parameters of the elementary cell determine the positions of the diffraction maxima whereas the positions of the atoms the intensities of the diffraction lines.

Our data evidence two polymorphs of *Indomethacine*. One can see, by inspection of the Fig. 1, different diffraction lines and different angular position and intensities of the lines for the samples of *Indomethacine* obtained by recristallization from toluene (form I) and methanol (form II). That means different parameters of the elementary cell and distinct positions of the atoms in the cell. The triclinic elementary cell having the parameters given in literature [1] is confirmed from X-ray diffraction spectrum of *Indomethacine* I.

Each polymorph, usually has typical, differential IR and NIR spectra by virtue of atomic vibrations in the molecule being influenced by their differential ordering in the crystal lattice. Infrared spectra of *Indomethacine* I and II registered in chloroform solution are identical while the spectra of these samples prepared using KBr pellet technique are different (Figure 2). This situation is characteristic for polymorphs and is due to difference in crystal structure.

For *Indomethacine*:

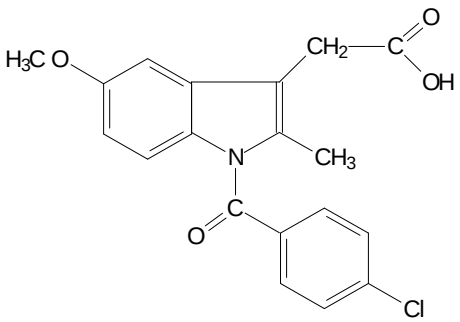

infrared spectra suggest that hydrogen bonds have an important role in structure of polymorphs. Comparative to *Indomethacine* I, the frequency of both C=O stretching vibrations is shifted to lower values.

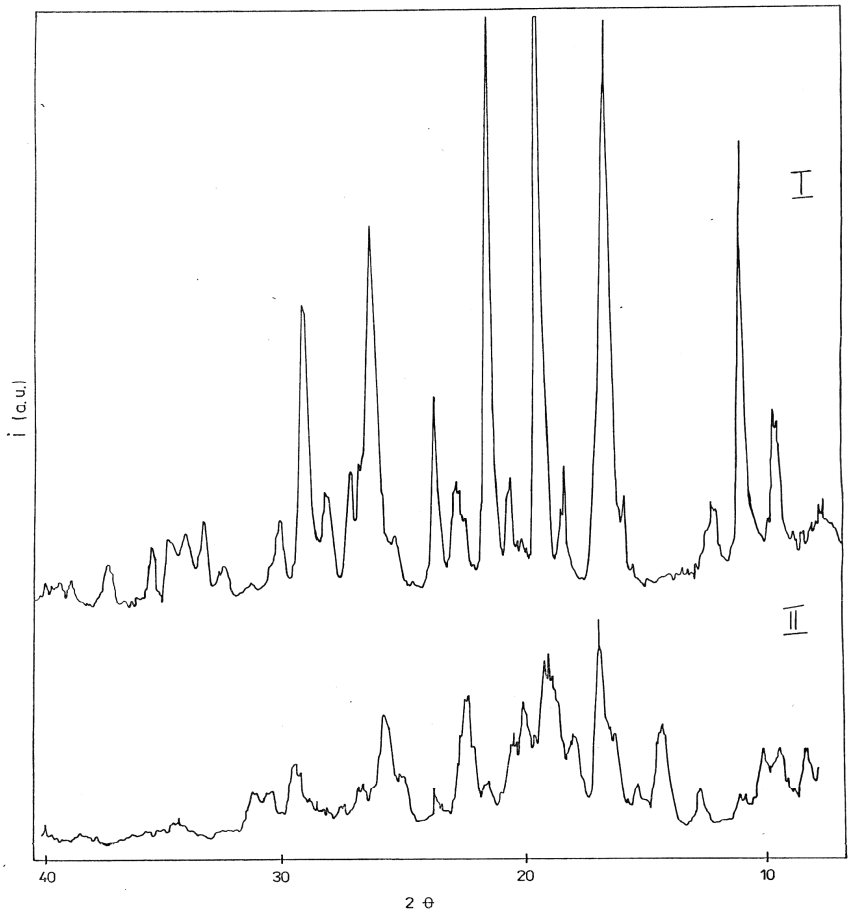

Figure 1. X-ray diffraction spectra for Indomethacine *I and II polimorphic forms.*

The thermal behaviour and infrared spectra indicate that *Indomethacine* sample recrystallized by us from chloroform (m.p. 95–104°) is a ˝peudo–polimorph˝; solvent molecules are included in the crystalline lattice. The position of ν(C=O) bands from infrared spectrum is significant. We assigned them as follows (in bracket is indicated the solvent used for recrystallization):

	ν(C=O)	ν(C=O)(carboxy)
Indomethacine I (toluene)	1717.3 cm^{-1}	1691.7 cm^{-1}
Indomethacine II (methanol)	1700.4 cm^{-1}	1677.8 cm^{-1}
Indomethacine (chloroform)	1696.1 cm^{-1}	1676.8 cm^{-1}
Indomethacine (ethanol)	1691.7 cm^{-1}	1679.7 cm^{-1}

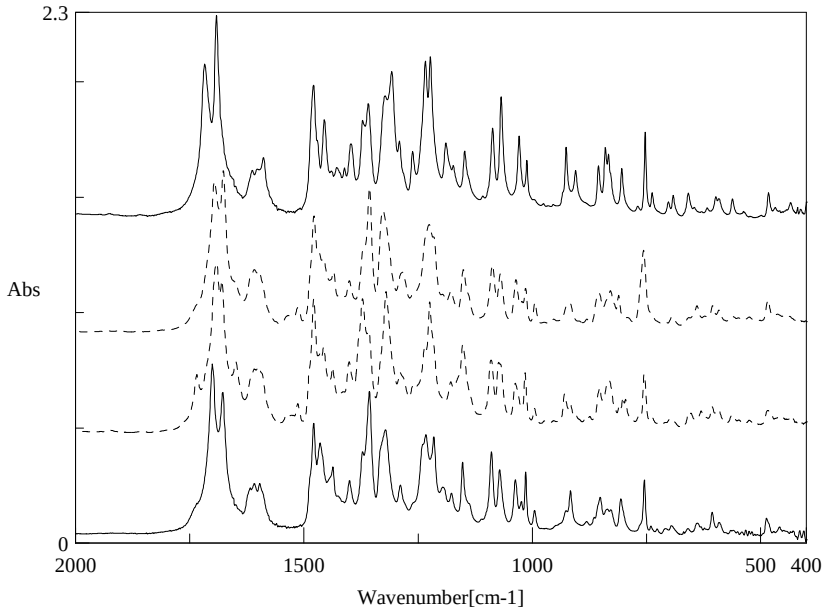

Figure 2. FTIR spectra of various samples of Indomethacine *polymorphs (—) (form I, up; form II, down) and "pseudo-polymorphs" (---) (recrystallized from chloroform, up; from ethanol, down).*

The use of benzene as solvent does not influence the structure of *Indomethacine* I. The sample obtained by recrystallization from ethyl ether has spectra alike *Indomethacine* II. The existence of two colored polymorphs prepared by Borka [5] using as solvent benzene and methanol is questionable.

Conclusions

Indomethacine has two polimorphic forms and the infrared spectra of the solid samples prepared by KBr technique can be used to identify the therapeutic active form (*Indomethacine* I). The frequency of ν(C=O) bands is quite characteristic and distinct from that of the other polymorphic form or solvates.

Acknowledgements

The authors are thankful to *"TERAPIA"* factory from Cluj-Napoca, Romania, for supplying with *Indomethacine* sample.

REFERENCES

[1]. I. Grecu, D. Monciu, "*Structura cristalina si biodisponibilitatea substantelor medicamentoase*", Ed. Medicala, Bucuresti, 1984, p. 183–184.
[2]. L. Beu, J. Russu, I. Farcasanu, Gh. Bora, *Rev. Chimie*, **36**, 400 (1985).
[3]. D.J. Allen, K.C. Kwau, *J.Pharm.Sci*., **58**, 1190 (1969)
[4]. D.C. Monkhouse, J.L. Lach, *J.Pharm.Sci*., **61**, 1435 (1972)
[5]. L. Borka, *Acta Pharm. Suecica*, 11(3). 295 (1979).

STUDIA UNIVERSITATIS BABEŞ-BOLYAI, PHYSICA, SPECIAL ISSUE, 2001

PROTON NMR SPECTROSCOPY STUDIES OF THE INCLUSION COMPLEX OF NIFLUMIC ACID WITH β - CYCLODEXTRIN

M. BOGDAN*, S.I. FARCAS*, MINO R. CAIRA**

**National R&D Institute of Isotopic and Molecular Technologies, P.O. Box 700, 3400 Cluj-Napoca, Romania*
*** Department of Chemistry, University of Cape Town, Rondebosch 7701, South Africa*

ABSTRACT. The inclusion complex of niflumic sodium salt with β-cyclodextrin has been studied by proton NMR at 300 MHz. The continuous variation technique was used to evidence the formation of a 1**:**1 complex in aqueous solution at pH = 12. The association constant of the niflumic Na salt with β-cyclodextrin has been obtained at 298 K, by fitting the experimental chemical shift difference, $\Delta\delta_{obs} = \delta_{obs} - \delta_{free,}$ (for a given proton) of the observed guest or host molecule, with a non-linear regression method. Besides the effective association constant, the fitting procedure allows a precise determination of all NMR parameters of the pure inclusion complex which are used for an analysis of the geometry of the molecular edifice in solution.

Introduction

The non-steroidal anti-inflammatory drugs (NSAIDS) are one of the most commonly used classes of drugs. However, at high-sustained dosages, most NSAIDS cause ulcerative side effects as gastric irritation and bleeding [1]. Several approaches have been tested for preventing or reducing these side effects, including prodrug formulation, microencapsulation and addition of neutralising excipients [2]. One of the more recent method tested is complexation of NSAIDS with cyclodextrins [3]. For a better understanding of the therapeutic properties of these complexes a complete characterisation in terms of stoichiometry, stability and molecular conformation has to be performed.

We report here a ^{1}H NMR study of the complex formed between niflumic acid **1** (anion form) and β-cyclodextrin in aqueous solution.

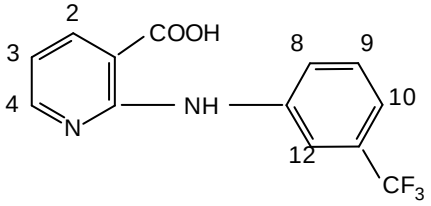

(**1**)

Analysis of our data by the continuous variation method indicates that the inclusion occurs and the complex has 1:1 stoichiometry. The association constant for the 1:1 complex was calculated by a non-linear least squares regression analysis of the observed chemical shift changes of the drug and β-cyclodextrin NMR lines, as a function of β-CD concentration.

Materials and Methods

β-CD (water content 8 mol/mol) was purchased from Sigma Chemie GmbH (Germany), D_2O (deuterium content 99.7 %) from Institute of Cryogenics and Isotope Separations (Rm. V>lcea, Romania) and niflumic acid was kindly donated by the Chem. Department, University Cape Town, South Africa (Prof. Mino Caira).

Proton NMR spectra were performed at 300 MHz using a Varian Gemini spectrometer. The NMR spectra were recorded in D_2O solution at 298 ± 0.5 K and all chemical shifts were measured relative to external TMS. Typical conditions were as follows: 32 K data points; sweep width 4500 Hz giving a digital resolution of 0.28 Hz/point. The pulse width was 5 μs (45^0) and the spectra were collected by co-addition of 32 or 64 scans.

Due to extremely low solubility of the niflumic acid in water, this was converted to sodium salt by titration with NaOD in D_2O to a final pH = 12 (uncorrected meter reading). At this pH value the niflumic acid was practically completely ionised and two stock solution (both 10 mm) of sodium niflumate and β-CD were prepared in D_2O.

The stoichiometry of the complex was determined by the continuous variation method. The overall concentration of the two species was kept constant ([H] + [G] = M = 10 mM) and the ratio $r = \frac{[H]}{[H]+[G]}$ was varied form 0 to 1. This was accomplished by using the equimolar solutions of H and G and mixing them to constant volume to the desired ratio r. [H] and [G] are the total concentrations of the host and guest respectively.

The quantity $\Delta\delta_{obs}^{(X)}[X]$ where X = H or G was plotted against r. $\Delta\delta_{obs}^{(X)}$ is the difference between the chemical shift of free X and the observed value for a given ratio r.

For determination of association constant (K), the same set of samples as that for the determination of stoichiometry was used. The data were evaluated according to eq. (1):

$$\Delta\delta_{obs}^{(X)} = \left\{ M + \frac{1}{K} - \left[\left(M + \frac{1}{K} \right)^2 - 4[H][G] \right]^{1/2} \right\} \frac{\Delta\delta_C^{(X)}}{2[X]}$$

In eq. (1), $\Delta\delta_C^{(X)}$ represents the chemical shift difference (for a given proton) between thefree molecule and the pure complex.

Inclusion of niflumic anion is shown by the change in the chemical shift of some of the guest and host protons in comparison with the chemical shifts of the same protons in the free compounds. Partial 300 MHz ^1H NMR spectra of the pure compounds and of niflumic-βCD complex are displayed in Figures 1 and 2.

Distinct peaks are not observed for a bound and a free form, indicating that complexation is a dynamic process, the included niflumate undergoing rapid exchange (on the NMR time scale) between the free and bound state.

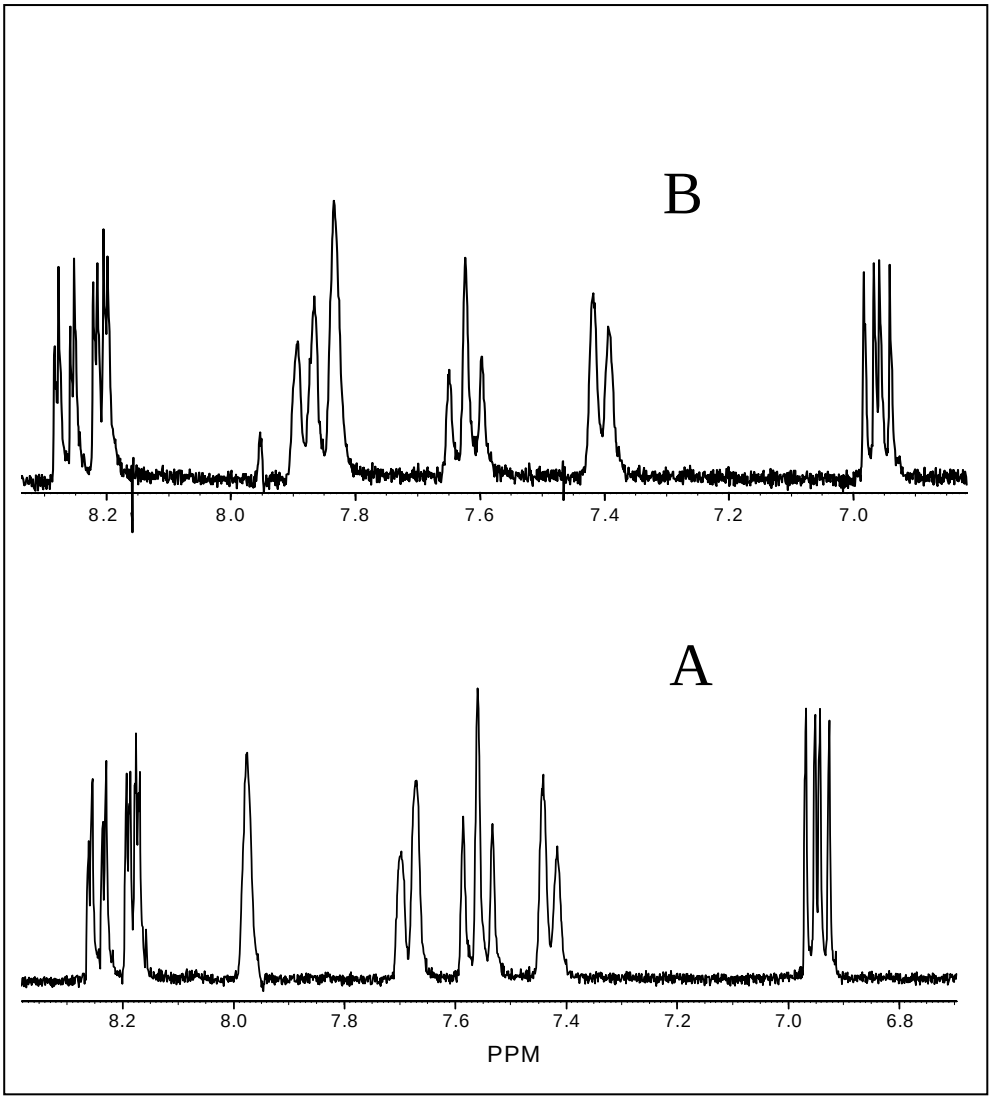

Fig. 1. Partial 300 MHz ^{1}H NMR spectra of (A) 10 mM Na niflumate and (B) 5 mM Na niflumate and 5 mM β-CD

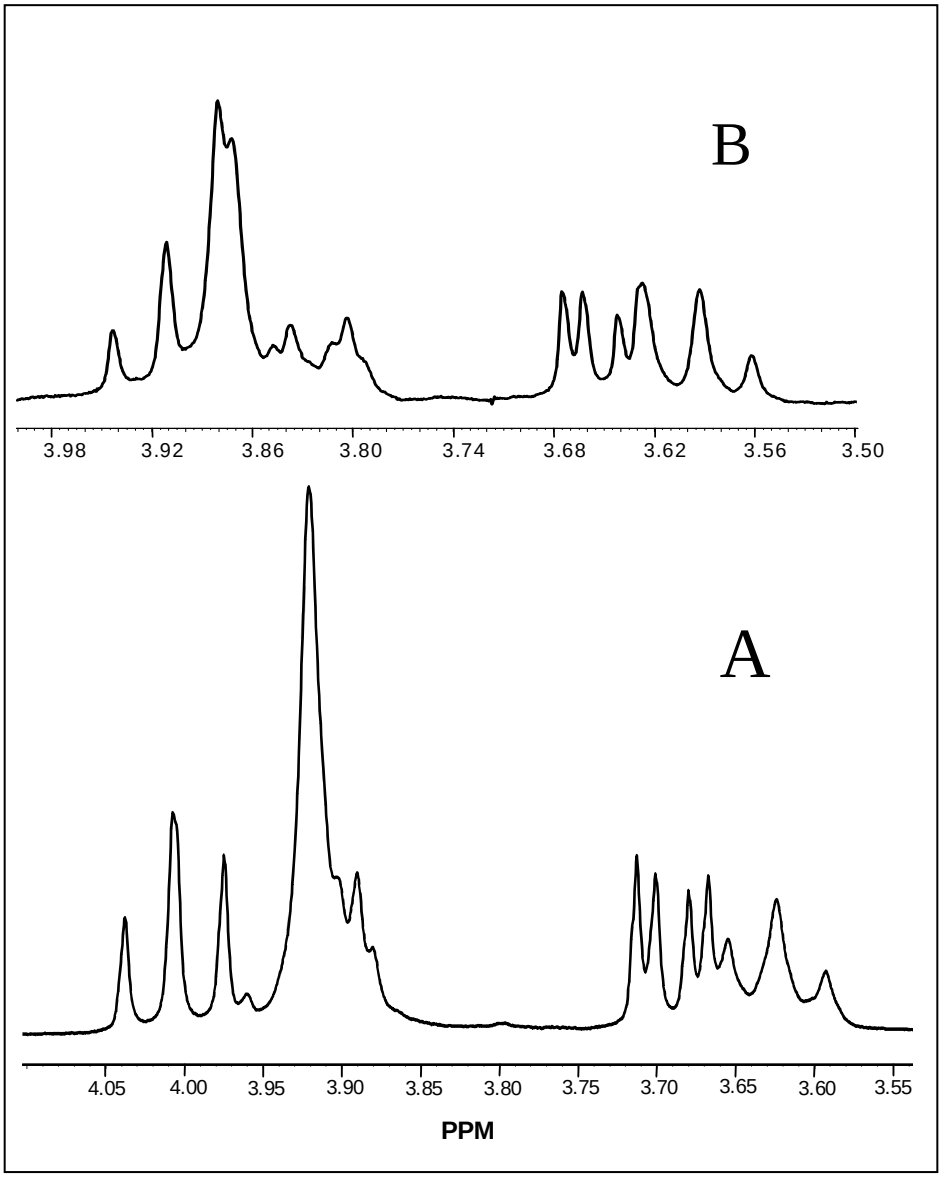

Fig. 2. Partial 300 MHz ^{1}H NMR spectra of (A) 10 mM β-CD and (B) 5 mM β-CD and 5 mM Na niflumate
Only the spectral region for protons H-2 to H-6 of β-CD is displayed

To establish the stoichiometry of the complex, the continuos variation method was used to follow the changes in chemical shifts of protons H-5, H-3, and H-6 of β-CD (Figure3) and protons 9, 10 and 12 of the ninflumate anion (Figure 4) which shows the most marked variations. Although the shape of the curves in Figures 3 and 4 are not highly symmetrical, the maximum does not deviate significantly from r = 0.5, indicating the existence of a 1:1 stoichiometry within the range of concentrations investigated. On the other hand, the changes in chemical shifts of protons H-3 ($\Delta\delta_{obs}^{max}$ = 0.133 ppm) and H-5 ($\Delta\delta_{obs}^{max}$ = 0.131 ppm) of β-CD do not conclusively indicate which side of the β-CD cavity is involved in complex formation, because no significant differences were detected. The signals of the included niflumate are shifted by complexation to a variable extent. The piridine ring protons experiences very little perturbation. Conversely, the phenyl ring protons are strongly affected by the formation of the inclusion complex. The chemical shift difference for the protons belonging to phenyl ring are higher than that for piridine ring by a factor of 10. These results clearly support the assumption that the niflumate anion is entering with the trifluoromethylphenyl residue in the β-CD cavity.

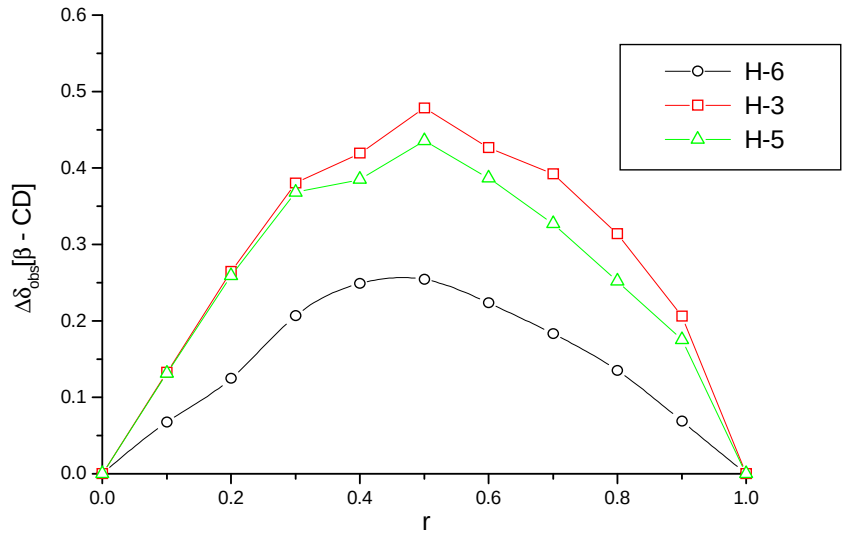

Fig. 3. Job plot for H-3, H-5 and H-6 protons of β-CD in the presence of different concentrations of niflumic acid anion.

The association constant K was evaluated form the observed differences in chemical shifts for niflumate (9, 10 and 12) and β-CD (H-3, H-5 and H-6) protons, based on eq. (1). This equation involves no approximations and correlates the total concentrations

of the guest and host molecules with the observed difference in chemical shift, $\Delta\delta_{obs}^{(X)}$. We developed a computer programme written in C^{++} based on an iteration procedure following specific algoritms in order to fit the experimental values of $\Delta\delta_{obs}^{(X)}$ to the appropriate equation. Each iteration sets up a quadratic programme to determine the direction of search and the loss function (ΔY^2, defined as the sum of the squared derivation about the predicted values), until the search converges. The programme is producing one single K value for the whole process and a set of calculated $\Delta\delta_{C}^{(X)}$ values. The programme is quite flexible since both the guest and host can be observed for spectroscopic perturbations as a function of variable guest or host concentrations.

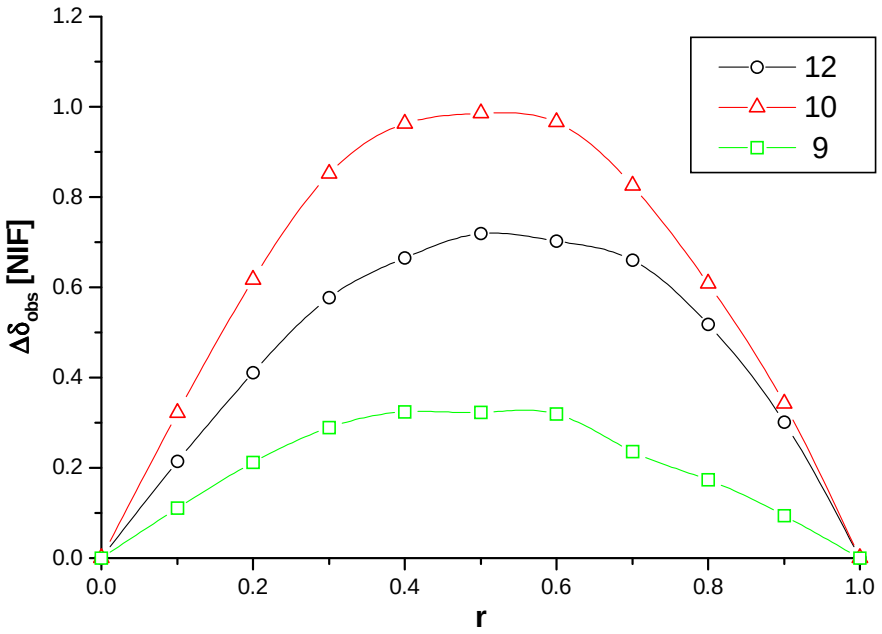

Fig. 4. Job plots for protons 9,10 and 12 of niflumic acid anion (NIF) in the presence of different concentrations of β-CD.

The overall K obtained from this procedure was 336 M^{-1} at 298 K, with $\Delta Y^2 = 1.38 \cdot 10^{-3}$ and the correlation factor r = 0.9992. The complete set of chemical shifts in the free state and pure complex are reported in Table 1.

Table 1.

Chemical shifts (ppm) of the niflumic acid anion and β - cyclodextrin protons in the free and complex states ($\Delta\delta_c = \delta_c - \delta_{free}$).

Proton	δ_{free}	δ_c	$\Delta\delta_c$
Niflumic acid anion			
2	8.182 (dd)	-	-
3	6.948 (dd)	-	-
4	8.246 (dd)	-	-
8	7.429 (d)	-	-
9	7.560 (t)	7.412	-0.148
10	7.685 (d)	7.248	-0.438
12	7.977 (s)	8.279	0.302
β - Cyclodextrin			
H1	5.111	-	-
H2	3.690	-	-
H3	4.007	4.199	0.192
H4	3.624	-	-
H5	3.907	4.090	0.183
H6	3.921	4.019	0.0981

Conclusions

Analysis of our data by the continuous variation method indicates that the inclusion occurs and the complex has 1:1 stoichiometry. The association constant K for the inclusion complex was evaluated from the observed differences in chemical shifts for niflumate and β-CD protons. Unfortunately not conclusive indication concerning which side of the β-CD cavity is involved in complex formation. The results clearly support the assumption that the niflumate anion is entering with trifluoromethylphenyl residue in the β-CD cavity.

REFERENCES

[1] T. Loftsson, B.J. Olafsdottir, H. Fridriksdottir, S. Jonsdottir, Eur. J. Pharm. Sci., **1,** 95 (1993).

[2] J.R. Nixon, M.S. Harris "Development of Drugs and Modern Medicines" J.W. Gorrod, G.G. Gibson and M. Mitchard Eds. Ellis Harwood, UK, 19.

[3] T. Irie, K. Uekama, J. Pharm. Sci., **86,** 147 (1997).

STUDIA UNIVERSITATIS BABEŞ-BOLYAI, PHYSICA, SPECIAL ISSUE, 2001

SOLID-STATE NMR AND FTIR CHARACTERIZATION OF 3-MERCAPTOPROPYL SILICA GEL R

VIRGINIA COMAN*, RODICA GRECU*, JÜRGEN WEGMANN, STEFAN BACHMANN** and KLAUS ALBERT****

**"Raluca Ripan" Institute of Chemistry, Str. Fântânele 30; P.O. Box 702, Of. P. 5, RO-3400 Cluj-Napoca, ROMANIA; E-mail: v.coman@icrr.cj.edu.ro*
***University of Tübingen, Institute of Organic Chemistry, Auf der Morgenstelle 18, D-72076 Tübingen, GERMANY; E-mail: klaus.albert@uni-tuebingen.de*

ABSTRACT. The surface modification of Romanian silica gel sample was performed by organosilanization reaction with 3-mercaptopropyltrimethoxysilane. The obtained stationary phase was investigated by ^{29}Si and ^{13}C CP/MAS NMR and FTIR spectroscopic solid-state techniques in order to put in evidence the presence of the modifier and the variety of bonded silyl species on the surface as well as to find out the modifier effect on the surface properties.

Keywords: 3-Mercaptopropyl chemically modified silica gel, FTIR, Solid-State NMR

1. INTRODUCTION

Stationary phases based on silica gel chemically modified with organic compounds are widely used in chromatography due to their practical advantages, especially the high separation selectivity [1]. The general and the most used method for the synthesis of modified nonpolar and polar stationary phases is the interaction of superficial hydroxyl groups of silica gel with organosilicon compounds. Owing to steric hindrance, the modification affects only about half of the surface silanol groups. With bi- or trifunctional modifiers, some Si–X reactive groups (X = –Cl, $–O–CH_3$) remains unreacted, that produce additional hydroxyls on silicon atom due to the hydrolysis [2].

The aim of this paper was to study the 3-mercaptopropyl chemically modified silica gel R (Romanian silica gel) surface using the Solid-State NMR and FTIR spectroscopic methods.

2. EXPERIMENTAL

The investigated sample was obtained by the organosilanization reaction of O–H groups of silica gel R with 3-mercaptopropyltrimethoxysilane as modifier [3].

Infrared spectra of samples were registered on a JASCO-610 FTIR spectrometer, using KBr pellet technique. To improve the sensibility of IR method, the difference and second-derivative spectra were also analysed.

^{29}Si and ^{13}C CP/MAS NMR spectra were recorded on Bruker ASX 300 and DSX 200 spectrometers in order to study the surface modification of the samples.

3. RESULTS AND DISSCUSIONS

The chemical modification of the silica gel surface is related to the presence of the free silanol groups (─Si─OH). The effects of silanization reaction are the reduction of the superficial ─OH group number and a greater variety of siloxane groups (─Si─O─Si─). For the studied compound, the following reaction takes place:

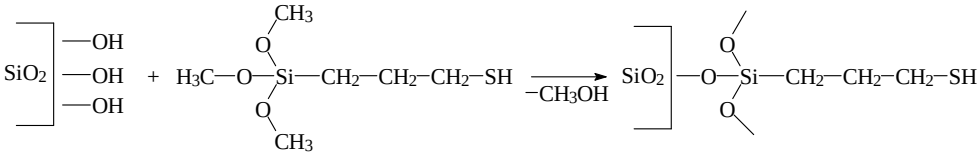

silica gel (inorganic support) — 3-mercaptopropyltrimethoxysilane (trifunctional modifier) — 3-mercaptopropyl silica gel (chemically modified stationary phase)

3.1. FTIR Study

When the samples are prepared using the well-known method of KBr pellet, infrared data are useful only to confirm the existence of the bonded species. Due to the low concentration of the organic part of modifier on the surface, the intensity of the new bands attesting the presence of CH_2 groups is weak. Hardly are observed any differences in the 2800–3000 cm^{-1} range, where ν(C─H) vibrations of the ─CH_2─ groups are evidenced (Figure 1). In the difference spectrum of 3-mercaptopropyl modified and unmodified silica gel R samples (Figure 2), we can easy to identify the $\nu_{as}(CH_2)$ and $\nu_{sym}(CH_2)$ bands at 2930 cm^{-1} and respectively 2855 cm^{-1}. The band at 2960 cm^{-1} is assigned to $\nu_{as}(CH_3)$ and this fact confirms that, due to steric reasons, the functionality of 3-mercaptopropyltrimethoxysilane is 2 and 3.

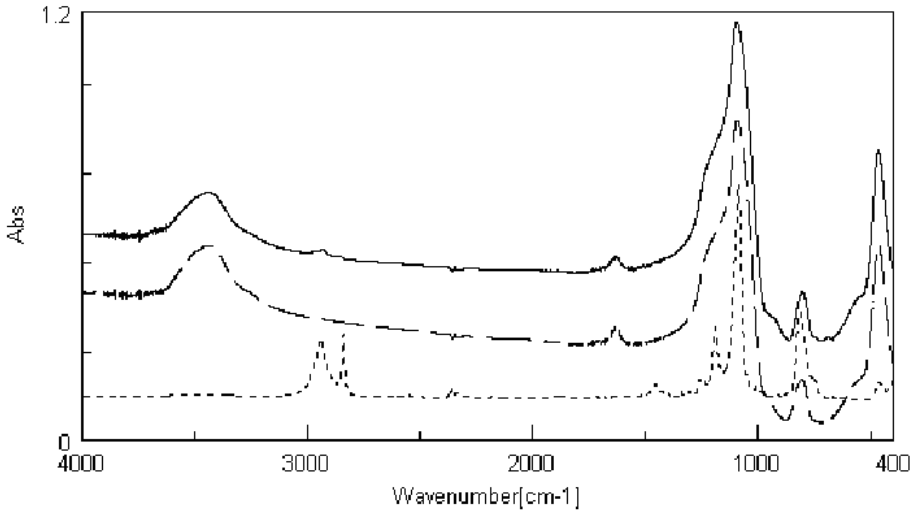

Figure 1. FTIR spectra of the following samples: (------) 3-mercaptopropyltrimethoxysilane modifier (liquid film technique),(– – –) silica gel R (KBr pellet technique), (——) 3-mercaptopropyl chemically modified silica gel R (KBr pellet technique).

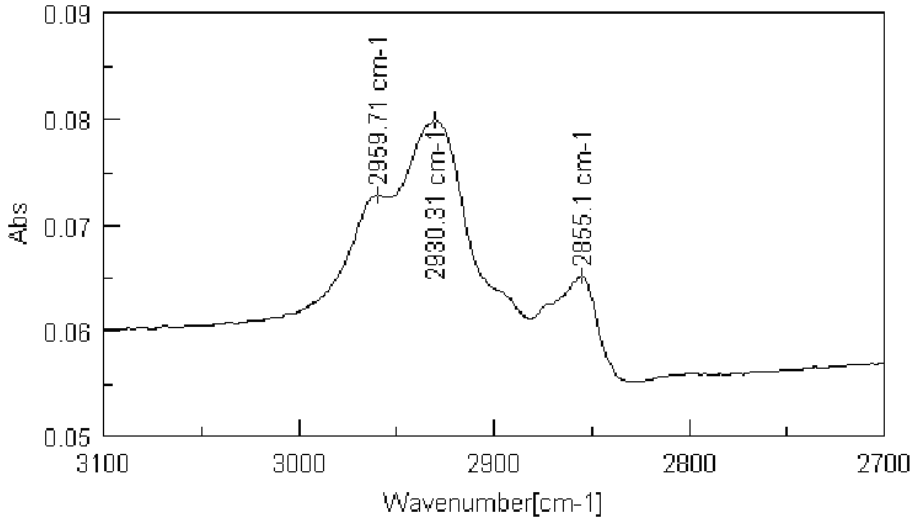

Figure 2. Difference FTIR spectrum of 3-mercaptopropyl modified and unmodified silica gel R samples.

A disadvantage of infrared spectra lies in the interference of the strong absorption by the skeletal modes of unmodified silica (900-1300 cm^{-1}) with the Si─O absorptions of silicoorganic part. However, there are some differences that reflect the effect of modifier and these could be evidenced comparing the second-derivatives of spectra of the unmodified and modified silica gel R samples (figure 3).

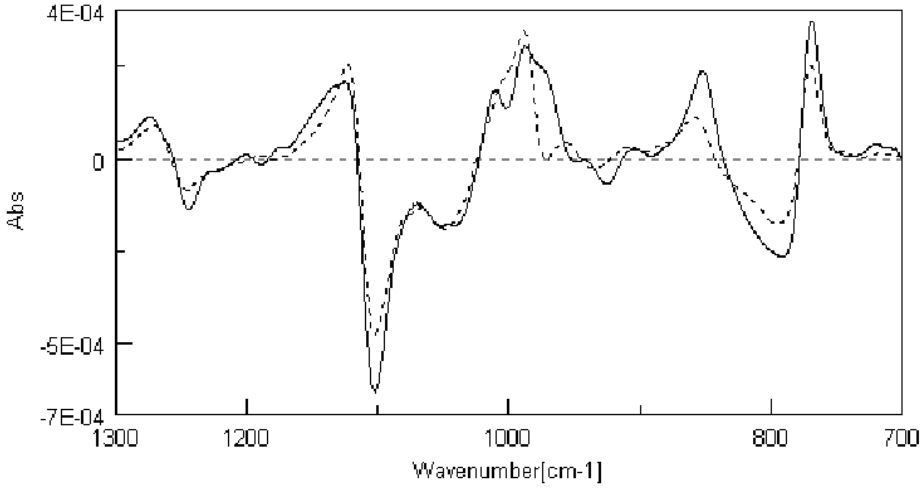

Figure 3. Second–derivative FTIR spectra for unmodified (– – –) and 3-mercaptopropyl modified (——) silica gel R samples.

3.2. Solid-State NMR Study

Valuable structural information about the silica gel and the chemically modified material can be obtained by means of Solid-State NMR spectroscopy. In solid state samples, due to the limited motion, strong dipolar-dipolar and chemical shift anisotropy interactions occur. The line broadening effects can be cancelled using magic angle spinning (**MAS**) technique. Other problems which arise in solid-state NMR spectroscopy related to the strong heteronuclear interactions and to the existence of very long spin-lattice relaxation times T_1 of the order of minutes to hours are solved in the cross polarization (**CP**) technique [4].

Silane functionality according to the used silane type, bonding chemistry and the different surface species that result can be distinguished by ^{29}Si and ^{13}C CP/MAS NMR measurements. So, the monofunctional species (M) appear in the region from 13 to –1 ppm, difunctional species (D^n) from –7 to –20 ppm, trifunctional species (T^n) from –49 to –66 ppm and signal from the starting silica gel from –91 to –110 ppm (Figure 4).

A higher degree of cross-linking of silyl species and/or of oxygen neighbors leads to an upfield shift in NMR spectra. Figure 5 presents the ^{29}Si CP/MAS NMR spectra of unmodified and 3-mercaptopropyl modified silica gel R. The spectrum of unmodified silica gel R contains the signals assigned to the Q species, Q^2 (–91 ppm) and Q^3 (–101 ppm) showing a high amount of free –OH groups on the surface. In the spectrum of 3-mercapto-propyl silica gel R one can be observed the signals of trifunctional species (T^n) assigned to T^2 (–56 ppm) and T^3 (–65 ppm) groups. The shoulder at –91 ppm is assigned to Q^2-groups which are still available on the surface. The signal of the Q^3-groups has a high intensity. This spectrum indicates a high cross linking on the modified surface and a lower surface coverage.

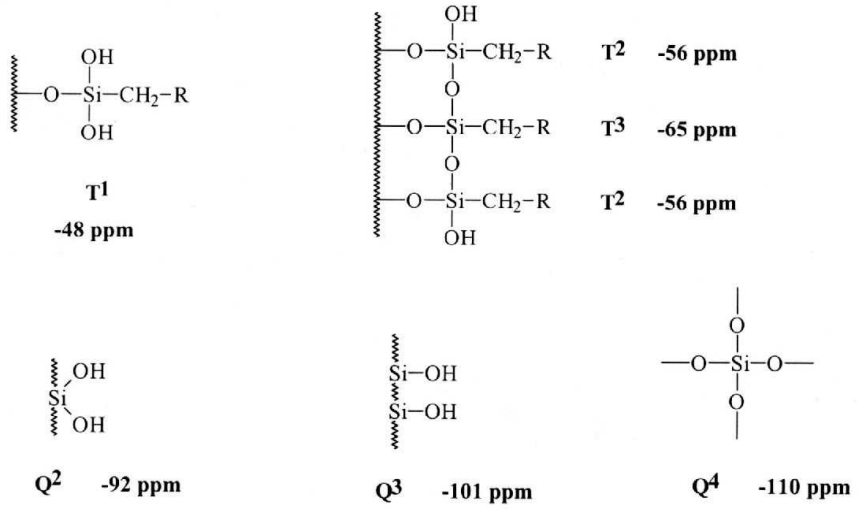

Figure 4. Nomenclature and chemical shifts of some silyl species.

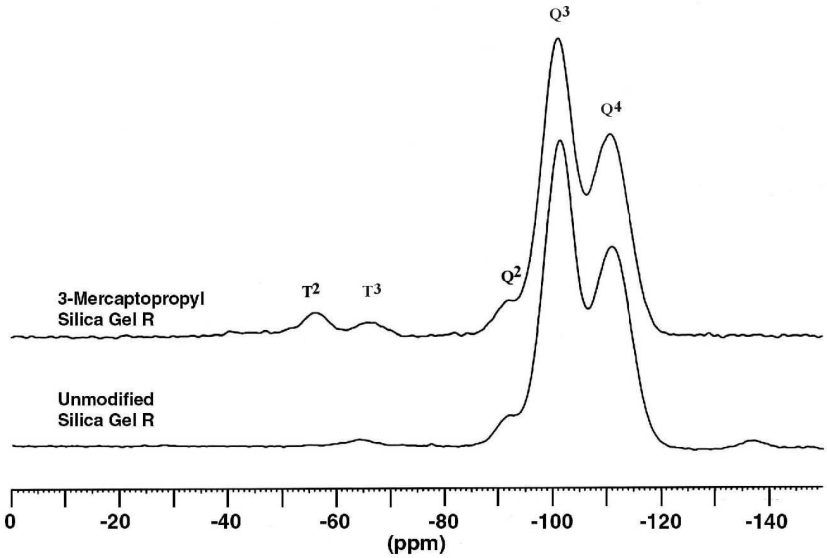

Figure 5. ^{29}Si CP/MAS NMR spectra of unmodified and 3-mercaptopropyl modified silica gel R samples.

The ^{13}C CP/MAS NMR spectrum of 3-mercaptopropyl modified silica gel R (Figure 6) indicates the presence of the modifier on the surface.

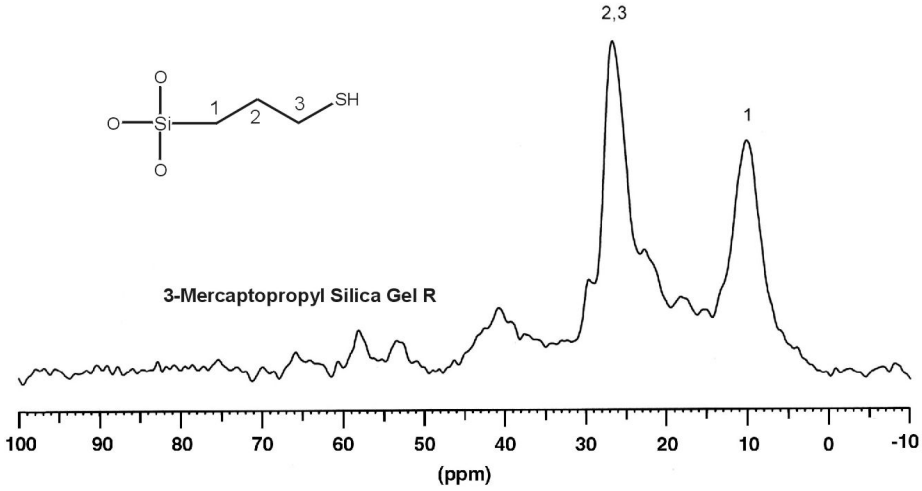

Figure 6. ^{13}C CP/MAS NMR spectrum of 3-mercaptopropyl modified silica gel R.

The high field shifted signal at 10 ppm belongs to the C-1 closest to the surface, in the neighborhood of the silicon. The signals at 23 and 27 ppm can be assigned to C-2 and C-3 carbons from 3-mercaptopropyl modifier.

4. CONCLUSIONS

The presence of the 3-mercaptopropyl modifier on the surface of silica gel R was evidenced using FTIR and ^{13}C CP/MAS NMR spectroscopic methods. The type of bonded silyl species resulted by the organosilanization reaction was investigated by ^{29}Si CP/MAS NMR technique. It was established the presence of different silyl species on the chemically modified support and the coverage of surface according to the results obtained from the measurements of specific surface area [3].

REFERENCES

1. S.M. Staroverov and A.Yu. Fadeev, *J. Chromatogr.*, 1991, **544**, 77-98.
2. S. Héron and A. Tchapla, *Analusis*, 1993, **21**, 327-347.
3. C. Măruțoiu, R. Constantinescu, F. Dogar and R. Grecu, *J. AOAC Int.*, 1999, **82**, 399-401.
4. K. Albert and E. Bayer, *J. Chromatogr.*, 1991, **544**, 345-370.

STUDIA UNIVERSITATIS BABEŞ-BOLYAI, PHYSICA, SPECIAL ISSUE, 2001

MICROSCOPIC PARAMETERS IN THE EXCITED STATES OF SOME ANTHRACENE DERIVATIVES

DANA DOROHOI and DAN DIMITRIU

"Al. I. Cuza" University, Faculty of Physics, 11 Bdv. Carol I, 6600 Iasi, Romania

ABSTRACT. The results obtained by Takehiro Abe's model for a non-polar, isotropic liquid and spectral measurements in the visible vibronic band of some anthracene derivatives were used to estimate the electric dipole moments and the polarizabilities in the molecular excited electronic states.

The study pointed out the applicability of the Takehiro Abe model in the case of non-polar solutions of the anthracene derivatives.

The value of microscopic parameters obtained using the three vibrational electronic bands emphasized very closed values for the electric dipole moment and for the polarizability in the first excited state of anthracene, comparable with those estimated using the value of the wavenumber corresponding to the pure electronic transition (calculated from the wavenumbers of absorption and fluorescence bands).

The values of the pure electronic transition in each solvent were used to estimate microscopic parameters of the anthracene derivatives.

1. Introduction

The sounding of the local reactive field in the liquids is usually achieved by solving spectrally active molecules, at low concentration, in a pure transparent liquid [1-3]. The solvation energies in the electronic states responsible for the electronic (absorption or fluorescence) band appearance determine spectral shifts compared to the gaseous state of the spectrally active molecule.

In Takehiro Abe model [1] the spectral shifts are expressed in function of the microscopic parameters of the molecules. The concentration of the spectrally active molecules is very low (10^{-5} mol/l), thus the solution can be divided into identical, independent subsystems consisting from a spectrally active molecule surrounded by solvation spheres with identical spherical molecules of the pure liquid, having their centers on the solvation sphere surface. The system of spheres is considered in two electronic states:

- ground state (g) in which all the molecules are in their ground electronic state;
- excited state (e) corresponding to the ground state of the solvent molecules and to the excited state of the spectrally active molecules.

The liquids used as solvents must be transparent in the absorption range of the spectrally active molecules. So, we can consider that, during spectra recordings, the solvent molecules do not change their electronic state. In Fig. 1 are shown the electronic levels participating to the absorption visible band appearance both for the gaseous and liquid states of the spectrally active molecule. Indexes *g* and *e* refer to the ground and to the excited state respectively; *u* and *v* refer to the spectrally active molecule and to the pure liquid molecule respectively.

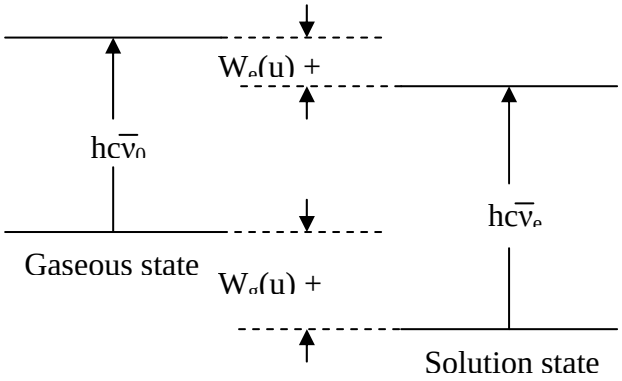

Fig. 1: The spectral shift by passing from gaseous to solution state

Because the solvent molecules do not change their electronic state, the total energy of these molecules interaction, $W_g(v)$, is the same in the both state of the subsystems. It result that spectral shift can be expressed by the following relation:

$$hc\left(\overline{\nu}_e - \overline{\nu}_0\right) = W_e(u) - W_g(u) \tag{1}$$

Formula (1) shows that the spectral shift is directly proportional with the solvation energy of the spectrally active molecule in its excited and ground states.

A final formula of the type:

$$\left[\mu_e^2(u) - \mu_g^2(u)\right] + a \cdot \alpha_e(u) = b \tag{2}$$

was obtained by Takehiro Abe [1] after expressing the solvation energies from (1) as functions of molecular microscopic parameters. In relation (2) μ and α are dipolar moment and polarizability of the spectrally active molecule, and a and b are parameters depending on the solvent characteristics:

$$a = \frac{\frac{3}{2} \cdot I_g(v) \cdot \alpha_g(u) \cdot \frac{I_g(u) - hc\overline{\upsilon}_1}{I_g(v) + I_g(u) - hc\overline{\upsilon}_1}}{\frac{3}{4\pi N_A} \cdot \frac{M_V}{\rho_V} \cdot \left[\frac{\left(\varepsilon_V - n_V^2\right) \cdot \left(2\varepsilon_V + n_V^2\right)}{\varepsilon_V \cdot \left(n_V^2 + 2\right)^2} + \frac{n_V^2 - 1}{n_V^2}\right]} \tag{3}$$

$$b = \frac{\frac{\overline{\upsilon}_1 - \overline{\upsilon}_v}{C} - \frac{3}{2} \cdot \frac{I_g(v) \cdot I_g(u)}{I_g(v) + I_g(u)} \cdot \alpha_g(v) \cdot \alpha_g(u)}{\frac{3}{4\pi N_A} \cdot \frac{M_V}{\rho_V} \cdot \left[\frac{\left(\varepsilon_V - n_V^2\right) \cdot \left(2\varepsilon_V + n_V^2\right)}{\varepsilon_V \cdot \left(n_V^2 + 2\right)^2} + \frac{n_V^2 - 1}{n_V^2}\right]} \tag{4}$$

where n - refractive index, I – ionization potential, ε - electric permitivity, α - polarizability, μ – electric dipole moment, M_V – molecular mass, ρ_V - density.

We intend to check the applicability of relation (2) in the case of some anthracene derivatives [4]. Three electronic bands are characteristic for these molecules. They are named α, p and β by Clar [5]. We refer to the longest wavelength as α-band in Clar's notation, or $A_{1g} - B_{3u}^{+}$ in group nomenclature [6].

2. Materials and methods

With a Specord UV-VIS spectrophotometer having a data acquisition system we have recorded the electronic absorption spectra of anthracene (A) and two anthracene derivatives, namely 9,10 dichloroanthracene (9,10-DClA) and 9,10 dibromoanthracene (9,10-DBrA) (Fig. 2). These compounds were purchased from Merck Company and used without purification. The concentration of the studied solutions was 10^{-5} mol/l. The simple liquids were spectrally grade and carefully dried by specific methods.

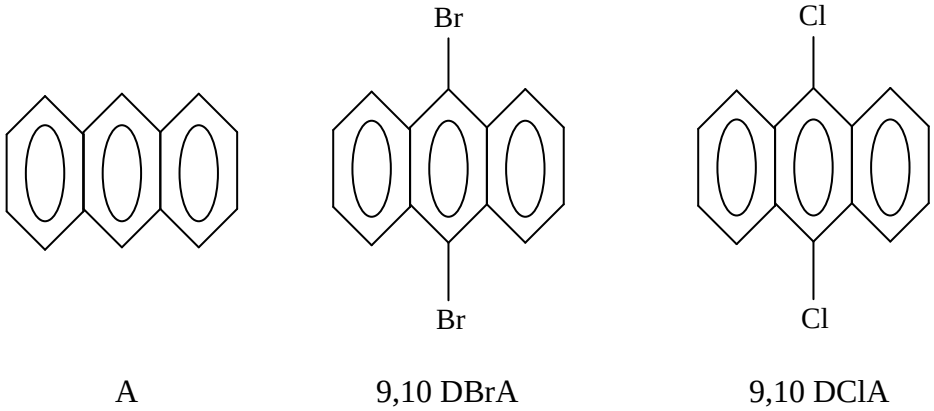

Fig. 2: Chemical formula of the studied anthracene derivatives

3. Results and discussion

The wavenumber of the vibronic absorption bands for anthracene and of the pure electronic transition for 9,10 DBrA and 9,10 DClA are listed in Tables 1-3. A linear relation exists between the parameters *a* and *b* (from the equations 3 and 4) (see Fig. 3). From this linear dependence we calculated the polarizability and the electric dipole moment for each excited state of molecules (Table 4, where R is the linear correlation coefficient). The obtained values are in good agreement with the structure of the studied compounds and with previous studies based on Bakhshiev's theory [2]. From Table 4 it result that the electronic transition responsible for α – band appearance induces an increase of the molecular dipole moment. The highest value of the first excited state has been obtained for 9,10 DBrA.

4. Conclusions

The spectral method derived from the result of Takehiro Abe can be successfully used for estimate some microscopic parameters in the excited states of anthracene and anthracene derivatives, like polarizabilities and electric dipole moments. The obtained results are in good agreement with those obtained by another methods.

Table 1:

Wavenumbers (cm^{-1}) of the visible absorption bands of anthracene

Solvent	$\upsilon_{exp.}$ (cm^{-1})		
	1	2	3
Cyclohexane	26500	27940	29400
Methyl acetate	26540	27980	29400
Ethanol	26540	27980	29400
Acetone	26480	27920	29340
Carbon tetrachloride	26335	27740	29160
Mesitilene	26375	27810	29230
Toluene	26375	27680	29425
Ethyl acetate	26500	27935	29360
Pyridine	26230	27670	29080
m-Xylene	26375	27820	29200
p-Xylene	26315	27745	29170
o-Xylene	26355	27810	29215
Propionic acid	26585	28000	29425
Chlorobenzene	26350	27660	29130
Benzene	26290	27700	29170
Methyl ethyl ketone	26500	27915	29340
Anisole	26290	27730	29145

Table 2:

Wavenumbers (cm^{-1}) of the pure electronic transition band of 9,10-DClA

Solvent	$\upsilon_{exp.}$ (cm^{-1})
Cyclohexane	25560
Methyl acetate	25650
Ethanol	25600
Acetone	25620
Ethyl acetate	25650
Pyridine	25320
Propionic acid	25630
Chlorobenzene	25320

Table 3:

Wavenumbers (cm^{-1}) of the pure electronic transition band of 9,10-DBrA

Solvent	$\upsilon_{exp.}$ (cm^{-1})
Cyclohexane	24630
Methyl acetate	24730
Acetone	24680
Carbon tetrachloride	24460
Ethyl acetate	24670
Pyridine	24390
Propionic acid	24760
Chlorobenzene	24340
Benzene	24450

Table 4:
Microscopic parameters in the excited state and the linear correlation coefficient (R) determined from the vibronic bands (1-3) of anthracene (A) and from the pure electronic transition of 9,10 DBrA and 9,10 DClA respectively

Anthracene and anthracene derivatives	α_e ($10^{-25}cm^3$)	$\mu_e^2 - \mu_g^2$ (D^2)	R	μ_g (D)	μ_e (D)
A (1)	590.91	0.52	0.997	0	0.72
A (2)	588.77	0.77	0.998	0	0.88
A (3)	551.83	1.10	0.998	0	1.05
9,10-DClA	514.25	2.42	0.999	0	1.55
9,10-DBrA	621.31	6.21	0.998	0	2.49

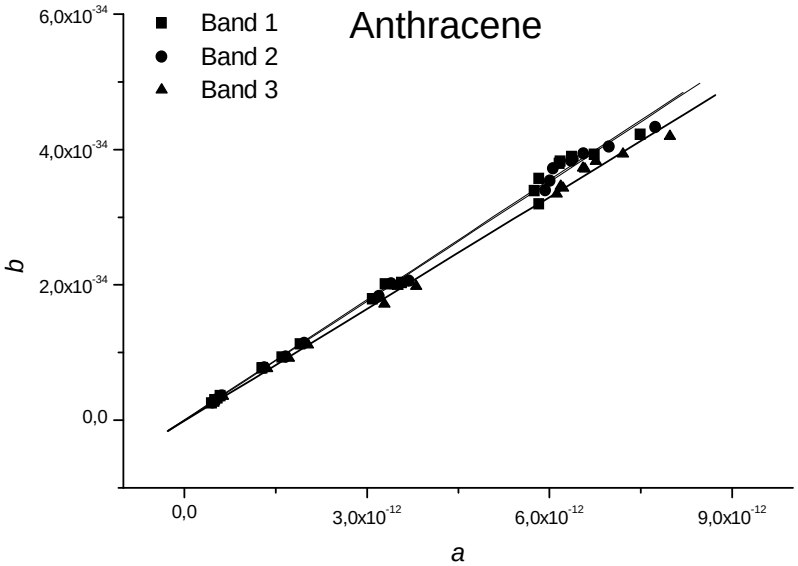

Fig. 3: The linear dependence between the coefficient *a* and *b* corresponding to the vibronic bands of anthracene (1-3) and to the pure electronic transition of anthracene derivatives

REFERENCES

[1] Takehiro Abe, *Bull. Chem. Soc. Japan* **38** (1965), 1314; **39** (1966), 936;
[2] N. G. Bakhshiev, *Spectroscopia Mejmolekuliarnih Vzaimodeistvii*, Izd. Nauka, Leningrad 1972;
[3] V. Pop, D. Dorohoi and V. Holban, *Spectrochimica Acta* **50A** (1994), 14, 2281;
[4] V. Pop, D. Dorohoi and V. Holban, *An. St. Univ. "Al. I. Cuza" Iasi, s. 1b, Fizica*, **XLIII – XLIV** (1997 – 1998), 37;
[5] E. Clar, *Aromatische Kohlenwasserstoffe, second edition*, Springer Verlag, 1952;
[6] Andrew Streitwieser Jr., *Molecular Orbital Theory for Organic Chemists*, John Wiley & Sons, 1961;

STUDIA UNIVERSITATIS BABEŞ-BOLYAI, PHYSICA, SPECIAL ISSUE, 2001

ELECTRIC DIPOLE MOMENTS OF SOME BENZO-[F]-QUINOLINIUM CYCLOADUCTS

DORINA CREANGĂ, DAN DIMITRIU and DANA DOROHOI

"Al.I.Cuza" University, Faculty of Physics, 11 Bdv. Carol I, 6600 Ia¿i, Romania

ABSTRACT. Electric dipole moments and polarizabilities of three benzo-[f]-quinolinium cycloaducts were estimated using a spectral method derived from the statistical cell model proposed by Takehiro Abe for the simple liquids.

1. Introduction

Benzo-[f]-quinolinium cycloaducts [1,2] are organic compounds used as initial substances in some chemical reactions, such as in antimicrobial and antifunginc drug obtaining. The values of the microscopic parameters of these compounds could help chemists in increasing the reaction output and physicist to explain the cycloaducts intermolecular interactions in their condensed states. Benzo-[f]-quinolinium cycloaducts have some characteristic visible bands corresponding to n-π^* or to π-π^* transitions [3,4]. The benzene rings from these cycloaducts structures assure a great polarizability and their spectral sensibility to the solvent nature.

Our purpose was to check if the statistical cell model proposed by Takehiro Abe [5] could be applied to the benzo-[f]-quinolinium cycloaducts solutions and to determine the electric dipole moments and polarizabilities of these spectrally active molecules.

Takehiro Abe developed his model in the following assumptions:

1) the model can be applied only to the solutions of spectrally active molecules in a solvent which is a simple liquid free of specific intermolecular interactions, having approximate spherical molecules with small values for their dipole moments;

2) the studied solutions contain spectrally active molecules solved, at very low concentrations, in the simple, pure liquid. Such a solution can be divided into identical subsystems consisting from only a single spectrally active molecule surrounded by the solvent molecules;

3) the solvents do not absorb in the range were the studied molecule is spectrally active. The solvent molecules are only in their ground state;

4) the studied system has only two energetic states, one in which all the molecules are in their ground state and another in which spectrally active molecule is in its excited state and the solvent molecules are in their ground state;

5) the electronic transitions are very fast, so the arrangement of the solvent molecules around the spectrally molecule is not changed after absorption.

2. Material and Methods

Three cycloaducts with the structures from Fig.1 were prepared in the laboratories of Organic Chemistry Department of "Al.I.Cuza" University, by the method described in [2]. The electronic absorption spectra were recorded with a Specord UV-VIS spectrophotometer having a data acquisition system. The concentration of the

studied solutions was 10^{-5} mol/l. The simple liquids were spectrally grade and carefully dried by specific methods.

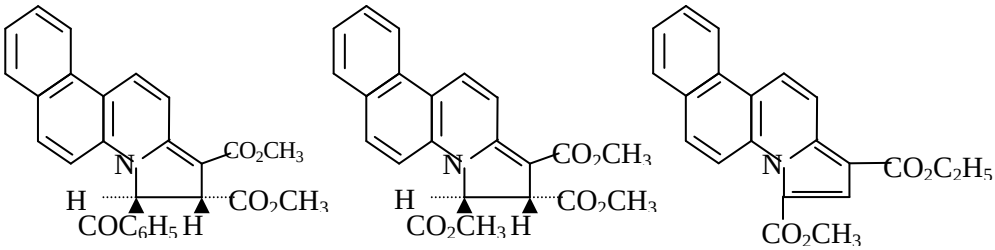

Fig. 1: Structural formula of the studied benzo-f-quinolinium cycloaducts

Table 1:

Wavenumbers (cm^{-1}) of the visible absorption bands of C_1 cycloaduct

Solvent	$\upsilon_{exp.}$ (cm^{-1})					
	1	2	3	4	5	6
Dichloroethane	18960	20160	21440	22800	27280	28240
Methyl alcohol	19440	20960	22000	23600	27920	28800
Ethyl alcohol	19360	20840	21900	23500	27700	28800
Acetone	19000	20260	21400	-	27560	28180
Chloroform	19000	20400	21640	22780	27520	28600
Toluene	18580	19920	21240	22580	26920	28040
Isoamil acetate	18700	20120	21500	22920	27220	28400
Methyl ethyl cetone	19000	20120	21440	22900	27420	28400
o-Xylene	18500	19960	21360	22900	26750	28100
Phenyl chloride	18750	20080	21420	22640	27120	28200
Benzene	18660	20080	21320	22920	27040	28100
Anisol	18620	20040	21400	22600	27180	28300

Table 2:

Wavenumbers (cm^{-1}) of the visible absorption bands of C_2 cycloaduct

Solvent	$\upsilon_{exp.}$ (cm^{-1})					
	1	2	3	4	5	6
Dichloroethane	19240	20420	21700	22920	27200	28200
Methyl alcohol	19700	21000	22080	23580	27700	28660
Ethyl alcohol	19600	20820	21960	23460	27500	28600
Acetone	19240	20540	21780	23160	27320	28360
Carbon tetrachloride	18920	20240	21540	22820	26660	27880
Toluene	18900	20320	21580	22900	26940	28120
Ethyl acetate	19140	20320	21580	22820	27200	28200
p-Xylene	18920	20480	21620	23000	26900	28100
o-Xylene	19000	20300	21620	22880	-	-
Phenyl chloride	19000	20280	21580	22740	26940	28000
Benzene	19000	20340	21640	22900	26920	28080
Anisol	19000	20300	21580	23160	27040	28160

Table 3:

Wavenumbers (cm^{-1}) of the visible absorption bands of C_3 cycloaduct

Solvent	$\upsilon_{exp.}$ (cm^{-1})				
	1	2	3	4	5
Dichloroethane	25540	26860	28160	-	32320
Methyl alcohol	25740	27080	28360	-	32420
Ethyl alcohol	25720	27060	28350	-	32400
Acetone	25720	27040	28300	29750	-
Toluene	25440	26740	28020	29480	32120
Isoamyl acetate	25600	26940	28260	29560	32300
Methyl ethyl cetone	25620	26920	28260	29720	-
o-Xylene	25420	27400	28120	29600	-
Phenyl chloride	25360	26700	28080	29500	32060
Carbon tetrachloride	25440	26800	28120	29580	32100
Ethyl acetate	25700	27020	28280	29680	32480
Anisol	25360	26700	27940	29560	32140

3. Results and Discussions

The wavenumber of the electronic absorption bands of the studied compounds are listed in Tables 1-3. The first four electronic absorption bands of C_1 and C_2 are attributed to an n-π^* transition, because they have a small intensity and disappear in acid media. This transition involves the unbounded electrons of the substituents attached to the addition cycle of the compounds C_1 and C_2. The addition cycle of these compounds isolates the substituents from the point of view of π conjugation with heterocycle. Otherwise, the addition cycle of C_3 cycloaduct permits [1,2] a large conjugation of the π electron cloud reflected in the aspect of the electronic absorption spectra that become very alike with the spectra of benzene derivatives having a number of benzene rings bigger than three [6]. Visible electronic bands of this compound do not disappear in the protic solutions. They are attributed to a π-π^* transition [1,3]. Two last peaks near UV spectral range were attributed to π-π^* transitions [3,4] because they are very intense and do not disappear in the protic solutions. Data analysis using Bakhshiev theory [7] indicated that, by passing from the ground to the excited electronic state, these compound change their dipole moments and the polarizabilities in a measurable ratio [3,4]. The final formula from the model proposed by Takehiro Abe [5]:

$$\left[\mu_e^2(u)-\mu_g^2(u)\right]+a\cdot\alpha_e(u) \quad = \quad b \tag{1}$$

was used to check the applicability of the model to benzo-[f]-quinolinium cycloaducts solutions. In equation (1) *a* and *b* are parameters dependent on the solvent characteristics as well as on the ionization potential of the spectrally active molecule:

$$a \quad = \quad \frac{\frac{3}{2}\cdot I_g(v)\cdot\alpha_g(u)\cdot\frac{I_g(u)-hc\overline{\upsilon}_1}{I_g(v)+I_g(u)-hc\overline{\upsilon}_1}}{\frac{3}{4\pi N_A}\cdot\frac{M_V}{\rho_V}\cdot\left[\frac{\left(\varepsilon_V-n_V^2\right)\cdot\left(2\varepsilon_V+n_V^2\right)}{\varepsilon_V\cdot\left(n_V^2+2\right)^2}+\frac{n_V^2-1}{n_V^2}\right]} \tag{2}$$

$$b = \frac{\frac{\overline{\upsilon}_1 - \overline{\upsilon}_v}{C} - \frac{3}{2}\cdot\frac{I_g(v)\cdot I_g(u)}{I_g(v)+I_g(u)}\cdot\alpha_g(v)\cdot\alpha_g(u)}{\frac{3}{4\pi N_A}\cdot\frac{M_V}{\rho_V}\cdot\left[\frac{\left(\varepsilon_V - n_V^2\right)\cdot\left(2\varepsilon_V + n_V^2\right)}{\varepsilon_V\cdot\left(n_V^2+2\right)^2} + \frac{n_V^2-1}{n_V^2}\right]} \quad (3)$$

where n - refractive index, I – ionization potential, ε - electric permitivity, α - polarizability, μ – electric dipole moment, M – molecular mass, ρ - density. In equations 1-3 u and v denominate the spectrally active molecules and the solvent molecules and, on the other hand, indices g and e refer to the ground and to the excited states of the electronic transition of the spectrally active molecules. A linear relation exists between a and b (see Fig. 2) with a high degree of correlation for all electronic absorption bands of the studied cycloaducts (Table 4-6, where R is the linear correlation coefficient). The slopes of the line signify the electric polarizability in the excited state of electronic transition and the cuts are equal with the difference $\mu_e^2 - \mu_g^2$. From Table 4-6 it result that the polarizability in the excited molecular state are higher for the π-π^* transitions compared with those for n-π^*.

The positive signs obtained for the differences $\mu_e^2 - \mu_g^2$ indicate an increase of the molecular dipole moment by excitation, excepting a UV π-π^* absorption band of C_1.

Table 4:

Cycloaduct C_1

Excited state	α_e ($10^{-25}cm^3$)	$\mu_e^2 - \mu_g^2$ (D^2)	R	μ_g (D)	μ_e (D)
1	488.68	20.49	0.998	3.67	5.82
2	517.75	14.06	0.998	3.67	5.24
3	583.57	12.33	0.998	3.67	5.07
4	357.28	4.01	0.973	3.67	4.18
5	1341.06	1.73	0.992	3.67	3.89
6	1438.78	-7.75	0.995	3.67	2.38

Table 5:

Cycloaduct C_2

Excited state	α_e ($10^{-25}cm^3$)	$\mu_e^2 - \mu_g^2$ (D^2)	R	μ_g (D)	μ_e (D)
1	434.53	17.18	0.998	4.10	5.83
2	443.42	8.17	0.998	4.10	4.99
3	440.12	4.00	0.998	4.10	4.56
4	496.66	3.38	0.997	4.10	4.49
5	1227.58	3.60	0.989	4.10	4.51
6	972.99	0.51	0.995	4.10	4.16

Table 6:

Cycloaduct C_3

Excited state	α_e ($10^{-25}cm^3$)	$\mu_e^2 - \mu_g^2$ (D^2)	R	μ_g (D)	μ_e (D)
1	1482.16	4.58	0.999	2.34	3.17
2	1508.54	5.02	0.999	2.34	3.24
3	1416.36	2.87	0.999	2.34	2.88
4	1441.30	3.42	0.999	2.34	2.98
5	1507.36	19.42	0.999	2.34	4.98

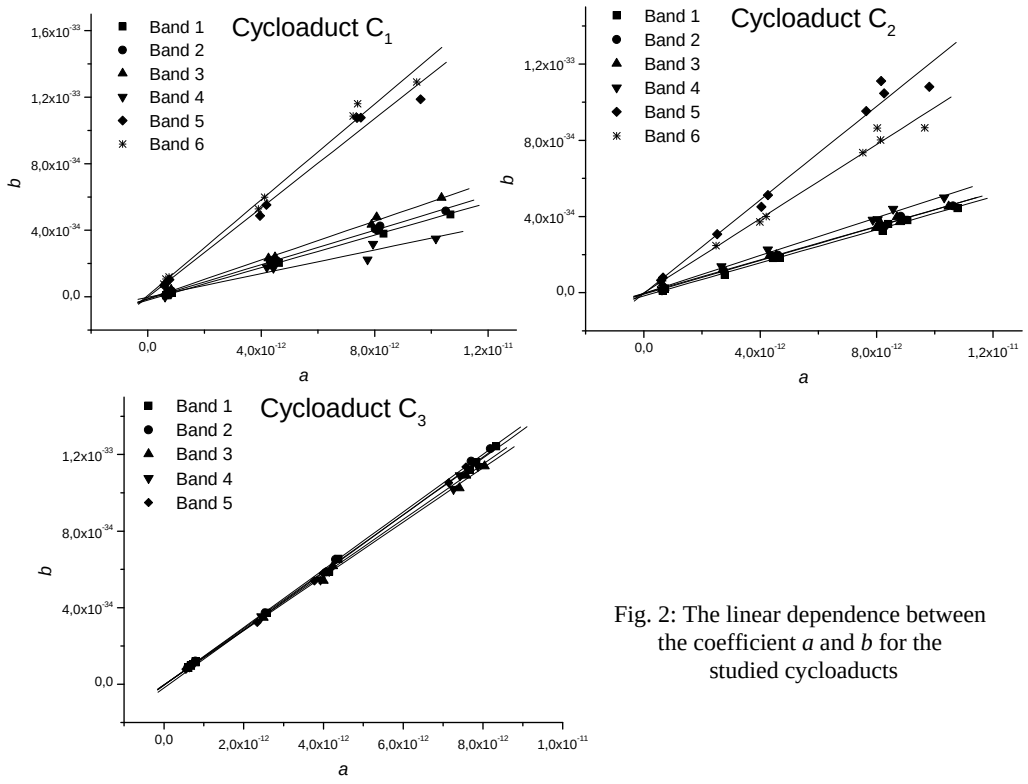

Fig. 2: The linear dependence between the coefficient *a* and *b* for the studied cycloaducts

The lack of π conjugation on the cycloadition cycle in the case of compounds C_1 and C_2 determines an important charge separation and a higher variation of electric dipole moments compared with C_3 cycloaduct.

4. Conclusions

There are a few methods that permit estimation of the microscopic parameters in the excited states of the molecules. This spectral method deriving from the results of Takehiro Abe gives information on these parameters and permits to estimate the

transition dipolar moments. We are looking for another specific methods permitting to evaluate electric dipole moments and polarizabilities in order to compare them with the values obtained by orbital molecular theories.

REFERENCES

1. I. Zugravescu and M. Petrovanu, N-Ylid Chemistry, Academic Press, New York, London 1976;
2. Do Nhat Van Ph.D. Thesis, "Al. I Cuza" University, Department of Chemistry 1976;
3. Dana Dorohoi, M. Guyre-Rotariuc and Dorina Iancu, An. St. Univ. Al.I.Cuza, Iasi, s.1b, Fizica, t. XXVI, 1980, p. 71-76;
4. Dana Dorohoi and Dorina Iancu, An. St. Univ. "Al. I. Cuza", Iasi, s.1b, Fizica, t. XXVII, 1981, p.49-54;
5. Takehiro Abe, Bull. Chem. Soc. Japan, 38, 1965, p. 1314 and 39, 1966, p. 936;
6. A. Streitwiser Jr., Teorija moleculjarnyh orbit, Izd. Mir, Moscova, 1965;
7. N. G. Bakhshiev, Spectroscopia mejmolekuliarnov vzaimodeistvii, Izd. Nauka, Leningrad, 1972.

STUDIA UNIVERSITATIS BABEŞ-BOLYAI, PHYSICA, SPECIAL ISSUE, 2001

AROMA COMPOUNDS AND ANTIOXIDANTS FROM RED WINE BY GC/MS

M. CULEA*, L. FROMONDI*, C. GHERMAN, R. PODEA* and O. COZAR****

**S.C. Natex s.r.l. Sos. Cluj-Oradea km8, P.O.Box 374 3400 Cluj-Napoca, Romania*
***Univ. Babes-Bolyai, Cluj-Napoca, Romania, Dept. of Physics, 1 Kogalniceanu, RO-3400 Cluj-Napoca, Romania e-mail: monica.culea@phys.utcluj.ro*

SUMMARY. The popularly French paradox suggests that the consumption of wine, particularly of red wine, reduces the incidence of mortality and morbidity from coronary heart disease. The cardioprotective effect has been attributed to antioxidants present in the polyphenol fraction of red wine. The aroma and nutraceutics compounds from some selected Romanian red wines produced in traditional wine-growing regions of the country were investigated by GC/MS, by using two different extraction methods, LLE and SPE. The extraction of the compounds from the matrix was performed with ethyl acetate-dichloromethane-hexane (5:1:1,v/v/v). The extracted red wines were analysed by gas chromatography and gas chromatography-mass spectrometry. A HP-5 capillary column, 30mx 0.32mm, 0.25µm film thickness was used in a temperature program from 50oC to 310oC for compounds of low and high volatility.

Introduction

Many scientific studies suggest that consumption of wine, particularly red wine, reduces the incidence of mortality and morbidity from coronary heart disease. Many natural compounds such as salicylates and flavonoids function as radical scavengers and thus as antioxidants. Flavonoids are components of fruits, vegetables and wines responsible for reducing heart disease mortality, acting as protective nutrients, including protection against cardiovascular diseases, osteoporosis and anticarcinogenic effects. Isolation and structure elucidation of these compounds are the initial steps to understanding their significance and action. Resveratrol (3,5,4'-trihydroxystilbene) is thought to be the active principle of red wines that were shown to reduce heart diseases /1,2/. Gas-chromatography (GC) and gas-chromatography coupled with mass spectrometry (GC/MS) are very much used methods for organic compounds identification and quantitative determination in wine samples /3-9/. High performance liquid chromatography (HPLC) by using RI/UV detection are also quantitative assay for major organic acids (tartric acid, malic acid, lactic acid, acetic acid, citric acid, succinic acid), glucose, fructose, glycerol and ethanol, most useful for fermentation monitoring during wine making.

The aroma and nutraceutics compounds from two selected Romanian red wines produced in traditional wine-growing regions of the country were investigated by GC/MS, by using two different extraction methods, LLE and SPE.

Experimental

Apparatus A Hewlett Packard (HP) GC 5890 coupled with a MS engine 5989B in the EI mode was used for compounds identification. A HP-5MS capillary column 30mx0.25mm diameter, 0.25µm film thickness, used the temperature program: 50 ^{o}C for 2 min, then increased to 250^{o}C with a rate of 8 ^{o}C /min, then 30 ^{o}C /min to 310^{o}C and kept 10min, helium flow rate 1ml/min. A HP 6890 gas chromatograph equipped with the same column was used in the same temperature program. The GC/MS interface line and the ion source were maintained to 200^{O}C and respective 280^{O}C, and quadrupol analyser at 100 ^{O}C. Electron energy was 70eV and electron emission 300µA.

Reagents and chemicals

Solvents and aroma standards: methylen chloride, hexane, ethyl acetate, purchased from Comchim (Bucharest, Romania) were purified by distillation, when necessary. The aroma compounds (Sigma-Aldrich, Germany): 1. isoamyl acetate purity 99.13%, 2. phenyl ethyl alcohol, purity 99.5% 3. diethyl succinate, purity 99.7% 4. gamma-decalactone, purity 98.7% 5. methyl myristate (C14:0), purity 99.99%, used as internal standard 6. benzyl salicylate, purity 99.12%. The purity of standards and solvents was tested by GC. The standards, 100µl each, formed the *standard mixture*, with the internal standard, C14:0, added separately after extraction for recovery study.

Wines: Commercial Romanian red wines: Murfatlar Pinot Noir 1996 and Cabernet Ausbruch 1999 (Vinaria), usually in 750-ml bottles, were opened and analysed within 24h or kept at 4^{o}C within a 3-day period.

LLE extraction. *Solvent A*, a mixture of three solvents, was prepared in the ratio 5:1:1, v/v/v from: ethyl acetate:hexane:methylen chloride. For the standards the LLE extraction procedure was as follows: 10 µl *standard mixture* in 6 ml distilled water and 1ml *solvent A*, were mixed with 0.5g NaCl for 5 minutes and then centrifugated 2 minutes. 1µl C14:0 was added to the supernatant and then 4µl were injected two times by using the autosampler injector.

Wine extraction procedure was the following: 6ml wine with 1ml *solvent A*, and 0.5g NaCl were mixed for 5 minutes and then centrifugated 2 minutes. The supernatant was separated and concentrated, then 4µl were injected into the chromatograph. The GC and GC/MS analysis was performed in the same day of the extraction.

SPE extraction LiChrolut RC (200mg) C18 cartridges(Merck, Germany) were preconditionated with 3ml ethyl acetate and 9ml distilled water pH2. Wine samples were diluted with equal volume of distilled water to bring the alcohol level to approximately 6%(v/v) and 20 ml were passed onto the preconditioned cartridge, then 1ml distilled water and drying for 10minutes followed. The aroma wine bouquet compounds were extracted with 3ml solvent A

Method validation Linearity was studied in the range 0– 100µg. The regression curves obtained for the standards gave good correlation coefficients, over 0.995. Precision gave relative standard deviation (R.S.D.) lower than 4%. The average values are resulted from four extraction procedures and two injections of each extract. Recovery of the standard mixture for SPE extraction was 93% and for LLE was 86%.

Results and discussion

Absolute recoveries were determined by using external calibration with the standard C14:0. The recovery study for LLE is presented in Table I. Average values are resulted from four extraction procedures and two injections of each extract. The relative standard deviation (RSD) values were bellow 4% for the extraction procedure. The recovery for LLE was 86% for the *standard mixture* and 93% for SPE. The LLE and SPE methods were used for comparative studies of the organic compounds of red wines. The compounds were identified by GC/MS. Table II presents the compounds found in Pinot Noir Murfatlar (1996) by LLE and SPE extraction and Table III presents the compounds found in Cabernety Ausbruch (1999) by LLE and SPE extraction (pH2 and pH7, pH2, wine 6% alcohol v/v). Some phenolic compounds found in the studied wines are shown in Fig.1. The comparison between LLE and SPE extractions at Pinot Noir Murfatlar wine is presented in Fig.2

The aroma bouquet and phenolic compounds are responsible for wine taste. The antioxidants, free radical scavengers inhibit lipid peroxidation and exhibit various physiological activities: anti-inflammatory, anti-allergic, anti-carcinogenic, antihypertensive and anti-arthritic activities/8/.

Conclusions

The extraction methods presented show good recovery mean values by LLE (86%) and SPE (93%). Precision gave R.S.D. lower than 4%. Better extraction was obtained for phenolic compounds at pH2 and for alcoholic wine concentration of 6%,v/v. The method is suitable to characterise trace amounts of active principles in plants. The polyphenolic compounds present in red wine in concentration of 1800-3000 mg/l are antioxidants, free radical scavengers and inhibit the lipid peroxidation. The moderate consumption of red wine have a beneficial effect on reducing coronary heart diseases /9/.

BIBLOGRAPHY

1. L. Bavaresco, C. Fregoni, E. Cantu, M. Trevisan, Drugs Exp& Clin Res **25**(2-3)53-6,1999.
2. R.M. Lamuela-Raventos, M.C. de la Torre-Boronat, Drugs Exp& Clin Res **25**(2-3)121-4,1999.
3. D. De la Calle-Garcia, M. Reichenbacher, K. Danzer, C. Hurlbeck, C. Bartzsch, K. Feller, J. High Resol. Chromatogr. **20**,665-68,1997.
4. G.P. Blanch, G. Reglero, M. Herraiz, J. Agric. Food Chem. **43**,1251-58, 1995.
5. E.F. Lopez, E.F.Gomez, J. Chromatogr. Sci.,**34**, 254 (1995).
6. A. Escobal, C. Iriondo, C. Laborra, E. Elejalde, I. Gonzalez, J. Chromatogr. A.,**823**, 349-54 (1998).
7. C. Andres-Lacueva, F. Mattivi, D. Tonon, J. Chromatography A.,**823**, 355-63 (1998).
8. K. Robards, M. Antolovich, Analyst, **122**, 11R-34R,1997.
9. A. Lugasi, A. Blazovics, E. Dworschk, J. Feher, Orvosi Hetilap. **138**(11)673-8,1997.

Table I

Precision and recovery results for LLE extraction procedure

compounds	tR(min)	LLE (n=4) mean	SD	RSD(%)	ETALON n=3	recovery (%)
1 i-amyl acetate(99.13%)	6.95	0.64	0.06	9.62	0.93	68.59
2 fenetol((99.5%)	11.67	1.43	0.04	3.00	2.26	63.29
3 diethyl succinate(99.7%)	12.73	0.87	0.03	3.08	1.05	82.71
4 gamma-decalactone(98.7%)	17.6	1.83	0.05	2.52	1.82	100.62
5 C14:0(99.99%)	21	1.00	0.00	0.00	1.00	100.00
6 benzyl salicylate((99.12%)	23.15	2.71	0.09	3.45	2.37	114.50
				3.61		85.94

t_R = retention time; R.S.D, = relative standard deviation

Table II

Wine bouchet compounds from Pinot Noir Murfatlar (1996)

Compound	t_R	LLE %MS	SPE %MS
1 1,3 butandiol(threo)	3.4	3.31	0.33
2 2,3 butandiol(erythreo)	3.6	1.09	0
3 isobutyl acetate	3.8	0	0.45
4 1-hexanol	4.8	0	0.10
5 gamma-butyrolactone	5.74	0.25	0.05
6 propylen glycol	6.06	2.87	0
7 ethyl lactate	6.13	1.08	0
8 3-methyl thiopropanol M=106	7.08	0.31	0
9 hexanoic acid	7.59	1.0	0.5
10 succinic anhydride	7.89	0.4	0
11 ethyl 4-hydroxy butanoate	8.6	0.22	0.40
12 glycerol	9.13	0.33	0
13 phenyl ethyl alcohol	9.87	18.34	15.39
14 sorbic acid M=112	10.95	37.44	56.79
15 diethyl succinate M=174	11.88	23.41	11.36
16 ethyl mallate M=190	12.55	0.25	0
17 3-methyl-3-hydroxypentanoic acid	12.92	0.26	0
18 gamma-nonalactone M=158	13.17	0.3	0
19 triacetin	13.9	0.3	0
20 decanoic acid M=172	14.39	0.68	1.16
21benzen ethanol 4-hydroxy M=138	15.41	3.07	2.00
22 * M=194	15.45	0	0.11
23 beta-phenethyl acetate+**M=166	15.8	0.1	0.1
24 (2-phenylethyl)-acetamide M=163	16.7	0	2.37
25 methyl gentisate M=168	16.94	0.1	0.1
26 ***M=168	16.84	0.1	0.1
27 vanillic acid M=168	17.58	0.4	0
28 ethyl vanillate M=196	17.6	0.1	0.1
29 ****M=194	18.57	0.22	0.38
30 M=228	19.44	0	0.52

31 1H-indole-3-ethanol M=161	20.12	0.37	0.65
32 ethyl phenethyl acetate M=164	20.6	0.1	0.1
33 M=198+226+192*****	20.95	0.34	1.05
34 benzyl salicylate	21.5	0.1	0.1
35 vanilmandelic acid M=198	22.56	0.1	0.1
36 M=228	28.1	0.1	0.1
37 M=228 resveratrol?	30	0.1	1.47

t_R=retention time; * ethyl-2-hydroxy-3-phenyl propanoate M=194
tertbutyl catechol M=166; * 5-methoxy-2-methoxymethylphenol M=168
****p-isopropoxyphenylacetic acid M=194
*****ethyl m-hydroxycinnamate M=192

Table III

Wine bouchet compounds in Cabernet Ausbruch (Vinaria 1999)

Compound	LLE	SPE:pH2	[a]pH7	[a]pH2	
	t_R	%MS	%MS	%MS	%MS
1 1,3 butandiol(threo)	3.4	1.92	0.64	0	0
2 isovaleric acid	4.7		0.27		0.22
3 1-hexanol	4.8	1.53	2.05	1.76	1.2
4 isoamyl acetate	4.98	0	0.31	0	0.13
5 ethyl lactate	6.13	1.25	0.53	0	0.1
6 ethyl hexanoate	7.08	0	0.30	1.76	1.02
7 hexanoic acid	7.59	0.98	1.25	1.65	1.02
8 limonene	8	0	0.23	0.55	0.28
9 benzyl alcohol	8.2	0	0	0	0.02
10 ethyl 4-hydroxy butanoate	8.6	0	1.03	1.14	0.34
11 phenyl ethyl alcohol	9.87	24.12	10.66	10	13.06
12 p-ethyl phenol	10.8	0	0	0.2	0
13 sorbic acid M=112	10.95	42.69	39.25	46.14	47.8
14 diethyl succinate M=174	11.88	13.41	17.2	15.6	17.36
15 coumarin M=120	11.79	0	0	0.37	0.3
16 undecane M=184	12.92	0	0	0.3	0.11
18 gamma-nonalactone M=158	13.17	0	0	0	0.23
19 decanoic acid M=172	14.39	0	1.06	0.64	0.6
20 diethy hydroxypentadieoate	14.41	0	0.5	0.3	0.5
21 tetradecane M=198	14.7	0	0	0	0.14
22 1,2,3-benzentriol	15.45	0	0	0	0.35
23 benzene ethanol 4-hydroxy M=138	15.3	0.55	1.68	0.8	1.8
24 * M=194	15.5	0	0.6	0.9	0
25 (2-phenylethyl)-acetamide M=163	16.7	0	1.10	0.32	0.72
26 vanillic acid M=168	17.58	0	0.38	0.32	0.21
27 ethyl vanillate M=196	17.6	0	0.22	0.32	0.66
28 1,3,5-benzentriol (phloroglucinol)	18.1	0	0.68	0.58	0.86
29 1H-indole-3-ethanol M=161	20.12	0	0.48	0.2	0.36
30 p-hydroxycinnamic acid M=164	20.6	0	0.44	0.1	0
31 M=192**	20.95	0	0.94	0.2	0.45
32 syringic acid M=198	21.09	0	0	0	0.47
33 M=226***	21.1	0	0.21	0.2	0

34 palmitic acid M=256	22.49	0	0.28	0	0.57
35 M=230****	28	0	0.83	0.63	0.55
36 M=272*****	28.9	0	0	0	0.1
37 M=228 resveratrol)	30	0	1.01	0.54	0.28
38. squalene M=410	30.1	0	0.62	0.33	0.3
39. anhydrosecoisolariciresol M=344	30.2	0	0.5	0.3	0.2

t_R=retention time; [a] alcoholic concentration:6°; * ethyl-2-hydroxy-3-phenyl propanoate M=194; **ethyl m-hydroxycinnamate M=192; *** 2-hydroxy-4'-methoxy stilbene M=226; **** trihydroxyphenyl lactic acid methyl ester M=230; *****2-hydroxy-4'-phenyl-stibene M=272

vanillic acid M=168 (tR=17.58)

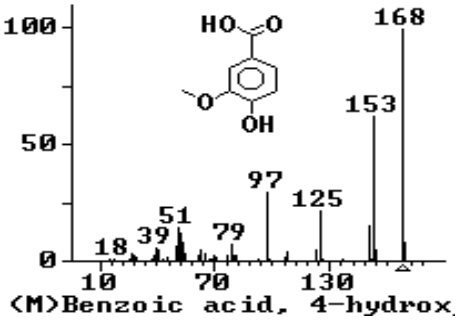

syringic acid M=198 (tR=21.09)

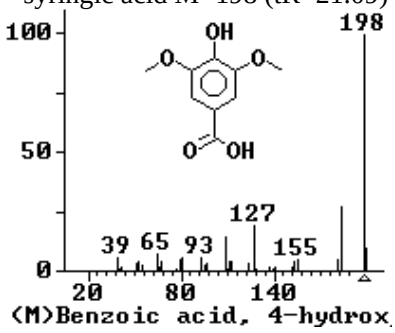

methyl gentisate M=168 (tR=16.84)

vanilmandelic acid M=198 (tR=24.8)

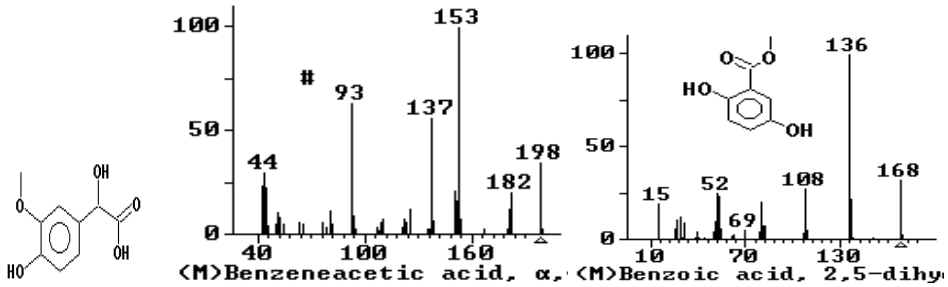

indole-3-ethanol M=161 (tR=20.12)

ethyl phenylacetate M=164 (tR=20.6)

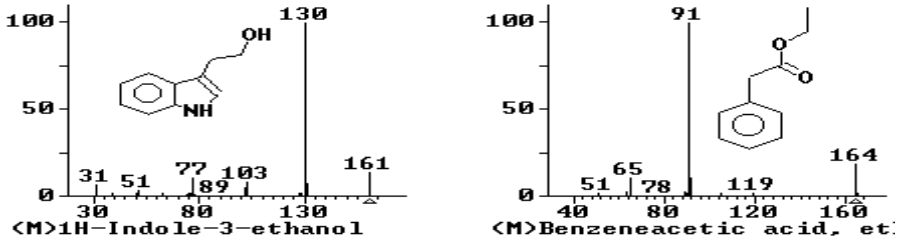

Fig. 1 Mass spectra and chemical structures of some phenolic compounds found in red wines

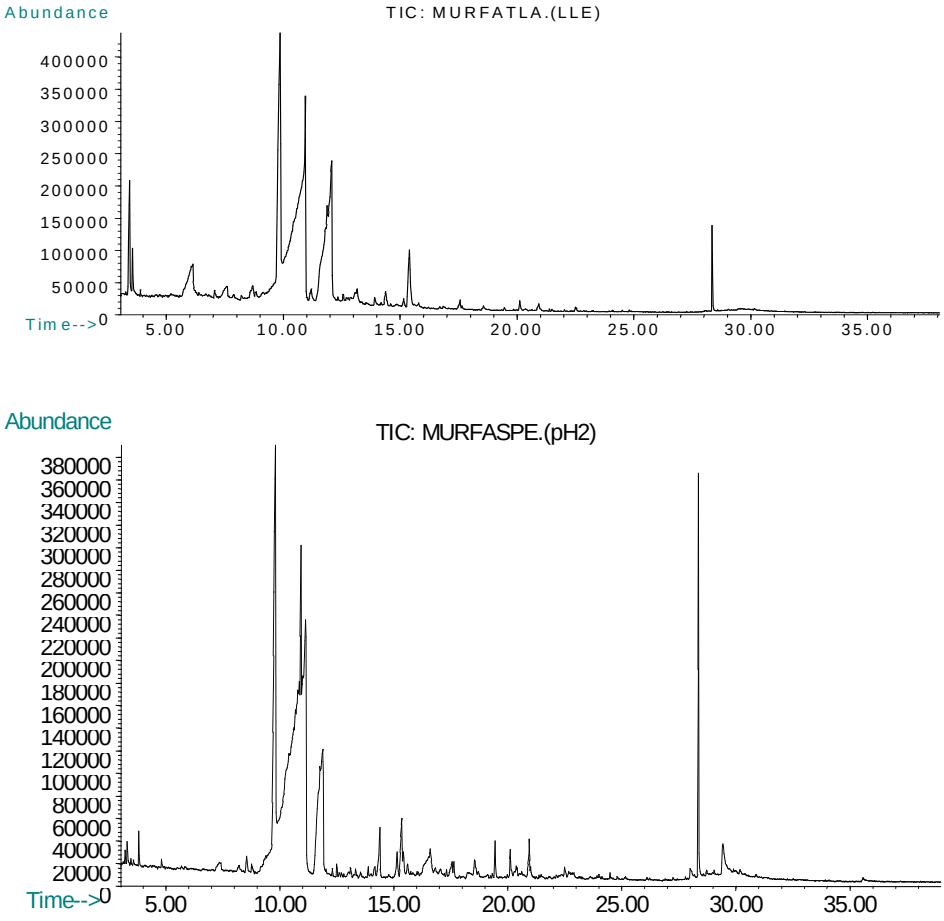

Fig. 2**.** Pinot Noir Murfatlar LLE and SPE chromatograms

STUDIA UNIVERSITATIS BABEŞ-BOLYAI, PHYSICA, SPECIAL ISSUE, 2001

DETERMINATION OF SOME ACTIVE PRINCIPLES OF TERAPEUTIC AND COSMETIC USE FROM *Camomile* BY GC/MS

R. PODEA, M. CULEA, L. FROMONDI

S.C. Natex s.r.l. Sos. Cluj-Oradea km8 , P.O. Box 374 3400 Cluj-Napoca

ABSTRACT. In this study some extraction methods and solvents are tested for the extraction of α-bisabolol, two en-in-dicycloethers and achilin from *Camomile.* These extraction methods and solvents are compared and the objective of the study is to find the most effective way of extracting active principles from *Camomile.* The analytical methods chosen are GC/MS and GC-FID for qualitative respectively quantitative determinations. Comparison of all experiments under the chosen conditions shows propylenglycol to be the most effective extraction solvent for these active compounds.

Introduction

Camomile is a plant that has been used in folk medicine for centuries. It is employed in many different ways both as an aqueous infusion (tea) and as oil of camomile. *Camomile* has been used for a long time, in many parts of the world, as a remedy against inflammation/1,2/. It has been used externally to heal lesions of the skin, as a mouth-rinse, and it has been taken internally against irritated conditions of the stomach and intestinal tract. Some important active principles of *Camomile* are α-bisabolol which is the main responsible for their anti-inflammatory activity, chamazulene, en-in-dicycloethers, mono and sesquiterpenes.

The objective of this work is to study the recovery of some active principle extracts of *Camomile* using different solvents. The solvents are compared for extraction of α-bisabolol, two en-in-dicycloethers and achilin from *Camomile*, the most important active principles found in our study.

Experimental

Extraction methods

In this study we have used different types of solvents and we have compared their efficency in extracting the most important active principles found in *Camomile.*

***A1**. Solvent: hydroalcoholic solution (1:1) at room temp.*

5 extracts were prepared in hydroalcoholic solution (1:1) at room temp;1g air dried and crushed plant was mixed with 5 ml. distilled water and 5 ml. ethanol. The extracts were kept for 5 days at room temperature.

***A2.** Solvent: hot water (infusion)*

5 extracts were prepared in hot water; 0.5 g air dried and crushed plant were mixed for 5 min with 20 ml hot water.

A3 .*Solvent: PG + water at room temp.*

3 kinds of extracts were prepared by mixing 0.5 g dried plant with three propylenglycol solutions of 10%, 25% and 50%. The extracts were kept for 5 days at room temperature.

A4. *Solvent: PG + hot water.*

2 kinds of extracts were prepared by mixing 0.5 g dried plant with two propylenglycol solutions of 25% and 50%. The extracts were mixed for 5 min.

A5. *Solvent: ethanol 100% at room temp.*

5 extracts were prepared by mixing 1g air dried and crushed plant with 10 ml. ethanol. The extracts were kept for 5 days at room temperature.

A6. *Solvent: PG 100% at room temp.*

5 extracts were prepared by mixing 0.5 g dried plant with 10 ml 100% PG. The extracts were kept for 5 days at room temperature.

B).

In the second part of the study we have used propylenglycol (PG, 100 %) as extraction solvent and we have prepared four kinds of extracts in different concentrations: 5 % (0.5 g plant + 10 ml PG), 10 % (1 g plant + 10 ml PG), 15 % (2 g plant + 13.4 ml PG), 20 % (2 g plant + 10 ml PG). The extracts were kept for 7 days at room temperature. Under vacuum filtration of the extracts we have obtained the following amounts of liquid extract:

-solution 5 % : 10 ml PG gave 8.6 ml extract
-solution 10 % : 10 ml PG gave 7.8 ml extract
-solution 15 % : 13,4 ml PG gave 8 ml extract
-solution 20 % : 10 ml PG gave 5.8 ml extract

Sample preparation for GC-FID and GC/MS

1.5 ml of each of the following extracts B, A3, A4 and A6 was mixed with 4.5 ml distilled water , 1ml solvent A (ethyl acetate:hexane:methylen chloride 5/1/1, v/v/v), 2 g NaCl and 1333 µg/g internal, standard methyl undecenoate, (C11:1) for 5 min and 4µl were injected in GC-FID.

3 ml of each of the following extracts A1, A5 was mixed with 3 ml distilled water, 1ml solvent A, 2 g NaCl and 1333 µg/g IS for 5 min, and 4µl were injected in GC-FID.

6 ml of extract A2 was mixed with 1ml solvent A, 2g NaCl and 1333 µg/g IS for 5 min and 4µl were injected in GC-FID.

GC-FID Analysis

GC-FID analysis was performed with a Hewlett Packard GC system 6890 with FID. Compounds were separated on a 30m x 0.25mm HP-5 fused-silica capillary column coated with 0.25µm film.

The column was maintained at 50°C for 2 min after injection, then programmed at 8°C/min to 250°C, then 30°C/min to 310°C which was maintained for 10 min. Helium was used as carrier gas with a flow rate of 1ml/min, split ratios 1:20. The injector and detector temperatures were 250°C.

GC-MS Analysis

GC-MS analysis was performed with a Hewlett Packard GC 5890 coupled with a MS engine 5989B in the EI mode. Compounds were separated on a 30m x 0.25mm HP-5MS fused-silica capillary column coated with 0.25µm film. The column was maintained at 50°C for 2 min after injection, then programmed at 8°C/min to 250°C, then 30°C/min to 310°C which was maintained for 10 min. Split ratio was 1:5 and helium flow rate 1ml/min. Injector, interface, ion source and quadrupol analyser temperatures were 250°C, 280°C, 200°C, 100°C, respectively. The mass spectrometer was operated in electron-impact (EI) mode; electron energy was 70 eV and electron emission 300 µA. Compounds were identified using the Wiley, NBS and NIST library spectra.

Results and discussions

Method validation:

The extraction methods were validated. The following parameters were studied: linearity, precision, recovery, limit of detection.

Quantitation of the active principles was obtained by using the internal standard methyl undecenoate (C11:1) and bisabolol 99.9% purity. The regression curve for bisabolol gave y=0.0011x-0.006, r=0.999.

Table I shows the relative standard deviation values obtained for the different extracts lower than 13%, n=2,3 or 5. Recovery for PG 100% extractions gave 70.5%. The limit of detection was o.5µg/g at a signal to noise of 10:1.

Table I

Precision for different extraction procedures

7days 10% PG µg/g	7days 25% PG µg/g	7days 50% PG µg/g	45oC 50% ET. µg/g	3 days 100% ET. µg/g	100oC infusion µg/g	25% PGinf µg/g	50%PG inf µg/g	5days 50% ET. µg/g	5days 50% ET. µg/g	7days 100% ET. µg/g
3.5	11.14	2.56	12.9	9.8	7.7	8.14	14.7	11.6	11.6	8
n=2	n=2	n=2	n=5	n=3	n=5	n=2	n=2	n=2	n=3	n=2

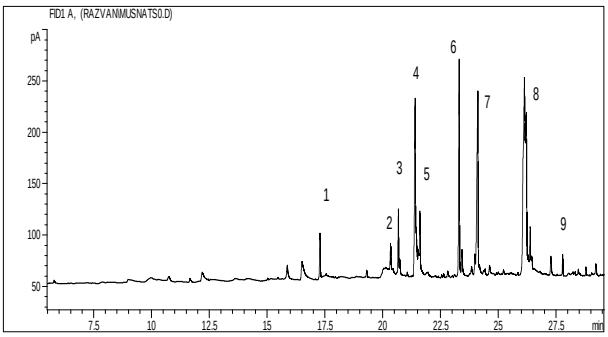

Fig. 1 Gas chromatogram for hydroalcoholic extraction of camomile: 1. spathulenol; 2. alpha-bisabolol oxide B M=238(20.2min); 3. alpha bisabolol M=220 (20.6min) 4. herniarin M=176(21.46min); 5.bisabolol oxide A(21.8min) M=238; 6. en-in-dicycloether M=200; 7. ethyl palmitate; 8. ethyl linoleate; 9.achilin M=246 (27min);

The active principles from camomile determined by different extraction procedures are presented in tables II and III.

Table II

Extracts in PG 100% (**B**)

Concentration of the extract g/ml	0.5g/10ml (5%)	1g/10ml (10%)	2g/13.4ml (15%)	2g/10ml (20%)
Active principle	µg/g	µg/g	µg/g	µg/g
bisabolol	86.99	73.57	90.47	94.8
en-in-dicycloether M=200	2111.84	2059.9	2694.75	2571.4
en-in-dicycloether M=200	332.19	234.26	296.28	294.12
achillin M=246	198.12	235.26	297.89	305.1
Active principle	µg/ml	µg/ml	µg/ml	µg/ml
bisabolol	4.35	7.36	13.5	18.96
en-in-dicycloether M=200	105.59	205.99	402.2	514.28
en-in-dicycloether M=200	16.61	23.43	44.22	58.82
achillin M=246	9.91	23.53	44.46	61.02
recovery	86%	78%	60%	58%

Table III

Extracts in other solvents

	A1	**A2**	**A3,a**	**A3, b**
active principle	µg/g	µg/g	µg/g	µg/g
bisabolol	282.20	29.03	11.78	12.12
en-in-dicycloether M=200	1493.06	170.90	114.40	177.62
en-in-dicycloether	252.22	142.57	55.45	69.37
achillin M=246	159.73	173.34	122.87	143.91
total	**2187.21**	**515.84**	**304.51**	**403.01**

A3, c	**A4, a**	**A4,b**	**A5**	**A6**
µg/g	µg/g	µg/g	µg/g	µg/g
29.01	19.38	35.87	99.15	329.98
880.14	252.14	366.68	1221.40	1259.3
202.33	122.72	130.23	313.13	230.18
211.36	143.63	113.54	134.16	167.44
1322.85	**537.88**	**646.32**	**1633.68**	**1986.9**

Fig.1 presents the gas chromatogram of separation of active principles from camomile extracts. The quantitative variability of active principles extracted from camomile in different procedures is present in Fig.2. The structure of some of the active compounds found in camomile is presented in Fig. 3.

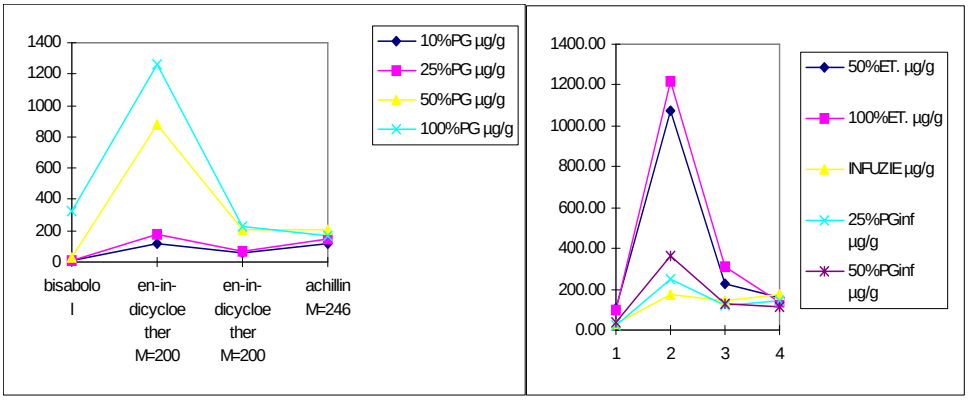

Fig. 2 Efficiency of extraction of active principles from camomile in different procedures

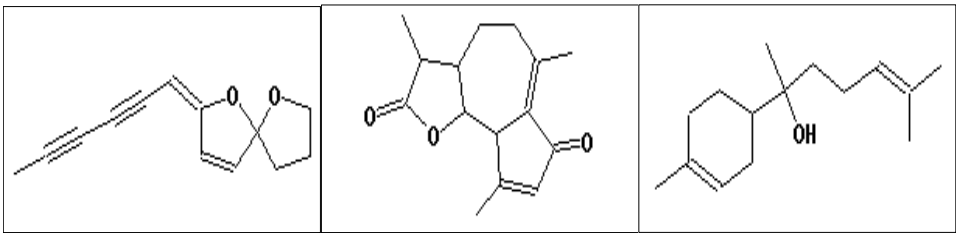

Fig. 3 en-in-dicycloeter achilin M=246 bisabolol

Conclusions

The analytical methods chosen are good for qualitative and quantitative determinations of active principles in camomile. Best recovery for propyleneglycol extracts was found for concentration of 10%-15% PG.

The comparison of different extraction procedures shows hydroalcoholic, alcoholic and propylenglycol to be the most effective extraction solvents for these active compounds.The concentration of the active principles decreases in extracts as follows: hydroalcoholic 1:1(B1)>PG100%(B6)>ethanol 100% (B5)> PG 50% r.temp. (B3c)> PG50% + hot water(B4b)>PG25% + hot water (B4a)>infusion(B2)> PG25% r.temp. (B3b)> in PG10% r.temp.(B3a) (Fig.2)

The good recovery for propylenglycol extraction method of active principles of camomile give important application in skin-care cosmetic preparation. The extraction procedure followed and the monitoring of the quantitaty of active principles in herb is very important in therapeutical and industrial application.

BIBLIOGRAPHY

1. Avallone R. Zanoli P. Puia G. Kleinschnitz M. Schreier P. Baraldi M. Biochem.l Pharmacol. 59(11):1387-94, 2000.

2. Scalia S. Giuffreda L. Pallado P. J.Pharm. Biomed. Anal. 21(3):549-58, 1999.

STUDIA UNIVERSITATIS BABEŞ-BOLYAI, PHYSICA, SPECIAL ISSUE, 2001

AN EPR INVESTIGATION OF GIANT MAGNETORESISTIVE PEROVSKITES DOPED WITH DIAMAGNETIC IONS

X. FILIP, N.M. GRECU, L.V. GIURGIU, AL. DARABONT[A], O. RAITA and J. BLASCO[B]

National Institute for Research & Development of Isotopic and Molecular Tehnology, P.O.Box 700, R-3400, Cluj-Napoca, Romania, giurgiu@L30.itim-cj.ro
National Institute of Materials Physics, 76900 Bucharest-Magurele, P.O.BoxMG-7, Romania
[a] "Babes-Bolyai" University, Faculty of Physics, Kogalniceanu 1, Cluj-Napoca, Romania
[b] Universidad de Zaragoza – CSIC,50009-Zaragoza, Spain

ABSTRACT. The effects of Mn site substitution by diamagnetic ions on the spin dynamics in the magnetoresistive $La_{2/3}Ca_{1/3}Mn_{1-x}D_xO_3$ (D=Al, In; $x \leq 0.05$) powders have been investigated by EPR. The temperature and x dependence of the resonance linewidth and integral intensity of the EPR signal have been investigated and discussed in terms of exchange narrowing and small polaron hopping model. In the paramagnetic regime, the exchange coupling integral,J,betweeen Mn^{3+} and Mn^{4+} ions shows a decrease with increasing x. It could arises from weakening of the double exchange interaction by D-doping which reduces the exchange field at the Mn sites.The activation energy, E_a, for the hopping motion of small polarons as function of x and D was evaluated and compared with the results of other experiments .

1.INTRODUCTION

The manganese perovskites have been widely studied since the discovery of colossal magnetoresistance(CMR) effects.They are mixed valent containing Mn^{3+} and Mn^{4+} ions.Coexistence of ferromagnetism and metallic conduction in these materials has been explained in terms of the double exchange machanism(DE)[1,2]. However, DE alone does not explain the CMR and an additional mechanism based on the polaronic effects was included.[3].Here a strong electron-phonon coupling is expected because the electronic ground state of the Mn^{3+} ions is degenerate giving rise to the Jahn-Teller (JT) effect.There are direct experimental evidences of JT polaron formation in $La_{1-x}Ca_xMnO_3$ compounds.[4,5,6]

The archetypul CMR compound $La_{2/3}Ca_{1/3}MnO_3$ undergoes a para-ferromagnetic (PM-FM) transition at $T_C \approx 260K$ accompanied by a metal-insulator transition.The study of substitution of diamagnetic ions (D) for manganese in this system has shown that it was possible to modify its magnetic and transport properties [7,8,9,10]. For low replacement values of Mn by Al or In, which have no magnetic moment and their atomic radii are $\langle r \rangle_{Al} < \langle r \rangle_{Mn} < \langle r \rangle_{In}$, a decrease of the T_C with increasing D content was observed, but the magnetoresistive properties do not change very much. [7].

EPR spectroscopy is a powerful tool to study the complex magnetic state in the manganese perovskites [11,12,13,14,15]. The linewidth in CMR perovskites was considered to be caused by spin - lattice relaxation of the exchange coupled Mn^{4+} ions via Mn^{3+} JT-ions to the lattice under the condition of a strong relaxation bottleneck [11].The energy transfer is provided by the activated hopping of small polarons in connection with the jumps of e_g charge carriers from Mn^{3+} ions to the Mn^{4+} ions [14]. The argument for the above assumption is based on the similar temperature dependence of EPR linewidth and conductivity in $La_{0.8}Ca_{0.2}MnO_3$ [14] . In the paramagnetic regime the conductivity of CMR perovskites arrises from the adiabatic hopping motion of small polarons and obeys a $T^{-1}\exp(-E\sigma/k_BT)$ law, E_σ beeing the activation energy [15].

In order to obtain further insight into physical mechanisms of the spin dynamics and the Mn-site doping effects, an X-band EPR investigation of $La_{2/3}Ca_{1/3}Mn_{1-x}D_xO_3$ (D=Al,In) fine powders was carried out . Some results concerning the destabilisation of the Mn sublattice by Al doping as seen by EPR have been already reported [12,13].

2. EXPERIMENTAL

Ceramic samples of $La_{2/3}Ca_{1/3}Mn_{1-x}D_xO_3$ (D=Al,In ; x=0; 0.01 ; 0.03 ; 0.05) were prepared by standard solid state reaction method [7,8] . Table 1 shows the Mn^{4+} content y, as determined by redox titration and the values for T_C defined as the inflection point of the susceptibility curves [16].

Table1.

Percentage of Mn^{4+} and the critical temperatures T_C for $La_{2/3}Ca_{1/3}Mn_{1-x}D_xO_3$

Parameter	x = 0	Al			In		
		x = 0.01	x = 0.03	x = 0.05	x = 0.01	x = 0.03	x = 0.05
y(% Mn^{4+})	0.30	0.34	0.34	0.35	0.31	0.32	0.28
T_C (K)	263	217	203	189	232	200	107

The samples with $x \leq 0.5$ and $x \leq 0.3$ for Al and In doping, respectively, are nominally stoichiometric and in order to preserve the charge equilibrum the substitution of D for Mn leads to an oxidation from Mn^{3+} to Mn^{4+} (Table 1). The T_C decreases with the increase of the D content and implies weaker ferromagnetic interactions.

In the paramagnetic regime the EPR spectrum for all investigated samples consists of a single line with $g \approx 1.99$ [12]. The line-shape of the ceramic samples reduced to fine powders was found to be Lorentzian over the investigated temperature range and for all x. It confirms the presence of the exchange-narrowed Mn dipolar fields [13]. Since the sample size effects due to magnetic losses affect the spectrum [12] we have used small amount of powder material, m=1mg, for each x. In order to evaluate the EPR parameters, the derivative spectra were fitted with a Lorentzian line-shape with fit parameters being the half-width at half-height, $\delta B_{1/2}$, of the corresponding absorption line and the resonance field, B_0.

3.RESULTS AND DISCUSSION

The temperature dependencies of the EPR linewidth $\delta B_{1/2}$ are shown in Fig.1 and Fig.2 for the samples with various Al and In concentration x, respectively.The linewidth decreases almost linearly with decreasing temperature and goes through a minimum at $T_{min} \approx 1.1\ T_C$, the behaviour similar to that observed for undoped compound [7] .Its increase below T_{min} is attributed to the usual critical slowing down in ferromagnets.The temperature T_{min} shows a decrease with increasing x in accordance with T_C variation.

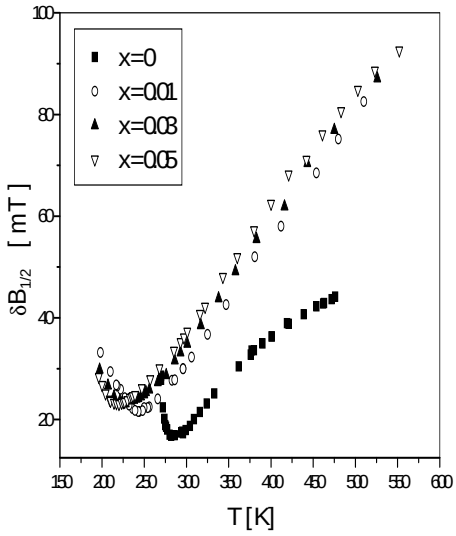

Fig.1 Temperature dependence of the linewidth $\delta B_{1/2}$ for $La_{2/3}Ca_{1/3}Mn_{1-x}Al_xO_3$

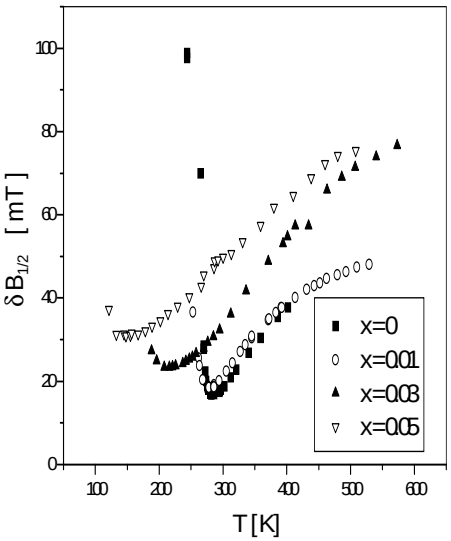

Fig.2 Temperature dependence of the linewidth $\delta B_{1/2}$ for $La_{2/3}Ca_{1/3}Mn_{1-x}In_xO_3$

The effect of Al substitution is to progressively broaden the resonance line and the linewidth at a fixed temperature shows an increase with increasing D concentration [13]. It could arises from the weakening of the double-exchange ferromagnetic interaction by D doping which reduces the exchange field at the Mn sites and consequently an increase of the dipolar broadening would be expected.

The analysis of the EPR integral intensity,I_{EPR}, shows that all Mn spins contribute to the EPR signal in the temperature range investigated [17]. In the bottleneck approach, a collective motion of the magnetic moments of Mn^{4+} and Mn^{3+} spin subsystems is involved [14]. Here the EPR integral intensity is proportional to the total susceptibility χ_{EPR} of the Mn^{4+} and Mn^{3+} spins:

$$I_{EPR} \approx \chi_{EPR} = \chi_s + \chi_\sigma \qquad (1)$$

where χ_s and χ_σ are the normalized static susceptibilities of the Mn^{4+} and Mn^{3+} spins, respectively [18].

We have found that at high temperatures $I_{EPR}(T)$ for $La_{2/3}Ca_{1/3}Mn_{1-x}D_xO_3$ samples follows a ferromagnetic Curie-Weiss (CW) temperature dependence

$$I_{EPR}(T) = C/(T-\theta) \quad (2)$$

arising from the FM coupling of the Mn^{4+} ($S_1 = 3/2$) and Mn^{3+} ($S_2 = 2$) subsystems [13].At lower temperatures in the paramagnetic regime, there is a deviation from the CW law.Fig.3 shows a plot of $1/I_{EPR}$ for Al and In doped samples with x=0.05.From the linear behaviour of $1/I_{EPR} = f(T)$ for $T \geq 1.9\ T_C$ and the extrapolation to lower temperatures, the CW temperature θ could be obtained.

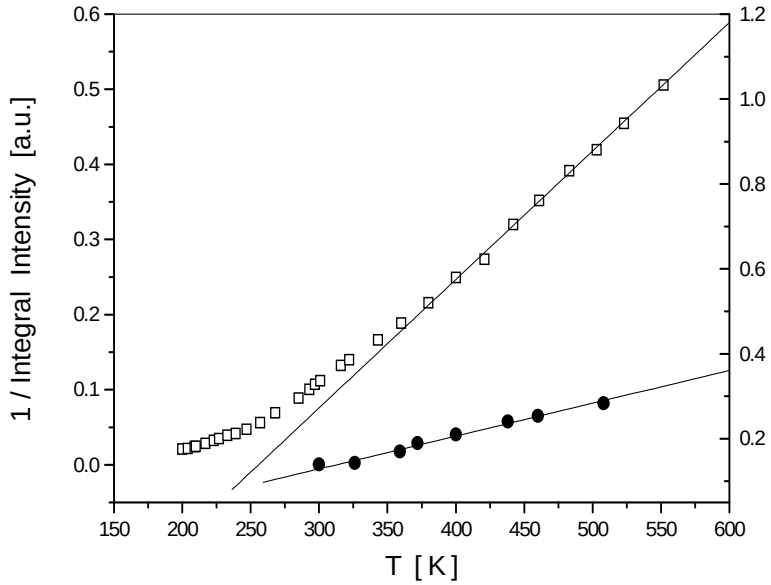

Fig.3. 1/ Integral intensity of EPR linewidth as function of T for $La_{2/3}Ca_{1/3}Mn_{0.95}D_{0.05}O_3$ (- D=Al ; • - D=In).The solid lines represent the best fits to the Eq.(2) at high temperatures.

In Table 2, we present θ values determined from the high temperature region as function of D concentration. For $x \leq 0.05$,θ is reduced as x is increased showing a general weakening of DE interaction.

Table 2.

Variation of θ and J as function of D concentration x in $La_{2/3}Ca_{1/3}Mn_{1-x}D_xO_3$

	x	θ [K]	T_C/θ	J [meV]
	0	325	0.80	4
Al	0.01	278	0.78	3.1
	0.03	263	0.77	2.9
	0.05	256	0.74	2.8
In	0.01	270	0.86	3.1
	0.03	267	0.74	3.0
	0.05	134	0.79	1.7

In the Weiss mean-field approximation for a system of two different spins, S_1 and S_2, the θ temperature may be expressed by [12].

$$k_B\theta / J = (4z/3)y(1-y)S_1(S_1+1)S_2(S_2+1) / [y S_1(S_1+1)+(1-y)S_2(S_2+1)] \quad (3)$$

where z is the number of nearest Mn neighbours and J represents the exchange integral between Mn ions in the PM regime.

Using the evaluated values of θ, the exchange coupling integrals J deduced by means of Eq.(3) are given in Table 2. As one can see, the effect of D doping is to perturbe DE coupling between Mn^{4+} and Mn^{3+} ions, causing a decrease in J [12,13]. It could arises from the bending of the Mn-O-Mn bonds in the (a-b) plane which is expected to slow down the carrier hopping and weaken the DE.

In the following we discuss the temperature dependence of the EPR linewidth, $\delta B_{1/2}$ (Fig.(1) and (2)).If one assumes that the polaronic charge carriers also exists in $La_{2/3}Ca_{1/3}Mn_{1-x}D_xO_3$ ($0 < x \leq 0.05$), than the temperature dependent part of the EPR linewidth should arrises from a thermally activated process involving the adiabatic hopping of small polarons.

In Fig.4 we plot the temperature dependences of the EPR linewidth corresponding to $La_{2/3}Ca_{1/3}Mn_{0.95}D_{0.05}$ samples where the solid lines represent the best fit to the data using the expression [14,19].

$$\delta B_{1/2}(T) = \delta B_0 + AT^{-1}\exp(-E_a / k_B T) \quad (4)$$

where δB_0 and E_a are the residual linewidth and the polaronic activation energy, respectively.

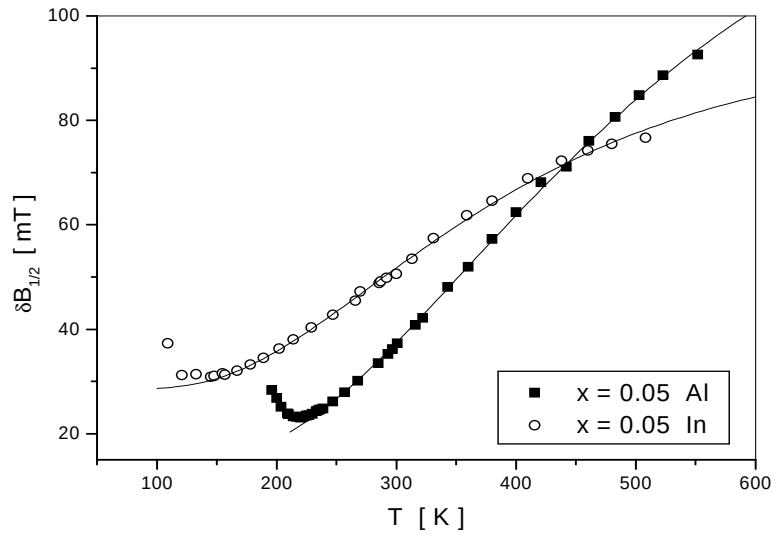

Fig.4. Temperature dependence of the EPR linewidth for $La_{2/3}Ca_{1/3}M_{0.95}D_{0.05}O_3$ (♦-D=Al, o-D=In).The solid line represents the best fit to the data above T_{min}(Eq.4)

The fitting parameters for D=Al,In samples with $x \leq 0.05$ are given in Table 3.

Table3.

The residual linewidth δB_0 and the activation energy,E_a, as function of D concentration x in $La_{2/3}Ca_{1/3}Mn_{1-x}D_xO_3$

	x	δB_0 [mT]	E_a [eV]
	0	60	0.12
Al	0.01	129	0.11
	0.03	139	0.10
	0.05	165	0.10
In	0.01	379	0.05
	0.03	153	0.09
	0.05	329	0.08

As one can see, the activation energies are of the same order of magnitude for all $La_{2/3}Ca_{1/3}Mn_{1-x}D_xO_3$ samples within the experimental uncertainty. The values of E_a for In doped samples seem to be a little smaller than Al doped ones.We suppose that this is a result of the larger ionic size of doped In ions which could perturb the polaron hopping procces.It is important to note that the activation energies deduced from the present EPR linewidth data for Al and In doped samples are very close to the value E_σ = 0.121 eV obtained from resistivity data of a $La_{2/3}Ca_{1/3}MnO_3$ thin film [5].More than that, the evaluated E_a values are nearly the same as the values 0.106 eV and 0.108 eV deduced from the corresponding temperature dependence of the EPR linewidth and tunneling experiments on $La_{0.8}Ca_{0..2}MnO_3$ samples, respectively [14, 20]

These results lead us to suggest that polaronic charge carriers should also exist in $La_{2/3}Ca_{1/3}MnO_3$ perovskites doped with Al and In ions.In the corresponding paramagnetic regime the spin-lattice relaxation could be determined by the thermaly activated motion of small polarons.

4.CONCLUSIONS

The effects of Al and In substitution in $La_{2/3}Ca_{1/3}MnO_3$ powders have been investigated by EPR. The weakening of the DE interaction by doping reduces the exchange field at Mn sites, which result in a broadening of the resonance lines and a decrease of the exchange coupling integral J between Mn^{4+} and Mn^{3+} ions. In the PM regime the temperature dependences of the EPR linewidth are well describe by the polaronic model.

From a comparison of the evaluated activation energies for the doped samples with the corresponding ones for undoped compounds, one can suggests the presence of small polarons in $La_{2/3}Ca_{1/3}Mn_{1-x}D_xO_3$ (D = Al, In) perovskites for $x < 0.5$.

REFERENCES

[1] Zener C., Phys. Rev. **B82**, 403(1951)
[2] P.G. de Gennes, Phys. Rev. **118**, 141(1960)
[3] Millis A.J., Zitlewood P.B.and Shraiman B.I., Phys. Rev. Lett. **74**, 5144(1995)
[4] Hock K.H.,Nickisch H. and Thomas H. Helv Phys.Acta **50**, 237 (1983)
[5] Worledge D.C., Snyder G.J., Beasley M.R., Geballe T.H., Hiskes R.and Di.Carolis S., J. Appl.Phys. **80**, 5158 (1996)
[6] Jaime M., Salamon M.B.,Rubinstein M.,Treece R.E., Horowitz J.S.and Chrisey D.B., Phys. Rev. **B54,** 11914 (1996)
[7] Blasco J.,García J., J.M. de Teresa, Ibarra M.R., Perez J., Algarabel P.A., Marquina C. and Ritter C., Phys. Rev. **B55**, 8905(1997)
[8] Sánchez M.C., Blasco J., García J., Stankiewicz J., J.M. de Teresa and Ibarra M.R., J.Solid State Chem. **138**, 226(1998)
[9] Sun J.R., Rao G.H., Gao X.R., Liang J.K., Wong H.K. and Shem B.G. J Apll.Phys. **85**, 3629 (1999)
[10] Turilli G and Licci F., Phys. Rev. **B54**,13052 (1996)
[11] Shengelaya A., Guo-meng Zhao, Keller H. and Müller K.A., Phys. Rev. Lett. **77**, 5296(1996)
[12] Giurgiu L.V., Grecu M.N., Filip X., Darabont A, Filip C.,Ordean R. and Popescu G.D., Proc. 30-th Congress AMPERE, Lisbon, Ed. A.F. Martins, Universidade Nova de Lisboa, Lisbon, Portugal, p.51. (2000)
[13] Giurgiu L.V., Grecu M.N, Filip X., Darabont A., Indrea E., Filip C., Ordean R., Popescu G.D., Surducan E., Blasco J.and Papavassiliou G., J.Optoelectronics and Adv.Mat. **2**, 375 (2000)
[14] Shengelaya A., Zhao G., Keller H., Muller K.A.and Kochelaev B.I., Phys.Rev **B61**, 5888 (2000)
[15] Atsarkin V.A., Demidov V.V., Vasneva G.A.and Conder K., Phys.Rev. **B63**, 092405 (2000)
[16] Deac I.G., Darbont A. and Giurgiu L.V.- to be published
[17] Causa M.T., Tovar M., Caneiro A.,Prado F.,Ibãnez G.,Ramos C.A.,Buter A.,AlascioB., ObradorsX., Piñol S,Rivadulla F.,Vázquez-Vázquez C.,López-Quitela M.A.,Rivas J., Tokura Y. and Oseroff S.B., Phys. Rev. **B58**, 3233(1998)
[18] Barnes S.E. Adv. Phys. **30**, 801 (1981)
[19] Zhao G.M., Keller H., Greene R.L.and Muller K.A., Physics of Manganites, Eds.Kaplan and Mahanti, Kluwer Academic, Plenum Publishers, p.231 (1999)
[20] Biswas A., Elizabeth S., Raychaudhuri A.K. and Bhat H.L., Phys.Rev. **B69**, 5368 (1999)

SPECTROSCOPIC STUDIES ON INCLUSION COMPLEX OF SULPHASALAZINE WITH CYCLODEXTRINS

LORENA FILIP, [1]DIANA BOGDAN, M. BOJITA, [1]M. BOGDAN

University of Medicine and Pharmacy "Iuliu Hatieganu" Cluj-Napoca
National Institute for R&D of Isotopic and Molecular Technologies,
P.O. Box 700, Cluj-Napoca

ABSTRACT. The complexing and amorphising abilities towards sulphasalazine of native α- and β-cyclodextrin were determined. The inclusion complexes prepared by different methods (kneading and co-precipitation) led to amorphous products. The influence of the preparation method on the physicochemical properties of sulphasalazine was studied by means of IR spectroscopy and X-ray diffraction analyses.

1. INTRODUCTION

Cyclodextrins have recently been recognized as useful pharmaceutical excipients, due to their potential to form inclusion complexes with appropriately sized drug molecules. The resulting complexes generally show some favorable changes of the characteristics of the guest molecule, such as increased solubility and reduced side effects [1].

Selections of the most suitable preparative method for a given drug requires careful evaluation because it should take into account not only factors such as simplicity, lower cost, high yield, swiftness, easy of scaling up, but also the performance of the obtained product.

Therefore, in the present work, we considered worthy of interest to investigate the influence of preparation method and the type of carrier on the physicochemical properties of a series of binary systems of sulphasalazine (**SF**) with α- and β-cyclodextrin.

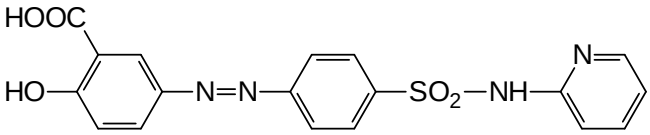

Acid 5[(4-(pyrid 2-ilsulfamoil)fenil)azo]salicylic
(Sulphasalazine)

2. MATERIALS AND METHODS

2.1. Materials

α- and β-cyclodextrin were supplied by Sigma Chemie GmbH, Germany, and were used without further purification. Sulphasalazine was kindly donated by AC Helcor, Baia Mare, Romania. All other solvents were of analytical reagent grade. Double distilled water was used.

2.2.Preparation of solid binary systems

Two different methods (kneading and coevaporation) were used for the preparation of drug-cyclodextrin solid system.

Kneading: a physical mixture of α(β)-cyclodextrin-sulphasalazine (1:1 mole ratio) was wetted in ethanol-water (1:1 v/v) solution and kneaded thoroughly for 60 min in a mortar with a pestle in order to obtain a uniform paste. During this process an appropriate quantity of the solvent mixture was added. The paste was dried under reduced pressure at room temperature for one day.

Co-evaporation: α(β)-cyclodextrin was solubilized at room temperature in 15 ml of water then sulphasalazine (1:1 mole ratio) was added with stirring. The suspension was heated at 45 ºC and stirred for 48 h until equilibrium was reached. The suspension was filtered and the filtrate was dried under vacuum at room temperature.

2.3.Infrared spectroscopy

Infrared spectra were obtained with a Carl Zeiss – Jena UR 20 infrared spectrophotometer.

2.4.X-ray powder diffractometry

X-ray diffraction patterns of powdered samples were recorded using a DRON 2 diffractometer. Experimental settings: Ni-filtered Cu K_α radiation (λ = 1.54178 Å); tube settings 40 kV, 30 mA; scan rate of 2 degree·min^{-1} over the 10 - 40 degree 2θ range.

3. RESULTS AND DISCUSSION

Infrared spectra of sulphasalazine, CDs as well as those of its different systems with CDs are presented in Fig. 1. We found no significant differences (comparing with the spectra of pure CDs) in the case of inclusion compounds obtained by co-evaporation. For the kneaded samples the IR spectra of SF-CDs products show no features similar to pure drug or CD. In these cases we observed a shift of some absorption bands to higher frequency.

This effect can be attributed to the formation of an inclusion complex between the monomeric drug with CD.

X-ray powder diffraction patterns, shown in Fig. 2, confirmed the results of IR spectroscopy. The patterns of the products obtained by co-evaporation method were practically a superposition of the patterns of the two starting components. In this case we presume that the complex between sulphasalazine and CDs does not form.

The spectra of the kneaded samples prove the appearance of a new solid phase having o lower crystallinity than the drug and CDs. The spectra of the kneaded sulphasalazine with α- and β-CD were practically the same, but the spectrum of SF with α-CD showed broader and less intense peaks than that of SF-βCD complex. This indicates a much stronger interaction between the two components and, as a result, the final product is transformed into an amorphous compound.

REFERENCES

[1] D. Duchene, F. Glamot, C. Vaution, *"Pharmaceutical applications of cyclodextrins"*. In D. Duchene (Ed.) *"Cyclodextrins and Their Industrial Uses"*, Edition De Santé, Paris, 1987.

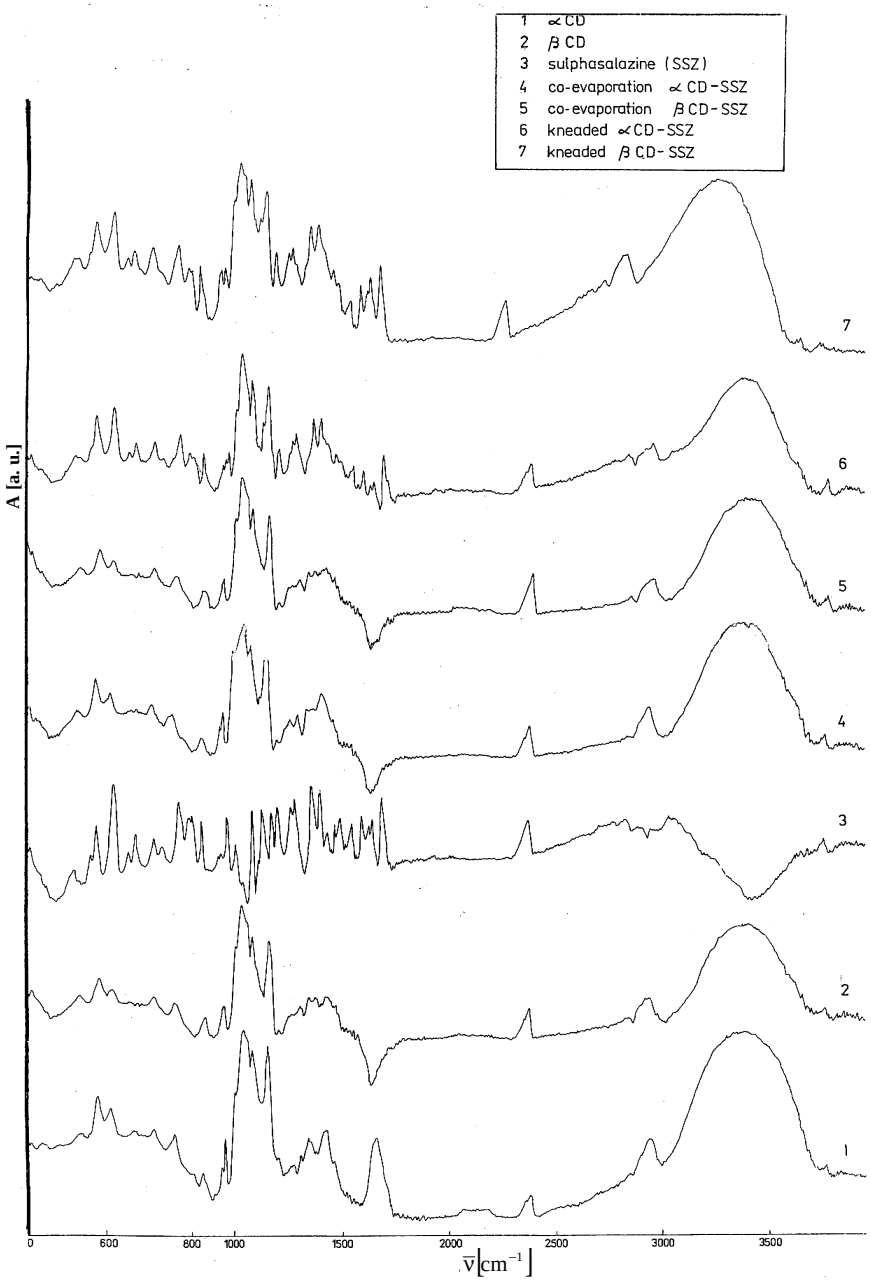

Fig. 1. IR spectra of sulphasalazine, CDs and its different systems

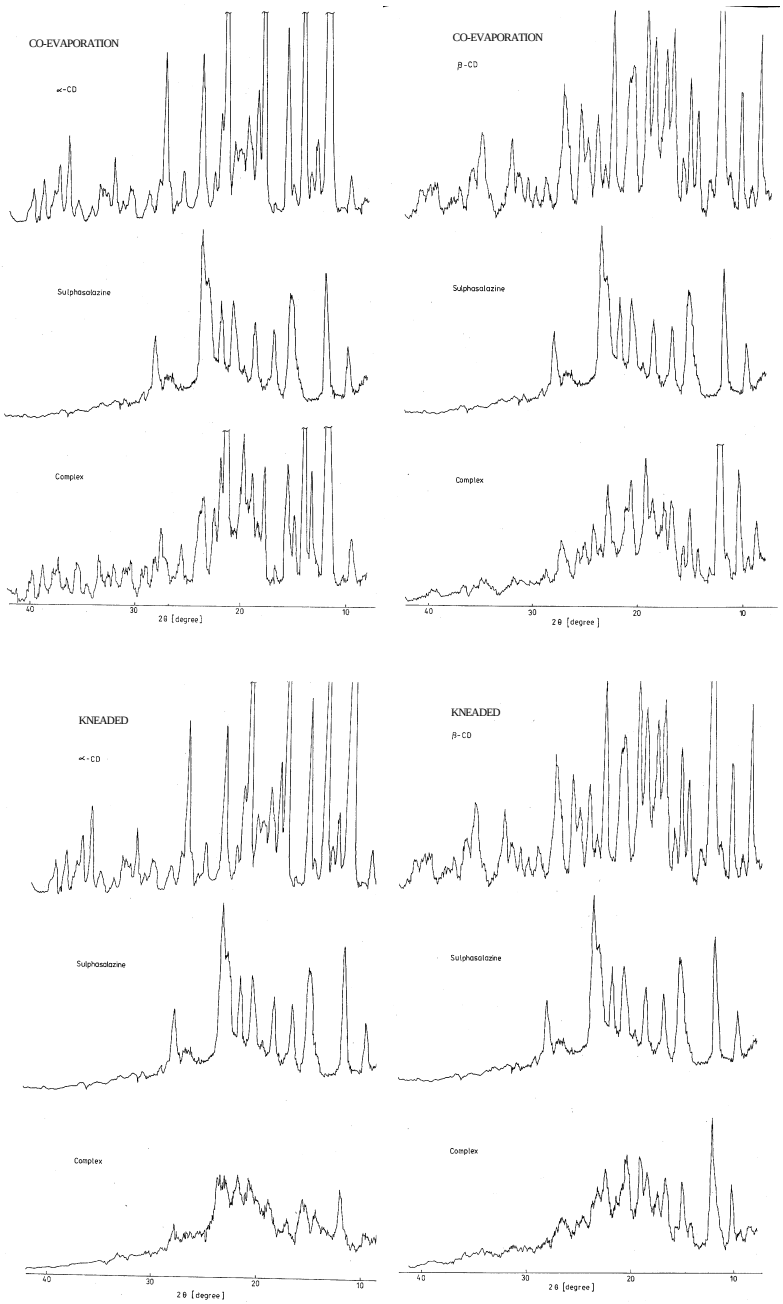

Fig. 2. X-ray powder diffraction patterns of single components and equimolar kneaded or co-evaporated products of SF with α- and β-CD

STUDIA UNIVERSITATIS BABEŞ-BOLYAI, PHYSICA, SPECIAL ISSUE, 2001

STUDIES OF BORATE VANADATE GLASSES USING RAMAN AND IR SPECTROSCOPY

D.MANIU[*1], T. ILIESCU[1], I. ARDELEAN[1], I. BRATU[2], C. DEM[3]

[1]*Babes Bolyai University, Faculty of Physics, Kog¾lniceanu 1, 3400 Cluj-Napoca, Romania*
[2] *Institute for Isotopic Molecular Technology, P.O. Box 700, 3400 Cluj-Napoca 5, Romania*
[3]*Institut für Physicaliche Chemie, Universitat Würzburg, Am Hubland, D-97074 Würzburg, Germany*

ABSTRACT. Raman and IR spectra of $xV_2O_5.(1-x)B_2O_3$ glasses (with $0.05 \le x \le 0.8$) have been measured and analysed.

The band characteristic to boroxol groups (806 cm^{-1}) is present only at very low V_2O_5 content. This band has small intensity and disappears when V_2O_5 content increases, while the Raman bands assigned to diborate groups and isolated BO_4 units are present in all spectra. The presence of V_2O_5 in B_2O_3 glasses determines the appearance of four-fold coordinated boron atom in diborate groups and isolated BO_4 units. In this glasses chain type metaborate groups are also identified. For high V_2O_5 content, the intensity of the band centered at 993 cm^{-1} does not decrease as that from 1022 cm^{-1} (both assigned to diborate groups). Therefore, we presume that at 993 cm^{-1} are overlap two bands: one is characteristic to diborate groups and the other one to vanadate structure.

IR spectra reveal same changes as in Raman spectra. For samples having $x \ge 0.6$ a peak characteristic to V_2O_5 appears. This is an indication that vanadate structure was forming.

Therefore, we conclude that the vanadium oxide acts as network modifier in these glasses for $0.05 \le x \le 0.5$. For $0.6 \le x \le 0.8$ vanadium oxide acts as glass forming.

Keywords: Raman, IR, borate glasses, vanadium oxide.

1. Introduction

Raman and IR spectroscopy become effective tools for resolving the structure of local arrangement in glasses.

The transition metal (TM) oxide glasses have been extensively studied by several authors during the last twenty years. These glasses are of importance due to their semiconducting properties and the electrical conduction is due to electron hopping [1-3] on account of the available reduced states of the TM ions. Some authors have studied the effect of single [4] and multiple [5] TM ions as dopants in alkali or alkaline earth oxide glasses. On the other hand some have reported the effect of glass formers on these TM oxides as regards the glass formation and have examined the electrical behavior [6] and performed spectroscopic studies [7].

In this paper we report the structure study of borate vanadate glasses using Raman and IR spectroscopy.

2. Experimental

Glasses of $xV_2O_5(1-x)B_2O_3$ system with $0.05 \leq x \leq 0.8$ were prepared by mixing H_3BO_3 and V_2O_5 having reagent grade purity in suitable proportions and melting this admixtures in sintered corundum crucibles at T = 1523 K for 0.5 hour. Vitrification was achieved by rapid cooling of the melts on stainless steel plates at room temperature and atmospheric pressure.

The Raman spectra were obtained using the micro-Raman technique. A Spectra Physics 166 Ar^+ laser (514.4 nm) was coupled with an optical microscope Olympus U-CMAD-2 with two objectives (DPLAN 20 160/0.17 and ULWD MSPLAN 80/0.75). The laser power was 350 mW at the sample. A 180° geometry was used as well as a Spex model 1404 double monochromator with a spectral slit width of 2 cm^{-1}. The spectra were recorded without a polarizer in the collection optics.

The IR spectra were recorded in 4000-400 cm^{-1} spectral range with a Brucker IFS 120 spectrometer using the KBr pellet technique. A MIR Glowbar source and a MCT detector cooled with liquid nitrogen were used. The measurements were carried out for a pressure less than 1 mbar, at the room temperature. For each spectrum 100 scans were made and the spectral resolution was 1 cm^{-1}.

3. Results and discussion

Raman spectra

Raman spectra of $xV_2O_5(1-x)B_2O_3$ glasses with various contents of copper oxide ($0.05 \leq x \leq 0.7$) are shown in Fig.1. The following bands are present in these spectra: 407 cm^{-1}, 471 cm^{-1}, 526 cm^{-1}, 694 cm^{-1}, 806 cm^{-1}, 993 cm^{-1} and 1022 cm^{-1}.

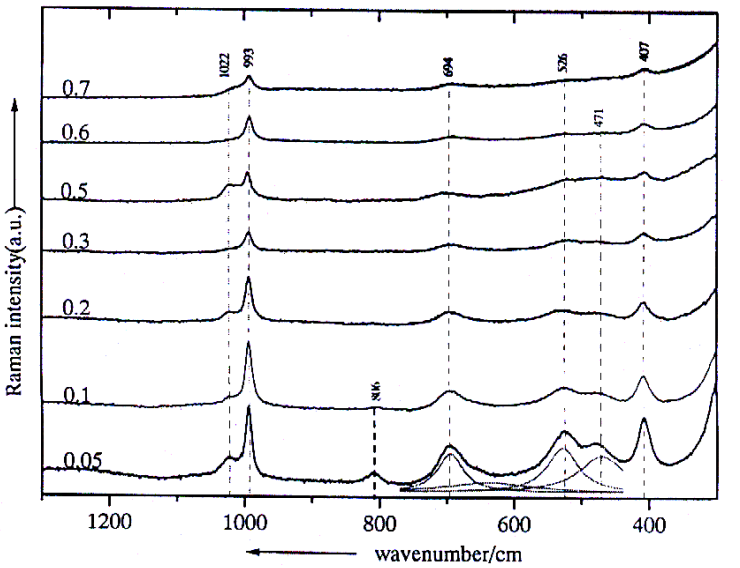

Fig. 1. Raman spectra of of $xV_2O_5(1-x)B_2O_3$ glasses with $0.05 \leq x \leq 0.7$

In the spectrum obtained for lowest V_2O_5 content, the main peaks appear at 993, 694, 526 and 407 cm^{-1}. The intensities of these peaks decrease as the V_2O_5 content increases. Some bands disappear at high content of vanadium oxide. The band centered at 806 cm^{-1} is present only at very low V_2O_5 content. The bands centered at 527 cm^{-1} and 471 cm^{-1} disappear for $x > 0.5$. For highest content of V_2O_5 ($x = 0.7$) the bands centered at 993 cm^{-1}, 694 cm^{-1} and 407 cm^{-1} are still observed and no new bands appear when V_2O_5 content further increases.

The Raman spectrum of vitreous B_2O_3 is dominated by a strong band centered at ~806 cm^{-1}. The 806 cm^{-1} band was assigned to the boroxol ring oxygen breathing involving a very little boron motion (boron atom coordinate is 3) [8]. (A list of borate groups found in borate compounds is given by Meera et al. [9]. This band (characteristic to boroxol rings) appears only for low V_2O_5 content. Therefore, the raising of vanadium oxide content determines a disruption of the boroxol network.

All recorded spectra exhibit peaks at: 407 cm^{-1}, 526 cm^{-1}, 694 cm^{-1}, 993 cm^{-1} and 1022 cm^{-1}. In order to assign these bands we took into account crystalline boron compounds.

Crystalline $ZnO\text{-}2B_2O_3$ and $Li_2O\text{-}2B_2O_3$, which consist only of diborate groups, have Raman peaks at 1050 cm^{-1} and 980 cm^{-1} [10]. On this basis we consider that the band at 993 cm^{-1} and the shoulder at 1022 cm^{-1} observed in our spectra indicate the presence of diborate groups in studied glasses. Diborate groups consist of six membered rings containing two BO_4 tetrahedra. The line occurring at 993 cm^{-1} could arise both from diborate groups [10] and from vanadate structures [11]. Because for high V_2O_5 content, the intensity if the Raman band centered at 993 cm^{-1} does not decrease as the other band assigned to diborate groups (1022 cm^{-1}), we presume that at 993 cm^{-1} are overlap two bands: one typical to diborate groups and the other one characteristic to vanadate structure.

The bands between 400 and 550 cm^{-1} were assigned by Kamitsos et all [12] to the symmetric stretching vibration of the isolated BO_4 units (tetrahedra connecting various segments without participating in the specific borate arrangements) and anti-symmetric stretching vibration of such BO_4 tetrahedra, respectively. Therefore the band at 407 cm^{-1} and 526 cm^{-1} can be assigned to the symmetric stretching vibrations of isolated BO_4 units. The 471 cm^{-1} band is assigned to a ring angle bending (B-O-B) [13] that is observed at 470 cm^{-1} for pure B_2O_3 [14].

Raman spectra of lithium and calcium borate glasses, which consist of chain type metaborate groups [13] exhibit a strong peak at 710 cm^{-1}. In our spectra (fig. 1) this band appears at 694 cm^{-1} and indicates the presence of the chain type metaborate groups.

Even for the Raman spectra obtained for lowest V_2O_5 content the 806 cm^{-1} are not dominant. There are another bands with higher intensities. These bands are characteristic in majority to borate groups containing BO_4 units as we just shown. Therefore, the addition of a very small amount of V_2O_5 ($x = 0.5$) leads to the formation of four coordination boron atoms. The incorporation of BO_4 units in the ring structure results in a weakening of the B-O bond and as consequence the ring opening.

Diborate groups, chain type metaborate groups and isolated BO_4 units are all evidenced beginning with the lowest vanadium oxide content. The decrease of all Raman bands intensities determined by the increase of the V_2O_5 content indicates the diminution of the number of these groups. At very high content of V_2O_5 Raman spectra indicate the formation of vanadate structure. These facts denote that vanadium oxide in the binary system V_2O_5-B_2O_3 acts like a glass modifier and only for very high content of V_2O_5 act as a glass former. The presence of boron oxide, a very strong glass former, permits to vanadium oxide to act as a glass former only at high concentrations.

IR spectra

IR spectra of $xV_2O_5(1\text{-}x)B_2O_3$ glasses with various contents of copper oxide ($0.05 \leq x \leq 0.8$) are shown in Fig.2. The following bands are present in these spectra: 642 cm^{-1}, 796 cm^{-1}, 883 cm^{-1}, 1023 cm^{-1}, 1195 cm^{-1}, 1384 cm^{-1}, 1465 cm^{-1}, 1630 cm^{-1}, 2260 cm^{-1}, 2360 cm^{-1}, 2520 cm^{-1}, 3220 cm^{-1}, and 3443 cm^{-1}.

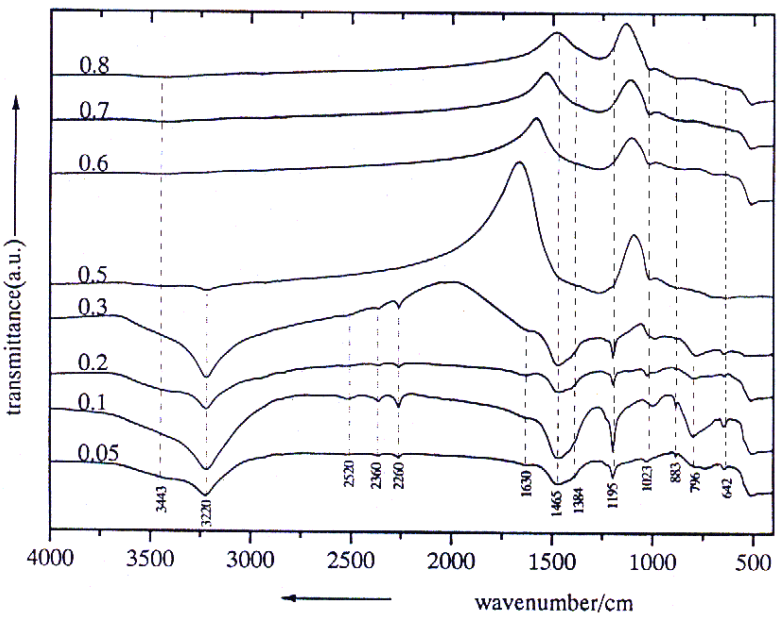

Fig. 2. IR spectra of $xV_2O_5(1\text{-}x)B_2O_3$ glasses with $0.05 \leq x \leq 0.8$

Samples having up to 0.5 V_2O_5 show a water band at 3220 cm^{-1} and -OH stretching peaks at 2520 cm^{-1}, 2360 cm^{-1} and 2260 cm^{-1}. These are intense for low V_2O_5 content as shown in fig 2. According to Borrellie et al. [15] these bands and peaks are due to the hygroscopic character of the powdered glass samples. Hence, it can be safely concluded that the samples are quite hygroscopic in nature at low x content.

An absorption peak was observed at 1630 cm^{-1}. The origin of this peak is not obvious, but the H-O-H bending mode gives rise to an absorption in this region [16] and the possibility of some adsorbed water giving rise to this peak cannot be ruled out.

A broad band at around 1450 cm^{-1} as observed in crystalline B_2O_3 is present in low composition V_2O_5 glasses, but its character changes in samples above 0.5 V_2O_5. As already reported in Na_2O-B_2O_3 glasses [17] the characteristic >B-O^- stretching band in the B_2O_3 glass network is assigned to a broad band from 1428 cm^{-1} to 1333 cm^{-1}. This band appears in our IR spectra, confirming the amorphous nature of studied glasses.

The low V_2O_5 content glasses show a very sharp absorption peak at 1195 cm^{-1}. This peak may be attributed to triangular B-O stretching vibrations [16]. This peak disappears when V_2O_5 content increases. The spectra corresponding to x >0.6 present a band at 1250 cm^{-1} and do not exhibit the 1195 cm^{-1} peak. The disappearance of the 1195 cm^{-1} peak and the progressively appearance of the band centered at 1250 cm^{-1} corresponds to a change from triangular to tetrahedral boron structure when the system goes to higher V_2O_5 content [16].

An absorption band at 1023 cm^{-1} was observed in all the samples, also at highest V_2O_5 content. This peak in attributed to V=O stretching vibrations [18].

The peak at 883 cm^{-1} which is observed for low V_2O_5 content disappear for x > 0.5. This disappear might be due to the rupture of boron ring structure when the V_2O_5 content increases [16]. A broad absorption peak between 740 cm^{-1} and 800 cm^{-1} in crystalline B_2O_3 and at 825 cm^{-1} in crystalline V_2O_5 is observed [16]. For higher compositions, this band disappears completely. The absence of this band indicates that either the structural units of V_2O_5 in V_2O_5-B_2O_3 glasses is not the same as that in crystallineV_2O_5 or the intensity of the peak becomes very weak and could not be detected.

Below 800 cm^{-1} there are several absorption peaks in crystalline B_2O_3 as well in V_2O_5 [16]. Therefore, we can not assume these bands to particular groups (borate or vanadate).

For low V_2O_5 content IR spectra reveal the presence of triangular and tetrahedral borate units. At high V_2O_5 content only IR bands corresponding to the tetrahedral borate units appear, in agreement with Raman conclusions. This indicates a modification of the structure of studied glasses, determined by the changes of the vanadium oxide content. Both Raman and IR analyses show the presence of vanadate groups at high concentration of vanadium oxide. Thus at high V_2O_5 content vanadium oxide starts to act as a glass former.

4. Conclusions

The vanadium oxide acts in the investigated x V_2O_5(1-x)B_2O_3 glass system as a modifier and only at very high content as a glass former. A very small V_2O_5 content determines the break of the regular structure of boroxol groups in B_2O_3 glass and the formation of diborate groups, chain type metaborate groups and isolated BO_4 units. The appearance of diborate groups and isolated BO_4 units is an indication for the four-fold coordinated boron atoms presence in the glasses studied. At very high content vanadium oxide acts as glass former.

The IR spectra of studied glasses have been qualitatively interpreted in the range of 4000 cm^{-1} to 500 cm^{-1}. The main characteristic is the disappearance of some bands when V_2O_5 content increases. For low vanadium oxide content, specifically borate units with triangular and tetrahedral configuration are present, while for high V_2O_5 content are present only borate units with tetrahedral configuration. In the same time, the feature of IR spectra reveal bands characteristic to vanadate structure.

Therefore, we conclude that vanadium oxide acts as network modifier in these glasses for $0.05 \leq x \leq 0.5$. For higher concentration, vanadium oxide starts to act as glass former. In the structure of $x\ V_2O_5(1\text{-}x)B_2O_3$ glasses boroxol rings (at low V_2O_5 content) chain type metaborate groups, diborate groups and isolated BO_4 units are present. For high V_2O_5 content vanadate groups appear, both borate and vanadate glass network been present in the glasses structure.

REFERENCES

[1] M. Sayer and A. Mansingh, Phys. Rev. B6 (1972) 4629.

[2] I. G. Austin and E. S. Garbett, Electronic and Structural Properties of Amorfous Semiconductors (Academic Press New York, 1973) p.393.

[3] L. Murawski, C. H. Chung and J. D. Mackenzie, J. Non-Cryst. Solids 32 (1979) 208.

[4] A. K. Bandyopadhyay, J. O. Isard and S. Parke, J. Phys.D: Appl.Phys.11 (1978) 2559.

[5] A. K. Bandyopadhyay J. Mat. Sci. 16 (1981)189.

[6] V. K. Dhawan, A. Man Singh and M. Sayer, J. Non-Chryst. Solids 51 (1982) 87.

[7] G. W. Anderson and W. D. Compton, J Chem Phys. 52 (1970) 6166.

[8] B. P. Dwivedi, M. H. Rahman, Y. Kumar and B. N. Knanna, J. Phys.Chem. Solids 54 (1993) 621.

[9] B. N. Meera, A. K. Sood, N. Chandrabhas and J. Ramakrishna, J. Non-Cryst. Solids 126 (1990) 224.

[10] A. M. Zahra and C. Y. Zahra, J. Non-Cryst. Solids 155 (1993) 45.

[11] S. Gunasekaran and K. Srinivasan, Asian Chem. Lett. 3 (1999) 227.

[12] E. I. Kamitsos, M. A. Karakassides and G. D. Chryssikos, Phys Chem Glasses, 30 (1989) 229.

[13] T. W. Brill, Philips Res. Rep. Suppl. 1 (1976) 117.

[14] W. L. Konijnedijk and J. M. Stevels, Mater. Sci. Res. 12 (1977) 259.

[15] N. F. Borrelli, B. D. McSwainand Gouq-Jen Su, phys. Chem. Glasses 4 (1963) 11.

[16] B. K. Sharma and D. C. Dube, J. Non-Cryst. Solids 65 (1984) 39.

[17] J. T. Quan and C. E. Adams, J. Phys. Chem. 70 (1966) 331.

[18] G. W. Anderson and W. D. Compton, J. Chem. Phys. 52 (1970) 6166.

STUDIA UNIVERSITATIS BABEŞ-BOLYAI, PHYSICA, SPECIAL ISSUE, 2001

Cu(II) AND Ni(II) COMPLEXES WITH 2-HYDRAZINO-4-R THIAZOLE DERIVATIVES

LUMINIȚA OPREAN*, ADRIANA COMȘA*, L.DAVID, O. CRIȘAN* MIOARA COMAN*, MARIA NEAMȚU***

**Dept. of Pharmacy, "Iuliu Haţieganu" University of Medicine & Pharmacy, 3400 Cluj-Napoca, Romania*
***Dept. of Physics, "Babeş-Bolyai" University, 3400 Cluj-Napoca, Romania*

ABSTRACT. Four new complexes of Cu(II) and Ni(II) with the ligands L_1 (2-N-acetyl-salicyliden-hydrazino-4-clormethyl thiazole) and L_2 (2-N-acetyl-salicyliden-hydrazino-4-thiazolyl acetic ester) were synthetized and investigated by IR, ESR and UV-VIS spectroscopy and by magnetic susceptibility measurements. A correlation of these data suggest that the complexes are of the type $[ML_1(CH_3COO)]H_2O$ and $[ML_2(CH_3COO)]$. L_1 and L_2 act as tridentate ligands and the complexes have a distorted tetrahedral (D_2d) local symmetry around the Cu(II) and Ni(II) ions.

1. Introduction

The recent studies on compounds containing the thiazole moiety has raised special interest due to their importance in different life-fields. The pharmacological activity and the chelating properties of thiazole derivatives were the premises for obtaining metallic complexes with therapeutic activity or serving as study models for metallo-enzymes [1-4].

In the present work, we report the synthesis and the physico-chemical study of 4 new complexes with possible antibacterial, antifungal or anti-inflammatory activity. The new complexes are $[ML_1(CH_3COO)]H_2O$ and $[ML_2(CH_3COO)]$,where M = Cu(II), Ni(II), L_1 = 2-N-acetyl-salicyliden-hydrazino-4-clormethyl thiazole, L_2 = 2-N-acetyl-salicyliden-hydrazino-4-thiazolyl acetic ester.

2. Experimental

2.1. Materials and measurements

The ligands were prepared as described in the literature [5]. Metal acetate and solvents were chemical reagent grade or analytical grade.

The elemental chemical analysis of the complexes was performed by the classical method. The Cu(II) and Ni(II) ions were determined gravimetrically as $Cu(py)_2(SCN)_2$ and $Ni(dmg)_2$, where py = pyridine and dmg = dimethylglioxime.

The IR spectra were recorded with a FTIR Nicolet 205 and a Specord IR 20 spectrophotometers in the 4000 – 400 cm^{-1} range, in KBr pellets.

The electronic spectra in the UV-Vis (190-900 nm) region were performed with a Spectronic Genesys 5 spectrophotometer using 10^{-5} M (UV) and 10^{-3} M (visible) DMSO solutions.

The powder ESR spectra of (1) and (2) complexes were obtained at room temperature in the X band (9.4 GHz) using a standard JEOL-JES-3B equipment.

Magnetic susceptibility measurements of all complexes were recorded using a horizontal Weiss balance. The values of magnetic moments were determined from the plot of $1/\chi_M$ versus T values.

2.2. Preparation of complexes

Synthesis of the $C_{15}H_{16}N_3OSClCu$ complex : $[CuL_1(CH_3COO)]\cdot H_2O$ (1)

50 ml ethanolic (EtOH) solution of $Cu(CH_3COO)_2\cdot H_2O$ (0.200 g, 1 mmol) was added to the solution of 0.309 g of the ligand L_1 (1 mmol) in 10 ml benzene with continuous stirring at 60 °C. After 30 minutes, a dark greenish precipitate was formed. The solid was isolated by filtration, washed with ethanol and dried until constant weight (0.216 g complex, η = 48 %) (Found: C 39.27%; H 3.00%; N 9.87%; S 7.21; Cl 7.44%; Cu 15.13%; $C_{15}H_{16}N_3O_5SClCu$ requires: C 40.07%; H 3.56%; N 9.34%; S 7.12%; Cl 7.09%; Cu 14.13%)

Synthesis of the $C_{18}H_{19}N_3O_6SCu$ complex: $[CuL_2(CH_3COO)]$ (2)

8 ml water solution of $Cu(CH_3COO)_2\cdot H_2O$ (0.200 g, 1 mmol) was added to the solution of 0.348 g of L_2 (1 mmol) in 50 ml acetonate with continuous stirring at room temperature. After about 10 minutes, a greenish precipitate was formed. After stirring for an hour, the solid was isolated by filtration, washed with acetone and ethylic ether and dried until constant weight (0.201 g complex, η = 43 %) (Found: C 45.13%; H 3.82%; N 9.58%; S 7.87; Cu 14.08%; $C_{18}H_{19}N_3O_6SCu$ requires: C 46.10%; H 4.05%; N 8.96%; S 6.83%; Cu 15.55%)

Synthesis of the $C_{15}H_{16}N_3O_5SClNi$ complex, $[NiL_1CH_3COO]\cdot H_2O$ (3)

5 ml ethanolic (EtOH) solution of $Ni(CH_3COO)_2\cdot 4H_2O$ (0.250 g, 1 mmol) was added to the solution of 0.310 g of the ligand L_1 (1 mmol) in 10 ml benzen with continuous stirring at room temperature. After an hour, a yellow-brown precipitate was formed. The solid was isolated by filtration after two hours, washed with benzene, ethanol and ether and dried until constant weight (0.140 g complex, η = 42.8 %) **(**Found: C 40.95%; H 4.24%; N 10.07%; S 6.78; Cl 8.12%; Ni 13.79%; $C_{15}H_{16}N_3O_5SClNi$ requires: C 40.05%; H 3.60%; N 9.45%; S 7.21%; Cl 7.98%; Ni 13.20%).

Synthesis of the $C_{18}H_{19}N_3O_6SNi$ complex, $[NiL_2CH_3COO]$ (4)

5 ml ethanolic (EtOH) solution of $Ni(CH_3COO)_2\cdot 4H_2O$ (0.248 g) was added to the solution of 0.309 g of the ligand L_2 (1 mmol) in 10 ml benzene with continuous stirring at room temperature. After an hour, an orange precipitate was formed. The solid was isolated by filtration after two hours, washed with ethanol, benzene and ether and dried until constant weight (0.265 g complex, η = 57.2 %). **(**Found: C 46.81%; H 4.65%; N 9.83%; S 6.64; Ni 13.10%; $C_{18}H_{19}N_3O_6SNi$ requires: C 46.54%; H 4.09%; N 9.04%; S 6.89%; Ni 12.64%).

3. Results and Discussion

3.1. IR Spectra

Information about the coordination mode of the Cu(II) and Ni(II) ions to the ligands was obtained by comparing the IR spectra of the metallic complexes with the IR spectra of the corresponding free ligands L_1 and L_2 (Table 1) and those of the other metal complexes [6-9]. The involvement of the OH phenolic group in deprotonated

form, in coordination to the metallic ions is indicated by the shift of the ν(OH) and ν(CO) phenolic bands in the IR spectra of complexes compared to the corresponding ligands.

The exocyclic –HC=N is another group from the ligands which is coordinated to the metallic ions. This is sustained by the shift of the ν(CN) exocyclic and ν(NN) hydrazonic groups vibrations.

The thiazolic ring coordinates the metallic center through its nitrogen atom, which arises in the lowering of the ν(CN) thiazole frequency and the increasing of the ν(NN) hydrazonic frequency.

The free acetate ion has characteristic bands at 1580 cm^{-1} (ν_{as}) and 1425 cm^{-1} (ν_s). The coordination of the acetate to the metallic ion is indicated by the complexes new IR bands.

Table 1

Some IR bands (cm^{-1}) of the ligands and Cu(II) and Ni(II) complexes

Band	**L_1**	**1**	**3**	**L_2**	**2**	**4**
ν(OH) phenolic	3450 m	3430 w	3420 b	3440 m	3430 w	3430 b
ν(CN) exocyclic	1650 m	1600 s	1600 s	1620 s	1600 s	1610 s
ν(CN) thiazol	1610 m	1570 w	1580 w	1600 m	1570 w	1590 s
ν(ring) thiazol	1570 w	1560 w	1540 m	1560 w	1550 w	1550 m
ν(acetate)	-	1430 m 1490 m	1430 m 1490 m	-	1430 m 1500 s	1445 m 1495 m
ν(CO) phenolic	1295 s	1340 w	1330 w	1300 s	1335 s	1310 s
ν(NN) hydrazonic	1010 m	1030 w	1030 m	1020 m	1035 m	1035 m

w – weak, m – medium, s – strong, b – broad

3.2. Electronic spectra

Information about geometry of complexes around the Cu(II) and Ni(II) ions was obtained from electronic spectra. The assignment of the bands of the electronic spectra of (**1**) – (**4**) complexes are set out in table 2.

Table 2

Electronic spectral data for (1) – (4) complexes in DMSO solutions

Complex	**M.C.(mol/l)**		**ν_{max} [cm^{-1}] (ε_{max} [$l \cdot mol^{-1} \cdot cm^{-1}$])**		
	UV	**Vis**	**Intraligand transitions**	**Charge transfer**	**d-d transitions**
1	$2.86 \cdot 10^{-5}$	$5.26 \cdot 10^{-3}$	47619 (6713) 37593 (14755)	24390 (12132)	17857 (141)
2	$4.3 \cdot 10^{-5}$	$5 \cdot 10^{-3}$	38028 (15744)	23529 (14348)	19083 (145)
3	$3 \cdot 10^{-5}$	$4.5 \cdot 10^{-3}$	38461 (13566) 31545 (9166)	24570 (8466)	18416 (136)
4	$6.3 \cdot 10^{-5}$	$3 \cdot 10^{-3}$	38461 (5063) 34843 (3968) 33222 (3687)	25974 (4777)	17064 (157)

This data suggest that (**1**) – (**4**) complexes have a distorted tetrahedral geometry around the central metal ion [6, 9-11].

3.3. ESR Spectra and magnetic susceptibility measurements

Powder ESR spectrum of the complex (**1**), obtained in the X band at room temperature, contains a broad signal at g = 2.103. The complex (**2**) has an axial powder spectrum, with the g_{II}= 2.281 and $g_{\perp}$ = 2.075 parameters. The obtained spectra (Fig. 1) are in agreement with a distorted tetrahedral symmetry and a CuN_2O_2 chromophore [12, 13]. The distortion is higher for the complex (**2**), as arises from the axial character of the spectrum. For obtaining information about the possible interactions between the copper (II) ions, the two complexes were studies by means of magnetic measurements. The magnetic susceptibility data have been corrected by the diamagnetic contribution using the Pascal constants.

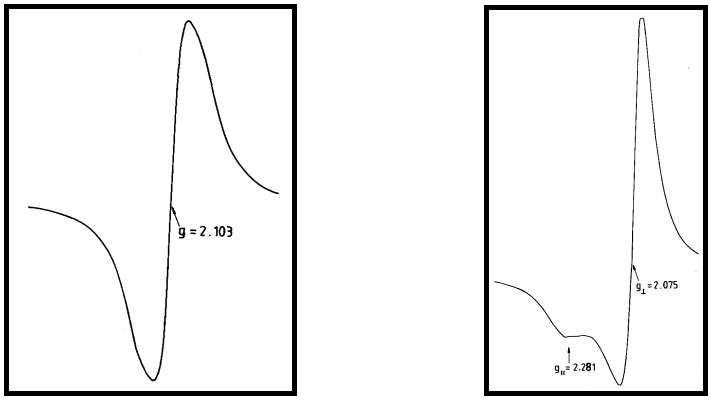

Fig.1 *ESR spectra of the complexes **1** and **2***

The magnetic moments μ_{eff} = 1.74 BM for (**1**) and μ_{eff} = 1.94 BM for (**2**) indicate the presence of monomeric species and the lake of any interaction between the Cu(II) ions from neighboring molecules (Fig.2) [8, 13-15].

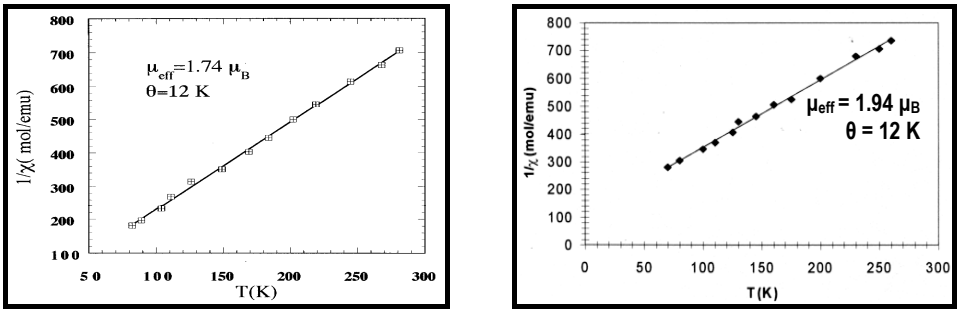

Fig.2 *Temperature dependence of the inverse of the magnetic susceptibility for the complexes **1** and **2***

The magnetic moment obtained for the complexes **3** and **4** indicate a distorted tetrahedral symmetry around the Ni(II) ions: μ_{eff} = 4.36 BM for (**3**) and μ_{eff} = 3.71 BM for (**4**) (Fig.3) [3,13].

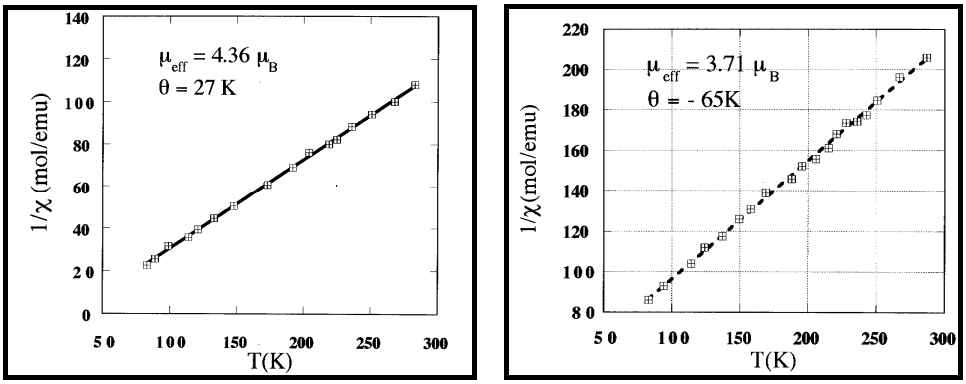

Fig.3 *Temperature dependence of the inverse of the magnetic susceptibility for the complexes **3** and **4***

4. CONCLUSION

A correlation of the results obtained from chemical analysis and spectral data afford the assignment of the most probable structural formulae. L_1 and L_2 act as tridentate ligands and the complexes have a distorted tetrahedral geometry. The proposed structures of the complexes is presented in Fig. 4.

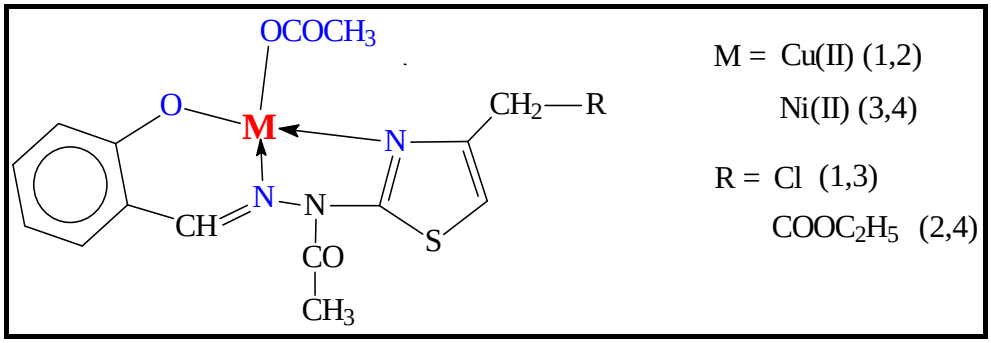

Fig.4 *Proposed structures of the complexes **(1) – (4)***

REFERENCES

1. J.V. Metzger, "*Thiazoles and Its Derivatives*", John Wiley & Sons Inc., New York, **1979**.
2. R.K. Gouch, T.W Kensler, L.V. Oberley, J.R.J. Sorenson, "*Biochemical and Inorganic Copper Chemistry*" (K.D. Karlin, J. Zubieta Eds.), Adenine Press, New York, **1986**.
3. L. Sacconi , F. Mani, A. Bencini, "*Nickel*" in "*Comprehensive Coordination Chemistry*" (G. Wilkinson, R. Gillard, J. McCleverty Eds.), Pergamon Press, Oxford, **1987**.

4. I. Puşcaş (Ed.), " *Anhidraza carbonică şi modelarea proceselor fiziologice şi patologice în organism. Activatorii şi inhibitorii enzimei.*", Ed. Helicon, Timişoara, **1994**
5. M. Coman, "*Studiul unor derivaţi de 2-hidrazino, 4 şi 5 substituiţi ai tiazolului*", Teza de doctorat, UBB, **1972**
6. A.M. Hammam, S.A. Ibrahim, M.H. Abo Elwafa, M.A. El-Gahami, W. Thabet, *Synth.React.Inorg.Met.-Org.Chem.*, **22**, 1401 (1992)
7. A. Bernalte-Garcia, F.J. Garcia-Barros, F.J. Higes-Rolando, A.M. Pizarro-Galan, C. Valenzuela-Calahorro, *Polyhedron*, **16**, 1137 (1997).
8. S. Jayasree, K.K. Aravindakshan, *Polyhedron*, **12**, 1187 (1993).
9. D.B. Wang, B.H. Chen, B. Zhang, Z.X. Ma, *Polyhedron*, **16**, 2625 (1997).
10. B.J. Hathaway, in "*Comprehensive Coordination Chemistry*", G. Wilkinson, R. Gillard, J. McCleverty Eds., Pergamon Press, Oxford, **1987**.
11. A.B.P. Lever, in "*Inorganic Electronic Spectroscopy*", Elsevier, New York, **1984**
12. T.K.R. Justin, P. Thrmaraj, V. Chandrasekhar, C.D. Brzan, A.W. Cordes, *Inorg. Chem.*, **33**, 821 (1994).
13. H. Yokoi, A.W. Addison, *Inorg. Chem.*, **6**, 16 (1977).
14. K.C. Satpathy, A.K. Panda, R. Mishra, A. Mahapatra, A. Patel, *Synth.React.Inorg.Met.-Org.Chem.*, **22**, 201 (1992).
15. K.K. Narang, J.P. Pandey, V.P. Singh, *Polyhedron*, **13**, 529 (1994).

STUDIA UNIVERSITATIS BABEŞ-BOLYAI, PHYSICA, SPECIAL ISSUE, 2001

THE DETERMINATION OF THE THERAPEUTIC COMPOUNDS FROM *Aristolochia Clematitis* BY GC/MS

R. PODEA, M. CULEA, L. FROMONDI

S.C. Natex s.r.l. Sos. Cluj-Oradea km8 , P.O. Box 374 3400 Cluj-Napoca

SUMMARY. Some extracts of the medicinal plant ***Aristolochia Clematitis*** from Romania have been investigated by GC-FID and GC/MS to identify compounds responsible for its therapeutical properties. Three kinds of extracts were investigated.

The **tincture** was prepared by mixing all parts of the plant (roots, steams, leaves) with an 50% alcoholic solution for 30 days. The **infusion** was also prepared by mixing all parts of the plant with hot water for 20 min. These two extraction methods were compared for extraction of the active therapeutic compounds of ***Aristolochia Clematitis***.

In parallel, another study was performed to identify the distribution and the concentration of the active compounds in the roots, steams and leaves of this plant. For this purpose we have prepared three alcoholic (96 % alcoholic solution) extracts from each part of the plant and we have studied them separately.

Introduction

Aristolochia Clematitis, a very toxic herb, member of the ***Aristolochiaceae*** family, popularly named Marul Lupului, is a rare medicinal plant which has a very long history of medicinal use, though it is little used by present-day herbalists. It is an aromatic tonic herb that stimulates the uterus, reduces inflammation, controls bacterial infections and promotes healing. The flowering herb, with or without the root, is abortifacient, antiinflammatory, antispasmodic, diaphoretic, emmenagogue, febrifuge, oxytonic and stimulant. The plant contains a complex of acids so called “aristolochic acids” which stimulate white blood cell activity and speeds the healing of wounds if it is used in correct concentration. Aristolochic acid is active in a concentration of 1:100000. Externally it is used in the treatment of slow-healing cuts, eczema, infected toe and finger nails etc., but internal consumption can cause damage to the kidneys and uterine bleeding.

The objective of this work is to identify and characterise the compounds of therapeutic value extracted from ***Aristolochia Clematitis***. The analytical methods chosen are gas-chromatography (GC-FID) and gas-chromatography/mass spectrometry (GC/MS). The methods were applied to characterise the infusion and tincture prepared from this plant and to make a comparison between the alcoholic extracts of the roots, stems and leaves.

Experimental

Aristolochia Clematitis plants were harvested in July 2001.

Extraction procedure

For the preparation of tincture and infusion we have used air dried, crushed and mixed plants, and for the alcoholic extract (96% alcoholic solution) fresh roots, steams and leaves. The tincture was prepared by mixing all parts of the plant (roots, steams, leaves) with an 50% alcoholic solution for 30 days. The infusion was also prepared by mixing all parts of the plant with hot water for 20 min, and the alcoholic extracts by mixing the fresh parts of the plant with a 96% alcoholic solution for 12 days.

Sample preparation for GC-FID and GC/MS

3 ml of tincture were mixed for 5 min with 3 ml distilled water, pH 3, 0.5g NaCl and 1 ml solvent A (ethyl acetate:hexane:methylen chloride 5/1/1, v/v/v). Then the organic phase was collected and 4 µl were injected in GC/MS.

6 ml of infusion, pH 3 and 0.5g NaCl were mixed for 5 min with 1 ml solvent A and 4 µl of the organic phase were injected in GC/MS.

3 ml of 96 % alcoholic extracts were mixed for 5 min with 3 ml distilled water, pH 3, 0.5g NaCl and 1 ml solvent A. Then the organic phase was collected and 4 µl were injected in GC-FID.

GC-FID Analysis

GC-FID analysis was performed with a Hewlett Packard GC system 6890 with FID. Compounds were separated on a 30m x 0.25mm HP-5 fused-silica capillary column coated with 0.25µm film.

The column was maintained at 50°C for 2 min, then it was programmed at 8°C/min to 250°C, then 30°C/min to 310°C which was maintained for 10 min. Helium was used as carrier gas with a flow rate of 1ml/min and split ratios 1:20. The injector and detector temperatures were 250°C.

GC-MS Analysis

GC-MS analysis was performed with a Hewlett Packard GC 5890 coupled with a MS engine 5989B in the EI mode. Compounds were separated on a 30m x 0.25mm HP-5MS fused-silica capillary column coated with 0.25µm film. The column was maintained at 50°C for 2 min after injection, then programmed at 8°C/min to 250°C, then 30°C/min to 310°C which was maintained for 10 min. Split ratio was 1:5 and helium flow rate 1ml/min. Injector, interface, ion source and quadrupol analyser temperatures were 250°C, 280°C, 200°C, 100°C, respectively. The mass spectrometer was operated in electron-impact (EI) mode; electron energy was 70 eV and electron emission 300 µA. Compounds were identified using the Wiley, NBS and NIST library spectra.

Results and discussion

Use of GC/MS (Fig.1), enabled identification of the most components in both samples tincture and infusion. The compounds identified are listed in **Table 1**. Some contaminants in as dibutylphtalate, tR 28.3min were neglected.

The predominant components of the tincture are terpenic compounds, fatty acids esters and aristolochic acid derivatives. We have studied the mass spectra of compounds no. 33 (M=294), 34 (M=293) and 35 (M=355) mass spectra and we have concluded that these are some aristolochic acid derivatives (Fig.2,a,b,c). The derivatives of the aristolochic acid seem to be present in root and stems of this plant. The derivatives have the same fragment ions as aristolochic acid (Fig. 2,d) as: M-15, M-31, M-43 in the case of the first two, or M-46 in the case of the last derivative. m/z 294 seems to be the molecular ion of a derivative of aristolochic acid by loosing 0=N-OH radical. The second derivative has m/z 293, as molecular ion containing odd number of nitrogen in the molecule. The third derivative has m/z 355 as molecular ion which represent m/z 341 (molecular ion of aristolochic acid) + 14.

a)

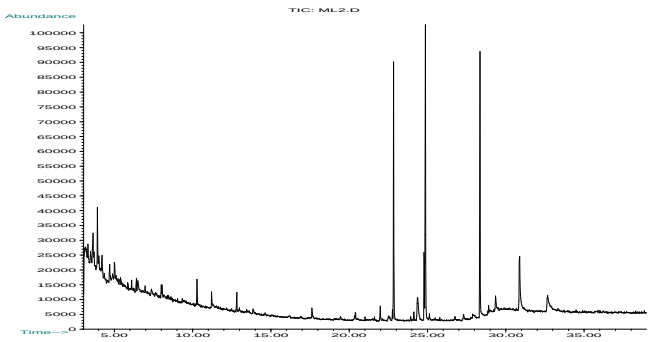

b)

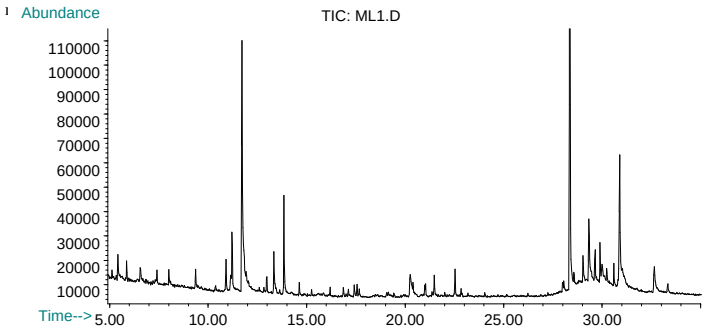

Fig. 1. The ion chromatograms obtained by GC/MS analysis for tincture(a) and infusion (b)

Table 1

Composition of the tincture and infusion

No.	Compounds	tR	Tincture %MS	Infusion %MS
1	alpha-pinene	6.1	0.89	0.00
2	camphene	6.4	1.60	0.00
3	beta-myrcene	6.96	0.44	0.00
4	limonen	8	1.13	3.03
5	eucalyptol	8.04	1.44	0.00
6	camphor	10.3	3.43	0.00
7	terpinen-4-ol	10.9	0.00	7.62
8	4-vinyl phenol	11.7	0.00	97.58
9	bornyl acetate	12.8	2.04	0.00
10	4-vinyl-2-metoxyphenol	13.3	0.00	13.02
11	dihydroactinidiolide	16.9	0.00	2.22
12	caryophyllene oxide	17.6	2.11	0.00
13	loliolide	20.3	0.00	16.85
14	benzyl salicylate	21.5	0.00	4.84
15	1-octadecanol	22.8	2.11	0.00
16	ethyl hexadecanoate	22.8	24.40	0.00
17	phytol	24.4	7.84	0.00
18	ethyl linoleate	24.8	8.48	0.00
19	octadecatrienoic acid, ethyl ester	24.9	31.87	0.00
20	M=297	29.3	3.18	26.14
21	M=294	30.9	13.97	57.77
22	M=293	32.7	8.16	12.97
23	M=355	33.3	0.00	3.13

t_R=the retention time

a)

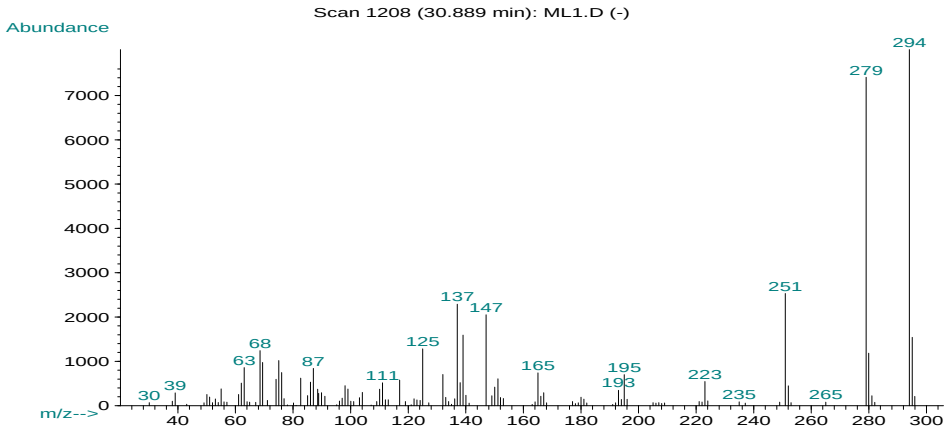

b)

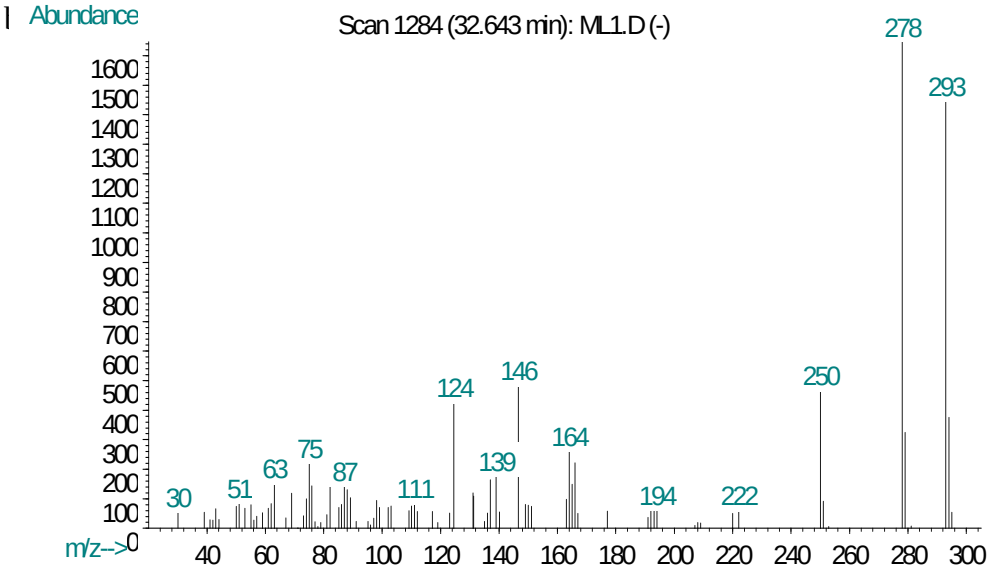
Abundance
Scan 1284 (32.643 min): ML1.D (-)
278
293
250
146
124
164
139
75
63
87
51
30
111
194
222
m/z-->
40 60 80 100 120 140 160 180 200 220 240 260 280 300

c)

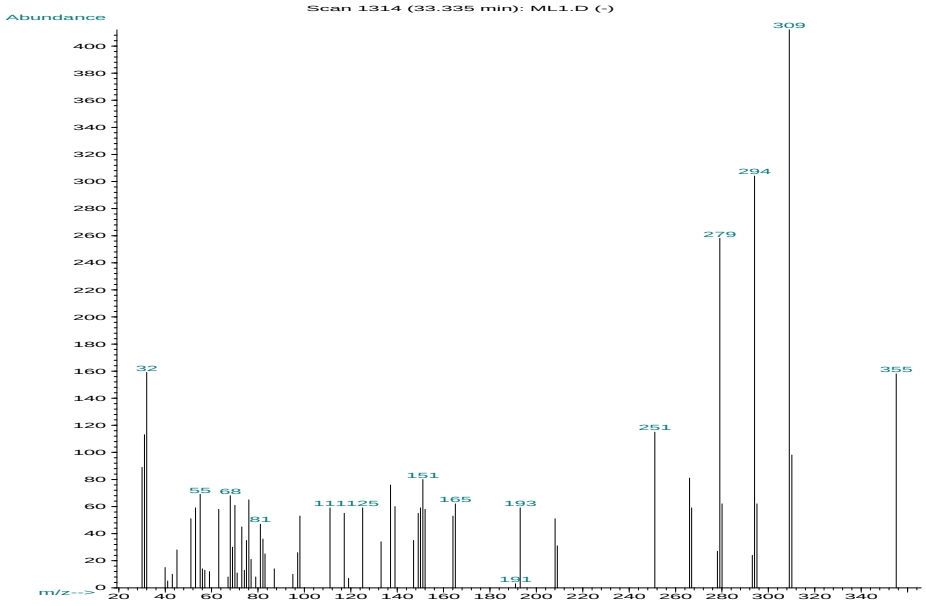
Scan 1314 (33.335 min): ML1.D (-)
Abundance
309
294
279
355
251
32
151
165
193
55
68
81
111
125
191
m/z-->
20 40 60 80 100 120 140 160 180 200 220 240 260 280 300 320 340

d)

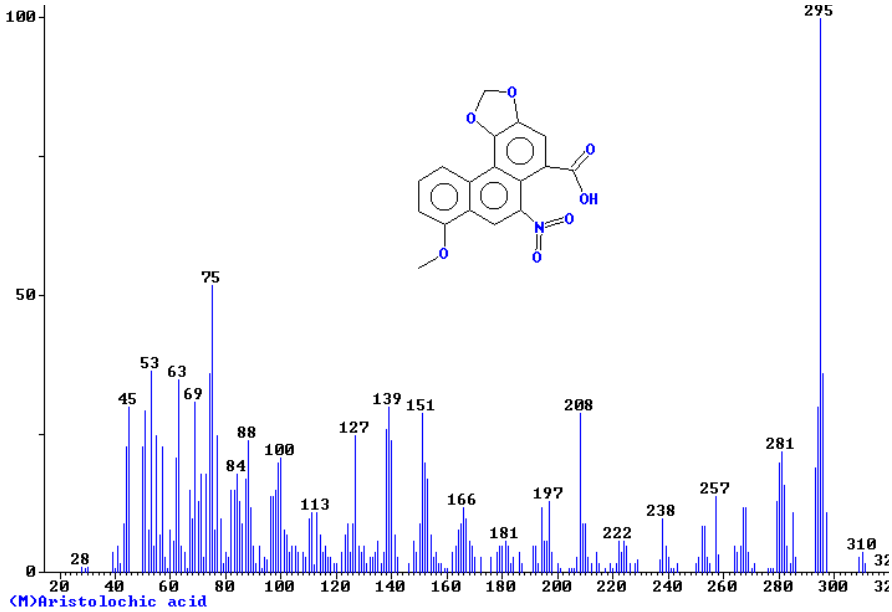

Fig. 2

The components of the infusion differ from those found in tincture except aristolochic acid derivatives. The concentrations (in %MS) of these derivatives in infusion and tincture are very closed, maybe that is why in traditional medicine are used both types of extracts with success.

The differences between the compounds that we have found in the roots, steams and leaves of Aristolochia Clematitis were studied by GC-FID. This study was performed on the alcoholic extracts of the three parts of the plant. From this study we have concluded that the compounds found in the root and steam are very similar. The aristolochic acid derivatives are present in both extracts, but in the leaves these derivatives are in very low concentration.

Conclusion

The analytical methods used, GC/MS and GC-FID are suitable for medicinal herb organic compounds determination. The sample preparation method is rapid and precise.

There is a difference between the compounds extracted from herb by infusion and tincture but the important thing is that the aristolochic acid derivatives are present in both of them. On the other side the study shows that their concentration is higher in the roots and steams. In the leave extracts aristolochic acid derivatives and vitamin F (polyunsaturated fatty acids) are very low or are absent. In conclusion terpenic

compounds, fatty acids, coumarins, alkaloids and especially aristolochic acid derivatives are responsible for the therapeutic activity of this plant.

REFERENCES

1. G. Host, A. Wahllander, U. von Mandach, R. Preisig,, Hepatology, 7:338-344,1987.
2. N. R. Scott, D. Stambuk, J. Chakraborty, V. Marks, M. Y. Morgan, Clin. Sci., 74:377-384, 1988.
3. A. Hostage, M. Staiger, K. Haag, W. Gerok,, Klin Wochenschr 67:6-15, 1989.
4. W. F. Balistreri, H. H. A-Kader, K.D.R. Setchell, D. Gremse, F.C. Ryckman, T. J. Schroeder, Annals of Clin, Lab. Sci., 22:162-174, 1992.

STUDIA UNIVERSITATIS BABEŞ-BOLYAI, PHYSICA, SPECIAL ISSUE, 2001

GAS-CHROMATOGRAPHY -MASS SPECTROMETRIC METHOD FOR LIVER FUNCTION TEST IN CHILDREN

MONICA CULEA*, M. NANULESCU, MIRELA POPA**, R. MIHALCA*****

**NATEX s.r.l., 3400 Cluj-Napoca,P.O.Box 374 România,*
E-mail:monica.culea@phys.utcluj.ro
***Pediatric Clinic III, Cluj-Napoca*
****University of Baia Mare*

ABSTRACT. A gas chromatography-mass spectrometric (GC/MS) method for caffeine levels determination in blood to children suffering of different forms of liver diseases is described. Caffeine clearance is a novel approach for assessing hepatic microsomal function. 10 µg/ml ^{15}N-theophylline has been used as internal standard. A Hewlett Packard GC/MS engine 5989B in the SIM mode was used equipped with a HP-5 capillary column 30mx 0.25mm diameter, 0,25µm film support, in the temperature program: 200-250^{o}C with a rate of 10^{o}C/min. The method was validated in the range 0-20µg/ml caffeine. A dose of 4mg/kg p.o. was used. Blood caffeine concentrations were measured before dose and timed intervals at 0, 30 min, 1, 3, 6, 9 and 12 h. Caffeine clearance, measured in patients with cirrhosis and chronic hepatitis, was reduced and half live time was increased in children with liver disease as compared with control. The decreased metabolism observed in patients with various forms of liver disease was correlated to the disease status.

1. INTRODUCTION

Liver function in humans has traditionally relied on static indices of hepatic structure, cellular integrity or function and is based on the release of substances from damaged tissues. The development of dynamic tests based on the measurement of substances metabolized or cleared from blood by the liver offers a more precise quantitative estimation of hepatic functional capacity. Recently, caffeine, which is a trimethylxanthine, has been introduced as a model compound for measuring the metabolic capacity of the liver and has the advantage of being well tolerated when administrated orally. Fasting plasma or saliva caffeine concentrations have been suggested to be a simple guide to the severity of chronic liver disease /1,3/. Tests of screening for the presence of liver disease or a reflection of deteriorating hepatic function must be studied in a serial manner and confirmed by many laboratories/4/. Caffeine clearance, measured as disappearance of the parent compound from the blood stream or as appearance of the end product of demethylation in breath, was validated as a dynamic test for assessing hepatic microsomal function.

The aim of the present investigation was to validate a method for plasma caffeine level determination for characterization of some pharmacokinetic parameters as plasma clearance and half-life time in children.

2. EXPERIMENTAL:

^{15}N-theophylline, 74,2 atom % ^{15}N, labeled at the nitrogen in the position 7, synthesized in Institute of Isotopic and Molecular Technology Cluj-Napoca, was used as internal standard. Solvents were purchased from Comchim, Bucuresti, Romania. The analyses were performed with a quadrupolar mass spectrometer HP 5989B couplet with a gas chromatograph HP 5890 with the following parameters: electron energy: 70 eV, electron emission: 300µA and ion source temperature of 200^{o}C,

A HP-5MS fused silica capillary column, 30mx0.25mm, 0.25µm film-thickness, was programmed from 200^{o}C to 270^{o}C at 10^{o}C/min with helium flow rate 1ml/min. Retention times for caffeine and the internal standard were 2.8min and respectively 3.5 minutes. The molecular masses m/z 194 for caffeine and m/z 181 for ^{15}N-theophylline were selected in the SIM mode. Fig.1 presents the SIM ion chromatogram and the mass spectrum of caffeine.

2.1. *Extraction procedure*:

The extraction was performed from by mixing 1.5 minutes 1ml plasma, 2ml solvent: chloroform:isopropanol (20:1.v/v), 10µlg internal standard and 0.5g NaCl. After 3 minutes centrifugation, 3µl of supernatant was analyzed.

2.2. *Study population*

Concentration measurements were performed in 32 hospitalized children: 10 controls, 18 with chronic hepatitis and 4 children with cirrhosis. A dose of 4 mg/kg of caffeine intravenous was given. Blood samples were collected at different hours: 0, 0.5h, 1h, 3h, 6h, 9h, 12h. Written informed consents were obtained from each subject parent prior to this study.

2.3. *Calculation* of caffeine levels was made by using the regression curve obtained from the aliquot samples measured by GC/MS method. The pharmacokinetic parameters were calculated with the formulas:

$$K_{el}=(\ln C_1-\ln C_2)\square t; \qquad t_{1/2}=\ln 2/k_{el} \qquad Cl=k_{el}xV_d$$

where:k_{el} is the elimination constant; C_1 and C_2 are the maximum plasma concentration and minimum plasma concentration of caffeine, $t_{1/2}$ is the half-live time and V_d is the distribution volume of 0.6l/kg body weight.

RESULTS AND DISCUSSION

Method validation. In the gas chromatograph-mass spectrometric (GC/MS) assay, m/z 194 and 181 ions were measured in the selected ion monitoring (SIM) mode, for caffeine and the internal standard respectively. The regression curve obtained in GC/MS assay **:** y=0.52 x - 0.13 (DI-MS); n=5 r=0.95 in the range 0-20µg. Precision gave R.S.D values lower than 5% for 5µg/ml (n=7) and lower 12% for 3µg/ml(n=7). Accuracy shows values lower than 6%. Sensitivity measured at a signal/noise 4/1 was 0.5µg/ml. Each value was obtained as an average between two measurements of the same sample.

The ion chromatograms in SIM mode for caffeine (m/z 194) and the internal standard (m/z 181) are presented in Fig. 1. The molecular ion is the basic peak for the both components as shown in the mass spectrum for caffeine in Fig.1.

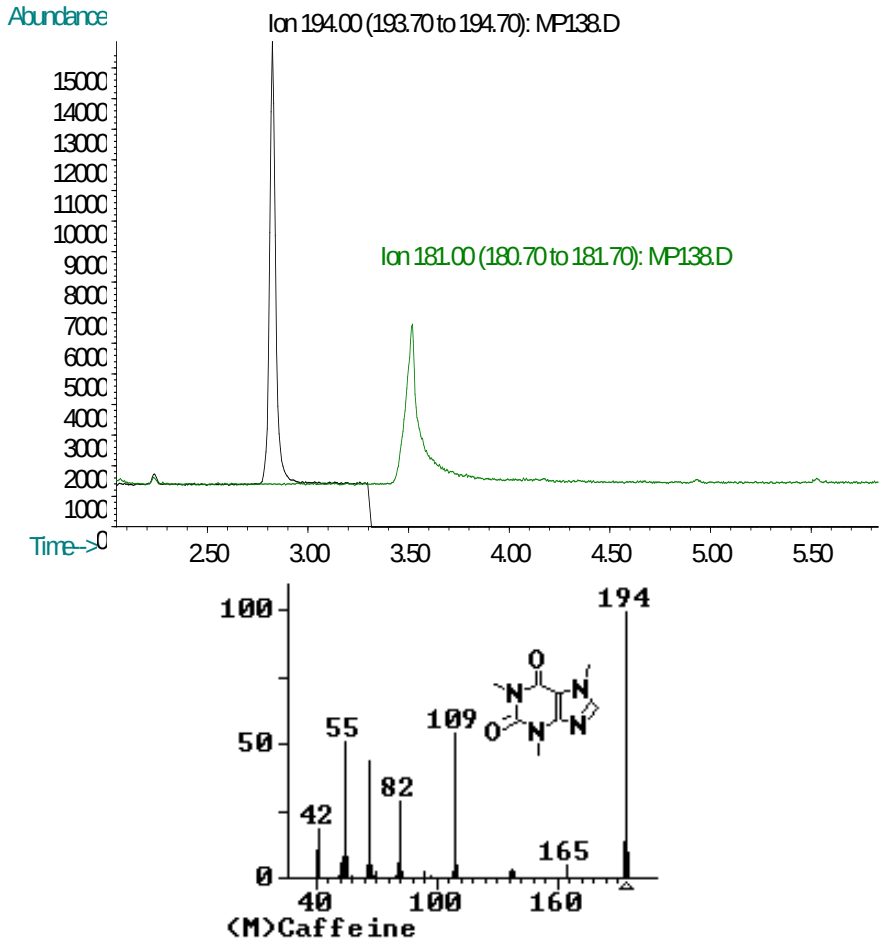

Fig.1 Caffeine determination by GC/MS SIM mode

The mean values of the two pharmacokinetic parameters studied, Cl and $t_{1/2}$, presented in Table I for patients with hepatic disease and control., show high differences especially between control and cirrhotics. Table II shows the pharmacokinetic parameter values for the patients with hepatic disease. Fig.2 presents the high plasma concentration values for caffeine in patients in comparison with the mean value of caffeine concentration obtained in control (n=10), as shown in Table III.

Table I

Mean values for half-live time and clearance for control and patients

	Cirrhosis (n=4)		Chronic hepatitis (n=22)		Control (n=10)	
	$t_{1/2}$(h)	Cl(ml min^{-1} kg^{-1}	$t_{1/2}$(h)	Cl(ml min^{-1} kg^{-1}	$t_{1/2}$(h)	Cl(ml min^{-1} kg^{-1}
mean	0.55	19.11	1.20	6.62	5.13	1.36
SD	0.41	14.90	0.46	2.44	0.85	0.23

Table II

Patients pharmacokinetic parameters

Subject[a]	Sex	Age (yr)	Body weight (kg)	Caffeine clearance (ml/min/kg)	Caffeine half-life (h)	
Normal values:	M			1.36±0.23	5.23±0.85	
P.F.	M	13		0.77	9	HEPATITIS
B.V.1	M	7	28	1.58	4.39	HEPATITIS
I.S.	M	10	24	1.8	3.84	HEPATITIS
B.V.2	M	11	30.5	0.78	8.87	HEPATITIS
S.V.	M	10	31.5	1.13	6.11	HEPATITIS
D.I.	M	8	22	0.97	7.18	HEPATITIS
P.O.	M	8	29	0.84	8.23	HEPATITIS
S.R.	M	9	39	1.31	5.28	HEPATITIS
R.M.	F	6	11	1.45	4.77	CIRRHOSIS
L.R.	M	5	16	0.19	35.74	CIRRHOSIS
M.A.m	M	7	32.6	0.99	6.98	CIRRHOSIS
S.M.	M	3	14	1.79	3.87	HEPATITIS
S.C.	M	8	22.5	1.65	4.21	HEPATITIS
I.F.	M	19		1.46	4.75	HEPATITIS
M.F.	M	11.5		0.47	14.62	CIRRHOSIS
B.A.	F			0.92	7.53	HEPATITIS
B.C.	M		38	0.95	7.31	HEPATITIS
C.M.I	M			0.88	7.88	HEPATITIS
C.M.II	M			0.60	11.55	HEPATITIS
G.A.	M	5	15.5	2.21	3.13	HEPATITIS
M.A.	F	15	47	1.25	5.54	HEPATITIS
T				0.66	10.51	HEPATITIS

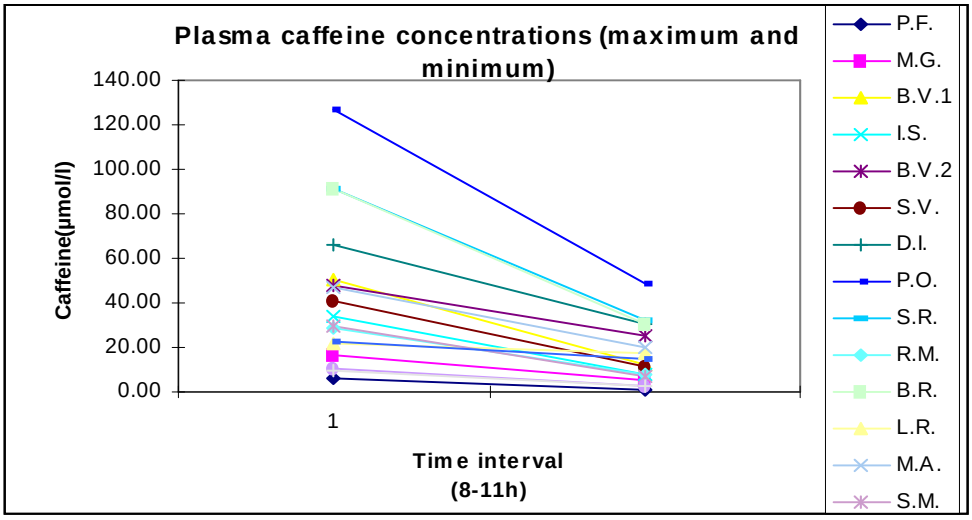

Fig.2 Plasma caffeine concentrations in patients

Table III

Caffeine plasma concentration mean values (maximum and minimum)

	C_1(1h)	C_2(9h)
CONTROL	16.84	5.28
CIRRHOSIS	29.96	15.12
HEPATITIS	37.41	13.43

3. CONCLUSIONS

The method presented is simple, precise and rapid, useful in the analysis of xantines. Isotopic labelled internal standard used avoids metabolites overlapping. Good linearity, precision, accuracy and sensitivity is obtained in the range 0-20µg/ml of drug.

Significant changes ($p<0.01$) were observed in caffeine metabolism in children with decompensated cirrhosis. The clearance values of 0.41±0.56ml min^{-1} kg^{-1} and half-life times of 14.34±14 are changed because of the reduction in "functioning hepatocyte mass". The control values for clearance and half-life time were 1.5±0.46 and $t_{1/2}$=5±1.8 in literature and our data of 1.36±0.23 and $t_{1/2}$=5.13±0.85 (n=10).

Patients with noncirrhotic liver disease showed intermediate values (Cl=1.2±0.46 and $t_{1/2}$=6.62±2.44) but higher values of caffeine plasma concentrations.

BIBLIOGRAPHY

1. G. Host, A. Wahllander, U. von Mandach, R. Preisig,, Hepatology, 7:338-344,1987.

2. N. R. Scott, D. Stambuk, J. Chakraborty, V. Marks, M. Y. Morgan, Clin. Sci., 74:377-384,1988.

3. A. Hostage, M. Staiger, K. Haag, W. Gerok,, Klin Wochenschr 67:6-15, 1989.

4. W. F. Balistreri, H. H. A-Kader, K.D.R. Setchell, D. Gremse, F.C. Ryckman, T. J. Schroeder, Annals of Clin, Lab. Sci., 22:162-174, 1992.

STUDIA UNIVERSITATIS BABEŞ-BOLYAI, PHYSICA, SPECIAL ISSUE, 2001

"MOLECULAR ORBITAL CALCULATIONS ON CONFIGURATIONAL ISOMERS OF DESFERRIOXAMINE B USING HYPERCHEM"

CORINA ANCA SIMION, EUGEN PREOTEASA

"Horia Hulubei" National Institute for Physics and Nuclear Engineering
409 Atomistilor St. Bucharest Romania

Desferrioxamine B is a hydroxamate iron (III) complex of N'-[5-[[4-[[5-(acetylhydroxyamino)pentyl]amino]-1,4-dioxobutyl]hydroxyamino]pentyl]-N-(5-aminopentyl)-N-hydroxybutanediamide. It shows promoting and antibiotic properties. Its stability is probably explained by the favorable distribution of hydroxamate radicals in the iron-free compound.

Five possible configurations for the Fe complex are presented.

The MO calculations using Hyperchem 5.02 program give us some relative information about stability, energies, and geometrical parameters for these configurations.

In this order, we focus our attention on central metallic ion as well as on the most stable configuration.

The calculation was developed on *"in vacuo"* conditions using both molecular mechanics (MM^+) and semi - empirical (ZINDO/1) as methods, with some restraints applied on central ion in the first stage of calculations. The final criterion of RMS gradient was 0.1 kcal/mol·Å and the optimization algorithm was the mathematical Polak-Ribière method.

In the UHF Calculation we used the sextet state calculation (five is the number of unpaired electrons). The number of electrons is 231 (118 Alpha Electrons, and respectively 113 Beta Electrons). The charge on the system is zero with a number of total orbitals of 210.

In the last step, the zero point energy of vibrations and normal mode frequencies of vibration in the ir spectrum were calculated.

Ferrioxamines A to F have been separated from cultures of *Streptomyces pilosus* soil type by chromatography in the early 60's. Ferrioxamine B is the N-[5-[3-[(5-amino pentyl) hydroxycarbamoyl] propionamido] pentyl]-3-[[5-(N-hydroxyacetamido) pentyl] carbamoyl] propionohidroxamic acid and its physical and chemical properties were studied in the last decades together with its ability to form chelates with a number of transitional metals, especially with iron (III). These complexes already have many applications in biology and medical fields [1, 2, 3, 4, 5].

The mechanism formation of Ferrioxamine B gives four possible isomers (**I, II, III, IV**) of the same compound and literature data indicate that the fourth undergoes a reaction with iron (III) ions to form five possible configurations of Desferrioxamine B complex [6]:

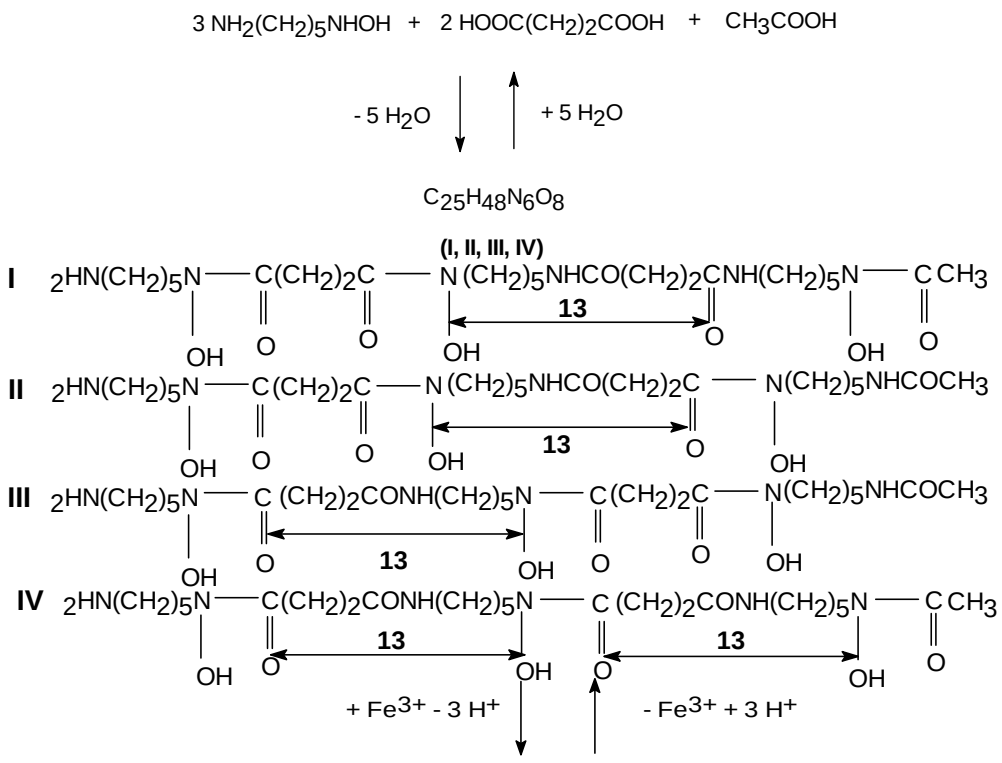
3 NH2(CH2)5NHOH + 2 HOOC(CH2)2COOH + CH3COOH
- 5 H2O
+ 5 H2O
C25H48N6O8
(I, II, III, IV)
I
II
III
IV
13
+ Fe3+ - 3 H+
- Fe3+ + 3 H+
C25H45N6O8Fe
(Va, Vb, Vc, Vd, Ve)

Va **Vb**

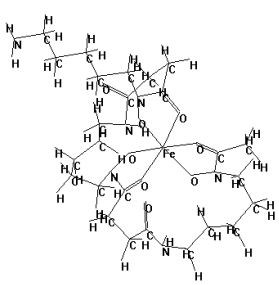

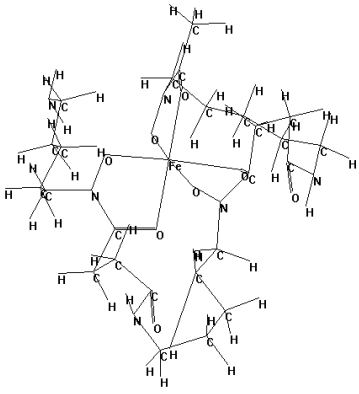

Vc **Vd**

Ve

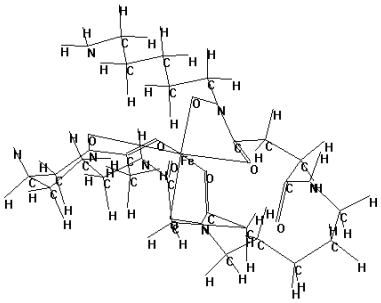

In the case of Ferrioxamine B, the MO calculations (AM1, Polak – Ribière Optimizer, RMS Gradient of 0.1 kcal/mol·Å) indicate that the most probable structure that may undergoes a metal complexation is **IV** (Heat of Formation of ~ -276.5 kcal/mol). For that compound, the number of atoms involved in sequence complexation (see below) are 13 – 13:

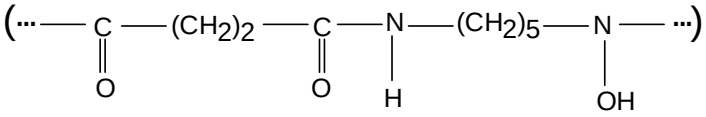

towards a singular "13" atoms distribution for the first, second and third structures. The semiotic 13 – 13 (**IV**) compound seems to be the most appropriate for the isomers **Va – e**, according to literature data [6].

The reaction of Ferrioxamine B with iron (III) ions affords five possible configurational isomers of Desferrioxamine B (**Va – e**). The paramagnetic complex may be estimated by EPR spectroscopy and the results suggest that the central ion have five unpaired electrons and an octahedral distribution of neighboring oxygen atoms. The total electrical charge of the molecule is zero [2].

According to these experimental information and HyperChem semi - empirical rules, we calculated some cuantic properties of compounds **Va – e**. For the initial geometry optimization, we applied some "Restraints" for the geometry around the central ion and for the geometry of oxygen and nitrogen atoms. From the log files, the next table presents some data issued from calculation steps:

Compound	**Va**	**Vb**	**Vc**	**Vd**	**Ve**
Energies and gradient:					
Total Energy (kcal/mol)	-261223.25	-261423.93	-261407.15	-261590.64	-261587.33
Total Energy (a.u.)	-416.27	-416.59	-416.57	-416.86	-416.85
Binding Energy (kcal/mol)	**-23274.95**	**-23475.63**	**-23458.84**	**-23642.34**	**-23639.02**
Isolated Atomic Energy	-237948.30	-237948.30	-237948.30	-237948.30	-237948.30

Compound	**Va**	**Vb**	**Vc**	**Vd**	**Ve**
(kcal/mol)					
Electronic Energy (kcal/mol)	-2128241.72	–2316831.45	-2244469.92	-2269682.89	-2298670.19
Core-Core Interaction (kcal/mol)	1866973.49	2055397.06	1983028.62	2008090.51	2037075.74
Restraint Energies:					
Tether Point Stretch Energy (kcal/mol)	19.46	0.00	0.00	0.00	0.00
Bond Stretch Energy (kcal/mol)	0.72	0.00	0.00	0.00	0.00
Bend Energy (kcal/mol)	24.78	10.45	34.14	1.73	7.12
Torsion Energy (kcal/mol)	0.00	0.00	0.00	0.00	0.00
Heat of Formation (kcal/mol)	-15449.30	-15615.47	-15622.37	-15773.46	-15775.53
Gradient (kcal/mol/Ang)	0.09	0.1	0.09	0.1	0.1

The Heat of Formation is not parameterized for ZINDO/1 by fitting to experimentally determined heats (enthalpies) of formation for a set of molecules at 298 K (like MINDO/3, MNDO, AM1, and PM3 methods).

The Heat of Formation is calculated for these methods by subtracting atomic heats of formation from the binding energy. Results are reported in the log file for a calculation. Heat of Formation is the value usually reported when describing results and is more useful than the directly calculated binding energy).

The values, in our case, are approximately four times greater than the usual H^0_f values (we don't use for MM^+ Options any "Cutoffs"), and the difference between experimental and computed Heat of Formation is estimated to be ~ 460 kcal/mol. For theoretical estimations, the most probable isomer is **Ve**.

Therefore, if energy binding remains the appropriate value to establish the most probable configurational isomer, **Vd** isomer is the most stable according to our estimations.

The difference between **Vd** and **Ve** is low (~ + 3.19 kcal/mol $_{\text{binding energy}}$ and - 2.07 kcal/mol $_{\text{heat of formation}}$), the both presenting 13-13 long chain atoms in the structure.

The distances between the two ends of the "13 atoms bridges" (oxygen atoms/ions) are 2.85 and 2.99 Å (**Va**), 3.08 and 3.23 Å (**Vb**), 3.02 and 3.19 Å (**Vc**), 3.09 and 3.19 Å (**Vd**), and 3.18 and 3.42 Å (**Ve**).

BIBLIOGRAPHY

1. H. Bickel, R. Bosshardt *et al.*, Helv. Chim. Acta, 43, 2118 (1960)
2. H. Bickel, H. Keberle *et al.*, Helv. Chim. Acta, 46, 1385 (1963)
3. S. P. Young, E. Backer *et al.*, J. Haematol., 41, 357 (1979)
4. C. L. Meyers, C.J. Weiss *et al.*, J. Moll. Cell. Cardiol., 17, 675 (1985)
5. E.A. Preoteasa, G. Schianchi *et al.*, Rom. J. Phys., 1995
6. H. Bickel, G. E. Hall *et al.*, Helv. Chim. Acta, 43, 2129 (1960)

STUDIA UNIVERSITATIS BABEŞ-BOLYAI, PHYSICA, SPECIAL ISSUE, 2001

COLLISIONAL EFFECTS IN INFRARED MULTIPHOTON DISSOCIATION OF Si_2F_6

VALER TOSA

National Institute for Isotopic amd Molecular Technologies, Cluj-Napoca, P.O.Box 700, Romania

ABSTRACT. The model of McRae et al is used to investigate the effect of laser fluence and collisions in the dissociation of vibrationally excited Si_2F_6. The parameters of the model are obtained and their dependence on laser fluence is discussed. Vibrational energy pooling mechanism dominates over quenching of vibrational excitation in homogeneous (Si_2F_6-Si_2F_6) collisions. Heterogeneous collisions between Si_2F_6 parent molecule and SiF_4 as dissociation product are found to hinder dissociation for low laser fluence and to enhance it, as fluence increases.

1. Introduction

The dependence of IRMPD on laser fluence and pressure is complex and difficult to predict. Extracting this dependence from experimental data can be complicated because, for practical reasons, it is desirable to have a substantial fractional decomposition. This usually requires a large number of pulses, during which the pressure and composition of the irradiated mixture significantly changes with the target gas disappearing and the products accumulating. The increase of pressure with the number of pulses must be taken into account in the study of collisional IRMPD process, as dissociation products may significantly affect the subsequent excitation process through their collisions with parent molecules. Although dissociation products generally increase vibrational quenching, sometimes they can help to overcome vibrational and rotational bottlenecks. We refer especially the cases when the reaction products absorb the infrared radiation, and, becoming vibrationally hot, enhance the dissociation process by vibrational energy pooling.

The multiphoton absorption and dissociation processes induced by the pulsed infrared radiation in the ν_7 normal mode of Si_2F_6 was investigated by us [1, 2] both as a potential method for Si isotope separation [4] and as the most efficient way of generating the SiF_2 long-lived radical [5, 6]. The purpose of the present work is to examine in more detail than our previous study [1] the effect of laser fluence on Si_2F_6 dissociation. The change of pressure during multipulse irradiation experiments as well as the above mentioned effects which the reaction products may have upon dissociation process were not taken into account in our previous work. In particular, by using the method proposed by McRae et al. [3], we will concentrate on dissociation processes occurring after the laser pulse, as a result of heterogenous and homogenous collisions. One benefit is that new information can be extracted concerning the

postpulse dissociation and additional conclusions may be drawn if the experiment is stopped for analysis after different number of pulses.

2. Methods

For MPD measurement we used a stainless steel cell of 10 cm long with KBr windows on both ends. A mixture of He and CO_2 of 6:1 was used for the CO_2 laser. The temporal profile, measured with a photon-drag detector (Hamamatsu), shows a pulse duration of 100 nsec FWHM with no tail. For 0.1 Torr of neat Si_2F_6 gas, the average time between collisions at room temperature is 1.5 μs, therefore we collisionless conditions hold. The fluence was varied from 0.1 to 2 J/cm^2 by putting various thickness of CaF_2 attenuators before the cell and by using two confocal BaF_2 lenses of focal length 40 cm and 20 cm. We also monitored the transmitted beam with a pyroelectric detector so that we could skip incomplete laser pulses. After irradiating with a number of pulses which was varied depending on the fluence, we measured the FTIR absorption spectrum (Perkin Elmer 1600 series FTIR, resolution 4 cm^{-1}). The amount of Si_2F_6 remaining in the cell is proportional to the integrated absorption of the ν_7 band. The gas contains SiF_4 as an impurity but most of it can be separated by fractional distillation, so that the concentration of SiF_4 in Si_2F_6 gas was around 2%.

The method proposed by McRae et al [3] is devoted to the analysis and quantification of the contributions from different collisional processes in multipulse dissociation experiments. The number of parent molecules N_n left in the cell after n irradiation pulses is given by

$$N_n = N_0 \prod_{k=1}^{n} \left[1 - \frac{V_I}{V_c} f_k\left(\Phi_k, \alpha_{k-1}, \beta_{k-1}\right) \right] \tag{1}$$

where N_0 is the initial number of molecules in the cell, V_I and V_C are, respectively, the irradiation and the total cell volumes (for our irradiation geometry V_I/V_C=0.191), and $f(\Phi,\alpha,\beta)$ is the single-pulse decomposition probability. This is a function of fluence, Φ, and the partial pressures of parent molecules, α, and of the dissociation products, β. The target gas partial pressure after n pulses, α_n can be expressed as

$$\alpha_n = \frac{N_n}{N_0} \alpha_0 \tag{2}$$

and the accumulated partial pressure of the products after n pulses is

$$\beta_n = \sum_p S_p (\alpha_0 - \alpha_n) \tag{3}$$

where the sum runs over all dissociation products. The proportionality constants S_p depends on the stoichiometry of the dissociation reaction and takes specific values for each dissociation product. The method takes into account the variation in the pulse-to-pulse yield induced by the change of the pressures α_n and β_n, during the time of the experiment.

It was assumed a power dependence of f on partial pressures given by:

$$f(\Phi,\alpha,\beta)=\sum_{i=1}\sum_{j=0}h_{ij}(\Phi)\alpha^{i-1}\beta^{j} \tag{4}$$

where the coefficients h_{ij} are associated with Lindenmann-like collision reactions. The sum *i+j-1* is inferred to be the number of effective collisions between *i* molecules of the target gas and *j* molecules of some buffer gas (in our case dissociation products). After *i+j-1* collisions, the target gas decomposes. If values of the h_{ij} coefficients are positive this indicates that the composition is enhanced by collision with target or buffer gas, while negative coefficients would correspond to collisional deactivation. As pressure is low, we restricted our fit to first order coefficients, i.e. *i+j-1= 1* so that Eq. 4 takes on the form:

$$f(\alpha,\beta)=h_{10}+h_{20}\alpha+h_{11}\sum_{p}S_p(\alpha_0-\alpha_n) \tag{5}$$

where the sum runs over all dissociation products. For a given fluence we fitted the experimental data (N_n *vs n*) to Eq.(1), by using a computer program written by us and standard minimization subroutines [8]. We started from the data corresponding to the lowest laser fluence with an initial guess of all $h_{ij}=0$ and use the obtained h_{ij} parameters for one fluence as initial guess for the next higher fluence.

3. Results and discussions

The h_{10} coefficient and the $h_{20}\alpha_0$ quantity are plotted in Fig. 1 as a function of laser fluence. Both quantities increase steadily with fluence. In particular, h_{10} follows closely the dependence of the dissociation probability on fluence (Fig. 4 of ref. [1]). It sharply increases for low values of fluence then asymptotically approaches unity for fluence values greater than 1.5 J/cm^2.

The h_{10} coefficient is responsible for that part of the dissociation which is only induced by the infrared radiation:

$$h_{10}\qquad \begin{cases} Si_2F_6 \xrightarrow{h\nu} Si_2F_6^{\,*} \\ Si_2F_6^{\,*} \xrightarrow{h\nu} SiF_4+SiF_2 \end{cases} \tag{6}$$

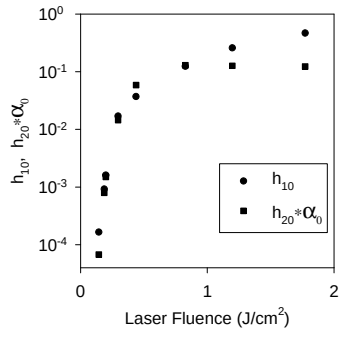

where the * superscripts indicate a generalized excitation energy distribution due to photon absorption or collision.

We represented in Fig.1 the dimensionless quantity $h_{20}\alpha_0$ (see Eq.5) in order to compare it with h_{10} coefficient. As one can see from Fig. 1, the contribution of homogenous collisions to dissociation probability is comparable, for low fluences, to the contribution of the laser field itself. This is consistent with recent results on CF_2HCl [8] IRMPD. By monitoring the CF_2 radical density in the interaction zone, it was found [8] that large

quantities of CF_2 are formed after the laser pulse, by collisions. As fluence increases the contribution of homogenous collisions to the dissociation saturates (even slowly decreases) for values of laser fluence greater than 1 J/cm^2, while the collisionless dissociation probability continues to grow. This means that, as fluence increases, more an more molecules will be dissociated by the laser field, while the fraction of molecules which are excited and then dissociated through homogenous collisions will saturate.

There are [9] at least three processes which can potentially contribute to the h_{20} coefficient: (a) weakening of the anharmonic barrier effect (through rotational hole filling and overcoming of the vibrational bottleneck via rotational-translational and vibrational-vibrational, V-V', intermolecular energy transfer, respectively), (b) quenching of the vibrational excitation via vibrational-translational energy transfer, and, (c) vibrational energy pooling which is a V-V' transfer between molecules excited to quasicontinuum:

$$h_{20}\begin{cases} Si_2F_6^{*} + Si_2F_6^{*} \longleftrightarrow Si_2F_6^{**} + Si_2F_6 \\ Si_2F_6^{**} \longrightarrow SiF_4 + SiF_2 \end{cases} \tag{7}$$

Here the $Si_2F_6^{**}$ is excited to where it can absorb further nonresonantly or can decompose with a unimolecular rate that is fast when compared with deactivation. For our case, i.e. when there are no collisions during the laser pulse, the process (a) does not contribute to the value of h_{20}. The positive sign of this coefficient indicates that mechanism (c) is dominant over (b), which means that the energy transfer described by Eq. 7 is very efficient.

The h_{11} parameters are associated with collisional-energy transfer between excited target molecules ($Si_2F_6^{*}$) and buffer gases. In our case the dissociation products are SiF_4 and the radical SiF_2,. This latter one easily combines to form $(SiF_2)_n$ polymer which usually adheres to the cell walls and windows, forming a whitish film [4, 6], so that SiF_4 remains the only collision partner to be considered for Si_2F_6.

The negative h_{11} values for low fluences indicate that SiF_4 collisions with $Si_2F_6^{*}$ will diminish the dissociation probability through a process like:

$$h_{11} < 0 \quad Si_2F_6^{**} + SiF_4 \longrightarrow Si_2F_6^{*} + SiF_4^{*} \tag{8}$$

For this low laser fluences SiF_4 does not absorb energy from laser field (see below), thus, heterogenous collisions could only produce Si_2F_6 vibrational deexcitation.

However, as fluence increases the h_{11} coefficient continuously increases and becomes positive. A positive h_{11} has been also observed in the CH_2Br-CH_2F IRMPD experiments [10] and has been explained by the collisions of the excited parent molecules with CH_2=CHF dissociation product which becomes vibrationally hot as a result of

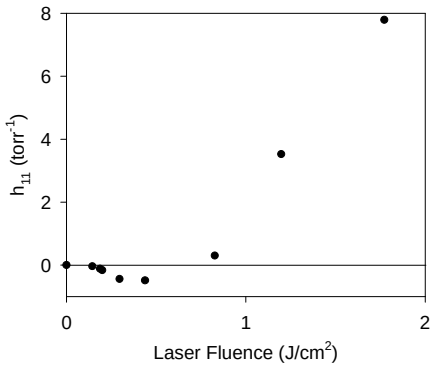

photons absorption. Previous investigations on the SiF_4 molecule shows that it absorbs both cw [11] and pulsed [12, 13] laser photons at 979.7 cm^{-1}. A decomposition reaction was observed to occur when irradiating SiF_4 with CO_2 cw laser in the spectral region of 974.6 to 982.1 cm^{-1}. The maximum of the multiphoton absorption in supersonic molecular beam [12] is reported to be around 1020 cm^{-1} , and to occur at 979.7 cm^{-1} only under two frequency irradiation. This suggests that multiphoton absorption and dissociation could be induced at this wavelength through combination bands of SiF_4. Indeed, room temperature SiF_4 irradiation [13] with pulses of 100 nsec and 979.7 cm^{-1} produces visible luminiscence, and the authors conclude that this is a direct proof of the multiphoton absorption and dissociation as a unimolecular process. Emission was observed within the duration of the laser pulse, even at pressure as low as 10 mTorr, but only starting from laser pulses higher than 60 mJ. The irradiation geometry was not fully specified to estimate the fluence but the threshold in energy to observe the luminiscence suggests that sizeable absorption will be produced at higher fluence values. We can therefore assume that, for higher laser fluences, SiF_4 will enhance the Si_2F_6 dissociation in a collisional process:

$$h_{11} > 0 \begin{cases} SiF_4 \xrightarrow{h\nu} SiF_4^{*} \\ Si_2F_6^{*} + SiF_4^{*} \longrightarrow Si_2F_6^{**} + SiF_4 \\ Si_2F_6^{**} \longrightarrow SiF_4^{*} + SiF_2 \end{cases} \tag{9}$$

We conclude that this is the main process responsible for the increase of h_{11} with laser fluence. It shoud be stressed, however, that there is another process which could not be taken into account by the McRae model. The laser diode spectroscopic studies [6] reported that in IRMPD of the Si_2F_6, the SiF_2 radical is produced in the ground vibrational state while SiF_4 results vibrationally hot. Postpulse collisions between hot SiF_4 and Si_2F_6 excited by the laser field close to dissociation, could give a contribution to the dissociation. As this is a unipulse contribution, it is proportional to the quantity of SiF_4 produced per pulse, thus, it will be much smaller than the contribution given by Eq. 9, which is proportional to the accumulated SiF_4 from pulse to pulse.

In conclusion, by using the model of McRae et al [3], we studied the importance of various dissociation processes of Si_2F_6 on the laser fluence. The emerging picture is that even when apparently dissociation takes place in collisionless conditions, the collisions play a significant role in enhancing or inhibiting dissociation. At low fluences homogenous collisions play a positive role and enhance dissociation through vibrational energy pooling while heterogenous collisions contribute to vibrational deactivation of the Si_2F_6 molecules. As fluence increases the contribution of laser field to dissociation becomes dominant, while homogenous collisions contribution slowly decreases. An interesting feature is that at higher fluence values the dissociation product, SiF_4 also absorbs IR photons, and, by collisions with Si_2F_6, contribute to the enhancement of the overall dissociation field.

REFERENCES

1) H. Okamura, V. Tosa, T. Ishii, and K. Takeuchi, , J. Photochem. & Photobiol., **95**, 203 (1996)

2) V. Tosa, S. Isomura, and K. Takeuchi, J. Photochem. & Photobiol. **91**, 173 (1995)

3) G. A. McRae, B. Yamashita, and J.W. Goodale, J. Chem. Phys. **92**, 5997 (1990)

4) M. Kamioka, Y. Ishikawa, H. Kaetsu, S. Isomura, and S. Arai, J. Phys. Chem. **90,** 5727 (1986)

5) F.W. Lampe and J. Biedrzycki, Spectrochim. Acta **46A**, 631 (1990)

6) K. Sugawara, F. Ito, T. Nakanaga, and H. Takeo, Chem. Phys. Lett. **232**, 561 (1995)

7) W.H. Press, B.P. Flannery, S.A. Teukolsky, W.T. Veterling, *Numerical Recipes*, Cambridge University Press, Cambridge, 1986

8) W. Stube, J. Wollbrandt, M. Rossberg and E Linke, J. Chem. Phys. **105** 9478 (1996)

9) J.A. Torresano and M. Santos, J. Phys. Chem. **100**, 9726 (1996)

10) G. A. McRae, D.K. Evans, and J.W. Goodale, J. Chem. Phys. **93**, 1689 (1990)

11) A.E. Darjiushkin, N.L. Kondratyev, A.N. Orlov, A.M. Prokhorov, V.I. Pustovoi, Laser Physics **5**, 747 (1995)

12) E. Borsella, L.Caneve, A. Giardini-Guidoni, A. Mele, in *Photons and Continuum States of Atoms and Molecules*, Ed N.K. Rahman, C. Guidotti, and M. Allegrini, Springer Verlag Berlin Heidelberg 1987

13) G. Yahav and Y. Haas, Chem. Phys. Lett. **83**, 493 (1981)

STUDIA UNIVERSITATIS BABEŞ-BOLYAI, PHYSICA, SPECIAL ISSUE, 2001

ELECTRICAL BEHAVIOUR OF Fe_2O_3 - B_2O_3 - CaO GLASSES

I. ARDELEAN and P. PĂŞCUŢĂ

Faculty of Physics, "Babes-Bolyai" University, 3400 Cluj-Napoca, Romania

ABSTRACT. Electric resistivity measurements have been performed on $xFe_2O_3 \cdot (100-x)[3B_2O_3 \cdot CaO]$ glasses with $0 < x \leq 50$ mol%.The electrical resistivity and the conductivity activation energy decreases with the Fe_2O_3 content. In order to analyze the electrical data, we have considered in these glasses a polaronic model for conduction.

1. Introduction

Fe_2O_3 containing oxide glasses as semiconductive glasses have attracted to investigate their electrical conduction [1-5]. The studies extended to vanadium [3, 6-8], mangan [3, 9] and copper [3, 10] oxide glasses. Austin and Mott [11] and Schnakenberg [12] have discussed the conduction process in terms of hopping between ions in two valence states. Mott [13] has proposed for the electric conductivity an expression of the form:

$$\sigma = (\nu n\, e^2 R^2 / kT) r(1-r) \cdot \exp(-2\alpha R) \cdot \exp(-W / kT), \qquad (1)$$

where R is the average intersite separation, n is the number of size of TMIs per volume unit, r is the fraction of sites occupied by an electron; ν is the phonon frequency, T is the absolute temperature, $\exp(-2\alpha R)$ is the tunneling probability, W is the hopping activation energy. The variation of conductivity with glass composition is difficult to interpret since the parameters n, r, R and W vary with the nature, the content of the TMIs, the preparation conditions [14] and the thermal treatments after preparation [15]. In homogeneous glass systems the electrical conductivity can be affected by the electron tendency to be localized at specific sites in the glass matrix [13, 16]. Such sites may arise from a particular type of short-range order and have been established to exist in vanadate glasses from magnetic resonance [17] and infrared [18] investigations and in iron-lead-borate glasses from Mössbauer effect data [19]. The growth of crystallites in the glasses can lead to a long-range order within the crystallites and to a barrier-layer polarization at the crystallite-glass interfaces. Finally, the correlation effect may vary the conductivity and their activation energy.

The present work reports our results concerning the electric behaviour of Fe_2O_3-B_2O_3-CaO glass system. The studies were made by means of electric resistivity measurements.

2. Experimental

We have studied $xFe_2O_3 \cdot (100-x)[3B_2O_3 \cdot CaO]$ glasses with $0<x\leq 50$ mol % using pure reagent grade Fe_2O_3, H_3BO_3, and $CaCO_3$. The mixtures, in suitable proportions corresponding to the desired concentration of Fe_2O_3, were mechanically homogenized and melted in sintered corundum crucibles in an electric furnace at 1200 ˚C. The molten material was kept at this temperature for 30 min, then quenched at room temperature by pouring onto a stainless-steel plate.

The structure of samples was analyzed by means of X-ray diffraction. The pattern obtained did not reveal any crystalline phase in the samples up to 50 mol%.

The electrical resistivity measurements were performed using a Keithley Electrometer (model 6517) with a technique previously described [4]. The samples have 0.5-1.2 cm^2 area and 1-3 mm thickness. For the control of the results we used current-voltage techniques. The dc I-V characteristic was linear. Concerning the surface polarization no dependence on time was observed in dc resistivity after the voltage was applied. The thermoelectric power indicated that the current carriers are electrons.

The glass sample density was determined using a picnometric technique.

3. Results and Discussion

In order to analyze the resistivity data we have considered a polaronic model. Equation (1) has been used for the description of electric behavior of $xFe_2O_3 \cdot (100-x)[3B_2O_3 \cdot CaO]$ glasses. For this reason the $\log(\rho \cdot T^{-1})$ versus T^{-1} is shown in Figure 1. Figure 2 indicates that the resistivity at 500 K decreases with six orders of magnitude when the Fe_2O_3 content increases from 3 to 50 mol %.

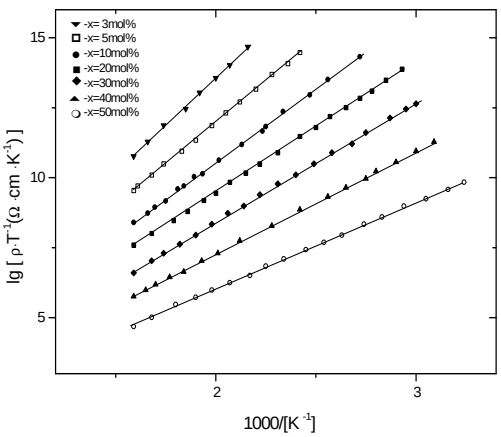

Fig 1. Reciprocal temperature dependence of the $\log(\rho T^{-1})$ for $xFe_2O_3 \cdot (100-x)$ $[3B_2O_3 \cdot CaO]$ glasses

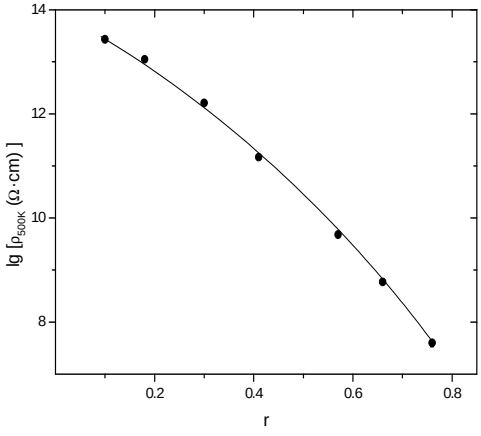

Fig 2.The log ρ at 500K dependence of r for $xFe_2O_3 \cdot (100-x)[3B_2O_3 \cdot CaO]$ glasses

The values of the conductivity activation energy are presented in Table 1. One remarks that the activation energy increases if the Fe_2O_3 content is descreased. The results are similar to those found for iron-lead-borate [4] and iron-phosphat [1-3] oxide glasses. This type of behaviour has been attributed to the fact that the charge transfer is due hopping of small polarons between Fe^{2+} and Fe^{3+} ions [3, 4] for which the intersite separation (R) is lower at high content of Fe_2O_3. The values of R and n in Eq. (1) were estimated using density data (Table 1). The existence of both Fe^{2+} and Fe^{3+} ions was evidenced for the studied glasses by magnetic measurements, from which was evaluated ratio r [20].

The phonon frequency estimated for the sample with x=5 mol %, using Eq. (1) and replacing R ~ 4.6 Å, $\alpha \sim 10^8$ cm^{-1} [13], W=1.18 eV, r = 0.10, $n_0 = 3.5 \cdot 10^{20}$ cm^{-3} at 500 K is $\nu \approx 8 \cdot 10^{12}$ s^{-1}. On the other hand for the glasses with x = 50 mol % and replacing corresponding values R ~ 4 Å, W=0.60 eV, $n_0 = 1.96 \cdot 10^{21}$ cm^{-3} at 500 K the phonon frequency is $\nu \approx 2 \cdot 10^{12}$ s^{-1}. Considering that ν is extremely sensitive to the conduction activation energy, the calculated values are very close to the lattice vibration frequency.

In contrast with Hansen`s [1] results the resistivity of xFe_2O_3 $(100-x)[3B_2O_3 \cdot CaO]$ glasses does not show the minimum at r = 0.5. It was noticed that the resistivity decreases for $0.10 \leq r \leq 0.76$ (Fig. 2). From this dependence we conclude that the minimum occurs at r>0.76, but minimum value of r it was not obtained in concentration range when our glasses are formed. Results obtained by Hansen [1] represent the behavior of the 55 FeO· 45 P_2O_5 (mol %) glass, when the valence state of the iron was adjusted by adding different amounts of dextrose to the batch. These samples were annealed between 475ºC and 500ºC. Kinser [15] resuming Hansen`s technique showed that after thermal treatments at 400ºC and 500ºC one observes a finely dispersed crystalline phase in the glasses. In this case due the presence of a long-range order within the crystallites and of a barrier-layer polarization at the crystallite-glass interfaces it is possible that the variation of the resistivity could be otherwise. The minimum at r = 0.5 has not been obtained for iron-lead-borate glasses [4] and other oxide glasses with TMIs [3, 6-10].

Table 1.

Ratio r of Fe^{2+} ions relative to all iron ions containing in the glasses, conduction activation energy, W, sample density, d and concentration of Fe^{2+} ions, n_0.

x [mol%Fe_2O_3]	r	W [eV]	d [g/cm^3]	$n_0 \cdot 10^{-21}$ [cm^{-3}]
3	0.10	1.34	3.78	0.22
5	0.18	1.18	3.98	0.35
10	0.30	1.04	4.17	0.64
20	0.41	0.91	4.46	1.08
30	0.57	0.83	4.61	1.45
40	0.66	0.72	5.02	1.75
50	0.76	0.60	5.43	1.96

In the analysis of these data we have considered that all the available carriers are “free” and therefore we can take the Fe^{2+} ions concentration as the carrier concentration [21]. In this case, the carriers mobility in $xFe_2O_3 \cdot (100-x)[3B_2O_3 \cdot CaO]$ glasses in the concentration range from 5 to 50 mol % has been estimated from the equation:

$$\sigma = n_0 e \mu \qquad (2)$$

The mobilities are very low, ranging from 10^{-15} to 10^{-8} $cm^2V^{-1}s^{-1}$ at 500 K and are in agreement with other results obtained for oxide glasses with TMIs [1, 13, 21].

An examination of the semiconduction processes in $3B_2O_3 \cdot CaO$ glass matrix containing iron ions suggests that a polaron model is applicable.

4. Conclusions

Electric resistivity measurements performed on $xFe_2O_3 \cdot (100-x)[3B_2O_3 \cdot CaO]$ glasses with $0 < x \leq 50$ mol % lead to data depending on the Fe_2O_3 content. The presence of the Fe^{2+} and Fe^{3+} ions determines the semiconducting behavior of these glasses. The semiconduction processes occurring in calcium-borate glasses containing iron ions suggest that a polaron model is applicable.

REFERENCES

1. K. W. Hansen, J. Electrochem. Soc. 112, 10 (1965)
2. K. W. Hansen and M. Splann, J. Electrochem. Soc. 113, 9 (1996)
3. M. Sayer and A. Mansingh, Phys. Rev. B, 6, 4629 (1972)
4. I. Ardelean, Solid State Commun. 27, 697 (1978)
5. Qui Hong-Hua, H. Mori, H. Sakata and T. Hirayama, J. Ceram. Soc. Japan, 103,32 (1995)
6. H. Hirashima, M. Mitsuhashi and T. Yoshida, Yogho-Kyokay-Shi, 90, 411 (1982)
7. R. Singh and K. Sethupathi, J. Phys. D, 22, L709 (1989)
8. K. Tanaka, T. Yoko, N. Nakamura and K. Kamiya, J. Non-Cryst. Solids, 125, 164 (1990)
9. I. Ardelean, V. Simon, V. Ioncu, S. Filip and M. Flora, Inter. J. Mod. Phys. B, 15 (17), 2359 (2001)
10. C. F. Drake, I. F. Scanlan and A. Engel, Phys. Status Sol. 32,193 (1969)
11. I. G. Austin and N. F. Mott, Advan. Phys. 18, 41 (1969)
12. J. Schnakenberg, Phys. Status Sol. 28, 623 (1968)
13. N. F. Mott, Advan. Phys. 16, 49 (1967); J. Non-Cryst. Solids, 1, 1 (1968)
14. E. Burzo, I. Ursu, D. Ungur and I. Ardelean, Mat. Res. Bull. 15, 1273 (1980)
15. D. L. Kinser,J. Electrochem. Soc. 117, 546 (1970)
16. T. Allersma and J. D. Mackenzie, J. Chem. Phys. 47, 1406 (1967)
17. R. F. Landberger and D. J. Bray, J. Chem. Phys. 53, 2757 (1970)
18. M. Sayer, A. Mansingh, J. M. Reyes and G. F. Lynch, in Proceedings of the Conference on Low Mobility Materials (Eliot, Israel, 1971) p. 115
19. I. Ardelean, E. Burzo and I. Pop, Solid State Commun. 23,211 (1977)
20. I. Ardelean, P. Păşcuţă and V. Ioncu, Mod. Phys. Letters B, accepted for publication (2001)
21. A. E. Owen, Contemp. Phys. 11, 227 (1970)

STUDIA UNIVERSITATIS BABEŞ-BOLYAI, PHYSICA, SPECIAL ISSUE, 2001

THE EFFECTS OF BALL-MILLING ON THE PROPERTIES OF AB_3 : AB_5 ALLOY MIXTURES

A. R. BIRIŞ, I. MIŞAN, E. INDREA, D. LUPU

National Institute for Research and Development of Isotopic and Molecular Technologies, PO Box 700, R-3400 Cluj-Napoca, Romania

ABSTRACT. The ball milling of a mixture of Laves phase and $LaNi_5$ type alloys results in a Laves phase type structures with XRD pattern characteristic to nanostruntured materials. The transformation leads also to changes in the hydrogen desorption isotherms and improves the discharge capacity of the hydride electrode.

1. Introduction

Nanocrystalline structure induced by mechanical alloying may improve the properties of hydrogen storage alloys. Ball milling involves heavy deformation of the powder and induces high concentration of strain and defects: favourable characteristics for activation and hydrogen absorption/desorption kinetics [1-5]. The current tendency in materials design strategies of hydrogen storage alloys is toward nanocrystalline, disordered and mesostructured materials [6] in order to achieve high electrochemical activity via a strict control of interfacial properties. The mechanical alloying process has recently emerged as a novel technique for producing nanostructured alloy powders which interesting electrochemical properties [7]. Advanced nanocrystalline of C15 type structure obtained by complete crystallisation of melt-spun alloys show also high performance as metal hydride electrodes [8].

2. Experimental

The AB_5 and AB_3 type alloys were prepared by arc melting the components under pure argon atmosphere.

The mixture of AB_5:AB_3 alloys (about 2 g) was ball milled with a vibromill, under argon, in a stainless steel reactor with a hard steel ball of 11 g.

The hydrogen desorption isotherms were measured in a Sievert type aparatus at room temperature and the electrochemical charge-discharge cycles were performed as described elsewhere [9].

3. Results and discussion

3.1 Structural characteristics

A mixture of $Zr_{0.6}Ti_{0.4}V_1Mn_{0.37}Cr_{0.3}Ni_{1.33}$ and $MmNi_{4.3}Mn_{0.7}$ (Mm = mischmetall) in the mole ratio 2:1, ball milled 145h show the XRD pattern reported in Fig. 1. The ball milling results in line broadening and decreasing intensity typical [4] for decrease in crystallite size and an increase of internal strain as a result of mechanical deformation and fracture. The remaining lines are characteristic to the C15 and C14 Laves phase structures while the lines of the AB_5 type structure allmost disapear after ball milling. It is interesting to note that by arc melting the same mixture of alloys a pure C15 type structure was obtained.

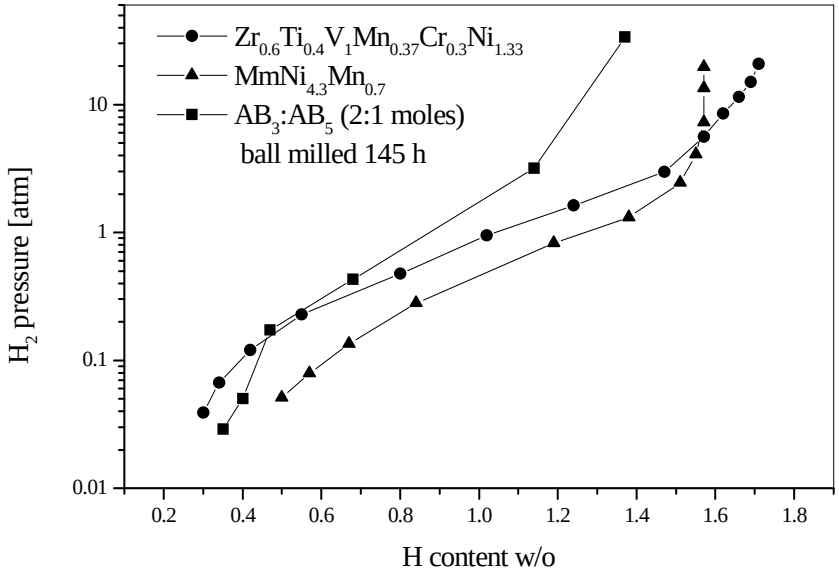

Fig. 1. The X ray diffraction profiles for the starting alloys and their ball milled mixture

Hydrogen desorption isotherms

The desorption isotherms for the starting alloys (AB_3 and AB_5) and the ball milled mixture are reported comparatively in Fig. 2.

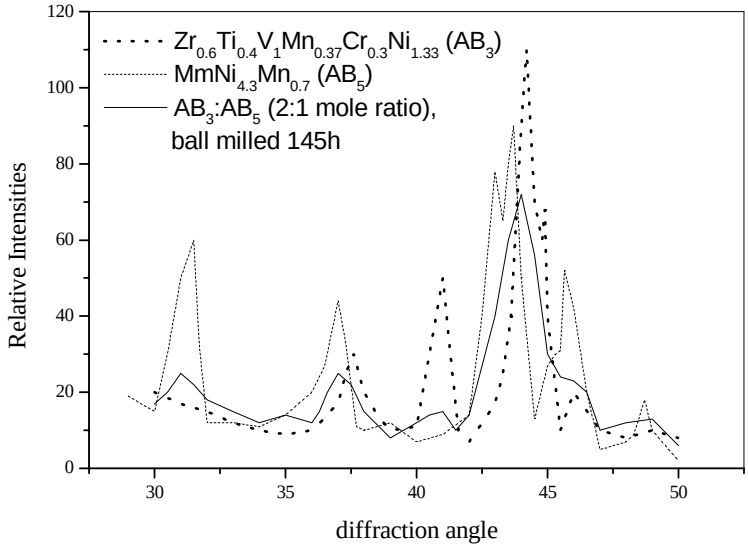

Fig. 2. Hydrogen desorption isotherms at 20 ^{o}C.

The effect of ball milling is a slight diminution of the overall amount of adsorbed hydrogen together with an increase of the equilibrium desorption pressure in the high pressure range. This could be due both to the formation of the Mm-substitution mixture Laves C15 and C14 structure and to the ball milling induced strain and deformations.

The arc melted mixture of the same composition, with pure C15 as mentioned above, showed, surprisingly, very low hydrogen absorption (0.39 % H).

3.2 The behaviour as hydride electrodes

The behaviour of the alloys as hydride electrodes an their capacities during charge-discharge cycling is reported in Fig. 3.

The comparison shows clearly the ball milled sample does not behave like an average weighted mixture of the starting alloys, the fast degradation with cycling of the AB_5 disappears. The electrode is fully activated after 15 cycles. After 95 cycles the electrode was sandwiched between two NiOOH electrodes and assembled in a sealed cell under 10 bar H_2 pressure. The discharge capacity increases, reaching a plateau at about 350 mAh/g, obviously because the materials with sloping plateaux in the desorption

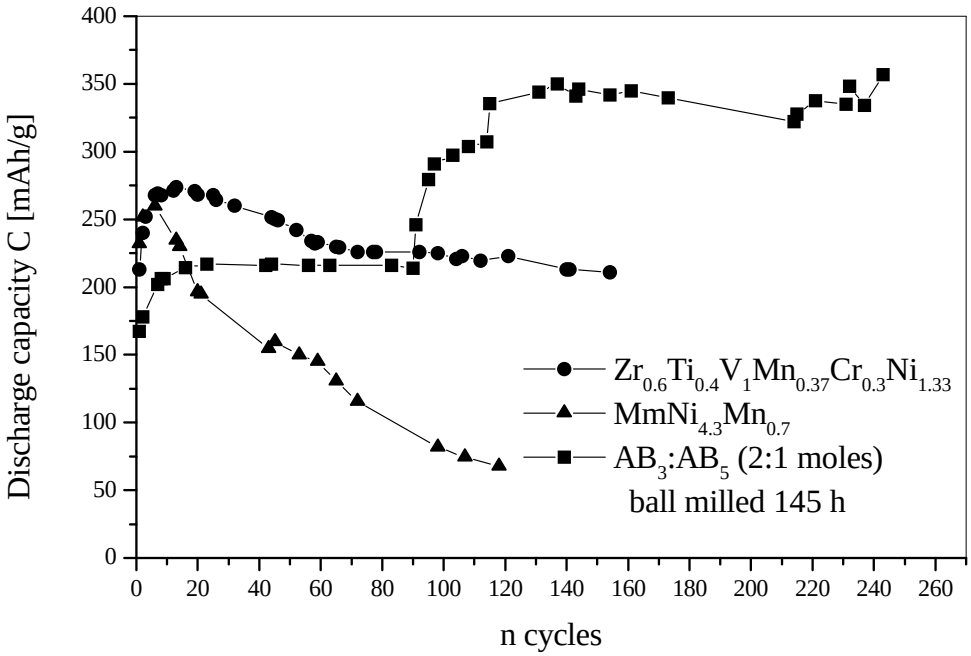

Fig. 3. Cycle life curves for the hydride electrodes at 160 mA/g discharge current at 20 °C in 6N KOH.

isotherms doe require higher pressures to reach the full charging with hydrogen. It has been shown [10] that good algorithm which accounts for the experimental discharge capacity is the amount of hydrogen desorbed in the range 10-0.1 bar H_2 at 20 °C. For

the ball milled sample Fig. 2 shows that this amount is 0.97 weight per cent H, corresponding to 260 mAh/g. The much higher capacity obtained experimentally shows that the ball milling method is very effective in increasing the discharge capacity. Such in increase has been also reported for the nanostructured alloys [8].

Conclusions

The ball milling of a mixture of Laves phase AB_3 with an AB_5 ($LaNi_5$ type structure) in 2:1 mole ratio results in a Laves phase alloy with the XRD pattern characteristic to C15 and C14 type structures. The line broadening suggests a nanostructured material.

The overall composition $AB_{3.67}$ explains the decreasing of the amount of absorbed hydrogen and the increasing equilibrium hydrogen pressure due to the increasing B:A ratio.

The ball milling has a beneficial effect on the discharge capacity as hydride electrode and deserves the research in this direction.

REFERENCES

1. L. Zaluski, A. Zalusca, P. Tessier, J.O. Ström-Olsem, R. Schulz, *J. Alloys Comp.*,227 (1995) 53.
2. L. Zaluski, A. Zalusca, J.O. Ström-Olsem, *J. Alloys Comp.*,253-254 (1997) 70.
3. A. Zalusca, L. Zaluski, J.O. Ström-Olsem, *J. Appl. Physics*, (2001), in press
4. R.A. Andrievski, B.P. Tarasov, I.I. Korobov, N.G. Mozgina, S.P. Shilkin, *Int. J. Hydrogen Energy*, 21 (1996) 949.
5. M. Zhu, W.H. Zhu, C.Y. Chung, Z.X. Che, Z.X. Li, *J. Alloys Comp.*,293-295 (1999) 531.
6. Z.S. Wrinski, *International Materials Reviews*, 46 (2001) 1.
7. M. Jurczyk, W. Majchrzycki, M. Nowak, E.Jankowska, *J. Alloys Comp.*, 322 (2001) 233.
8. L. Chen, F. Wu, M. Tong, D.M. Chen, R.B. Long, Z.Q. Shang, H. Liu, W.S. Sun, K. Yang, L.B. Wang, Y.Y. Li, *J. Alloys Comp.*, 293-295 (1999) 508.
9. D. Lupu, A.R. Biriş, E. Indrea, A.S. Biriş, G. Bele, L. Schlapbach, A. Züttel, *J. Alloys Comp.*,291 (1999) 289.
10. J.-M. Joubert, D. Sun, M. Latroche, A. Percheron-Guégan, *J. Alloys Comp.*,253-254 (1997) 564.

STUDIA UNIVERSITATIS BABEŞ-BOLYAI, PHYSICA, SPECIAL ISSUE, 2001

FRONT PHOTOPYROELECTRIC METHOD FOR THERMAL EFFUSIVITY MEASUREMENTS OF SOME FOODSTUFFS

D. DADARLAT, X. FILIP, C. NEAMTU, G. NAGY, V. SURDUCAN, A. PASCA

National Institute for Research and Development of Isotopic and Molecular Technologies, POB 700, Cluj-Napoca 5, R-3400, Romania.

ABSTRACT. The photopyroelectric calorimetry, in the front configuration, was applied in order to measure the thermal effusivity of some foodstuffs. The front configuration with thermally thick sensor and sample, and optically opaque sensor, was used for analysing the thermal properties of some fats. The information was obtained via a frequency scan of the phase of the pyroelectric signal. The main advantages of this configuration on the other two front schemes proposed before are: (i) one has not to use very thin foils or expensive semitransparent sensors; (ii) the information is contained in the phase of the signal (and not in the amplitude - as usual) which is not dependent on the power fluctuations of the radiation source.

INTRODUCTION

In the photopyroelectric (PPE) technique, the temperature variation of a sample exposed to a modulated radiation is measured with a pyroelectric sensor. In the last few years the method has been applied for investigating various optical and thermal properties of the materials. There were practically two detection configurations proposed for PPE calorimetry - the standard (back) and inverse (front) one, respectively [1, 2] – and all the four static (specific heat) and dynamic (thermal diffusivity, conductivity and effusivity) thermal parameters can be measured by combining different particular cases [3].

Concerning the front configuration, until now, there were proposed two detection schemes: the front configuration with thermally thin and optically opaque sensor, and with thermally thick and optically semitransparent sensor [4, 5]. In both cases, the sample must be thermally thick, and the information (the value of the thermal effusivity) is contained in the amplitude of the PPE signal. We want to stress on the fact that the main advantage of the front configuration (compared with the standard one) is the elimination of all optical problems (especially transparency) connected with the sample. This is why the configuration is very recommended when measuring the thermal properties of "non-classical" samples, as foodstuffs.

Unfortunately, sometimes it is not easy to handle very thin PVDF foils or expensive semitransparent sensors. On the other hand, it is well known that the amplitude of the PPE signal is very dependent on the power fluctuations of the laser and on the quality of the incident surface.

In this paper we applied a PPE front configuration scheme with thermally thick and optically opaque sensor for measuring the thermal effusivity of some (semi)liquid foodstuffs using the information coming from the phase of the PPE signal.

THEORY

Mandelis and Zver [6] and Chirtoc and Mihailescu [7] demonstrated that the general formula of the complex PPE signal is analytically exact, but it contains too many parameters, and it is often difficult to handle it when analysing results of ordinary experiments. Consequently, a lot of work has been devoted to simplifying this formula in order to obtain expressions in which the amplitude and/or the phase of the signal depends on one or, in a simple manner, on two thermal parameters [3].

For the purposes of this paper, we consider the simple situation when the detection cell is composed by a sensor situated on a (semi)liquid sample, and the medium in front of the sensor (where the radiation is coming from) is air.

If the detector works in a current mode, and the substrate is thermally thick, one gets the following expression for the PPE signal [8]:

$$V(f) = V_0(b_{ap} + 1)^{-1}(\exp(\sigma_p L_p) + R_{sp}\exp(-\sigma_p L_p) - (1+R_{sp}))\,(\exp(\sigma_p L_p) - R_{ap}R_{sp}\exp(-\sigma_p L_p))^{-1} \quad (1)$$

where V_0 is a factor depending on the pyroelectric coefficient of the sensor, the flux of the incident radiation, the thickness (L_p) and the volume specific heat of the sensor.

$$\sigma = (1+j)/\mu\,;\ \ \mu = (\alpha/\pi f)^{1/2} \quad (2)$$

where $j = (-1)^{1/2}$, μ is the thermal diffusion length, f is the modulation chopping frequency , and α is the thermal diffusivity, related to the other thermal parameters, the volume specific heat C, thermal conductivity k, and thermal effusivity e, by:

$$k = C\alpha; \qquad e = (Ck)^{1/2} \quad (3)$$

$$R_{ij} = (b_{ij} - 1)(b_{ij} + 1) \quad (4)$$

R_{ij} represents the reflection coefficient of the thermal waves between two media, where $b_{ij} = e_i/e_j$.

The symbols a, p, and s refer to the front medium (air), pyroelectric sensor and sample, respectively.

If we consider the pyroelectric sensor thermally thick too, than we can approximate in Eq. 1 $\exp(-2\sigma_p L_p) \rightarrow 0$, and we get:

$$V(f) = V_0(b_{ap} + 1)^{-1}\,(1 - (1+R_{sp})\,(\exp(-\sigma_p L_p)) \quad (5)$$

The phase of the signal defined by Eq.(5) is:

$$\tan\Theta = (((1+R_{sp})\,(\exp(-L_p/\mu_p))\sin(L_p/\mu_p))(\,1 - (1+R_{sp})\,(\exp(-\sigma_p L_p)\cos(L_p/\mu_p))^{-1} \quad (6)$$

where from,

$$R_{sp} = tg\,(\Theta)/[\sin(L_p/\mu_p)\exp(-L_p/\mu_p) + tg(\Theta)\cos(L_p/\mu_p)\exp(-L_p/\mu_p)] - 1 \quad (7)$$

An inspection of Eq.(7) leads to the conclusion that, one can obtain, in this configuration, the room temperature value of the thermal effusivity of the sample, performing only a frequency scan for the phase of the PPE signal.

EXPERIMENT

The experimental set-up was a classical one, and it was largely described elsewhere [3]. We will give here only some details.

The radiation source was a Spectra-Physics Argon Laser (type 177602, λ = 5.40 μm), and the radiation was modulated by an (Intra Action AOM40 model) acousto-optical modulator. A 7260 EG&G lock-in amplifier was used for data processing, and a PC for data acquisitions. During the measurements the signal to noise ratio was better than 1000. The frequency step was 0.5 Hz. The pyroelectric sensor was a 520μm thick $LiTaO_3$ single crystal in good thermal contact with a 5 mm thick sample.

The measurements were normalised to the data obtained with the empty sensor (both sample and front medium are air), in order to eliminate the influence of the electronics.

RESULTS

A typical plot of Rsp as a function of frequency, for a margarine is presented in Fig.1.

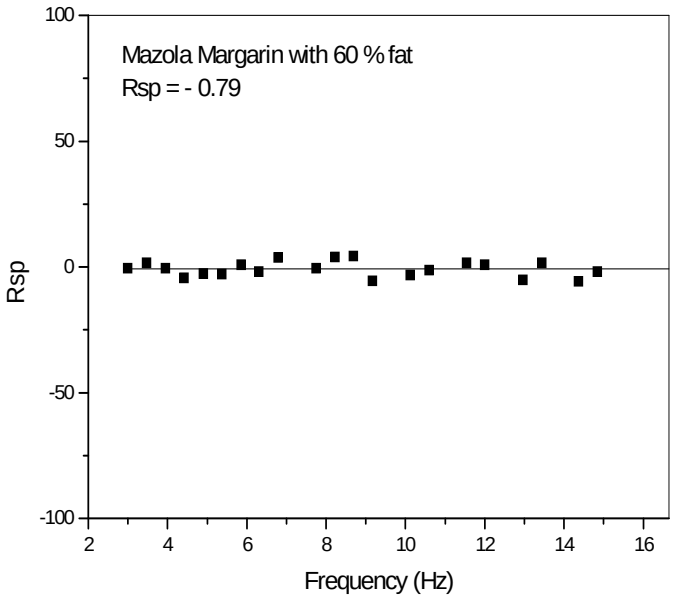

Fig. 1. The frequency behaviour of the reflection coefficient of the thermal waves at the interface sensor/sample for a margarine sample.

In table 1, the values of the thermal effusivity obtained for some Brazilian fats are listed.

TABLE 1.

The room temperature values of the thermal effusivity for some Brazlian oils and margarines.

SAMPLE	MEASURED THERMAL EFFUSIVITY ($Ws^{1/2}/m^2K$)	LITERATURE DATA ($Ws^{1/2}/m^2K$)
WATER	1593	1600
BORAGE OIL	985	
REFINED BORAGE OIL	986	
MAZOLA MARGARINE	526	
MILA MARGARINE	583	

Fig. 2 contains the frequency behaviour of the normalized amplitude and phase for a butter sample. The measurements were performed on the same sample in identical experimental conditions, at about 1 hour time interval. The purpose of this figure is to compare the reproducibility of the results obtained by the amplitude and phase of the PPE signal.

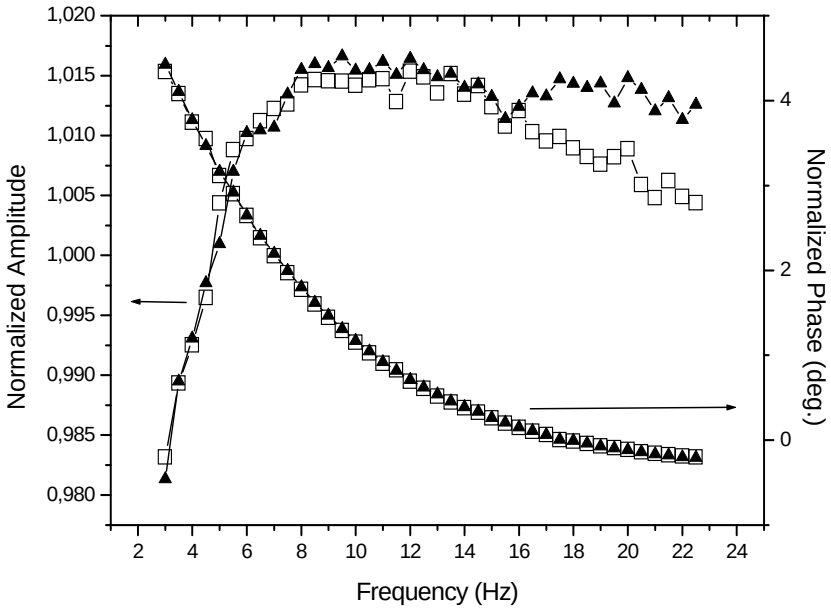

Fig. 2. The frequency dependence of the amplitude and the phase of the PPE signal for the same sample of butter at 1 hour time interval.

CONCLUDING REMARKS

The front (inverse) PPE configuration , with opaque sensor and thermally thick sensor and sample, was used to measure the thermal effusivity of some fats.

There are three main advantages of this configuration, compared with the previously reported inverse configurations (with thermally thin and optically opaque sensor, and thermally thick and semitransparent sensor):

(i) a rigid opaque and thick sensor is easier to be handle than a thin PVDF foil, and it is cheaper than a semitransparent sensor;

(ii) the information (the value of the thermal effusivity) is contained in the phase of the PPE signal and not in the amplitude as usually happens in the inverse configurations, so, the accuracy and reproducibility of the measurement is much better, as revealed by Fig. 2,

(iii) all the components of the detection cell are thermally thick, leading to a very easy selection of the chopping frequency range.

Additionally, as mentioned before, the liquid foodstuffs are very suitable samples for this type of investigations.

REFERENCES

1. M. Marinelli, U. Zammit, F. Mercuri, R. Pizzoferrato, J. Appl. Phys.,**72**, 1906 (1992)
2. D. Dadarlat, M. Chirtoc, C. Neamtu, R. Candea, D. Bicanic, Phys. Stat. Sol **(a) 121**, K231 (1990)
3. D. Dadarlat, D. Bicanic, H. Visser, F. Mercuri, A. Frandas**,** J. Amer. Oil Chem. Soc., part I, **72,** 273 (1995); part II, **72**, 281 (1995)
4. D. Dadarlat, A. Frandas, Appl. Phys. **A56**, 235 (1993)
5. D. Dadarlat, A Frandas, M. Marinelli, F. Mercuri, D. Bicanic, Appl. Phys. **A61**, 183 (1995)
6. A Mandelis, M. M. Zver, J. Appl. Phys., **57**, 4421 (1985)
7. M. Chirtoc, G. Mihailescu, Phys. Rev., **B40**, 906 (1989)
8. S. Delenclos, M. Chirtoc, A. Hadj Sahraoui, C. Kolinsky, J. M. Buisine**,** Analytical Sciences, **17**, s161 (2001)

STUDIA UNIVERSITATIS BABEŞ-BOLYAI, PHYSICA, SPECIAL ISSUE, 2001

APPLICATION OF ELECTROACTIVE POLYPYRROLE FOR METAL UPTAKE

I. PETER, R. TURCU, C. BINDEA, A. BOT

Institutul National de Cercetare-Dezvoltare pentru Tehnologii Izotopice si Moleculare, Cluj-Napoca

ABSTRACT. Conducting polymers like polypyrrole are very promising materials for uptake the metal ions from solution. Polypyrrole is one of the most frequently investigated. This is owing to its ease of preparation relatively high stability compared to other conducting polymer and the ready commercial availability of many of its derivatives.

The electroactive polypyrrole used in this study has been synthesized in the form of nanocomposites using ultra fine SiO_2 particles, through chemical oxidative polymerization of pyrrole in the presence of $FeCl_3$. The rates of metals uptake from acidic solution is indicated by the decrease of the metal concentration in solution, which was determined by atomic absorbtion spectroscopy. The effects of the reduction of metals from acid solution by PPy-SiO_2 nanocomposites are also investigated using UV-VIS absorption spectroscopy.

Our results demonstrate that this simple procedure could be successfully applied for the treatment of industry wastewater containing metal ions of need to be extracted or their concentration lowered, before the effluents can be discharge into the environment.

INTRODUCTION

Polypyrrole (PPY) is one of the extensively investigated conducting polymers that have potential application in many domains.It is one of the most stable known conducting polymers ansd aslo one of the easiest to synthesize.

Recently PPy have been synthesized in the form of nanocomposites using ultra-fine SiO_2 particles. [2,3] This materials have been potential comercial application. [4]

The precipitating conducting polymer coats the sol particles and "glues" them together.

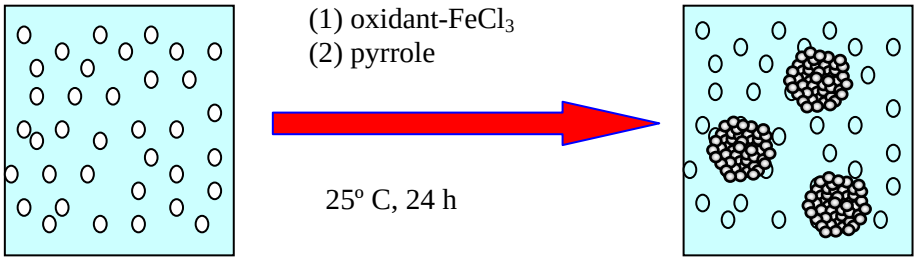

The reaction of pyrrole with $FeCl_3$ is considered follows:

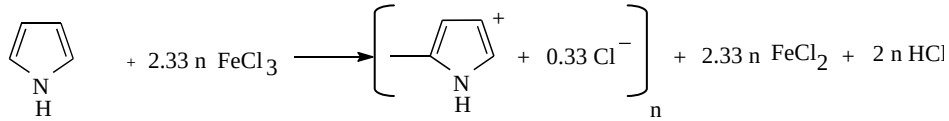

From this reaction one chlorine atom accept one electron from three pyrrole monomer units to became a doping anion.

In this paper we describe the use of these materials for gold uptake. Our interest in these materials stems from the fact that they possess a surface area substantially higher than that estimated from the particle size [4] and hence could aid the process of gold uptake.

EXPERIMENTAL

1.Synthesis of nanocomposites

Reactions at room temperature were carried out as follows: a colloidal silica solution was added to a deionized water a $FeCl_3$ solution, followed by pyrrole. The polymerization was allowed to proceed for 24 h. The resulting reaction solution was centrifuged at 6000 rpp for 30 min, and the supernatant containing the excess silica solution and inorganic byproducts was decanted and discarded. The black sediment was then redispersed in deionized water. This centrifugation – redispersion cycle was repeated three times in order to remove excess non-aggregated silica and soluble (in) organic byproducts.

2. Uptake of gold from solution

The gold uptake experiments were conducted using a range of PPy/gold mole ratios. The volume of nanoparticles suspension added to the chloride solution was calculated from the Py/gold concentration. After the nanoparticles were added to the solution, under constant stirring, samples of the solution were removed at regular intervals for the determination of the gold concentration using atomic absorption spectroscopy.

RESULTS AND DISCUSSION

The synthesis of PPy-SiO_2 was monitored by FTIR spectrometry (fig. 1)

The effects of the reduction of gold from acid solution by PPy-SiO_2 nanocomposites were also investigated using UV-Vis absorption spectroscopy (Fig.2). The absorbance was monitored at 314 nm for gold chloride. The estimation of the gold concentration from UV-VIS spectra is not posible due to the shift of the characteristic absorption band of gold chloride. The shift of this band is attributed to the pH decrease (Fig 3).

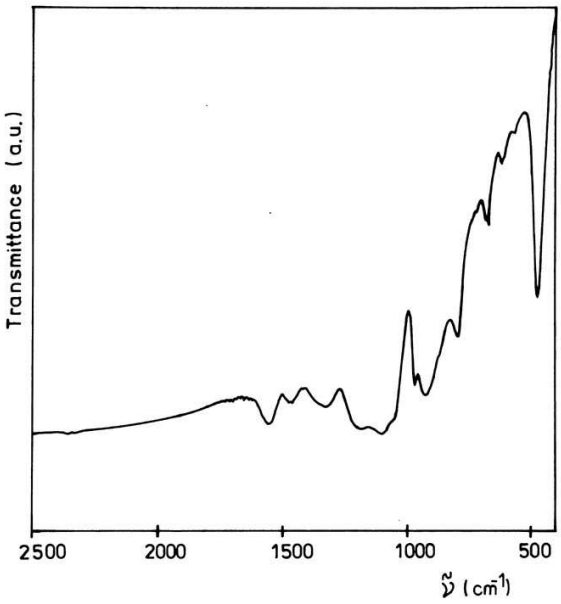

Fig.1. FT-IR spectra of PPy-SiO_2 synhesized by $FeCl_3$

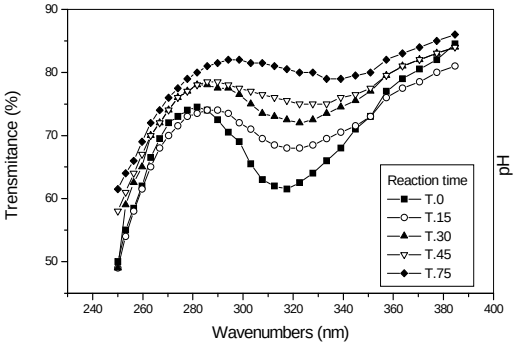

Fig.2 The evidence of gold concentration decrease in the solution containing PPy-SiO_2 nanocomposites

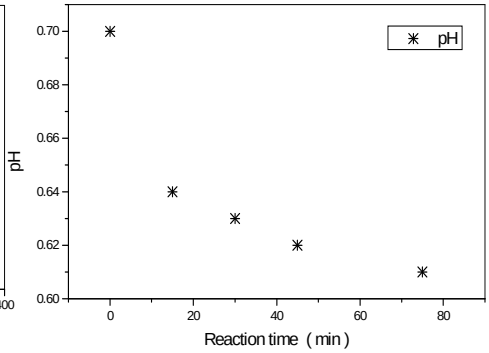

Fig.3. The pH decrease in the gold chloride solution during the metal uptake by PPy-SiO_2

The rates of gold uptake from acidic solution by PPy-SiO_2 indicated by the decrease of the gold concentration was determined by atomic absorption spectroscopy. This decrease is present in Fig. 4. The concentration of gold ions in solution decreased by about 50 % within the first 15-min.

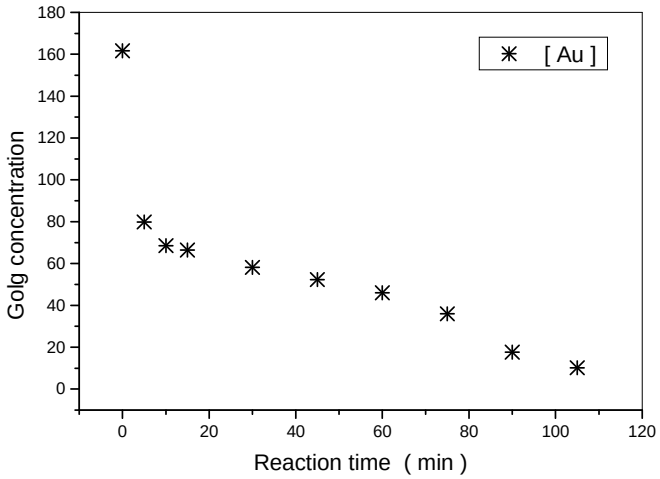

Fig. 4. The decrease of the gold concentration determined by atomic absorption spectroscopy

CONCLUSION

The PPy-SiO_2 nanocomposites posses a high surface area for reaction.
The rate of gold uptake from chloroauric acid by PPy-SiO_2 highly depends on nanocomposites concentration.

The surface Au/PPySiO_2 ratio can be higher or lower than the bulk value depending on the reaction condition.

The results show that the electroactive polypyrrole - SiO_2 nanocomposites represents a potentially useful material for recovery of precious metal.

REFERENCES

1. Terje A. Skotheim, *Handbook of conducting polymers*, vol 1

2. Maeda S, Armes SP, *J Colloid Interfaces Sci*, 1993;**159**:257

3. Gill M, Mykytiuk J, Armes SP, Edwards JL, Yeates T, Moreland PJ, Mollet C, *J Chem Soc*, Chem *Commun*, 1992;**108**:256

4. Maeda S, Armes SP, *Synth Metals*,1995;**73:**151

5. Lascelles SF, McCarthey GP, Butterworth MD, Armes SP, *Colloid Polym Sci*, 1998;**276**:893

STUDIA UNIVERSITATIS BABEŞ-BOLYAI, PHYSICA, SPECIAL ISSUE, 2001

SPECTROSCOPICAL CHARACTERISATION OF PRECURSORS FOR CALCIUM HYDROXIDE SYNTHESIS

CRINA DAN, ELISABETH-JEANNE POPOVICI, LAURA UNGUR, LIGIA PASCU, CRISTINA CIOCAN and RODICA GRECU

"Raluca Ripan" Institute of Chemistry, 30 Fântânele, 3400-Cluj-Napoca, Romania

ABSTRACT. The present work refers to the preparation and characterisation of calcium carbonate and calcium oxide precursors for the manufacture of high quality calcium hydroxide for dentistry use. Calcium carbonate precursors were prepared from high purity calcium chloride and ammonium carbonate as precipitating agents, by using the simultaneous reagent addition technique. The as-obtained precipitates were maturated, washed and dried and finally converted into CaO-precursors. Chemical and thermal analysis, FTIR and UV-Vis spectroscopy were used to characterise both $CaCO_3$ and CaO precursors. The influence of some synthesis conditions on $CaCO_3$ and CaO precursor quality was illustrated.

Key words: calcium carbonate, calcium hydroxide, calcium oxide, dental compositions

1. INTRODUCTION

High quality calcium hydroxide is largely used in dental compositions [1-3]. The present work refers to the preparation and characterisation of $CaCO_3$- and CaO-precursors for the manufacture of calcium hydroxide for dentistry use.

High purity calcium carbonate is usually prepared either by treating $Ca(OH)_2$ solutions or suspensions with CO_2 or by adding ammonium carbonate to calcium containing solutions, by the sequential reagent addition technique[4-6]. Our studies have in view the precipitation of $CaCO_3$ precursor by using the *simultaneous reagent addition technique*. The as-obtained $CaCO_3$-precipitates (precursors # 1) is converted into CaO (precursors # 2) and finally into calcium hydroxide-sample for dental compositions.

In order to establish the correlation between the synthesis parameters and the quality of precursors that can generate $Ca(OH)_2$ product for dentistry use, the intermediates quality is evaluated by thermal analysis and FTIR spectroscopy. In this manner, the influence of synthesis conditions on precursors quality is to be illustrated.

2. EXPERIMENTAL PART

Equal volumes of 1 mol/l solutions of high purity calcium chloride and ammonium carbonate were simultaneously added with constant flow rate (peristaltic pump) into water or 0.1 mol/l $CaCl_2$ solution. The process developed under continuous stirring, at 20 °C or 70° C and the medium acidity was continuously checked with pH sensors. The precipitates were one hour maturated, filtered, well washed and dried at 110°C to give the $CaCO_3$- precursors. These ones were put into un-covered quartz crucibles and were fired at high temperature. After the firing period was over, the CaO containing crucibles were quickly cooled at room temperature, by using P_2O_5+ KOH

filled dryers. By adding small amounts of water, CaO-precursors were converted into high quality (h.q.) $Ca(OH)_2$ samples. In this purpose, special designed device provided with nitrogen atmosphere and stirrer was used.

Precursors characterisation was performed by Atomic Absorbtion Spectroscopy, chemical analysis (EDTA-Na titration), thermal analysis (Paulik Erdely Derivatograph-MOM OD -102) and infrared spectroscopy (JASCO 610 -FTIR Spectrophotometer).

3. RESULTS AND DISCUSSION

Five $CaCO_3$-precursors were prepared by the simultaneous addition of equal quantities of calcium chloride and ammonium carbonate solutions into a bottom solution containing calcium chloride. In addition, one precursor (CC-0) was also prepared by CO_2 (g) and NH_3 (g) simultaneous bubbling into the calcium chloride solution. The general preparation conditions and precursor codification are indicated in table 1.

The as-prepared calcium carbonate samples i.e. precursors # 1 were converted into calcium oxide samples i.e. precursors # 2 and successively into calcium hydroxide products. The main chemical processes are described by equations (1) ÷ (3):

- precipitation stage:

$$CaCl_2 + 2NH_4HCO_3 \longrightarrow CaCO_3 + 2NH_4Cl + CO_2 + H_2O \quad (1)$$

- decomposition stage:

$$CaCO_3 \longrightarrow CaO + CO_2 \qquad \Delta w_{theor} = 43{,}97\% \quad (2)$$

- "hydration" stage

$$CaO + H_2O \longrightarrow Ca(OH)_2 + Q \quad (3)$$

Depending on precipitation conditions (medium pH and temperature, reagent ratio, bottom solution composition), some other by-products could be formed beside $CaCO_3$.

Supposing that $Ca(OH)_2$ or $Ca(HCO_3)_2$ are also formed during the precipitation stage, the thermal decomposition could proceed as follows:

$$CaCO_3 \cdot xCa(OH)_2 \longrightarrow (1+x)CaO + CO_2 + xH_2O \qquad \Delta w < 43{,}97\% \quad (4)$$

$$CaCO_3 \cdot yCa(HCO_3)_2 \longrightarrow (1+y)CaO + (2y+1)CO_2 + yH_2O \qquad \Delta w > 43{,}97\% \quad (5)$$

Table 1.

The main preparation conditions and the as -obtained precursor codes

Code	$CaCO_3$ – Precursor # 1					CaO – Precursor # 2	
	Precipitation / maturation conditions					Firing regime	Code
	Bottom solution	$\bar{pH}$	Thermal regime (°C)		η (%)		
			Precipitation	Maturation			
CC-0	$CaCl_2$ (1M)	-	20	20	78.8	1000 °C	**CO-0**
CC-1	$CaCl_2$ (0.1M) pH=6.75	7.77	20	20	80.6	1000 °C	**CO-1**
CC-2	$CaCl_2$ (0.1M) pH=6.75	7.65	20	100	72.0	1000 °C	**CO-2**

Code	$CaCO_3$ – Precursor # 1					CaO – Precursor # 2	
	Precipitation / maturation conditions						
	Bottom solution	$\overline{pH}$	Thermal regime (°C)		η (%)	Firing regime	Code
			Precipitation	Maturation			
CC-3	$CaCl_2$ (0.1M) pH=8.5	6.00	75	100	81.0	1000 °C	**CO-3**
CC-4	$CaCl_2$ (0.1M) pH=8.5	6.57	75	100	92.2	1000 °C	**CO-4**
CC-5	H_2O pH=5.75	7.30	75	100	79.5	1000 °C	**CO-5**

Obs. Precipitation of CC-4 and CC-5 was performed with 25% NH_4HCO_3 in excess .

AAS- method confirmed that $CaCO_3$- and CaO-precursors contain under 10^{-4} % Fe, Cu and Pb. In these condition, h.q. $Ca(OH)_2$ could be generated during the hydration stage. The calcium salt conversion into $CaCO_3$ and CaO, evaluated by *chemical analysis* varies between 72.0 % (CC-2 precursor) and 92.2% (CC-4 precursor).

The *thermal analysis* data (table 2) indicate that, in our work conditions, three $CaCO_3$ precursor categories were obtained i.e.:

- CC-0 precursor is characterised by a relative high decomposition temperature (965 °C) and a weight loss (Δw) slightly higher then the theoretical value;
- CC-1, CC-2 and CC-3 precursors are characterised by strong endothermic effects at 950 - 960 °C and $\Delta w < \Delta w_{theor}$; $Ca(OH)_2$ traces are probable contained.
- CC-4 and CC-5 precursors are characterised by a relatively low decomposition temperature (920-935°C) and $\Delta w > \Delta w_{theor,}$ thus suggesting $Ca(HCO_3)_2$ traces; additional decomposition stage could be observed at 440÷460 °C (HCO_3 decomposition).

Table 2.

Thermal analysis data for various $CaCO_3$-precursors types.

Code	*Weight loss*			*Thermal effect*		
	Temperature domain (^{0}C)	T max (^{0}C)	Δw (%)	Temperature domain (^{0}C)	T max (^{0}C)	Effect nature
CC-0	745-1000	955	44,28	805 -	965	endothermic
CC-1	640-960	940	43,92	850 -	950	endothermic
CC-2	605-980	950	43,71	860 -	960	endothermic
CC-3	650-980	940	43,71	855 -	950	endothermic
CC-4	380-520 650-950	440 920	1,16 43,33	800 -	920	endothermic
CC-5	420-520 650-940	460 910	1,16 43,33	820 -	935	endothermic

Infrared spectroscopy illustrate the difference between various precursor characteristics such as CaO-sensitivity to atmospheric H_2O and CO_2 (figure 1 and 2) or aragonite/ calcite ratio into the $CaCO_3$-precursors (figure 3 and 4).

The main absorbtion band of $CaCO_3$-precursors are situated at 3640 cm^{-1} (absorbed H_2O), ~2510 cm^{-1} (HCO_3); 1458, 1422.7, 876 and 712.5 cm^{-1} (CO_3). Thermal decomposition gives relatively "clean" CaO-products; CO-3 sample is relatively more sensitive to both atmospheric H_2O and CO_2.

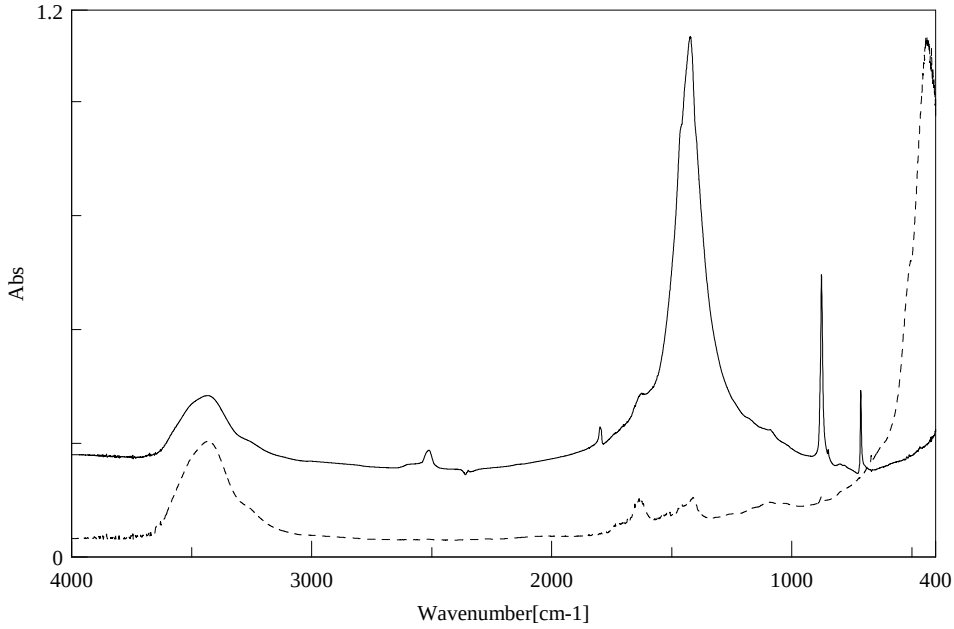

Figure 1. FT-IR spectra of precursors CC-0 calcium carbonate (—) and CO-0 calcium oxide (----).

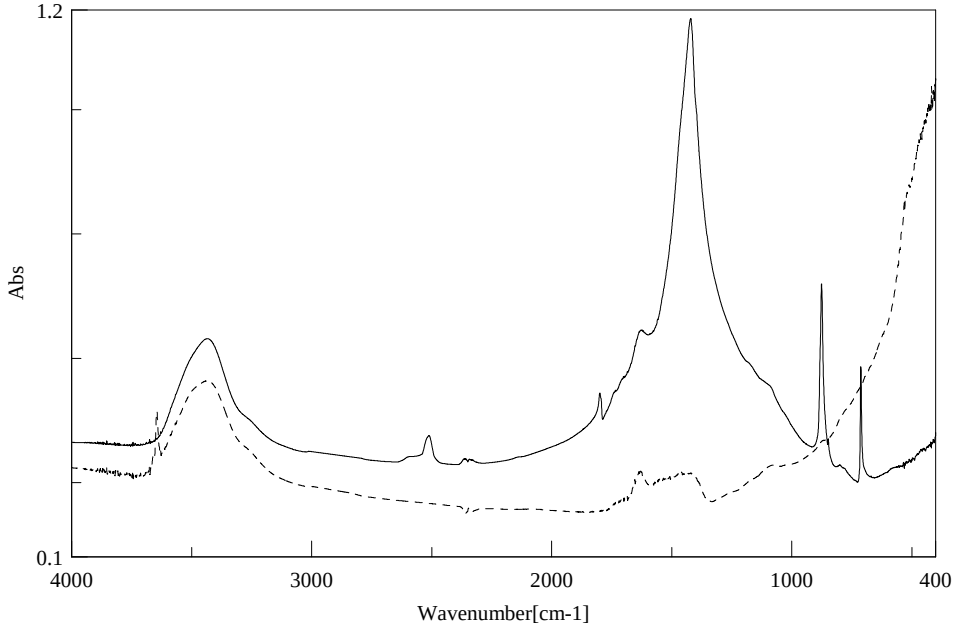

Figure 2. FT-IR spectra of precursors CC-3 calcium carbonate (—) and CO-3 calcium oxide (---).

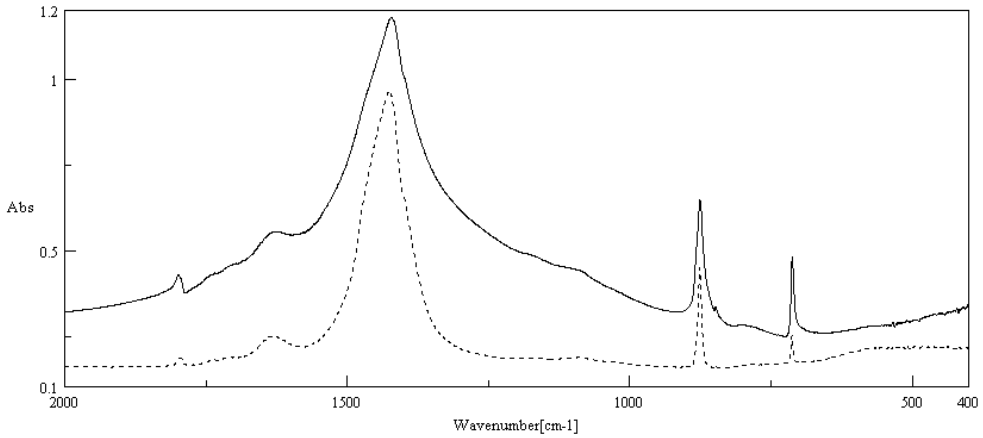

Figure 3. FT-IR spectra of calcium carbonate precursor CC-3 (—) and CC-1 (---) samples

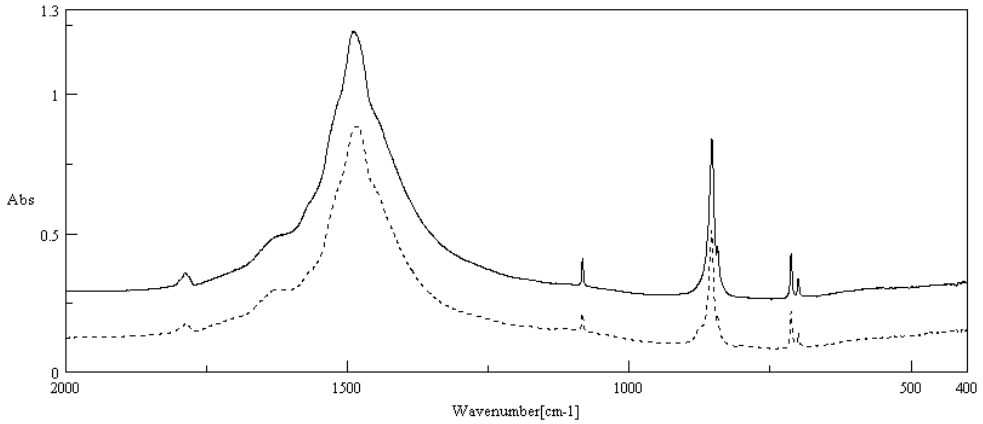

Figure 4. FT-IR spectra of calcium carbonate precursors CC-4 (—) and CC-5 (---) samples

The width of the CO_3 specific absorbtion band (~1485 cm^{-1}) depends on thermal precipitation regime. One presumes that the structural disorder degree of precursors is responsible for the shape of the CO_3 band of the carbonate samples. It is well known that the aragonite structure show two bands at 1492 and 1504 cm^{-1} whereas calcite modification show only one band at 1429 ÷ 1492 cm^{-1}. As a result, the aragonite-rich samples (prepared in warm solution and with ammonium carbonate surplus) show larger CO_3- bands then the calcite-rich ones (obtained in cold solution).

The lowest aragonite content seems to be in the CC-0 sample whereas the highest one appears in CC-4 and CC-5. This relatively higher structural disorder could be the cause of the relative low decomposition temperature (see table 2). By comparing the results, one can conclude that $CaCO_3$ precipitate prepared at 75/100 °C, in calcium chloride bottom solution with a medium pH of 6.57, is the most convenient precursor for the conversion sequence $CaCO_3 \rightarrow CaO \rightarrow Ca(OH)_2$ for dentistry purposes.

REFERENCES

1. Moszner, N., Salz, U. and Rheinberger, V., *U.S. 5733968* (March, 1998).

2. Shibuya, M., Ishii, S., *US 5236496* (August 1993).

3. Dietz G., Barth H.H., *U.S. 4311528* (January 1982).

4. Ota, Y., Inui, S., Iwashita T., *Jpn.Kokai Tokkyo Koho JP 04 46013* (February 1992), cf. CA 116, 258553.

5.Yu, H., Xiong, H., *Faming Zhuanli Shenquing Gongkai, Shuomingshu CN 1 150 125* (May 1997), cf. CA 131, 312 212.

6.Valiullin, A.K., Rastorgueva, K.V., Satrigunov, F.I., *SU 1685871* (October 1991).

STUDIA UNIVERSITATIS BABEŞ-BOLYAI, PHYSICA, SPECIAL ISSUE, 2001

RESIDUAL DIPOLAR COUPLINGS IN CROSSLINKED ELASTOMERS INVESTIGATED BY MAGNETIC EXCHANGE NMR

XENIA FILIP, C. FILIP[1], D.E. DEMCO[2]

National Institute for R&D of Isotopic and Molecular Technologies, P.O.Box 700, R-3400 Cluj-Napoca, Romania
[1]Francis Bitter National Magnet Laboratory, MIT, Cambridge, Massachusetts
[2]Institute of Technical Chemistry, RWTH Aachen, Germany

ABSTRACT. Solid-state one-dimensional proton magnetization-exchange is used to investigate intergroup residual dipolar couplings in cis-1,4-polybutadiene and poly(styrene-co-butadiene). A three spin model is employed, in which the CH – and CH_2 – group are considered to be coupled by residual dipolar interactions.

1. Introduction

Crosslinking of technical elastomers is of crucial importance for the mechanical properties of rubber products. From the viewpoint of NMR, crosslinked elastomers exhibit both solid- and liquid-like features. The presence of topological constrains and permanent crosslinks in these materials leads to a non-zero average of anisotropic spin interactions, such as dipole-dipole couplings. In this work one uses solid-state NMR magnetization exchange for investigating intergroup residual dipolar couplings in cis-1,4-polybutadiene and poly(styrene-co-butadiene) (SBR 1500) elastomers.

2. Spin-system model

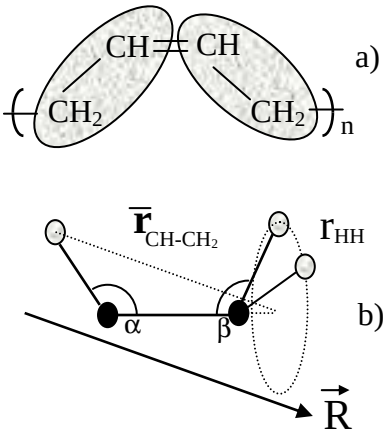

Fig.1.The CH-CH_2 spin system

The model which will be considered in the following to describe the proton magnetization-exchange in cis-1,4-polybutadiene and SBR 1500 is based on the following assumptions and properties of the polymer chain:

i) SBR 1500 is a copolymer with 23.5% styrene units and 76.5% butadiene units distributed in a random sequence [1]. The majority of functional groups ($a \equiv CH_2$, $b \equiv$ CH) are arranged in a pair sequence *aabbaa*…. This pair sequence is present also in cis-1,4-polybutadiene. The alternating sequence *abab*… is less frequent. The relevant spin system is depicted in Figure 1a.

ii) Chemical crosslinks lead to restrictions of the chain motions and hence to a non-zero average of the dipolar interactions between the protons of the CH_2 – and CH – group along the chain. Depending on the degree of motional averaging,

these residual dipolar interactions may be scaled to quite small values. They reflect single-chain properties because the fast molecular motions of the polymer chains effectively average the interchain dipolar interaction [2]. The validity of these assumptions was proven by a 2D magnetization-exchange experiment performed with a short mixing time [3].

iii) Fast anisotropic molecular motions lead to partially narrowed static proton spectra. At room temperature, two lines are resolved in the static proton spectrum (for cis-1,4-polybutadiene and SBR 1500). One line corresponds to the CH-groups and the other to the CH_2- groups.

iv) The dipolar couplings between two neighboring CH groups or two neighboring CH_2 groups, respectively, are not relevant with respect to measurements of the magnetization-exchange dynamics at short mixing times [4,5].

In conclusion, the measurable exchange of longitudinal proton magnetization predominantly takes place between the protons belonging to nearest-neighbor CH– and CH_2– groups. The spin system that has to be considered for describing this process thus is a three-spin system in which the two strongly coupled protons of the CH_2-group interact with the remote proton of CH-group. At longer mixing times, however, a much larger spin system along the polimer chain must be considered.

3. **Magnetization-exchange observables**

In the rotating-frame representation the Hamiltonian for a static sample (characterized by the three spin system model described before) is:

$$H = H_z^{CH} + H_z^{CH_2} + \overline{H}_d^{CH_2} + \overline{H}_d^{CH-CH_2} \tag{1}$$

The chemical-shift anisotropy and heteronuclear couplings are neglected. Thus the Zeeman Hamiltonians are:

$$H_z^{CH} = -\Delta\omega_{CH}\, I_z \qquad H_z^{CH_2} = -\Delta\omega_{CH_2}\, F_z \tag{2}$$

where $\Delta\omega_i = (\omega_0 + \delta_i) - \omega$, for $i \equiv$ CH or CH_2. The spin operator for the proton of the CH–group is denoted by **I** and the spin – pair represented by the methylene protons can be replaced by a quasi-particle with spin F = 1 and o total spin operator $\mathbf{F} = \mathbf{I_1} + \mathbf{I_2}$. The intra- and intergroup residual dipolar Hamiltonians may be expressed in secular approximations as [6]:

$$\overline{H}_d^{CH_2} = \overline{d}^{CH_2}\, Y_{2,0}(\Omega) T_{2,0}^{CH_2}; \quad \overline{H}_d^{CH-CH_2} \cong \overline{d}^{CH-CH_2}\, Y_{2,0}(\Omega) T_{2,0}^{CH-CH_2} \tag{3}$$

where $\overline{d}^{j}$ (j ≡ CH_2, CH-CH_2) denote the strengths of the residual dipolar couplings. The spherical harmonics $Y_{2,0}(\Omega)$ depend on the azimuthal angle between the local chain vector $\vec{R}$ and the direction of the magnetic field $\vec{B}_0$. $T_{2,0}^{j}$ are irreducible tensor-operators. The distance between the functional groups is fluctuating due to local conformational jumps. Therefore, the CH-CH_2 dipolar coupling of the protons is approximated by the dipolar coupling between the CH-proton and an effective spin 1 nucleus located at an average distance $\vec{r}_{CH-CH_2}$ (cf. Fig.1b).

In the 1D-version of the magnetization-exchange experiment, the separation of the NMR lines enables one to apply a chemical-shift filter [7] in order to select the longitudinal magnetization of either CH– or CH_2– group. The sequence starts with an evolution period that acts as a chemical-shift filter by an appropriate choice of the rf-irradiation frequency and the duration t_1. The remaining transverse magnetization after the second 90° pulse and the excited multiple-quantum coherences are removed from the aquired signal by phase cycling ant the application of a short gradient pulse of duration t_d, where $t_d \le t_m$ (cf. Fig.2). As an example, the selection of the CH signal (for cis-1,4-polybutadiene) is shown in Fig.3. After a mixing time of t_m=15ms magnetization exchange is complete and the CH_2 signal is fully recovered at the expense of the CH intensity.

The CH – or CH_2 – group is selected by the conditions:

$$\text{CH:} \quad \Delta\omega_{CH} = 0, \quad \Delta\omega_{CH_2} t_1 = \pi/2 \qquad \rho^{CH}(t_1) = a I_z \tag{4}$$

$$\text{CH}_2\text{:} \quad \Delta\omega_{CH_2} = 0, \quad \Delta\omega_{CH} t_1 = \pi/2 \qquad \rho^{CH_2}(t_1) = a\left\langle \cos\left(\sqrt{\frac{3}{2}}\,\overline{D}^{CH_2} t_1\right)\right\rangle F_z \tag{5}$$

where $\rho^i(t_1)$ (i = CH, CH_2) are the density operators at the beginning of the mixing period, *a* is the prefactor of the density operator of thermal equilibrium in the high-field/high temperature approximation, $\overline{D}^{CH_2} \equiv \overline{d}^{CH_2} Y_{2,0}(\Omega)$. The symbol $\langle ... \rangle$ represents the statistical ensemble average [7] of the space part of the dipolar coupling in the disordered elastomer.

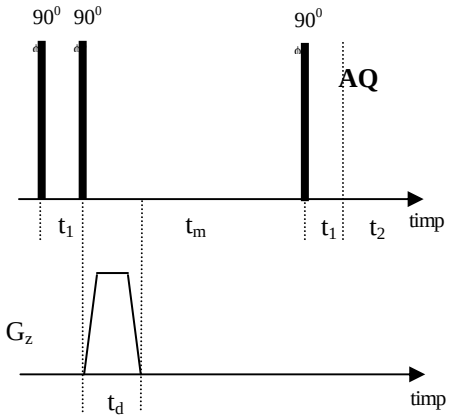

Fig.2. Basic scheme for magnetic-exchange spectroscopy

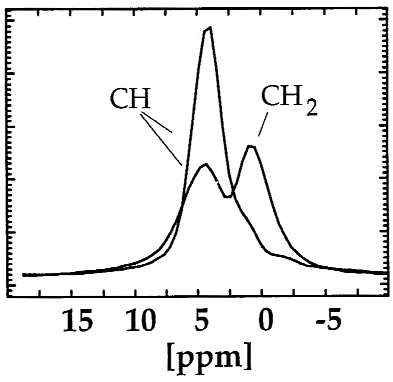

Fig.3. Proton spectra of cis-1,4-polybutadiene recorded in D magnetization-exchange experiments

The NMR observables of the 1D magnetization-exchange experiment with chemical-shift filter are:

$$\left\langle\left\langle I_z(t_m)\right\rangle\right\rangle = \left\langle \frac{Tr\left\{I_z\rho^{CH}(t_m+t_1)\right\}}{Tr\left\{I_z\rho^{CH}(t_1)\right\}}\right\rangle; \left\langle\left\langle F_z(t_m)\right\rangle\right\rangle = \left\langle \frac{Tr\left\{F_z\rho^{CH_2}(t_m+t_1)\right\}}{Tr\left\{F_z\rho^{CH_2}(t_1)\right\}}\right\rangle \quad (6)$$

which, in the limit of short mixing time, $\left(3\left\langle\overline{D}^{CH_2}\right\rangle - \delta\right)t_m << 1$ transforms to:

$$\left\langle\left\langle I_z(t_m)\right\rangle\right\rangle = 1 - \frac{1}{2}\left\langle\left(\overline{D}^{CH-CH_2}\right)^2\right\rangle t_m^2; \left\langle\left\langle F_z(t_m)\right\rangle\right\rangle = 1 - \frac{1}{4}\left\langle\left(\overline{D}^{CH-CH_2}\right)^2\right\rangle t_m^2 \quad (7)$$

where $\overline{D}^{CH-CH_2} \equiv \overline{d}^{CH-CH_2}Y_{2,0}(\Omega)$. In this short mixing time, the initial decay rates depend only on the intergroup residual dipolar coupling. The longitudinal magnetization transfer from CH to CH_2 is twice as fast as that from CH_2 to CH.

4. **Experimental results**

The investigated elastomers systems are based on a cis-1,4-polybutadiene and SBR 1500 synthetic rubbers. The NMR experiments were performed at a ^{1}H frequnecy of 300 MHz on a Bruker MSL spectrometer using a variable temperature probe.

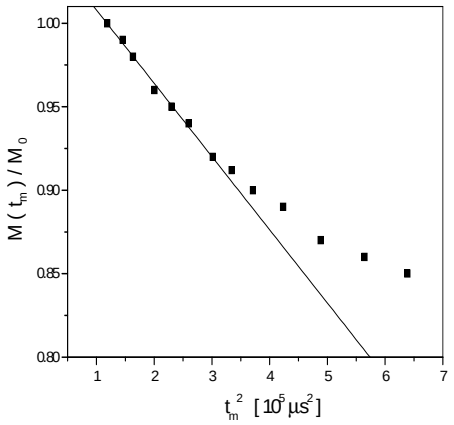

Fig.4. The initial decay of proton magnetization for cis-1,4-polybutadiene

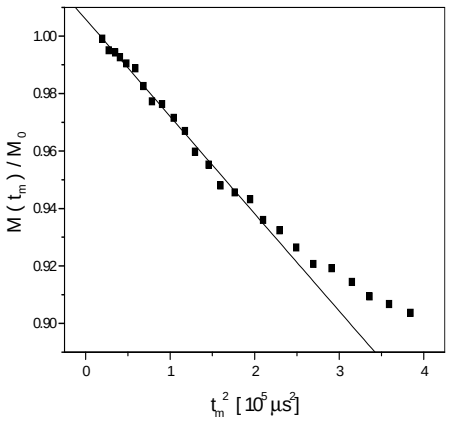

Fig.5. The initial decay of proton magnetization for SBR 1500

The decay of the longitudinal magnetization $M(t_m)$ normalized to the value M_0 that corresponds to zero mixing time, is recorded for short mixing times using the CH chemical-shift filter. According to Eq.(7), the magnetization-exchange dynamics should show an initial quadratic dependence on t_m. This dependence indeed is found in the experiments and is shown in Fig.4 (cis-1,4-polybutadine) and Fig.5 (SBR 1500). The solid-like behavior of the magnetization decay is valid for mixing times $t_m << \left(3\left\langle\overline{D}^{CH_2}\right\rangle - \delta\right)^{-1}$. This expression can be estimate using data of protonic spectrum

(the line width at half-intensity and the distance from lines). A deviation from the t_m^2 dependence is expected for mixing times t_m > 500 μs (for cis-1,4-polybutadiene) and t_m > 400 μs (for SBR 1500). This deviation is confirmed by experiments (Figs. 4 and 5).

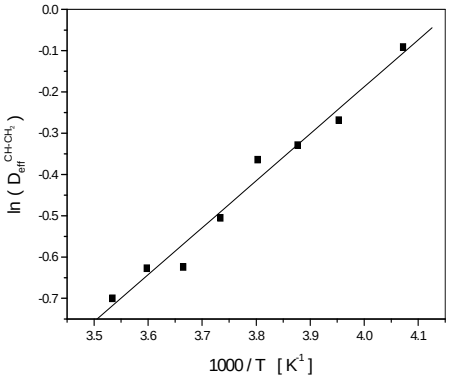

Fig.6.

Defining the efective dipolar coupling constant as $D_{eff}^{CH-CH_2} \equiv \left\langle \left(\overline{D}^{CH-CH_2} \right)^2 \right\rangle^{1/2}$, this can be evaluate from the initial magnetization decays in the 1D exchange experiments. The measuremnets of $D_{eff}^{CH-CH_2}$ versus temperature (for cis-1,4-polybutadiene) is presented in Fig.6. In the investigated temperature range 245-285 K, the temperature dependence can be in a good approximation fitted with an exponential function. Finally based on a gaussian distribution [8] of polymer chains where $D_{eff}^{CH-CH_2} \propto N^{-1}$ [7], one can readily extract the temperature dependence of the crosslink density, N.

5. **Conclusions**

In this work it was shown that proton NMR magnetization exchange experimets are very well suited to probe small intergroup rezidual dipolar couplings in elastomers. For the investigated systems it was demonstarted that in the short mixing-time limit the measurable exchange of longitudinal proton magnetization predominantly takes place between the protons belonging to nearest-neighbor CH– and CH_2– groups. Within this regime the residual dipolar couplings and hence the cross link density in cis-1,4-polybutadiene and poly(styrene-co-butadiene) were accurately determined. At longer mixing times, however, a much larger spin system along the polymer chain must be considered.

REFERENCES

[1] J.A. Brydson, *Rubber Chemistry*, Applied Science Publishers, London, 1978

[2] J.P. Cohen-Addad, A. Viallat, Ph. Huchot, *Macromolecules*, **20**, 2146 (1987)

[3] P. Sota, C. Fulber, D.E. Demco, B. Blumich, H.W. Spiess, *Macromolecules* **29**, 6222 (1996)

[4] D.E. Demco, S. Hafner, C. Fulber, R. Graf, H.W. Spiess, *J. Chem. Phys.* **105**, 11285 (1996)

[5] J.P. Cohen-Addad, *J. Chem. Phys.* **63**, 4880 (1975)

[6] J.P. Cohen-Addad, *J. Chem. Phys.* **60**, 2440 (1974)

[7] K. Schmidt-Rohr and H.W. Spiess, *Multimdimensional Solid-State NMR and Polymers*, London, Academic Press, 1994

[8] M. Todica, *Fizica polimerilor*, Babes-Bolyai Univ., Physics Faculty, Cluj-Napoca 1996

STUDIA UNIVERSITATIS BABEŞ-BOLYAI, PHYSICA, SPECIAL ISSUE, 2001

MICROWAVE POWER ASSISTED SAMPLE PREPARATION. EXTRACTION STUDIES

E.SURDUCAN, CAMELIA NEAMTU, V.SURDUCAN, GABRIELA NAGY, S.FILIP

National Institute for Research and Development of Isotopic and Molecular Technologies, P.O.Box 700, 3400 Cluj Napoca 5, ROMANIA.

The nonconventional microwave power sample preparation is a well-known method. Our purpose is to use the microwave field distribution to perform probe extraction using nontoxic polar solvents. This is a new technique because in the classical microwave samples preparation nonpolar solvents, most of them toxic, are used.

This paper presents our studies on extractions from natural samples by the microwave power-assisted method, in polar and nonpolar solvents.

1. PRINCIPLES OF THE MICROWAVES EXTRACTION PROCESS

The microwave extraction is based on the selectivity of the microwaves absorption in materials. The key of this selectivity is the permittivity loss (or the loss tangent) of the materials irradiated by microwaves. The interaction microwaves-matter is characterized by the relative dielectric permittivity :

$$\varepsilon = \varepsilon' - j\,\varepsilon'' \qquad j = (-1)^{1/2} \qquad tg(\delta) = \varepsilon''/\varepsilon' \qquad \textbf{(1)}$$

where:

- ε' is the relative permittivity of the material and represents the amount of microwave energy cumulated in the material by dipoles orientations (or dipole structures orientations);
- ε'' is the permittivity loss and represents the microwave energy lost in different conductive processes or by the dipoles vibrations;
- $tg(\delta)$ is the loss tangent;

The expression of the microwave power absorbed in the unity volume of the material is:

$$P_a = \omega\varepsilon_o\,\varepsilon'\,tg\delta\,E_i^2 \quad \text{or} \quad P_a = 2\pi f\,\varepsilon_o\,\varepsilon''\,E_i^2 \quad \text{in } (W/m^3) \qquad \textbf{(2)}$$

where: $\varepsilon_o = 8.856\ 10^{-12}$ F/m; E_i - internal electric field (in the material), proportional with the incident microwave power; f - microwave frequency; ω - microwave pulsation.

If we assume that all the absorbed microwave power is transformed in heat, the raising rate of the material temperature is:

$$(\Delta T/\delta t) = (\omega\varepsilon_o\,\varepsilon'\,tg\delta\,E_o^2)/\rho cv \qquad \textbf{(3)}$$

where ΔT is the temperature rise in the δt time, ρ is the density of the material, in Kg/m^3, and c is the specific heat of the material, in J/Kg^oC.

If a mixture of different materials is irradiated with microwave power, the microwave absorption and the local rise of temperature would be selective for the different values of the permittivity of the constituents. This is an important fact in the microwave extraction process. Usually, the natural probe, from which we intend to extract one component, is immersed in a nonpolar solvent (microwave loss-less). By microwave irradiation, the temperature rising rate of the natural probe is bigger then that of the solvent (usually by one or two magnitude orders) and the natural tissues (vegetal or animal) are broken up. The different temperatures between the probe and the solvent determine a local convection, which favorises the transport of the component (esther, volatile oil, organic oil, etc.), in the solvent [1,2,3].

2. USING THE MICROWAVE FIELD DISTRIBUTIONS TO STIMULATE THE CONVECTION IN THE EXTRACTION PROCESS

Most of the nonpolar solvents used in the classical microwave samples preparation are toxic (one of the usual solvent is the hexane). This is an inconvenient for the alimentary use of the end product, even after multiple steps distillations. This is one of the reasons of the present research.

The common alimentary solvents are polar (water, alcohol) with high microwaves loss. The use of these solvents destroy the local convection in the process of extraction. One way to restore the convection is to use the microwaves particular distribution in the extraction cell. It is well known that in the microwave cavities the microwave field has a specific distribution of the power with local maximums. These microwave distributions imply local maximums distribution of temperature in a homogenous material and local convection processes.

In our experiments we used a coaxial cavity. In Figure 1 is presented the microwave field pattern [4] in the longitudinal plane of the cavity for the following cases: (1) empty coaxial cavity, (2) coaxial cavity with Teflon vessel, vessel filed with (3) ethanol, (4) 3% acetic acid, (5) water. The figure presents also the schematic microwave circuit used in the extraction experiments .

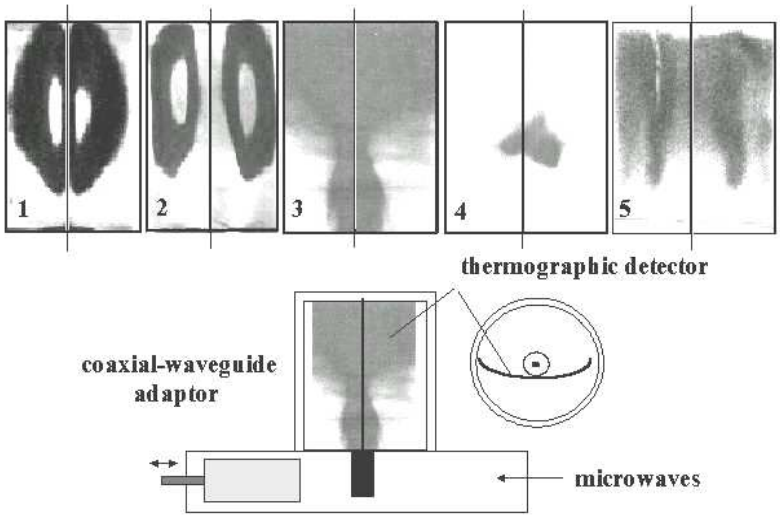

FIG. 1

3. EXTRACTION STUDIES

The extraction studies were done on *pelargonium zonale* green leaves using eight solvents, five of them polar (distilled water, ethanol, 3% acetic acid, isopropylic alcohol, acetone) and three nonpolar (hexane, benzene, petroleum ether).

Our purpose was to establish the optimal microwave extraction parameters and to compare the results with the classical method of extraction by studying the optical absorption spectra of the extraction compounds. The microwave treatment cell configuration for a six cells arrangement is presented in Figure 2. In this experiment a coaxial cavity with eight Teflon cells of 1ml each was used.The 0.025g of probe (rectangular shape) and 1ml of solvent were put in each Teflon cell. The microwave treatment parameters are:

- microwave power: 80W at 2.45 GHz;
- exposure time: 10 min in sequences of 5s ON power, 24s OFF power.

A photo of the probes after microwave irradiation is presented in fig.3.

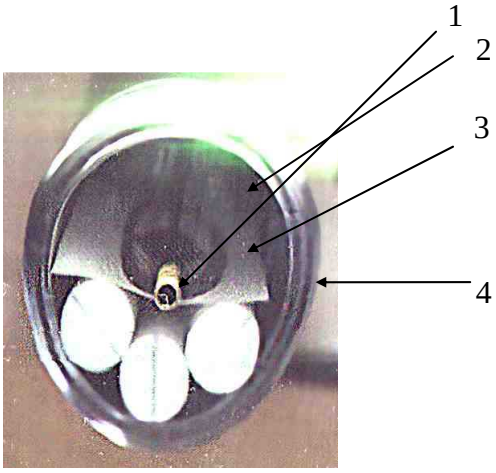

FIG.2 Coaxial cavity with six Teflon cells; 1- coaxial line, 2- thermographic detector; 3 - Teflon cell; 4- coaxial cavity;

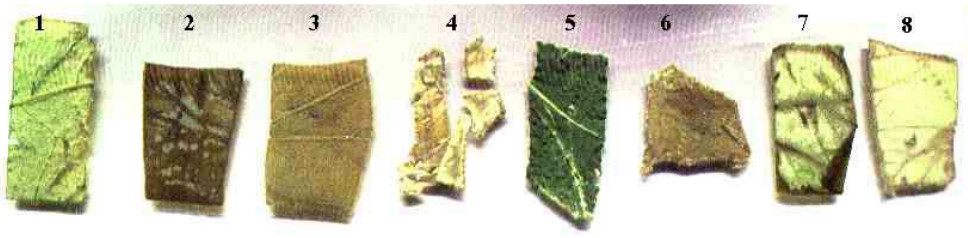

Fig.3 *Pelargonium zonale* leaves after extraction in: 1- ethanol, 2- 3% acetic acid, 3-n-hexane, 4- acetone, 5- isopropylic alcohol, 6- benzene, 7-distilled water, 8- petroleum ether.

The UV-VIS spectrophotometric analyses evidentiate the presence of **chlorophyll** (460nm) and **menthol** (275nm) in the extraction compound.

Figures 4 and 5 present the chlorophyll and menthol extraction in various solvents from samples of *Pelargonium* green leaves after different treatments.The corresponding periods of maceration are T_1=115 min and T_2 = 10s.

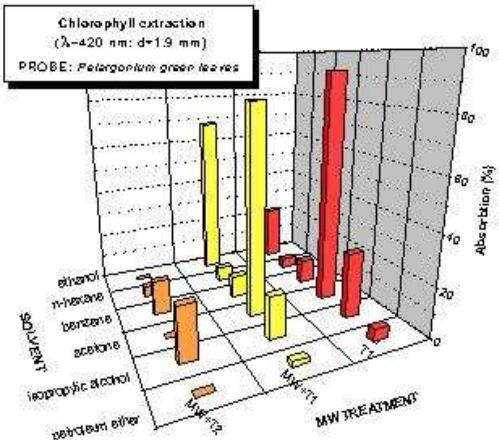

FIG.4 Chlorophyll extraction in various solvents from samples of *Pelargonium* green leaves after different treatments (from right to left): *(T1)* after a maceration time T1; *(MW+T1)* after a microwave-assisted treatment, followed by a maceration time T1; *(MW+T2)* after a microwave-assisted treatment, followed by a maceration time T2<T1.

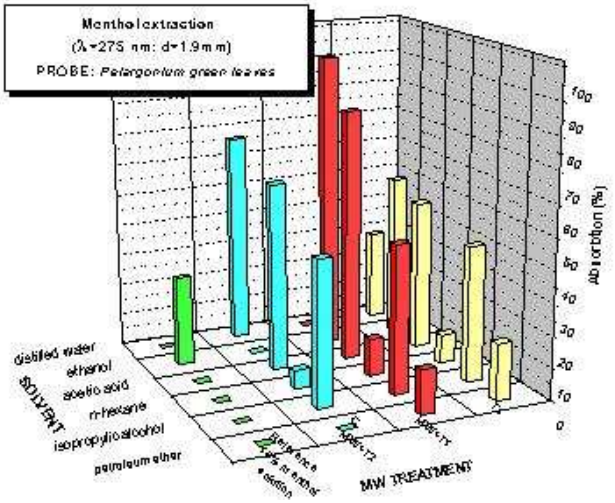

FIG.5 Menthol extraction in various solvents from samples of *Pelargonium* green leaves, after different treatments (from right to left): *(T1)* after a maceration time T1; *(MW+T1)* after a microwave-assisted treatment, followed by a maceration time T1; *(MW+T2)* after a microwave-assisted treatment, followed by a maceration time T2<T1; *(Reference 10% menthol solution)* reference sample of 10% menthol solution in ethanol.

The effect of the microwave irradiation is enhanced for ethanol. No chlorophyll is extracted in distilled water and 3% acetic acid.

4. CONCLUSIONS

Our experiments prove that the microwave extractions offer better or comparable efficiences of extraction at shorter or comparable periods of time, if the proper solvent is chosed for a specific product. For menthol extraction, the microwave method offers a better efficiency for all solvents used. Particularly, the good efficiency of 3% acetic acid extraction of menthol represents the achievement of our initial purpose.

From this experiments it is not possible to compare polar-nonpolar solvents extraction in the microwave technique.

Also, in order to establish a microwave-assisted extraction technology, further work is necessary.

REFERENCES

1. D. Barclay, Today's Chemist at Work, 9(3), 40 (2000)
2. J.R.Pare, "Microwave-assisted extraction from materials containing organic matter", US patent 05458897/1995
3. E.Surducan, V.Surducan, S.V.Filip, C.Neamtu, Balkan Phys. Lett. 5, 235 (1997)
4. E.Surducan, V.Surducan " Traductor termografic pentru radiatie de microunde de putere", brevet RO 116506 B1/2001

STUDIES OF THE MICROWAVE DISTRIBUTIONS IN MICROWAVE POWER APPLICATIONS

E.SURDUCAN, V.SURDUCAN, CAMELIA NEAMTU

National Institute for Research and Development of Isotopic and Molecular Technologies, P.O.Box 700, 3400 Cluj Napoca 5, ROMANIA

The microwave power applications are very attractive because of the energy saving rate (2 to 100 comparatively with classical processes). The microwave technologies are very elaborate and specific to the nature of the treated materials. One of the most important facts in the elaboration of the technology is the microwave field distribution in the reaction chamber.

This paper presents three categories of applications and the specific microwave field distributions studies: the microwave power adaptations, the microwave field distributions in the cavities of microwave plasma generators and microwave cavities for chemical applications and samples preparation.

1. INTRODUCTION

To achieve the microwave power field distributions images we used one **microwave termographic transducer,** Romanian patent [1](fig.1). This transducer is a composite of three materials :

- ***dielectric support*** (1b),
- ***thermographic substance*** (1a) and
- ***microwave absorber*** substance (1c).

One of the transducer structure looks like a thin film white paper .To obtain the images of the microwave power field distribution, the transducer is introduced in the microwave lines (circuits or cavities) and is exposed to the microwave a time of 5 to 120 seconds, depending on the value of the incident power. The images are black and white colour and are very easy to interpret (fig.)

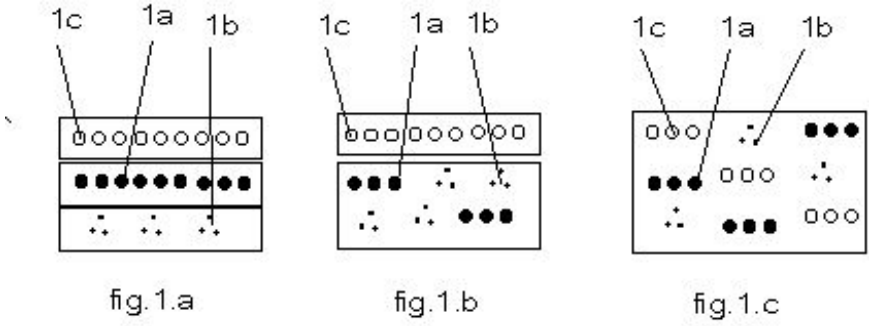

FIG.1

2. THEORY

For microwaves power applications it is desirable to know the field pattern in microwave cavity (with or without probe), or in (or on surface of) dielectric material placed in microwave cavity. For this purpose, thermography is a convenient measurement method because there is no need for a probe to measure the E-field, and entire cross-section of the cavity / microwave lines, or surface of the dielectric material, can be observed simultaneously by thermal effect of microwave power. Thermographic method used an microwave absorber mixture, on sheet form, which temperature rise according to (1) and make colors modifications in absorber mixture, in IR or visible [1,2,3].

(1)
$$\frac{\Delta T}{\Delta t} = \frac{\omega \varepsilon_o K_i \int_{Vi} \varepsilon_{ri} Fi(\varepsilon_{ri}) E_i^2 dV_i}{m_i c}$$

where :

$\Delta T/\Delta t$ is temperature rate rising;

$\omega = 2\pi f$, f- microwave frequency;

E_i - microwave E field in "i" point ;

K_i - coupling coefficient for "i" point and F_i - filling factor;

ε_{ri} - absorber mixture relative permittivity in point "i" and εo - free space permittivity;

m_i,c are absorber material characteristics, respectively, local mass and specific heat;

In figure 2 is presented the theoretical (fig.2a) and experimental (fig.2.b) microwaves field distribution in one TM104 rectangular cavity. The images of the figures 2b correspond at different exposure times.

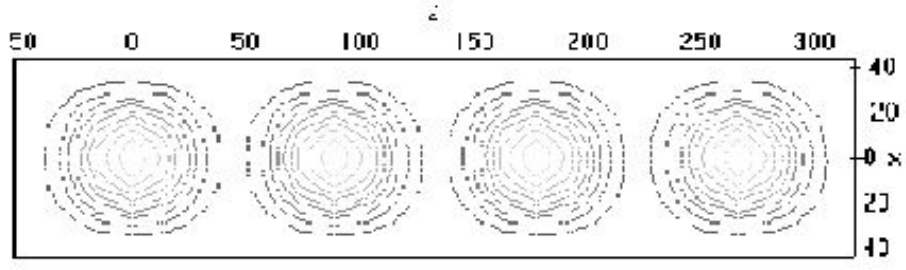

FIG. 2a

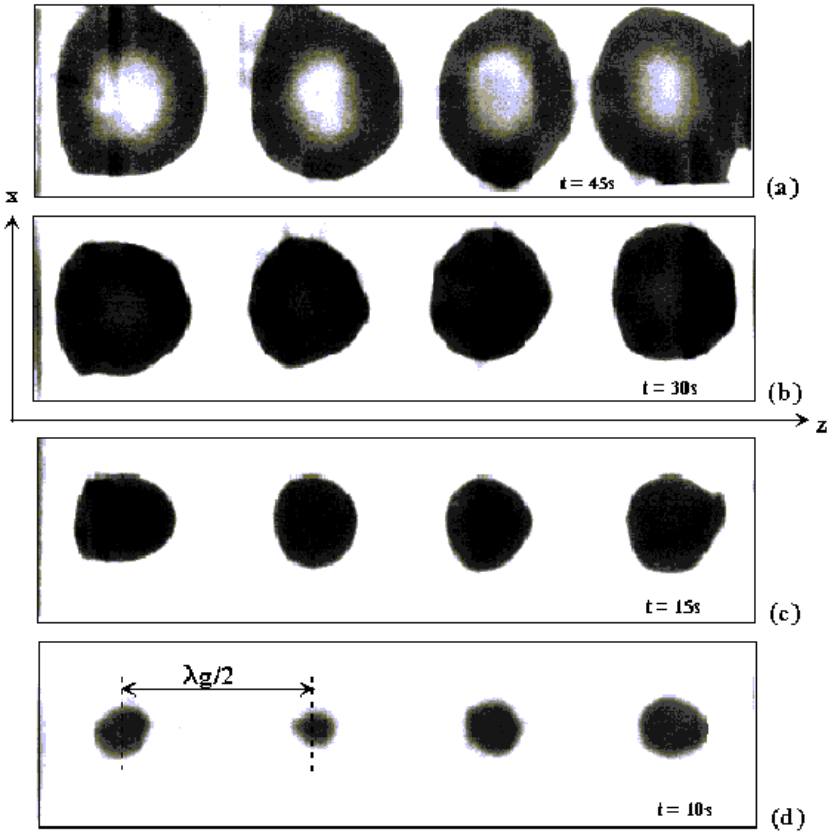

FIG. 2b

3. APPLICATIONS

The following pictures present the microwave power distributions in different applications. All this distributions are obtained using the thermographic transducer. The image of fig.3 is used to adapt one coaxial to waveguide transition. In figure 4 is the image of the microwave distributions in one cylindrical cavity middle coupled to one waveguide.

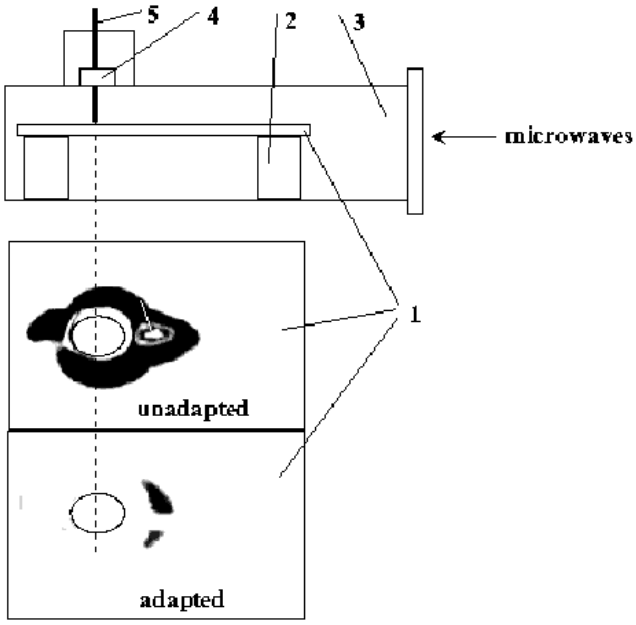

FIG.3

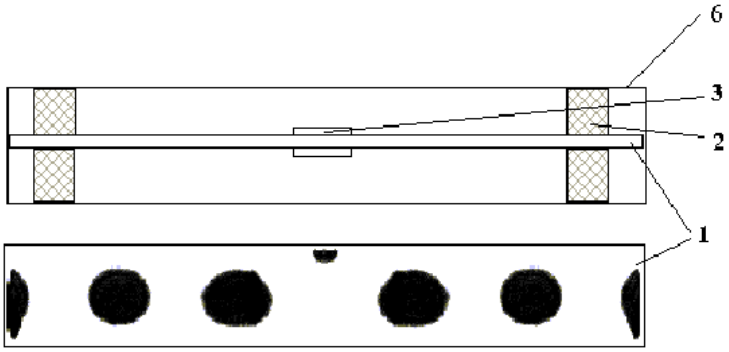

FIG.4

The notation in the fig.3 and 4 are : 1-thermographic; 2-dielectric support; 3-waveguide; 4-ceramic window; 5-coaxial line; 6- cylindrical cavity.

The figure 5 present one microwave plasma generator configuration and the images of the microwave thermographic transducer for the microwave power distribution characterisation. The "A,B,C,D,E,F,G,H" images represent the microwave power field distributions in the coaxial exciter (A,B,C,D,E) and in the TM100 cavity (F,G,H). The “E” image represent the adaptation situation between coaxial eciter and cylindrical cavity. The position of the thermographic transducer in the microwave circuit is indicated with dash line.

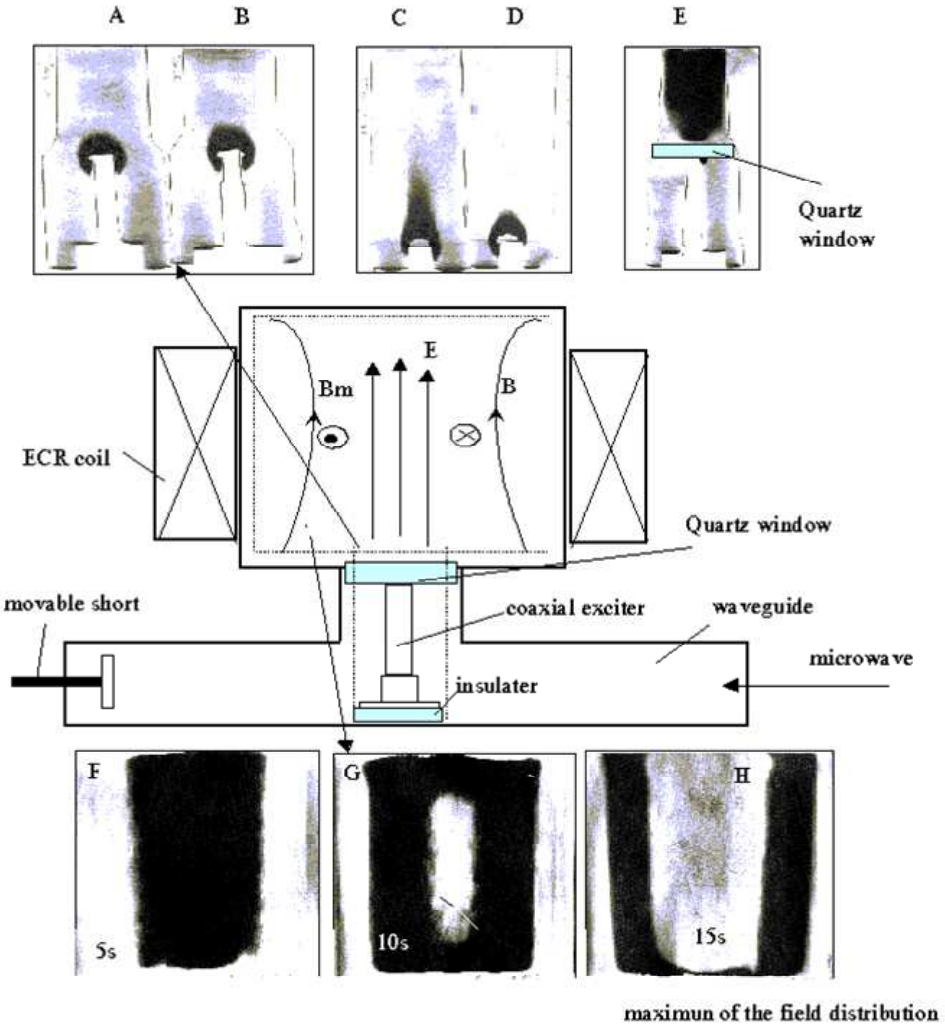

FIG.5

4. CONCLUSION

The microwave distribution images are the most important instruments in elaboration of the microwaves power nonconventional technologies. Our method is low cost, easy to use and simple to interpret.

The bronze medal acquired at ***"The Invention Saloon of Geneva 2001"*** represent the international appreciation of the microwave thermographic transducer [4].

BIBLIOGRAPHY

1. E.Surducan, V.Surducan " Thermographic transducer for microwave power distributions" Romanian Patent No. RO-116506 B1 /2001

2.M.F.Iskander -" Computer modeling and numerical simulation of microwave heating system" MRS Bulletin, no.11, 1993, pag.30-35;

3. T.Kashiwa, et all - A New Transducer for Thermography to Observe the Electric Field Distributions in a Microwave Oven - MICROWAVE AND OPTICAL TECHN LETT, Vol.4(2)92. pp. 81-83;

4. E.Surducan, V.Surducan - “Le traducteur thermographic pour les microondes de puissance” GENEVA – PALEXPO, The 29th International Exhibition of Inventions, New Techniques and Products, 11th – 15th April 2001, Geneva

STUDIA UNIVERSITATIS BABEŞ-BOLYAI, PHYSICA, SPECIAL ISSUE, 2001

CHARACTERISATION OF OXIDIC MATERIALS WITH LUMINESCENT PROPERTIES

LAURA UNGUR*, ELISABETH-JEANNE POPOVICI*, MARIA VăDAN*, LIGIA PASCU*, MARILENA VASILESCU and M.NAZAROV*****

** "Raluca Ripan" Institute of Chemistry, 30 Fântânele, 3400-Cluj-Napoca, Romania*
***"I.G. Murgulescu" Institute of Physical Chemistry of the Romanian Academy, 202 Spl. Independentei, Bucureşti, Romania*
****Technical University of Moldova, Bd. Stefan cel Mare 168, Chişinău, R.. Moldova*

ABSTRACT. Under UV or cathode ray excitation, europium activated yttrium oxide phosphor shows bright characteristic red luminescence. Y_2O_3: Eu phosphor is especially used in the manufacture of coloured fluorescent lamps and plasma display panels. Phosphor utilisation depends both on powder characteristics and luminescent properties and sensitivity to various excitation radiation. The paper reveals the correlation between photoluminescence (PL) and cathodoluminescence (CL) properties and the synthesis conditions. Polycrystalline phosphor samples were prepared by thermal synthesis at 1100-1400°C, from homogeneous mixtures containing yttrium oxide (host lattice), Eu_2O_3 (activator source) and alkaline earth salts (flux). PL spectra and CL defectoscopy measurements put in evidence the influence of thermal synthesis conditions on europium incorporation degree into the yttrium oxide host lattice.

Key words: phosphors, luminescent materials, yttrium oxide; red emitting material

1. INTRODUCTION

Under UV or cathode ray excitation, europium activated yttrium oxide phosphor shows bright characteristic red luminescence and could be used in the manufacture of coloured fluorescent lamps, cathode ray tubes and plasma display panels[1].

Usually, Y_2O_3: Eu phosphor synthesis is performed by ceramic techniques i.e. the direct firing of oxide mixtures [2,3.] The phosphor manufacture could proceed also by the firing of some precursors that were previously prepared by sol-gel method[4] or homogeneous precipitation[5].

Y_2O_3:Eu phosphor utilisation depends both on powder characteristics and luminescent properties and sensitivity to various excitation radiation. Photoluminescence and cathodoluminescence properties as well as morpho-structural characteristics strongly depend on phosphor synthesis conditions [6-8.] This paper is the first in a series referring to Y_2O_3: Eu synthesis by both ceramic techniques and homogeneous precipitation route and is aiming at illustrating the correlation between PL and CL characteristics and the synthesis conditions.

2. EXPERIMENTAL PART

Polycrystalline phosphor samples were prepared by thermal synthesis from homogeneous mixtures containing yttrium oxide (p.a. Merck) as host lattice, Eu_2O_3 (Merck) as activator source and luminescent grade $BaCl_2$ and borax as flux. Phosphors were fired for 2 hrs, in air (un-closed system), at 1100-1400°C; the as-prepared material was washed, dried and sieved.

Phosphor samples were characterised by emission and excitation spectra that were performed with 204 Perkin Elmer Spectrofluorimeter. The registration conditions were as follows: emission spectra were registered under 360 nm excitation (S=4x1/10) whereas the excitation spectra were registered for the 618 nm emission (S=3x1/10); excitation: λ_{max} =;. Y_2O_3: Eu phosphor sample produced by KEMIRA-Finland was used as standard. Phosphor powders were examined also by Colour Cathodoluminescence-Scanning Electronic Microscopy method (CCL_SEM) by using a special CCL-SEM attachment.

3. RESULTS AND DISCUSSION

Phosphor synthesis was performed by ceramic technique, by firing homogeneous and well defined mixtures of yttrium oxides, europium oxide and barium chloride or borax. Phosphor synthesis conditions and some of their general properties are presented in table 1. The phosphor formation could be described by the equation #1

$$\mathbf{(1\text{-}x)Y_2O_3 + xEu_2O_3} \xrightarrow[\text{flux}]{\textit{firing stage}} \mathbf{Y_{2\text{-}2x}\,Eu_{2x}O_3} \qquad (1)$$

Under UV excitation, europium activated yttrium oxide phosphor shows bright characteristic red luminescence. The most important emission and excitation bands of some samples are revealed by their photoluminescence spectra (fig.1-3).

Our experimental technique permitted us to observe the following Eu-emission bands: ~ 460 nm band, in the blue part of the spectrum, and 589, 611 and 650 nm bands, in the red spectral domain. The main peak position and its relative intensity (I_{max}) are shown in table 1.

Excitation spectra shows that the 611 nm emission band is well excited in the UV-Vis domain. The main excitation bands are disposed at 267; 317; 366; 397; 416; 472 and 537 nm.

Eu-specific luminescence (the red domain bands) are the result of some $^5D_0 \rightarrow {}^7F_J$ electronic transitions inside the activator ion, these ones generating many narrow emission bands into the emission spectrum. Their exact position and relative intensity depend on the activator incorporation degree (AID) into the Y_2O_3 host lattice and this one is strongly influenced by the flux presence (fig.4).

Table 1.

General properties of some phosphor samples prepared in various conditions.

Code	Phosphor formula	Synthesis conditions			**PL** colour	PL characteristics	
		Europium (mol %)	Flux	Firing temperature		λ_{max} (nm)	I_{max} (%)
L1	$Y_{1.990}Eu_{0.010}O_3$	1.0	-	1300^0C	pink	608.4	47.0
L2	$Y_{1.970}Eu_{0.030}O_3$	3.0	-	1300^0C	reddish	610.0	54.8
L3	$Y_{1.950}Eu_{0.05}O_3$	5.0	-	1300^0C	reddish	611.7	64.6
L4	$Y_{1.925}Eu_{0.075}O_3$	7.5	-	1300^0C	red	611.7	66.2
L5	$Y_{1.990}Eu_{0.010}O_3$	1.0	$BaCl_2$ (2%)	1300^0C	reddish	610.6	55.3

Code	Phosphor formula	Synthesis conditions			**PL** colour	PL characteristics	
		Europium (mol %)	Flux	Firing temperature		λ_{max} (nm)	I_{max} (%)
L6	$Y_{1.970}Eu_{0.030}O_3$	3.0	$BaCl_2$ (2%)	1300^0C	red	610.0	68.0
L7	$Y_{1.950}Eu_{0.05}O_3$	5.0	$BaCl_2$ (2%)	1300^0C	red	610.6	72.5
L8	$Y_{1.925}Eu_{0.075}O_3$	7.5	$BaCl_2$ (2%)	1300^0C	red	610.6	96.2
L9	$Y_{1.950}Eu_{0.05}O_3$	5.0	-	1100^0C	pink	608.4	47.9
L10	$Y_{1.950}Eu_{0.05}O_3$	5.0	$BaCl_2$ (2%)	1100^0C	pink	609.5	50.4
L11	$Y_{1.950}Eu_{0.05}O_3$	5.0	-	1400^0C	red	610.6	67.9
L12	$Y_{1.950}Eu_{0.05}O_3$	5.0	$BaCl_2$ (2%)	1400^0C	red	610.6	96.9
L19	$Y_{1.925}Eu_{0.075}O_3$	7.5	$BaCl_2$ (5%)	1300^0C	red	610.6	106.0
L20	$Y_{1.925}Eu_{0.075}O_3$	7.5	Borax (5%)	1300^0C	red	611.7	146.5
	STANDARD	-	-	-	***RED***	***610.6***	***100.0***

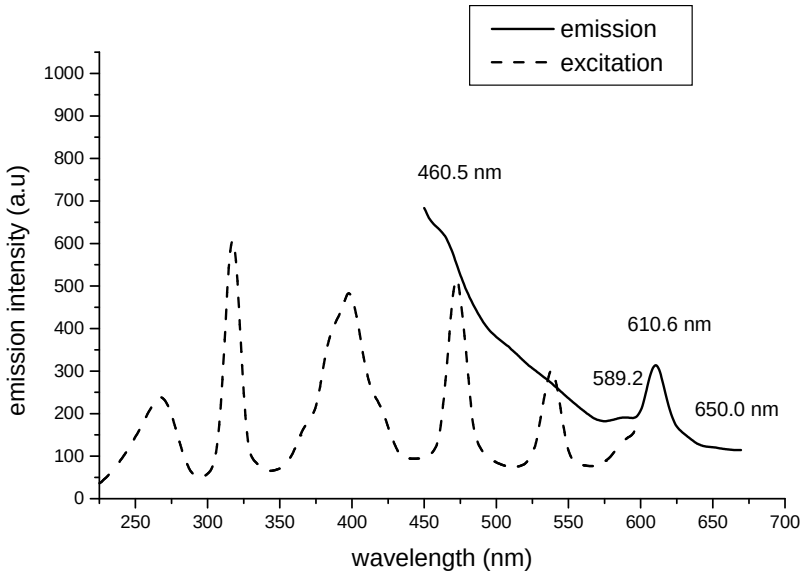

Figure 1. Emission and excitation spectra of L12-samples
[5 mol% Eu; 2% $BaCl_2$ 1400°C]

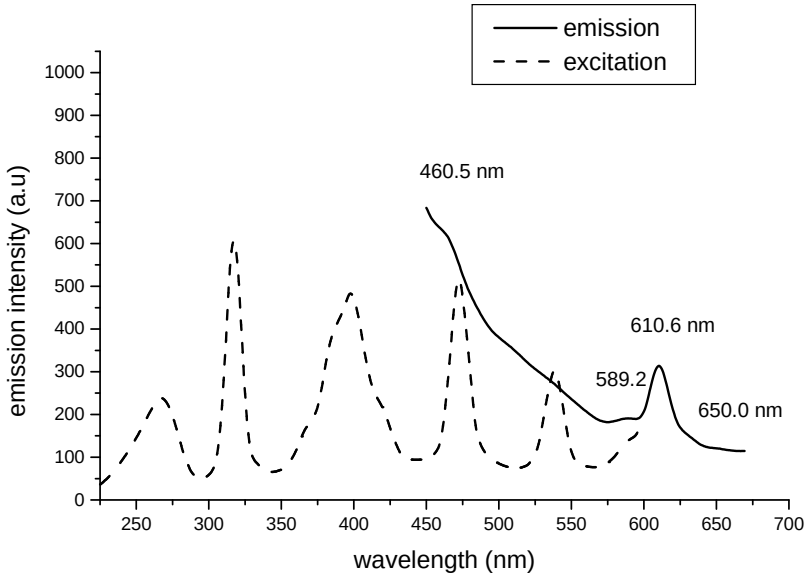

Figure 2 .Emission spectra of some Y_2O_3: Eu samples: L8 [7.5 mol % Eu; 2% $BaCl_2$] ; L19 [7.5 mol % Eu; 5% $BaCl_2$] and L20 [7.5 mol % Eu; 5% Borax]

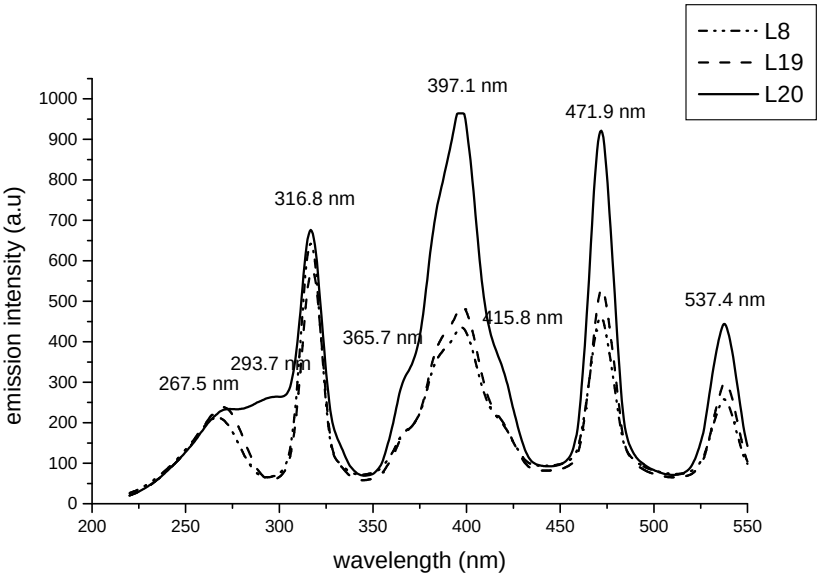

Figure 3. Excitation spectra of some Y_2O_3: Eu samples: L8 [7.5 mol % Eu; 2% $BaCl_2$]; L19 [7.5 mol % Eu; 5% $BaCl_2$] and L20 [7.5 mol % Eu; 5% Borax]

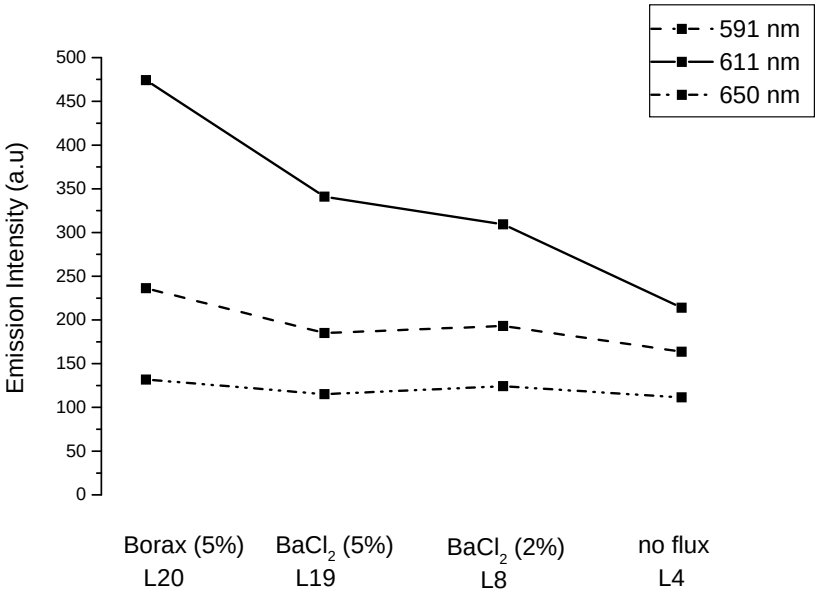

Figure 4. Dependence of the Eu- emission bands intensity on flux nature and concentration - phosphor samples L20; L19; L8 and L4 $\Leftrightarrow$ Y_2O_3:Eu (7.5 mol %)

The preparation conditions i.e. quality of the host lattice generating material, activator amount, mineralising agent nature and concentration, thermal synthesis conditions and conditioning regime determines the Y_2O_3:Eu sample characteristics.

The activator incorporation degree (AID) depends on phosphor synthesis conditions. The specific emission band of L1-L20 samples is disposed between 608.4 and 611.7 nm whereas the relative emission intensity vary from 47.9 % to 146.5 %.

Colour Cathodoluminescence - Scanning Electronic Microscopy images are very illustrative for the specific luminescence colour of the Y_2O_3: Eu powders. CCL-SEM photos illustrate the effect of firing temperature on the chromatic hue of powder surfaces. One observes that the higher the temperature, the more saturated the red colour.

The preparation conditions i.e. quality of the host lattice generating material, activator amount, mineralising agent nature and concentration, thermal synthesis conditions and conditioning regime determines the Y_2O_3:Eu sample characteristics.

PL spectra and CL defectoscopy measurements put in evidence the influence of thermal synthesis conditions on Eu- incorporation degree into the yttrium oxide host lattice.

One can conclude that:

The presence of mineralising agent as well as the high firing temperature facilitate the formation of the cubic Y_2O_3 - Eu_2O_3 solid solution and consequently an efficient activator distribution. The highest AID seems to be attained at 1300^{o}C in the presence of 5% borax. The very high PL brightness of the sample is due to its very high excitability, especially in the ~ 398 band. The optimal activator concentration is de 7.5 mol%.

In order to obtain high AID and consequently efficient Y_2O_3:Eu samples, flux nature and concentration, firing temperature and activator amount have to be carefully chosen.

REFERENCES

1.X. Jing, T. Ireland, C. Gibbons, *J. Electrochem. Soc*., **1999**, 146 (12), 4654-4658.

2.B. Djuricic, D. Kolar, M. Memic, *J. Eur. Ceram. Soc*., **1992**, 9, 75-82.

3. Y.D. Jiang, Z.L. Wang, *J. Mater. Res*., **1998**, 13(10), 2950-2955.

4. R.P. Rao, *J. Electrochem. Soc*., **1996**, 143(1), 189-197.

5. E.L. Shea, J. McKittrick, *J. Am. Ceram. Soc*., **1996**, 79(12), 3257-3265.

6. B. Bihari, H. Eilers, M. B. Tissue, *J. Lumin*., **1997**, 75, 1-10.

7.M. I. Martinez-Rubio, T. G. Ireland, *Electrochem. Solid-State Lett*., **2000**, 3(9), 446-449.

8. H. Eilers, B.M. Tissue, *Chem. Phys. Lett*., **1996**, 251, 74-78.

STUDIA UNIVERSITATIS BABEŞ-BOLYAI, PHYSICA, SPECIAL ISSUE, 2001

THE EFFECT OF MAGNETIC FIELD ON Na^+ TRANSPORT THROUGH HUMAN ERYTHROCYTE MEMBRANES

C.BINDEA, T.SIMPLĂCEANU, ST.POPESCU

National Institute of Research and Development for Isotopic and Molecular Technology, PO Box 700, 3.400 Cluj-Napoca, Romania

ABSTRACT. Human erythrocytes were exposed to magnetic field, the intensity domain being 0.59-0.62T, and the Na^+ efflux was measured. It was found that the loading of erythrocytes with sodium (Na^+ erythrocyte) was higher in exposing cells than in controls.

The rate constant K of Na^+ efflux by passive diffusion mechanism increased by about 60% and by Na^+- K^+ pump mechanism decreased with about 50%.

Key words: Na^+ efflux, passive diffusion, Na^+-K^+ pump, ion transport, erythrocytes, and magnetic field.

INTRODUCTION

The efflux of natrium ions through human erythrocyte membranes is known to occur through the following mechanism: a). passive diffusion along its electrochemical gradient and b). active transport by the Na^+-K^+ ATPase pump.

The present work is concerned with Na^+ transport through erythrocyte membranes under the influence of magnetic field.

The values of the magnetic fields in offices and homes reach no more than 0.3 μT, while along the telephone wires and high tension networks they go up to 15 μT.

The values of these magnetic fields tend to increase in the neighborhood of plants using electric power engines or hating electric systems. For example in steel industrialization production magnetic field of 8-70 mT may occur.

Considering the data above we have come to study the behavior of the human erythrocyte membrane concerning the permeability of ions and water in a magnetic field larger than the terrestrial one.

We have done research about the influence of the gamma radiation of the electric and magnetic field upon the movement of Li^+- Na^+ and the rate exchange of the water through the human erythrocyte membranes /1-13/.

MATERIALS AND METHODS

The human blood in citrate was collected from aparent healthy subjects. Human erythrocytes were exposed to magnetic field, the intensity domain being 0.59-0.62T, and the Na^+ efflux was measured.

The measurement in vitro of Na^+ efflux by the passive diffusion and Na^+- K^+ pump mechanism was performed using the technique of Smith et. al. [14].

We adapted it to the investigation of drug effects on the Na^+ efflux through human erythrocyte membranes and the Na^+ efflux alterations in various disease [15-19].

The erythrocytes are washed in a solution (75mM $MgCl_2$, 85mM mannitol, 10mm TRIS, pH 7.4 at 4^o C) with 5 times the erythrocyte volume. An approximately 50% suspension of the final erythrocyte pellet is prepared in the same solution and the hematocrit was measured.

The two efflux media have a pH of 7.4 at 37^o C and an osmolality of 290-305 mOs: (1) 75mM $MgCl_2$, 85mM mannitol, 10mM TRIS, 1mM ouabain and 1mM glucose; (2) 72mM $MgCl_2$, 83mM mannitol, 10mM TRIS, 10mM KCl and 1mM glucose. One mililliter of the erythrocyte suspension is added to 5ml of each of the efflux media. Duplicate tubes of each solution are removed at t=0.5 and 15 min. The suspension are immediately centrifuged at 4000 rot/min. for 5 min. and the supernatants removed and stored in capped tubes until the Na^+ concentration is measured by atomic absorption spectrophotometry. The Na^+ efflux via passive diffusion is represented by the efflux into solution (1), while Na^+ efflux via Na^+- K^+ pump is the difference in the Na^+ efflux into the two media.

The Na^+ efflux rate constant $K=Na^+_{efflux} / Na^+_{erythrocyte}$ was calculated, where Na^+_{efflux} is the Na^+ efflux measured in $mmol/l_{erythrocyte}$* h and $Na^+_{erythrocyte}$ represents the Na^+ concentration of the erythrocytes measured in $mmol/l_{erythrocyte}$.

RESULTS

Human erythrocytes were exposed to magnetic field, the intensity domain being 0.59-0.62T, and the Na^+ efflux was measured. These has been performed an average of about two experiments for every exposure time in a magnetic fields. There haven't been performed experiments with exposures longer than 20 hours considering the dangers for the erythrocytes to hemolysis.

It was found that the loading of erythrocytes with sodium was higher in exposing cells than in controls (tab. 1).

Table 1

The average measurement of the Na^+ intraerythrocytar concentration after its exposure in an intense magnetic field.

Nr. exp.	**Time of exp.**	**$Na^+_{erythrocyte}$ [$mmol/l_{eryth.}$] controls**	**$Na^+_{erythrocyte}$ [$mmol/l_{eryth.}$] magnetic field**	**$\Delta Na^+_{erythrocyte}$ [$mmol/l_{eryth.}$]**	**$\frac{\Delta Na^+_{erythrocyte}}{Na^+_{eryth.\ control}} * 100$ [%]**
3	2	4.81±0.98	4.89±0.52	0.23±0.39	4.8±10.6
4	1	4.06	4.43	0.37	9.1
6	2	4.50±0.23	5.16±0.63	0.66±0.46	14.6±11.5
8	2	4.79±0.26	5.53±0.03	0.74±0.28	15.9±6.8
10	2	4.61±0.00	5.33±0.36	0.76±0.42	15.4±7.0
12	2	4.12±0.44	5.66±0.09	1.54±0.53	39.1±16.9
14	2	5.06±0.75	8.18±0.38	3.12±0.37	64.2±16.8
16	1	5.12	10.94	5.82	113.7
18	1	5.03	8.35	3.32	66.0
20	2	4.75±0.10	9.82±0.16	5.07±0.25	107±7.4

By exposing the human erythrocytes to a magnetic field for 12 hours it results, an increase of intracell Na^+ of about 40% while after exposing it to more than 12 hours, the intracellular Na^+ concentration increased to about 100%.

The experimental results concerning Na^+ through passive diffusion mechanism from the human erythrocyte after its exposure in an intense magnetic field compared to

the Na^+ efflux through the same mechanism from the none exposed control erythrocytes are shown in the 2 table.

There has been obtained an increase of the Na^+ efflux using the passive diffusion from the human erythrocytes exposed to an intense magnetic field compared to the Na^+ efflux using the same mechanism from the none exposed control erythrocytes.

The increase of the Na^+ using the passive diffusion is larger in the first 12 hours of exposure in an intense magnetic field.

The rate constant of the Na^+ efflux using the passive diffusion from the human erythrocytes after being exposed to an intense magnetic field compared to the rate constant of the Na^+ using the same mechanism from the none exposed control human erythrocytes are shown in table 3.

Table 2

The average values of the Na^+ efflux through the mechanism of the passive diffusion from the human erythrocytes after being exposed in an intense magnetic field.

Time of exposition [h]	Na^+_{efflux} [mmol/$l_{erythrocyte}$ *h]		ΔNa^+_{efflux} [mmol/$l_{erythrocyte}$ *h]	$\frac{\Delta Na^+_{efflux}}{Na^+_{efflux\ control}} \times 100$ [%]
	controls	magnetic field		
2	0.34±0.19	0.49±0.13	+ 0.15±0.12	+ 81.6±76.1
4	0.54	0.85	+ 0.31	+ 57.4
6	0.43±0.23	0.80±0.39	+ 0.37±0.17	+ 90.2±10.1
8	0.53±0.13	0.63±0.24	+ 0.10±0.11	+ 14.7±17.2
10	0.35±0.00	0.68±0.03	+ 0.33±0.03	+ 94.3±8.6
12	0.42±0.03	0.65±0.07	+ 0.25±0.05	+ 57.6±9.0
14	0.47	0.64	+ 0.17	+ 36.2
20	0.75±0.16	0.97±0.10	+ 0.22±0.25	+ 37.7±42.0

Table 3

The average values of the rate constant of the Na^+ efflux using the passive diffusion from the human erythrocytes after being exposed to an intense magnetic field.

Time of exposition [h]	K [h^{-1}] controls	K [h^{-1}] magnetic field	ΔK [h^{-1}]	$\frac{\Delta K}{K_{control}} \times 100$ [%]
2	0.082±0.045	0.103±0.20	+ 0.021±0.028	+ 80.7±85.2
4	0.133	0.191	+ 0.058	+ 43.6
6	0.099±0.057	0.147±0.061	+ 0.048±0.02	+ 70.9±38.6
8	0.131	0.158	+ 0.017	+ 20.6
10	0.076±0.00	0.129±0.015	+ 0.053±0.015	+ 69.1±19.1
12	0.104±0.018	0.115±0.011	+ 0.011±0.007	+ 11.7±9.2
14	0.150±0.041	0.073±0.010	- 0.078±0.051	- 45.9±21.1
16	0.104	0.037	- 0.067	- 64.4

There has been obtained an increase of the rate constant of the Na^+ efflux using the passive diffusion from the human erythrocytes after an exposure of no more

than 12 hours in an intense magnetic field and a decrease of the rate constant with the exposures longer then 12 hours, compared to the Na^+ efflux rate constant using the passive diffusion from the none exposed control erythrocytes.

Therefore, although the Na^+ efflux using the passive diffusion from human erythrocytes exposed to the intense magnetic field increase with exposures longer then 12 hours, the rate constant of the Na^+ efflux decreases also in exposures longer then 12 hours, the rate constant of Na^+ efflux decrease with the exposures longer then 12 hours. This effect is due to the strong decrease of intraerythrocytes Na^+ concentration.

The experimental results concerning Na^+ efflux and rate constant of Na^+ efflux using the Na^+-K^+ pump mechanism from the human erythrocytes after being exposed to an intense magnetic field compared to the Na^+ efflux using the same mechanism from the none exposed control erythrocytes, are shown in table 4 and table 5.

Table 4

The average values of the Na^+ efflux through the Na^+- K^+ pump using from the human erythrocytes after being exposed to an intense magnetic field.

Time of exposition [h]	**Na^+_{efflux} [mmol/$l_{erythrocyte}$ *h]**		**ΔNa^+_{efflux} [mmol/$l_{erythrocyte}$*h]**	$\frac{\Delta Na^+_{efflux}}{Na^+_{efflux\ control}} \times 100$ [**%]**
	controls	**magnetic field**		
2	1.02±0.07	0.54±0.19	- 0.48±0.10	- 47.5±13.2
4	0.86	0.48	- 0.38	- 44.2
6	0.58±0.25	0.28±0.03	- 0.30±0.28	- 37.8±31.7
10	1.23±0.19	0.72±0.52	- 0.51±0.34	- 46.5±34.4
12	0.92±0.07	0.81±0.15	- 0.11±0.22	- 10.2±23.1
14	0.68±0.41	0.53±0.26	- 0.15±0.16	- 11.9±15.6
18	0.59	0.31	- 0.28	- 47.5
20	0.82±0.30	0.20±0.03	- 0.62±0.27	- 734±6.1

A decrease of about 50% of the Na^+ efflux using the Na^+-K^+ pump mechanism from the human erythrocytes exposed to an intense magnetic field has been noticed compared to the Na^+ efflux using the same mechanism from the non exposed control erythrocytes.

Table 5

The average values of the rate constant of the Na^+ efflux through the Na^+- K^+ pump mechanism from the human erythrocytes after being exposed in an intense magnetic field.

Time of exposition [h]	**K [h^{-1}] controls**	**K [h^{-1}] magnetic field**	**Δ K [h^{-1}]**	$\frac{\Delta K}{K_{control}} \times 100$ **[%]**
2	0.222±0.050	0.111±0.037	- 0.111±0.070	- 47.1±25.7
4	0.212	0.108	- 0.104	- 49.1
6	0.131±0.061	0.056±0.012	- 0.076±0.073	- 40.2±37.4

Time of exposition [h]	K $[h^{-1}]$ controls	K $[h^{-1}]$ magnetic field	ΔK $[h^{-1}]$	$\frac{\Delta K}{K_{control}} \times 100$ [%]
10	0.266±0.050	0.129±0.089	- 0.137±0.048	- 55.5±26.7
12	0.228±0.042	0.144±0.029	- 0.084±0.070	- 32.4±24.8
14	0.149±0.104	0.067±0.035	- 0.083±0.070	- 44.5±15.6
18	0.117	0.037	- 0.080	- 68.4
20	0.172±0.060	0.021±0.003	- 0.151±0.056	- 87.2±2.4

There has been noticed decrease of about 50% of the rate constant of the Na^+ efflux from the human erythrocyte with an exposure of up to 20 hours to an intense magnetic field compared with the rate constant of the Na^+ efflux through the Na^+- K^+ pump mechanism from the non exposed control erythrocytes.

CONCLUSIONS

Human erythrocytes were exposed to magnetic field, the intensity domain being 0.59-0.62T, and the Na^+ efflux was measured.

There has been obtained an increase of about 60% of the Na^+ efflux through the passive diffusion from the human erythrocytes exposed to a magnetic field compared the Na^+ efflux from the non exposed control erythrocytes using the same mechanism.

The Na^+ efflux through the Na^+- K^+ pump mechanism from the human erythrocytes exposed to the magnetic field has been diminished with about 50% compared with the Na^+ efflux through the same mechanism from the non exposed control erythrocytes.

We may conclude that there is an effect of the magnetic field upon the channel protein, namely an increase of the Na^+ permeability - upon Na^+- K^+ ATPase namely a decrease in its activity.

The present results coincide with our previous research on the influence of the magnetic field upon Li^+ transport through the human erythrocyte membranes [10, 11] as well as with the erythrocyte permeability for water [8].

REFERENCES

1. C.BINDEA, T.SIMPL{CEANU, I.CHEREJI, V.V.MORARIU V.V. “Influen□a radia□iilor γ asupra influxului Li^+ în eritrocitele umane”. Analele Universitã□ii din Oradea, Fizic| Tom IV, p. 42-50 (1996).
2. T. SIMPL{CEANU, C.BINDEA, I.CHEREJI V.V.MORARIU “Influen□a radia□iilor nucleare asupra timpului de schimb al apei prin membrana eritrocitelor umane”.Analele Universitã□ii din Oradea, Fizicã Tom IV, p 135-144 (1996).
3. C.BINDEA, V.V.MORARIU, I.CHEREJI “The effect of gamma radiation on Li^+ transport through human erythrocyte membranes”. Cytobios (Cambridge), 93, 23-31 (1998).

4. C.BINDEA, T.SIMPL{CEANU, I.CHEREJI "Efectul radiațiilor γ asupra efluxului Li^+ din eritrocitele umane."Analele Universității din Oradea, Fizică Tom VIII, 63-72, (1998).
5. C.BINDEA, T.SIMPL{CEANU, S.KREIBIK, S.POPESCU "Efectul câmpului electric asupra influxului Li^+ în eritrocitele umane."Analele Universității din Oradea, Fizică Tom VIII, 55-62, (1998).
6. C.BINDEA, T.SIMPL{CEANU, S.KREIBIK, S.POPESCU "Efectul câmpului electric asupra efluxului Li^+ din eritrocitele umane."Analele Universității din Oradea, Fizică Tom VIII, 45-54, (1998).
7. T.SIMPL{CEANU, C.BINDEA, S.POPESCU, G.CRISTEA "Efectul câmpului electric asupra timpului de schimb al apei prin membranele eritrocitare umane." Analele Universității din Oradea, Fizică Tom VIII, 225-232, (1998).
8. T.SIMPL{CEANU, C.BINDEA, S.POPESCU, G.CRISTEA "Efectul câmpului magnetic asupra timpului de schimb al apei prin membranele eritrocitare umane." Analele Universității din Oradea, Fizică Tom VIII, 233-244, (1998).
9. C.BINDEA, I.CHEREJI, T.SIMPLĂCEANU, V.TARBA "Efectul radiațiilor gamma asupra efluxului Na^+ din eritrocitele umane." Analele Universității din Oradea, Fizică Tom IX 39-50, (1999).
10. C.BINDEA, T.SIMPLĂCEANU, T.MÎRȚ "Efectul câmpului magnetic asupra influxului Li^+ prin membranele eritrocitare umane." Analele Universității din Oradea, Fizică Tom IX, 27-38, (1999).
11. C.BINDEA, T.SIMPLĂCEANU, T.MÎRȚ "Efectul câmpului magnetic asupra efluxului Li^+ prin membranele eritrocitare umane." Analele Universității din Oradea, Fizică Tom IX, 17-26, (1999)
12. C.BINDEA, ALINA MUREȘAN, St.POPESCU, T.SIMPLĂCEANU. "Efectul câmpului electric asupra efluxului Na^+ din eritrocitele umane prin mecanismul difuziei pasive." Analele Universității din Oradea, Fizică - A Tom X 133-138, (2000).
13. C.BINDEA, ALINA MUREȘAN T.SIMPLĂCEANU, St.POPESCU. "Efectul câmpului electric asupra efluxului Na^+ din eritrocitele umane prin mecanismul pompei Na^+- K^+." Analele Universității din Oradea, Fizică - A Tom X 139-144, (2000).
14. J.B.SMITH, K.O.ASH, W.M.HENTSCHEL, W.L.SPROWELL, R.R.WILLIAMS An improved nonradioisotopic method for measuring ouabain-sensitive Na^+ efflux from erythrocytes – Clin.Chim.Acta. 143, 295 (1984).
15. C.BINDEA, T.SIMPL{CEANU, V.V.MORARIU. "Efectul anestezicelor locale asupra transportului activ al pompei Na^+-K^+ prin membrana celulelor roõii umane". Analele Universit|ii din Oradea, Tom.IV, Fizic|, p. 33-36 (1994).
16. C.BINDEA, T.SIMPL{CEANU, L.PETROV, V.V.MORARIU, ANCA GHIURTZ, ANCA VASILACHE, A.CUCUIANU. "Modific|ri ale efluxului Na^+ din eritrocitele umane în leucemie".Cancerul (Serie nou|) nr. 13 p. 43-47 (1996).
17. C.BINDEA, T.SIMPL{CEANU, V.V.MORARIU "Efluxul Na^+ din eritrocitele umane". Analele Universitãûii din Oradea, Fizica Tom IV, p. 31-41 (1996).
18. C.BINDEA, S.R=NDAÔU, V.V.MORARIU "Na^+ efflux through erythrocyte membranes from patients with affective psychosis". Biomedical Letters (Cambridge), 56, 111-114 (1997).
19. C.BINDEA, M.COLDEA, T.SIMPL{CEANU, L.SR=MBU "The Na^+ efflux through human erythrocyte membranes in hypertension". Romanian Journal of Biophysics 8(1), 51-57 (1998).

SPECTROSCOPICAL INVESTIGATION OF SOME CALIX[N]ARENES DERIVATIVES UTILISABLE AS METAL EXTRACTING AGENTS

CRISTINA CIOCAN, ELISABETH-JEANNE POPOVICI, CRINA DAN, MARIA VĂDAN, RODICA GRECU and N. POPOVICI

"Raluca Ripan" Institute of Chemistry, 30 Fântânele, 3400-Cluj-Napoca ROMANIA

ABSTRACT. p-tert-butil-calix[n]arene [n=4,6] and their corresponding acetate-derivatives were prepared by specific procedures. The calix[n]arenes' purity was checked by elemental analysis and various spectroscopic methods such as RMN, MS-GC, UV-Vis and FTIR. The ability of calixarenes acetates to extract precious metallic ions from aqueous solutions was tested. The high effectiveness of O-acetilated p-t-butil calix[6] arene to extract Pt(II) ions was demonstrated in relation with Pd^{2+} and Rh^{3+} species.

Key words: calixarenes; liquid extraction; precious metal ions extraction.

1. INTRODUCTION

Calix[n]arenes are polinuclear compounds that act as selective complexation agents for electrical charged or neutral species. The high complex-formation ability of calix[n]arenes offers them large utilization possibilities in the manufacture of sensitive membranes, elaboration of some selective extraction methods for various cations and anions, realization of modern metal recovery procedures and for the environmental protection.

The purpose of this study is to present our attempt to prepare some O-acetilated p-tert-butil-calix[n]arene in order to test their ability to co-ordinate precious metallic ions.

2. EXPERIMENTAL PART

p-tert-butyl -calix[4]arene and calix[6]arene were prepared and purified by C.D.Gutsche' technique[1,2]. The as mentioned calixarenes were converted into the corresponding acetate derivatives by using acetic acid anhydride as O-acetilating reagent (reaction #1). In this respect, about 2 mmol of p-tert-butyl calix[n]arene was treated with 50 ml of acetic acid anhydride and two drops of concentrated sulfuric acid[3]. The mixture was heated and refluxed for 2 hours.

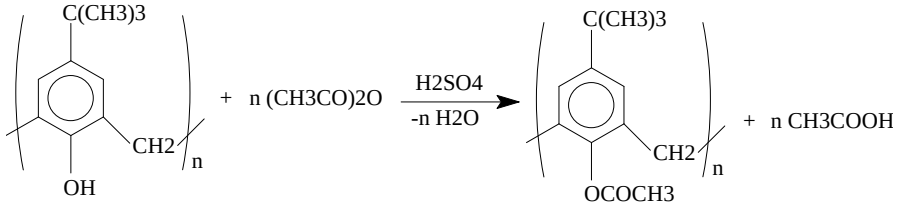

(**1**)

The crude product was recrystallised from chloroform/methanol. White platelets were obtained with a yield of 45-47%.

The purity of as prepared products was checked out by elemental analysis as well as by IR, UV-Vis, ^{1}H NMR and mass spectroscopy.

The metallic ions extraction was performed by using chloroform solutions of calix[4]arene tetraacetate (noted **C4Ta**) or calix[6]arene hexaacetate (noted **C6Ha**) as extraction agents[4,5]. In this respect, 10 ml aliquots oh hydrochloric acid solutions of palladium, platinum or rhodium ions (100 μg M^{z+} /ml) were quantitatively transferred into separating funnels and vigorously shaken with 10 ml 5.10^{-4} mol/l solutions of **C4Ta** or **C6Ha**. The precious metallic ions concentration into the aqueous medium was determined before and after the liquid-liquid extraction and the metal extraction degree was evaluated.

3. RESULTS AND DISCUSSIONS

3.1. Characterisation of calix[n]arene derivatives

The spectral characteristics of p-tert-butyl calix(4)arene (noted **C4A**) were as follows: IR(KBr): 3400, 3150 cm^{-1} (OH stretching) and the fingerprint in the 1500-1000 cm^{-1}domain; UV-Vis: 243 nm, 279.5 nm, 287.5 nm. The elemental analysis results are 79.35%C, 8.72%H as compared with the theoretical values 81.44%C, 8.70%H.

The spectral characteristics of p-tert-butyl calix(6)arene (noted **C6A**) were as follows: IR(KBr): 3400, 3120 cm^{-1} (OH stretching) and the fingerprint in the 1500-1000 cm^{-1}domain; ^1H NMR ($CDCl_3$): δ 10.55 (s, 1, ArOH), δ 7.16 (s, 2, ArH), δ 3.90 (s, 2, CH_2), δ 1.27 (s, 9, $C(CH_3)_3$); UV-Vis: 244 nm, 284 nm, 291nm. The elemental analysis results are 77.91%C, 7.80%H.as compared with the theoretical data 81.44%C, 8.70%H.

The main spectral characteristics of tetraacetato-calix(4)arene (noted **C4Ta**) were: IR(KBr): 1758 cm^{-1} (>C=O stretching) and the fingerprint in the 1500-1000 cm^{-1} domain; UV-Vis: 244 nm, 267.5 nm, 276 nm; MS(3kV; 240°C): m/e= 817(10); 816(28); 775(29); 774(100); 733(34); 732 (64); 691(17); 690(36);…57(43); 43(82). The elemental analysis results are 75.24%C, 7.82%H.as compared with the theoretical values 76.44%C, 7.90%H.

The main spectral characteristics of hexaacetato-calix(6)arene (noted **C6Ta**) were: IR(KBr): 1762 cm^{-1} (>C=O stretching) and the fingerprint in the 1500-1000 cm^{-1} domain; UV-Vis: 245 nm, 266.5 nm, 275 nm; MS(2kV; 270°C): m/e =1225(2); 1224(3); 1205(5); 1204(9); 1182(7); 1165(36); 1164(40); 1123(31)…57(70); 43(100) The elemental analysis results are 75.23%C, 7.95%H as compared with the theoretical values 76.44%C, 7.90%H.

The calix[n]arenes derivatives formation was confirmed by the spectroscopic methods used for samples characterisation (fig. 1-4).

Elemental analysis indicates relatively lower values for carbon and hydrogen amounts thus suggesting a certain degree of solvent absorption into the calix[n]arene cavity.

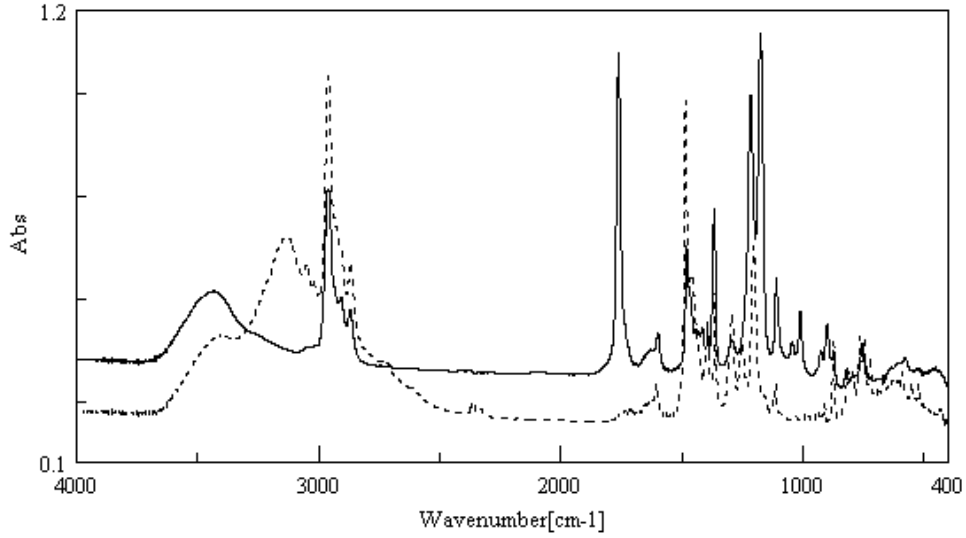

Figure 1: Infrared spectra of t-Butylcalix[6]arene hexaacetate **C6Ha** (straight line) as compared with the original t-Butylcalix[6]arene **C6A** (dashed line).

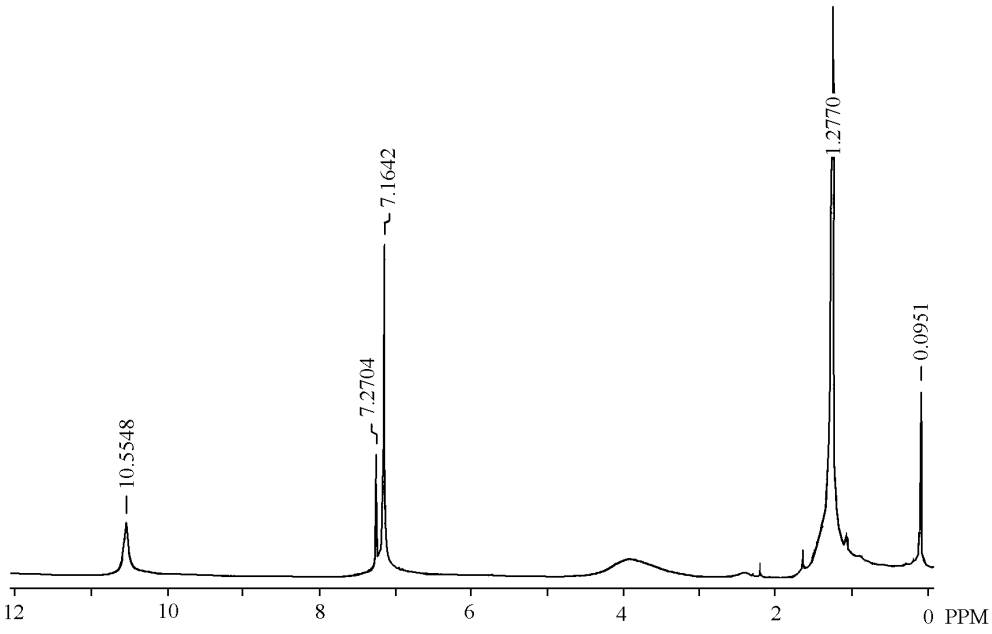

Figure 2: RMN spectrum of p-tert-butylcalix[6]arene **C6A**.

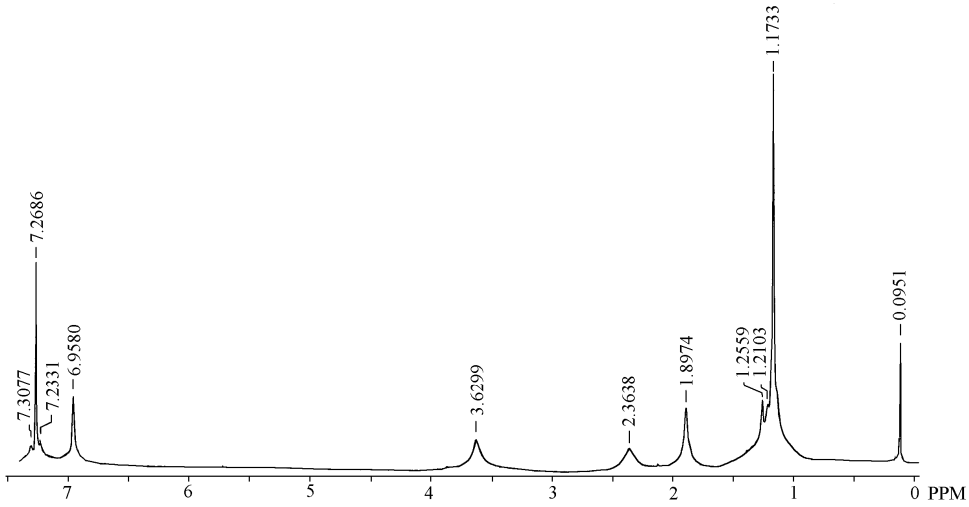

Figure 3: RMN spectrum of p-tert-butylcalix[6]arene hexaacetate **C6Ha**.

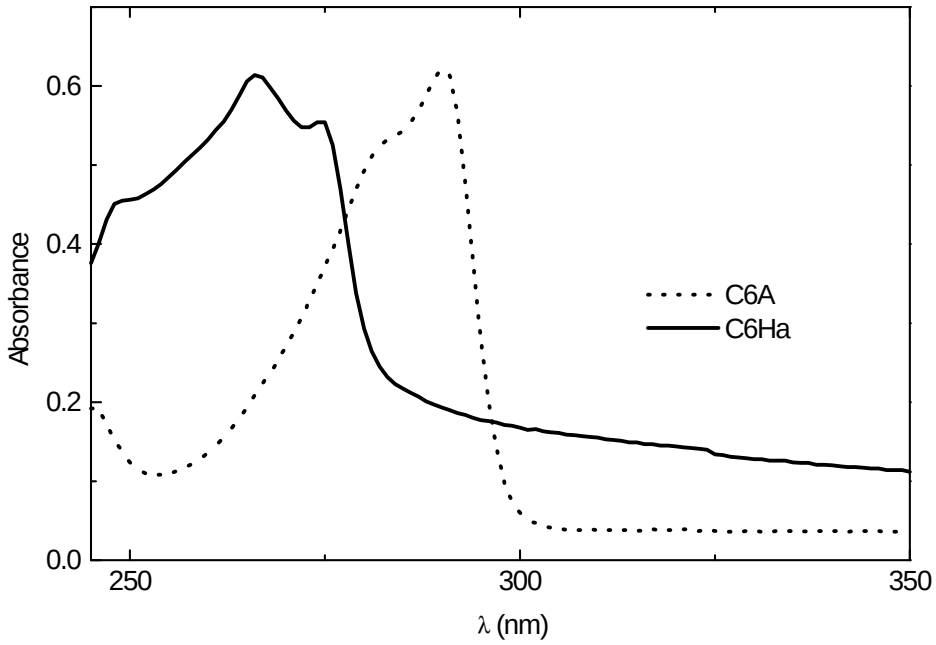

Figure 4: UV-Vis spectra of p-tert-butylcalix[6]arene hexaacetate **C6Ha** as compared with the original p-tert-butylcalix[6]arene **C6A** .

3.2. Extraction results

Precious metallic ions were extracted from aqueous medium by using C4Ta/$CHCl_3$ and C6Ha/$CHCl_3$ solutions. The extraction degree (ED) of Pd^{2+}, Pt^{2+} and Rh^3 was evaluated and compared (table 1).

C6Ha/$CHCl_3$ system shows the highest extraction ability for Pt^{2+} (II) ions and the lowest for Rh^{3+} species. One can state that, in our extraction conditions, no Rh(III) removal from aqueous solution could be observed.

By comparing Pd(II) extraction with C6Ha/$CHCl_3$ and C4Ta/$CHCl_3$ respectively, one can observe a relatively higher ED for the latter extraction system.

Table 1:

Metal ion extraction from aqueous solution with **C4Ta/$CHCl_3$** or **C6Ha/$CHCl_3$**

Aqueous phase	**Organic phase**	**pH value**	**Metal ion concentration (μg/ml)**		**Extractibility degree**
			Initial	**Final**	
Pd^{2+}(aq)	C4Ta($CHCl_3$)	5.0	1000	112.5	88.7%
Pd^{2+}(aq)	C6Ha($CHCl_3$)	5.0	1000	150.0	85.0%
Pt^{2+}(aq)	C6Ha($CHCl_3$)	5.0	1000	49.5	95.1%
Rh^{3+}(aq)	C6Ha($CHCl_3$)	6.0	1000	990.0	1.0%

4. Conclusions

p-tert-butil-calix[n]arene [where n=4,6] noted C4A and C6A and their corresponding acetate-derivatives i.e. C4Ta and C6Ha were prepared and characterized. The elemental analysis and FTIR, UV-Vis or NMR spectroscopy confirmed the purity of as prepared material.

The acetate derivatives were used as extraction reagents for Pt^{2+}, Pd^{2+} and Rh^{3+} ions. Liquid extraction was used for Pt^{2+}, Pd^{2+} and Rh^{3+} species removal from aqueous medium by using C4Ta/$CHCl_3$ and C6Ha/$CHCl_3$ systems. The extraction degree (ED) values shows that C6Ha/$CHCl_3$ is an efficient extracting agent for Pd^{2+} (ED>84%) and Pt^{2+} (ED>90%) species. For Pd^{2+} ions, the C4Ta/$CHCl_3$ system seems to be a better extracting agent than the C6Ha/$CHCl_3$ solution. Moreover, no Rh^{3+} ions extraction could be observed (ED ~ 1%) in our experimental conditions

REFERENCES

1. C.D. Gutsche, M. Iqbal, “Organic Synthesis”, **1989**, 68, 234-237.
2. C.D. Gutsche, B. Dhawan, M. Leonis, D. Stewart, “Organic Synthesis”, **1989**, 68, 238-242.
3. C.D. Gutsche, B. Dhawan, K. Hyun No, R. Muthukrishnan, “J. Am. Chem. Soc.” **1981**, 103, 3782-3792.
4. A.Gupta, S.M.Khopkar, “Talanta”, **1995**, 42, 1493-1496.
5. V.J.Mathew, S.M.Khopkar, “Talanta”, **1997**, 44, 1699-1703.

STUDIA UNIVERSITATIS BABEŞ-BOLYAI, PHYSICA, SPECIAL ISSUE, 2001

HEMOGLOBIN AND HUMAN BLOOD ADSORPTION ON SILVER COLLOIDAL PARTICLES: SURFACE ENHANCED RESONANCE RAMAN STUDIES

S. CÎNTĂ PÎNZARU*, S. CAVALU, N. LEOPOLD*, W. KIEFER*****

**Babes-Bolyai University,Physics Faculty, Optics and Spectroscopy Dept. Kogalniceanu 1, RO 3400 Cluj-Napoca, Romania*
***University of Oradea, Faculty of Medicine and Pharmacy, Biophysics Dept., 1 Dec. Square 10, RO-3700 Oradea*
****Institut für Physikalische Chemie, Universität Würzburg, Am Hubland, 97074 Würzburg, Germany*

ABSTRACT. These studies summarize the applications of surface enhanced resonance Raman scattering (SERRS) technique to the study of complicate biosamples like human blood, in comparison to a largely studied molecule: hemoglobin.

Introduction

Due to the high sensitivity and selectivity combined with the fluorescence quenching, surface enhanced Raman spectroscopy has been recently applied to investigate single molecule behaviour. [1, 2]. A single hemoglobin molecule adsorbed onto Ag nanoparticle was found to "respond" to the light excitation, being received SERRS signal under a laser focus radius of 1 micrometer [1]. Further, methemoglobin was found to reveal SERRS spectra dominated by the heme group, similar with the SERS and resonance Raman results previously reported [3, 4]. Evidencing single molecule opens new directions in the applied spectroscopy, mainly for the biological active samples or *in-vivo* studies. Following these pioneering studies, many other researchers have continued to demonstrate the immense potential of this approach for solving a number of problems in biochemistry, biophysics and molecular biology.

In the present work, surface enhanced resonance Raman spectra (SERRS) of hemoglobin (Hb) and freshly acquired integral human blood samples on colloidal silver particles have been recorded and discussed. Vibrational analysis and potential biological applications are further discussed.

Experimental

Hb powder was received from Sigma. Ag sol has been prepared according to the Lee-Meisel procedure [5]. A small amount from the Hb aqueous solution was dropped on the Ag sol, resulting in a final concentration for SERRS experiment of $2x10^{-9}$ mol l^{-1}.

The 514.5 nm line from an Ar ion laser Spectra Physics was employed for excitation of the Raman spectra. Back scattering configuration was performed with a micro-Raman set-up. The scattered light was focused on the entrance slit of a Dilor-Jobin Yvon Spex Groupe Horiba spectrometer equipped with 1800 grooves/mm holographic gratings. A CCD camera detection system and analysing software package LabSpec_3.01C were employed for the acquisition of data. The spectral resolution was 4 cm^{-1}.

Results and discussions

It is known that the hemoglobin molecule presents a strong fluorescence background at the green light (514.5 nm) excitation. Conventional Raman technique being inadequate, SERRS technique overcomes such difficulties by quenching fluorescence (Fig 1).

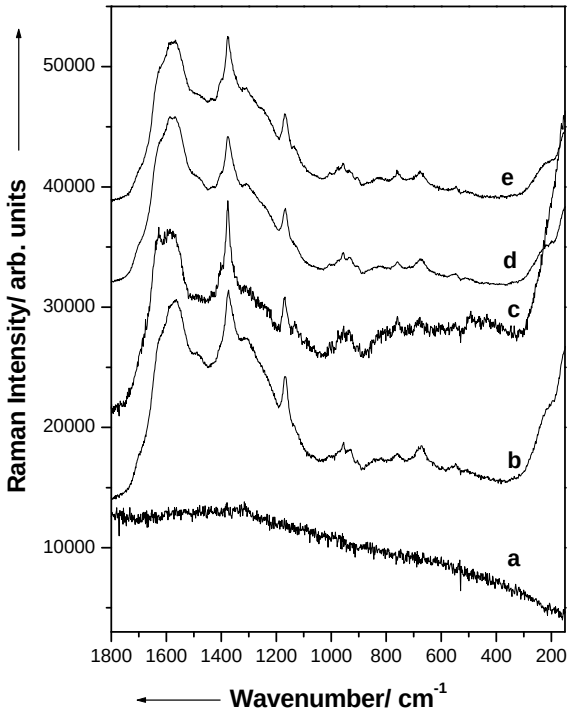

Fig. 1. a) Raman spectrum of pure haemoglobin covered by a fluorescence background. SERS spectra of haemoglobin b) 36, c) 75, d) 360, e) 720 nmol/l concentration in Lee-Meisel Ag colloid. Excitation 514.5 nm, power 120 mW on the sample.

A near-IR excitation with 1064 nm, which was previously used, could very well give rise to a certain degree of resonance enhancement [6], due to the several weak and broad optical absorption bands in the region 900-1100 nm. The presence of intense bands near 1370-1372 cm^{-1} HbF, metHb, hemin and its absence in NiHb and deoxyHb confirms this band to be a FT-Raman marker for Fe^{3+} [6]. The FT-Raman bands at 1370 and 1354 cm^{-1} in oxyHb and deoxyHb have been assigned to ν4 in good agreement with previous reports [3, 6]. The other prominent FT-Raman bands observed in all derivatives of Hb, but absent in hemin, around 1000 cm^{-1} can be correlated to the phenyl mode of the aromatic amino acid residues in globin part of Hb. Other representative band observed around 1654 cm^{-1} for Hb derivatives, which is absent in

hemin spectrum indicates that it is of globin origin [6]. This band is absent in the RR spectra of Hb derivatives spectra with visible excitation indicating non-resonant nature of globin moiety.

Modification of the Ag colloid with chloride ions was unnecessary for obtaining the SERRS signal. This modification generated only the typical Ag-Cl mode at 244 cm^{-1} in the SERRS spectrum.

According to the recent literature [1, 2], excitation with the 514.5 nm line leads to a SERRS spectrum characterised by three prominent haemoglobin bands: 1375, 1586, 1640 cm^{-1}. These bands are called "markers" of the hemic group packed in the polipeptidic chain and are assigned to in plane vibrations of the porphyrine ring. The dominant SERRS bands (Fig. 1) are located at 1610, 1586, 1568 cm^{-1} being assigned to the $\nu_{C=C}$ and $\nu_{C=N}$ modes. The bands at 1375, 1167, cm^{-1} were assigned to $\nu_{=C-N}$, and C-H bending respectively. The out of plane porphyrine bending vibrations are located at 957, 761 and 674 cm^{-1} respectively. Increasing concentration of haemoglobin solution dropped in Ag sol, very good reproducibility of SERRS signal was observed. Once optimised the SERRS acquiring procedure, increasing concentration does not affect significantly the intensity of the SERRS signal. This fact reflects that the signal was received only from the first monolayer of adsorbed molecules, further added molecules being already too far to the SERS active surface which could be completely covered. However, by increasing concentration, we can notice a little modification in relative intensity of 1375 cm^{-1} band with respect to 1586-1610 cm^{-1} spectral range, meaning the enhancement of $\nu_{=C-N}$ detrimental to the $\nu_{C=C}$ and $\nu_{C=N}$ modes. This observation suggests an electronic dellocalization of cromophore group.

In the present case, the SERRS signal represents a double resonance contribution, first a plasmon resonance of the colloidal particles excited with green light, representing the electromagnetic contribution to the total enhancement and second, the pre-resonance contribution of hemoglobin excited with green light. Fig. 2 presents the absorption spectrum of haemoglobin aqueous solution together with the human blood, in order to have a better eye-guide of the laser line position near the Soret band (420 nm). Hence, the total amplification is greater than the usual SERS amplification due to the well-known mechanisms (EM and CT). These results are in agreement with the previous report of oxihemoglobin adsorbed onto colloidal silver [7].

SERRS spectrum of integral human blood was successfully obtained and compared to that one of haemoglobin (Fig. 3 b, a). A time dependence study was also carried out (Fig. 3 b-e). A small amount of human blood freshly isolated was dropped into 2.5 ml Ag sol resulting a rapid change in colloid colour. The SERRS sample was putted under laser excitation and different acquiring times were employed successively. The main hemoglobin marker bands (1610, 1586, 1568, 1375, 1167, 957, 761 and 674 cm^{-1}) were observed in all the SERRS spectra of blood, even if some little changes in relative intensities are observed in the 1375-1586 cm^{-1} spectral range. Those changes are probably due to the photo- or thermal-induced coagulation of blood. Further oxidation of blood lead to the transition from oxihemoglobin (Fe^{2+}) to methemoglobin (Fe^{3+}) with a dellocalization of iron from porphyrine plane.

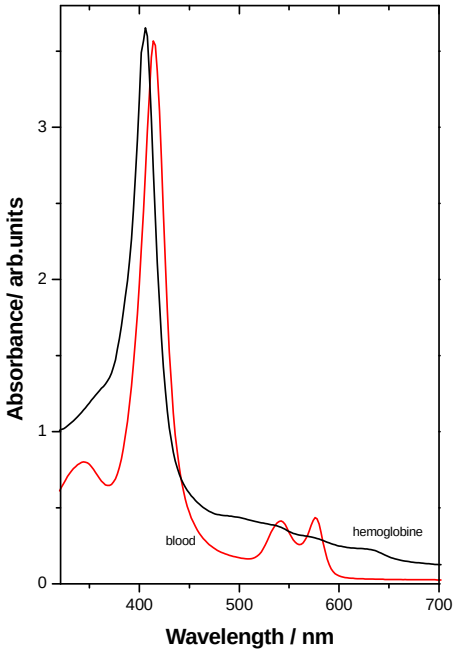

Fig. 2. Absorption spectra of hemoglobin and freshly isolated human blood.

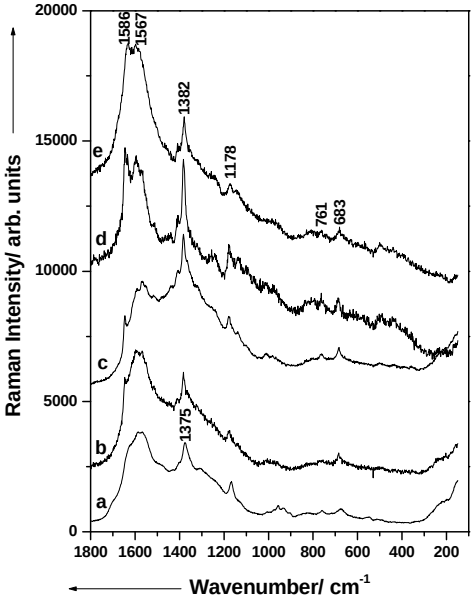

Fig. 3. Time evolution SERRS spectra of human blood (b) 10 s, c) 100 s, d) 200 s, e) 300 s acqiring time, in comparison to the SERRS spectrum of pure hemoglobin (a).

Hence, SERRS technique was employed as a very important tool for detecting small amounts of hemoglobin (nano-, picomolar concentrations and even lower) in complicate biosamples, due to its high selectivity and huge enhancement of the Raman signal, combined with (pre-) resonance amplification contribution of a defined species from a biological mixture.

Conclusions

Surface enhanced resonance Raman spectra of hemoglobin have been recorded and compared to those of human blood. The SERRS signal of hemoglobin was found to be independent on the increasing concentration after attempting the monolayer coverage. SERRS spectra of the human blood reveal the same hemoglobin marker bands, emphasising the high selectivity of this technique for complicate biosamples.

Acknowledgement.

Financial support from Grant T 131 BM is highly acknowledged.

REFERENCES

1. K. Kneipp, H. Kneipp, I. Itzkan, R.R. Dasari, M. S. Feld, Chem. Rew. 1999, 99, 2957-2975.
2. Hongxing Xu, Erik J. Bjerneld, M. Kall, L. Börjesson, Phys. Rew. Lett., 83, 21, 1999, 4357.
3. T. G. Spiro, T. C. Strekas, J. Am. Chem. Soc. 1974, 96, 338.
4. H. Brunner, H. Sussner, Biohim. Biophys. Acta, 310, 1973, 20-31.
5. P. C. Lee, D. Meisel, J. Phys. Chem., 1982, 86, 3391.
6. M. Mylrajan, Proceedings of the XVIIth International Conference on Raman Spectroscopy 2000, Eds., J. Wiley &Sons, Ltd, Chichester, New-York, Weinheim, p.956.
7. J. de Groot, R. E. Hester, J. Phys. Chem., 91, 1987, 1694.

STUDIA UNIVERSITATIS BABEŞ-BOLYAI, PHYSICA, SPECIAL ISSUE, 2001

SCALING CHARACTERISTICS OF THE STRUCTURE OF HUMAN HAEMOGLOBIN

AUREL COZA*, VASILE V. MORARIU**

**Faculty of Physics, Babes-Bolyai University, Cluj-Napoca, Romania*
***Department of Biophysics, Institute for Isotopic and Molecular Technologies, 3400 Cluj-Napoca, P.O.Box 700 Romania, E-mail: vvm@L40.itim-cj.ro and Faculty of Physics, Babes-Bolyai University, Cluj-Napoca, Romania*

The structure of proteins was described in terms of fractal characteristics both in relation to the position of the aminoacids and properties such as the hydrophobicity of the aminoacids. The methods of analysis involved typical procedures for measuring the fractal dimension. The goal of our study was to characterize the series of the temperature factors (Tf) of the hemoglobin heavy atoms (all excepting hydrogen).

The method used for analysis was the Detrended Fluctuations Analysis (DFA). DFA method consists in integration of the series and divides the integrated series in intervals of lag n, every interval being fitted with a line ($y_n(k)$). For different lag of n calculate $F(n)=\{1/N \sum_{k=1}^{N} [y(k)-y_n(k)]^2\}^{1/2}$, the value of F(n) typically will increase with n, and the slope of the plot relating F(n) with n gives the scaling exponent α.

We have calculated the scaling exponent from the series representing Tf of heavy atoms of human hemoglobin (chains A and B). We found that the hemoglobin is characterized by a complex DFA pattern, the slopes of the fitting lines (i.e. scaling exponents) of the DFA plot depend on *n.* It can be seen that hemoglobin is characterized by three slopes i.e. three scaling exponents. These three scaling exponents correspond to the three structural levels of protein (primary, secondary and tertiary). In this respect we have obtained α=0.96, α=0.81 and α=1 from the three levels. We have also found that mutant hemoglobin display a different pattern from that of normal hemoglobin, in this case only one or two slopes appeared and the values of the scaling exponents are different from that of normal protein. This changes in the vibrations pattern may be involved in the misfolding or the dysfunction of these proteins.

1.INTRODUCTION

It is well known from many theoretical and experimental studies that proteins behave like space defined fractals. The 3D structure of proteins is characterized by a fractal shape both in relation to position of the main chain atoms and surface[1]. Another fractal shape of proteins is that relating the amplitude of vibrations and frequencies[2]. In this respect we have analyzed the temperature factors (Tf) of the main chain atoms (C_{alpha}, N, C_{betta}). Tf is a measure of vibration amplitude of a certain atom and can be related with the amplitude (represented here by the rot mean square displacement from the position of equilibrium of a certain atom) by:

$$Tf = 8\pi^2 \left\langle u^2 \right\rangle ,$$

were *u* is the displacement from the equilibrium position.

The goal of this study was to find if there are certain relations between the frequency of vibrations of atoms in the main chain and their amplitude and if there are correlation between vibrations of atoms along the main chain.

In the present paper we have 'constructed' series of data representing the Tf of main chain atoms of hemoglobin (*chain A*) in their physical (natural) order: beginning with the first N atom and ending with the last C_{betta} atom. In this way were obtained series of more than 400 data for two hemoglobin: R state and a mutant form. The Tf were taken from Protein Data Bank (PDB)[3]. The series of data were analyzed using the now classical Fourier Transform (FT) and the more recently Detrended Fluctuations Analysis (DFA)[4]. We have also constructed a random walker using the series of Tf in order to find the mobility of certain parts of the protein main chain.

In the present work we bring evidence that the mobility of main chain hemoglobin atoms display fractal shape characterized by different scaling exponents for normal (R state) and mutant hemoglobin.

2.METHODS

The temperature factors of main chain atoms of hemoglobin where taken from (PDB) and where adjusted in their natural order, in this way we have obtained series of data that can be analyzed in order to find correlation between atomic fluctuations along the chain.

The methods used from analysis are:

1. DFA, according to this algorithm, the fluctuations are first integrated:

$$y(k) = \sum_{i=1}^{k} (x_i - x_{mean}) \tag{1}$$

where x(i) is the *i*-th number and x_{mean} is the mean value of the numbers in the series. The next step is to divide the integrated time series into boxes of equal length, *n* in each box of length *n* a least squares line is fit to the data (representing the trend in that box). The *y* co-ordinate of the straight line segments is denoted by $y_n(k)$. For a given box *n*, the characteristic size of fluctuation is calculated by:

$$F(n) = \sqrt{\frac{1}{N}\sum_{k=1}^{N}[y(k) - y_n(k)]^2} \tag{2}$$

Typically, *F(n)* will increase with box size *n*, the slope of the line relating *log F(n)* to *log n* determines the scaling exponent (self-similarity parameter) α.. The index α and β (FFT) are related as $\beta = 2\alpha-1$.

2.FFT used, especially, in order to find the nonstationarities of the series by comparing the β exponent (from the log-log slope of the FFT transform of the series) with the calculated with the relation $\beta=2\alpha-1$.

3. RW analysis consisting in the integration of the series using the relation:

$$M(i) = \sum_{i} (Tf(i) - m) \tag{3}$$

where $Tf(i)$ represent the *i*-th atom temperature factor and *m* is the average over all main chain atoms *Tf*. Plotting *M(i)* vs. *i* we find information about the mobility of different regions of the main chain.

3.RESULTS

DFA plots of both normal and mutant hemoglobin display a straight line in the log-log representation of *F(n) vs. n*, but the alpha coefficient resulting from the slope of the lines in different form the two mentioned hemoglobin. We have obtained α=1.36 for normal hemoglobin (fig1a) and α=1.16 for mutant form (fig. 1b)

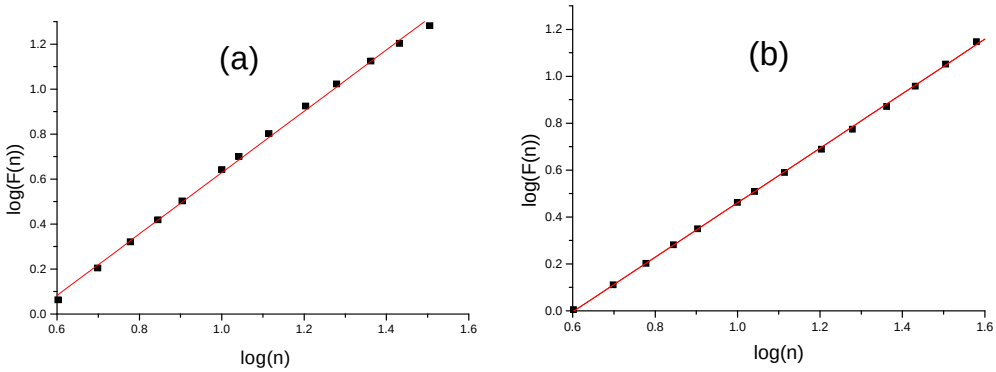

Fig. 1: DFA plot from Tf series of main chain atoms from normal (a) and mutant (b) hemoglobin

The value of β coefficient obtained from FFT for the two hemoglobin is 1.95 for normal and 1.58 for mutant form (fig 2a,b). Comparing the β_{FFT} whit $\beta_{calculated}$ we find a difference of 0.26 between both normal and mutant corresponding coefficients.

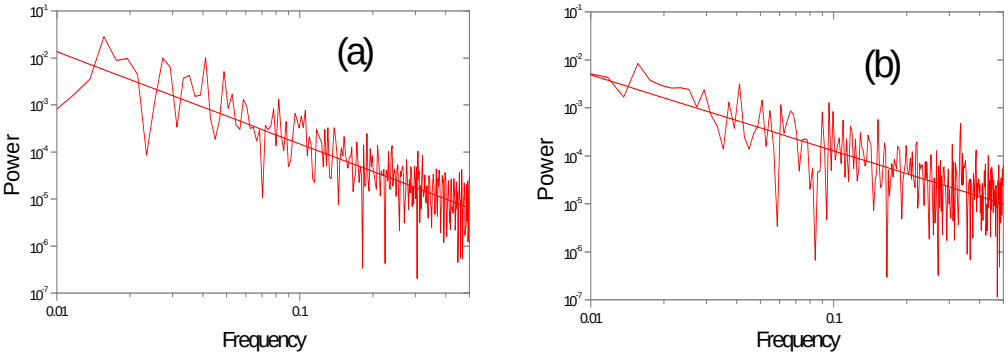

Fig.2: Log-log plot of FFT from normal (a) and mutant (b) hemoglobin main chain atoms.

The RW plots of *M(i)* vs *i* for the two forms is shown in the figure 3a,b. It can be seen that there are alternating portions of high and low mobility along the normal hemoglobin main chain (ascending and descending slopes of the plot correspond to

high and low mobility respectively) and only few large portions of high and low mobility from mutant form.

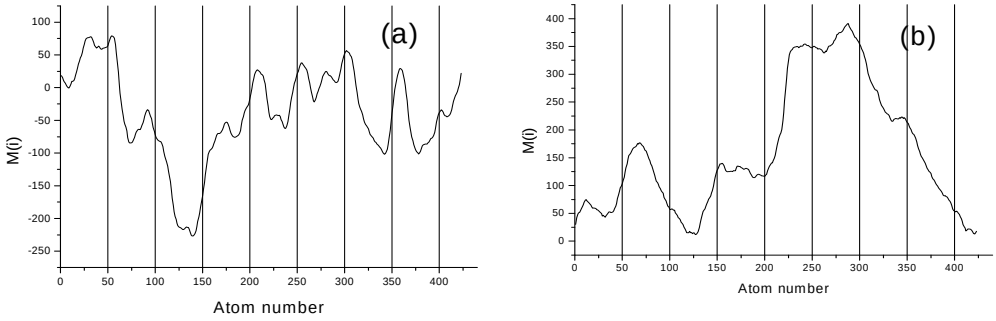

Fig.3 RW plots of the atomic Tf of normal (a) and mutant form (b) of human hemoglobin

4.CONCLUSIONS

From the data presented in the preceding section we may conclude that:

1. There is a strong correlation between the atomic Tf along the protein main chain in both normal and mutant hemoglobin. It also can be seen that the scaling exponent of the two chains is different, α=1.36 and 1.16 for normal and mutant form respectively. A possible explanation for this difference can be the fact that mutant form is unproper folded in this case the pattern of landscape energy became rugous and the correlation between movements of different atoms is weakened by random high potential barriers.

2. From the differences between the values of β_{FFT} and $\beta_{calculated}$ we can conclude that the two series are nonstationary and have the same nonsatationarity expressed by a difference of 0.26 between the two calculated and experimental coefficients.

3. From the RW plots presented in fig.3a,b it can be seen that there are significant differences between normal and mutant hemoglobin. Normal form presents strong irregularities (alternating portions of high and low mobility) and the mutant form is characterized by few such irregularities. One possible explanation for the misfunctioning of the mutant form can be this low varying mobility portions.

REFERENCES

1. Dewey, T.G., "Fractal Aspects of Protein Structure and Dynamics", *Fractals* **1**, 179-189 (1993).
2. Isvoran A., Morariu V.V., "Comparison of the Behavior of Sea Hare Myoglobin when it Forms two Different Complexes" *Chaos Solitions and Fractals* **12,** 1041-1045 (2001).
3. Protein Data Bank web address (www.rcsb.org).
4. C-K. Peng, S. Havlin, H. E. Stanley and A. L. Goldberger, "Detrended fluctuation analysis," *Chaos*, **5,** 82-87 (1995).

STUDIA UNIVERSITATIS BABEŞ-BOLYAI, PHYSICA, SPECIAL ISSUE, 2001

EPR INVESTIGATIONS OF NON COVALENT SPIN LABELLED CYTOCHROME C AND OVALBUMIN

G. DAMIAN[1], S. CAVALU[2], M. DÂNŞOREANU[3], S.SIMON[1], C. M. LUCACIU[4]

[1] "Babes-Bolyai" University, Dpt. of Physics, RO-3400 Cluj-Napoca, Romania
[2] University of Oradea, Faculty of Medicine, RO-3700, Oradea, Romania
[3] University of Medicine and Pharmacy "Iuliu Hatieganu", Dept. of Biophysics, RO-3400 Cluj-Napoca, Romania
[4] University of Medicine and Pharmacy, "Iuliu Haţieganu", Dept. of Biophysics and Radiopharmacy, RO-3400 Cluj-Napoca, Romania

ABSTRACT. Nitroxide radicals exhibit a number of chemical and physical properties that make them extremely useful molecules for studying biochemical systems, especially the metalloporphyrins. The aim of this work was to investigate the Tempyo spin label as a report group for the interactions and the conformational changes of lyophilized Cytochrome c and Ovalbumin, as function of pH. values in the range 2.5÷12. The EPR spectra are similar with those of other noncovalently spin label porphyrins in frozen solution at very low temperatures. This behavior indicated a possible spin-spin interaction between the hemic iron and the nitroxide group. The changes in the EPR spectra as function of the pH are discussed in terms of conformational changes of the proteins.

Introduction

The successful application of spin labeling to protein structure investigations is limited by the possibility to chemically change specific side chains in proteins. However, useful information on protein properties can be obtained by noncovalent spin labeling if the affinity of the protein for the label molecules is great enough to affect their motional freedom [1-4]. In the same time, EPR has been an invaluable tool for probing microscopic molecular motions in a variety of systems, including isotropic solvents [5,6], liquid crystals [7,8], model membranes and biomolecules [9,10]. The EPR spectrum of a nitroxide radical depends not only on the magnetic interactions of the unpaired electron spin but also on the reorientational motion of the probe molecule. The dependence is relatively simple when the reorientation is sufficiently fast, or more specifically, when $\tau\Delta\omega \ll 1$, where τ is the correlation time characterizing the motion and $\Delta\omega$ is a measure of magnitude of the orientation dependent part of the spin Hamiltonian. In this case the EPR spectrum is a simple superposition of Lorentzian lines. For slower rotations, i.e., when $\tau\Delta\omega \geq 1$, the EPR spectrum depends in a much more complicated fashion on the combined influences of molecular motion and magnetic interactions and the line shape can be analyzed only by using a theoretical approach [11]. These "slow-motional" line shapes are most often calculated using the stochastic Liouville equation, which can be solved numerically [12] to obtain the EPR spectra for fast or slow motions and for various Markovian models for reorientation.

In the present work, noncovalent spin labeled Cytochrome c and Ovalbumin with Tempyo spin label (3-carbamoyl-2,2,5,5-tetramethyl-3-pyrrolin-1-yloxy) were investigated both in liquid and lyophilized samples, in the pH range $2.5 \div 11$, in order to obtain useful information related to the interaction between the nitroxide group and the active site of the proteins. Interactions of spin label with hemic or nonhemic proteins might affect the spin label spectra and in the same time it is well known that the pH stronglyy influences the conformation of proteins leading to significant changes in the type and degree of these interactions [13]. In this pH range, we followed the effect of protein conformational changes on the interactions between the nitroxide and the active site of proteins and also the pH influence on molecular motion emphasized by the EPR spectra of the spin label.

Materials and Methods

Powder Cytochrome c and Ovalbumin from SIGMA Chemicals, were used without further purification. Proteins were hydrated in phosphate buffer physiological saline at a final concentration of 10^{-3} M. Tempyo spin-label (3-carbamoyl-2,2,5,5-tetramethyl-3-pyrrolin-1-yloxy), from SIGMA Chemicals, was added to the liquid samples of each protein in a final concentration of 10^{-3} M (protein/spin label molar ratio 1:1) and the pH values were adjusted to the desired value in the range $2.5 \div 11$. The amount of 5 ml from each sample was lyophilized for 30 hours at -5^{o}C and used for the EPR measurement, at room temperature.

EPR spectra for both liquid and lyophilized samples, were recorded at room temperature with a JEOL-JES-3B spectrometer, operating in X-band (9.5 GHz), equipped with a computer acquisition system. Samples were placed in quartz capillary tubes. The spectrometer settings were: modulation frequency 100 KHz, field modulation 1 G, microwave power 20mW. The computer simulation analysis of spectra, for obtaining the magnetic characteristic parameters, was made by using a program that is available to the public through the Internet (http://alfred.niehs.nih/LMB).

Results and Discussion

EPR spectra of liquid samples are typical for fast motion nitroxide radicals in liquid environment, being similar for both proteins, at all pH values. The characteristic powder EPR spectrum of a nitroxyl radical at X band is due primarily to anisotropy in the nitrogen hiperfine coupling. Fig.1 display the experimental and simulated spectra for Tempyo labeled Ovalbumin, lyophilized, at various pH values.

The z-axis of the g and hyperfine matrices is approximately along the axis of the nitrogen p orbital that is involved in π bonding to the nitroxyl oxygen. When the external magnetic field is along this axis, the nitrogen hyperfine splitting, A_{zz} , is about 35 G, while in the perpendicular plane, A_{xx} =5.33 G and A_{yy}=8.46 G. Generally, in studying the motional effects in spin label spectra, the changes in g-factor are not relevant and hence, A_{zz} parameter is the one which offers the substantial information concerning the rotational motion of the molecule in different environment [4,10]. Computer simulation analysis of Tempyo labeled Ovalbumin emphasize a Gaussian lineshape and a single paramagnetic spices for the best fit of experimental spectra.

According with [12,14], when rotational motion is slow enough that the spectra approach the powder spectrum limit, the rotational correlation time (τ) can be evaluated using the relation:

$$\tau = \alpha\,(1 - A_{zz'}/A_{zz})^{\beta}, \text{ where } \alpha = 2.25\cdot 10^{-9},\ \beta = -0.615$$

and A_{zz}/A_{zz} is the ratio of the observed splitting between the derivative extrema $2A_{zz}$ and the principal value of A_{zz} determined from the powder spectrum. The results are consistent with the "moderate jump diffusion" model for rotational diffusion [11,14] in which the molecule has a fixed orientation for some average residence time τ and then "jumps" through an average angle of $(6D\tau)^{1/2}$ radians, where D is the diffusion coefficient.

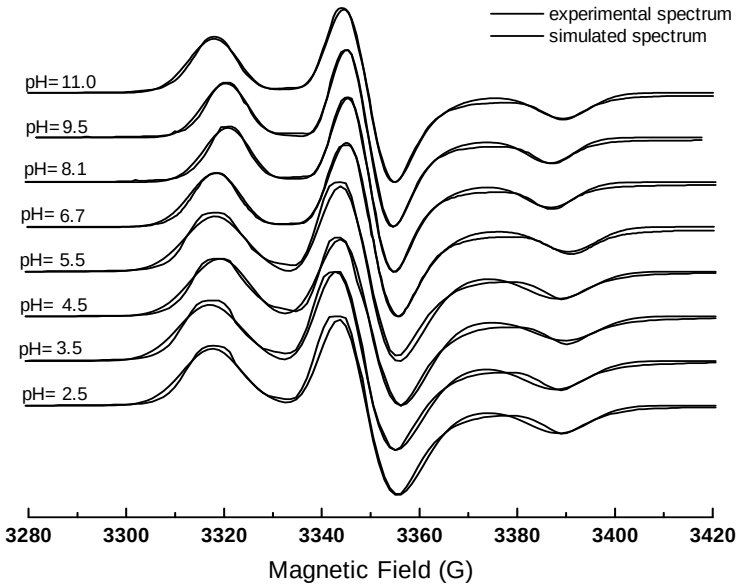

Fig.1. Experimental and simulated spectra of Tempyo labeled Ovalbumin

As showed in Fig. 3, the pH strongly influence the rotational correlation time with respect to Ovalbumin. In acid pH range, the NH_2 groups of the label molecule as well as those of the aminoacids residues are protonated. The fact that τ shows greater values in this range followed by a significant decrease in basic pH range, indicate a low mobility of Tempyo label in acid environment while a significant increase of mobility can be noticed in basic pH range. A minimum mobility can be observed around the izoelectric point ($pH_i = 4.5$) of this protein. The pH dependence of correlation time (involving the mobility of the label as well) results on the one hand from the electrostatic interactions which are stronger in acid environment, and on the other hand, the mobility is reduced by forming hydrogen bonding with the exposed aminoacids residues of the protein [15].

Figure 2 display the experimental and simulated spectra for Tempyo labeled Cytochrome c, lyophilized, at various pH values. In perpendicular plane, the nitrogen hyperfine splittings are A_{xx} = 4.51G and A_{yy} = 4.77G, on the average. Along the z axis, A_{zz} = 30G on the average, the values being similar to those calculated for covalently labelled methemoglobin and other porphyrins in frozen samples under 50 K [18,19].

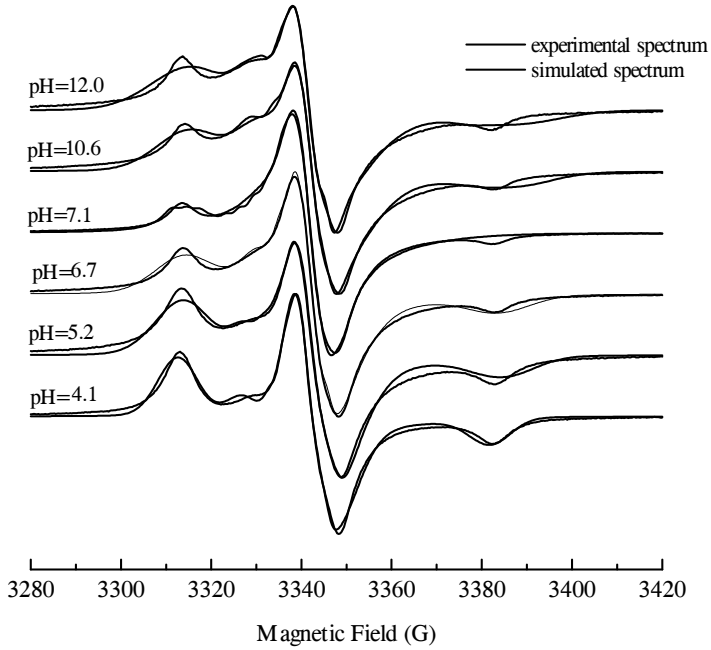

Fig.2. Experimental and simulated spectrum of Tempyo labelled Cytochrome c.

In the present study of noncovalent labelled Cytochrome c, the best fit of the experimental spectra can be obtained by assuming the presence of two sites in Cytochrome c, associated with two nonequivalent paramagnetic species [10]. Computer simulations indicate weighted sum of Gaussian lineshapes (static case) and Lorentzian lineshapes (dinamic case). The first species, with Gaussian lineshape and well resolved hyperfine splitting, is not influenced by the presence of the hemic iron.The correlation time versus pH (Fig. 3) reveals that in acid pH range the mobility of Tempyo decreased and has a mimimum value near the pH=5.5. By comparing with Ovalbumin case, we can notice that the mobility of Tempyo is greater with respect to Cytochrome c then to Ovalbumin. The second species in Cytochrome c,with Lorentzian lineshape, is obviously influenced by the presence of the hemic iron. The lack of hyperfine structure of this species is due to the dipolar and spin-spin interaction between the nitroxide radical and the paramagnetic iron of the hem group. As shown in Fig.3 the mobility of this species is very little affected by the pH variation. We suggest

that in basic pH range, where the label is not subject to strong electrostatic interactions, dipolar and spin-spin interactions are preferential manifested. However, the latter are less intense than the former, as results from Fig.3.

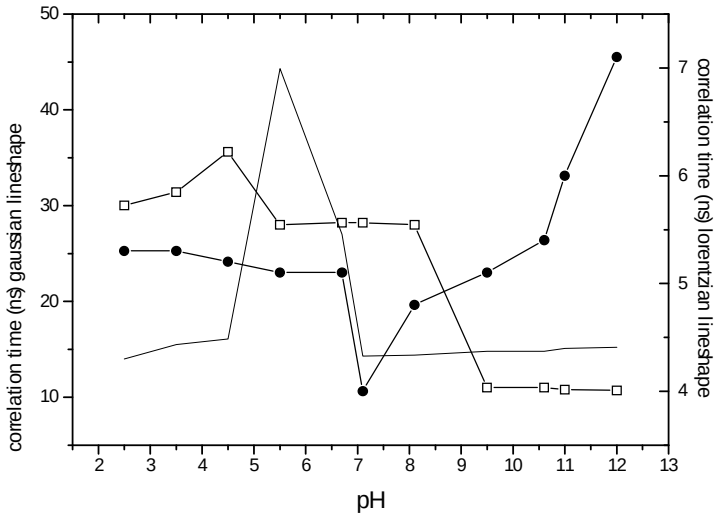

Fig.3. Correlation times vs pH:(——)Cytochrome c-Tempyo (gaussian lineshape); (—□—) Ovalbumin–Tempyo (gaussian lineshape); (—●—)Cytochrome c-Tempyo (lorentzian lineshape).

Conclusion

Noncovalent labeling of proteins can give valuable informations on the magnetic interactions between the label molecule and the paramagnetic center of the proteins. The relevance of this interaction can be obtained from lineshape analysis: computer simulation for nonhemic protein assume a Gaussian lineshape, while for hemic protein is assumed a weighted sum of Lorentzian and Gaussian components. In the framework of the "moderate jump diffusion" model for rotational diffusion, the rotational correlation time is strongly influenced by pH, due to the electrostatic interactions and hydrogen bonding.

REFERENCES

[1] Morrisett, J.D., Wien, R.W., McConnell, H.M. (1973), *Ann. N.Y. Acad. Sci*. (1973), 222, 149-162.

[2] Jost, P., Griffith, O.H. (1972) in *Methods in Pharmacology*, Chignell C. Ed., Appleton, New York (1972), p.223-276.

[3] Morrisett, J.D., Pownall, H.J., Gotto, A.M., *J.Biol.Chem.* (1975), 250, 2487-2494.

[4] Morrisett, J.D. in *Spin Labelling – Theory and application*, Berliner J. Ed., Acad.Press, (1975) pp. 273-331.

[5] Hwang, J.S., Mason, R.P., Hwang, L-P., Freed, J.H., *J.Phys.Chem*. (1975), 79, 489.

[6] Zager, S.A., Freed, J.H., *J.Chem.Phys.* (1982), 77, 3344-3360.

[7] Polnaszek, C.F., Freed, J.H., *J.Phys.Chem*. (1975), 79, 2283.

[8] Meirovitch, E., Igner, D., Moro, G., Freed, J.H., *J.Chem.Phys.* (1982), 77, 3915.

[9] Tanaka, H., Freed, J.H., *J.Phys.Chem*. (1985), 89, 350.

[10] Marsh, D., Horvath, L. I., in *Advance EPR – Application in Biology and Biochemistry* Hoff, A.J. Ed., Elsevier, Amsterdam (1989), p.707-752.

[11] Earle, K.A., Budil, D.E., Freed, J.H., *J.Phys.Chem*. (1993), 97, 13289-13297.

[12] Schneider, D.J., Freed, J.H., in *Biological Magnetic Resonance*, Berliner, L.J., Reuben, J., Eds., Plenum, New York (1989), vol.8, p.1.

[13] Eaton, G.R., Eaton, S.S.,C*oord.Chem. Rev.* (1978), 26, p.207-262.

[14] Schreider, S., Polnaszek, C.F., Smith, I., C., P., *Biochim.Biophys.Acta*, (1978), 515, 375-436.

[15] Du,J.L.,Eaton G.R.,Eaton S.S.,*J.Magn.Res*.(1995),series A,115,213-221.

[16] Foster, J.R., in *Albumin structure, Function and Uses*, Rosenoer, V.M., Oratz, M., Rothschild, M.A., Eds., Pergamon, Oxford (1977), p.53-84.

[17] Carter, D.C., Ho, J.X., *Adv. Protein. Chem*. (1994), 45, 153-203.

[18] Carter, D.C., He, X.M., Munson, S.H., Twigg, P.D., Gernerd, K.M., Broom, M.B., Miller, T.Y., *Science* (1989), 244, 1195-1198.

[19] Budker, V., Du, J-L., Seiter, M., Eaton G.R., Eaton, S.S., *Biophys. J*., (1995), 68, 2531-2542.

STUDIA UNIVERSITATIS BABEŞ-BOLYAI, PHYSICA, SPECIAL ISSUE, 2001

ALUMINA MEMBRANES USED AS MOLECULAR FILTERS FOR HUMAN RED BLOOD CELLS AND BOVINE SERUM ALBUMIN

GH.MIHAILESCU, STELA PRUNEANU, SILVIA NEAMTU, LILIANA OLENIC

National Institute of R&D for Isotopic and Molecular Technologies
P.O.BOX 700, 3400 Cluj-Napoca, Romania

ABSTRACT. Nanoporous alumina membranes were electrochemically prepared in sulfuric or phosphoric acid. After preparation they were used for microfiltration of biological media, such as human red blood cells and bovine serum albumin. The filtration efficiency was studied by UV-Vis absorption spectroscopy.

1. INTRODUCTION

Aluminum oxide (Al_2O_3) has attracted a great attention as template material for fabrication of nano-devices and for application to micro and ultrafiltration.

Filters can be divided into two general categories according to whether particle retention occurs on the surface or throughout the filter's depth. A wide variety of filter membranes are currently produced. Filters based on cellulose membranes are the most widely used for routine applications. If high filtration performance is required, a microporous inorganic membrane (Al_2O_3) is recommended /1/. The tightly- packed capillary pores produce a filtration mechanism, which operates by surface sieving particles. The alumina membranes have several features that indicate the practical benefit in analytical and diagnostic separations. They are transparent, allowing the view of the retained materials from either side of the membrane. The capillary pore structure allows no lateral diffusion of liquids along the membrane /2/.

In this paper we present the filtration efficiency of alumina membranes, for solutions of human red blood cells and bovine serum albumin.

2. EXPERIMENTAL

High purity (99.9%) aluminum foil was vertically mounted between the two parts of an electrochemical cell. One side was exposed to electrolyte while the other side was exposed to distilled water. A large area aluminum disk was used as counter electrode. The electrolyte employed during oxidation was either an aqueous solution of 15% sulfuric acid or 32% phosphoric acid with 1% sulfuric acid.

The oxidation was performed at low temperature ($4\ldots8^0$ C) for about 3 hours, at a current density of 17 $mAcm^{-2}$ (15% H_2SO_4) and respectively 10 $mAcm^{-2}$ (32% H_3PO_4 + 1% H_2SO_4). The stirring of the electrolyte during oxidation was a necessary condition for the formation of an ordered structure oxide.

In order to obtain nanoporous alumina membranes, the Al_2O_3/Al layer was treated as following: the residual Al from the backside was removed, by etching in a solution of $CuCl_2$ and HCl; after that, the barrier layer was dissolved in 32% phosphoric acid. At the end of these steps we obtained nanoporous membranes having pores' diameter between 20 and 100 nm. We have used these membranes as filters for biological media.

3. RESULTS AND DISCUSSIONS

Filtration of human red blood cells

Red blood cells (erythrocytes) were isolated from the blood by centrifugation and repeatedly washing with buffered serum (150 mM NaCl, HEPES 4mM, pH 7.4). After the last centrifugation, the erythrocyte pallet was suspended in a buffered medium, at a concentration of 0.1%. The cell suspension was then filtered through a 20 nm porous alumina membrane (the membrane was prepared in 15% sulfuric acid) and also through a 100 nm porous membrane.

The filtration was performed by mounting the alumina membrane into a cell and than connecting the cell to a vacuum pump. Both the initial and the filtered solutions were analyzed by UV-Vis absorption spectroscopy, using a SPECORD UV-Vis spectrophotometer.

The hemoglobin, the main protein of the erythrocytes (98%), presents a characteristic absorption maximum at 410 nm. Since its intensity is proportional with the hemoglobin concentration, we could evaluate the filtration efficiency of the alumina membrane. The results are presented in fig.1and fig.2. In fig.1, curve 1 represents the spectrum of 0.1% aqueous erythrocytes solution (obtained by hemolysis of erythrocytes in water) while curve 2 represents the spectrum of 0.1% erythrocytes in buffered medium.

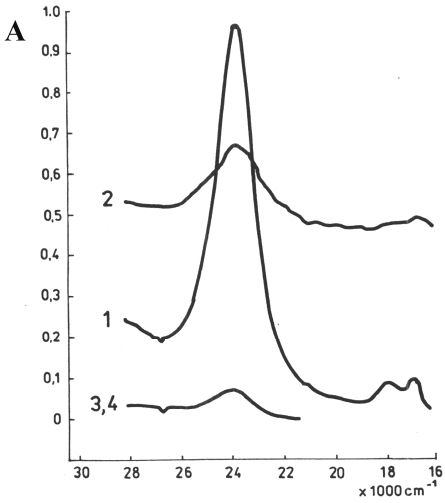

Fig1: Absorption spectra of initials (1,2) and filtered (3,4) solutions of human red blood cells, through 20 nm alumina membrane

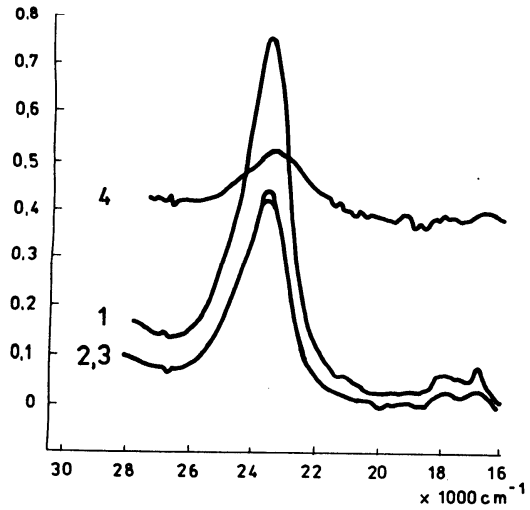

Fig2: Absorption spectra of initials (1,4) and filtered (2,3) solutions of human red blood cells through a 100 nm alumina membrane

Although the two solutions have the same hemoglobin concentration, the intensity of the two curves is different. This is due to the fact that in the first solution, the hemoglobin is released from the cell and it absorbs a large quantity of the incident radiation.

In the second case, the erythrocytes' membranes prevent the absorption of the radiation, by hemoglobin. Also, one can observe that in this case (curve 2) the baseline is far from zero, due to the light scattering on the cell membrane.

Curve 3 represents the absorption spectra of the filtered erythrocyte suspension, through 20nm porous alumina membranes. Curve 4, that overlaps curve 3, was characteristic for the filtered suspension, hemolysed with water. Both spectra have baselines close to zero and that suggests the absence of the erythrocytes after filtration.

In fig.2, curve 1 represents the absorption spectrum of 0.1% aqueous erythrocytes solution while curve 4 represents the spectrum of 0.1% erythrocytes in buffered medium. After filtration through a 100nm porous membrane, we have obtained two identical curves (2 and 3).

The filtration efficiency is given by the rejection factor, which is defined as:

$$\mathbf{R=1-(C_f / C_I)}$$

where C_f and C_I represent the concentration of the filtered and initial solutions. In our case, the concentration of the filtered solutions was 0.007% (for a 20nm porous membrane) and 0.038% (for a 100nm porous membrane) and that gives rejection factors of 0.93 respectively 0.62.

Filtration of bovine serum albumin

A solution of 0.1% bovine serum albumin (M_w=67000) was filtered through porous alumina membranes, having the pore diameter of 20nm and 100nm. The filtration efficiency was determined by analyzing the content of albumin, from the filtered solutions, with an UV-Vis spectrophotometer.

The albumin has three main absorption maxima, at 278nm (due to the presence of tyrosine), 203nm and 190nm (due to the presence of other aminoacids). In fig.3 is illustrated the absorption spectra of 0.1% albumin solution filtered through a 100nm porous membrane (P_1) and 20nm membrane (P_2).

In order to determine the concentration of these solutions, the spectra were compared with those of some standard solutions, obtained by successive dilutions of the 0.1% albumin solution (M_1 respectively M_2).

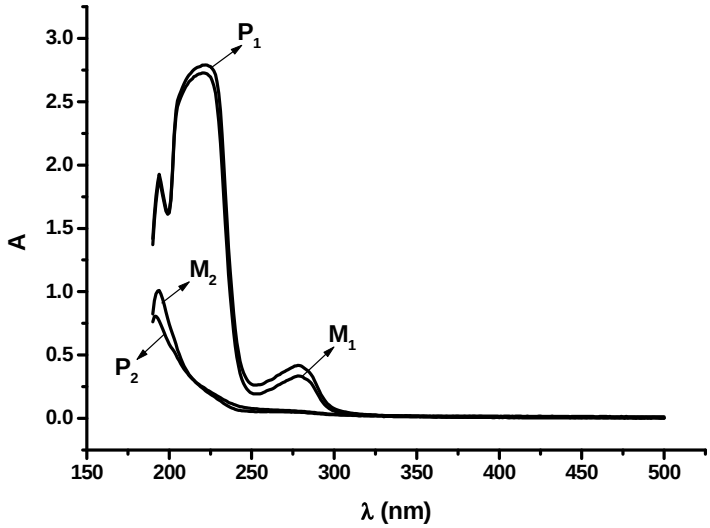

Fig.3 Absorption spectra of filtered solutions of bovine serum albumin through a 100nm alumina filter (P_1) and 20nm alumina filter (P_2)

The albumin concentration of M_1 standard solution was 0.058% and that corresponds to the concentration of filtered solution, P_1. In the case of M_2 standard solution, the albumin concentration was very low (0.0014%), suggesting that the 20nm porous membrane retained almost the entire albumin. The rejection factor of the two membranes has the value of 0.42 (100nm membrane) and 0.986 (20nm membrane). These results show very good filtration efficiency for the 20nm alumina filter.

4. CONCLUSIONS

Porous alumina membranes prepared in sulfuric and phosphoric acids, were used as molecular filters for human red blood cells solutions and bovine serum albumin solution. A very good filtration efficiency was obtained with the 20 nm porous membranes, that gave rejection factors higher than 0.92.

REFERENCES

1. C.H.McKenzie, R.Heller, D.Diebel, Applied and Environmental Microbiology 58(1992)773
2. J.Kong, A.M.Cassell, H.Dai, Chem.Phys.Lett. 292(1998)567

STUDIA UNIVERSITATIS BABEŞ-BOLYAI, PHYSICA, SPECIAL ISSUE, 2001

CHARACTERISTICS OF THE ATOMIC VIBRATION OF CYTOSKELETON PROTEINS

V.V. MORARIU*, LAVINIA GHEORGHE**

**Department of Biophysics, Institute for Isotopic and Molecular Technologies, 3400 Cluj-Napoca, P.O.Box 700 Romania, E-mail: vvm@L40.itim-cj. ro*
***Faculty of Physics, Babes-Bolyai University, Cluj-Napoca, Romania*

1.INTRODUCTION

The functionality of the proteins is due to their flexibility properties. A similar rigid structure would not be able to perform the task the protein is designed for. The flexibility of the proteins is due to the fact that there are internal degrees of freedom of the atoms in the protein. As a result the intrastructural mobility of proteins is an important feature which received much attention during the last years. The present work is intended to investigate the correlation of this mobility of the atoms inside the protein chain for a particular class of proteins, namely the cytoskeleton proteins.

Eukariotic cells have distinct shapes and a high degree of internal organization. They are capable of changing their shape and, in many cases, of migrating from one place to another. These properties of shape and movement depend on networks of filaments in the cytoplasm that serve as the cell's cytoskeleton. Among the most important types of filaments in the cytoskeleton are the actin filaments. They are composed of globular protein units or actin monomers. These monomers, also known as actin G, has a molecular weight of 42.000. The structure of the molecule is stabilized by binding a calcium ion and an ATP molecule noncovalently bound.

There are some clues in the literature that the temperature factor of the proteins, which is related to the internal mobility, might have a fractal structure (1-2). This has never been checked up directly until present. In a series of investigations on proteins alone and bound proteins to their substrate it was revealed that temperature factor series of all atoms have a fractal character. To be more specific these papers searched for a deterministic chaos behavior when the protein binds to the substrate. Suppose the temperature factor series for the free protein is $\{T^{free}_i\}$ and $\{T^{bound}_i\}$ is the similar series when the substrate is bound to the protein. The procedure was to subtract these two series, and to search for attractors in the resulting series $\{T^{free}_i\}$ - $\{T^{bound}_i\}$. Preliminary to the attractor analysis it was also performed a Fast Fourier Analysis (FFT) on the subtracted series which resulted typically in a fractal plot (log of amplitude versus log of frequency can BE fitted by a line whose slope represents the scaling exponent β). As the result of subtraction of the two series is a fractal object, it means that also the two initial series are fractal. This is what we want to prove directly in this work. Besides, it is known that if the series is nonstationary, then FFT procedure introduce further correlation into the spectrum which to not directly reflect the correlation of the fluctuations. In order to avoid this problem we used a supplementary method of analysis.

We have also explored the random walk plot of the temperature factor series in order to draw preliminary conclusions on the changes induced by the binding of proteins.

2. MATERIALS AND METHODS

The protein of choice was actin. In the Protein Data Bank we found structural and temperature factor series for two complexed forms of actin with other two proteins: an actin-gelsolin complex and a an actin-deoxyribonuclease complex. In both cases actin has calcium and ATP bound which are necessary conditions for the stability of this protein. Therefore we have, in fact, available data for four proteins. We can make therefore interprotein and same protein bound to different proteins comparisons.

The series of data used for analysis was limited to the main chain atoms:

$$N — C_\alpha — C — N — C_\alpha — C — ...$$

where C_α is the alpha carbon, or the central atom in the amino acid.

The series was subjected to FFT and the spectrum was plot as a double log plot. The spectrum was fitted with a line with slope β. The series were also subjected to Detrended Fluctuation Analysis which removes the nonstationarities in the series. The resulting scaling exponent is a "pure" one and denoted as α. The relationship between the two exponents is:

$$\beta = 2\alpha - 1$$

This is a theoretical relationship as the calculated value of a $\beta_{calculated}$ from an α value may be different to the experimental value β. When $\beta_{calculated} \neq \beta$, then the series contains nonstationarities.

It is instructive to explore the series of the temperature factors either in the raw form or as or as a random walk curve. This latter plot involves integration of the fluctuation step by step. We shall refer to this procedure as random walk analysis (RWA). The difference between the raw plot and RWA plot is that the latter gives a simpler picture in respect to the average level of fluctuation.

3. RESULTS

Fig 1 illustrates the temperature factor series for actin complexed with gelsolin and deoxyribonuclease respectively. We can notice that there is a central region in actin where mobility is significantly increased and is characterized by a triplet more resolved in the complex with gelsolin. It can also be noticed that the binding proteins are shorter chain length structures and both of them imprint their characteristically higher mobility on actin. The RWA plots are presented in fig.2 for the same proteins and complexes.

The RWA plots are illustrated in fig.2. They contain similar information as in fig.1 but they better reflect the change of the mobility in respect to the average value of the fluctuations. For example the significant change of the mobility occur at atom no. $\approx$ 530 and continue beyond the number 600. It is interesting to note that the binding of either of the proteins to actin does not change significantly the mobility of this region. At contrary, there appears to be a susceptibility of actin to mobile parts of the complexing proteins. They "imprint" or "transfer" their mobility to actin. This finding should be confirmed by studying other complexed forms of proteins.

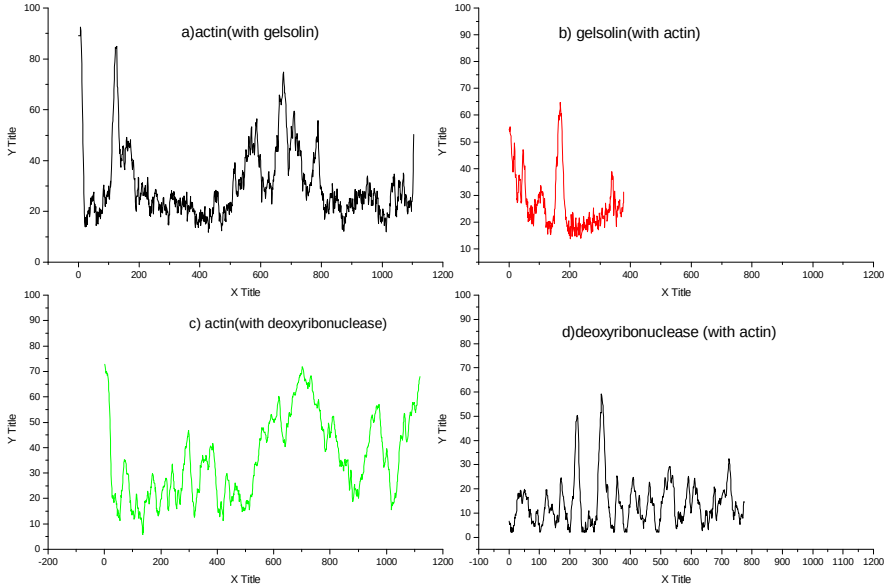

Fig.1 The temperature factor series for the atoms of the main chain for actin complexes.

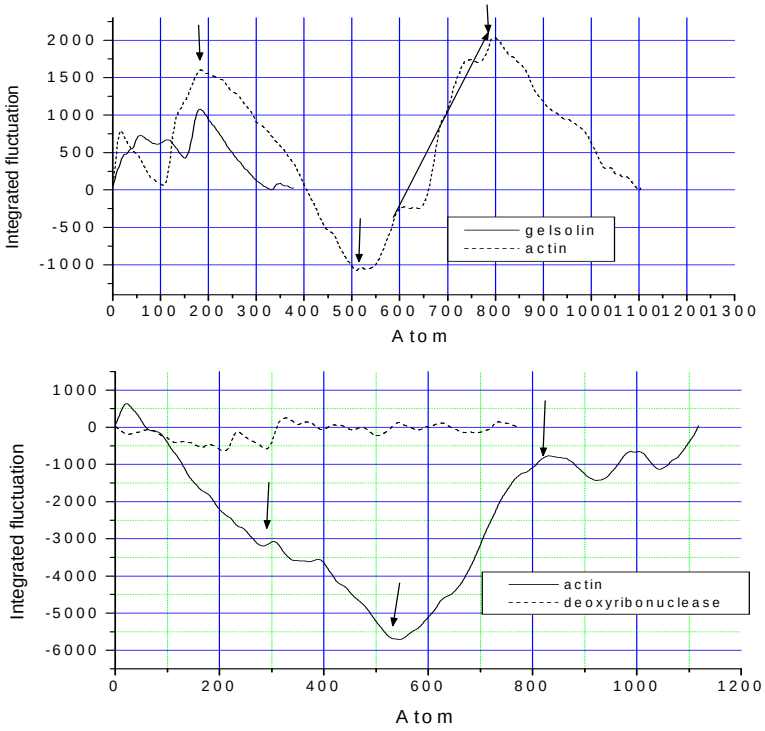

Fig.2 Random walk analysis for actin complexes with gelsolin (upper plot) and deoxyribonuclease respectively (lower plot).

Example of FFT and DFA are further presented in fig. 3 and 4. The results for the scaling exponents are included in table 1. We can notice that the α scaling exponents vary around the value 1.33 which is exactly the mean value which was found for other proteins (3). There appear to be no strict rule concerning the change of the α scaling exponent upon binding of actin to another protein i.e. in one case its value increases while in the other it decreases.

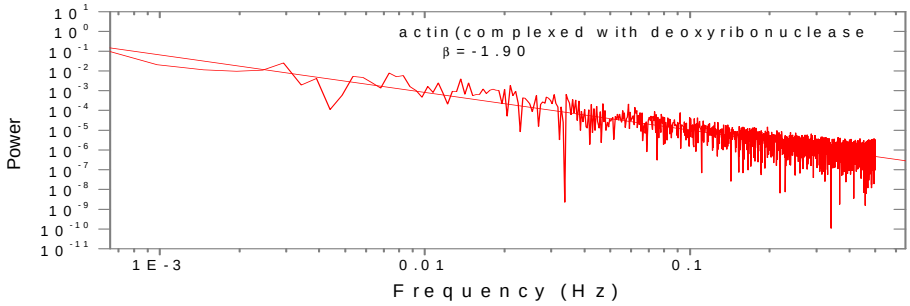

Fig.3 Fast Fourier Transform of the temperature factor series of actin complexed with deoxyrybonuclease. The slope of the fitting line is -1.9.

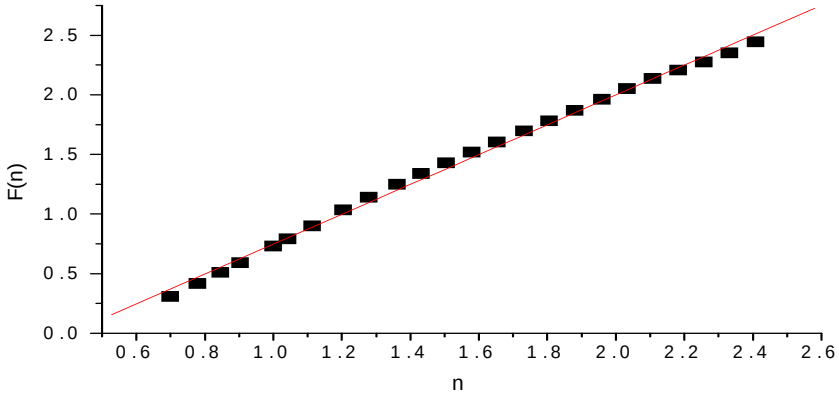

Fig.4 Detrended Fluctuation Analysis of actin complexed with deoxyribonuclease

Table 1

Scaling exponents for proteins as resulting from DFA -(α exponent) and FFT- (β exponent).

No.	**Protein**	**Complex**	**Species**	**α**	**β calcul.**	**β(FFT)**	Δβ
1	gelsolin	CaATP actin with gelsolin	*homo sapiens*	1.40	1.80	1.80	0
2	actin	CaATP actin with gelsolin	*dictyostelium discoideum*	1.25	1.50	1.77	0.27
3	actin	deoxiribonuclease with actin	*oryctolagus cuniculus*	1.39	1.78	1.90	0.12
4	deoxyribo-nuclease	deoxyribonuclease with actin	*bos taurus*	1.29	1.58	2.31	0.73

βcalculat=2α-1; Δβ=|βcalculat-βFFT|

4. CONCLUSIONS

- The scaling exponent of actin complex with gelsolin or deoxyribonuclease has a value around 4./3 which confirms the findings in ref.3. This may suggest that the mobility in the proteins is organized according to a single universal scaling law.

- Biding of two different proteins to actin leaves unchanged the central mobile part of acting while it "imprints" their own mobility characteristics to actin.

REFERENCES

1. A.Isvoran, V.V.Morariu, Comparison of the behavior of sea hare myoglobin when it forms two different complexes, Chaos, Solitons and Fractals, vol.12 1041-1045, 2001
2. A.Isvoran, V.V.Morariu, Analysis of the nonlinear behavior of ascaris trypsin inhibitor from NMR data, Chaos, Solitons and Fractals, vol.12, 1485-1488, 2001
3. V.V.Morariu, Scaling in the temperature factor series proteins, in Proceedings of the Second Conference "Isotopic and Molecular Processes" PIM 2001, Sept.27-29, 2001, Studia Universitatis Babes-Bolyai, Special Issue 2001

STUDIA UNIVERSITATIS BABEŞ-BOLYAI, PHYSICA, SPECIAL ISSUE, 2001

LOCAL CHARACTERIZATION OF TIME SERIES BY DETRENDED FLUCTUATION ANALYSIS (DFA)

CRISTIAN V.L. POP, IOAN TURCU, LORELAI I. CIORTEA

National Institute for Research and Development of Isotopic and Molecular Technologies, P.O.Box 700, 3400 Cluj-Napoca 5, e-mail:popcl@l40.itim-cj.ro

ABSTRACT. The data obtained in experiments performed on dynamic processes in biophysical systems are generally very long time series and have significant temporal non-stationary fluctuations. Such a time series are obtained, for example, by measuring the coherent light intensity scattered at small angles by a human erythrocyte suspension during the sedimentation process. The purpose of our work was to investigate the sedimentation process and to characterize the local temporal correlation using two modified versions of the DFA method. Each version give a set of local scaling exponents obtained by applying the DFA on successive shorter data domains. The information given only by one value of the scaling exponent has a global character and cannot describe the local temporal correlation for long processes.

INTRODUCTION

The erytrocyte sedimentation rate (ESR) is one of the most useful test used by clinicians in medical diagnosis. Usually ESR mesurement focus on the movement of the boundary between sedimenting erythrocytes and plasma. Detailed analysis of the process reveals complex dynamic and self-organizing properties [1].

In our work a light scattering technique was used to capture and characterize the dynamic aspects of the ESR process for two groups of volunters: healty subjects on one side and persons with different disease (with increased values of the ESR) on the other side. The dynamic parameter that we have measured was the intensity of the light scattered at small angles by the erythrocyte suspensions. The light intensity scattered by the samples has a very complex spatio-temporal pattern. In the present work we investigate the temporal aspects of the processes applying the DFA method [2,3] on time series obtained by converting the analogic signal into a digital one.

MATERIALS AND METHODS

The scattering experiments were performed with a 5-mW He-Ne laser at 632,8-nm wavelength. The laser beam was applied on an erythrocyte suspension of about 1mm thin. The light scattered by suspension was detected by a photodiode and the signal was amplified and transferred to a PC computer by an A/D converter. For good temporal resolution we used a 20 Hz sapling rate of the A/D convertor for processes with characteristic times of about 10^4 seconds.

The investigated samples were human erythrocyte suspension in sanguine plasma with hematocrit 5% and different values of ESR. Erythrocyte cells were obtained from human blood of healthy and sick donors collected on Na citrate 3,8%. Cells were separated from plasma by centrifugation, washed three times with buffered

solution (150 mM NaCl, 5 mM Hepes/HCl, pH 7,4) and resuspended in plasma. There was two type of blood samples: erythrocyte suspensions from healthy donors with small values of the ESR parameter taken as control and samples with high ESR values from subjects with pathological problems.

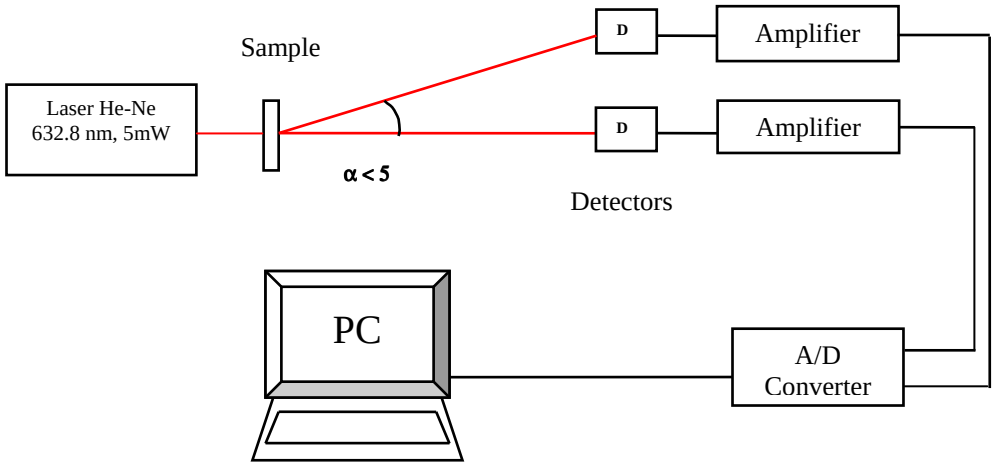

Figure 1: Experimental Setup of the Light Scattering

RESULTS

The coupling of the experimental set-up with the computer allow the on line registration of the data as time series. With a 20 Hz sampling rate, the dynamics of the sedimentation processes was captured with relatively high accuracy over time domains of about 2 hours. The intensity of the scattered light has a very complex fluctuation pattern. At the beginning the intensity of scattered light has uncorrelated fluctuations the dynamic patern being similar to that of a random process (white noise) Figure 2A. As the time increase the fluctuations becomes more and more correlated and the dynamic patern change significantly (Figure 2B).

A **first** characteristic property of this dynamic parameter is his self-similar fluctuating behaviour. Self-similarity means that the fluctuations for sorter sub-units are statistically equivalent with the fluctuations for the whole time series.

The sedimentation process of human erythrocyte is described in our experiment by the intensity of scattered light given as a long time series of 130000 data corresponding to 6500 seconds.

For graphical reasons we present in figure 3A a local domain of 120 seconds (2400 data) that we have pick up from the whole process, and also two steps of temporal rescaled sub-domains of the series B. Figure 3 show, in graphic terms, the local self-similar behavior of the sedimentation process.

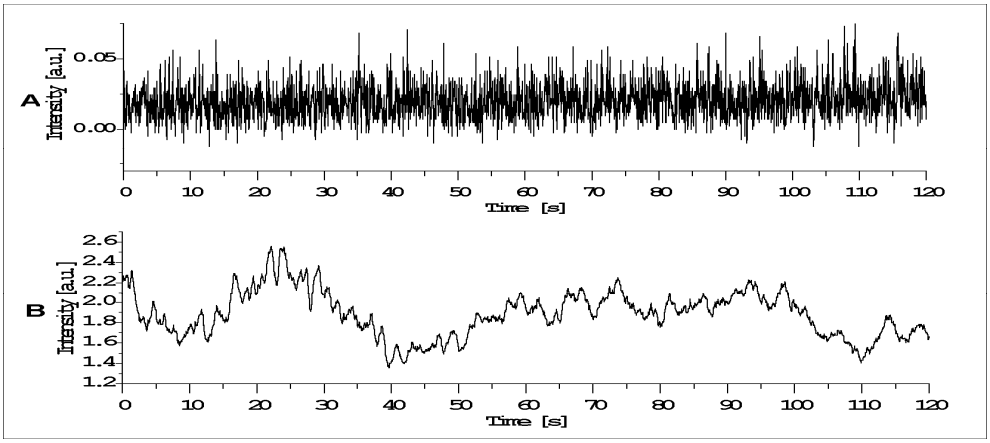

Figure 2 The fluctuation of the scattered light intensity for two short temporal domains pick up from the entire erythrocytes sedimentation process

A **second** important property, present only for local domains, is the stationarity of the fluctuation of the scattered light intensity.

The parameter that is usualy computed in the literature for stationary time series with self-similar behaviours is the scaling exponent (self-similarity parameter). The scaling exponent **α** characterize the power law dependence of the fluctuation standard deviation **s** on the domain length **n** (the number of data in the domain):

$$\alpha = \log(s) / \log(n)$$

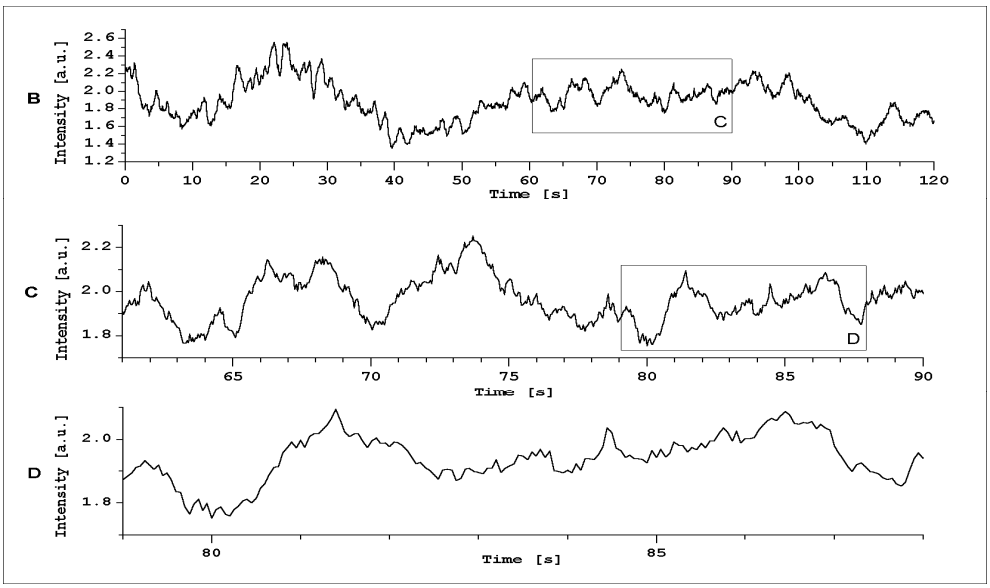

Figure 3: The intensity fluctuation of the scattered light for three self-similarity time series (B) original time series, (C) detail rescaled of time series B, (D) detail rescaled of time series C

Figure 4a show the three gaussian curves that were obtained by fitting the distributions of experimental data from the series B, C and D. The standard deviations of the probability densities increases with the number of the data in each of the three series with a power dependence (Figure 4b - linear behaviour in a log – log plot).

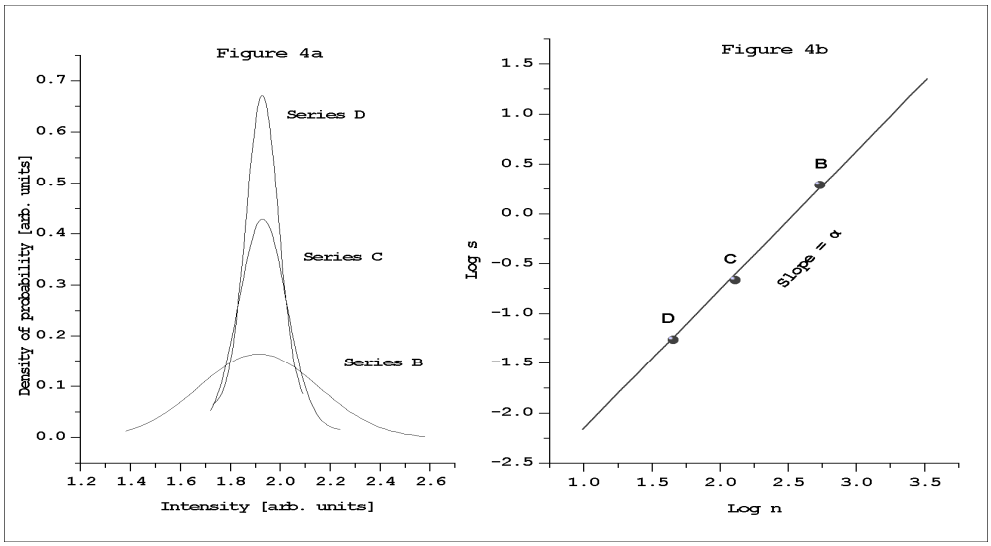

Figure 4: Scaling properties of the scattered light intensity

The stationarity is lost for such a long and complex process such as the erythrocyte sedimentation. To describe the scaling properties of nonstationary processes the algorithm usually used by the research teams, working in the field is the Detrended Fluctuation Analysis (DFA).

The complexity of the sedimentation phenomenon introduces also important temporal correlations. Different types of correlations correspond to different values of the scaling exponent that consequently can be used as an indicator of the system behavior:

- $0 < \boldsymbol{\alpha} < 0.5$, power-law anti-correlations (large values are more likely to be followed by small values and vice versa);
- $\boldsymbol{\alpha} = 0.5$ completely uncorrelated systems (white noise - the value at one instant is independent by any previous values);
- $0.5 < \boldsymbol{\alpha} \leq 1$, long-range power-law correlations;
- $\boldsymbol{\alpha} > 1$ correlations exist but cease to be of a power-law form; $\boldsymbol{\alpha} = 1.5$ indicates brown noise.

The **third** important characteristic, is the variation of self-similarity parameter (the scaling exponent) during the sedimentation process. The temporal correlations are almost absent at the beginning of the process the corresponding scaling exponent being close to 0.5 and increase in 20 minutes to values as high as 1.5. This means that applying the DFA method on the entire temporal series we will obtain a sort of global value of the scaling exponent the detailed information on smaller temporal domains being lost. The local temporal correlations can be correctly described only if the original DFA method is modified in order to give local values of the scaling exponent.

To obtain local scaling exponents, two modified versions of the original DFA method was developed, each of them applying the DFA on successive shorter data domains. The difference between the two versions was that the first one use successive nonoverlapping domains of 10^3 data and the second allow the partial overlapping of the successive domains. The temporal evolution of the scattered light intensity and of the scaling exponents are given in Figures 5 and 6 for control samples (healthy donors with low ESR) and blood samples from sick donors (high ESR values), respectively.

The scattered light intensity has a fluctuating dynamics with a 'latent domain' in first part of curve followed by an relatively fast increase, a large maximum in the middle and a long tail decrease in the final part of the sedimentation process.

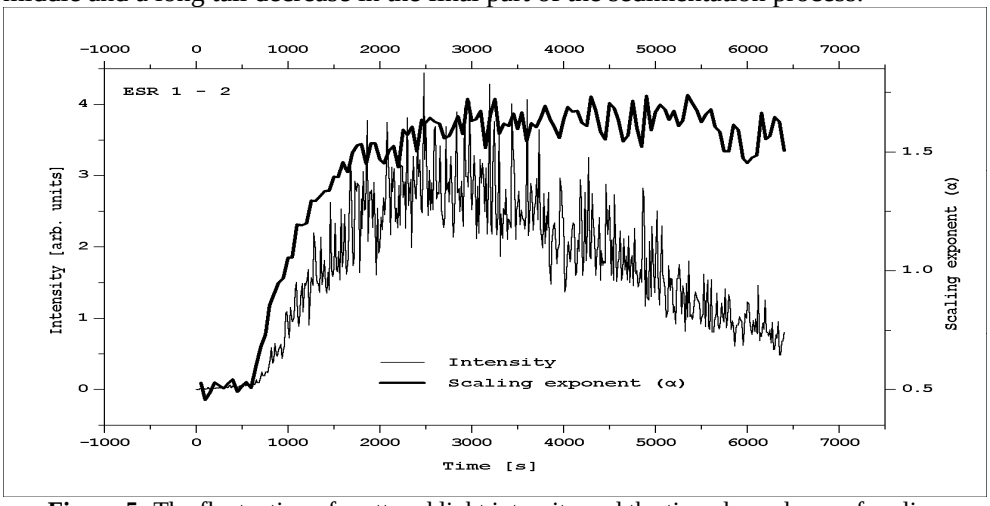

Figure 5: The fluctuation of scattered light intensity and the time dependence of scaling exponent during sedimentation process for healthy donor

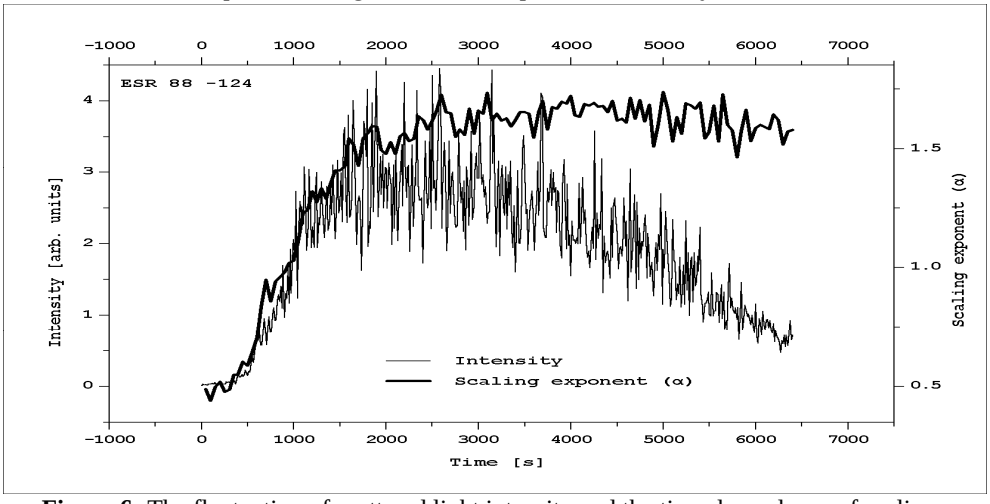

Figure 6: The fluctuation of scattered light intensity and the time dependence of scaling exponent during sedimentation process for sick donors

The temporal evolution of the scaling exponent has a similar behavior in the first part of the process. To the 'latent domain' corresponds completely uncorrelated fluctuation ($\boldsymbol{\alpha} \cong 0.5$). To the increase in the intensity of the scattered light corresponds a very quick increase in the scaling exponent from noncorrelations ($\boldsymbol{\alpha} \cong 0.5$) to strong correlation. ($\boldsymbol{\alpha} \cong 1.5$). The last zone indicates persistent of brown noise ($\boldsymbol{\alpha}$ is about 1.5) for the rest of process. The same behavior was observed for each sample without significant differences.

Differences between the two modified DFA versions was not significant and consist only in a higher resolution for the overlapping version.

CONCLUSIONS

The coherent light intensity scattered at small angles by a human erythrocyte suspension during the sedimentation process has a very complex dynamic behavior. In the present work we focus on the local characterization of temporal correlation using two modified versions of the DFA method. Each version gives a set of local scaling exponents for successive shorter data domains.

The sedimentation process begins with a random dynamics characterized by the absence of temporal correlation, and relatively fast switch to a strongly correlated dynamics. The method gives similar results for healthy and sick donors. In our opinion the complexity of the process needs a detailed analysis and certainly more parameters to improve the sensibility and the selectivity of these optical methods as potentially diagnosis procedures.

REFERENCES

1. Voeikov V., Kondakov S.E., Buravleva E., Kaganovsky I. and Reznikov M., "Computerized video-enhanced high temporal resolution of erythrocytes sedimentation rate (ESR-graphy) reveals complex dynamic and self-organizing proprieties of whole blood", In: *Optical Diagnostics of Biological Fluids V.* SPIE Proc. Priezzhev A.V., Asakura T., eds. San Jose, CA, Vol. 3923, pp. 32-43, 2000.
2. Peng C-K, Hausdorff JM, Goldberger AL., "Fractal mechanisms in neural control: Human heartbeat and gait dynamics in health and disease", In: *Nonlinear Dynamics, Self-Organization, and Biomedicine.* Walleczek J, ed. Cambridge: Cambridge University Press, 1999.
3. "Fractals in Science", Brude A. and Havlin S. Eds. Springer-Verlag Berlin Heidelberg, 1994.

STUDIA UNIVERSITATIS BABEŞ-BOLYAI, PHYSICA, SPECIAL ISSUE, 2001

CONTROL SYSTEM TO DELIMIT THE GRASSING AREA

ST.POPESCU, T.SIMPLĂCEANU, C.BINDEA

National Institute of Research and Development for Isotopic and Molecular Technology, PO Box 700, 3.400 Cluj-Napoca, Romania

1. General overview

As a direct outcome of the small and average farms for the breeding of the herbivorous animals, in limited groups (5-50 heads), it is necessary to do a controlled administration of the grassing areas.

The grassing land control requires:

a) The surface magnitude delimitation in ratio with the animals number.
b) The recurency rate of grassing, considering the grass regenerating on the exploited field.

2. The economic justification

For a efficient exploatation it is necessary a rational organization of the grassing surface. It can make same age groups, same weight groups, same purpose groups (for milk, for cutting), so on.

Different enclojures might be built for these animal groups.

High technical supervision is assured with no human asistace. Unlike the old metods of encosing a grassing surface, our proposed method is much more economical and simple from the point of view of the building materials.

The fence mode of wood loth and wickerwork is practically replaced by a only a metal wire suspended here and there on wood pillars.

The system is conceived in such a way as not to jepartize the animals health and life inside the enclosure.

The wathing system is based on the researches of electric field effects known from biofisics.

3. The system structure

There are two components

a) One high voltage pulses generator, mounted in a hermetic plastic box.
b) One metal wire fixed on wood pillars through ceramics isolators.

The entire assembly is shown in this picture:

Network sector and the box generator are found in a refuge, provided with a 220 V network To assure a better security a double grounding is required. The high voltage line can be one isoled cable. The high voltage enclosure must necessarily be a unisoleted wire.

The height of the pillars depend upon the animal rize (sheeps, caws).

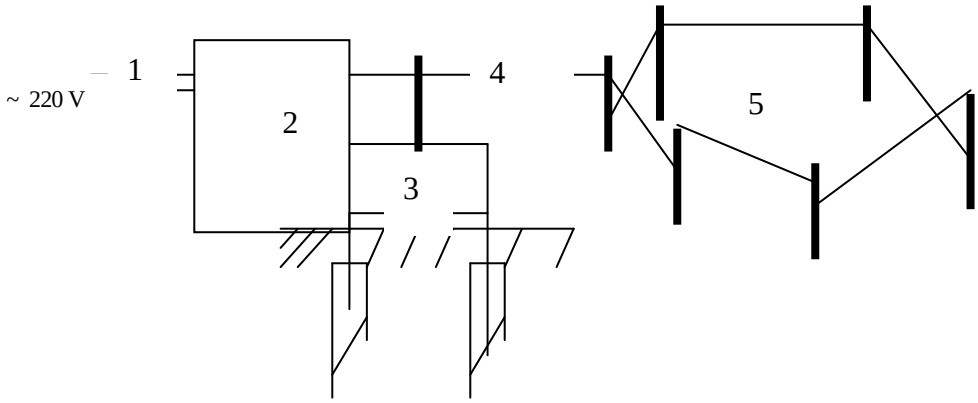

Network sector

1. High voltage pulse generator
2. Graunded shield
3. High voltage line
4. High voltage enclosure

4. Technical characteristics

- ♦ Pulse amplitude without charge: 8÷10kV
- ♦ Power absorption 7 ÷ 10W
- ♦ Enclasure length : max 5km
- ♦ Quality isolations toke two aspects:
  - the isolation between electronical devices and the wals of box
  - the isolation between electronical enclosure and the ground

5. Warnings

Precautions wich have to be taken into account while using the system:

a) Before toching any of the components of the system, the supply cable should be unpluged from the supply network.

b) The entire area should be marked with worning plates to keep people away from the zone.

STUDIA UNIVERSITATIS BABEŞ-BOLYAI, PHYSICA, SPECIAL ISSUE, 2001

SINGLE CRYSTAL GROWTH AND SOME PHYSICAL PROPERTIES OF $CeCl_3 \times 7\ H_2O$

CAMELIA NEAMȚU*, AL. DARABONT, GH. BORODI*, OANA RAITA***

**National Institute for Research and Development of Isotopic and Molecular Technologies, 65-103 Donath St., P.O.Box 700, RO-3400 Cluj-Napoca 5, Romania (e-mail: cneamtu@L30.itim-cj.ro)*
***"Babeş-Bolyai" University, Faculty of Physics, 1 M.Kogălniceanu St., Cluj-Napoca, Romania (e-mail: daal@physics.ubbcluj.ro)*

ABSTRACT. The paper describes the preparation of $CeCl_3 \times 7\ H_2O$ polycrystalline material and the growth of pure and Gd^{3+} doped single crystals of this type. The crystal structure was identified by X-ray diffraction methods. The absorption spectra in the UV, VIS and IR domains were studied. The EPR spectrum, consisting from the fine structure transition lines, was determined for the Gd^{3+} doped single crystals.

INTRODUCTION

Although the lanthanides were discovered for a long time, the lanthanide compounds are still not entirely characterized till now. The interaction of the 4f electrons of lanthanide ions with the host lattice is weak. Nevertheless, this interaction has a large influence on the optical and magnetic properties of lanthanide ions [1] and can be evidenced by EPR spectroscopy .

Because of these specific characteristics, the lanthanide halides hydrates and their related systems are a class of materials of potential interest [2]. From the large variety of possible compounds, we have chosen for our study $CeCl_3 \times 7\ H_2O$ (cerium chloride heptahydrate) which was less investigated, probably because this substance is highly hygroscopic and therefore is difficult to handle. The literature reports recent studies only of the dehydration process of some rare earth (Nd, Tb, Dy) chloride hydrates [3, 4] and rare earth chloride hydrates with organic inclusions [5, 6] and gives data on their dielectric properties [7].

The aim of the present paper is to study some physical properties of the $CeCl_3 \times 7\ H_2O$ single crystals by X-ray diffraction, UV-VIS and IR spectroscopy, and the influence of the first neighborhood on the EPR spectra of the gadolinium trivalent ion in Gd^{3+} doped $CeCl_3 \times 7\ H_2O$ single crystals.

EXPERIMENTAL

The $CeCl_3$ compound has two possible forms:

A. $CeCl_3$ without H_2O – it can be prepared in the following ways:

a) from cerium oxide and chloride:

$$2\ Ce_2O_3 + 6\ Cl_2 = 4\ CeCl_3 + 3O_2$$

b) from cerium oxide and carbontetrachloride:

$$2\ Ce_2O_3 + 3\ CCl_4 = 4\ CeCl_3 + 3\ CO_2$$

B. $CeCl_3$ hydrate – for the preparation of this compound, data from the literature indicates the two following possibilities:

a) from the solution obtained by the reaction of cerium hydroxide with hydrochloric acid:

$$Ce(OH)_3 + 3\ HCl = CeCl_3 + 3\ H_2O$$

b) from the solution obtained by the reaction of cerium carbonate with hydrochloric acid:

$$Ce_2(CO_3)_3 + 6\ HCl = 2CeCl_3 + 3\ H_2O + 3\ CO_2$$

A third possibility, not mentioned in the literature, is the preparation from the aqueous solution of CeF_3 and $BaCl_2$. We applied this method because we had CeF_3 available as starting material:

$$2\ CeF_3 + 3\ BaCl_2 = 2\ CeCl_3 + 3\ BaF_2 \downarrow$$

The major advantage of this method is that BaF_2 is insoluble in water, and can be separated by simple filtration from the solution. According to the above-mentioned reaction, we have obtained $CeCl_3$ hydrate in polycrystalline form.

$CeCl_3 \times 7\ H_2O$ is extremely soluble in water. This property allows both the purification and the preparation of the material from aqueous solutions. Therefore, after multiple recrystallization processes, we obtained a starting material for the single crystal growth without diamagnetic impurities. This fact was confirmed by EPR measurements.

RESULTS

The transparent, colorless single crystalline samples were obtained by slow evaporation of the $CeCl_3$ aqueous solution in approximately 2 to 3 weeks. One of these samples is shown in Figure 1. Up to the present, our experiments indicate that the crystal growing process can be accomplished at a temperature around 30^oC.

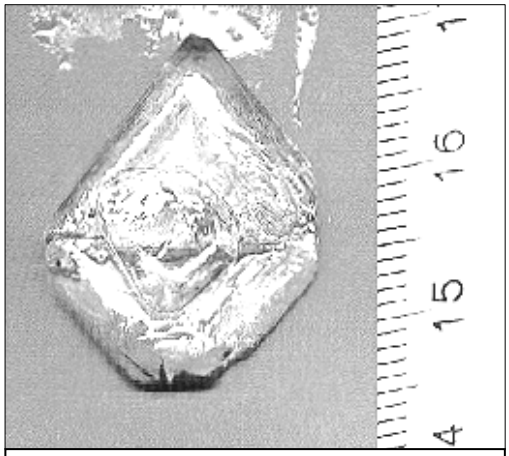

Figure 1. $CeCl_3 \times 7\ H_2O$ single crystal grown from solution

The Gd^{3+} doped samples were obtained in the same way when we added to the aqueous solution of $CeCl_3$ small quantities of $GdCl_3$ in a molar ratio of 1/500 (Gd^{3+}/Ce^{3+}).

In order to identify the exact structure of the single crystals obtained by us we effectuated X-Ray diffraction measurements on polycrystalline samples. The experimental X-ray powder pattern is presented in Figure 2.

These measurements have confirmed that the crystals contain indeed seven H_2O molecules. The single crystals have a monoclinic system and their space group is P1. Using these data, we generated the unit cell and the possible positions of the atoms in it (Figure 3).

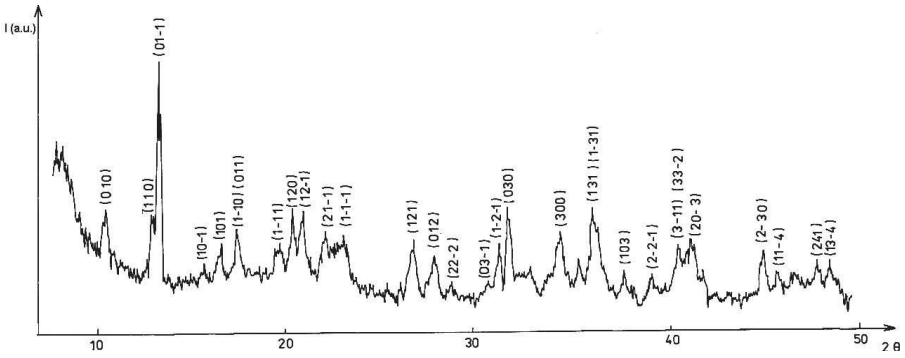

Figure 2. The X-ray diffraction powder pattern measured for polycrystalline $CeCl_3 \times 7\ H_2O$ samples

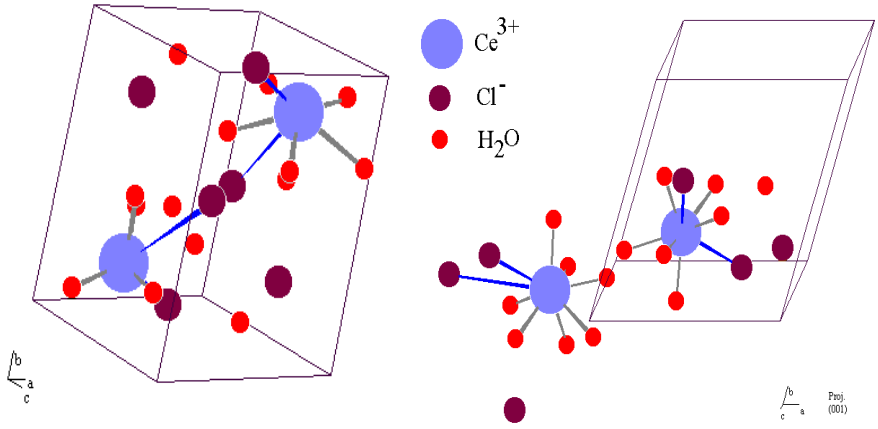

Figure 3. The unit cell (left) and the asymmetric unit (right) proposed for the $CeCl_3 \times 7\ H_2O$ single crystal

The UV-VIS and IR transmission spectra show that the $CeCl_3 \times 7\ H_2O$ single crystals prepared by us are not transparent in the UV, transparent in the VIS and partially transparent in the 400-1500 cm^{-1} range of the IR domain.

We have to mention that the investigated single crystalline samples were rather thick (2-3 mm), so the results are not very conclusive. Further measurements are in progress.

The EPR spectrum of Gd^{3+} doped $CeCl_3 \times 7\ H_2O$ single crystals has been measured with an X-band Radiopan SE/X - 2453 spectrometer at room temperature (Figure 4).

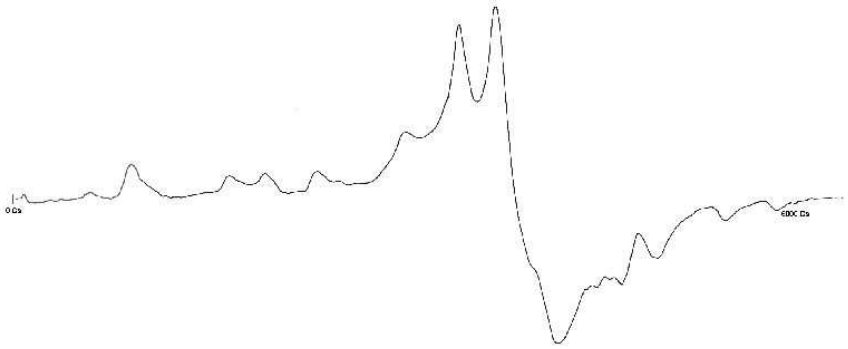

Figure 4. The EPR spectrum of the Gd^{3+} ion in the $CeCl_3 \times 7\ H_2O$ diamagnetic base at an arbitrary orientation of the external magnetic field

From the preliminary analysis of the spectra, we consider that the symmetry of the magnetic complex is lower then axial. The EPR spectra is described by the following spin Hamiltonian that can be expressed in the standard notation [8]:

$$\hat{H} = \beta \vec{H} \cdot g \cdot \vec{S} + \sum_{l=2,4,6} B_l^m O_l^m; \quad 0 \le m\,(even) \le l$$

After preliminary investigations, we consider that there are two magnetically equivalent centers in the unit cell - if we consider only the next nearest neighborhood of Ce^{3+} ions and if the Gd^{3+} ions occupy their sites. However, the symmetry axes of these magnetic centers are differently oriented.

CONCLUSIONS

We have obtained $CeCl_3$ heptahydrate single crystals of relatively large size using the growth method as described above. This fact was confirmed by X-ray diffraction measurements.

Based on the UV-VIS and IR absorption spectra, we can affirm that our samples may prove a good material for the visible domain. No transmission was observed in the UV domain. The IR absorption measurements carried out till now were not conclusive enough because the single crystalline samples were too thick. Investigations with the polycrystalline base material included in KBr pellets were not made.

The preliminary analysis of the EPR spectra confirmed the presence of two magnetic centers with differently oriented symmetry axes. The thorough study and the exact determination of the spin-Hamiltonian parameters are in progress.

REFERENCES

1. J.C. Bünzli, N. André, M. Elhabiri, G. Muller, C. Piquet, J. Alloys and Compounds 303-304, 409 (2000)
2. G. Meyer, J. Alloys and Compounds 303-304, 66 (2000)
3. J. Sundstrom, V.H. Vu, Thermochimica Acta 306 (1-2), 13 (1997)
4. V.H. Vu, J. Sundstrom, Thermochimica Acta 307 (1), 37 (1997)
5. L.G. Hubert-Pfalzgraf, L. Machado, J. Vaissermann, Polyhedron 15 (3), 545 (1996)
6. W.Y. Xu, J.W. Zhen, R.L. Jian, R.Fei, L.G. Sheng, Thermochimica Acta 311 (1-2), 29 (1998)
7. "High Frequency Properties of Dielectric Crystals – Nonlinear Dielectric Susceptibilities", Landolt-Börnstein – Condensed Matter III/30B, 433-485 (2000)
8. A. Abragam, B. Bleaney, "Electron Paramagnetic Resonance of Transition Ions", Clarendon, Oxford (1970)

STUDY OF MAGNETIC PROPERTIES OF $5Fe_2O_3 \cdot 3Gd_2O_3$ MICRO AND NANOPARTICLES

ILIOARA COROIU[1], Al. DARABONT[2], M. BOGDAN[3], E. CULEA[1]

[1]*Technical University, 3400 Cluj-Napoca, Romania*
[2]*Babes-Bolyai University, 3400 Cluj-Napoca, Romania*
[3]*National Institute for Research and Development of Isotopic and Molecular Technology, P.O. Box 700, 3400 Cluj-Napoca, Romania*

ABSTRACT. $5Fe_2O_3 \cdot 3Gd_2O_3$ micropowder and $5Fe_2O_3 \cdot 3Gd_2O_3$–dextran nanoparticles were prepared and studied by magnetic susceptibility and nuclear magnetic resonance measurements. Magnetic susceptibility data suggest the presence of antiferromagnetic interactions between the magnetic ions (Fe^{+3}, Fe^{+2} and Gd^{+3}) of the samples. These interactions are stronger for the micropowder sample. The relaxivities are almost the same but the R_1 relaxivity of the nanoparticles is higher than that of the micropowder sample. The decrease of the particles size in the $5Fe_2O_3 \cdot 3Gd_2O_3$–dextran to nanometer range determines modifications of their magnetic properties.

INTRODUCTION

In the last years the study of the nanoparticles have received increasing attention. Altered electrical, magnetical, electrooptical and chemical properties accompany reducing of particle size to nanometer range. These special properties are caused by the changes of band structure with quantum – size effect [1].

In this paper we studied the magnetic properties of $5Fe_2O_3 \cdot 3Gd_2O_3$ micropowder and $5Fe_2O_3 \cdot 3Gd_2O_3$–dextran nanoparticles by magnetic susceptibility and nuclear magnetic resonance measurements.

EXPERIMENTAL

Synthesis of $5Fe_2O_3 \cdot 3Gd_2O_3$ microparticles was made in the following way: to iron oxide and gadolinium oxide taken in ratio $3Gd_2O_3$: $5Fe_2O_3$ methanol was added and the suspension was stirred about 6h with a magnetic agitator. The homogeneous mixture was dried for 5h at 105°C. Furthermore, the mixture was calcined for more than 2h at 1200°C in air atmosphere and then transformed into micropowder [2]. The size of the $5Fe_2O_3$ $3Gd_2O_3$ micropowder was about $2\text{-}10 \cdot 10^{-2}$ μm. The particles size was determined by width of the peaks from X-ray diffraction spectrum. X-ray diffraction analyses were performed on a DRON3 diffractometer using CuK_α radiation.

The $5Fe_2O_3 \cdot 3Gd_2O_3$–dextran nanoparticles were prepared by microemulsion method using a water and toluene system. The starting materials $FeCl_3/GdCl_3$ in molar ratio of 5:3 were converted to the corresponding oxides by treating then in a system of 420ml of water and 120ml of toluene on a water bath for about 10-12 hours. We used oxides/dextran molar ratio of 1:1. The molecular weight of dextran was 40000. We appreciated that the median diameter of the dextran-stabilized particles was distributed between 800Å and 1200Å, whereas the ($5Fe_2O_3 \cdot 3Gd_2O_3$) core mean diameters were about 35-45Å.

The source of $Fe_2O_3 \cdot$ and Gd_2O_3 (99.9% purity) was E. Merck, Darmstadt.

Magnetic susceptibility measurements were performed on a Faraday type balance in the temperature range 80-300K.

Measurements of the longitudinal and transverse relaxation rates T_1^{-1} and T_2^{-1} respectively, of dextran coated nanoparticles have been carried out on ^1H in aqueous solutions as a function of molar concentrations, while the water-insoluble micropowder was maintained in carboxymethylcellulose solutions. All measurements have been made at room temperature (about 25°C) at a proton Larmor frequency ν_0 = 90MHz.

The pulsed NMR spectrometer utilized was a commercial Bruker SXP4/100 spectrometer. Transverse relaxation rates were measured using the Carr-Purcell method, while longitudinal relaxation rates measurements using the inversion recovery pulse sequence, 180°-τ-90°. All data exhibited single – exponential behavior.

The $T_{1,2}^{-1}$ values were obtained by fitting experimental data with the expression

$$Y_i(t_i) = A + B\exp(-t_i / T_{1,2}) \quad (1)$$

t_i being the times at which the magnetization values Y_i was measured. The fitting error was about 1% and the accuracy for the longitudinal rates was about 2-3% while the accuracy for the transverse relaxation rates was about 5-7%.

R_1 and R_2 relaxivities, in $mM^{-1}s^{-1}$ were obtained from the least-squares determination of the slopes of plots $1/ T_{1,2}$ versus molar concentration of the compound, using at least five independent measurements at several concentration between 0 and 2mM.

RESULTS AND DISCUSSION

Figure 1 shows the dependence of the inverse magnetic susceptibility as a function of temperature for the $5Fe_2O_3{\cdot}3Gd_2O_3$–dextran nanoparticles and also for the $5Fe_2O_3{\cdot}3Gd_2O_3$ micropowder. The data collapse to straight lines indicating that the magnetic susceptibility follows a Curie-Weiss type behavior.

$$\chi^{-1} = (T - \theta_p) / C \quad (2)$$

where C is the Curie constant and θ_p is the paramagnetic Curie temperature. The solid lines in Figure 1 represents the computer fit of experimental data according to Eq. (2). These plots permitted to derive the two important magnetic parameters namely θ_p and C_m (the molar Curie constant). The values obtained for these constant are θ_p= -40K, C_m=103.68emu·K/mole for $5Fe_2O_3{\cdot}3Gd_2O_3$–dextran nanoparticles and θ_p= -52K, C_m=66.74emu·K/mole for $5Fe_2O_3{\cdot}3Gd_2O_3$ micropowder. The paramagnetic Curie temperature θ_p is a rough indicator of magnetic interaction between the iron and gadolinium ions (Fe^{+3}, Fe^{+2} and Gd^{+3}). The negative values obtained for θ_p suggest that the interaction between the magnetic ions is antiferromagnetic and its intensity is higher for the micropowder sample.

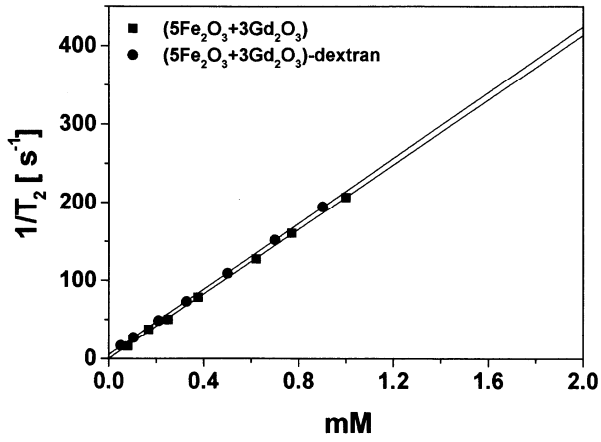

Fig.3. ***Proton transverse relaxation rates as a function of particle concentration***

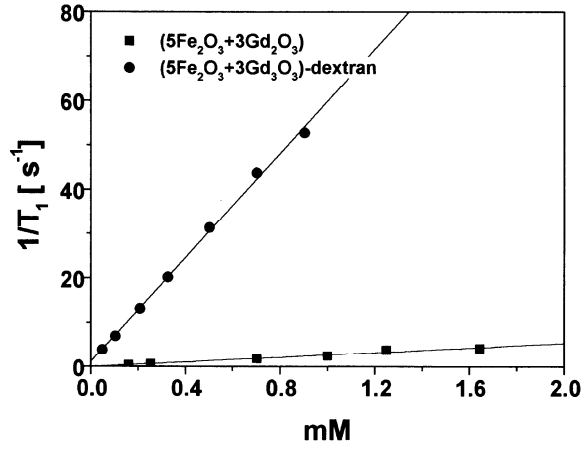

Fig. 2. ***Proton longitudinal relaxation rates as a function of particle concentration***

The measured R_1 and R_2 relaxivities of nanoparticles and micropowder studied in aqueous and carboximethylcellulose solutions are shown in table 1. For purpose of comparison the R_1 and R_2 relaxivities of magnetite and SPIOs (the commercial magnetite coated in dextran) are shown too.

Table 1.

R_1 and R_2 relaxivities for the studied particles

Compound	$R_1(mM^{-1}s^{-1})$	$R_2(mM^{-1}s^{-1})$	R_2/R_1
$5Fe_2O_3 \cdot 3Gd_2O_3$	2.54	207.83	81.82
$5Fe_2O_3 \cdot 3Gd_2O_3$ – dextran	61.78	201.4	3.26
Magnetite [3]	3.02	55.29	18.31
SPIOs [4]	30	100	3.33

The proton relaxation rates (Figures 2 and 3) are linearly dependent on concentration of compounds. This certifies the absence of solute – solute interaction [5].

The relaxation rate increase produced by magnetic particles is a contribution of several complex mechanisms. The size and the composition of these particles represent the essential parameters. The particles possess very large magnetic moments in the presence of a static magnetic field. Dipolar interactions between the magnetic cores and surrounding solvent protons results in increasing both longitudinal and transverse relaxation rates, especially for nanoparticles (below 100Å). Smaller particles are adequately described by the microscopic outersphere theory [6] which predicts that the transverse relaxivity R_2 of water will increase with the radius of the particle, whereas the longitudinal relaxivity R_1, will first increase then reach a maximum for $\omega_I\tau_R \approx 1$ and finally decrease. ω_I is the proton Larmor frequency and τ_R is the time required for a water molecule to diffuse over a distance equal with radius of the particle. Due to the small dimension of the magnetic core, iron oxide – gadolinium oxide –dextran nanoparticles and also SPIOs have higher values for R_1 and consequently lower values for the ratios R_2/R_1.

The susceptibility difference between the particles and the surrounding medium generates strong magnetic field gradients, particularly around the periphery of each inclusion. Diffusion of protons leads to an irreversible dephasing of the transverse magnetization that cannot be completely rephased by application of a 180° radio-frequency pulse. Thus in a Carr-Purcell (90 - τ -180) sequence, where τ is the spacing between the 90° and 180° pulse, the estimated transverse relaxation rate is considerably increased. The magnetized particles with large size domains (up to 100 Å) affect T_2 more that T_1. For this case the mechanism of action can be related more to diffusion-induced magnetic field gradients than to dipole-dipole interactions.

CONCLUSIONS

$5Fe_2O_3 \cdot 3Gd_2O_3$ micropowder and $5Fe_2O_3 \cdot 3Gd_2O_3$–dextran nanoparticles were prepared and their magnetic susceptibilities and R_1 and R_2 relaxivities were measured. Magnetic susceptibility data suggest the presence of antiferromagnetic interactions between the magnetic ions (Fe^{+3}, Fe^{+2} and Gd^{+3}) of the samples, these interactions being stronger for the micropowder sample. The increase or decrease of R_1 and R_2 relaxivities depends on the number of factors as compound mass, size and composition, and is the combined result of more than one type of relaxation processes.

REFERENCES

[1] Y. Wang, N. Herron, J.Phys.Chem., 95, 525 (1991)

[2] I. Coroiu, Al. Darabont, M.Bogdan, D.E. Demco, Rom.J.Biophys., 7, 103 (1997)

[3] P.F. Renshaw, C.S. Owen, A.C. Mc.Laughlin, T.C. Frey, J.S. Leigh Jr., Mag.Reson.Med., 3, 217 (1986)

[4] D.E. Canet, D.Revel, R.Forrat, G. Baldy-Porcher, M. De Lorgeril, L. Sebbag, J.P. Vallee, D. Didier, M.Amiel, Magn.Res.Imaging, 11, 1139 (1993)

[5] K. Marcus, in: Ion Solvation, chap.5, Wiley Chichester, U.K., 1985

[6] R.N. Muller, P. Gillis, F. Moiny, A. Roch, Magn.Reson.Med., 22, 178 (1991)